UAB
Universitat Autònoma de Barcelona

Synthesis and device integration of two-dimensional MOCVD MoS₂ films

Christian Martin Schäfer

A thesis submitted for the degree of
Doctor of Philosophy

PhD program in Materials Science
Autonomous University of Barcelona

Supervisor: Prof. Dr. Jose Antonio Garrido Ariza

Tutor: Prof. Dr. Jordi Sort Viñas

Catalan Institute of Nanoscience and Nanotechnology (ICN2)

Barcelona, February 2023

"What could we do with layered structures with just the right layers? What would the properties of materials be if we could really arrange the atoms the way we want them? They would be very interesting to investigate theoretically. I can't see exactly what would happen, but I can hardly doubt that when we have some control of the arrangement of things on a small scale we will get an enormously greater range of possible properties that substances can have, and of different things that we can do."

There's Plenty of Room at the Bottom, 1959

— **RICHARD P. FEYNMAN**

Acknowledgements

Abstract

Two-dimensional (2D) layered transition-metal dichalcogenides, such as MoS_2, possess a unique combination of electronic and mechanical properties making them appealing materials for atomically-thin transistors and flexible electronics. However, the implementation of MoS_2 thin films on industrially relevant large areas faces manifold manufacturing challenges, heavily relying on the development of scalable, industry-compatible synthesis and integration processes to reach target applications.

This work investigates metal-organic chemical vapor deposition (MOCVD) as a promising and technologically relevant method for the large-scale synthesis of MoS_2 thin films. MoS_2 films were grown from molybdenum hexacarbonyl and organosulfide precursors on commercial, insulating substrates, such as silicon oxide, glass and sapphire. To gain fundamental understanding of the MOCVD process and to optimize the growth of high-quality MoS_2 thin films, a comprehensive growth parameter study coupled with microscopic and spectroscopic film characterization was conducted. A particular focus was given to understanding the underlying mechanisms and mitigation of carbon incorporation that may arise from the use of organic precursor chemistry and that may affect the morphological and (opto)electronic film properties. Furthermore, the study explored strategies to minimize grain boundary defects in polycrystalline films by enhancing grain size and by growing substrate-aligned MoS_2 films on crystalline sapphire substrates via van der Waals heteroepitaxy. For the latter, the impact of sapphire surface preparation and growth conditions on the orientation-selective domain epitaxy was studied. A framework of microscopic and grazing incidence surface diffraction techniques was established to assess film quality in terms of epitaxial relationship and in-plane mosaic spread, working towards the goal of single-crystalline MoS_2 thin films.

The device integration and fabrication of a MoS_2 field effect transistor (FET) technology was developed, including residue-reduced layer transfer, oxide encapsulation by a seed layer strategy and wafer-level batch process. Along the fabrication flow, microscopic and spectroscopic film analyses were performed from as-grown to fully

integrated MoS$_2$ thin films up to the final electrical characterization of FET devices. The reduction of interface trap densities was identified as a central challenge for interface engineering. Moreover, MoS$_2$ films with different grain sizes obtained during thin film growth optimization were benchmarked, highlighting the importance of reducing channel defects for improving the film transport properties. Several generations of FET devices were fabricated spanning from simple liquid-gate to fully oxide-encapsulated solid-gate architectures, including the successful translation from rigid silicon wafers to flexible polyimide substrates. To this end, as the target application, neural interface electrocorticography (ECoG) probes were developed. First prototypes of these ECoG devices made use of active MoS$_2$ FETs serving as monolithically integrated, serial switches to graphene-based neural sensor pixels in a 1×8 matrix arrangement. The addressing and multiplexing capability of MoS$_2$-FET arrays in ECoG devices was demonstrated *in vitro* as a proof-of-concept. This is a significant step towards the development of a flexible, high-density neural interface technology based on 2D materials.

Thesis framework

This dissertation has been prepared within the Doctoral program in Materials Science of the Autonomous University of Barcelona (UAB).

The presented work is part of the collaborative *BrainCom* and Graphene Flagship *Core 3* projects, funded by the Horizon 2020 program of the European Commission. Within this frame, it is aimed at the development of a new generation of flexible, neuroprosthetic devices for large-scale and high-density recording and stimulation of brain activity, using novel technologies based on two-dimensional materials, such as graphene and MoS_2.

The main body of experimentation was carried out in the Advanced Electronic Materials and Devices laboratory led by Prof. Jose A. Garrido at the Catalan Institute of Nanoscience and Nanotechnology (ICN2), and taking advantage of ICN2's associated research support units with facilities for nanomaterials growth, electron microscopy, photoemission spectroscopy, X-ray diffraction, and nanofabrication. Additionally, some of the device fabrication was carried out at the clean room facility of the Institute of Microelectronics of Barcelona (CNM-IMB, CSIC).

Experiments concerning the epitaxial growth of MoS_2 thin films have been performed during a research stay at Yonsei University (Seoul, South Korea), with acknowledged funding from ICN2's Severo Ochoa Mobility program, and in close collaboration with the Flexible Electronics and Devices Group led by Prof. Jong-Hyun Ahn.

Epitaxial MoS_2 thin films were further analyzed during a synchrotron experiment at the French CRG surface and interfaces beamline BM32 at the European Synchrotron Radiation Facility (ESRF) in Grenoble, in which the author was the main proposer.

Contents

List of figures

List of tables

Nomenclature

Acronyms / Abbreviations

2D   Two-dimensional

3D   Three-dimensional

AFM   Atomic force microscopy

ALD   Atomic layer deposition

BDE   Bond dissociation energy

BSE   Back-scattered electrons

BTBMMo Bis(t-butylimido)bis(dimethylamino)molybdenum(VI)

CB   Conduction band

CMOS Complementary metal-oxide-semiconductor

CNP   Charge neutrality point

CVD   Chemical vapor deposition

CVT   Chemical vapor transport

DEDS Diethyl disulfide

DES   Diethyl sulfide

DFT   Density functional theory

DLI   Direct liquid injection

DMDS Dimethyl disulfide

DMS Dimethyl sulfide

DTBS Di-*tert*-butyl sulfide

ECoG Electrocorticography

EDL Electric double layer

EDX Energy-dispersive X-ray spectroscopy

EEG Electroencephalography

EELS Electron energy loss spectroscopy

ESRF European Synchrotron Radiation Facility

FE Field emission

BEOL Back-end of line

FEOL Front-end of line

FET Field-effect transistor

FIB Focused ion beam

FWHM Full-width-at-half-maximum

GIXRD Grazing incidence X-ray diffraction

GL Gaussian-Lorentzian

Gr Graphene

HAADF High-angular annual dark field

HER Hydrogen evolution reaction

HRTEM High-resolution transmission electron Microscopy

ICN2 Catalan Institute of Nanoscience and Nanotechnology

ICP-RIE Inductively-coupled plasma reactive ion etching

IP Ionization potential

IRDS International Roadmap for Devices and Systems

IT   Interface trap

MBE   Molecular beam epitaxy

MFC   Mass flow controller

MHC   Molybdenum hexacarbonyl

MIM   Metal-insulator-metal

MISM   Metal-insulator-semiconductor-metal

MOCVD Metal-organic chemical vapor deposition

MOMBE Metal-organic molecular beam epitaxy

PBS   Phosphate buffered saline

PCB   Printed circuit board

PDMS   Polydimethylsiloxane

PI   Polyimide

PLD   Pulsed laser deposition

PL   Photoluminescence

PMMA Poly(methyl methacrylate)

PVD   Physical vapor deposition

RGA   Residual gas analyzer

RHEED Reflection high-energy electron diffraction

RMS   Root-mean-square

RSF   Relative sensitivity factor

SEM   Scanning electron microscopy

SE   Secondary electrons

SGFET Solution-gated field-effect transistor

SOC   Spin-orbit coupling

SS   Subthreshold slope

STEM   Scanning transmission electron microscopy

TEM   Transmission electron microscopy

TFT   Thin film transistor matrix

TMAH   Tetramethylammonium hydroxide

TMA   Trimethylaluminium

TMD   Transition-metal dichalcogenide

TRT   Thermal release tape

UHV   Ultra-high vacuum

UPS   Ultra-violet photoelectron spectroscopy

UV   Ultra-violet

VB   Valence band

vdW   van der Waals

XPS   X-ray photoelectron spectroscopy

XRR   X-ray reflectometry

ZA   Zone axis

ZIF   Zero insertion force

Chapter 1

Introduction & Motivation

1.1   2D materials: A diverse and thriving research field

Two-dimensional (2D) materials are a class of atomically-thin, sheet-like crystalline solids with strong in-plane intralayer covalent bonds and weak out-of-plane interlayer van der Waals (vdW) bonds, also referred to as "van der Waals materials". Owing to their structure, density function theory calculations have found more than 1000 types of "easily exfoliable", layered materials from their over 100 000 experimentally known 3D-layered, bulk parents [1]. Among them, almost all conduction types are represented, including metals, semi-metals, semiconductors, insulators, topological insulators, and superconductors, forming a broad material family [2], as shown in Fig. 1.1a.

Thanks to their reduced dimensionality and ultra-thin nature with extreme surface-to-volume ratio, 2D materials exhibit a unique combination of electrical, optical, chemical, and mechanical properties; for this reason, they have been widely investigated by both fundamental and application-oriented research communities in recent years. They do not only provide a platform for basic understanding of condensed matter and quantum confinement phenomena in the single- and few-layer limit, such as "exotic" physics in spin- [3], valley- [4], and twistronics [5], but have also shown high potential for practical applications in multidisciplinary fields like (opto)electronics [6], photonics [7], catalysis [8], chemical sensing [9], neuromorphic computing [10, 11], and neuroscience [12, 13].
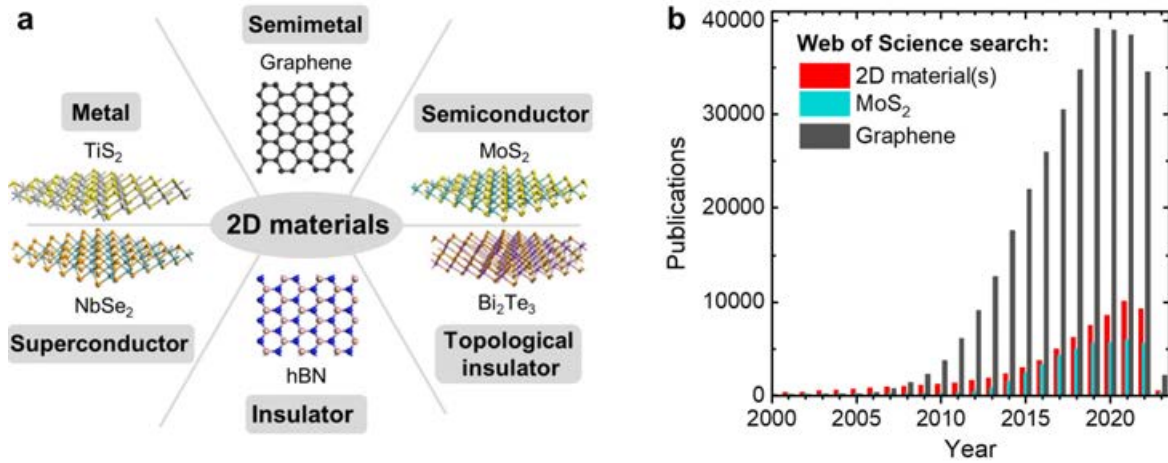
Figure 1.1 2D materials family and research interest. **(a)** Classes of 2D materials by conduction type with specific material examples. Adapted from Li et al. [2]. © 2017 Author(s). Published by AIP Publishing.**(b)** Number of publications per year found for keyword searches on the literature data base *Web of Science.*

The tremendous surge in interest over the last two decades is illustrated by the largely increasing number of publications per year shown in Fig. 1.1b, which refers to a literature search on the data base *Web of Science* using the exemplary keywords "2D material(s)", "graphene" and "MoS$_2$".[1] While the literature statistics document the rapid advancements of the topic, the trend also suggests a saturation after year 2020. This may be interpreted as a sign of the field reaching its research and funding limits and entering into a new phase of commercialization and implementation. Therein, more focus is given to realizing practical and profitable applications thriving from the research rather than continuing to publish academic papers.

1.2 Opportunities and challenges of 2D materials for next-generation electronics

The unique set of material properties makes 2D materials especially promising for advanced and versatile electronic applications. As illustrated in Fig. 1.2, this can be discussed in terms of the "More Moore" and "More than Moore" paradigms [14], which have served as guiding principles for the continued evolution of the microelectronics industry and the development of new technologies and devices.

---

[1]https://www.webofscience.com, accessed on 31 january 2023. A search after "topic" was performed, including titles, abstracts and author keywords.

"More Moore" refers to the classical transistor scaling approach in complex integrated circuits seen over the last decades [14]. According to Moore's Law, the number of transistors in microchips doubles approximately every two years. The "More Moore" strategy focuses on performance improvements and miniaturization based on increased transistor densities by continued feature size shrinking in traditional Si-based complementary metal-oxide-semiconductors (CMOS). However, this approach is reaching ultimate physical limits, where device performance becomes dominated and deteriorated by so called short-channel effects [15]. These concerns have been addressed by geometrical design considerations in sub-14 nm technology nodes, such as non-planar FinFET architectures [16]. However, sub-5 nm Si devices suffer serious mobility degradation through increased scattering events [17]. In this context, replacing bulk Si through alternative, sub-1nm-thin 2D semiconductors provides superior channel performance in the atomic limit and has been considered a plausible solution on the beyond-CMOS roadmap [16, 17]. In 2010, Kis and coworkers demonstrated the first 2D single-layer transistor based on bulk exfoliated MoS_2 [18], a semiconductor with a direct bandgap of 1.8 eV. For this proof-of-concept device, a field-effect charge carrier mobility of 217 $cm^2 V^{-1} s^{-1}$ (although the latter value was later downcorrected to 15 $cm^2 V^{-1} s^{-1}$ [19]) and remarkable on/off current ratio of $> 10^8$ was reported, demonstrating its suitability for logic circuitry with enhanced electrostatic control and low power dissipation. In 2016, Eric Pop's research group demonstrated scaled MoS_2 transistors with 10 nm gate length approaching ballistic transport with on-currents $>400 \mu A \mu m^{-1}$ and near-ideal subthreshold slope down to 80 $mV dec^{-1}$ [20]. In 2019, imec, one of Europe's leading micro-and nanoelectronics research centers, followed with 30 nm gate length MoS_2 transistors with oxide dielectric thickness scaled down to 4 nm, showing on/off ratios of $> 10^8$, and subthreshold swing of 90 $mV dec^{-1}$. In 2022, the world's largest semiconductor manufacturer TSMC presented the first gate-all-around MoS_2 nanosheet transistor with 40 nm gate length with high on-current density of $\sim 410 \mu A \mu m^{-1}$, high on/off ratio $> 10^8$ and nearly zero drain-induced barrier lowering [21]. These collective efforts of research and industry give reason to be optimistic about the potential of 2D semiconductors to keep Moore's law alive [16].

"More than Moore" seeks to improve device performance beyond the traditional CMOS scaling and has become an integral part of the International Roadmap for Devices and Systems (IRDS) [22]. Determined by application-specific requirements, the goal is to add new functionalities to integrated circuits that complement traditional Si-based devices by smart systems, new architectures and materials [14, 23]. For the latter, the 2D materials family offers many opportunities for functional, on-chip diver-

sification. Their ready "stackability" without lattice matching constraints, compared to conventional 3D bulk materials, facilitates their heterogeneous integration [24], such as for logic, high-speed communication [25], sensors, energy harvesting, and flexible, transparent devices. The (opto)electronic properties, in particular of the semi-metal graphene, may be exploited for CMOS-compatible, high frequency THz devices [26], high data transmission photonic waveguides [27], high responsivity photo-detection [28] and modulation [29]. The various 2D semiconductors offer bandgaps interesting for applications over a wide optical spectrum [30, 31, 32] and for logic operation [18]. Furthermore, the inherently large surface-to-volume ratio enables high sensitivity for
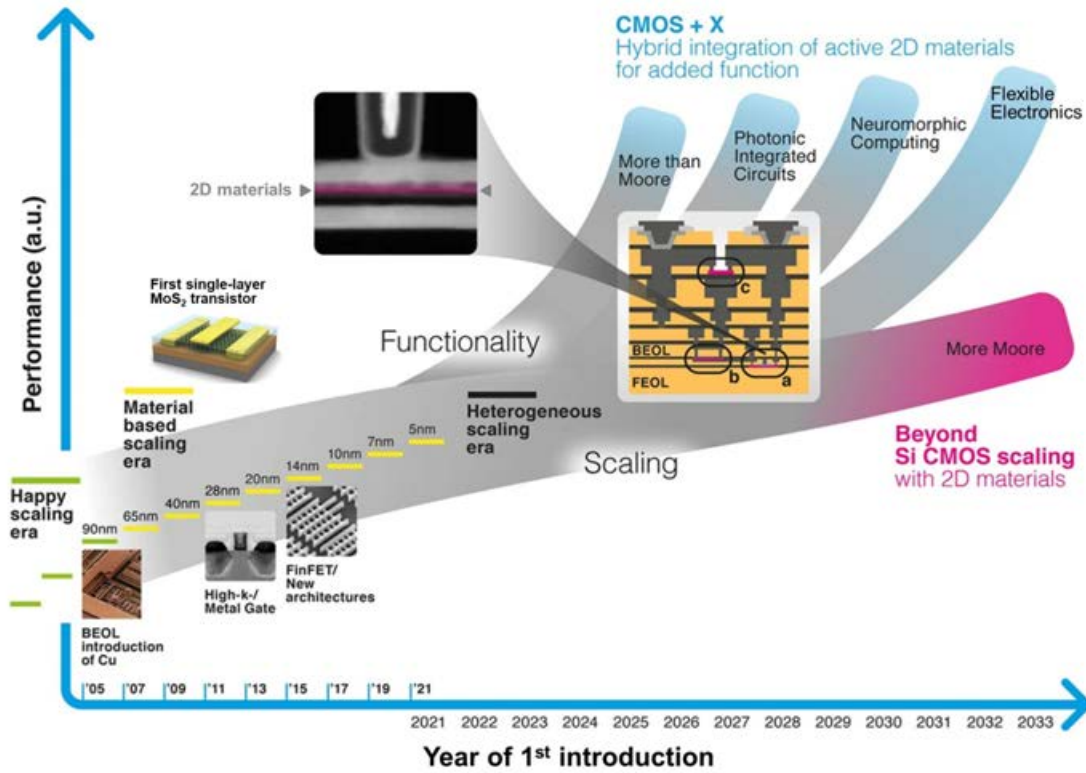
Figure 1.2 Opportunities of 2D materials for next-generation electronics in the context of "More Moore" scaling and "More than Moore" functional diversification. On the one hand, 2D material provide an alternative beyond bulk Si CMOS to enable continued miniaturization (feature size shrinking, higher device density), such as by nanosheet transistors. On the other hand, their heterogeneous integration may provide an "X-factor" for application-specific, CMOS-complementary hybrid functionalities, data transmission and novel processing capabilities (sensors, photonic circuits, in-memory neuromorphic computing, flexible electronics). Therefore, 2D materials may improve device performance determined by many combined factors in the heterogeneous scaling era (power consumption and efficiency, high-speed communication, capability to perform pattern recognition, multi-functional sensors, conformable devices etc.). Adapted from [14]. © 2022 by the Author(s) under creative commons license.

chemical sensing of gas- or biomolecules and electrical sensing of charge potentials in vicinity to 2D surfaces [9, 12], which may be selectively tuned by defect engineering and functionalization [33]. Moreover, the unique mechanical properties make 2D materials appealing for micro- and nanoelectromechanical systems [34], where movable, suspended 2D membranes provide high sensitivity and efficient signal transduction in oscillators, accelerometers, pressure sensors and gas sensors among others [34]. 2D materials have been also considered for brain-inspired neuromorphic computing approaches going beyond classical von-Neumann integrated circuit architecture [10]. This involves merging the processing and memory units at the hardware level of integrated 2D memristive systems [35], allowing for faster and highly energy-efficient data processing in the future [36, 11]. Notably, the high tensile strength/strain and their bendability [37] could make 2D materials excellent candidates for variants of above mentioned applications in flexible electronic circuitry and wearable applications [38, 39, 40, 41, 42]. For instance, this could enable novel technologies with disruptive potential in the field of bioelectronics, such as for 2D material based brain-computer interfaces, where shape conformability with the cerebral tissue is desired [43]. This has been exploited in graphene-based flexible neural interface arrays for brain activity mapping [12, 13, 44].

However, there are several challenges that must be overcome to realize the full potential of 2D materials for their widespread implementation into electronic devices [45, 14, 17]. This implies a transition from "lab to fab"; a major bottleneck for this to happen is the currently low "manufacturing readiness level" [14] of wafer-scale 2D semiconductor technologies for front-end (FEOL) and back-end (BEOL) of line integration [46]. A critical goal is to establish the large-area synthesis of high crystalline quality thin films by an industry-compatible growth method, ideally, on commercially available wafer substrates. The growth method must fulfill stringent scalability, reliability and controllability criteria, for which metal-organic chemical vapor deposition (MOCVD) has shown to be one of the most promising approaches [47, 48]. However, despite being an established method for conventional compound semiconductor manufacturing and recent advances in the wafer-scale growth of pristine, electronic-grade 2D semiconductors [49], it is still challenging to comply with the strict semiconductor manufacturing standards. Importantly to say, a fundamental understanding of the complex growth behaviour and epitaxy of this novel class of vdW materials is still required. Furthermore, direct growth of high quality films is often constrained by thermal budgets, chemical process incompatibilities or template choice, which typically makes 2D layer transfer from the growth substrate to a target wafer necessary; yet, such transfer processes are

often manually performed in research laboratories [50]. Automatization of more reliable transfer methods with industry-compatible wafer processing tools are still under development [51, 52, 53], and achieving wrinkle-, damage-, and process residue-free transfer of atomically-thin sheets is not trivial [54]. Moreover, 2D materials are highly sensitive to their surroundings owing to their extreme surface-to-volume ratio. While the latter property may be desirable for sensing applications, it may be detrimental for electronic device applications, where channel defects, substrate roughness, charged impurities and dangling bonds may strongly alter electronic transport properties. Therefore, attention must be given to prevention or removal of fabrication residues [55], design of innovative fabrication flows [56], the processing conditions [57], material selection [58] and interface engineering to ensure clean, passivated van der Waals interfaces. In this context, research into scalable integration of conventional oxide dielectrics [59] and identifying (better) suited insulators [60, 61, 62] is of upmost importance to demonstrate hysteresis-free and high-performance devices with low variability [63, 64, 65]. Other challenges include the need for ultra-low resistance ohmic contacts [66, 67, 68, 69], patterning and etching technologies with atomic precision and selectivity [70, 71], and intentional doping for tuned device performance [72, 73, 74].

1.3   Thesis scope & structure

The main objective of this thesis is the development and validation of a scalable 2D semiconductor thin film technology based on the material MoS_2. This includes the study and optimization of large-area **synthesis**, in-depth film **characterization**, device **integration** and wafer batch device fabrication towards the prospective **application** in flexible transistors for multiplexed neural sensing. This work follows a materials science and engineering methodology aiming to elucidate synthesis-structure-property-performance relationships, where material and device characterization play a central role, as illustrated by the "materials tetrahedron" in Fig. 1.3. This paradigm acts as the recurring theme throughout this thesis aiming to advance fundamental scientific understanding and technological engineering aspects in a holistic approach. Therefore, the work is expected to provide a comprehensive and significant contribution in multidisciplinary fields from large-scale 2D semiconductor growth, characterization and integration to flexible electronics and beyond.

The thesis is structured into the following six chapters, to which supporting information can be found in separate, dedicated appendices at the end of this manuscript.
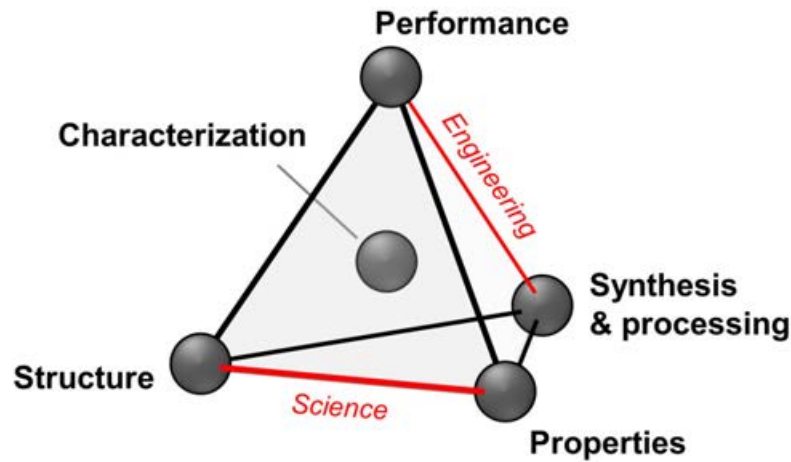
Figure 1.3 Materials science and engineering tetrahedron.

- The **first chapter** provides a brief introduction into 2D materials, their opportunities and integration challenges for use in electronic devices. The objective and structure of this thesis are presented.

- The **second chapter** contains background knowledge concerning the specific material properties of MoS_2 and an overview of available vapor-phase techniques. Suitable precursors for bottom-up synthesis, with a focus on the MOCVD method and epitaxy, are introduced. Moreover, this chapter provides the experimental details regarding the MOCVD reactors and analysis tools used for thin film synthesis and metrology, as well as methods for microfabrication and electrical device characterization.

- The **third chapter** studies the MOCVD of mono-to few layer MoS_2 thin films on amorphous silicon dioxide (SiO_2/Si) substrates; the work focuses on understanding the growth parameter space and finding optimized growth conditions. A central research aspect is the analysis of carbon impurity incorporation that can be an undesired side-product owing to the use of low-cost, low-toxicity organosulfide precursors. The effects of carbon incorporation on the morphological and (opto)electronic layer properties are discussed in detail. Moreover, MoS_2 grain size enhancement strategies for improved quality of polycrystalline thin films are introduced.

- The **fourth chapter** focuses on the large-area MOCVD of epitaxial MoS_2 thin films on crystalline sapphire [$Al_2O_3(0001)$] wafer substrates. The role of substrate surface preparation and growth parameters in the van der Waals heteroepitaxy

is investigated, contributing fundamental understanding towards the goal of synthesizing high-quality, single-crystalline MoS_2 thin films. Complementary microscopic inspection and grazing incidence diffraction techniques are used to reveal the oriented domain alignment, including angular dispersion, and selectivity of the film-substrate epitaxial relationships.

- The **fifth chapter** covers device integration aspects (2D layer transfer, interface cleanliness, oxide encapsulation) using the MOCVD-grown MoS_2 thin films for the wafer-scale fabrication of field-effect transistors; this includes translation from rigid to flexible substrates and benchmarking of the electrical performance of optimized thin films. A proof-of-concept of a monolithically integrated 2D MoS_2/graphene-based, flexible sensing array technology aiming at brain-computer-interface applications is demonstrated.

- The **sixth chapter** summarizes the achievements of this work, giving conclusions, an outlook for 2D electronics and opportunities for alternative and new directions based on this research.

Chapter 2

Background, Materials & Methods

This chapter provides the necessary background information regarding material properties, bottom-up fabrication of MoS_2 thin films by vapor-phase synthesis, including experimental details about the growth reactors and analysis methods for thin film and device characterization.

2.1   MoS$_2$ – A prototypical, layered 2D TMD

Layered transition-metal dichalcogenides (TMDs) have become a forefront of 2D material research due to their combination of mechanical and (opto)electronic properties [75, 76]. TMDs have the general formula MX$_2$, where M is a transition metal and X a chalcogen within the periodic table of elements (Fig. 2.1). The most widely studied compound of the TMD family is the prototypical layered TMD MoS$_2$. This section will introduce its basic, material properties.

Figure 2.1 Periodic table of elements highlighting transition-metals (M) and chalcogens (X) that predominantly crystallize in around 40 different, layered MX$_2$ compounds. Partial highlights for group 9–10 metals indicate that only some of the dichalcogenides form layered structures. Adapted from Chhowalla et al. [77]

2.1.1   Crystal structure

The crystal structure of monolayer 1H-MoS$_2$ consists of a hexagonally-packed layer of Mo atoms sandwiched between two layers of S atoms, as shown in Fig. 2.2a. The S-Mo-S sandwich structure is linked by polar covalent bonds between the Mo and S atoms, where the Mo atoms have a trigonal prismatic (D$_{3h}$) coordination by the S atoms (Fig. 2.2b). The Mo-S distance is 2.35 Å and the S-S distance along c-direction is 2.98 Å [78]. This monolayer structure forms the 1H phase, which has an in-plane lattice constant of 3.16 Å (Fig. 2.2c) and corresponds to the space group P$\bar{6}$m2 (#187) [79]. It has a 6-fold rotoinversion axis that implies a characteristic 3-fold, in-plane rotational symmetry, which has consequences for epitaxial thin film growth.
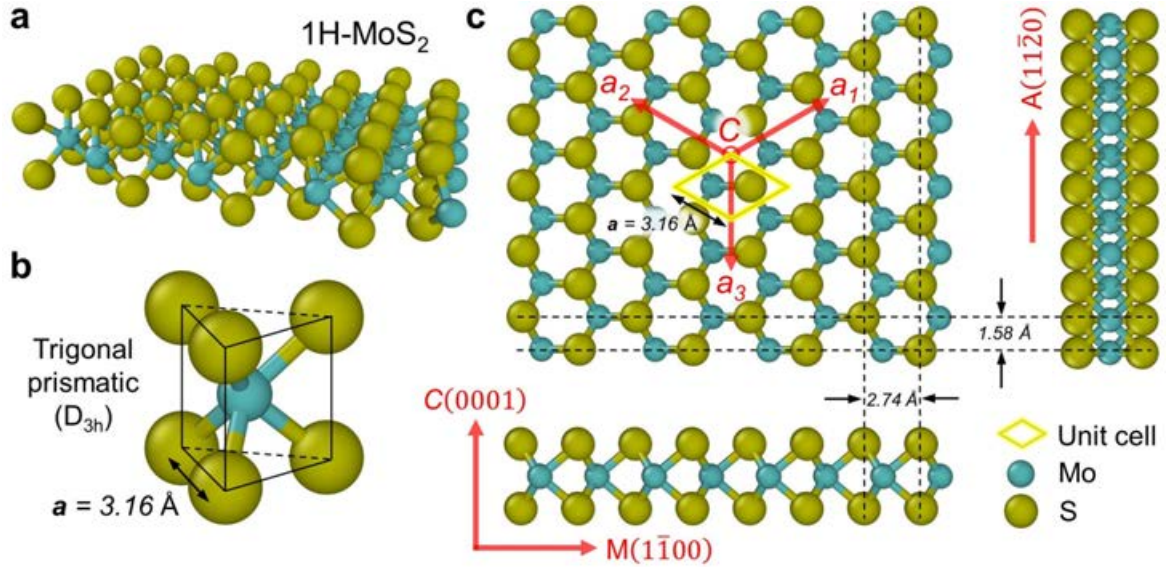
Figure 2.2 Crystal structure of monolayer 1H-MoS$_2$ produced from crystallographic data published on *materialsproject.org* [80] and visualized with the open-source software OVITO v3.6.0 [81]. **(a)** Perspective view of ball–and–stick model. **(b)** Polyhedron displaying the trigonal prismatic coordination (D$_{3h}$) of Mo by S atoms. **(c)** Top–, side–, and front view of the monolayer displaying its hexagonal structure, including coordinate system (red), primitive unit cell (yellow-highlighted rhombus), in-plane lattice parameter a_{MoS_2}, and characteristic $(1\bar{1}00)$ and $(11\bar{2}0)$ lattice plane distances indicated by dashed lines.

Besides the thermodynamically most stable H-phase there also exists a metastable T-phase with octahedral (O$_h$) coordination depicted in Fig. 2.3, where the upper and lower tetrahedra are rotated by 180° opposed to the symmetrical arrangement in the H-phase [82]. If multiple layers are vertically arranged along the c-axis, the stacking sequence of the individual layers becomes important, defining the so-called polytype, which determines the crystal symmetry and material properties [79]. Among all polytpes, the most common is the 2H polytype, which consists of layers with prismatic coordination and AB stacking; Mo and S atoms are arranged on top of S and Mo atoms, respectively. The two-layer unit cell 2H polytype has space group P6$_3$/mmc (#194) that adds a screw displacement to the single-layer unit cell 1H polytype while maintaining the hexagonal crystal system. In the three-layer 3R polytype, with ABC stacking, the rotation symmetry is reduced from 6-fold to 3-fold, resulting in a trigonal (rhombohedral) lattice with space group R3m (#160). In structures of multiple layers and in the bulk, crystallizing in the thermodynamically most stable 2H-phase, the individual layers are held together by weak van der Waals interlayer bonds and strong intralayer covalent bonds [83].
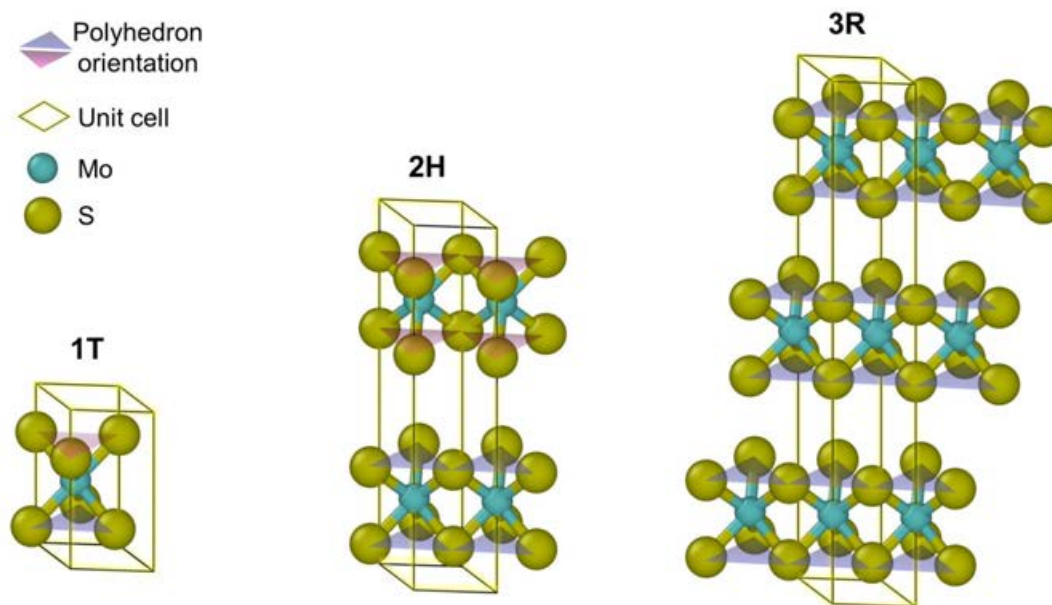
Figure 2.3 Polytypes of MoS$_2$. The conventional unit cells are drawn and the coordination polyhedra symmetries are highlighted by colored triangles.

2.1.2 Physical and mechanical properties

MoS$_2$ is naturally occuring in form of the mineral molybdenite (Fig. 2.4a). Bulk crystals have a silvery, dark gray physical appearance with a metallic luster, similar to graphite [84]. Their layered, crystalline structure with weak interplanar bonds allows to easily delaminate flakes from the basal planes perpendicular to the c-axis [Fig. 2.4c(i)]. Therefore, MoS$_2$ has been traditionally used in tribological applications as a dry lubricant. Since the advent of 2D materials research, the ease of delamination has allowed researchers to explore MoS$_2$'s layer-dependent properties down to the monolayer limit by bulk exfoliation via the scotch tape method [85], as depicted in Fig. 2.4b.

Monolayer (1L) MoS$_2$ has extraordinary mechanical properties exhibiting high in-plane stiffness (Young's modulus ~ 270 GPa) while having a low flexural rigidity [bending modulus ~ 11.7 eV, see Fig. 2.4c(ii)] [37, 89]. As listed in table 2.1, exfoliated 1L-MoS$_2$ has a high fracture strength of up to 30 GPa and fracture strain of up to 11 %. These values are about an order of magnitude higher than the ones for steel. Moreover, the fracture strain is in the range of common polymer substrate materials, such as polyimide (PI) or polydimethylsiloxane (PDMS), suggesting that 2D MoS$_2$ can be readily integrated with PI or PDMS for use in flexible applications [90]. It must be
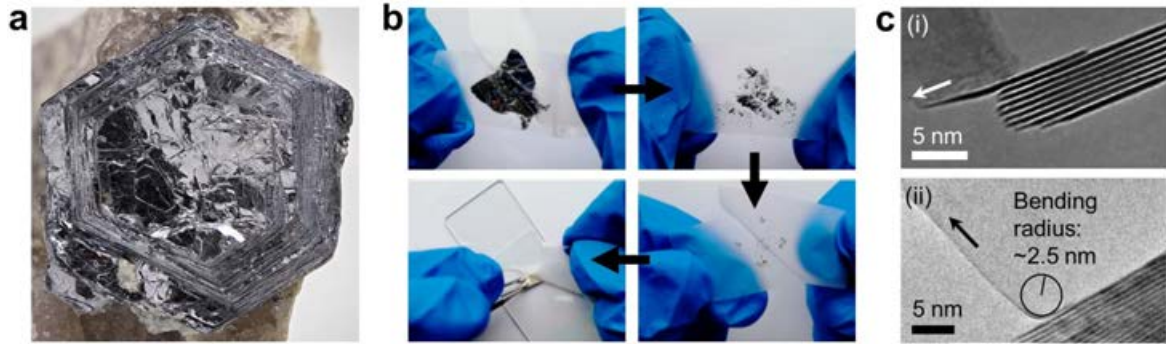
Figure 2.4 MoS$_2$ bulk crystal and exfoliation. **(a)** Natural molybdenite crystal.[1] © 2020 Harold Moritz. **(b)** Layer delamination by scotch tape method. Adapted from [86]. © 2019 by the Author(s) under creative commons license. **(c)** High-resolution transmission electron microscope images of nanomechanical cleavage of MoS$_2$ flake during (i) shearing, adapted from [87]. © 2015 American Chemical Society, and during (ii) bending, adapted from [88]. © 2014 Nature Publishing Group.

remarked though that the mechanical properties of MoS$_2$ also depend on its crystalline quality. Compared to exfoliated MoS$_2$ sheets [90], synthetic polycrystalline MoS$_2$ films may exhibit lowered fracture strength and strain due to crack propagation along defects, such as grain boundaries [91, 90]. However, even non-ideal, defect-rich MoS$_2$ films have shown fracture strains greater than 5 % [91, 40] that is superior to brittle materials, such as silicon. Therefore, the elastic properties make MoS$_2$ an interesting candidate for bendable, stretchable and wearable device applications [92, 93, 94, 37], in particular for flexible electronics in combination with its unique (opto)electronic properties [38].

Table 2.1 Mechanical properties of several materials, including monolayer (1L) MoS$_2$.

Material	Young's modulus (GPa)	Fracture strength (GPa)	Fracture strain (%)	Ref
Stainless steel	205	0.9	0.4	[95]
Polyimide (PI)	2.5	0.23	7 – 9	[92]
Polydimethyl-Siloxane (PDMS)	0.3 – 0.9	2.2	9	[96]
Silicon nanomembrane (thickness)	108–160 (50–200 nm)	6	∼ 1 – 2.5	[92, 93, 94]
Graphene	1000	130	13	[97]
1L MoS$_2$ (exfoliated)	270	16 – 30	6 – 11	[90]
1L MoS$_2$ (synthetic, polycrystalline)	n. a.	0.9 – 1.0	5	[91, 40]

---

[1]Unnamed quarry, White Rock Mining District, Middletown, Middlesex Co., Connecticut, USA. Source: https://www.mindat.org/photo-298192.html

2.1.3 Electronic and optical properties

Large part of the interest in 2D TMDs has been due to their electronic and optical properties. These are rooted in their electronic band structure, which is dominated by the crystal structure (coordination) and by the electronic configuration of the transition-metal atoms (to lesser extent by the chalcogen atoms) [98, 82]. In the case of MoS_2, the H-phase has semiconducting and the T-phase has metallic properties. This work focuses on the thermodynamically most stable, semiconducting H-phase; this phase exhibits a significant change in its electronic structure due to a layer number dependent bandgap transition. As the calculated band structure of Fig. 2.5 shows, MoS_2 is an indirect semiconductor in its bulk and few layer form with the lowest energy transition at the Γ-point; it gradually shifts towards a direct semiconductor in the monolayer limit, with the lowest energy transition at the K-point. This evolution with layer number is due to quantum confinement and the resulting change in hybridization between p_z orbitals in S atoms and d orbitals in Mo atoms [75].
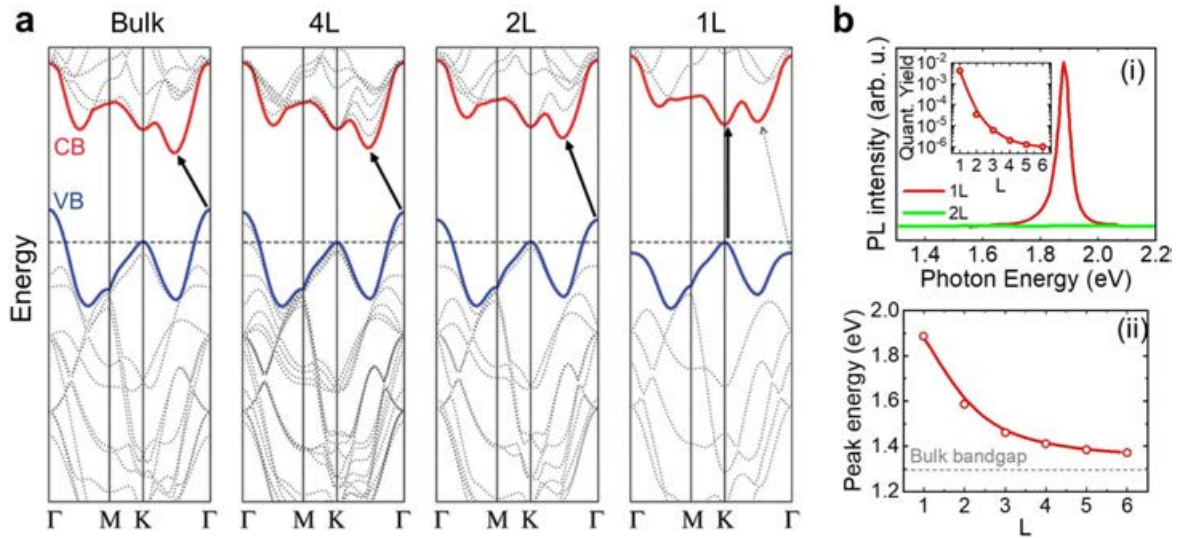
Figure 2.5 (Opto)electronic properties of MoS_2. **(a)** Calculated band structure of bulk, quadrilayer (4L), bilayer (2L), and monolayer (1L) MoS_2. The black arrows indicate the lowest energy transitions in the bandgap from the valence band maxima (VB, blue) to the conduction band minima (CB, red). While bulk and few layer MoS_2 show an indirect bandgap with transitions from the Γ-point, monolayer MoS_2 is characterized by a direct bandgap at the K-point. Adapted from Splendiani et al. [99] © 2010 American Chemical Society. **(b)**(i) Photoluminescence (PL) spectra of 1L- and 2L-MoS_2. The inset shows the quantum yield as function of layer number L. (ii) Layer-dependent bandgap energies inferred from the PL peak position. The dashed line represents the (indirect) energy bandgap of the bulk. Adapted from Mak et al. [100] © 2010 American Physical Society.

The indirect-to-direct bandgap transition has strong implications for the electronic and optical properties of MoS$_2$. In the monolayer limit, MoS$_2$ shows intense photoluminescence due to orders of magnitude higher quantum efficiency than for few layer and bulk material (Fig. 2.5b). Because of this, there exists a huge interest to exploit 1L MoS$_2$ for electronic and optoelectronics device applications [75]. The optical bandgap is tunable from around 1.9 eV (1L) to around 1.3 eV (bulk) covering a wide bandgap range [99, 100], as depicted in Fig. 2.5b(ii). Moreover, due to the lack of inversion symmetry in 1H-MoS$_2$ there exist inequivalent spin-polarizable K/K' valleys, which has attracted great attention for valleytronics [101, 4].

Due to its semiconducting properties, MoS$_2$ is a promising material for electronic devices, such as field-effect transistors with high on/off current ratios ($\sim 10^8$) and charge carrier mobility $\gtrsim 15\,\mathrm{cm^2\,V^{-1}\,s^{-1}}$ [18, 19]. Although in practice the electrical transport and carrier mobility may be limited by scattering at acoustic and optical phonons, surface interface phonons, substrate roughness, and charged impurities [75], researchers have mitigated these effects by interface engineering [102, 103]. With a theoretically predicted mobility of up to $400\,\mathrm{cm^2\,V^{-1}\,s^{-1}}$ at room temperature, 1L MoS$_2$ exhibits a higher value than Si for thicknesses below $\sim 5\,\mathrm{nm}$, giving a perspective for the use of 2D MoS$_2$ as an alternative material beyond conventional CMOS in ultra-scaled devices [104, 16]. Therefore, MoS$_2$ represents the prototype of a new class of atomically thin semiconductors with an unprecedented performance and unique combination of properties for next-generation (opto)electronic applications.

2.1.4 Catalytic edge properties

Pristine, dangling-bond free basal planes make MoS$_2$ a rather chemically inert material that is stable in many acidic and weak alkaline aqueous solutions at room temperature [84]. However, coordinatively unsaturated edge sites of MoS$_2$ sheets exhibit a high reactivity [105] and their catalytic activity has long been exploited as a hydrotreating catalyst for selective hydrogenation [106] and hydrodesulfurization [107, 108], such as for refining of crude oils in petroleum industry. Moreover, MoS$_2$ has also been investigated in electrochemical (photo)catalysis [109, 110], in particular for the hydrogen evolution reaction (HER) in water splitting [111, 112]. While catalysis applications are not the objective of this work, the catalytic properties and edge structure of MoS$_2$ are also relevant for the gas-phase synthesis of MoS$_2$ thin films. Lauritsen and coworkers have extensively studied MoS$_2$ nanocatalysts [107, 115, 105, 116, 114] prepared on Au(111) surfaces by atomically-resolving scanning tunneling microscopy and density functional

theory. They found that the nanocluster shape is determined by the relative stability of the most stable, low-index $(1\,0\,\bar{1}\,0)$ Mo and $(\bar{1}\,0\,1\,0)$ S edges, as given by the ratio of their free energies γ_{Mo} and γ_S, respectively. A hypothetical nanocluster is depicted in Fig. 2.6a. Under sulfiding conditions $(\gamma_S/\gamma_{Mo} \geq 2)$, triangular domains with Mo edges are the thermodynamically most stable morphology [114]. However, the Mo edge termination may exhibit varying degrees of S coverage depending on the hydrotreating conditions (temperature, chemical potentials of S and H) [117, 108], as illustrated by the ball models and the phase diagram in Fig. 2.6b. This has implications for precursor feeding and reaction stoichiometry during MoS_2 synthesis [118, 119], which impact the domain shape and edge configuration of growing domains. S-rich conditions result in Mo edges with fully saturated S dimers, whereas S-deficient and H-rich conditions may lead to edge desulfurization according to the phase diagram in Fig. 2.6b.
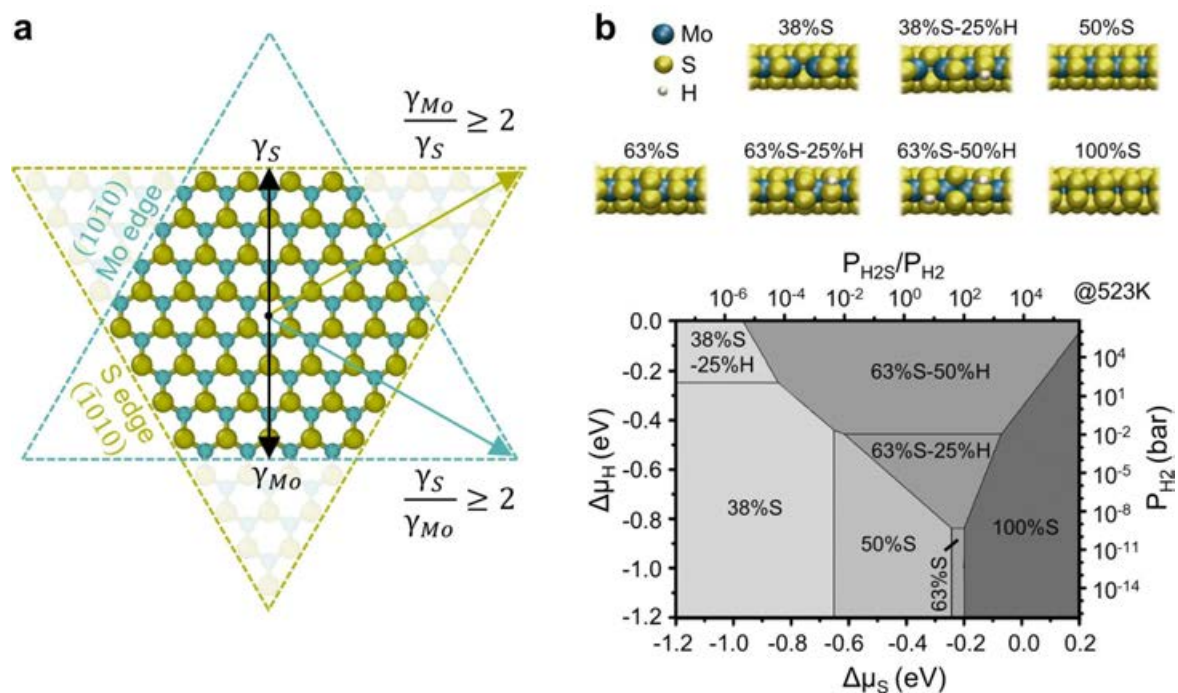
Figure 2.6 MoS_2 domain shape and edge termination. **(a)** Wulff construction of a hexagonal, truncated MoS_2 domain exposing the $(0\,0\,0\,1)$ basal plane with low-index $(1\,0\,\bar{1}\,0)$ Mo and $(\bar{1}\,0\,1\,0)$ S edges. The figure illustrates the dependence of the equilibrium domain morphology on the relative edge free energies (γ). For γ-ratios between 1 and 2 the domain shape results in a truncated hexagon, whereas values exceeding 2 result in perfect triangles with either Mo or S edges. Based on [113, 114]. **(b)** Top: Side view ball models of different MoS_2 edge terminations. Bottom: *Ab initio* thermodynamics phase diagram of the edge termination in H_2/H_2S gas mixtures. $\Delta\mu_S$ and $\Delta\mu_H$ designate the entropic parts of the chemical potentials of S and H atoms in the gas phase, respectively. These are directly related to the temperature, the H_2S pressure, and the H_2 pressure. Adapted from [108]. © 2019 The Author(s).

2.1.5 Phase diagram and stability

Figure 2.7a shows the calculated heat of formation of 216 MX$_2$ TMD compounds crystallized in 2H and 1T phases, reported by Rasmussen et al. [120]. The color-coding (blue: stable, red: unstable) visualizes the stability trends within the matrices. In general, oxides are most stable, followed by sulfides, selenides, and tellurides. This means that there exists a tendency for the sulfides, selenides and tellurides to oxidize in ambient conditions, with sulfides being the most air-stable compounds. Typically, defect-rich, synthetic TMDs age more quickly than pristine, exfoliated sheets due to defect-mediated oxidation, which affects their long-term stability [121, 122]; this has important implications for device processing conditions [57, 123]. For further air sensitivity and thermal degradation studies the reader is referred to the literature [121, 124, 125]. The 2H Mo- and W- based sulfides belong to the most stable, semiconducting compounds, explaining their ease of synthesis and popularity for research into their electronic applications.
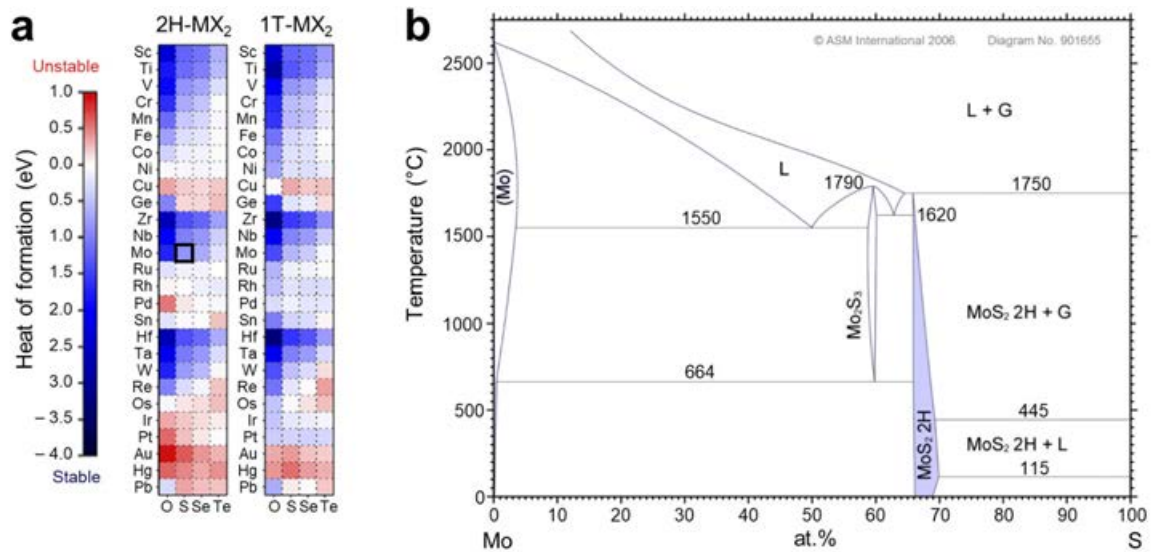
Figure 2.7 Phase stability and phase diagram of TMD compounds. **(a)** Calculated heat of formation for monolayers of 2H– and 1T–phase MX$_2$ compounds (M = transition-metal, X = chalcogen). Adapted from Rasmussen et al. [120] **(b)** Binary phase diagram of the Mo-S system. "L" indicates liquid, "G" indicates gaseous. Adapted from ASM phase diagram database [126].

TMD synthesis requires knowledge of occuring/coexisting phases during synthesis depending on the reaction stoichiometry and temperature regime. Figure 2.7b shows the binary phase diagram of the Mo-S system, which is characterized by the significant

discrepancy in melting points between elemental Mo and S. According to the phase diagram, stoichiometric MoS_2 melts at 1750 °C forming a Mo-rich liquid phase in equilibrium with gaseous S. Therefore, it is not possible to synthesize MoS_2 via melt growth techniques and, instead, vapor phase methods are employed for synthesis of bulk crystal and thin films in S-rich conditions [82]. For S:Mo ratios $\gtrsim 2$ and temperatures between 445 and 1750 °C, MoS_2 is in equilibrium with S vapor. Above 664 °C, and in the case of S-deficient conditions (S:Mo$\lesssim 2$) a Mo_2S_3 phase can potentially form and result in phase impurities. A peculiarity of the Mo-S system is the wide 2H-MoS_2 phase region (blue) as function of temperature, which is typical for Mo-based TMDs (MoS_2, $MoSe_2$, $MoTe_2$) existing over a broad range of chalcogen concentrations [127]. This is distinct from W-based TMDs (WS_2, WSe_2), which exhibit line compounds easier to obtain in stoichiometrically pure form compared to the Mo chalcogenides [127].

2.2 Vapor-phase synthesis

2.2.1 Overview of synthesis techniques

Figure 2.8 gives an overview of common TMD preparation techniques for a wide range of MX_2 compounds [76, 128], including MoS_2. Generally, they can be classified into top-down (e.g. dry mechanical or wet chemical exfoliation [129, 130, 131] from natural or synthetic bulk crystals) and bottom-up (e.g. synthetic liquid- or vapor-phase methods) approaches. While top-down exfoliation via scotch tape [132] and visco-elastic stamping [133] have been widely used in laboratories to isolate and integrate pristine TMD layers into proof-of-concept devices with high electronic performance [18], this method is not suitable for commercial batch fabrication, which requires a scalable, controllable, and reproducible manufacturing process. Spray pyrolysis [134] or solution processing and printing methods [135, 136] may provide scalable routes, but are not ideal for producing thin films with controlled layer numbers down to the monolayer limit for high-performance electronic devices. Therefore, extensive efforts have been dedicated to develop a variety of bottom-up vapor-phase techniques, discussed in the following.

Already in the 1970s and 1980s chemical vapor transport (CVT) had been commonly used to synthesize layered, centimeter-scale TMD crystals; this method is based on the evaporation of stoichiometric quantities of M and X constituents inside a closed vacuum tube across a thermal gradient [137, 138, 139], often by using transport agents such as
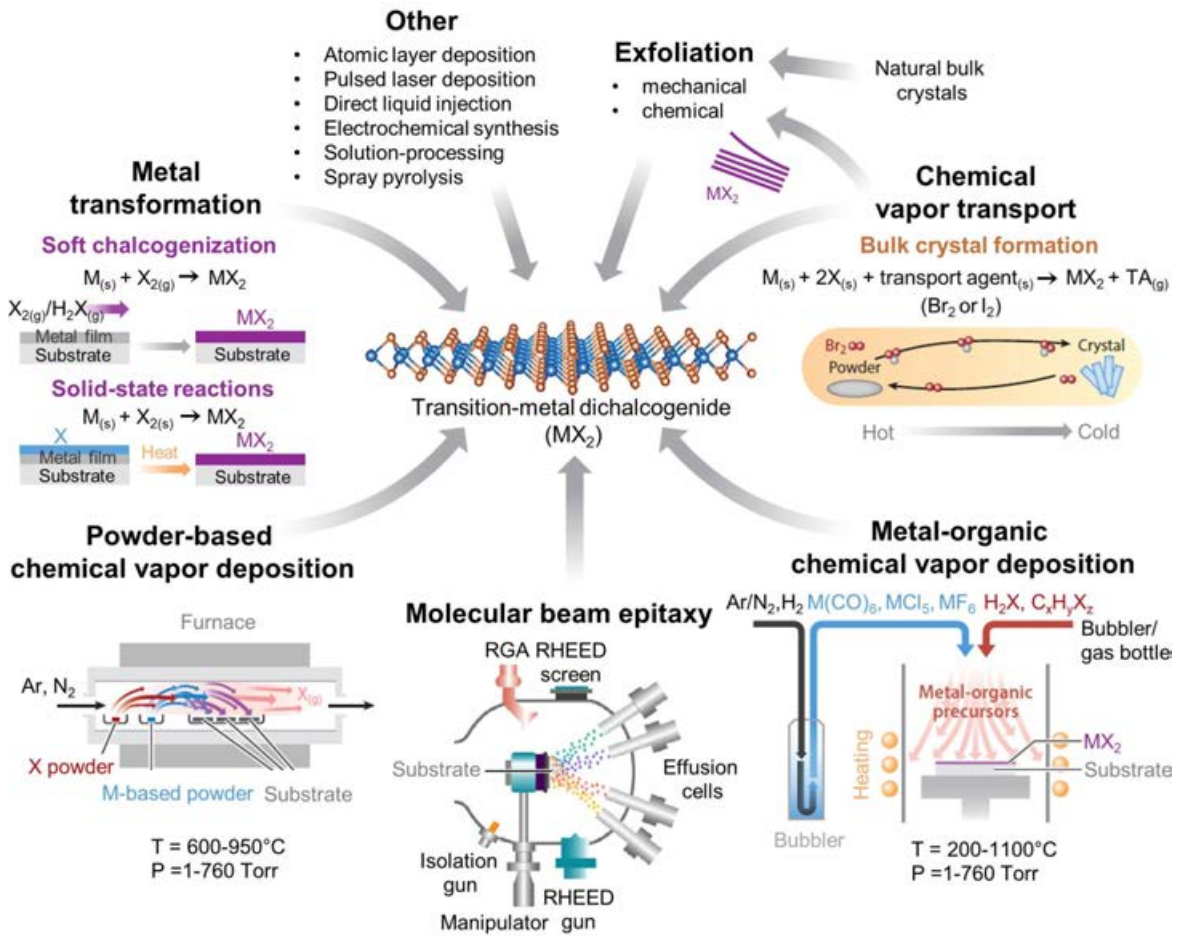
Figure 2.8 Overview of TMD synthesis techniques. Adapted from Das et al. [76] © 2015 Annual Reviews, and Briggs et al. [128] © 2019 IOP Publishing Ltd.

Br_2 and I_2. Single-crystalline TMDs can be obtained by CVT upon recrystallization at the cold end of the vessel; however, this near equilibrium process typically requires days or weeks to complete and produces bulk crystals that require layer isolation by aforementioned exfoliation techniques. A simple method able to directly produce 2D TMDs on wafer-scale down to a few- and single-layers consists in metal transformation by soft chalcogenization of a nm-thin transition metal film via exposure to a chalcogen vapor (e.g. sulfurization of a sputtered Mo film by S or H_2S) or solid-state reactions upon annealing a chalcogen on a metal film [140, 141, 142]. Similarly, a pre-deposited transition-metal oxide layer, such as MoO_2 or MoO_3, can be transformed in this way [143, 144, 145]. These approaches typically yield polycrystalline films with grain sizes below or only a few 10 nm depending on the annealing temperature; they provide limited control over the grain growth, although capped epitaxial conversion may result in enhanced crystallinity [146]. A more sophisticated method known from semiconductor

manufacturing is molecular beam epitaxy (MBE) [147, 148, 149, 150, 151] providing better control over film nucleation, growth rate and layer thickness, stoichiometry, and epitaxial film-substrate orientation by well-dosed, high-purity M/X source supply in an (ultra) high vacuum chamber. MBE enables pristine van der Waals interfaces and heterostructures. Furthermore, there are other techniques, such as atomic layer deposition (ALD) [152, 153, 154, 155], pulsed laser deposition (PLD [156, 157, 158], or direct liquid injection (DLI) [159] for controllable and scalable film deposition; however, these methods typically produce films with high nucleation densities and grain boundary defects. Most research efforts have focused on powder-based chemical vapor deposition ("powder CVD") [160, 161, 162, 163] using solid-source evaporation of elemental chalcogen (e.g. S) and transition-metal powders (e.g. MoO_3) to form MX_2 (e.g. MoS_2). Typically, horizontal, multi-zone tube furnaces are used, where the chalcogen powder is evaporated from a crucible at a low-temperature zone ($\sim$ 150–250 °C) upstream the hot zone ($\sim$ 600–950 °C), the latter of which carrying a crucible filled with the metal oxide powder. The substrate is placed downstream of the oxide powder or face-down on top of the oxide powder crucible. Upon heating, the vapors are transported by an inert carrier gas (Ar or N_2) and often H_2 for reduction to form the MX_2 film on the substrate. The widespread use of this method can be explained by the rather simple setup that can be straightforward implemented at affordable cost in many research laboratories, while achieving mono- to few layer TMD films with relatively large grain sizes (up to mm^2) over large areas ($>cm^2$) and remarkable electronic properties [164]. However, this process typically yields non-uniform films highly dependent on the relative crucible/substrate positions and powder distribution, causing gradients in coverage, thickness, domain shape and continuity due to uncontrollable and temporally unstable powder evaporation rates. These difficulties can be overcome by metal-organic chemical vapor deposition (MOCVD), which provides well-dosed introduction of independent molecular precursors from external bubblers or gas bottles into the reactor chamber. Therefore, the controllable and reliable source supply enables superior control over vapor-phase chemistry and constant growth rates over time compared to powder CVD [165]. MOCVD is an established manufacturing method for traditional compound semiconductors [166], and, thus, one of the most promising candidates to meet industrial criteria for high-throughput [167, 168], homogeneous deposition of high-quality 2D TMDs with layer-by-layer thickness control [169] on wafer-scale [47, 48, 170].

2.2.2 Precursor selection for MoS₂ synthesis

The previously presented vapor-phase synthesis methods are distinguished by the utilized sources, whose choice plays a decisive role for the thin film deposition process. A good understanding of the precursor properties in interplay with the growth conditions is essential for MOCVD process design. In this section, criteria for precursor selection will be discussed. The implications of precursor choice made for the MOCVD of MoS_2 thin films studied in this thesis will be explained in a broader context.

Selection criteria

In order to find suitable precursors, several criteria regarding optimal precursor selection should be taken into account [171, 172]. The following list notes some important precursor characteristics to consider:

- Volatility
- Thermal stability
- Purity
- Reaction pathway

- Availability
- Cost
- Safety
- Sustainability

Generally, an "ideal" precursor should have physico-chemical properties serving its purpose to optimally deliver the starting substances in the right dose for film deposition, including 1) adequate volatility to obtain acceptable growth rates at moderate evaporation temperatures (i.e. typical vapor pressures $\gtrsim 0.1\,\mathrm{Torr}$ [171]), 2) good thermal stability upon evaporation, gas-phase transport to the reaction zone and sufficiently large thermal decomposition and film deposition window (e.g. depending on the bond dissociation energy), 3) high chemical purity, having compatibility with co-precursors allowing a reaction pathway for clean decomposition without incorporation of residual film impurities (e.g. carbon in case of organic precursors), thus, not being contaminated nor being contaminating. The reaction pathways are also determined by the precursor oxidation state. Moreover, from practical and economic reasons the precursor should be 4) readily available in sufficient and consistent quality and quantities at low cost, 5) have a long a shelf-life for storage with stability under ambient conditions (i.e. unaffected by air or moisture), and stability in the source container at a low consumption rate. Finally, from a safety and environmental "green" chemistry

perspective, the precursor, including its by-products, should be 6) non-hazardous with regard to health and fire risks (i.e. no/low toxicity and pyrophoricity), where solids/liquids are generally considered safer to handle than gases, while having a 7) sustainable chemical life cycle from its design over its production and use, until its ultimate disposal. While aiming at optimal results, considering all these factors certainly imply compromises and also depend on site-specific circumstances, such as in academic research or industrial production environments.

Mo and S sources

Representative for the targetted synthesis of MoS_2 in this work, table 2.2 specifically lists Mo and S source literature examples, including their chemical formulas, names and physical properties. Their structural formulas and vapor pressure curves plotted from Antoine parameters (see also appendix Fig. A1, eq. (A.1)) are given in Fig. 2.9 to compare their volatility. As pure elements, Mo and S exhibit a significant difference in vapor pressures, which has implications for precursor delivery, reaction conditions and surface kinetics during MoS_2 synthesis.

Table 2.2 Mo and S precursors used for vapor-phase MoS_2 synthesis. Physical state and melting/boiling points were extracted from tabulated data [173] if not otherwise stated.

Short name/ formula	Chemical name	State (25°C)	Melting/Boiling (°C)	Employed in [Ref]
Mo	Molybdenum(0)	solid	2622/4639	[174], [115], [175], [176]
$Mo(CO)_6$	Molybdenum(0) hexacarbonyl	solid	148/155 decomp.	[47], [177], [178], This work
$Mo(thd)_3$	Tris(2,2,6,6-tetramethylheptane-3,5-dionato) molybdenum(III)	solid	n.a./150-265	[155]
$MoCl_5$ (Mo_2Cl_{10})	Molybdenum(V) chloride	solid	194/268	[179], [180], [181]
MoF_6	Molybdenum(VI) fluoride	liquid	17.5/34	[182], [183]
MoO_3	Molybdenum(VI) oxide	solid	801/1155	[162] [184]
BTBMMo	Bis(tert-butylimido)-bis(dimethylamido) molybdenum(VI)	liquid	n.a./∼225 [185]	[167], [186], [169], [187]
S	Sulfur	solid	115.2/444.6	[162], [184], [175], [176]
H_2S	Hydrogen sulfide	gas	-85.5/-59.5	[188], [189], [190], [191]
DMS	Dimethyl sulfide	liquid	-98.24/37.33	[180], [192], [193], This work
DES	Diethyl sulfide	liquid	-103.91/92.1	[47], [190], [194], [195], This work
DMDS	Dimethyl disulfide	liquid	-84.67/109.74	[196], [115]
DEDS	Diethyl disulfide	liquid	-101.5/154	[167], [197]
DTBS	Di-*tert*-butyl sulfide	liquid	-105.5/171	[177], [198], [199]

Mo is a refractory metal with high bond strengths resulting in high melting/boiling point; It has extremely low vapor pressure even above 1000 °C, which is at the upper limit of commonly used MoS_2 growth temperatures. Therefore, effusion of elemental Mo sources presents a significant challenge, which can be achieved by electron beam evaporation in high vacuum MBE environments [82, 200] or thermal laser evaporation [201,

202]. MoO_3 can be evaporated in powder CVD with appreciable vapor flux at elevated temperatures ($\gtrsim 600\,°C$). Molecular Mo compounds with significantly increased volatility are employed for gas-phase delivery from external sources in metal-organic synthesis processes, such as MOCVD [203] and MOMBE [204, 205]. Hexacarbonyls have been long studied and used for transition-metal deposition upon decarbonylation [206, 207, 208, 209] and have become one of the most popular transition-metal sources for MOCVD of TMDs, such as $Mo(CO)_6$ for MoS_2 synthesis [47, 177, 192, 178]. $Mo(CO)_6$ is a solid powder with a moderate vapor pressure above $0.1\,Torr$ at room temperature [210] and is widely available at low cost. Due to its toxicity it has to be kept in sealed canisters and precautions need to be taken due to formation of poisonous CO gas upon decomposition and reaction [211, 82]. As CO is a rather stable gas-phase by-product there is reduced chance of C incorporation stemming from $Mo(CO)_6$ at elevated temperatures according to theoretical and experimental studies [188]. Furthermore, transition-metal chlorides (e.g. $MoCl_5$ [179, 180]) and fluorides (e.g. MoF_6 [182, 183]) exhibit increased volatility for increased growth rates. However, these compounds are air-sensitive and form HCl and HF, which are corrosive and dangerous by-products requiring increased safety precautions. Recently, also BTBMMo has been used in a variety of gas-phase synthesis processes [167, 212, 186, 169, 187], but may introduce N impurities due to uncomplete decomposition [212]. While development of novel precursors apart from the aforementioned Mo sources has been rare, Mattinen et al. [155] synthesized an $Mo(thd)_3$ beta-diketonate for a specialized ALD process with oxidation state Mo^{III} that is closer to the final Mo^{IV} state in MoS_2 and that may be benefitial compared to other precursors. As marked in table 2.2 the Mo oxidation state varies among the precursors, which has implications for reaction mechanisms and pathways requiring either oxidation or reduction to obtain $Mo^{IV)}$. The oxidation state in molecular precursors and reaction intermediates influence thermodynamics and reaction kinetics during growth. For instance, higher volatility and diffusivity reaction intermediates have been widely exploited for catalyzed TMD growth upon addition of alkali growth promotors [178, 213].

Turning to the sulfur precursors, elemental S provides sufficient vapor pressure $\gtrsim 150\,°C$, explaining its popular use in powder CVD to create an S-rich growth environment for efficient sulfurization. However, for gas-phase delivery from external canisters in MOCVD, precursors with higher volatility are desired. Gaseous hydrides, such as H_2S, have been used as viable sources in TMD synthesis [203, 188, 190, 169], but impose stringent safety requirements due to their high toxicity compared to their less harmful organic chalcogen counterparts. Considering S sources, a large variety

of organosulfide precursors has been employed in TMD synthesis (DMS [180, 192, 115, 193], DMDS [196, 115], DES [47, 190, 194, 195], DEDS [167, 197], DTBS [177, 198, 199]). Regarding their relative volatility, the vapor pressure of organosulfides decreases along the series DMS > DES > DMDS > DTBS > DEDS (Fig. 2.9b). There is few literature data available on the relative toxicity profiles of sulfides, for which
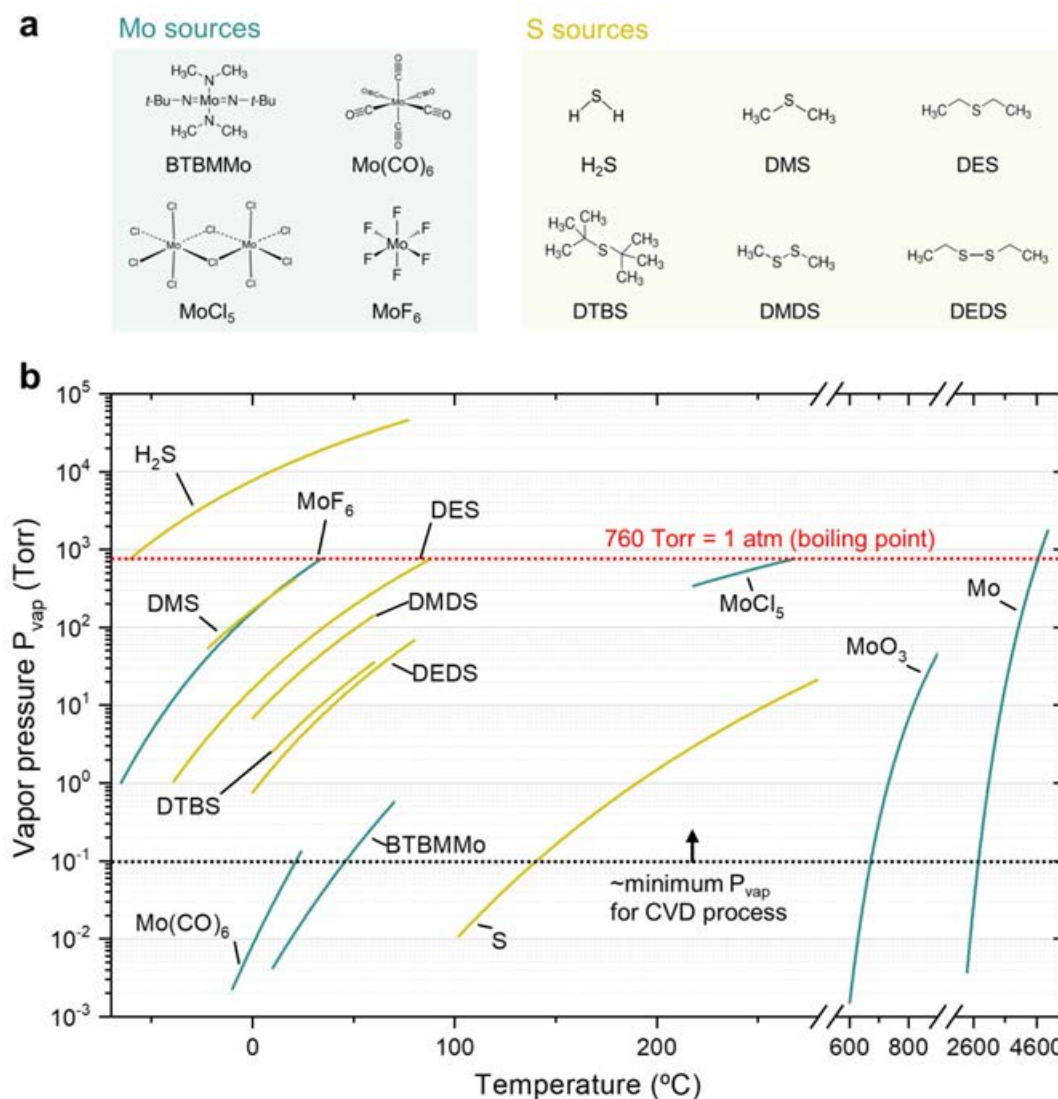
Figure 2.9 Vapor pressure P_{vap} of diverse Mo and S sources. **(a)** Chemical formulas of several molecular Mo (turquoise) and S compounds (yellow). **(b)** Vapor pressure curves based on Antoine parameters reported for the respective temperature ranges: Mo [214], MoO_3 [215] $MoCl_5$ [214], BTBMMo [185], $Mo(CO)_6$ [210], MoF_6 [214], S [214], DEDS [216], DTBS [217], DMDS [218], DES [215], DMS [219], H_2S [215]. Boiling points are indicated by intersection of the vapor pressure curves with the 760 Torr line (atmospheric pressure). The precursor volatility requirement for a CVD process typically demands vapor pressures $\gtrsim 0.1$ Torr [171].

the reader is referred to studies found for H_2S [220, 221, 222], DMS/DMDS [223], and DES [224]. Nevertheless, the main safety argument for the use of organosulfides is their comparatively low vapor pressure/liquid state at room temperature, making their handling safer compared to the gaseous hydride stored and supplied from pressurized gas bottles. However, the use of less harmful organic chalcogen precursors in TMD synthesis has raised concerns about C contamination stemming from carbonaceous radicals during their thermal decomposition [225, 190]. The thermal decomposition behaviour is crucial for the MOCVD process and is closely related to the bond strength of the precursor molecules, quantifiable by the bond dissociation energies (BDEs). A list of BDEs calculated by density funtional theory for a wide range of metal-transition and chalcogen precursors used in MOCVD of TMDs is given in the appendix (table A1). The organosulfide compounds differ in their ligand chemistry, affecting the different BDEs at C-S bonds in monosulfides and C-S/S-S bonds in disulfides. Typical BDEs of C-S bonds lie in the range of 2.6–3.4 eV with a general trend of lowered BDE for larger (branched) ligand chains around the C-S bond. Disulfides show lower BDEs of around 2.0–2.8 eV at their S-S bonds [153]. These BDEs translate into experimentally observed, condition- and time-dependent pyrolysis temperature windows of $\gtrsim$341–560 °C for DMDS [226, 227], representative for a disulfide, and $\gtrsim$408–709 °C for DMS [227, 228], representative for a monosulfide, which show different radical dissociation mechanisms and pathways [227, 228, 229, 230]. Therefore, the different BDEs and decomposition behaviours under liberation of S and C components may affect the sulfurization potential and carbon incorporation upon choice of different organosulfide sources for MoS_2 synthesis [152, 115, 153].

Considering $Mo(CO)_6$ as a popular Mo source, its volatilization and thermolytic properties have been experimentally analyzed by a coupled thermogravimetry-mass spectroscopy study in argon atmosphere by Fillman et al. [231], as shown in Fig. 2.10a. Upon heating, noticeable one-step weight loss appears above $\sim$100 °C, indicating the start of volatilization; rapid weight loss and peaking CO evolution indicate sublimation with simultaneous decomposition (decarbonylation) above $\sim$150 °C. For reference, $W(CO)_6$ (not shown in the graph) has higher thermal stability and sublimes without decomposition up to a temperature of $\sim$180 °C when CO evolution begins [231]. Furthermore, the decomposition behaviour of $Mo(CO)_6$ in a dynamic flow reactor has been analyzed by Usoltsev et al. [232, 233], as depicted in Fig. 2.10b. They measured the survival probability of $Mo(CO)_6$ as a function of temperature and inert carrier gas flow rate. Apparently, the survival probability due to decomposition drops above $\sim$200 °C with steepest slope at $\sim$300 °C for a flow rate of 0.3 L min^{-1}, whereas
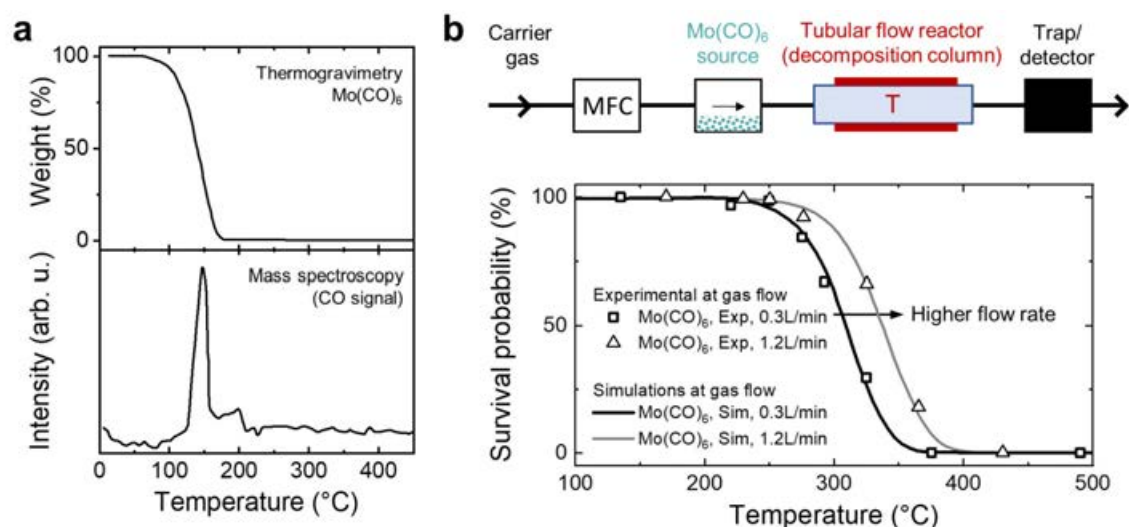
Figure 2.10 Volatilization and thermal decomposition of $Mo(CO)_6$. **(a)** Top: Thermogravimetric analysis in argon atmosphere. Bottom: Mass spectroscopic analysis of thermal evolution profile of CO. Adapted from Fillman et al. [231] © 1984 Elsevier Science Publishers B.V. **(b)** Adapted illustration of transition-metal hexacarbonyl decomposition study in a hot-wall flow tube reactor according to Usoltsev et al. [232] Experimental and simulated temperature-dependent survival probability of $Mo(CO)_6$ at different flow rates adapted from [233]. © 2015 Walter de Gruyter Berlin/Boston.

the decomposition profile shifts to higher temperatures for increased flow rates of $1.2\,L\,min^{-1}$. This shows the dynamic nature of the decomposition behaviour in a flow reactor closer to the real situation of a typical, non-equilibrium CVD process opposed to the static thermogravimetrical analysis. The decomposition behaviour has important implications for MOCVD of MoS_2 thin films from $Mo(CO)_6$, as the effective Mo concentration (partial pressure) determining the growth rate [47, 234] is highly dependent on the temperature, flow conditions, reactor geometry and sample position in the growth reactor [203, 235, 236]. In particular, in the case of a hot-wall reactor, decomposition gradients along the longitudinal tube axis of flow reactors play a critical role due to the comparatively low thermal stability of $Mo(CO)_6$ [237]. For reference, the higher thermal stability of $W(CO)_6$ (not shown in the graph) is indicated by a thermal decomposition profile shifted by $\sim 100\,°C$ to higher temperatures compared to $Mo(CO)_6$ [232, 233], related to the respective BDEs of ~ 1.7 and $\sim 2.1\,eV$ for $Mo(CO)_6$ and $W(CO)_6$ [232, 233] (also see appendix, table A1). This relative precursor stability has implications for the TMD growth processes of Mo- and W-based chalcogenides from hexacarbonyls.

For the studied MOCVD processes in this work, the precursors $Mo(CO)_6$ and DES/DMS were selected due to their commercial availability, low cost, comparatively low toxicity, and succesful utilization in previous MOCVD processes [47, 192]. Moreover, $Mo(CO)_6$ has with CO a non-corrosive, although toxic, but very stable gaseous dissociation product leaving the reaction (BDE $8.3\,eV$ [238]), and is thus expected to enable low C impurity introduction, while providing sufficient volatility. DMS/DES were chosen over hydrides due to their appropriate vapor pressures and due to safety considerations. Therefore, from the choice of this precursor system two major challenges can be anticipated: 1) Control of $Mo(CO)_6$ decomposition, effective Mo flux, and MoS_2 nucleation control [47, 237], and 2) organosulfide precursors as potential source of C incorporation [225, 190, 239].

2.2.3   Epitaxy

Epitaxy is defined as *"the process of growing a crystal of a particular orientation on top of another crystal, where the orientation is determined by the underlying crystal"*.[2] The term *epitaxy* is derived from the Greek prefix "epi" meaning "above" or "on" and "taxis" meaning "arrangement" or "order". The atoms of an epitaxially deposited layer are guided by the particular registry with the underlying crystal, which enables the growth of highly crystalline thin films in a layer-by-layer manner. In *homoepitaxy*, from greek "homo" meaning "same", these films may be made of the same material and structure as the substrate (e.g. Si on Si); in *heteroepitaxy*, from greek "hetero" meaning "other" or "different", they may be made of a material different from the substrate (e.g. Ge_xSi_{1-x} on Si, or AlAs on GaAs). In vapor-phase epitaxy the atoms are deposited from a vapor or molecules decomposed on the hot crystalline substrate surface, so that growth occurs at the solid-gas interface. This method is commercially used in III-V (and to a lesser extent II-VI and IV-VI) compound semiconductor manufacturing [240] to deposit thin films and quantum wells for applications in electronic and optoelectronic devices. However, the epitaxy concept can be generally applied for other material classes, such as metals and oxides, and 2D materials [241].

The type of epitaxy can be categorized based on the nature of the interactions at the interface between the crystalline film and the crystalline substrate, as illustrated in Fig. 2.11. In conventional epitaxy the interactions consist in a strong coupling between the conventional 3D crystal epilayer and the 3D bulk substrate by covalent,

---

[2]Retrieved from https://www.britannica.com/science/epitaxy, 8 january 2023

ionic or metallic bonds. While in homoepitaxy the epilayer can grow seamlessly with low defect density due to the same chemical composition and structure, conventional heteroepitaxy is more challenging due to the structural lattice mismatch of different materials. This mismatch arises from the difference in lattice parameters and thermal expansion and leads to the build-up of strain in the epilayer. A coherent strain can be accommodated in the *pseudomorphic* (from greek "pseudo" meaning "false"; "morph" meaning "form") growth regime only up to a critical epilayer thickness, at which strain relaxation occurs, for instance, by chemical intermixing, surface roughening or formation of misfit dislocations [240].

In van der Waals (vdW) epitaxy the interactions at the interface are formed by weak vdW forces. This type of epitaxy was discovered by A. Koma and coworkers at the University of Tokyo in Japan[3], which enables heteroepitaxy of single-crystalline films and atomically sharp vdW interfaces even for highly lattice-mismatched systems [241]. In their first report dated from 1984, Koma et. al. described vdW heteroepitaxy of 2D materials on 2D materials, such as strain-free $NbSe_2$ on MoS_2, where the epilayer can grow with its bulk lattice parameter despite large mismatch exceeding $10\,\%$ [243] and up to as much as $58\,\%$ [244]. Later, they reported vdW heteroepitaxy of 2D materials on 3D bulk materials [245], for which the preparation of a passivated, dangling-bond free 3D bulk surface was highlighted to form an ideal vdW interface [246], such as for
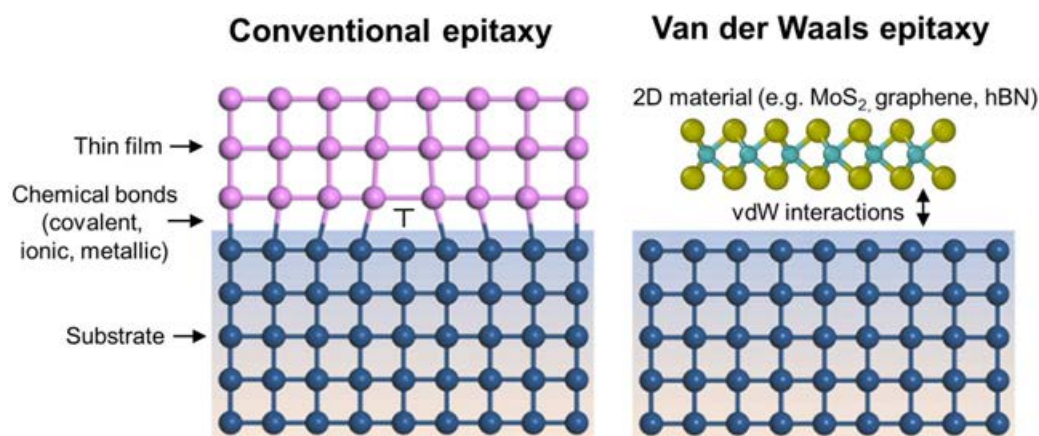
Figure 2.11 Effect of lattice mismatch in heteroepitaxy. **(a)** Schematic of a thin film grown on a lattice-mismatched substrate in conventional heteroepitaxy, where lattice strain is relaxed by formation of a dislocation ($\perp$). **(b)** Schematic of a 2D material grown on a lattice-mismatched substrate by quasi van der Waals (vdW) heteroepitaxy. Adapted from [242] © American Chemical Society.

---

[3]http://van-der-waals-epitaxy.info

MoSe$_2$ growth on a S-terminated GaAs(111) [247] and MoS$_2$ growth on F-terminated CaF$_2$(111). Recently, there is experimental evidence for the presence of such passivation layer in 2D-on-3D heteroepitaxy imaged by high-resolution, cross-sectional transmission electron microscopy and chemical profiling by electron energy loss spectroscopy [248] for WSe$_2$ and MoS$_2$ [249, 248] grown on chalcogen-terminated sapphire [Al$_2$O$_3$(0001)].

While lattice mismatch in weakly coupled vdW systems is less relevant than in conventional heteroepitaxial systems [250], the vdW epitaxy is still governed by the electrostatic forces and orbital overlap with the underlying substrate [82]. This has consequences for the long-range, rotationally commensurate registry of 2D layers on other 2D [251] or passivated 3D bulk substrates [48], where the preferred epitaxial relationship depends on the film-substrate symmetry and the orientation-dependent binding energy "landscape" [163]. Typically, binding energy minima occur along high symmetry directions [252, 253, 242] of the underlying substrate, determining the energetically favorable film-substrate configuration in substrate-lattice guided growth [175]. Other important factors controlling the film orientation, particularly in 2D-on-3D heteroepitaxy, include substrate properties like surface energy [254] and surface morphology [82], such as vicinal, stepped miscut surfaces in the case of edge-guided growth [255, 248, 256]. Growth conditions are also important, such as temperature to provide energy for epitaxial film alignment [49, 195] and gas-phase composition affecting the epitaxial relationship [257, 258, 259].

2.3 Experimental details

This section presents the used MOCVD reactor setups and growth processes, used substrates, and analysis techniques for film and device characterization.

2.3.1 MOCVD reactors and growth processes

ICN2 reactor

For growth of MoS$_2$ thin films on SiO$_2$ and soda-lime glass on up to $\sim 2 \times 2 \, \text{cm}^2$ areas in chapter 3, a home-built reactor located at ICN2 was used, subsequently referred to as "ICN2 reactor". Photographs and a scheme of the setup are shown in Fig. 2.12. The vertical setup with sample position normal to the gas flow direction has advantages over horizontal flow reactors in terms of gas flow homogeneity and spatial uniformity of the
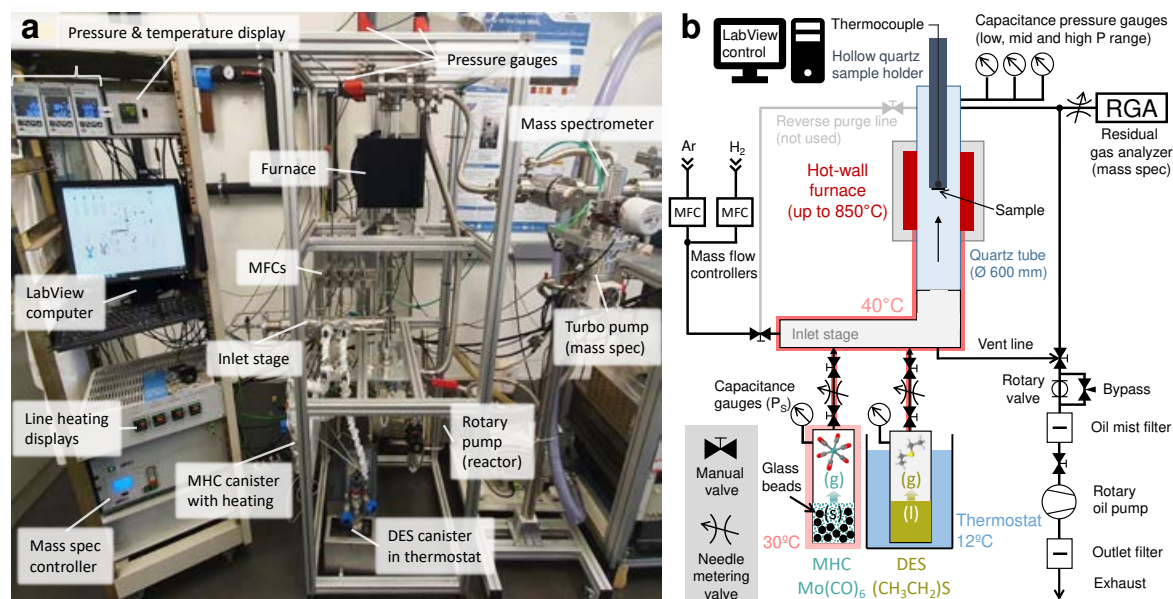
Figure 2.12 Home-built MOCVD reactor at ICN2 ("ICN2 reactor"). **(a)** Photograph with designated components. **(b)** Schematic illustration of setup and gas circuit.

film deposition [184]. A special feature of the reactor is the residual gas analyzer (mass spectrometer) connected downstream the sample position for gas-phase monitoring. The reactor operates in vapor draw mode, in which the precursors [$Mo(CO)_6$ and DES] are drawn by a pressure gradient from independent source canisters into the low-pressure reactor chamber without carrier gas. Typical working pressures used in this work were between 1×10^{-2} and 1×10^{-1} Torr and can be controlled by manual rotary valves and a bypass upstream the pump. Precursor flow was dosed by manual needle metering valves and estimated based on vapor pressure data (see appendix, Fig. A1). Precursor flow is started/stopped by manually operated 2-way valves at the inlet stage. A computer with LABVIEW interface is used to set the growth temperature, measured at the sample position, and controlled by a feedback-loop temperature controller. Moreover, Ar inert gas and H_2 flow fed by mass flow controllers (MFCs) can be added to the gas mixture. A typical growth process is illustrated in Fig. 2.13a. Between runs, the reactor was annealed according to Fig. 2.13b. A more detailed description of the used precursors and growth procedure can be found in the appendix (section A.2).
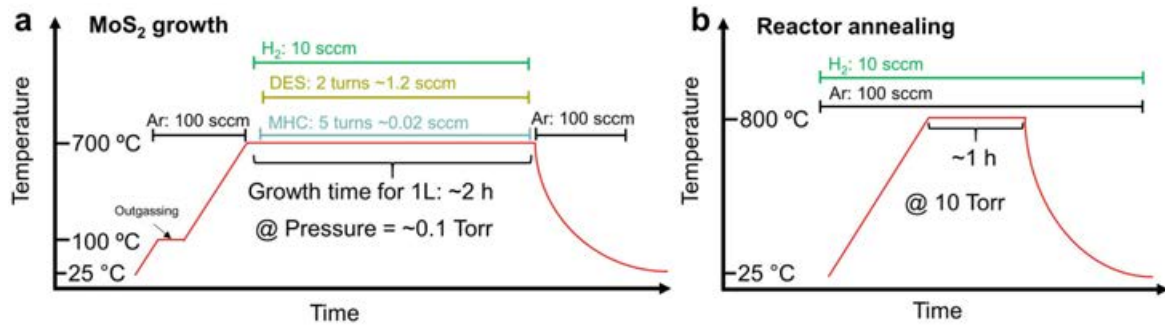
Figure 2.13 (a) Scheme of a typical growth process following an outgassing step at 100 °C, temperature ramp to the growth temperature of 700 °C under Ar flow, co-injection of Mo(CO)$_6$, DES precursors and additional H$_2$ flow upon reaching the growth temperature for a specified growth time, and cool down under Ar flow. **(b)** Reactor annealing step performed between consecutive growth runs at 800 °C with Ar/H$_2$ purge.

Yonsei reactor

For low growth rate MOCVD of MoS$_2$ thin films on SiO$_2$ substrate (chapter 3, section 3.4.2) and epitaxial growth on sapphire (chapter 4), another MOCVD setup was used; this was located at Yonsei university (Seoul, Rep. of Korea) and will be referred to as "Yonsei reactor". Photographs and a scheme of the reactor are shown in Fig. 2.14.
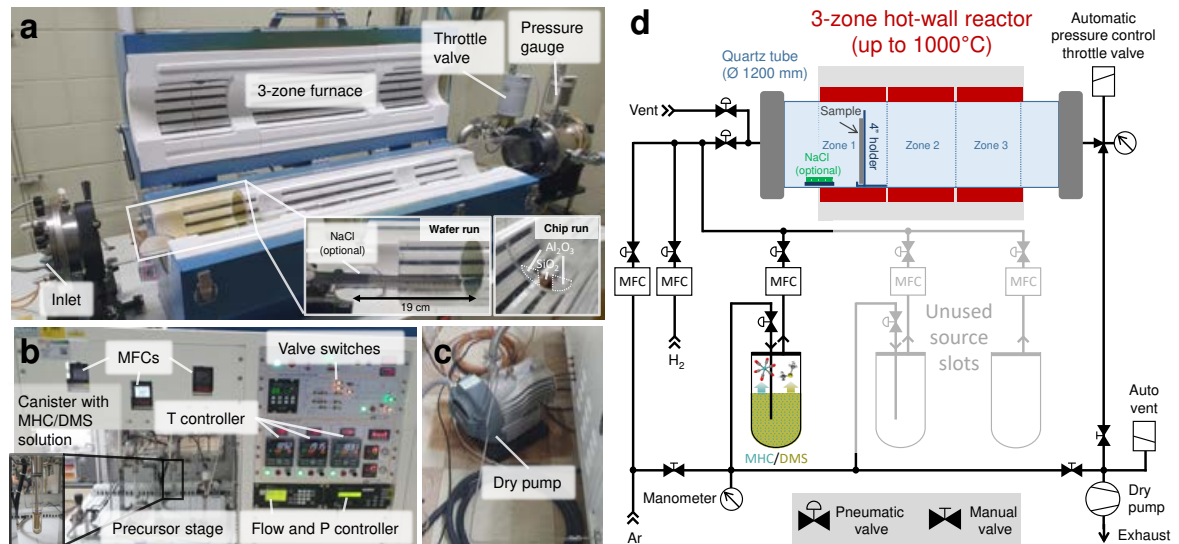
Figure 2.14 MOCVD reactor setup at Yonsei university ("Yonsei reactor"). **(a-c)** Photographs with designated system components. **(d)** Scheme of setup and gas circuit.

The customized, commercial setup (SCEN - Scientific Engineering, Rep. of Korea[4]) consists of a horizontal, three-zone hot-wall furnace with a 12 cm diameter quartz tube for deposition on wafers of up to 4" diameter. Samples were placed vertically (perpendicular to the flow directions) at an optimized position within the first reactor zone, and optionally NaCl was placed upstream at the reactor entrance for alkali-assisted growth. Control units for setting temperature, pressure, gas flows, and manual switches of pneumatic valves in the gas circuit are located in the control panel (Fig. 2.14b). The precursor stage offers three ports to be equipped with sealed glass canisters, from which only a single slot with the canister containing a liquid solution of $Mo(CO)_6$/DMS was used in this work. Precursor delivery is provided by bubbling Ar carrier gas through the solution and is controlled by a MFC downstream the source canister. Precursor flow estimations for this precursor injection method by a pick-up gas are given in section A.2. Additionally, Ar and H_2 are injected controlled by MFCs that enter the chamber together with the $Mo(CO)_6$/DMS flow pre-mixed at the reactor inlet. Pressure is controlled by an automatic throttle valve to a typical working pressure of 10 Torr. A dry pump is used in order to avoid backstreaming of inflicting organic hydrocarbon contaminants, as it may occur in the case of oil-sealed, rotary pumps [260]. A typical growth process is illustrated in Fig. 2.15a. Between runs, the reactor was annealed open to air according to Fig. 2.15b. A more detailed description of the used precursors and growth procedure can be found in the appendix (section A.2).
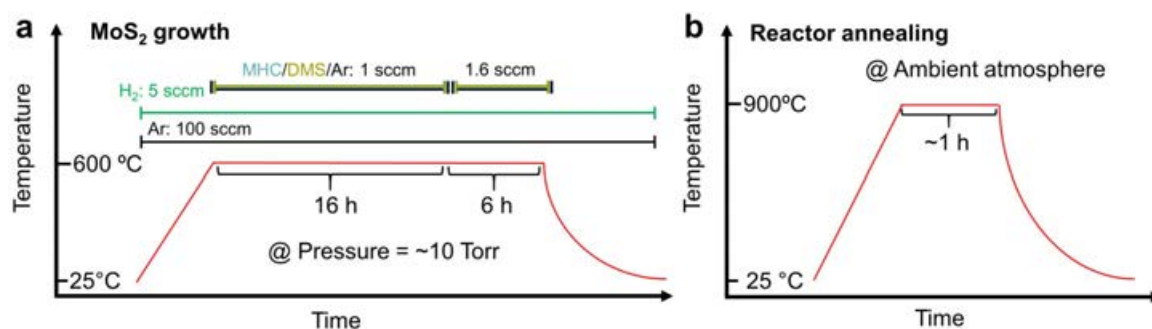
Figure 2.15 (a) Scheme of a typical growth process involves temperature ramp to the growth temperature of 600 °C under Ar/H_2 flow, start of growth by injection of $Mo(CO)_6$/DMS precursor provided from solution in a single canister, and fed by Ar carrier gas. First, domain nucleation and slow submonolayer film growth is carried out with 1 sccm Ar carrier during 16h, and can be extended to another 6h under higher 1.6 sccm Ar carrier flow to achieve 1-2L MoS_2. Ar/H_2 flow is kept during the whole growth phase, and is further maintained during cool down. **(b)** Reactor annealing step in ambient atmosphere at 900 °C is performed between consecutive growth runs to clean the quartz tube.

---

[4]http://www.scen.kr/

2.3.2 Substrates

The substrate plays an important role in the growth of MoS$_2$ thin films, as illustrated in Fig. 2.16. Amorphous substrates, such as SiO$_2$, result in the nucleation and growth of randomly aligned domains, which form polycrystalline thin films with large angle grain boundaries upon coalescence. Grain boundary defect densities can be reduced by decreasing the nucleation density and increasing the grain size. In contrast, growth on crystalline substrates, such as Al$_2$O$_3$(0 0 0 1), allows vdW heteroepitaxy of aligned domains with a preferred epitaxial relationship with respect to the underlying substrate, which can be a route towards single-crystalline films in the ideal case of unidirectionally merged domains without translational offsets [48, 261]. In this thesis, MoS$_2$ thin films have been grown on the following insulating substrates.
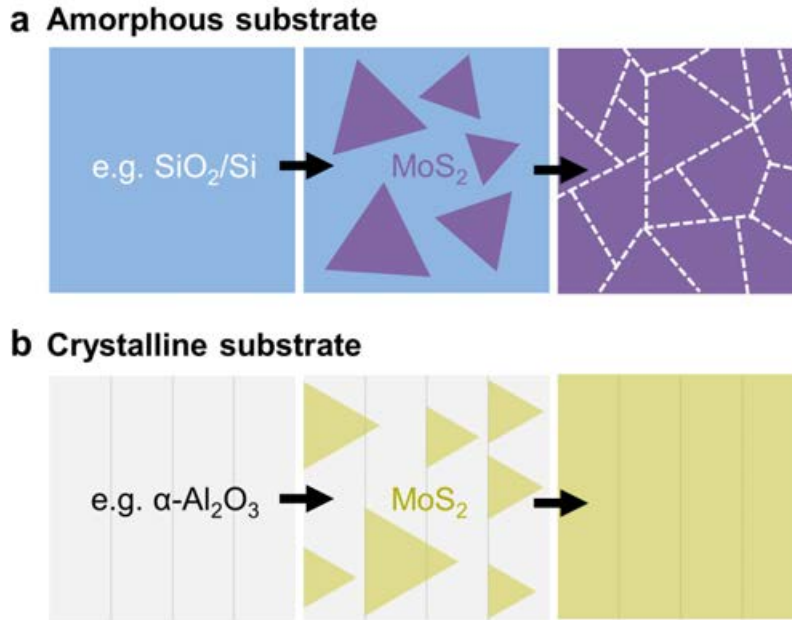
Figure 2.16 Influence of the substrate on MoS$_2$ growth. Schematic illustrations of nucleation and coalescence of MoS$_2$ thin films grown on **(a)** an amorphous substrate (e.g. SiO$_2$/Si), and **(b)** a crystalline substrate (e.g. α-Al$_2$O$_3$) with a vicinal, stepped surface.

Silicon oxide

SiO$_2$/Si^{++} substrates (SIEGERT Wafer GmbH, Germany) with 285 nm thick dry thermal oxide were used. Because of its semiconductor industry relevance, SiO$_2$ has been widely used for TMD synthesis taking advantage of its chemical inertness at high growth temperatures. SiO$_2$ also provides an ideal platform for optical characterization

by means of Raman and PL spectroscopy [262]. The highly boron-doped Si substrate ($<0.005\,\Omega\,\mathrm{cm}$) also offers the possibility to build simple, back-gated field-effect transistor devices (see appendix, Fig. D13).

Soda-lime glasses

For growth of MoS_2 thin films in section 3.4.1, three different, commercial soda-lime silicate glasses were used: 1) SCG 94 (Plan Optik AG, Germany) [263], 2) Marienfeld Superior (Paul Marienfeld GmbH & Co. KG, Germany) [264], and 3) B270®i (Schott AG, Germany) [265]. Due to their alkali (Na, K) content these substrates provide catalytic properties for growth of MoS_2 thin films with enhanced grain size [266, 267, 268]. More information about the glass composition and material characteristics is given in the appendix (table A2).

Sapphire

Sapphire is a commercially available, thermally stable and chemically robust substrate interesting for wafer-scale MoS_2 epitaxy [48, 255]. Double-side polished 2" c-plane $Al_2O_3(0\,0\,0\,1)$ wafers (99.998 % purity, Kyropolous-grown, SIEGERT Wafer GmbH, Germany) with nominal miscuts of 0.05° and 0.2° were used. For studying the impact of miscut direction, single-side polished $Al_2O_3(0\,0\,0\,1)$ with nominal miscut of 0.2±0.1° off the $A[1\,1\,\bar{2}\,0]$ and $M[1\,\bar{1}\,0\,0]$ directions were used (99.999 % purity, Kyropolous-grown, Cryscore Optoelectronic Ltd, China). For surface preparation, the substrates were sonicated in acetone/isopropanol for 5 min each and placed into covered alumina crucibles. Then, high-temperature annealing was performed to obtain "epi-ready", stepped surfaces with atomically-smooth terraces [269, 270]. Depending on the annealing requirements, substrates were annealed in a muffle furnace or alumina tube furnace [(]Fig. 2.17(a-b)]. Annealing programs with different dwell times (2, 6, 12 h), temperatures (1050 – 1350 °C) and gas atmospheres (H_2, Ar/5 %, Ar, O_2) were used [Fig. 2.17(b-c)]; the different annealing conditions aimed at preparing distinct starting surfaces (e.g. step morphologies and surface reconstructions) to test their effect on MoS_2 epitaxy. More details about the sapphire surface preparation are given in the appendix (section A.2).
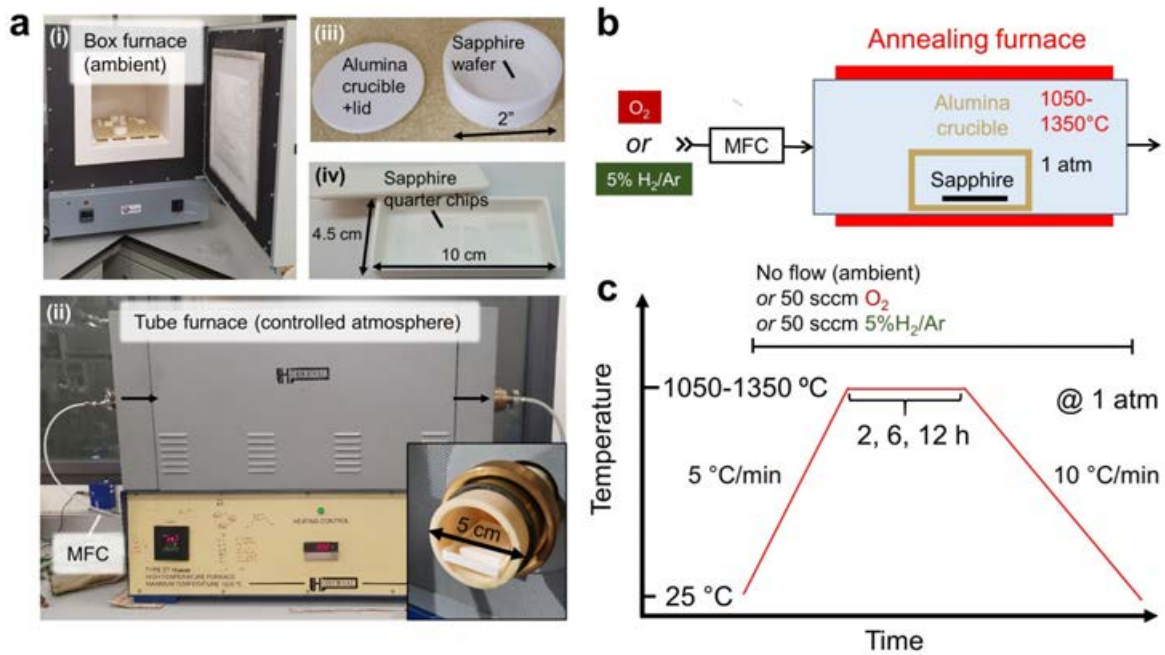
Figure 2.17 Sapphire substrate annealing. **(a)**(i) Box furnace for annealing in ambient air at 1050 °C, (ii) tubular furnace for high-temperature annealing up to 1350 °C in controlled atmosphere, (iii) alumina crucible for annealing of up to 2″ wafers in the box furnace, and (iv) 10×4 cm^2 rectangular crucible with maximum size fitting into the tube furnace. **(b)** Schematic of the tube furnace operable in oxidative or reductive conditions by flowing O$_2$ *or* 5 %H$_2$/Ar gas via a mass flow controller (MFC). **(c)** Schematic of annealing process.

2.3.3 Characterization methods

Surface analysis and thin film metrology are an essential part of the methodology of this thesis. A variety of characterization techniques ranging from microscopy, optical spectroscopy, and diffraction methods were used to investigate domain morphology and orientation, layer thickness, chemical compositions, crystalline structure, and (opto)electronic properties of as-grown, transferred and device-integrated MoS$_2$ thin films. Moreover, mass spectroscopy was employed for *in situ* gas-phase monitoring of the MOCVD process. In this section, specific methodologies and experimental parameters for the used techniques and equipments are described.

Scanning electron microscopy (SEM)

The morphology of MoS$_2$ thin films was analyzed by scanning electron microscopy (SEM) in different phases of the growth, from nucleation, over lateral domain expansion

until monolayer coalescence and growth of few-layer films. For high-resolution field emission SEM (FE-SEM) imaging, an FEI Magellan 400L XHR FE-SEM was used in immersion mode at low accelerating voltages of $2\,kV$ and $0.1\,nA$ beam current at a working distance of typically $4\,mm$. A sample bias of $4\,kV$ was used to compensate charging effects and a low-voltage, high-contrast detector (vCD) was used for back-scattered electron (BSE) material contrast imaging. This equipment and parameter choice allowed high-resolution routine imaging of MoS_2 domains with sizes from several tens of nanometers to micrometers even on the insulating growth substrates.

SEM image analysis was performed with the open-source program IMAGEJ 1.53 [271]. Thresholding of the film-substrate contrast was employed for creating binary images, removing image noise and segmenting stitching grains into separated domains. Starting from an original SEM image, the automatized algorithm included the following sequence of IMAGEJ operations: 1) Set scale (from original image), 2) Crop (remove original image caption), 3) Make binary, 4) Remove outliers, 5) Close, 6) Watershed, 7) Analyze particles. Figure 2.18 shows an exemplary SEM image after each execution step of the aforementioned algorithm. It is remarked that this method based on the film-substrate contrast only works well for non-coalesced films with isolated domains. Some images with high contrast noise had to be treated manually with added process steps, such as "Despeckle" or "Fill holes" commands.

Finally, the particle analysis tool was used to extract several film characteristics, including nucleation density N, film coverage χ, and domain size d_i of a domain with index i. N is defined as the domain count n_i per unit area A_{sub} of an SEM image, see eq. (2.2). χ is defined as the percentage of substrate area covered by the n_i domains with respective domain areas A_i per unit area A_{sub} of an SEM image, see eq. (2.1). The domain size d_i is defined as the side length of an equilateral triangle formed by the domain area A_i, see eq. (2.3), assuming that all domains have equilateral triangle shape. This might not always be the case, but is reasonable for comparison of equally extracted domain sizes.

$$\chi = \frac{n_i A_i}{A_{sub}} \cdot 100\,\% \tag{2.1}$$

$$N = \frac{n_i}{A_{sub}} \tag{2.2}$$

$$A_i = \frac{\sqrt{3}}{4}d_i^2 \tag{2.3}$$

Grain size histograms were created by data binning and plotting the frequency (domain count in each bin) over the calculated domain size. Then, the histograms were fitted by Gaussian or LogNormal functions depending on the best fit for the
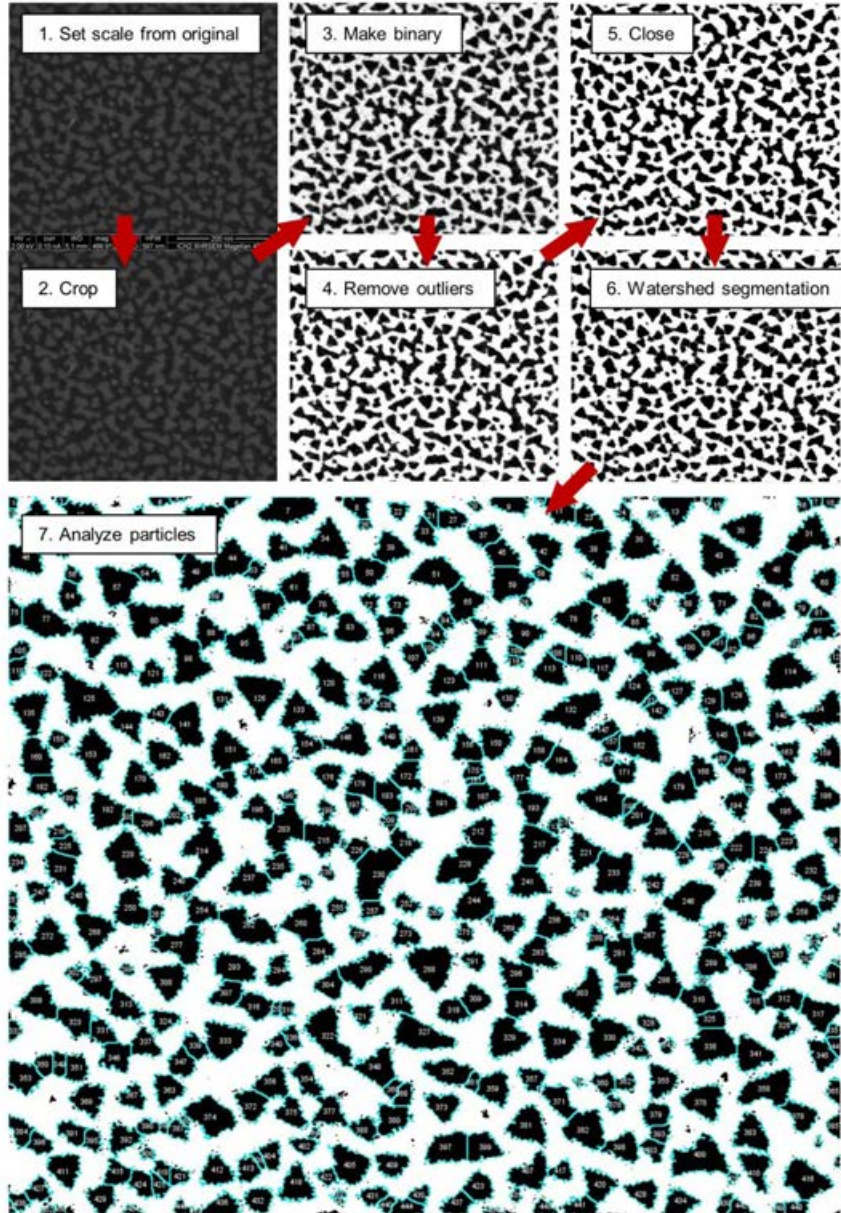
Figure 2.18 SEM image analysis algorithm with exemplary sequence of execution steps applied to a typical SEM image of MoS$_2$ domains grown on SiO$_2$ substrate.

distribution and the peak centers from the fitted distribution functions were extracted as mean grain sizes d_{mean}.

Atomic force microscopy (AFM)

Further morphological analysis of thin films was performed by atomic force microscopy (AFM), which gives additional information on the layer topography (e.g. thickness determination at layer step edges, roughness analysis). Moreover, AFM was used for analysis of substrate morphology of SiO_2, soda-lime glasses, sapphire starting surfaces and, in particular, the step morphology of the annealed sapphire surfaces.

AFM images were acquired with an Oxford Instruments Asylum Research MFP-3D in tapping mode using BudgetSensor Tap150Al-G tips ($5\,N\,m^{-1}$ spring constant, $150\,kHz$ resonance frequency), typically at 0.5–$0.8\,Hz$ scan rate. IGOR Pro 6.38B01 software was used for image corrections (flattening, plane-fitting, line artifact correction), and extraction of root-mean-square (RMS) surface roughness values.

For MoS_2 thin films grown in the Yonsei reactor (section 3.4.2 and chapter 4) AFM images were acquired with a Park Systems NX10 in non-contact mode using Olympus AC160TS tips ($26\,N\,m^{-1}$ spring constant, $300\,kHz$ resonance frequency) at $0.5\,Hz$ scan rate. MoS_2 domain orientation distribution were assessed from binarized images with the open-source IMAGEJ plugin ORIENTATIONJ v2.0.5 [272].

Transmission electron microscopy (TEM)

Transmission electron microscopy (TEM) was used for high resolution top-view (in-plane film morphology) and cross-sectional (out-of-plane film morphology) imaging of MoS_2 thin films. Furthermore, it was used to analyze crystallinity and domain orientation within polycrystalline thin films by electron diffraction.

TEM was carried out with a FEI Tecnai G2 F20 S-TWIN operating at $200\,kV$. For dark-field imaging in scanning TEM mode an off-axis, high-angle annular dark-field (HAADF) detector was used. For high-resolution TEM mode and selected-area diffraction a large $730\,nm$ aperture was employed to obtain signal averaged over many domains. The intensity profiles of diffraction patterns were analyzed with the software GATAN DIGITALMICROGRAPH v2.30.

For top-view analysis of MoS_2 thin films along the $[0\,0\,0\,1]$ axis, samples were prepared by spin-coating PMMA A4 950K (MicroChem, USA) onto MoS_2 thin films,

releasing them from their growth substrate (SiO_2 or sapphire) in $1\,mol\,L^{-1}$ NaOH (aq) and suspend them onto a holey carbon grid by a wet fishing transfer. For analysis of transfer-free sample, MoS_2 thin films were directly grown onto 18 nm thin PELCO™ SiO_2 support membranes (Ted Pella Inc., USA).

For cross-sectional analysis of MoS_2/SiO_2, $AlO_x/MoS_2/SiO_2$ and $MoS_2/hBN/Al_2O_3$ interfaces, a metal capping layer was deposited for protection during lamella preparation by a focused ion beam (FIB) in a Zeiss 1560XB Cross Beam. Then, the interfaces were imaged in STEM mode and the chemical line profiles across the interface were analyzed by EDX with a "super ultra-thin window" X-ray detector. For chemical profiling by electron energy loss spectroscopy (EELS), a Gatan imaging filter Quantum SE 963 fitted was employed to produce energy filtered images.

Raman and photoluminescence (PL) spectroscopy

Raman spectroscopy was used to detect phonon modes in MoS_2 thin films, which can give information about crystallinity and layer thickness/number, and allows to detect incorporated carbon impurities in the films. Moreover, semi-quantitative analysis of Raman peaks was used for monitoring trends of relative MoS_2 and C amounts within the growth parameter space.

The MoS_2 thin films were characterized under ambient conditions with a confocal Witec alpha300R A300M+ microscope at $100\times$ magnification using a laser with 488 nm excitation wavelength and a spot size of around $1\,\mu m$. If not otherwise highlighted in this work, a laser power of 0.2 mW was used to minimize laser heating effects, and to avoid optical doping and multiexciton dynamics in the PL measurements [273]. Integration times of 5 s and two accumulations were used. For parameter studies in chapter 3 for each sample, three spots were measured along the sample diagonal for averaged data and corresponding standard deviations as statistical errors. E^1_{2g} and A_{1g} Raman modes of MoS_2, Si, and carbon D and G bands were measured with a 600 grooves/mm diffraction grating within the same spectral window. For semi-quantitative Raman integral analysis, MoS_2 bands were fitted with double Lorentzians, Si bands with single Lorentzians, and the carbon D and G bands with double-Gaussians after first-order background subtraction. Within the fitting strategy, boundary conditions were used to exclude the contribution of a band appearing in the low-frequency shoulder of the D band and that could not be correlated to the growth conditions. For precise measurement of the E^1_{2g} and A_{1g} band positions and determination of the frequency

difference $\Delta(A_{1g} - E_{2g}^1)$, which can be used as a measure for layer thickness [274, 169], a high-resolution 1800 grooves/mm grating was used.

Photoluminescence (PL) spectroscopy was used to analyze the (opto)electronic properties, charge transfer, and quality of MoS_2 thin films. For PL measurements, a 600 grooves/mm grating was used. After background subtraction, Lorentzian peak fitting was performed with the Witec PROJECT 5.0 software to account for the charged trion A^-, neutral exciton A^0, and B exciton contributions. Fitting constraints were used for the peak positions based on the literature review of Lee et. al. [274] (see appendix for PL fitting parameters, table B2). The normalized PL intensity is used as a measure of sample quality, and is defined as the relative $(A^- + A^0)/B$ intensity ratio [275], i.e. as the peak integral ratio of summed A^- and A^0 contributions with respect to the B exciton.

X-ray and ultra-violet photoelectron spectroscopy (XPS/UPS)

The chemical composition and stoichiometry of the films was investigated by X-ray photoelectron spectroscopy (XPS) in ultra-high vacuum (UHV, $<1 \times 10^{-9}$ mbar) with a SPECS PHOIBOS 150 hemispherical analyzer using monochromatic Al Kα radiation with an energy of 1486.6 eV. To compensate for sample charging, in particular for non-conducting samples or samples on insulating substrate, spectra have to be energy-corrected against a reference peak. Often the C1s peak from adventitious carbon is chosen for practical purposes. However, this is not convenient when C is the sample material of interest. For analysis of MoS_2 thin films, the substrate peak of the thermally oxidized SiO_2/Si substrates (Si 2p, 103.3 eV [276]) or sapphire Al_2O_3 (Al 2p, 74.4 eV [277]) were chosen as reference peak. Peak fitting of the high-resolution core level spectra was performed with the software CASAXPS v2.3.17 employing Gaussian-Lorentzian (GL) line shapes and Shirley backgrounds. Details about analyzed transitions, peak assignment, fitting parameters and constraints are given in the appendix (table B1). As indicated, reference samples were used to set constraints for peak positions, FWHM, and peak shape. A natural MoS_2 crystal was measured as a reference for binding energy positions, FWHM and shape of Mo 3d, S 2s and S 2p core level peaks of the as-grown films, and was found in accordance to literature data [278]. For fitting of C 1s peaks, area constraints extracted from an adventitious carbon reference were utilized, as will be discussed in section 3.2.3. For fitting of Mo 3d and S 2p doublets an area constraint was applied satisfying 3:2 and 2:1

intensity ratios as per the electron population of d and p orbitals [277]. Equal FWHM was used for peaks within the same doublet.

Ultra-violet photoelectron spectroscopy (UPS) allows to extract valence band edge positions, work functions and ionization potentials, which is helpful to analyze valence band shifts resulting from doping, and to determine band alignment models of heterostructure interfaces. In this work, the interfaces of MoS_2/C in C-contaminated MoS_2 thin films and MoS_2/AlO_x in oxide encapsulated MoS_2 thin films were studied. UPS measurements were performed using a He-I lamp (21.2 eV). For determination of ionization potentials from the spectral width between the secondary electron cut-off and the valence band egde, a -10 V sample bias was applied to shift the secondary electron background above the work function of the analyzer, following the procedure of Diaz et al. [279]. Valence band edges were determined by extrapolation onto the energy axis.

Mass spectroscopy with residual gas analyzer (RGA)

Mass spectroscopy by a residual gas analyzer (RGA) allows to diagnose the residual gas composition in vacuum system, such as growth reactors. Furthermore, it can be used for gas-phase monitoring during MOCVD processes. In this work, it was used to study temperature-dependent pyrolysis processes of the used organosulfide precursor DES, which affects the film quality. This provides *in situ* information complementary to *ex situ* film analyses.

A Hiden Analytical HPR-30 RGA equipped with a triple filter quadrupole mass spectrometer was used for vacuum diagnosis and *in situ* gas-phase monitoring. The RGA is connected downstream the reaction zone in the ICN2 reactor via a sampling needle valve (see Fig. 2.12). The pressure inside the RGA was set to 1×10^{-6} Torr. Soft electron ionization at a low electron emission energy of 12 eV and 100 μA emission current was used to minimize electron-ionization-induced fragmentation of the DES molecular ion and for selective detection of DES pyrolysis products. A secondary electron multiplier detector was used for high sensitivity detection in the acquisition range of 1×10^{-11} Torr. For the temperature-dependent DES pyrolysis study, the reactor temperature was ramped at $10\,°C\,min^{-1}$ from room temperature to $800\,°C$ while introducing different $DES/Mo(CO)_6/H_2$ mixtures and continuously monitoring the partial pressure of gas-phase constituents; for example, the partial pressure evolution of unfragmented DES molecular ion ($m/z = 90$) and main pyrolysis products, such as ethyl radicals ($m/z = 29$) and ethylene ($m/z = 28$) was followed. Selective ionization

of ethylene is ensured by the low ionization energy, which avoids the formation of hard-to-distinguish isobaric ions of N_2 and CO, requiring higher ionization energies than used in this experiment. This also means that H_2 could not be detected under these conditions due to its higher ionization energy.

Reflection high-energy electron diffraction (RHEED)

Reflection high-energy electron diffraction (RHEED) was used for analysis of MoS_2 thin films grown on sapphire to determine crystallinity and the in-plane epitaxial relationship of the $MoS_2/Al_2O_2(0001)$ heterostructure. Furthermore, it was used to determine the surface reconstruction of annealed Al_2O_3 surfaces.

Ex situ RHEED measurements were done within a high vacuum chamber, with a base pressure of around 1×10^{-7} Torr. An RDA-002G electron-gun with remote control power supply RDA-004P (R-DEC Co. Ltd., Japan) was used, allowing for beam alignment via an XYZ lens, and setting the acceleration voltage (24 kV) and filament emission current (34 μA). The sample was mounted face-down onto the specimen holder that allows manual control over azimuthal rotation. A kSA 400 system (k-Space Associates, Inc., USA) equipped with a digital camera to record the fluorescence screen was used to capture the projected RHEED patterns. A related software package (v4.76) was used for line profile analysis. To convert the reciprocal distances from pixels measured on the screen to reciprocal space units (Å^{-1}), a calibration factor of 6.5×10^{-3} Å^{-1}/pixel was determined by means of a c-plane sapphire reference sample with known lattice constant of 4.76 Å.

Grazing Incidence X-ray Diffraction (GIXRD)

Grazing incidence X-ray diffraction (GIXRD) was used as another, complementary tool to determine the in-plane $MoS_2/Al_2O_2(0001)$ epitaxial relationship and orientational domain dispersion (mosaic spread) as figures of merit of epitaxial film quality. It was also used for fine analysis of sapphire surface reconstruction patterns and reciprocal space mapping of the $MoS_2/Al_2O_2(0001)$ heterostructure.

Laboratory GIXRD was carried out with a PANalytical X'PERT PRO MRD using a horizontal ω-2θ goniometer (320 mm radius) in a four-circle geometry under ambient conditions (see appendix Fig. C23). An X-ray tube with Cu Kα anode ($\lambda = 1.540$ Å) is used operating at 40 kV accelerating voltage and 45 mA filament current. The generated X-ray beam is directed onto the sample with a low incidence angle of around 0.3°.

The sample was placed and adjusted in-plane on a XYZ double-tilt sample stage by maximizing the sapphire substrate signal. In the primary beam a Ni filter was used to remove Cu Kβ radiation of the X-ray source in order to avoid polychromatic diffraction peaks, and a polycapillary lense was used for improved sample illumination intensity. While the use of a soller slit was omitted for improved intensity, a 0.27° parallel plate collimator was used to reduce divergence of the diffracted beam, which was captured by a 256×256 array PIXcel X-ray detector. Azimuthal (ϕ) line scans were performed over a full 360° wafer rotation around the normal axis [280], where $\phi = 0°$ is defined along the $(1\,1\,\overline{2}\,0)$ direction corresponding to the normal of the A-plane primary wafer flat of the c-sapphire wafer. Such measurements required long integration times and took about 10 h due to the low-intensity signal coming from the 2D MoS$_2$ thin films.

Synchrotron GIXRD was carried out at beamline BM32 at the European Synchrotron Radiation facility (ESRF), allowing faster data aquisition compared to the lab experiment due to the use of highly brilliant X-ray radiation. Experiments were performed in the INS2 setup dedicated to surfaces and interfaces in an UHV system with a base pressure of 3×10^{-10} mbar equipped with a z-axis diffractometer (see photos and schematics in the appendix Fig. C24a). For an enhanced MoS$_2$ signal over background, a beam energy of 11.19 keV was chosen and the grazing incidence angle was set below the critical angle of total external reflection at 0.175°. The diffraction signal was aquired with a 256×1280 pixels MAXIPIX 2D detector (ESRF, France). Appropriate regions of interest were defined on the detector for signal integration. For the measurement, the specimen has to be placed in vertical position on the six-motion goniometer head, for which $\sim 0.7 \times 0.7$ cm^2 sized samples were sticked onto the specimen holders heated on a hotplate by using molten In shots (40338, Alfa Aesar GmbH & Co KG, Germany). Samples were inserted into the UHV system and outgassed in a pre-chamber at 200 °C (1 h) before transfer into the measurement chamber. Then, beam and sample alignment procedures (t_x, t_y, t_z) were performed to set the sample in the homocenter of the in-plane diffraction configuration (see appendix, Fig. C24c). For in-plane scans, the ω and δ motors were moved: radial scans are performed by rotating around ω and in two-fold increments of δ (equivalent to the commonly used definition ω-2θ in the lab setup), and azimuthal scans were performed by rotation around ω (equivalent to ϕ-scans in the lab setup). For consistency, ϕ will be used to refer to in-plane, azimuthal scans for both laboratory and synchrotron experiments.

For extraction of the angular, in-plane domain dispersion (mosaic spread) from azimuthal line scans, diffractograms were background-subtracted with a constant baseline and fitted with Pseudo-Voigt functions using the software ORIGINPRO 2018.

For quantifying the domain dispersion, FWHM values of the diffraction peaks were averaged and standard deviations were calculated.

2.3.4   MoS$_2$ FET device fabrication and characterization

In semiconductor and integrated circuit manufacturing, microfabrication techniques have been established to produce electronic devices on wafer-scale with high throughput and high yield. Despite being mature technologies for conventional semiconductors, their use to process 2D materials is relatively recent and still requires adaptation. The techniques used in this thesis include photolithography, etching, metallization, and oxide integration, which will be briefly described in the appendix (section A.3). Microfabrication and wafer processing was carried out at the ICN2 Nanofabrication facility and CNM-IMB (CSIC) cleanroom. Detailed protocols, process parameters and used equipment and chemicals are given in the appendix (section D.4).

Electrical characterization of FETs

FETs are three-terminal devices and the classical building blocks of electronics, as schematically illustrated in Fig. 2.19a. A FET allows modulation of a current I_{DS} flowing through a semiconducting channel between two contacts called "drain" and "source" by applying an electric field in form of a gate voltage V_G. The gate bias generates an electric field across a dielectric layer (often an oxide, such as Al_2O_3), which is separating the gate electrode from the channel. This concept is the foundation of logic circuitry, where control of V_G allows to switch between a charge-carrier-depleted, low conductivity state (off-state) and an enhanced charge carrier concentration, high conductivity state (on-state). The correlation between I_{DS} and V_G is represented in the characteristic transfer curve. The I_{DS} is further controlled by the source-drain voltage V_{DS} represented in the output curve (Fig. 2.19b). In the following, FET characteristics and key figures of merit are defined and formulas for their extraction are introduced.
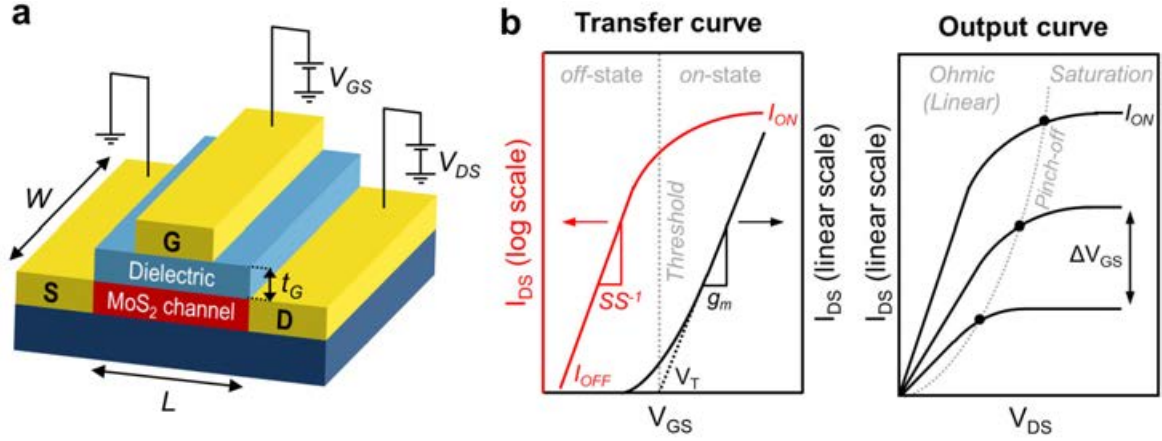
Figure 2.19 MoS$_2$ field-effect transistor (FET) device structure and electrical characteristics. **(a)** Sketch of the three-terminal device consisting of the semiconducting channel, source (S) and drain (D) metal contacts, gate (G) metal electrode and dielectric, typically an oxide insulator or ionic liquid/gel in case of electric double layer (EDL) gated devices. Potentials applied to the terminals are defined as the drain-source voltage V_{DS} and gate-source voltage V_G. Important geometrical dimensions are the width W, length L, and dielectric thickness t_G. **(b)** Schematic representation of an idealized I_{DS}-V_G transfer curve both in logarithmic (left axis) and linear scale (right axis) and I_{DS}-V_{DS} output curve for different gate voltages, where key device characteristics and working regimes are highlighted.

On/off-current ratio

The on/off-current ratio I_{ON}/I_{OFF} is the ratio between the drain-source currents in the "on" state and the "off" state. In this work, I_{ON}/I_{OFF} is extracted as the ratio of maximum and minimum currents within the V_G-switching window. In certain cases full accumulation (depletion) regimes for on (off) states might not be reached within the used switching window (typically $\pm 9\,\mathrm{V}$); however, higher bias values were avoided anticipating that the maximum $\pm 9\,\mathrm{V}$ switching window was limited by the electronics used in the test station for characterization of flexible neuroprosthetic devices.

Field-effect mobility

The field-effect mobility μ_{FE} is an important characteristic determined by the 2D channel material quality and its environment. It can be extracted from the transfer curve by eq. (2.4) [281]:

$$\mu_{FE} = \left(\frac{\partial I_{DS}}{\partial V_G} \right) \frac{W}{L} \frac{1}{C_G V_{DS}} = g_m \frac{W}{L} \frac{1}{C_G V_{DS}} \tag{2.4}$$

Here, $g_m = \left(\frac{\partial I_{DS}}{\partial V_G}\right)$ is the transconductance, W and L are the width and length of the channel, respectively, C_G is the capacitance of the gate dielectric, and V_{DS} is the applied voltage between drain and source. While intrinsic mobility is a material property, the field-effect mobility can be dominated by extrinsic effects, such as device structure/geometry and in particular the contact resistance R_C [282, 283], and may also depend on the method used to calculate the mobility. In this work, μ_{FE} is extracted at the peak transconductance.

Threshold voltage V_T

The threshold voltage V_T is the minimum V_G at which a significant current starts to flow between the source and drain terminals. V_T is an important scaling factor to control power efficiency and a stable V_T is important for device reliability. Many different methods have been proposed for V_T-extraction [284, 283]. In this work, the popular linear extrapolation method is chosen. It consists in finding the interception point of the linear extrapolation of the I_{DS}-V_G curve at its maximum slope (i.e. peak transconductance g_m), as illustrated in the transfer curve plotted for the linear scale in Fig. 2.19b. Although, the maximum slope point might be uncertain in some cases and the extrapolated V_T can be influenced by parasitic series resistances, mobility degradation and may be impacted by hysteresis threshold voltage shifts ΔV_T [63, 61]; however, this method has the advantage of simplicity and practicality compared to other methods, often yielding very similar results [284].

Subthreshold slope

The subthreshold slope SS is the gate voltage required to increase the drain current by a factor of 10, which characterizes the switching speed of the FET. It is typically extracted from the transfer curve plotted in log_{10} scale [285] according to eq. (2.5):

$$SS = \frac{\partial(log_{10} \ I_{DS})}{\partial V_G} \tag{2.5}$$

The ideal SS limit is $60\,\mathrm{mV\,dec^{-1}}$ at room temperature [282]. In this work, SS is extracted from the maximum slope of the transfer curve in logarithmic scale (yielding the lowest SS value, as the SS may be variable with V_G) [282]. The switching behaviour and SS are highly dependent on channel defects and the interface trap density D_{IT} that can be obtained from eq. (2.6) [282]:

$$SS = \frac{mk_BT}{q}ln(10); m = \left(1 + \frac{C_{MoS2}}{C_G} + \frac{C_{IT}}{C_G}\right); C_{IT} = qD_{IT} \qquad (2.6)$$

Here, q is the elementary charge., C_{MoS_2} is the quantum capacitance of MoS$_2$ (which will be assumed as $C_{MoS_2} = 0$ for fully depleted FETs [282]), and C_{IT} is the interface trap capacitance. It is noted that for 2D semiconductor devices it is difficult to differentiate the channel and interface defects contributing to D_{IT} [61].

Gate capacitance and dielectric constant

The gate dielectric can be understood from the model of a parallel plate capacitor with plates of area A_G and capacitance C_G. Its value can be measured by capacitance-voltage measurements of metal-insulator-metal (MIM) test structures, such as in the case of solid(oxide)-gated devices [286], or by cyclic voltammetry in case of liquid(EDL)-gated devices [136]. Here, $C_G = C_{OX}$ was only determined for MIM test structures. Literature values were considered for $C_G = C_{EDL}$ of EDL-gated devices. CV-measurements of MIM test structures were performed with a potentiostat at room temperature at 100 kHz for voltages between -9 and 9 V, to determine the dielectric constant κ of ALD-deposited AlO$_x$ gate dielectric and its stability in the common gate bias working range of flexible, monolithically integrated FET devices studied in chapter 5. For a ring capacitor geometry with area $A_G = A_{OX}$ the unit area capacitance C_{OX} of the gate oxide is described by eq. (2.7):

$$C_G = \frac{\epsilon_0\epsilon_r}{t_G A_G} \qquad (2.7)$$

Here, ϵ_0 is the vacuum permittivity and ϵ_r is the relative permittivity, often referred to as the dielectric constant κ in case of oxide dielectrics, and t_G ($= t_{OX}$) is the thickness of the dielectric (oxide). Formula eq. (2.7) can also be applied to ionic gel/liquid-gated FETs [287]. Under gate bias, mobile ions in solution form an electric double layer (EDL) at the channel-electrolyte interface, which can be regarded as an ultra-thin capacitor with thickness $t_G = t_{EDL}$ of around 1 nm. This results in very high C_{EDL} values of typically on the order of 1 to 4 µF cm^{-2} [287]. Here, a value of $C_{EDL} = 2$ µF cm^{-2} was chosen for calculation of field-effect mobilities of EDL-gated FET devices. For more precise determination of mobility values of EDL-gated FET devices, C_{EDL} should be determined experimentally [136].

Additionally, multi-frequency CV-measurements were performed on metal-insulator-semiconductor-metal (MISM) test structures for voltages between $-9\,\text{V}$ and $9\,\text{V}$ to analyze traps at the $\text{MoS}_2/\text{AlO}_x$ interface via the conductance method [288, 289, 286]. For this purpose, the parallel conductance G_p as function of the frequency f (angular frequency $\omega = 2\pi f$) was extracted from the measured capacitance C_m and the measured conductance G_m by eq. (2.8):

$$G_p = \frac{\omega^2 G_m C_{OX}^2}{G_m^2 + \omega^2(C_{OX} - C_m)^2} \tag{2.8}$$

The relation between G_p/ω and the interface trap density D_{IT} is given by eq. (2.9):

$$\frac{G_p}{\omega} = \frac{q D_{IT}}{2\omega\tau_{IT}} ln[1 + \omega(\tau_{IT})^2], \tag{2.9}$$

The interface trap density D_{IT} and the respective time constant τ_{IT} can be deduced from the following relations eq. (2.10) andeq. (2.11):

$$D_{IT} = \frac{2.5}{q}\left(\frac{G_p}{\omega}\right)_{peak} \tag{2.10}$$

$$\tau_{IT} = \frac{1.98}{2\pi f_0} \tag{2.11}$$

Here, $(G_p/\omega)_{peak}$ is the maximum G_p/ω value and f_0 is the frequency at this maximum value.

Chapter 3

MOCVD of MoS$_2$ thin films grown from organosulfide precursors

For the technological adoption of semiconducting 2D TMDs and their prospective commercial use in (opto)electronic applications, it is essential to develop large-scale and reliable methods for the synthesis of homogeneous, electronic-grade and low-defect density thin films. MOCVD is established in conventional compound semiconductor manufacturing and has emerged as a promising synthesis method for 2D TMDs. However, unintentional carbon incorporation has ever since been a concern in MOCVD and more recently in the field of 2D TMD growth — in particular due to the widespread use of organic chalcogen precursors as less harmful alternatives to toxic chalcogen hydrides. Therefore, it is necessary to elucidate the underlying mechanisms of carbon incorporation, and mitigate its undesired impact on 2D TMD growth and film properties. This requires a fundamental understanding of the influence of key growth parameters and process engineering to tailor thin films with well-controlled impurities and large grain size for high-performance electronic device applications.

This chapter provides a brief review on the MOCVD of TMDs, particularly focussing on carbon incorporation, which is a central research topic of this thesis. MoS$_2$, as a prototypical TMD example, is synthesized from Mo(CO)$_6$ and organosulfides (DES, DMS) on amorphous SiO$_2$ substrate as model systems to investigate key growth parameters, highlighting the crucial role of C-containing side-products arising from organosulfide pyrolysis. For this purpose, *in situ* gas-phase monitoring (mass spectroscopy) and a wide range of *ex situ* microscopy (SEM, AFM, TEM) and spectroscopy (Raman, PL, EDX, XPS/UPS) film analysis techniques are used to systematically

study the effect of growth time, temperature and precursor/gas mixture ratios on film morphology, composition, stoichiometry and (opto)electronic properties. It is found that high chalcogen-to-metal ratios and elevated temperatures above organosulfide pyrolysis onset ($\gtrsim 600\,°C$) are aggravating the formation of nanographitic carbon that competes with and disrupts lateral 2D MoS$_2$ growth. Furthermore, photoluminescence and photoelectron emission studies suggest that the process-induced C impurities result in doping of MoS$_2$ at the MoS$_2$/C heterointerface and produce trap states in the MoS$_2$ midgap. Adding optimized flows of H$_2$ gas to the growth process allows to control and reduce C impurities, enabling the growth of continuous mono- to few layer thin films. Alkali-assisted and low-growth-rate approaches are further discussed aiming at polycrystalline MoS$_2$ films with enlarged grain sizes for reduced grain boundary defects and improved electrical transport properties.

The main content of this chapter has been published in [234]:

Schaefer, C. M.; Caicedo Roque, J. M.; Sauthier, G.; Bousquet, J.; Hébert, C.; Sperling, J. R.; Pérez-Tomás, A.; Santiso, J.; del Corro, E.; Garrido, J. A., Carbon Incorporation in MOCVD of MoS2 Thin Films Grown from an Organosulfide Precursor. Chem. Mat. 2021, 33 (12), 4474-4487.

3.1   Review and roadmap of MOCVD-grown TMDs

Before entering into the experimental part of this chapter, the following section will summarize the promise and recent advances of MOCVD of 2D TMD semiconductors while discussing open challenges. Among many of them C incorporation and grain size enhancement are pointed out as the relevant research topics for this thesis.

Promise and state-of-the-art

Over the past decade, the pressing demand for mass production of 2D TMDs has attracted great interest in large-scale, bottom-up vapor-phase synthesis methods. MOCVD is a promising technique because it fulfills important industrial criteria, such as controllability, reliability, scalability, and versatility. This is thanks to the MOCVD working principle, which relies on precisely dosing and spatially even gas supply from external precursor sources into a heated reaction zone for uniform film growth across large substrate areas. The strict control over vapor-phase chemistry allows homogeneous

and fine-tuned film composition, and the steady delivery over extended times guarantees stable and reproducible conditions. Precursor selection enables the growth of a variety of materials; moreover, independently selectable precursor sources may be used for in-process composition control, doping and heterostructure growth. The exploitation of these benefitial aspects and successful adoption of MOCVD for layered TMD synthesis is well documented by recent literature examples. In 2015, the work of Kang et al. published in *Nature* marked an important milestone by demonstrating the controllable deposition of homogeneous, atomically-thin MoS_2 and WS_2 films on 4" wafers [47]; this was soon followed by reports on the reliable and precise monolayer [290] and layer-by-layer thickness control [291, 169]. The scalable, wafer-compatible synthesis process was further advanced by the use of industry-standard reactor technology, such as showerhead-type injectors [197, 170], and rapid growth for high-throughput manufacturing [167]. More recent studies have shown the versatile engineering opportunities of versatile source supply for tunable TMD composition in $WS_{2x}Se_{2(1-x)}$ alloys [292], *in situ* substitutional doping of MoS_2 via Nb [72], or WSe_2 via Re [293] atoms, as well as different combinations of lateral, in-plane $(Mo,W)(S/Se)_2$ heterostructures [294, 295] and vertically stacked heteroepitaxial MoS_2/WS_2 vdW superlattices [195]. Besides the quickly rising number of MOCVD-related publications documenting the growing academic interest, also an increasing industry interest can be observed. An indicator for the latter trend is the market entry of semiconductor deposition equipment manufacturers, such as AIXTRON, CVD EQUIPMENT CORPORATION / FIRSTNANO or OXFORD INSTRUMENTS, which have targeted the field of 2D materials by adding adapted research and small scale production systems to their product portfolio [296]. This highlights the fast-paced adoption of MOCVD for 2D thin film manufacturing.

Despite the recent advances and maturation of MOCVD for large-scale fabrication of TMD semiconductors, there are still many challenges to be overcome, as summarized in the roadmap shown in Fig. 3.1. Namely, precursor selection, epitaxy, optimization of growth conditions and growth modes, improvement of crystalline film qualities and transport properties, as well as gaining full control over doping and defect engineering, can be mentioned. For more detailed explanations on the specific topics, the interested reader is referred to the comprehensive review by Lee et al. [203] It should be commented that the current status in solving these issues might not always move along a linear path, as suggested by the illustration. Instead, the research advances on parallel fronts while facing the multiple challenges related to the multi-factor nature of the MOCVD process, involving complex surface and gas-phase processes with often interrelated dependencies that complicate technology progression.
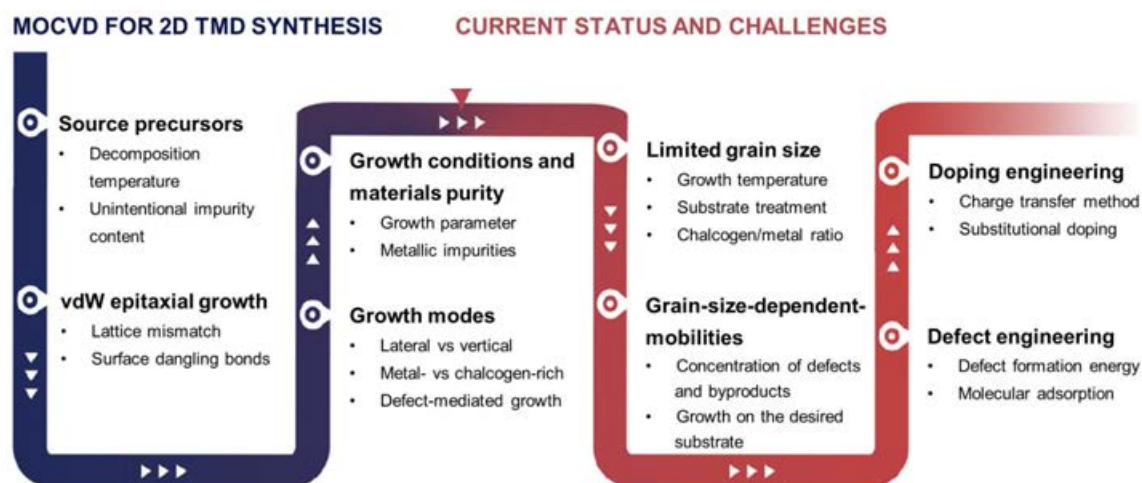
Figure 3.1 Roadmap for MOCVD of TMDs. Recent advances, current status, and open challenges. Adapted from [203]. © 2020 American Chemical Society.

Carbon incorporation as prime challenge

Among the numerous challenges, in particular, the choice of precursors is fundamental to every MOCVD process. It is obvious that the starting material and purity of the used source compounds determine the elements entering the reaction environment for deposition of the final thin films, including the possibility of unintentional impurity incorporation if undesired species do not leave the reaction as gaseous side-products. For example, and as MOCVD employs by definition carbon-containing (metal)-organic precursor, carbon impurities are a common concern. Such impurity incorporation may affect various other synthesis aspects marked on the roadmap (Fig. 3.1), such as the optimal growth conditions, resulting growth modes, grain sizes and (opto)electronic film properties. Therefore, MOCVD process engineering is generally dependent on the selected precursor chemistry [172], and the same holds for 2D TMD synthesis.

Theoretical phase diagram modelling has predicted the broadly used transition-metal hexacarbonyl precursors [Mo(CO)$_6$, W(CO)$_6$] to be a potential source of C impurities for temperatures $\lesssim 575\,°C$ [188, 297, 298]. Furthermore, the selected chalcogen source has shown to play a crucial role in the realization of electronic-grade TMDs, for which typically elevated temperatures $\gtrsim 800\,°C$ are desired to achieve high crystalline quality thin films [239, 190]. While carbon-free chalcogen hydrides (H$_2$S, H$_2$Se) are viable precursors according to thermodynamic predictions [188, 297, 298], and may be preferable from a film purity perspective according to experimental studies [239, 190], their high toxicity[220] raise cost and safety concerns, thus motivating further

research into "hydride-free" processes [198] using the less hazardous organic chalcogen counterparts. Focussing on organosulfides for the case of MoS_2/WS_2 synthesis, a variety of precursors have been employed (DMS [180, 192, 115, 193], DMDS [196, 115], DES [47, 190, 194, 195], DEDS [167, 197], DTBS [177, 198, 199]), as listed and compared in the introduction section 2.2.2 in view of their physicochemical properties . Among the many options, following the pioneering work of Kang et al. [47], and due to low-cost and easy availability, DES has become a popular choice, and as such, was also used in this work alongside DMS as representative, organic chalcogen precursors.

As mentioned, this selection implies the challenge of C incorporation, and therefore, remains to be a highly relevant topic that raises a series of research questions about the potentially introduced C impurities:

- What are the underlying reaction mechanisms for their formation?

- What is the their chemical form?

- Are they incorporated into the film or at the interface?

- How is the TMD film growth mode impacted?

- How does the C content depend on the growth parameters?

- How are film morphology, composition, and (opto)electronic properties impacted?

- How can undesired C impurities be mitigated?

The formation of highly reactive C radicals [299] during organosulfide pyrolysis is expected to be a main mechanism behind C impurity formation in TMD films [225, 190], which is supported by various thermal decomposition studies for DMS [228, 227, 229], DES [300], DMDS [226, 227, 230], and DTBS [301, 302]. The type of carbon introduction into TMD thin films is controversially discussed, which might be related to the particular TMD, individual process conditions and/or the capability of material characterization in each specific case. Some researchers observed codeposited "amorphous carbon" [180] or "defective graphene [225] to form simultaneously with the TMD layer at the substrate/TMD interface; others discuss carbon inclusion into TMD crystals through substitutional doping of the TMD basal-planes, such as C atoms at chalcogen sites in MoS_2 [303], CH functionalization in WS_2/WSe_2 [73, 304], or carbide transformation of the TMD edge [305]. Edge carbidization of MoS_2 nano-catalysts is well-known in the field of refining and hydrodesulfurization of organic fuels [306], referred

to as "coking/deactivation" [307, 308]. From atomistic hydrodesulfurization studies it is also known that H$_2$/H$_2$S hydrotreating conditions sensitively affect termination and edge sulfidation degree of MoS$_2$ nano clusters [105, 108], from which important mechanistic insights can be deduced for the role of sulfiding agents during domain edge expansion and shape evolution in MoS$_2$ synthesis. While the use of H$_2$S with its high sulfiding potential can yield the thermodynamically favored triangular MoS$_2$ domain shape, the use of organosulfides like DMS or DES may result in disturbed crystallinity and more roundish domain shape [115, 190]. Despite this disturbance Tuxen et al. did not find any sign of C inclusion at the edges or inside the MoS$_2$ sheet after sulfidation [115] raising the question about the exact role of carbonaceous species in the atomistic processes during MoS$_2$ edge reactions and reconfiguration. Nevertheless, it has been commonly observed in MOCVD studies that the lateral 2D TMD growth is impeded by C impurities, resulting in disrupted film morphologies and limited grain sizes [177, 225, 190]. Furthermore, C impurities alter the (opto)electronic properties of TMD films. Recent reports have suggested intentional C incorporation for *p*-doping and tailoring electronic TMD devices [225, 190]; unintentional C incorporation, on the other hand, may have unfavorable effects, such as quenched photoluminescence [190, 303] and/or a shift from semiconducting to conducting film properties, thus resulting in poor on/off transistor performance [180, 58]. Consequently, it is crucial to monitor and be in control of the C impurity level in TMD films.

Several mitigation strategies have been used to reduce C incorporation, such as alkali-assisted growth [180], water-assisted growth [309, 199, 170], low-pressure conditions [177], high-temperature substrate pre-treatment in H$_2$-atmosphere [177], and most commonly by working under reductive H$_2$ conditions while avoiding the thermodynamically unfavorable use of inert carrier gases [188, 310, 225, 190]. However, systematic studies especially dedicated to C incorporation are sparse and common practice in most studies relies solely on post-growth film characterization by qualitative Raman spectroscopy as the single method of carbon analysis. At present, little effort has been devoted to *in situ* gas-phase monitoring and a more quantitative and systematic approach is desired to correlate the C content with different growth parameters, such as temperature and gas-phase composition, by multiple, independent analysis techniques. In this regard, also hot- and cold-wall reactor designs and their impact on C formation rates are subject of ongoing research [190]. Therefore, the role of organosulfide precursor pyrolysis in TMD growth depending on the reaction conditions is not fully explored. Better understanding the origin, effect and mitigation of C incorporation is essential in the search of optimal growth conditions to produce thin films with desirable properties.

3.2   MoS$_2$ growth parameter study

The MOCVD synthesis of mono- to few layer MoS$_2$ thin films was chosen as a model system for TMD growth from organic chalcogen precursors. Thin films were grown from the gas-source precursors Mo(CO)$_6$ and DES in a home-built, vertical, hot-wall reactor described in section 2.3.1. To address the previously formulated research questions on C incorporation in section 3.1, a systematic study was performed for single- and multisource DES, Mo(CO)$_6$, DES/Mo(CO)$_6$, and DES/Mo(CO)$_6$/H$_2$ gas mixtures and varied growth times and temperatures. Extensive *ex situ* film characterization, such as by SEM, TEM, AFM, semi-quantitative Raman, PL spectrocopy and XPS are correlated with *in situ* gas-phase monitoring to elucidate the role of DES pyrolysis in C incorporation and impact on thin film morphology, composition, stoichiometry and (opto)electronic properties.

A schematic of the MOCVD reactor and growth process is shown in Fig. 3.2. Low-pressure conditions (10^{-2} to 10^{-1} Torr) during the growth phase were chosen for vapor draw of the Mo and S precursors into the vacuum reaction chamber without any inert carrier gas, which was motivated by the previously reported benefits for (carbon) contamination-free growth windows [311, 177, 188, 297, 298]. SiO$_2$/Si was chosen as substrate due to its technological relevance in semiconductor industry and because of its chemical inertness at high growth temperatures, while offering an excellent platform for optical characterization by Raman and PL spectroscopy [262]. The choice of 285 nm oxide thickness allows enhanced optical MoS$_2$ visibility [312] and signal intensity due to optical interference [313].

The illustration contains a simplified model of the MOCVD process, including (1) the delivery of vaporized Mo(CO)$_6$ and DES precursors from the external bubblers into the reaction chamber that is precisely dosed by needle metering valves, (2) gas-phase pyrolysis of Mo(CO)$_6$ and DES at high temperature, (3) adsorption and diffusion of Mo and S species on the SiO$_2$ substrate, (4) partial S desorption, and (5) nucleation and lateral growth of MoS$_2$ domains, while simultaneous deposition of graphitic C(sp^2) impurities may occur, and (6) release of gaseous byproducts, such as carbon monoxide CO, ethylene C$_2$H$_4$, hydrogen H$_2$, and hydrogen sulfide H$_2$S. It has to be mentioned that the real growth process may be far more complex than this simplified model, with numerous surface and gas-phase processes involved [314].

Surface processes include physisorption and chemisorption [315], and substrate-mediated precursor decomposition, such as the decarbonylation of Mo(CO)$_6$ on
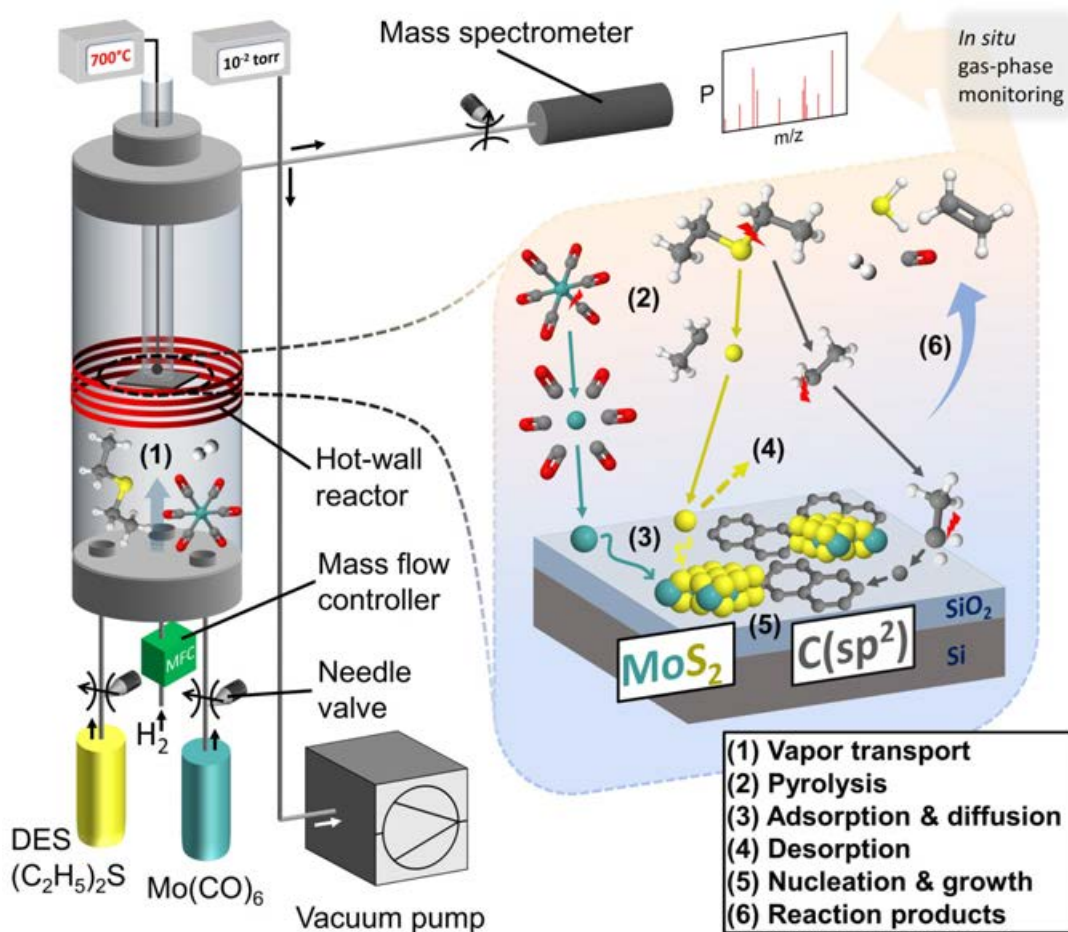
Figure 3.2 MOCVD setup and simplified growth model. Left: Schematic of the vertical, hot-wall MOCVD reactor. Molybdenum hexacarbonyl Mo(CO)$_6$ and diethyl sulfide [DES; ((CH$_3$CH$_2$)$_2$S)] are injected from external canisters together with H$_2$ into the reaction chamber at growth temperatures from 500 to 800 °C and at a working pressure of ca. 10^{-2} to 10^{-1} Torr. Right: Different MOCVD gas-phase and surface processes marked and annotated in the legend. *In situ* gas-phase monitoring of the reaction and pyrolysis products is enabled by a residual gas analyzer (mass spectrometer) attached downstream the reaction zone.

SiO$_2$ [316, 317]. The sulfidation of Mo adatoms results in the nucleation of MoS$_2$ grains, which can grow laterally through edge-attachment of additional Mo and S species [168, 47]. During sulfidation, a sufficiently high chalcogen-to-metal ratio is crucial to prevent Mo accumulation and metal-rich cluster formation [310]. The DES/Mo(CO)$_6$ precursor ratio requires tuning by independent source control to achieve the desired, effective chalcogen-to-metal ratios on the surface. Typically, high chalcogen-to-metal ratio are necessary to obtain stoichiometric TMD films, because the large discrepancy in vapor pressures, sticking coefficients, and diffusion kinetics of the metal and chalcogen species must be compensated [82].

Gas-phase reactions include the thermal decomposition of Mo(CO)$_6$ [232, 233] and DES [300]; moreover, premature reactions between pyrolyzed gas-phase species may occur before precursors reach the substrate surface [318, 319]. Such reactions and involved vapor-phase constituents can be monitored in this setup with a residual gas analyzer (mass spectrometer) connected at the reactor exhaust. In this study, this capability is used to investigate the role of DES pyrolysis during MoS$_2$ synthesis.

3.2.1   Assessment of MoS$_2$ monolayer and C incorporation

In a first experiment, it was aimed at synthesizing a MoS$_2$ thin film to demonstrate the ability of monolayer growth control and providing an exemplary sample for initial thin film assessment. The MoS$_2$ film was grown by co-injection of approximately 0.02 sccm Mo(CO)$_6$ and 0.3 sccm DES at 700 °C *without* added H$_2$ gas, and the growth time was set at 60 min, which yielded a virtually coalesced, nominally monolayer film. After SEM check of the as-grown sample on SiO$_2$ [Fig. 3.3a(i)], the film was succesfully transferred to a holey carbon TEM grid [Fig. 3.3a(ii-iii)] for high-magnification TEM imaging of the film's morphology. STEM in Fig. 3.3b shows the continuous nature of the monolayer film (1L, grey contrast), while revealing the presence of some non-coalesced (0L, black holes) and bilayer regions (2L, white contrast) corresponding to the hardly identifiable white dots previously seen in the lower resolution SEM images. Fully coalesced layers without holes and few layer thin films can be easily achieved by further increasing the growth time (section 3.2.2). However, strictly self-limited, layer-by-layer growth behaviour can be difficult to achieve by a continuous MOCVD process. This might be solved by low growth rate process controlled by decreased Mo flux [47], Mo flux ramp down with increasing monolayer domain coverage [320], and sequential dosing giving time for metal adatom diffusion [321, 322] and vertical Ostwald ripening [197] during interrupted precursor pulses. Another possibility is a thermally and H$_2$/Cl$_2$-controlled bilayer back-etching approach [291, 323] to remove superficial islands and to obtain a monolayer with more uniform properties. Further magnification in Fig. 3.3c(i) shows slight contrast variations with a whitish haze in the continuous 1L areas, which suggests the presence of another species. This might be attributed to organic residues from the PMMA-based layer transfer [324], and/or growth-induced carbon contamination that will be discussed in the subsequent paragraph. Qualitative EDX analysis confirms the expected Mo and S elemental composition, whereas the Cu signal can be assigned to the Cu-support grid, C signal to the holey carbon, and/or growth/transfer induced C residues, while no other elements could be found within the detection limit of EDX.

The plateau-like HAADF line profile intensity scan gives further evidence of the white contrast regions being bilayers [Fig. 3.3c(iii)]. HRTEM imaging displays the nanocrystalline nature in Fig. 3.3d and the inset shows an atomically-resolved 1L region of the hexagonal 1H-MoS$_2$ crystal structure with characteristic $\{10\overline{1}0\}$ and $\{11\overline{2}0\}$ lattice plane distances of 0.27 nm and 0.16 nm, respectively, as introduced in Fig. 2.2. The
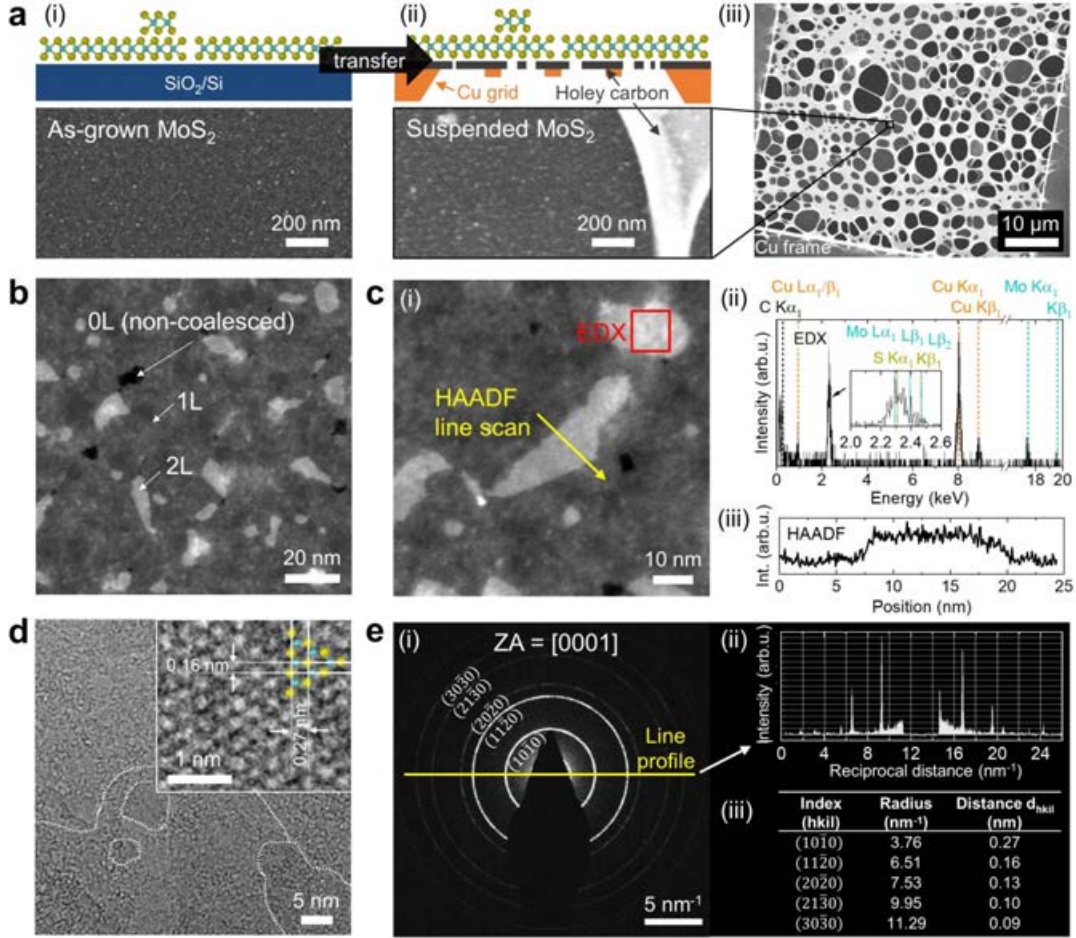
Figure 3.3 Transmission electron spectroscopy (TEM) of a MOCVD-grown, nominal 1L-MoS$_2$ thin film. **(a)** Schematic illustrations and SEM images of (i) as-grown MoS$_2$ film, and (ii) transferred MoS$_2$ film suspended over a (iii) Cu-supported, holey carbon TEM grid. **(b)** STEM of the continuous monolayer thin film, with non-coalesced (black holes), monolayer (1L, grey), and bilayer regions (2L, white). **(c)** (i) Magnified STEM image of 2L regions, over which (ii) elemental energy-dispersive X-ray spectroscopy (EDX, red box), and (iii) a high-angle annular dark-field (HAADF, yellow line) intensity profile scan were performed. **(d)** High-resolution (HR)TEM image of atomic MoS$_2$ structure, revealing the hexagonal lattice and characteristic lattice plane distances in the magnified inset. **(e)**(i) Selected-area electron diffraction (SAED) ring pattern seen along the out-of-plane [001] zone axis, (ii) extracted intensity line profile with (iii) table of corresponding diffraction ring radii and determined interplanar distances d_{hkl} of indexed (hkl) lattice planes.

ring-like selected-area electron diffraction pattern recorded with a 730 nm wide aperture and averaged signal from many domains highlights the polycrystalline nature of the MoS$_2$ film [Fig. 3.3e(i)] with random, in-plane grain orientations, as it can be expected for non-epitaxial TMD growth on amorphous SiO$_2$ substrate [82]. Figure 3.3e(ii-iii)] displays the intensity line profile through the indexed ring pattern for extraction of reciprocal distances and allowing the calculation of corresponding interplanar lattice distances d_{hkl}, which are in agreement with simulated values for the MoS$_2$ crystal structure in the CARINE CRYSTALLOGRAPHY v3.1 software database [325].
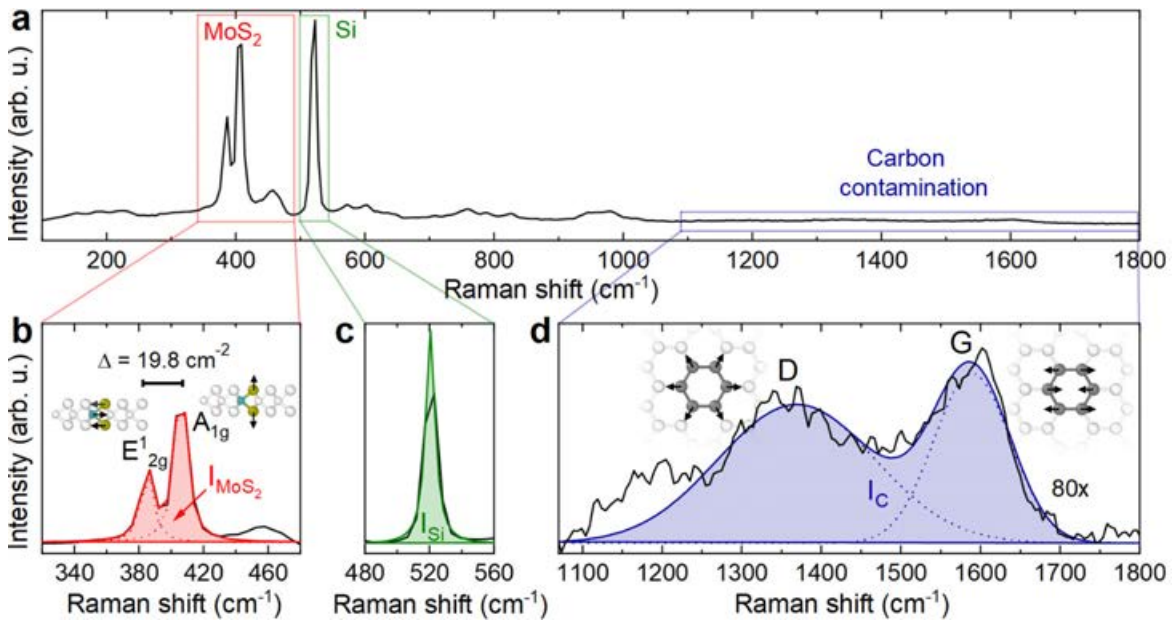
Figure 3.4 Semi-quantitative Raman analysis of 1L-MoS$_2$ grown at 700 °C by co-injection of 0.3 sccm DES and 0.02 sccm Mo(CO)$_6$ precursor flow *without* reductive H$_2$ gas flow. **(a)** Overview Raman spectrum, and three regions of interest for peak area analysis: **(b)** MoS$_2$-related modes fitted with a double-Lorentzian, **(c)** Si mode fitted with a single-Lorentzian, and **(d)** C-related D and G bands fitted with a double-Gaussian and magnified by a factor of 80. The peak integrals for the Raman modes associated to MoS$_2$, Si, and C are defined as I_{MoS_2} (red), I_{Si} (green), and I_C (blue), respectively.

Figure 3.4a displays an exemplary Raman overview spectrum of the coalesced 1L-MoS$_2$ thin film and three highlighted regions. The first region in Fig. 3.4b belongs to the characteristic MoS$_2$ in-plane (E_{2g}^1) and out-of-plane (A_{1g}) phonon modes at 382.6 and 402.4 cm^{-1}, respectively. The full width at half-maximum (FWHM) values of E_{2g}^1 and A_{1g} peaks are 5.7 and 5.0 cm^{-1}, respectively. The frequency difference $\Delta = A_{1g} - E_{2g}^1$, which is commonly used as a layer thickness indicator, is $\Delta = 19.8$ cm^{-1} and confirms the monolayer thickness of the film [274, 169]. Figure 3.4c shows the Si

substrate band at $521 \, \text{cm}^{-1}$. The third region in Fig. 3.4d depicts broad carbon D and G modes at around 1360 and $1590 \, \text{cm}^{-1}$, revealing the presence of incorporated C in the film, as previously observed in TMD growth from organic chalcogen precursors [190, 225]. The observed D and G band positions and the I_D/I_G intensity ratio of around 1.7 has strong characteristic of sp^2-bonded carbon (later also corroborated by XPS), such as in pyrolytic graphite [326]. According to the formula of Cancado et al. [327], the crystallite size $L_a = 560/E_l^4 \, (I_D/I_G)^{-1}$ for the used laser energy of $E_l = 2.54 \, \text{eV}$ can be estimated to be $\lesssim 10 \, \text{nm}$ for this carbon. Therefore, it will be subsequently termed as "graphitic carbon" C(sp^2), in agreement to previously described nano-grained, defective graphene incorporation during TMD synthesis [225]. Possibly, this C incorporation may also contain sp^3-bonded carbon, typical for "amorphous carbon", according to the amorphization trajectory of disordered carbons proposed by Ferrari and Robertson [328].

Raman spectroscopy has been used in this work as a rapid, semi-quantitative analysis tool. For this purpose, the MoS$_2$, Si, and C Raman bands are fitted and the respective peak integrals are defined as $I_{MoS_2} = I_{E_{2g}^1} + I_{A_{1g}}$, I_{Si}, and $I_C = I_D + I_G$. The normalized Raman integral ratios I_{MoS_2}/I_{Si} and I_C/I_{Si}, relying on the Si substrate reference peak, are used as indicators for monitoring the contents of MoS$_2$ and C(sp^2), respectively. This allows to follow their evolution and relative composition and to deduce trends within the growth parameter space. In the following, this method will be used as a tool to systematically investigate the influence of growth time, DES/Mo(CO)$_6$ ratio, temperature, and H$_2$ gas flow on MoS$_2$ growth and C incorporation.

3.2.2 Time – Nucleation, coalescence, and thickness control

The first parameter of interest is growth time, a basic control knob for layer coverage and thickness during MOCVD. MoS$_2$ films were synthesized by co-injection of $0.02 \, \text{sccm}$ Mo(CO)$_6$ and $0.3 \, \text{sccm}$ DES *without* added H$_2$ at $700 \, °\text{C}$, while varying growth time. Analysis of the morphology, composition, and (opto)electronic properties is shown in Fig. 3.5 by SEM, Raman and PL spectroscopy. The summarized trends and evolution of film properties are extracted from each method in panel Fig. 3.5d.

The SEM images in Fig. 3.5a for films grown between $15 \, \text{min}$ to $240 \, \text{min}$ at $700 \, °\text{C}$ display the characteristic nucleation, lateral domain expansion, monolayer coalescence and multilayer formation, as illustrated by the schematics on top. The analysis of sub-monolayer films allows the assessment of domain density N and evolution of the surface coverage χ of monolayer domains (gray) on the SiO$_2$ substrate (black) based on
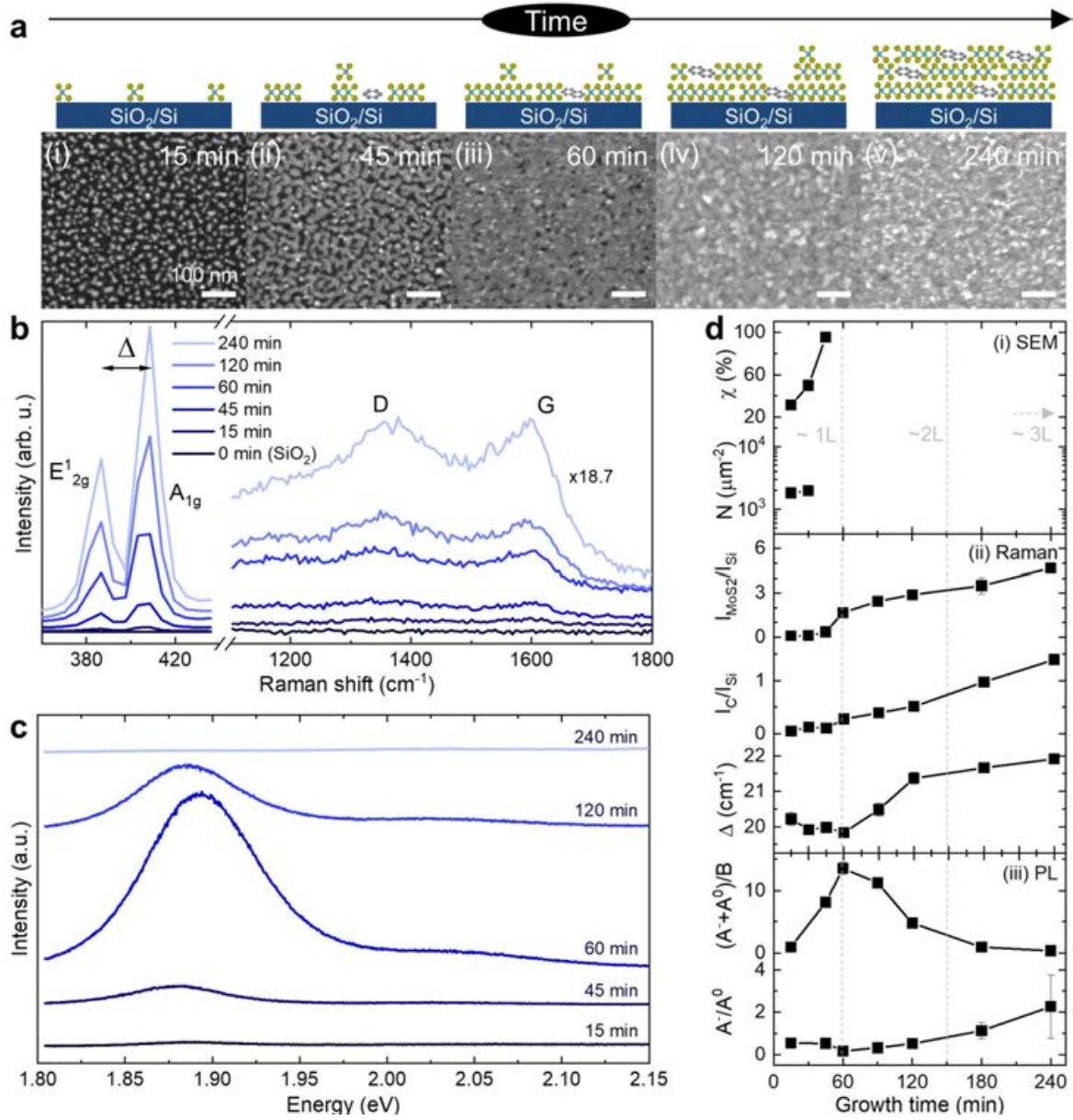
Figure 3.5 Growth time study. Mono– to few layer MoS$_2$ thin films grown at 700 °C from 0.02 sccm Mo(CO)$_6$ and 0.3 sccm DES flow for growth times varying between 15 and 240 min. [**a(i–v)**] Schematic illustrations of layer morphology and SEM images. **(b)** Raman spectra normalized to the Si peak (521 cm^{-1}, not shown), displaying MoS$_2$, and C regions. The intensities for carbon-related D and G bands are magnified. **(c)** PL spectra. **(d)** Summary of thin film characteristics as a function of growth time extracted from (i) SEM (coverage χ, and domain density N), (ii) Raman spectroscopy [I_{MoS_2}/I_{Si} and I_C/I_{Si} integral ratios, and $\Delta(A_{1g} - E_2^1 g)$ frequency difference], and (iii) PL spectroscopy [$(A^0 + A^-)/B$ and A^-/A^0 exciton intensity ratios.]

the film-substrate contrast [Fig. 3.5d(i)], as per the image analysis algorithm described in section 2.3.3. It can be clearly observed again that bilayer nucleation (white contrast spots, cf. TEM analysis in section 3.2.1) already starts prior monolayer coalescence (60 min), as previously discussed [197, 329, 320]. The nucleation density of the first layer is on the order of $\sim 10^3$ µm^{-2}, which has been consistently observed throughout this work for alkali-free growth in this reactor, and largely unaffected by the growth parameters (see appendix Fig. B4). This produces a nanocrystalline MoS$_2$ monolayer with small grain sizes on the order of 20 to 30 nm (more detailed grain size statistics are shown in Fig. B25). This high nucleation density can be explained by high Mo-flux-controlled growth rates [197, 47, 329], high Mo gas-phase supersaturation at low working pressure [188, 310], low diffusivity of Mo adatoms [320] and their anchoring at surface groups of the SiO$_2$ surface [330]. As larger grain sizes ($\gtrsim$ µm-scale) are typically desired for high-performance (opto)electronic devices and require suppression of nucleation events [180, 178], this issue will be later addressed by alkali-assisted and low-growth rate approaches in section 3.4.

While contrast-based SEM analysis is well-suited for determination of sub-monolayer coverage, its use for layer thickness determination is not sufficiently reliable. For the latter purpose, the frequency difference Δ of the E_{2g}^1 and A_{1g} MoS$_2$-modes is a useful thickness indicator (Fig. 3.5b). In Fig. 3.5d(ii) Δ-values below ~ 20 cm^{-1} correspond to 1L films up to 60 min; then, Δ widens with increased layer number due to softening (red-shift) of in-plane E_{2g}^1 modes and stiffening (blue-shift) of out-of-plane A_{1g} modes, in agreement with literature [274, 169]. Gray lines for 1L, 2L, and 3L are added to Fig. 3.5d(ii) according to AFM-calibrated thickness-data for MOCVD-grown MoS$_2$ from Shinde et al. [169] The full data set of E_{2g}^1 and A_{1g} positions is shown in the appendix Fig. B5. Interestingly, below 30 min an anomalous tail above Δ-values above 20 cm is observed. XPS analysis of these samples (not shown in the figure) found that the nano-scale MoS$_2$ domains (<15 nm) in the early nucleation phase exhibit a high MoO$_3$:MoS$_2$ content. This might be related to post-growth oxidation of ambient-exposed domain edges [331], resulting in oxidized domains with high perimeter-to-volume ratio, and thus, an elevated MoO$_3$:MoS$_2$ composition. Such edge-oxidation might constrain the MoS$_2$-phonon modes and impact Δ-values, as seen for the short growth times. The monotonically increasing I_{MoS_2}/I_{Si} and I_C/I_{Si} signals in Fig. 3.5d(ii) indicate the increasing amount of deposited MoS$_2$, while C is incorporated simultaneously.

The PL evolution during layer growth is also followed. The PL signal consists of several exciton peak contributions, as will be later discussed. PL intensity measured by the normalized $(A^0 + A^-)/B$ exciton ratio [275] first increases with sub-monolayer

coverage χ, reaching a maximum at full monolayer coverage around 60 min before declining again due to the layer-dependent direct-to-indirect bandgap transition of few layer MoS$_2$ thin films [99] [332]. The PL peak position may be affected by the decreasing bandgap with increasing layer number [99], see section 3.3.2. Furthermore, the A^-/A^0-ratio increases for increased layer number and C incorporation, which will be discussed in a more detailed PL study in section 3.3.2.1. Therefore, PL measurements can be used as another layer-thickness indicator for MOCVD of TMDs [169].

In summary, the steady precursor supply in MOCVD allows time-controlled growth of mono- to few layer MoS$_2$ thin films with determined coverage and thicknesses. This capability will be exploited to obtain 2-3L films for transistor application in chapter 5, which are expected to have improved transport properties compared to 1L films [291, 248, 333]. The subsequent studies will primarily focus on surface coverages χ between 0 to 100 % for further study of film growth and the role of C incorporation.

3.2.3   S:Mo ratio − Film composition and stoichiometry

The chalcogen-to-metal ratio is a key parameter during MOCVD of TMDs and chalcogen-rich conditions are commonly highlighted as preferred for stoichiometric, lateral 2D growth [310, 82]. Here, the effect of DES:Mo(CO)$_6$ ratio was investigated for MoS$_2$ films grown at 700 °C for 60 min and 0.02 sccm Mo(CO)$_6$ flow, and with DES flow varying between 0.3 and 13.2 sccm, corresponding to DES:Mo(CO)$_6$ ratios of $\sim$15 to $\sim$660. The SEM images in Fig. 3.6a and their analysis in Fig. 3.6d show that starting from a coalesced monolayer, increasing DES flow results in a significant coverage decrease with a constant, high nucleation density N of $\sim 10^3 \mathrm{\mu m}^{-2}$. Furthermore, MoS$_2$ domains change towards more irregular and fractal shapes with increasing DES flow. This morphological evolution is also evident in the Raman spectra in Fig. 3.6b; the decreasing E_{2g}^1 and A_{1g} MoS$_2$-mode intensity suggest a reduced amount of MoS$_2$, which is accompanied by rising D- and G-band intensities. Accordingly, the semi-quantitative analysis exhibits decreasing I_{MoS_2}/I_{Si} and increasing I_{MoS2}/I_{Si} values (Fig. 3.6d[ii]). These trends suggest that C incorporation introduced at elevated DES flow competes with and hinders the lateral MoS$_2$ growth. Similar observations of interrupted TMD morphology in presence of carbon have been reported for MOCVD of WS$_2$ [190] and WSe$_2$ [225] synthesized from organic chalcogen precursors. Moreover, the MoS$_2$ layer thickness indicator Δ increases despite the decreasing MoS$_2$ surface coverage and strongly suggests the tendency to form vertically, layer-stacked MoS$_2$ islands instead of laterally expanded 1L domains. This growth mode transition will

be further corroborated by topographical AFM and cross-sectional TEM analysis in Fig. 3.17. The PL spectra in Fig. 3.6c show quenched intensity $[(A^0 + A^-)/B]$ and
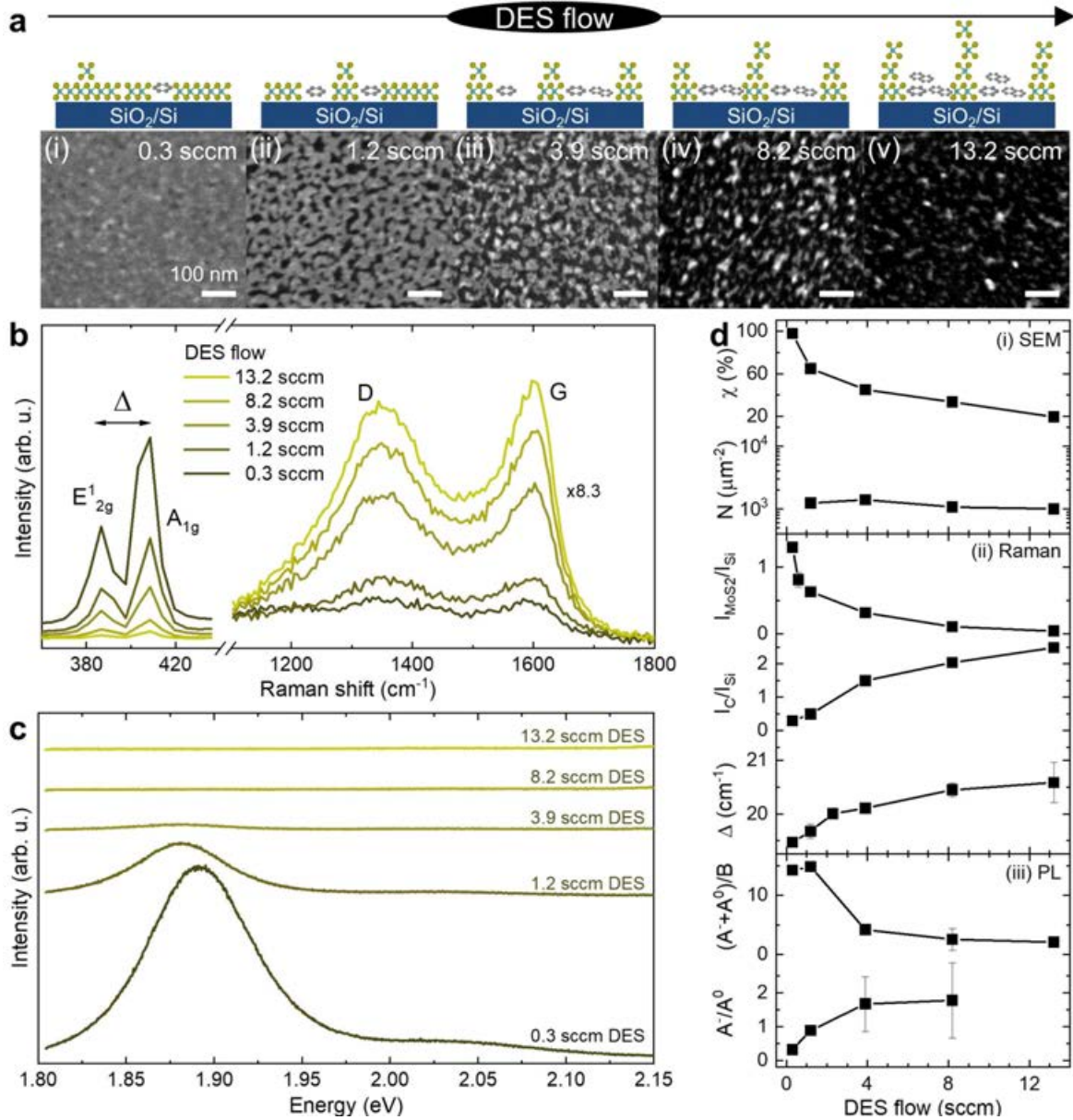
Figure 3.6 DES/Mo(CO)$_6$ precursor ratio study. MoS$_2$ thin films grown at 700 °C (60 min) from 0.02 sccm Mo(CO)$_6$ and DES flow varying between 0.3 to 13.2 sccm. **[a(i–v)]** Schematic illustrations of layer morphology and SEM images for indicated DES flows. **(b)** Raman spectra normalized to the Si peak (521 cm^{-1}, not shown). The carbon-related D and G bands are magnified by a factor of 8.3. **(c)** PL spectra. **(d)** Summary of film characteristics as a function of the DES flow, extracted from (i) SEM (coverage χ, and domain density N), (ii) Raman spectroscopy [I_{MoS_2}/I_{Si} and I_C/I_{Si} integral ratios, and $\Delta(A_{1g} - E_2^1g)$ frequency difference], and (iii) PL spectroscopy [$(A^0 + A^-)/B$ and A^-/A^0 exciton intensity ratios].

peak shift due to modulation of the trion-to-exciton ratio (A^-/A^0) as a consequence of decreased layer coverage and C incorporation at elevated DES flow. This will be explained more precisely in section 3.3.2.1.

The morphological evolution during DES flow increase could indicate that agglomerates of an amorphous MoS$_x$ phase are formed in place of crystalline 2D MoS$_2$ domains. However, amorphous phases, such as MoS$_3$ are known to be thermally unstable and to crystallize into the 2H-MoS$_2$ phase above 400 °C [334, 335], which is much lower than the growth temperature of 700 °C. Indeed, no obvious signs of MoS$_3$-related phases [112] were found in the XPS analysis, as discussed in the following. Figure 3.7 displays the fitted XPS spectra of thin films grown on SiO$_2$ for DES flows from 0.3 to 13.2 sccm, after energy correction to the Si^{IV} substrate reference peak at 103.3 eV [276] (see appendix for table of fitting parameters, table B1). The high-resolution Mo 3 d core-level spectra in Fig. 3.7b show three different Mo oxidation states, each fitted by a doublet peak. *First*, the most prominent doublet (blue) is attributed to the Mo^{IV} oxidation state and corresponds to stoichiometric MoS$_2$, with the Mo 3 d$_{5/2}$ and Mo 3 d$_{3/2}$ spin-orbit components positioned at 229.3 ± 0.1 eV and 232.5 ± 0.1 eV, respectively, in agreement with literature values for MOCVD-grown MoS$_2$ [167]. *Second*, the higher binding energy doublet (red) observed at 232.5 ± 0.2 eV and 235.6 ± 0.2 eV is attributed to the Mo^{VI} oxidation state ascribed to MoO$_3$. A fraction of MoO$_3$ has been generally detected in as-grown samples, which may be explained by post-growth oxidation of the defective, sulfur-deficient film upon air exposure [336, 190, 156], and is commonly found in aged, natural MoS$_2$ crystals [121]. Despite being grown under vacuum conditions, low water background levels in the reaction chamber monitored with the residual gas analyzer (see appendix, Fig. B7) might also explain a partial oxidation already during MoS$_2$ synthesis or reactor cool-down [337]. *Third*, the doublet (light green) observed at lower binding energies within slight shifts at 229.0 ± 0.2 eV and 232.2 ± 0.2 eV, is assigned to a Mo^{IV-y} oxidation state related to a defective, sub-stoichiometric MoS$_{2-x}$ phase, for which the doublet position depends on the MoS$_{2-x}$ stoichiometry [338]. The presence of this sub-stoichiometric phase can be accounted to S vacancies due to incomplete sulfidation, a frequent observation in CVD-grown MoS$_2$ [339]. The S:Mo stoichiometry of this S-deficient phase fraction lies approximately between 1.6 and 1.9 according to the Mo 3 d$_{5/2}$ peak positions [338]. For better visualizing the evolution of sub-stoichiometric MoS$_{2-x}$ phase fraction as a function of DES flow, the corresponding Mo^{IV-y} 3 d peak areas normalized to the stoichiometric MoS$_2$ phase (Mo^{IV} 3 d area) are plotted in Fig. 3.9a. With increasing DES flow, a vanishing MoS$_{2-x}$ phase can be observed, corresponding with a phase fraction reduction from 0.17 to 0.07, as

shown in Fig. 3.9d. This trend clearly indicates that a higher DES flow (i.e., higher sulfidation potential) can result in MoS$_2$ films closer to the ideal stoichiometry relation. Despite the advantage for stoichiometric growth, a high DES flow leads to increased incorporation of C impurities and hampered lateral MoS$_2$ growth, as shown in the previous SEM and Raman analysis. This conclusion is further supported by the XPS in Fig. 3.7 showing overall increased C 1 s peak areas together with concurrently decreased Mo 3 d peak areas for raised DES flow.

The following discussion of the C 1 s peaks aims at better understanding the chemical nature of the incorporated carbon. Such analysis is challenging because ambient-exposed samples typically build up an adventitious hydrocarbon layer with carbon components in different oxidation states [340]. XPS control experiments were performed on *in situ*-annealed samples for hydrocarbon desorption (Fig. 3.8) [315] and a reference-sample-based peak fitting model was developed to differentiate between adventitious, post-growth C contribution from ambient exposure and the growth-related C contribution from the MOCVD process. As shown in Fig. 3.8a, a bare SiO$_2$ substrate after air-exposure served as reference for the commonly observed, physisorbed C components (light gray peak areas) ascribed to aliphatic C-C/C-H species at 284.7 ± 0.2 eV, and oxidized C-O-C and O-C=O species upshifted by $+1.7$ eV and $+4.3$ eV, respectively (also see appendix, table B1). The individual peak area fractions of C-O-C and O-C=O species compared to aliphatic C-C/C-H reflecting the composition of adventitious carbons were found to be 0.1 and 0.17, respectively. Assuming these fractions of the aliphatic C-C/C-H peak as a standard, they were set as an area constraint for fitting the adventitious carbon components in MoS$_2$ samples (see appendix, table B1). The total fraction R of these oxidized carbonaceous species was found in the common range of $0.1 < R = 0.1 + 0.17 = 0.27 < 0.3$ [340]. It is remarked that this composition can depend on ambient factors like humidity or the storage time; however, to guarantee comparability, samples were processed and handled similarly. The adventitious carbon layer could be desorbed at $500\,°C$, as apparent from the vanishing peak components after *in situ* annealing and consistent with literature [315]. Then, MoS$_2$ samples grown with low 0.3 sccm and high 13.2 sccm DES flow were measured before and after annealing [Fig. 3.8(b-c)]. While the adventitious overlayer was removed, a thermally stable carbon component persisted the annealing step. This allowed identification of the growth-induced C incorporation as graphitic C(sp^2) (dark gray areas) with its asymmetric peak found at 284.2 ± 0.2 eV. Figure 3.9 shows the evolution of the graphitic C(sp^2) peak for MoS$_2$ thin films grown with DES flows from 0.3 to 13.2 sccm, exhibiting an almost 20-fold increase in the fraction of codeposited

C(sp^2) when normalized to the MoS$_2$-related Mo^{IV} 3 d$_{5/2}$ peak; this is characteristic of heavily contaminated films. When further studying the chemical nature of C impurities, no evidence was found in XPS spectra for the formation of possible C-Mo bondings, which should have otherwise been apparent in the C 1 s region at low binding energies
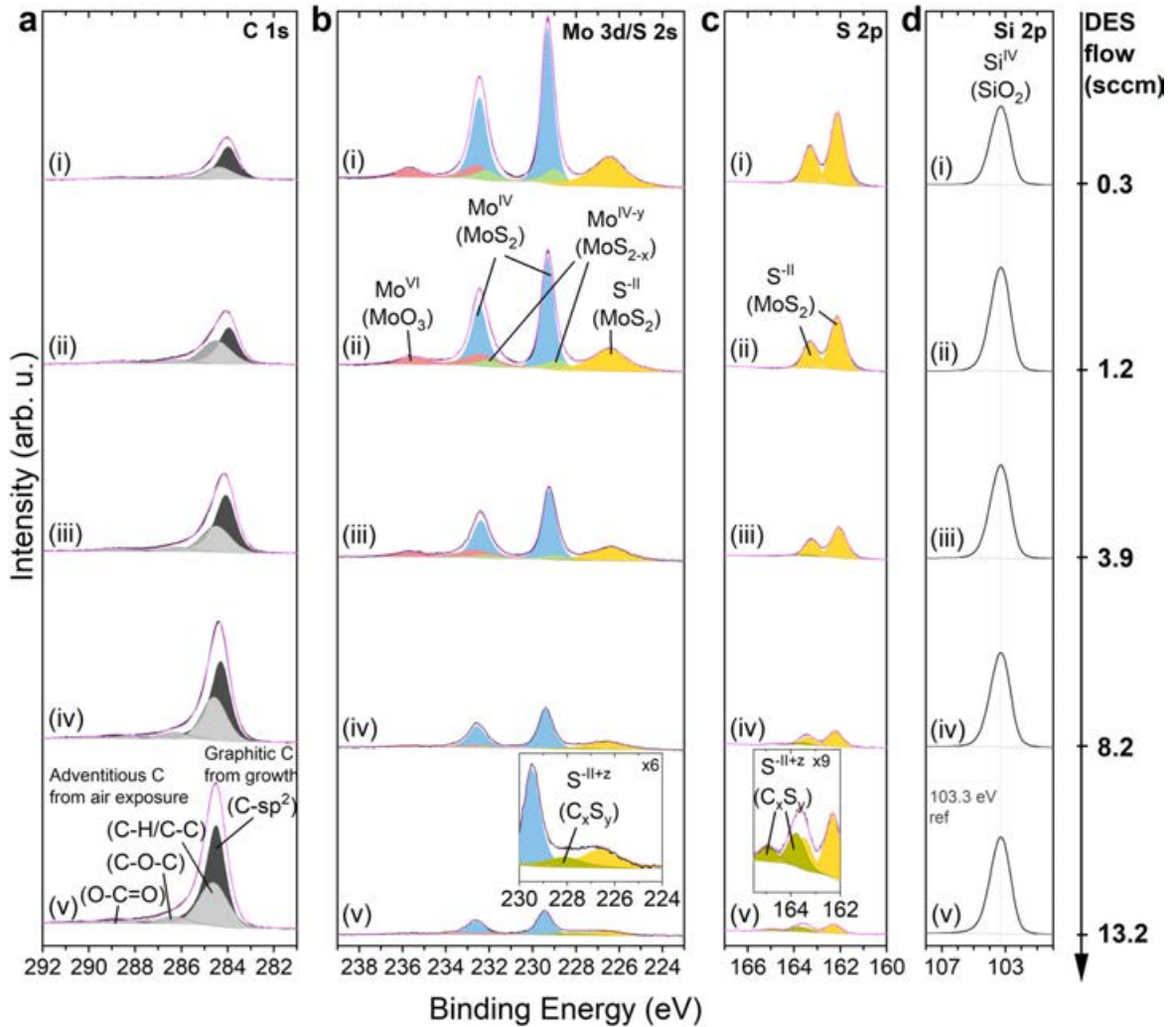
Figure 3.7 XPS analysis showing the effect of DES:Mo(CO)$_6$ precursor ratio on chemical composition of MoS$_2$ thin films grown on SiO$_2$ at 700 °C (60 min) from 0.02 sccm Mo(CO)$_6$ and varying DES flow, as indicated by the scale on the right; The following core level regions are shown: **a(i–v)** C 1s, **b(i–v)** Mo 3d / S 2s, **c(i–v)** S 2p, and **d(i–v)** Si 2p, where black lines in (i-v) correspond to the measured spectra for DES flow between 0.3 sccm and 13.2 sccm; colored areas under singlet/doublets represent fits assigned to the same chemical species and pink lines show the synthetic fitting envelopes of summed peaks. All spectra are calibrated to the SiO$_2$ substrate peak at 103.3 eV and are plotted with the same intensity scale. Insets in **(b–c)(v)** show the respective S 2s and S 2p peaks of the C_xS_y organosulfur compound emerging at increased DES flows.
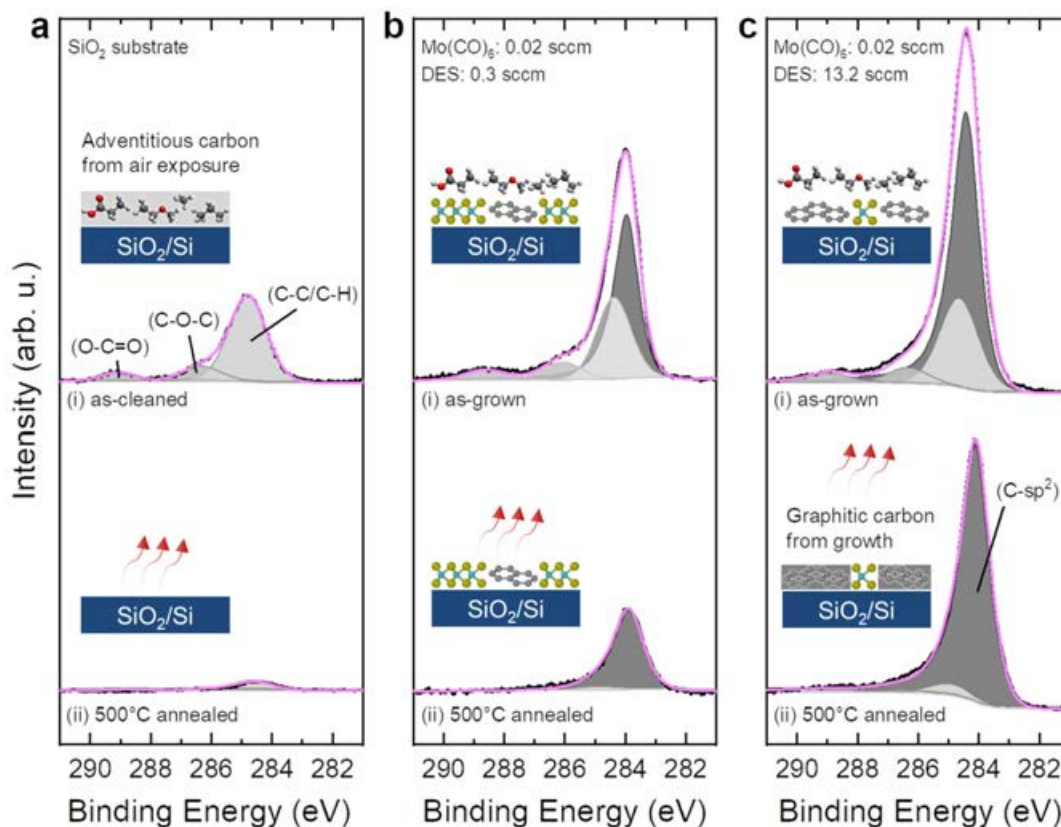
Figure 3.8 XPS *in situ* annealing experiment for differentiation of adventitious and growth-induced carbon components in the C 1s core level spectra (DES flow series). **(a)** SiO$_2$ reference substrate prior to deposition; and MoS$_2$ grown on SiO$_2$ at 700 °C (60 min) by co-injection of 0.02 sccm Mo(CO)$_6$ and **(a)** 0.3 sccm DES and **(c)** 13.2 sccm DES. The samples were analyzed (i) before and (ii) after annealing at 500 °C (∼1 min) inside the XPS chamber. Measured data is shown as black lines. The synthetic fitting envelopes of summed peaks are shown in pink. Fitting components assigned to adventitious carbon species (C-C/C-H, C-O-C, O-C=O) are colored with light gray peak areas and graphitic carbon (C-*sp^2*) with dark gray peak areas. All spectra are plotted with the same intensity scale. Insets show schematic illustrations of the SiO$_2$ surface before/after thermal desorption of adventitious carbon and grown thin films composed of MoS$_2$ and graphitic C(*sp^2*).

at around 282.8 eV [305]. Therefore, within the detection limit of the XPS study, it is believed that the incorporated C impurities for the used growth conditions are mainly composed of graphitic C(*sp^2*) patches codeposited alongside the MoS$_2$ layer rather than incorporated into the MoS$_2$ crystal [341]. This excludes the formation of Mo$_2$C carbide [193, 305] and CH functional groups at chalcogen sites, as previously reported for synthetic TMDs [304]. The latter is in good agreement with the theoretical prediction that substitution of S with C atoms at the MoS$_2$ edge is thermodynamically unfavorable [115] and is further supported by the experimental observation that carbide

conversion of MoS$_2$ does not occur below 800 °C [305]. It is remarked that different transition-metal elements used for TMD synthesis, most commonly Mo and W, vary in their susceptibility to form bonds with carbon[342], which explains the ongoing controversy on the type of C incorporation.
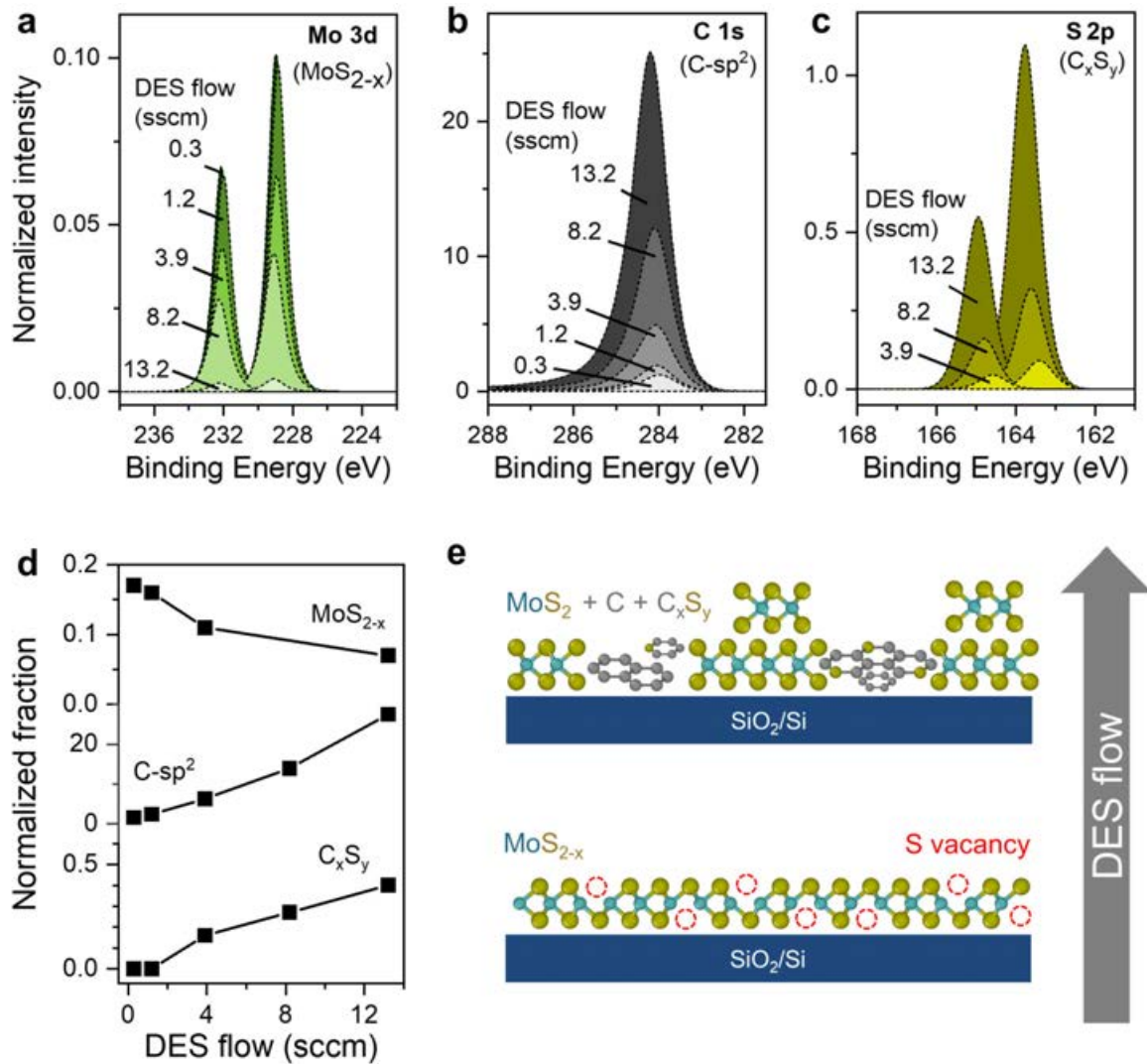
Figure 3.9 XPS analysis showing the evolution of film components as function of DES flow. **(a)** Sub-stoichiometric MoS$_{2-x}$ phase **(b)** graphitic C-sp^2 phase, and **(c)** organosulfur compound C$_x$S$_y$; Spectra are shown after Shirley background subtraction and normalization to the MoS$_2$-related Mo^{IV} 3 d$_{5/2}$ peak and after consideration of RSF factors. **(d)** Summary panel showing the phase fractions of sub-stoichiometric MoS$_{2-x}$, C-sp^2, and C$_x$S$_y$ relative to MoS$_2$.**(e)** Schematic illustration of MoS$_2$ thin film grown with low DES flow, containing S vacancies / sub-stoichiometric MoS$_{2-x}$ phase, and grown with high DES flow with reduced S vacancies, but codeposited C-sp^2 and C$_x$S$_y$ impurities.

Regarding the XPS analysis of sulfur core levels (Fig. 3.7c), the characteristic MoS$_2$ fingerprints attributed to the S^{-II} oxidation state are observed according to literature data [167]: an S 2s singlet peak at 226.5 ± 0.1 eV (Fig. 3.7b), and a S 2p doublet with S 2p$_{1/2}$ and S 2p$_{3/2}$ spin-orbit components at 162.1 ± 0.1 eV and 163.3 ± 0.1 eV, respectively, as marked by the yellow peak areas in Fig. 3.9c. Another S 2p doublet (yellow-green) emerges at higher binding energies for DES flows above 3.9 sccm, positioned at 163.6 ± 0.2 eV and 164.8 ± 0.2 eV. A magnified inset is shown in Fig. 3.7c(v) for the 13.2 sccm DES flow. A similar S 2p doublet was previously observed in WS$_2$ growth using DES and was attributed to either MoS$_x$O$_y$ oxysulfide or C$_x$S$_y$ organosulfur compounds [190]. Here, the presence of an intermediate MoS$_x$O$_y$ oxysulfide phase is discarded, as the S 2p spectra do not show evidence of the distinct sulfur oxidation state characteristic for MoS$_x$O$_y$ [343]. Instead, the additional doublet is assigned to a C$_x$S$_y$ organosulfur compound arising for excessive DES flow [Fig. 3.9(c-d)]. Such organosulfur compounds have been previously reported at binding energies of 163.7 ± 0.3 eV [344] for sulfurized carbon black, activated carbon, charcoal and in S-doped graphene [345]. Therefore, such additional C$_x$S$_y$ compounds may also form part of the complex carbonaceous impurity components incorporated into the film.

In summary, two significant conclusions can be drawn from the analyses of the effect of DES:Mo(CO)$_6$ ratio, which are highlighted by the trends in Fig. 3.9d and illustrated in the schematic in Fig. 3.9e. On the one hand, high DES flow is beneficial for a S-rich reaction environment and helps reducing S vacancies and the fraction of the sub-stoichiometric MoS$_{2-x}$ phase. On the other hand, excessive DES results in a C-rich environment that can cause codeposition of graphitic C(sp^2) and C$_x$S$_y$ organosulfur compounds competing with MoS$_2$. Therefore, the use of an organic chalcogen precursor can impose limitations on the maximal appropriate chalcogen-to-metal ratios due to the trade-off between film stoichiometry and purity.

3.2.4   Temperature – DES pyrolysis causing C incorporation

The reported temperature range for MOCVD of TMDs spans widely between around 400 to 1000 °C, for which the upper end is typically desired for improved crystalline TMD quality [346]. Thermal energy is an important factor in MOCVD to activate the thermal decomposition of precursors providing the source elements for the reaction and thin film formation. It was found that MoS$_2$ could be synthesized in the here used hot-wall reactor using Mo(CO)$_6$ and DES within a temperature window from roughly 550 to 750 °C according to a detailed XPS study (see appendix, Fig. B6), with

some uncertainty due to the large 100 °C temperature steps used in the study. Lower temperatures were not sufficient to initiate thermal DES dissociation for the sulfidation reaction and yielded MoO$_{3-x}$/MoO$_3$ thin films upon air exposure. Within the growth window and with rising temperature, a decreasing MoS$_2$ phase fraction was observed accompanied by an increased fraction of C($sp2$), up to about 850 °C at which only trace amounts of Mo^0 metal in absence of MoS$_2$ and C($sp2$) could be observed. The latter result might be caused by early decomposition and full depletion of the DES source upstream the sample position along the hot-wall tube due to long residence times.

To clarify the origin and main mechanism behind C incorporation within the identified growth window, first, single precursor source experiments were conducted, in which SiO$_2$/Si substrates were exposed to either 0.02 sccm Mo(CO)$_6$ or 13.2 sccm DES, for 60 min at 700 °C (Fig. 3.10). The only Mo(CO)$_6$-exposed samples exhibit Mo-cluster formation, as visible in SEM (Fig. 3.10a). Interestingly, the extracted nucleation density of around $N \sim 552 \pm 92 \,\mu\text{m}^{-2}$ is around two to four times below typical MoS$_2$ nucleation densities (see appendix, Fig. B4), suggesting that simultaneous injection of S increases the nucleation density; this may be explained by the diffusion-controlled ripening behaviour depending on the chalcogen-to-metal ratio [321, 322, 197]. Importantly, Raman spectra for only Mo(CO)$_6$-exposed in Fig. 3.10b are free of carbon-related D and G bands. In contrast, DES-exposed samples, for which C
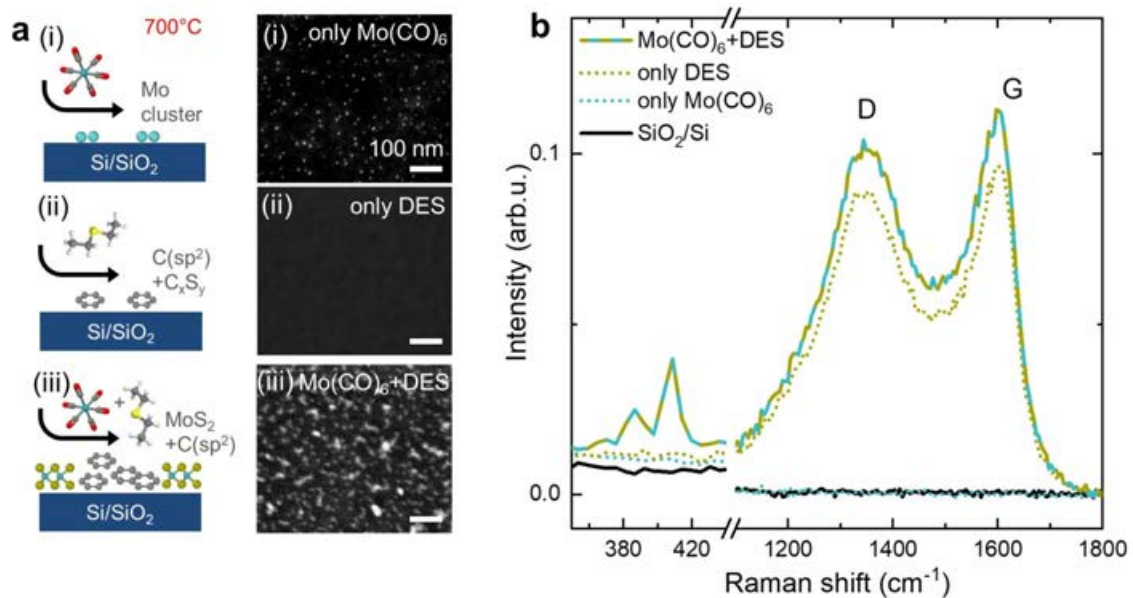
Figure 3.10 Single precursor source and precursor co-injection experiment. **(a)** Schematic illustrations and SEM images of (i) Mo(CO)$_6$, and (ii) DES single-source exposure, and (iii) co-injection experiments. **(b)** Raman spectra normalized to the Si peak at 521 cm^{-1}.

deposition is not visible from SEM images, exhibit intense D and G Raman signatures ($I_C/I_{Si} = 2.1$) stemming from C incorporation. The lack of C deposition in the case of only Mo(CO)$_6$ exposure at 700 °C is reasonable because the decomposition product CO, which might be a potential carbon-source, is a rather inert and thermally stable gas-phase compound [300]. Thus, it is not expected to participate in side reactions resulting in C incorporation at the tested growth conditions [188, 177]. Therefore, DES is identified as the source of C incorporation, which is consistent with previous reports of TMD growth processes using organic chalcogen precursors [193, 177, 225]. Another important observation is that co-injection of Mo(CO)$_6$ together with DES results in slightly higher C levels compared to single-source DES exposure, which suggests catalytic gas-phase and/or surface reactions in presence of gaseous Mo(CO)$_6$ and/or catalytically active MoS$_2$ domains on the surface.

After these preliminary experiments, the role of DES as a source of C incorporation was studied more precisely by Raman spectroscopy, investigating only DES-exposed SiO$_2$ substrates at growth temperatures from 550 to 800 °C. As shown in Fig. 3.11a, increasing temperature produces increasing carbon-related D and G bands. In previous studies, it has been assumed that such C incorporation is caused by organic chalcogen pyrolysis by-products [190, 225]; here, this phenomenon is explicitly assessed by gas-phase monitoring within the MOCVD reactor. For this purpose, the mass spectrometer was used to detect relative partial pressure changes of DES fragmentation products. Indeed, when comparing fragmentation patterns of DES (at constant DES flow), a lowered partial pressure of the single-charged DES molecular ion at mass-to-charge ratio $m/z = 90$ is detected at 700 °C compared to room temperature (Fig. 3.11b). Also, especially the partial pressure increase at $m/z = 29$ and $m/z = 28$ can be pointed out at the elevated temperature, which is a clear indication of the dissociation of the DES parent molecule into these fragments. This unimolecular dissociation mechanism is highlighted in Fig. 3.11c as an important pathway during the complex reactions of DES pyrolysis [300]. The dissociation is initiated at the C-S bond and produces ethyl radicals ($m/z = 29$), which further decompose into the more thermally stable ethylene ($m/z = 28$) after H abstraction [299].
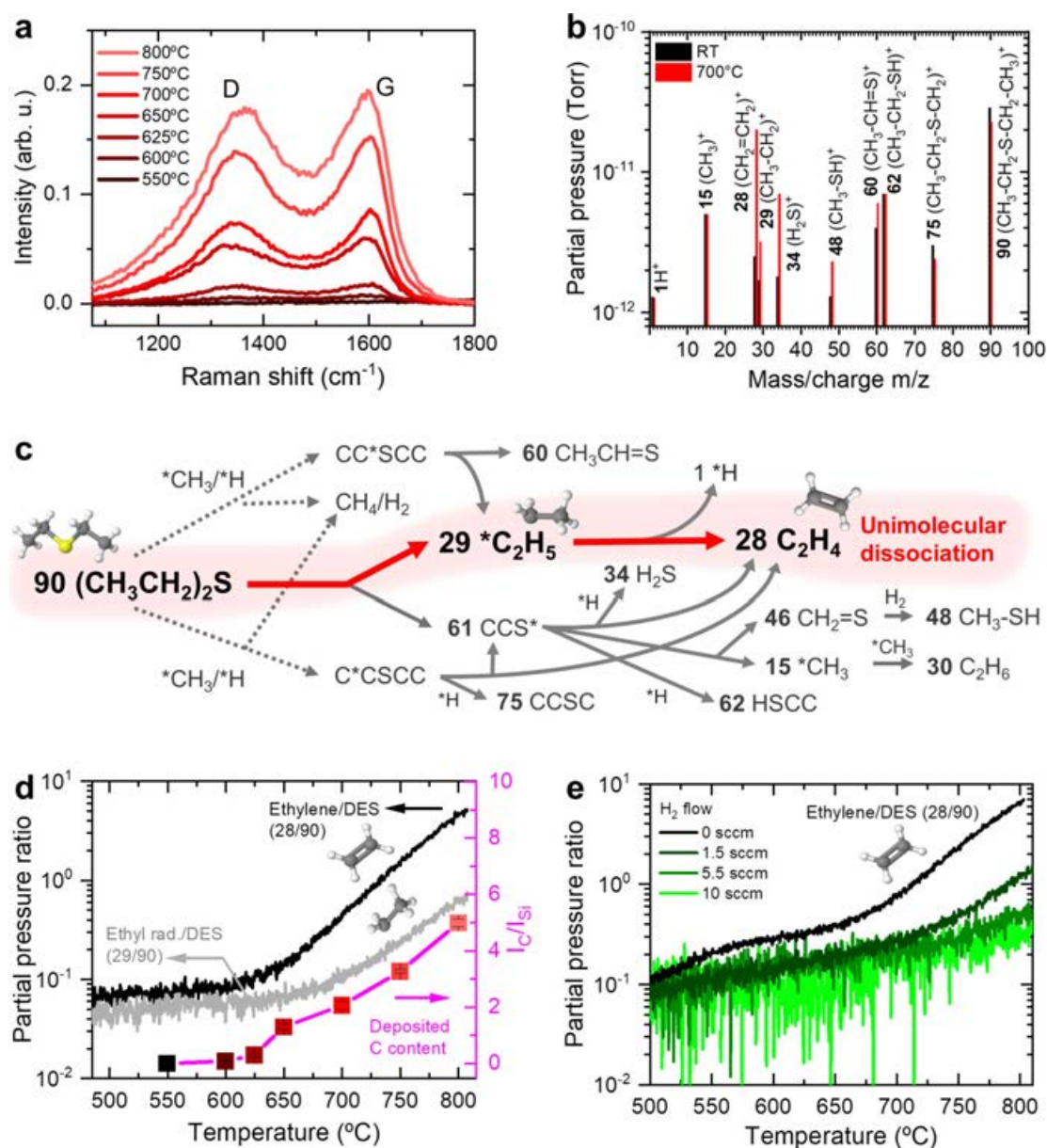
Figure 3.11 Growth temperature study correlating *ex situ* Raman analysis of C incorporation with *in situ* gas-phase monitoring of DES pyrolysis. **(a)** Raman spectra for single-source exposure of SiO$_2$ substrates to 13.2 sccm DES (60 min), *without* H$_2$ injection, at temperatures from 550 to 800 °C. **(b)** Mass spectra recorded for a DES flow of 13.2 sccm recorded at room temperature (black) and 700 °C (red). **(c)** Reaction pathways of DES pyrolysis adapted from [300]. Numbers in front of chemical species indicate molecular masses. H atoms are omitted in large fragments. Dotted lines mark radical attack reactions. The asterisks (*) mark radical species. The reaction pathway of relevance for this study, involving unimolecular dissociation of DES under production of ethyl radicals and ethylene, is highlighted in red. **(d)** Temperature dependence of partial pressure ratio of ethyl radicals ($m/z = 29$) and ethylene ($m/z = 28$) to unfragmented DES ($m/z = 90$) monitored by *in situ* mass spectrometry (left axis), and I_C/I_{Si} Raman integral ratio as an indicator of deposited C (right axis), as extracted from spectra in (a). **(e)** Temperature dependent partial pressure ratio of ethylene to unfragmented DES for typical reaction conditions of 0.02 sccm Mo(CO)$_6$, 1.2 sccm DES, and varying H$_2$ flow of 0 (black), 1.5 (blue), 5.5 (red), and 10 sccm (green).

The partial pressure ratios of these main fragments relative to the unfragmented DES molecular ion are displayed in Fig. 3.11d (left axis) and can be used for continuous DES pyrolysis monitoring as a function of temperature (for detailed analysis of other gas-phase constituents the reader is referred to the appendix, Fig. B8). The ethyl radical/DES and ethylene/DES ratios start to exponentially increase at around 600 °C, marking the onset of DES pyrolysis that is initiated by H effusion around this temperature [347].

Importantly, the pyrolysis onset coincides with increased C deposition above this point, as extracted from *ex situ* Raman analysis of the I_C/I_{Si} integral ratio in Fig. B8d (right axis). This correlation gives strong support to the hypothesis that C-containing products, resulting from the thermally activated pyrolysis of DES along the *hot-wall* reactor tube result in C formation with a temperature-dependent rate. In contrast, for WS$_2$ growth from DES in a *cold-wall* reactor, a rather constant C formation rate was found over a wide range of temperatures [190], which is likely due to limited, premature DES pyrolysis upstream the sample along the water-cooled tube [190]. Moreover, Choudhury et al. [190] speculated that the reason of C-reduced MoS$_2$ growth from DES using a hot-wall reactor in the pioneering work of Kang et al. [47] was a result of early depletion of C radicals and C deposition on upstream tube walls. However, our investigation suggests that Kang et al. may have avoided C incorporation by choice of a comparatively low growth temperature of 550 °C and additional use of reductive H$_2$, which is helpful in reducing carbon, as discussed later. This highlights the crucial importance of growth temperature in combination with reactor design for organic chalcogen precursor based TMD growth.

After the DES single-source experiment, the temperature-dependent DES pyrolysis degree was monitored under MoS$_2$ reaction conditions for a gas mixture of 0.02 sccm sccm Mo(CO)$_6$ 1.2 sccm DES (Fig. 3.11e, black line). It was observed that the DES pyrolysis onset shifted to lower temperatures of around 500 °C. This suggests the Mo(CO)$_6$-catalyzed DES pyrolysis, as shown in Fig. 3.10 and previously reported [225]. This finding is corroborated by the systematically increasing C content for co-exposure with both DES and Mo(CO)$_6$ when compared to single-source DES exposure (Fig. B10).

3.2.5   H$_2$ flow – Carbon reduction and MoS$_2$ etching

While reduced growth temperatures are a viable option to mitigate C incorporation, a high growth temperature is preferred for the deposition of TMDs with high crystalline

quality [239, 310, 178]. Therefore, H$_2$ gas has been used to limit C incorporation in TMDs grown from organic chalcogen precursors in high temperature regimes [47, 188, 190, 310]. To investigate its role, H$_2$ was added to Mo(CO)$_6$/DES gas mixtures during temperature-dependent DES pyrolysis monitoring. By using ethylene as the main indicator, it can be observed in Fig. 3.11e that H$_2$ introduction significantly lowers the partial pressure ratio of ethylene by over an order of magnitude upon H$_2$ increase to 10 sccm (the evolution of other pyrolysis fragments is reported in Fig. B9), indicating a reduced DES pyrolysis degree even above 700 °C. This result suggests that a H$_2$-rich gas phase effectively suppresses DES dissociation, possibly by counterbalancing the common H-abstraction mechanisms that are involved to initiate DES pyrolysis [300].

Next, a series of MoS$_2$ thin films were grown at 700 °C for 60 min by varying H$_2$ flows from 0 to 30 sccm, while keeping DES flow at 1.2 sccm and Mo(CO)$_6$ flow at 0.02 sccm. SEM, Raman, and PL analyses are presented in Fig. 3.12. The SEM images (Fig. 3.12a) and their analysis [Fig. 3.12d(i)], it is revealed that the MoS$_2$ surface coverage χ increases initially from 46 % (0 sccm H$_2$) to a maximum coverage of 77 % (5.5 sccm), coinciding with highest PL intensity [Fig. 3.12c and d(iii)]; subsequently, χ declines monotonically for H$_2$ flows greater than 5.5 sccm; the nucleation density remains roughly constant regardless of the H$_2$ flow (Fig. B4c). This suggests that it is possible to achieve a H$_2$-induced growth rate modulation with an optimized H$_2$ flow for time-efficient layer coalescence.

The I_{MoS_2}/I_{Si} Raman integral ratio [Fig. 3.12d(ii)], extracted from the corresponding Raman spectra (Fig. 3.12b), follows the same H$_2$-dependence than the surface coverage χ, in agreement with the SEM analysis. Notably, the initial increase in MoS$_2$ film coverage correlates with a steeply dropping I_C/I_{Si} signal, which suggests an enhanced lateral growth of MoS$_2$ domains in absence of growth-hindering C contamination. This promoted 2D growth mode is also supported by the Raman frequency shift Δ, indicating a decrease in MoS$_2$ layer thicknesses (bilayer fraction) with increasing H$_2$; Δ decreases from about 20.1 to around 19.6 cm^{-1}, as lateral MoS$_2$ domain expansion becomes thermodynamically favored over vertical (0 0 0 1)layer-stacked nucleation on the low-carbon, high-energy SiO$_2$ surface [329]. Indeed, MoS$_2$ thin films grown on a carbon (graphene) reference surface showed an increased tendency for vertical growth by second layer nucleation (see appendix, Fig. B16). In the SEM images for growth on SiO$_2$ (Fig. 3.12a) the reduced bilayer nucleation can be noticed by the vanishing white-contrast spots on top of the monolayer MoS$_2$ domains upon H$_2$ addition and carbon removal (see appendix for full set of SEM images, Fig. B3).

Furthermore, the MoS$_2$ domain shape gradually converts from irregular/roundish to triangular shape upon increasing H$_2$ and lowered carbon amount. Above 10 sccm
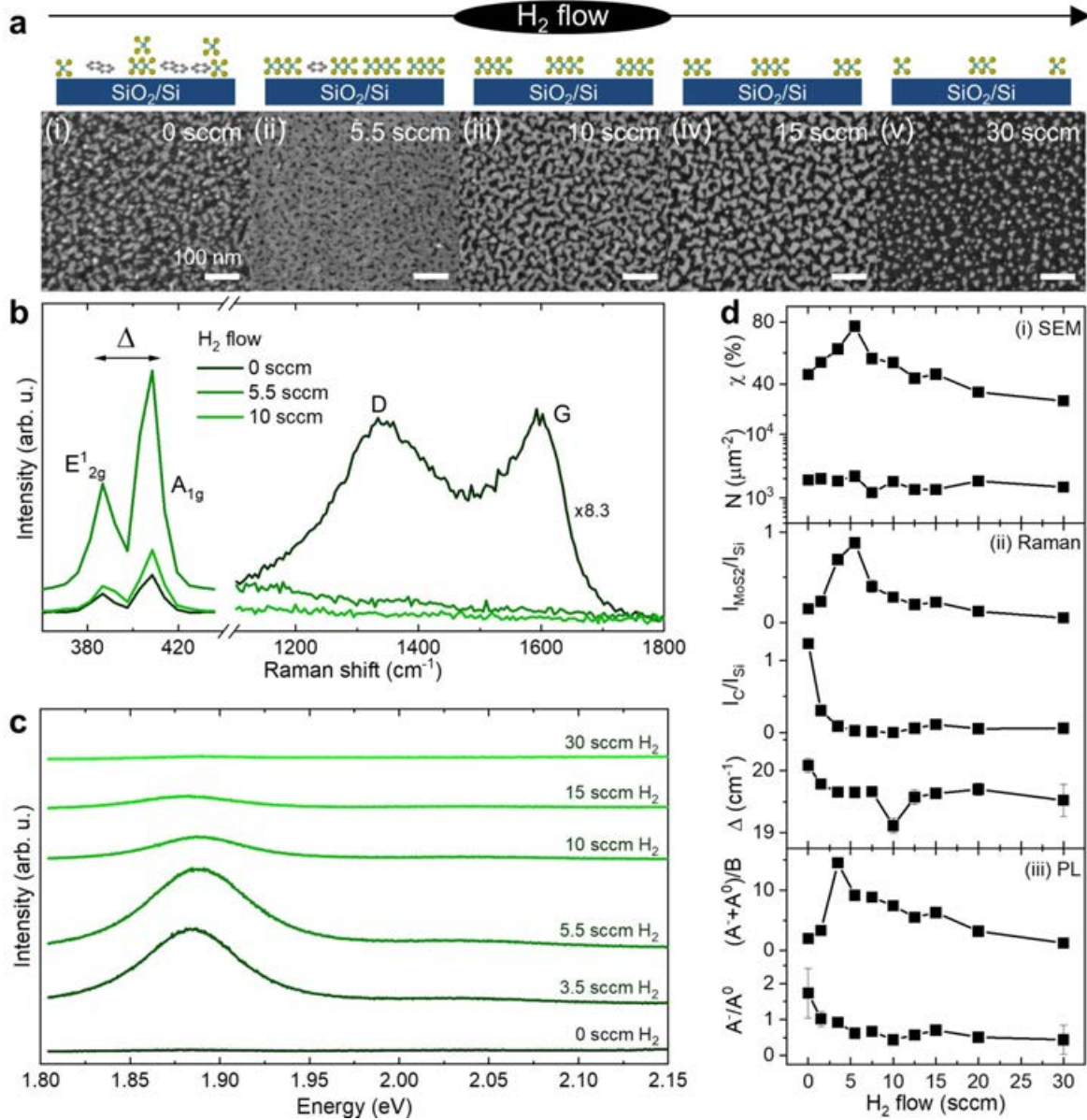
Figure 3.12 H$_2$ flow study, showing effect of H$_2$ on MoS$_2$ thin films grown at 700 °C (60 min) from 0.02 sccm Mo(CO)$_6$, 1.2 sccm DES flow, and H$_2$ flow varying between 0 to 30 sccm. [**a(i-v)**] Schematic illustrations of layer morphology and SEM images for indicated H$_2$ flows. **(b)** Raman spectra normalized to the Si peak (521 cm^{-1}, not shown). C-related D and G bands are magnified by a factor of 8.3. **(c)** PL spectra **(d)** Summary of thin film characteristics as a function of the H$_2$ flow, extracted from (i) SEM (coverage χ, and domain density N), (ii) Raman spectroscopy [I_{MoS_2}/I_{Si} and I_C/I_{Si} integral ratios, and $\Delta(A_{1g} - E_2^1 g)$ frequency difference], and (iii) PL spectroscopy (($A^0 + A^-$)/B and A^-/A^0 exciton intensity ratios].

H$_2$, ensuring negligible, growth-induced C incorporation, dominantly triangular shaped domains can be observed on SiO$_2$, while for growth on a graphene reference surface under the same conditions rounded/hexagonal-shaped domains are observed (see appendix, Fig. B15). This hints at substrate-dependent grain shape influenced by the thermodynamics [329] and kinetics (adatom diffusivities, sticking coefficients, effective S:Mo ratio) [148, 348] on the two distinct growth surfaces. As another hypothesis, the irregular grain shape on SiO$_2$ in the absence of H$_2$ could also imply disturbed crystallization due to the use of an organic sulfiding agent and low sulfidation potential [115, 116]. Although post-growth XPS analysis (Fig. 3.13) does not show signs of C-Mo bondings within the detection limit (i.e. by substitutional C doping of the MoS$_2$ crystal lattice), it is speculated that intermediate MoS$_x$C$_y$ edge compounds [116, 305, 306] might play a role during attachment of S species at the catalytically active edge sites of laterally expanding MoS$_2$ crystals. This might impede the ideal S dimer saturation of the Mo-terminated edge that is preferred in triangular MoS$_2$ crystals, as reported in atomic-resolution tunneling microscopy studies [108]. As known from hydrodesulfurization catalysts, such "deactivation" of edge sites through carbonaceous species can be recovered in H$_2$ ambient [349, 114] and could explain the shape evolution towards triangular domains when H$_2$ is added. On the other hand, it can be clearly observed that excessive H$_2$ flow above 5.5 sccm results in descending grain coverage at rather constant nucleation density (Fig. B4c). This demonstrates a reduced lateral MoS$_2$ growth rate, which may be attributed to H$_2$-induced domain etching [47, 291, 194]. Indeed, Raman analysis of the I_{MoS_2}/I_{Si} ratio for growth time studies with and without H$_2$ confirm lowered growth rates in the presence of H$_2$, as will be summarized in Fig. 3.15. This means that with elevated H$_2$ flow, longer growth times are required to achieve similar coverages, which was further deduced from growth parameter studies for two sets of H$_2$ flows (growth times) of 5.5 sccm (60 min growth) and 12.5 sccm (180 min), as summarized in the appendix (Fig. B4d).

Figure 3.13 shows XPS analysis of the air-exposed films grown *without* (0) and *with* H$_2$ (1.5, 10 sccm). The expected Mo^{IV} 3 d doublets (blue) and S^{-II} 2 p doublets (yellow) ascribed to MoS$_2$ are observed, as well as Mo^{VI} 3 d doublets (red) assigned to MoO$_3$. The lowest fraction of sub-stoichiometric MoS$_{2-x}$ phase (Mo^{IV-y} 3 d doublet, green) of $\sim 5\%$ is observed for the 10 sccm H$_2$ sample (Fig. 3.13b) and could be explained by an H$_2$-activated edge sulfidation mechanism [108]. Moreover, compared to H$_2$-free growth, the 10 sccm H$_2$ sample exhibits a reduced fraction of C(sp^2), which is further confirmed by an XPS study using the formerly established *in situ* annealing approach for removal of physisorbed adventitious carbons (Fig. 3.14). Interestingly,
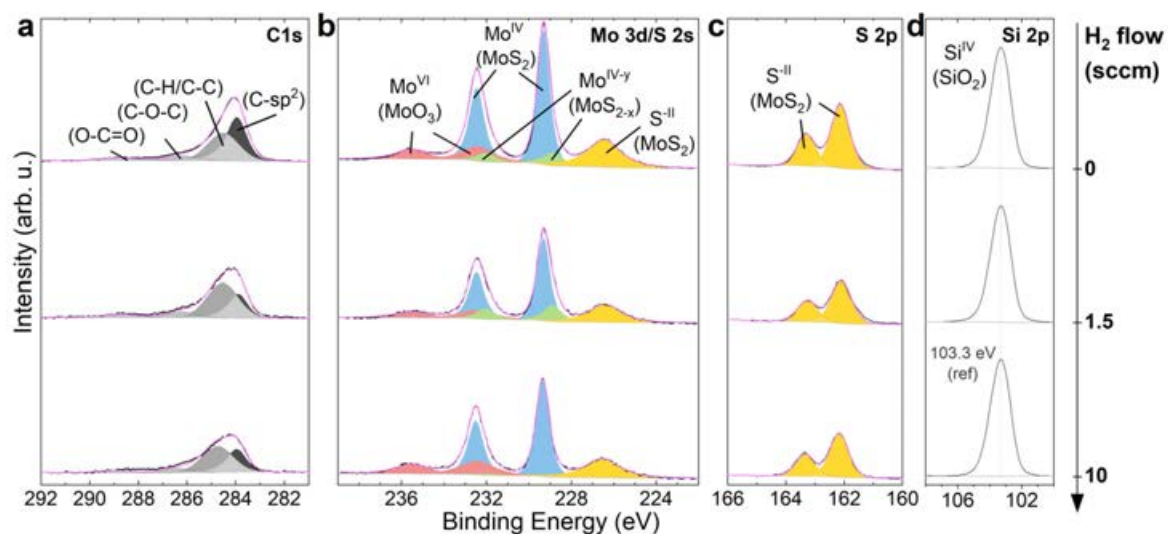
Figure 3.13 XPS analysis showing the effect of H$_2$ on the chemical composition of MoS$_2$ thin films grown on SiO$_2$ at 700 °C (60 min) from 0.02 sccm Mo(CO)$_6$ and 1.2 sccm DES flow with varying H$_2$ flow of 0, 1.5, and 10 sccm, as indicated by the scale on the right. The following core level regions are shown: **(a)** C 1 s, **(b)** Mo 3 d/S 2 s, **(c)** S 2 p, and **(d)** Si 2 p, where black lines in (i-v) show the spectra for H$_2$ flow between 0 sccm and 10 sccm; colored areas under singlet/doublets represent fits assigned to the same chemical species and pink lines show the fitting envelopes of summed peaks. All spectra are calibrated to the SiO$_2$ substrate peak at 103.3 eV and are plotted with the same intensity scale.

and in contrast to what might have been expected from the fully diminished Raman D and G bands in Fig. 3.13b above 5.5 sccm, a persisting C 1 s fraction is still present even for the 10 sccm H$_2$ condition after annealing (Fig. 3.14d(ii)). This observation suggests that despite the significant reduction of graphitic C(sp^2) in H$_2$-ambient, a non-negligible C impurity content still remains in the film. More detailed analysis of the C 1 s peak suggests that the composition of this residual carbon shifts from graphitic C(sp^2) to another form of C(sp^3) with increasing H$_2$ flow, as summarized and illustrated in Fig. 3.14(e-f).

As a final remark, it is noted that the thermal annealing step, apart from adventitious carbon removal, might have led to modifications of the C chemistry and influenced the interpretation. Therefore, further studies are required to fully understand the type and full mitigation of C impurities during MOCVD of TMDs, which recent studies have often covered only by Raman analysis; as shown above, Raman analysis does not seem to be sufficient for a comprehensive characterization of C impurities in TMD films.
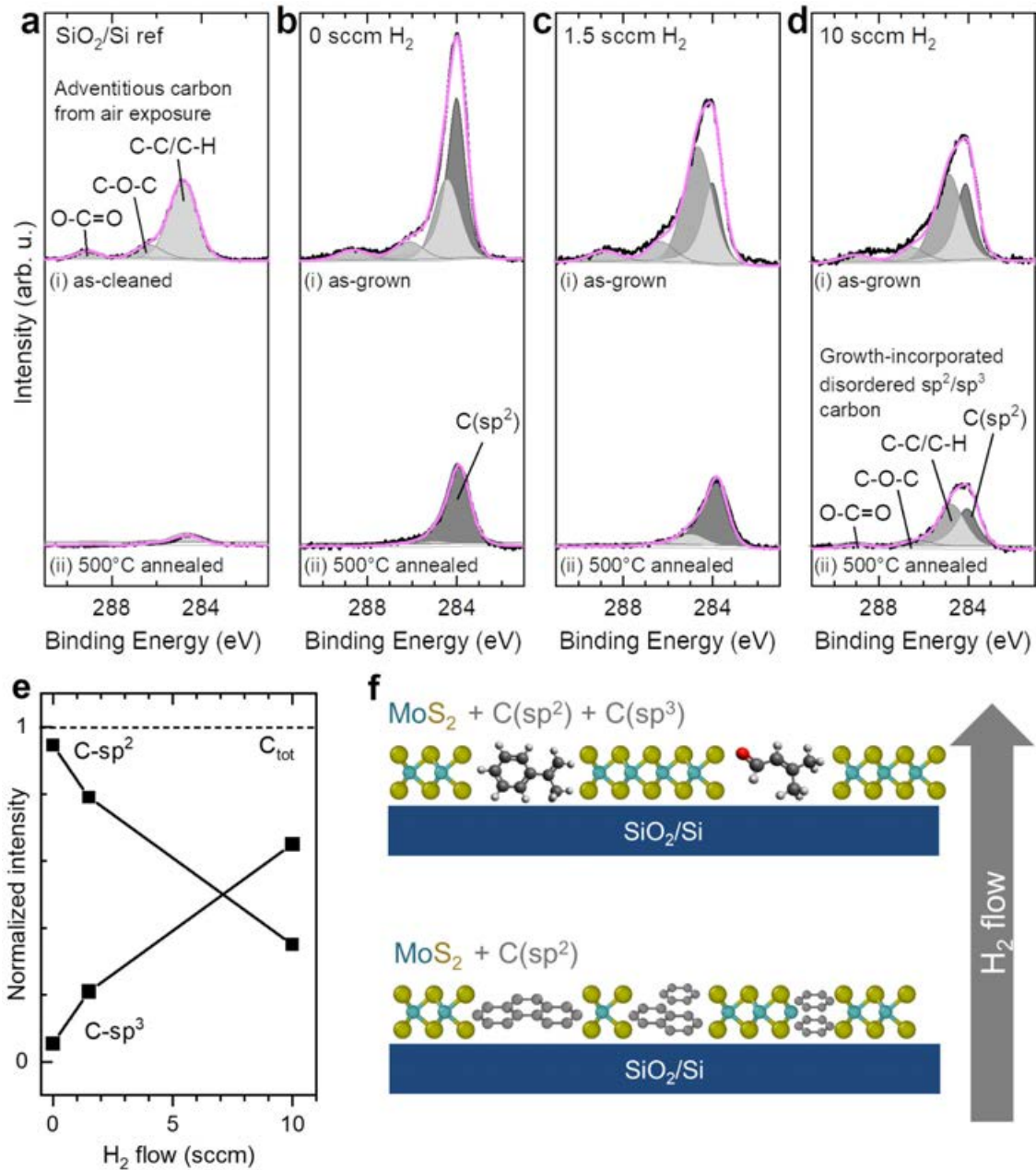
Figure 3.14 XPS *in situ* annealing experiment for differentiation of adventitious and growth-induced carbon components in the C 1s core level spectra (H$_2$ flow series). Films were grown on SiO$_2$ at 700 °C (60 min) from 0.02 sccm Mo(CO)$_6$ and 0.2 sccm DES flow for varying H$_2$ flows of 0, 1.5, and 10 sccm. **(a-d)** C 1s core level spectra of SiO$_2$ substrate reference and MoS$_2$ thin films grown with indicated H$_2$ flows (i) before and (ii) after *in situ* annealing. **(e)** Summarizing panel of phase fractions C(sp^2) and C(sp^3) normalized to the total amount of carbon $C_{tot} = C(sp^2) + C(sp^3)$. **(f)** Schematic illustration of the effect of H$_2$ on composition of disordered carbon in the MoS$_2$ thin film.

3.2.6 Overview of growth studies and reaction balance

To summarize the interplay of investigated growth parameters, such as growth time, DES flow, temperature, and H$_2$ flow, and to conclude the link between DES pyrolysis and competing MoS$_2$ and C deposition, an overview of the trends seen by the semi-quantitative Raman analysis using I_{MoS_2}/I_{Si} and I_C/I_{Si} indicators, is given in Fig. 3.15. The following, simplified reaction scheme can be postulated:

$$(CH_3{-}CH_2)_2S\,(g) \xleftrightarrow{\gtrsim 600\,°C} H_2S\,(g) + 2\,CH_2{=}CH_2\,(g) \tag{3.1}$$

$$Mo(CO)_6\,(g) + 2\,H_2S\,(g) \longleftrightarrow MoS_2(s) + 6\,CO\,(g) + 2\,H_2\,(g) \tag{3.2}$$

$$2\,CH_2{=}CH_2\,(g) \longleftrightarrow 2\,C\,(s) + 2\,H_2\,(g) \tag{3.3}$$

$$Mo(CO)_6\,(g) + 2\,(CH_3{-}CH_2)_2S\,(g) \longleftrightarrow MoS_2(s) + 6\,CO\,(g) + 8\,C\,(s) + 10\,H_2\,(g) \tag{3.4}$$
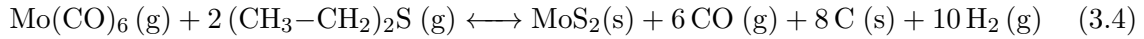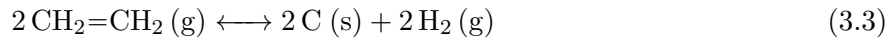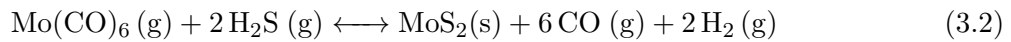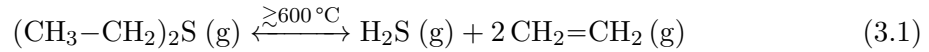
For simplicity, full conversion of DES to H$_2$S and ethylene is assumed in eq. (3.1), which were main constituents detected by mass spectroscopy. It is remarked that other intermediate compounds and radicals (e.g. ethyl radicals) are involved in the actual, more complex gas-phase reactions. While H$_2$S is consumed in the sulfidation reaction in eq. (3.2) for MoS$_2$ synthesis, ethylene decomposition in eq. (3.3) acts as a source of C deposition [350]. If H$_2$ is added to the gas phase, the thermodynamic equilibrium in eq. (3.4) shifts to the left side, therefore, resulting in reduced C deposition [Fig. 3.15d(ii)]. However, excessive H$_2$ concentration in reaction eq. (3.2) can also imply reduced MoS$_2$ growth, as seen after the I_{MoS_2}/I_{Si} culmination point in Fig. 3.15d(i) and differing slopes in comparative growth time studies with and without the use of H$_2$ in Fig. 3.15a(i). The reaction pathway eq. (3.1) through DES pyrolysis, with thermal onset around 600 °C can also occur at even lower temperatures in the presence of Mo(CO)$_6$ (Fig. 3.11e), which then leads to increased C formation through eq. (3.3) [Fig. 3.15c(ii)]; this may possibly be due to gas-phase reactions [318], surface-templated reactions on the SiO$_2$ substrate [351] and/or hydrodesulfurization of DES at the catalytically active edge sites of growing MoS$_2$ domains [105]. The reaction eq. (3.4) corresponds to the sum of eq. (3.1), eq. (3.2), and eq. (3.3).

While this study focuses on MoS$_2$ growth, the results are found consistent with MOCVD of other TMDs grown from organic chalcogen precursors, such as WS$_2$ [190] and WSe$_2$ [310, 225]. These studies have highlighted the importance of high chalcogen-to-metal ratios for optimized sulfidation [190, 310], which was confirmed by the XPS stoichiometry study in Fig. 3.14d. Nevertheless, if organic chalcogen precursors are used, excessive chalcogen-to-metal ratios cause detrimental codeposition of C(sp^2) hindering the lateral 2D TMD growth. Up to now, in-depth root-cause studies on

the mechanisms of C incorporation have been rare. Previous works speculated on the role of organic chalcogen pyrolysis for C incorporation without providing experimental evidence. This work confirms this hypothesis by combining *in situ* gas-phase monitoring with post-growth *ex situ* analysis, such as semi-quantitative Raman analysis. In this way, the thermally activated chalcogen precursor pyrolysis could be correlated with the C impurities in the as-grown films. If H_2 is used to mitigate C incorporation, careful tuning of H_2 flow is required to limit H_2-induced etching [291] and to control MoS_2 growth rate and film continuity.
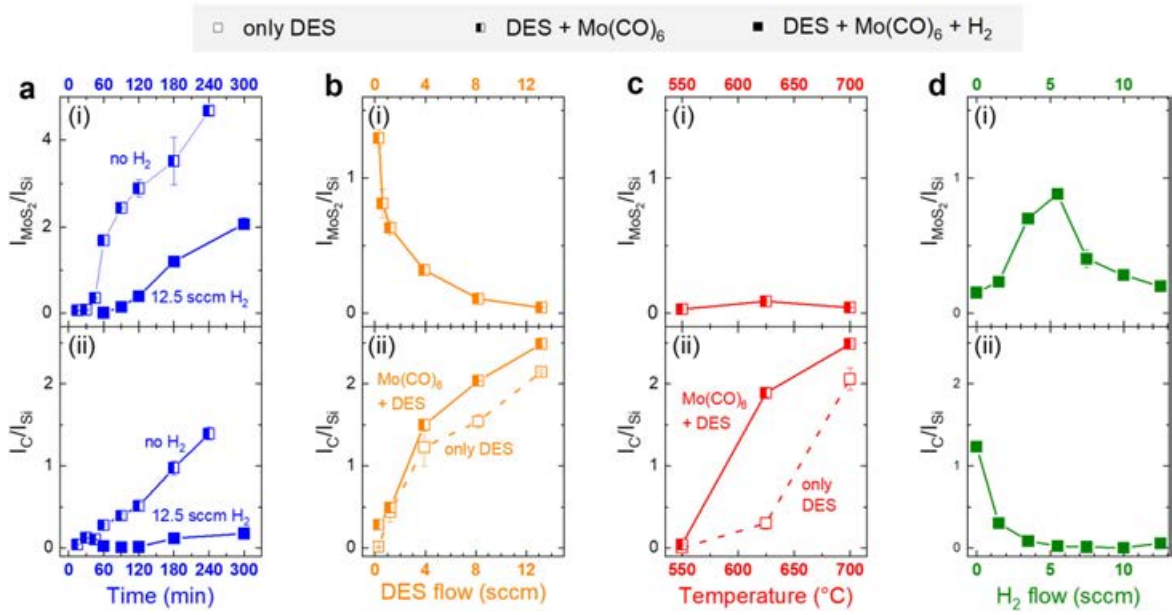
Figure 3.15 Overview of semi-quantitative Raman spectroscopy analysis of growth parameter study: **(a)** Growth time, **(b)** DES flow, **(c)** Growth temperature, and **(d)** H_2 flow, where the Raman band integral ratios (i) I_{MoS_2}/I_{Si} and (ii) I_C/I_{Si} serve as indicators for the deposited MoS_2 and carbon amount in the films, respectively. Open symbols correspond to series for single-source DES exposure, half-filled symbols to $Mo(CO)_6$ co-injection without H_2, and filled symbols co-injection together with H_2. Raw data of Raman spectra can be found in the appendix (Fig. B10).

3.3 Impact of C incorporation on film properties

So far, the variation of the growth parameters has allowed precise control over MoS_2 layer growth and C incorporation. The next sections will further clarify the impact of C incorporation on thin film morphology and (opto)electronic properties by using

additional AFM, cross-sectional TEM, PL, and XPS/UPS analysis. This analysis will point out relevant thin film characteristics for the intended transistor application.

3.3.1   Layer morphology and 2D-to-3D growth mode transition

Previous SEM and Raman studies based on image contrast and Δ-value analysis have suggested the growth of vertically, few-layer-stacked MoS$_2$ domains in presence of C impurities. To confirm this hypothesis, additional topographical AFM imaging was performed on MoS$_2$ samples grown with increasing C content, controlled by increasing DES flows between 0.3 sccm and 13.2 sccm, as shown in Fig. 3.16(b-f).

For this purpose, images were first processed by masking MoS$_2$-covered regions on the SiO$_2$ substrate and define the averaged height of the SiO$_2$ substrate plane
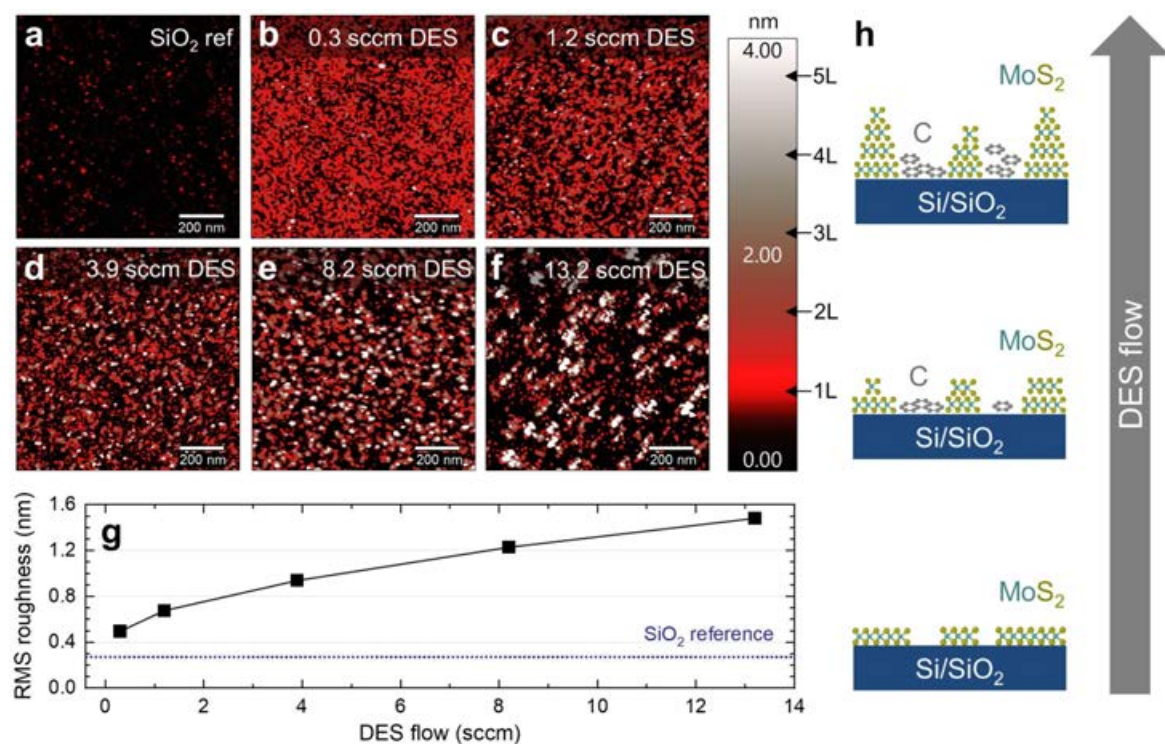
Figure 3.16 2D-to-3D growth mode transition studied by plane-fitted AFM topographic images of **(a)** a SiO$_2$ substrate reference, and **(b–f)** MoS$_2$ films grown at 700 °C (60 min) by co-injection of 0.02 sccm Mo(CO)$_6$ and DES flow varying between 0.3 and 13.2 sccm, as indicated. **(g)** Root-mean-square (RMS) roughness as a function of DES flow, as extracted from the AFM images. **(h)** Schematic illustration of growth model for MoS$_2$ thin films synthesized with increasing DES flow that results in increased C incorporation and transition from laterally-expanded to vertically-stacked MoS$_2$ domains.

as zero of the topographic scale. It has to be noted that the SiO_2 substrate, as shown in Fig. 3.16a, has a RMS roughness of around 0.27 nm. Due to the higher incorporation of C impurities with increasing DES flow the MoS_2 monolayer coverage (red in the height scale considering a monolayer step height of ~ 0.7 nm) decreases; at the same time an increased tendency of second and few-layer MoS_2 growth is observed, according to the red-to-grey/white transition in Fig. 3.16. In the case of very high DES flows (8.2 sccm and 13.2 sccm) formation of particle-like islands with heights up to ~ 4 nm can be observed. This transition from a lateral 2D to a vertical, layer-stacked 3D growth mode is also indicated by the increasing root-mean-square (RMS) film roughness as function of DES flow (Fig. 3.16g), and demonstrates the pronounced impact of C incorporation on film morphology. It is speculated that the high-energy SiO_2 surface preferred for lateral MoS_2 growth becomes increasingly covered by low-surface-energy graphitic $C(sp^2)$ patches, hindering the 2D lateral growth of MoS_2 domains according to thermodynamic [329] and kinetic [348] arguments. Thus, the presence of carbon impurities disturbs film coalescence and can result in interrupted TMD film morphologies [190, 225].

Furthermore, thin layers aiming at continuous, few-layer films for transistor channels, were synthesized at 700 °C using longer growth times (180 min), 1.2 sccm DES flow, *without* and *with* 10 sccm H_2 flow to compare carbon-contaminated and low-carbon conditions, respectively. First, AFM scans were performed over intentionally introduced step edges, in which the carbon-contaminated film show the expected roughened, particle-like morphology Fig. 3.17a), whereas the use of H_2 results in a more homogeneous and smooth 2-3L film morphology, according to the height profiles (Fig. 3.17b). Cross-sectional TEM imaging in Fig. 3.17(c-d) has been used to gain further insight into the thin film interfaces for the two growth conditions [Fig. 3.17(c-d); for a comparison at a shorter growth time of 60 min see also appendix, Fig. B12]. The C-contaminated film grown without H_2 unequivocally identifies the interrupted film morphology exhibiting layer-stacked MoS_2 islands due to 2D-to-3D growth mode transition. However, due to limited atomic resolution and contrast the location of carbon in the film can only be vaguely discerned. The rather enlarged interplanar spacing between some of the stacked MoS_2 layers in the inset in Fig. 3.17c might be due to interface contamination, but could have also been caused by the sample preparation. The changing contrast next to the multi-layer stacked domains could also speak for carbon patches between the laterally interrupted islands. Unfortunately, chemical EDX line profile analysis (not shown here) was not able to give more precise answers on the C location due to limited spatial resolution. Moreover, an overlaid C
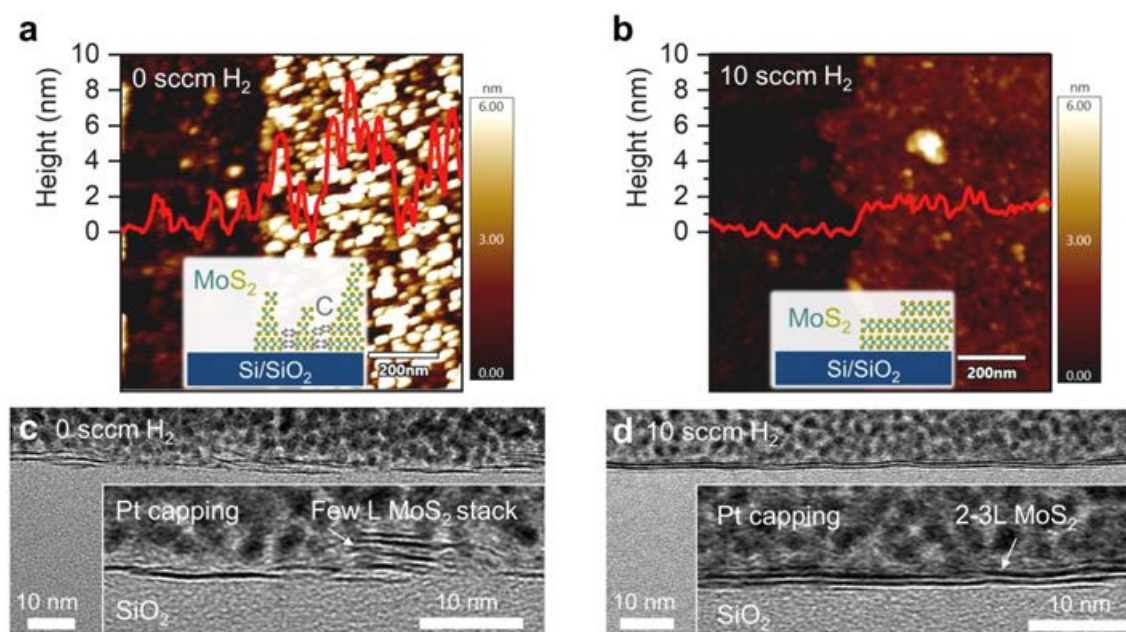
Figure 3.17 Layer continuity study, showing the morphology of MoS$_2$ films grown at 700 °C (180 min) from 0.02 sccm Mo(CO)$_6$ and 1.2 sccm DES flow. AFM step-edge topography images of **(a)** film grown without H$_2$, and **(b)** a film grown with 10 sccm H$_2$. Representative AFM line profiles along the step edges are drawn in red. Insets illustrate the hypothesized growth models. **(c–d)** Cross-sectional TEM images with magnified insets show the C-contaminated, interrupted film of multi-layer stacked islands, and low-carbon, continuous 2-3L MoS$_2$ thin films, respectively. MoS$_2$ films were protected by a Pt capping layer for FIB preparation of the TEM lamella.

signal coming from the Pt-capping layer that also contains C-contamination from the deposition process with organic precursors (see also Fig. 5.23) complicates the analysis. On the other hand, the growth conditions with added H$_2$ (10 sccm demonstrate the growth of more homogeneous and, importantly, continuous MoS$_2$ thin films with better suitability for transistor application. Nevertheless, it is remarked that the 2-3L MoS$_2$ film shows small grain size of only a few tens of nanometers with overlapping grain regions and corrugations due to substrate roughness.

3.3.2 (Opto)electronic properties

Carbon impurities in MoS$_2$ thin films are expected to alter the (opto)electronic film properties and, thus, performance of transistor [180] and photodetector [352] devices. This can be related to doping, and/or creation of defects and trap states at the MoS$_2$ interface, which was studied by PL, and XPS/UPS film analyses.

3.3.2.1   PL study and charge transfer doping

Fine-tuning of growth parameters has shown precise control over film morphology and coverage, as well as C incorporation. Although the modulation of the PL signal has already been discussed, here, a more detailed analysis of the PL spectra is used for better understanding the impact of surface coverage (χ) and C incorporation (I_C/I_{Si}) on the (opto)electronic properties. Laser excitation (488 nm, 2.54 eV) above the optical bandgap of monolayer MoS_2 induces two pronounced PL absorption features associated to neutral A^0 and B excitons at around 1.98 and 2.04 eV, respectively, as illustrated in Fig. 3.18a. These excitons originate from optical transitions from the highest spin-split valence bands due to spin-orbit coupling (SOC) within the direct electronic bandgap E_g at the K point of the Brillouin zone [332]. In the quasi-particle model, they can also be thought of as bound electron-hole pairs with exciton binding energy E_b^E. Furthermore, there exist negatively charged trions A^-, which are three-body quasi-particles formed by a hole and two electrons with trion binding energy E_b^T. Trions are typically observed as a consequence of increased electron density in MoS_2 [332, 353]. Figure 3.18b displays the PL spectra of MoS_2 films grown with different H_2 flows (films discussed in section 3.2.5, fitted by the respective A^0, B, and A^- components (see appendix for the used fitting parameters, table B2). Figure 3.18c shows that the PL intensity normalized to the B exciton intensity, considering the $(A^- + A^0)/B$ integral ratio as a quality factor [275], follows the H_2-controlled film coverage dependence, according to the overlaid SEM image insets; The PL intensity maximum corresponds to the highest film coverage at 5.5 sccm H_2 flow. This PL intensity modulation is determined by the surface coverage and grain size and was similarly observed for the series of films grown with different DES flows (Fig. B13); larger monolayer coverages (larger grain sizes) generally result in stronger A exciton peak intensity due to enhanced A exciton recombination lifetimes and reduced non-radiative recombination channels [354]. Importantly, however, the $(A^- + A^0)/B$ intensity ratio as a function of coverage χ (Fig. 3.18c) does not show a merely monotonic dependence.
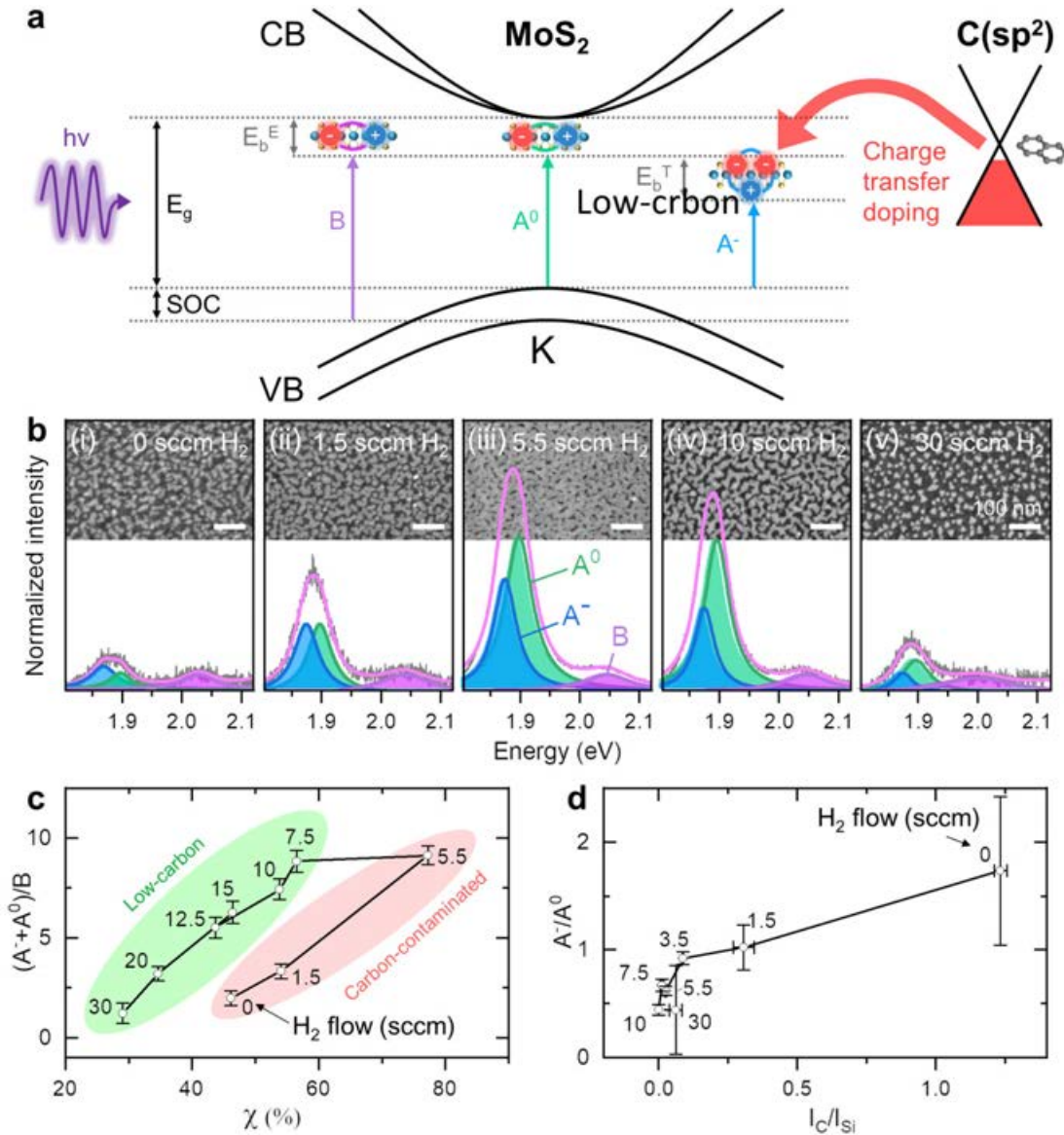
Figure 3.18 Photoluminescence study and charge-transfer doping model. **(a)** Schematic representation of the electronic band structure of MoS$_2$ at the K point with bandgap E$_g$ between the conduction band (CB) and valence band (VB). The VB is spin-split due to spin-orbit coupling (SOC). Laser irradiation excites neutral A^0 and B excitons with binding energy E$_b^E$ and negative trions with binding energy E$_b^T$. In the hypothesized model trion formation is induced by negative charge transfer from graphitic C(sp^2) in contact with MoS$_2$. [**b(i–v)**] PL spectra of MoS$_2$ thin films grown at 700 °C (60 min) from 0.02 sccm Mo(CO)$_6$, 1.2 sccm DES flow, and different H$_2$ flows varying between 0 and 30 sccm, including corresponding SEM images in background. Lorentzian peak deconvolution marks contributions of trions A^- (blue), neutral excitons A^0 (green), and B excitons (purple). The fitting envelopes are shown by the pink lines. Spectra are normalized to the B exciton intensity. **(c)** PL integral ratio $(A^- + A^0)/B$ as a function of coverage χ for MoS$_2$ films grown with different H$_2$ flows, as indicated next to each measurement point. **(d)** Trion-to-exciton ratio A$^-$/A^0 as a function of graphitic C(sp^2) content, represented by the I_C/I_{Si} Raman integral ratio, for MoS$_2$ films grown with different H$_2$ flows, as indicated.

Instead, two branches can be distinguished for films grown with H_2 flows below and above 5.5 sccm, which belongs to the growth condition yielding maximum coverage and separating films with high from films with low C impurity content, as previously discussed in section 3.2.5. As an example films grown with 0 and 10 sccm H_2 show comparable coverage but differ in $(A^- + A^0)/B$ intensity ratio by almost an order of magnitude, suggesting that the reduced PL intensity in the sample grown without H_2 results from its high $C(sp^2)$ content. Therefore, it may be concluded that the presence of $C(sp^2)$ results in strong PL quenching, which has also been observed for a MoS_2/graphene heterostructures (see appendix, Fig. B15), and might be a sign of electronic doping of MoS_2 via charge transfer, consistent with previous reports [355, 356]. Nevertheless, it must be remarked that both n-type [355, 279] and p-type [356] doping of MoS_2 interfaced with $C(sp^2)$ have been discussed controversially in the literature. To confirm the hypothesis of charge transfer doping, the A exciton peak was analyzed in more detail. By the Lorentzian peak deconvolution the neutral A^0 exciton and charged A^- trion contributions are revealed, which are separated by the trion binding energy E_b^T of around 20 to 30 meV in agreement with previous reports [273, 332]. As the trion is induced by an increased negative charge density within the MoS_2 sheet, a prominent A^- signal and increased A^-/A^0 ratio are indicators for electron doping [357, 355, 332, 353]. As shown in Fig. 3.18d, all the analyzed samples show trion contributions with A^-/A^0 ratios $\gtrsim 0.5$, which can be attributed to doping effects, such as S vacancies, strain, and/or charged impurities at the MoS_2/SiO$_2$ interface [353]. It is notable though that the increasing A^-/A^0 ratio correlates with rising I_C/I_{Si}, controlled by the H_2 flow. In other words, for higher C content the emerging trion peak dominates the PL spectra, suggesting an increased n-type tendency of MoS_2. This trend was also observed for films grown with increased DES flow and C content (see appendix, Fig. B13). Moreover, a Stokes red-shift of PL emission peaks in the range of 10 to 30 meV was found within the various, conducted growth parameter series (Fig. B14), which may further support the hypothesis of the n-type doping of MoS_2 depending on the C impurity content [332]. Interface dipoles [279] and bandgap renormalization effects [358, 359] might also play a role to explain this phenomenon. From an electrostatic point of view, the n-type doping of MoS_2 could be tentatively explained by a negative charge transfer from donor states of nanographitic $C(sp^2)$ located within the bandgap of MoS_2, as proposed in the band diagram model in Fig. 3.18a [58, 355]. This band line-up will be analyzed more closely in the following section.

3.3.2.2   XPS/UPS study and band diagram model

To support the findings of previous PL studies, including the proposed charge transfer doping of MoS$_2$ by C(sp^2), further photoemission studies by XPS/UPS were carried out. Such measurements allow to construct a band structure model that gives insight into the band alignment and potential impact of C impurities on the (opto)electronic MoS$_2$ film properties. For example, in case of doping, shifts in the MoS$_2$ valence band edge position with respect to the Fermi level are expected in XPS/UPS measurements. As the valence band spectrum of MoS$_2$/C(sp^2) grown on SiO$_2$ can be assumed as a superposition of several contributions from SiO$_2$, C(sp^2) and MoS$_2$ valences in first approximation, a series of (reference) samples were prepared and analyzed to disentangle the individual valence contributions and differentiate between possible doped/undoped MoS$_2$ state. The different samples are illustrated in the upper legend of Fig. 3.19: 1) SiO$_2$, 2) pyrolytic C(sp^2)/SiO$_2$; grown at 700 °C from single-source DES exposure, 3) graphene-C(sp^2)/SiO$_2$; CVD-graphene grown on Cu foil and transferred to SiO$_2$, 4) MoS$_2$/SiO$_2$; grown at 700 °C from DES+Mo(CO)$_6$ *with* 10 sccm H$_2$ flow, 5) MoS$_2$/C(sp^2)/SiO$_2$; grown at 700 °C from DES+Mo(CO)$_6$ *without* H$_2$, and 6) MoS$_2$/graphene-C(sp^2)/SiO$_2$; grown from DES+Mo(CO)$_6$ *with* 10 sccm H$_2$ (see appendix, Fig. B15, Fig. B16). Samples were *in situ* annealed at 500 °C (1 min) for adventitious carbon and adsorbate removal prior measurement [315].

High resolution XPS scans (Al $K\alpha$, 1486.6 eV) of the valence band region are shown in Fig. 3.19a. Spectra were energy corrected with respect to the Si 2 p substrate peak and normalized to the spectral intensity at 10.2 eV, at which the spectra of all samples are mainly dominated by the SiO$_2$-related valence contributions. First, for determining the energy difference E_{VB}^F of the valence band maximum E_{VB} with regard to the Fermi level E_F, the valence band edges were extrapolated onto the baseline of the energy axis. The valence band edge of the SiO$_2$ substrate (dark blue) can be extracted as $E_{VB}^F = 5.0$ eV. The SiO$_2$/C(sp^2) reference sample grown from pyrolyzed DES (dark green) shows a similar valence band spectrum due to the SiO$_2$ substrate contribution, but an additional C(sp^2)-related tail of π-states is clearly discernible for energies beyond the valence band maximum of the underlying SiO$_2$. The extrapolation line of the π-states from the pyrolytic C(sp^2) intersects at $\sim$0 eV, resembling the semi-metal graphene [360]. Indeed, the π valence states of the pyrolytic C(sp^2) show similar shape compared to a C(sp^2) reference of the CVD-graphene reference (light green). Therefore, in a simplified approximation, a Dirac-cone was chosen in the band structure model to represent the pyrolytic C(sp^2) in the MOCVD-grown films (Fig. 3.19d).
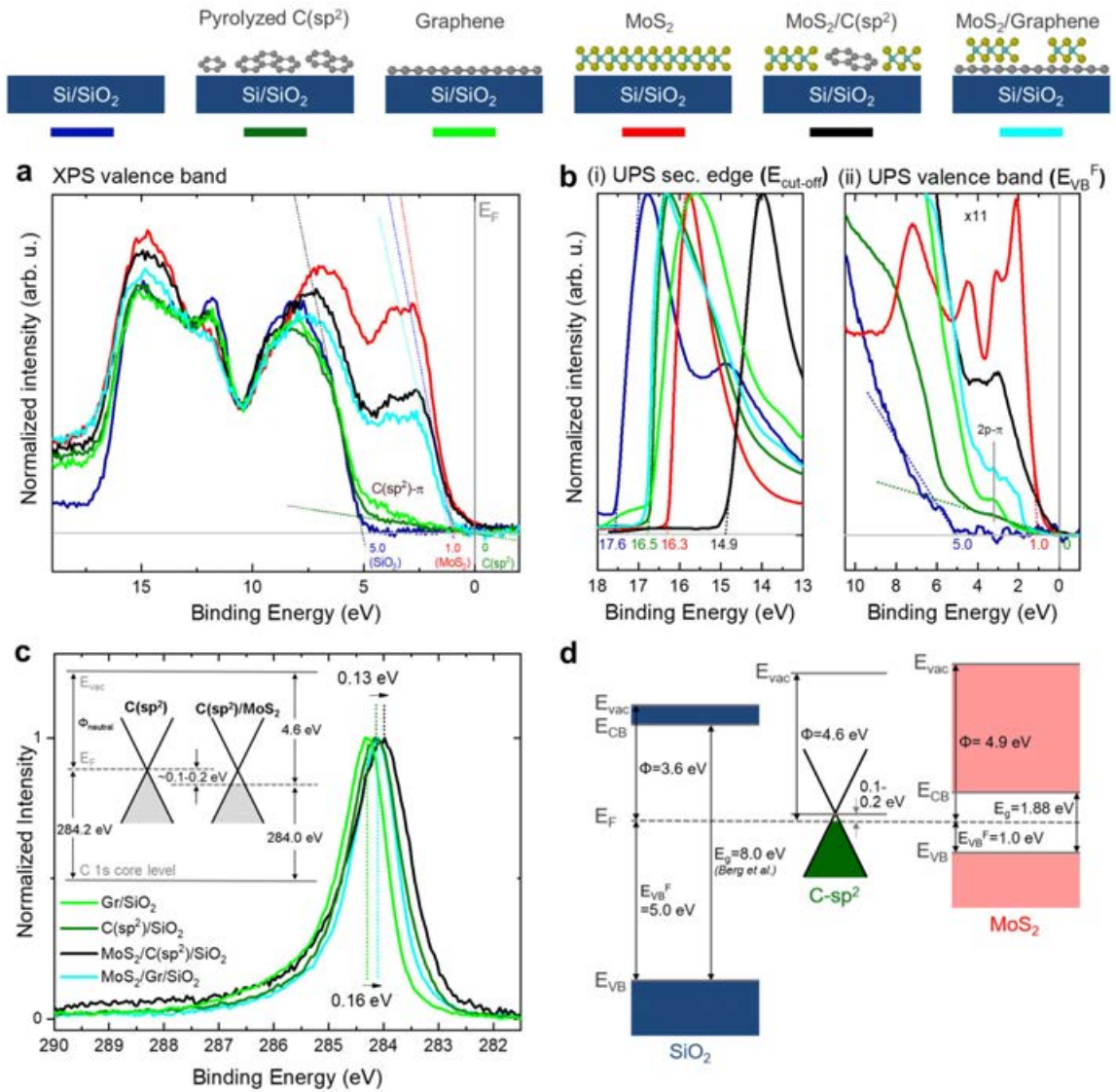
Figure 3.19 XPS/UPS valence band analysis and band diagram model of the $SiO_2/C(sp^2)/MoS_2$ heterostructure interface, as derived from the samples illustrated on the top: SiO_2, pyrolyzed-$C(sp^2)/SiO_2$, graphene-$C(sp^2)/SiO_2$, MoS_2/SiO_2, $MoS_2/$pyrolyzed-$C(sp^2)/SiO_2$, and $MoS_2/$graphene-$C(sp^2)/SiO_2$. **(a)** XPS (Al Kα, 1486.6 eV) valence band spectra for extraction of the energy difference E_{VB}^F between Fermi level E_F and valence band maximum E_{VB} of SiO_2, $C(sp^2)$ and MoS_2. **(b)** UPS spectra (He-I, 21.2 eV) showing the (i) secondary electron edge and (ii) valence band edge extraction to determine the spectral width ($E_{cut-off} - E_{VB}^F$). The UPS spectra were corrected with respect to the valence band edges obtained in the XPS valence band analysis in (a). **(c)** XPS C1s core-level spectra show downward shifts of 0.1–0.2 eV of the Fermi levels E_F below the Dirac point, suggesting p-type doping of pyrolyzed- and graphene-$C(sp^2)$ in contact with MoS_2. **(d)** Proposed band diagram model of $SiO_2/C(sp^2)/MoS_2$ interface derived from photoemission studies. Energy levels are designated as the vacuum level E_{vac}, the conduction band minimum E_{CB}, and the valence band maximum E_{VB}. E_{VB}^F were extracted from the XPS valence band in (a) and work functions ϕ were obtained from the UPS measurement in (b-c). The bandgap of SiO_2 was extracted from literature [361], and the optical bandgap of MoS_2 from the PL study.

Therefore, in a simplified approximation, a Dirac-cone was chosen in the band structure model as representation for the pyrolytic C(sp^2) incorporated in the MOCVD-grown films (Fig. 3.19d). However, it should be noted that the real band structure is likely to deviate from the ideal Dirac-cone shape; for instance, bandgap opening might arise due to the nano-crystalline nature [362] and the likely presence of C(sp^3)/hydrogenated carbon fraction [363] in the amorphous carbon incorporation, which have been detected in the previous Raman and XPS study. Further analyzing the XPS valence band spectra, the valence band edge of the "carbon-free" SiO$_2$/MoS$_2$ reference sample (red line) is determined at 1.0 eV in good agreement with literature [279]. The valence spectrum of the mixed SiO$_2$/C(sp^2)/MoS$_2$ sample (black) shows lowered MoS$_2$ intensity as expected from the lowered MoS$_2$ coverage due to C-hindered MoS$_2$ growth, and a slightly shifted MoS$_2$ valence edge of around +0.1 eV, which is in the limit of XPS resolution though. The SiO$_2$/graphene/MoS$_2$ sample (light blue) shows a more clearly observable shift of around +0.2 eV. These upshifts may indicate an n-doping effect for MoS$_2$ in contact with C(sp^2) carbon, and are comparable to the 0.3 eV shift reported for the MoS$_2$/graphene heterostructure reported by Diaz et al. [279] As another literature reference, KPFM measurements found surface potential (Fermi level) differences between 0.22 [257] and 0.28 V [364] for the MoS$_2$/graphene heterointerface.

To further test the hypothesis of n-doping MoS$_2$ by C(sp^2), a simultaneous p-doping of C(sp^2) is expected due to the negative charge transfer from C(sp^2) to MoS$_2$. Indeed, when comparing C 1 s core level spectra of the SiO$_2$/C(sp^2) reference sample with the MoS$_2$/C(sp^2)/SiO$_2$ sample, a $\sim$0.13-0.16 eV downshift for C(sp^2) in contact with MoS$_2$ is observed (Fig. 3.19c). This can be interpreted as a rigid band shift consistent with p-doping of C(sp^2) and gives further evidence to the interface charge transfer from C(sp^2) donor states to MoS$_2$ [279].

For building the band diagram model, it is necessary to focus on the SiO$_2$, C(sp^2)/SiO$_2$ and MoS$_2$/SiO$_2$ samples to extract the ionization potentials and work functions. For this purpose, UPS (He-I, 21.2 eV) measurements were performed under application of -10 V sample bias to shift the secondary electron background above the work function of the analyzer. The ionization potential IP was determined from the spectral width between the secondary electron cut-off $E_{cut-off}$ and the valence band edge E_{VB}^F according to eq. (3.5), following the procedure of Diaz et al. [279]

$$IP = 21.2 \, \text{eV} - E_{cut-off} - E_{VB}^F \tag{3.5}$$

Although charging effects due to the insulating SiO_2 substrate were affecting the absolute position of the secondary electron cut-off and valence band edge positions, extraction of the relative spectral width ($E_{cut-off} - E_{VB}^F$) delivers meaningful results for the IP. Figure 3.19b shows the (i) extraction of the secondary cut-off and (ii)valence band maxima from the UPS spectra. For plotting the UPS spectra, the valence band edges E_{VB}^F were aligned to the charge corrected XPS data. The work function Φ was determined by eq. (3.6) from the UPS-derived IP and the XPS-derived E_{VB}^F.

$$\Phi = IP - E_{VB}^F \tag{3.6}$$

Table 3.1 Band structure extraction from XPS/UPS. Energy difference E_{VB}^F between Fermi level and valence band maximum E_{VB}, secondary electron cut-off $E_{cut-off}$, ionization potential IP and work function Φ, as extracted from XPS/UPS photoemission spectra of the SiO_2, $C(sp^2)$ and MoS_2 reference samples.

Sample	$E_{VB}^F(eV)$	$E_{cut-off} - E_{VB}^F(eV)$	$IP(eV)$	$\Phi(eV)$
SiO_2	5.0	12.6	8.6	3.6
$C(sp^2)/SiO_2$	0	16.6	4.6	4.6
MoS_2/SiO_2	1.0	15.3	5.9	4.9

Table 3.1 summarizes the extracted E_{VB}^F, ($E_{cut-off} - E_{VB}^F$), IP and Φ values from the UPS/XPS analysis. IP and Φ values are in good agreement with literature values for MoS_2 on SiO_2 [365, 361] and MoS_2/graphene heterostructures [360, 279, 352]. Therefore, the analogy between C-contaminated MoS_2 thin films with MoS_2/graphene heterostructures can be drawn. Figure 3.19d shows the band alignment diagram of the $MoS_2/C(sp^2)/SiO_2$ heterostructure, using the work functions and valence band edge positions derived from the photoemission studies. As a general remark, it has to be noted that work function/ionization potential measurements are very sensitive to the sample surface condition (charging effects, presence of defects, adsorbates, dipoles at interfaces), which may have influenced the measurement of the effective work functions and band positions. This is in particular the case for the here analyzed 2D materials interfaces [365, 366, 367]. Nevertheless, the approximate band alignment of carbon states located within the MoS_2 bandgap may explain charge transfer doping at the $MoS_2/C(sp^2)$ interface, as it has been previously reported for oxide encapsulation with C-contaminated ALD layers [58]. Moreover, the midgap carbon states can be expected to act as interface traps for non-radiative recombination of excitons, and therefore

explain the observed PL quenching in the C-contaminated MoS$_2$ thin films. Furthermore, these trap states in proximity to MoS$_2$ may detrimentally deteriorate charge transport properties, highlighting the importance of an optimized, low-carbon synthesis process for lowered interface defect densities and improved electronic performance.

3.4   Grain size enhancement

The grain size determines the density of grain boundaries in a coalesced, polycrystalline thin film and is generally used as a figure of merit to describe the electronic performance of thin film transistors. This is because grain boundaries act as 2D line defect scattering centers and can deteriorate the electron transport properties. Therefore, it is desired to suppress nucleation and reduce grain boundary defect densities during synthesis of thin films. In this section, two approaches were employed to obtain MoS$_2$ thin films with enhanced grain sizes: First, alkali-assisted growth by the use of catalytically active NaCl salt, and various alkali-containing soda-lime glasses growth substrates are investigated. Second, MOCVD at highly decreased Mo flow and growth rates ($\sim$1 day/monolayer) is performed under 2D growth mode equilibrium conditions. The different growth outcomes are compared by their statistical grain sizes distributions and evaluated regarding their suitability and prospect for transistor devices.

3.4.1   Alkali-assisted growth

In the literature exists a myriad of reports documenting the grain size enhancing effect for TMD growth in the presence of alkali elements with demonstration of domain sizes reaching up to several tens of µm in MOCVD [213], and up to mm in powder CVD processes [368]. Common approaches include, placing/evaporation of alkali-halide salts, such as NaCl, in the reactor upstream the sample [47, 180, 178, 369], spin-coating of aqueous alkali-containing precursors, such as Na$_2$MoO$_4$, onto the substrate prior growth [196, 194, 170], using alkali-containing substrates, such as soda-lime glass [266, 267, 268], and more recently, adopting gas-phase MOCVD alkali-precursors, such as Na-propionate (CH)$_3$(CH)$_2$CO$_2$Na [213]. In the pioneering work from Kang et al. [47] the grain size enhancing effect of alkali halide salts was attributed to their role as desiccants. However, subsequent explanation models proposed that alkali salts suppressed nucleation density [178], and theoretical simulations highlighted the catalyzed TMD domain expansion by lowering edge adsorption energy barriers for

increased growth rates [268, 370, 371]. However, there is still a controversial discussion about the role of alkali-halides, for which the catalyzing effect has been been attributed both to the alkali and/or the halogen species. The growth promoting role of alkali ions was explained by a vapor-liquid-solid mechanism [372]: the formation of low-melting point, intermediate alkali metal oxides facilitate adatom mobilities and overall reaction rates for lateral domain growth [373, 374]. On the other hand, the role of halogens was emphasized for low-energy-barrier bond substitution reactions at domain edges and formation of volatile oxy-halides for accelerated growth dynamics [370, 368, 315, 375]. Moreover, and with particular relevance for organic chalcogen based MOCVD processes the use of alkali halide salts has shown to promote TMD growth by thermal decomposition of the sulfur source and formation of intermediate NaS_x compounds, while also enhancing film purity by reduced C incorporation from the organic precursor [180]. In the following section, alkali-assisted routes are investigated for better understanding the underlying mechanisms during the MOCVD process, compared and evaluated for the scaled growth of large grain size MoS_2 thin films.

3.4.1.1   NaCl co-evaporation

In a first approach, the co-evaporation of NaCl from a crucible upstream the substrate position was explored for growth conditions at $700\,°C$. The SEM images in Fig. 3.20a and the corresponding grain size histograms in Fig. 3.20b show the enhancement from an average grain size d_{mean} of 32 to $84\,nm$ when comparing NaCl-free and NaCl-assisted processes, respectively. Occasionally, grain sizes reaching $>200\,nm$ could be observed with NaCl. However, it was quickly noticed that the use of solid NaCl catalyst inside the reactor tube is difficult to control for reproducible growth outcomes, as documented by the SEM images of samples A and B of subsequent runs with otherwise same growth parameters. While sample A shows a rather clean surface with white nucleation spots in the center of triangular domains, sample B exhibits heterogeneous domain growth and particle-like residues. By analyzing the overview XPS spectra of the as-grown samples in Fig. 3.20c, these particles were likely Na-rich residues capturing the uncompleted reaction due the uncontrolled concentration by solid source evaporation.

A closer look at Mo 3 d core level spectra gives further insight into the chemical composition of the different samples. As expected, all samples exhibit the Mo^{IV} oxidation state (blue doublet) corresponding to MoS_2 [167] with Mo $3\,d_{5/2}$- and Mo $3\,d_{3/2}$-components positioned at $229.3 \pm 0.1\,eV$ and $232.5 \pm 0.1\,eV$, respectively. As observed in previous XPS results, the Na-free sample additionally contains MoO_3 according to

the Mo^{VI} oxidation state (red doublet) with peaks positioned at 232.6 ± 0.1 eV and 235.8 ± 0.1 eV, respectively. Interestingly, correlated with increasing number of white particles (SEM, Fig. 3.20a), MoS$_2$ grain size (histograms, Fig. 3.20b)) and Na concentration (XPS, Fig. 3.20c), the phase fraction of the Mo$^{VI-\delta}$ oxide phase normalized
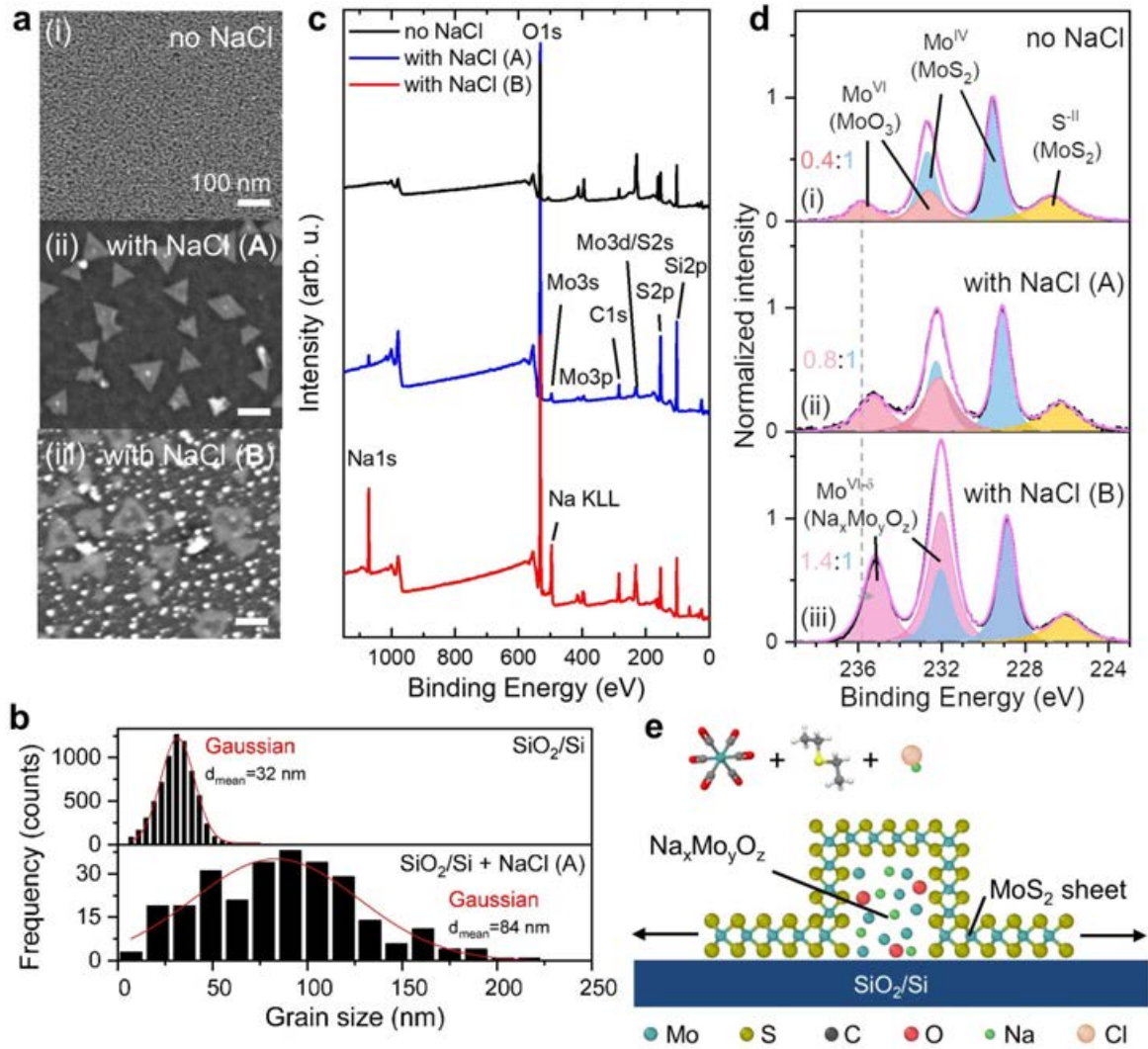
Figure 3.20 NaCl-assisted MoS$_2$ growth on SiO$_2$. **(a)** SEM images for MoS$_2$ grown (i) without NaCl, and (ii-iii) two different samples A and B grown with 100 mg NaCl and nominally identical growth parameters, but different growth outcome. **(b)** Histograms of grain size distribution (side length of assumed equilateral triangle). Data fitted with Gaussians and the mean grain sizes d_{mean} were extracted as depicted. **(c)** XPS overview spectra with designated peaks, and **(d)** Mo 3d core level region with assigned MoS$_2$-related Mo^{IV} doublet (blue) and S^{-II} singlet (yellow), and MoO$_3$-related Mo^{VI} doublet (red). Peak intensities are normalized to the Mo^{IV} 3 d$_{5/2}$ peak. MoO$_3$:MoS$_2$ area ratios of their respective Mo^{IV} 3 d$_{5/2}$ components are given. **(e)** Simplified model of the alkali-assisted growth mechanism illustrating a low-melting point Na$_x$Mo$_y$O$_z$ compound that transforms into monolayer MoS$_2$ upon sulfurization.

to the Mo^{IV} (MoS_2) increases concurrently, while a simultaneous downshift by $0.6\,eV$ towards lower binding energies can be observed towards sample B. This suggests the presence of another Mo oxide phase, indicated by the red-to-pink color gradient for the $Mo^{VI-\delta}$ doublet, in case of the alkali-assisted samples, in which the Mo oxidation state is slightly reduced compared to the MoO_3 state. This can be explained by the presence of an $Na_xMo_yO_z$ compound consistent with the $Na\,1\,s$ signal [376]. Such low melting point Na-Mo-O intermediate compounds forming molten nucleation clusters have been reported to mediate MoS_2 growth through a vapor-liquid-solid mechanism [372, 377, 374, 378], as illustrated in Fig. 3.20e.

To further test the hypothesis of Na-Mo-O-rich nucleation centers, a locally resolved analysis of the clusters was conducted by direct growth of MoS_2 onto a $18\,nm$-thin SiO_2 membrane TEM grid (Fig. 3.21a). In this way, while not changing the growth substrate material, a water-based transfer onto a standard TEM grid and the risk of washing away water-soluble intermediate compounds of interest could be avoided, allowing for high-resolution imaging and further chemical analysis of the sample in its as-grown state. The STEM image in Fig. 3.21b shows triangular MoS_2 domains on the size of $\sim100\,nm$ together with nucleation and residual particles consistent with previous SEM images.

EDX analysis was performed to analyze the elemental composition in various spots (EDX regions A, B, C in Fig. 3.21b). Si and O substrate signals and C attributed to adventitious carbons and/or growth-induced carbon incorporation are detected in all EDX spectra. Spectrum B was recorded on a MoS_2 domain containing a centered nucleation cluster, and exhibits the expected, overlapping Mo and S spectral regions, as previously assigned in Fig. 3.3. Importantly, Na is detected in the absence of Cl within the detection limit, suggesting the role of a Na-enriched nuclei, possibly a $Na_xMo_yO_z$ compound in agreement with previous XPS analysis. The absence of Cl can be explained by the evaporation of highly volatile MoO_xCl_y oxysulfide reaction side-products [372, 374]. The particle in spectrum B contains Mn and Ca impurities, which can be assigned to corrosion products from the metallic sample holder [Fig. 3.21a(iii)], which was only used for this particular experiment due to the challenge of sample mounting in the vertical reactor design (otherwise an inert, quartz-made sample holder was used). EDX C located on the white particle between MoS_2 domains showing both increased Na and Cl signals can be attributed to a condensated NaCl particle and highlights the uncontrolled, oversaturated NaCl concentration in the growth environment. A magnified image of a typical MoS_2 domain with a, centered nucleation particle is shown in Fig. 3.21d. In addition to the Na-rich concentration shown in Fig. 3.21c(i), the

EDX line scan (Fig. 3.21) qualitatively identifies the particle further to be Mo-rich, although no increased O signal attributable to the expected Na$_x$Mo$_y$O$_z$ compound is apparent. It is possible that the strong overlaying O signal contribution from the 18 nm-thick SiO$_2$ substrate and the limited spatial resolution do not allow to detect the comparatively low intensity O-contribution from the likely present Na$_x$Mo$_y$O$_z$
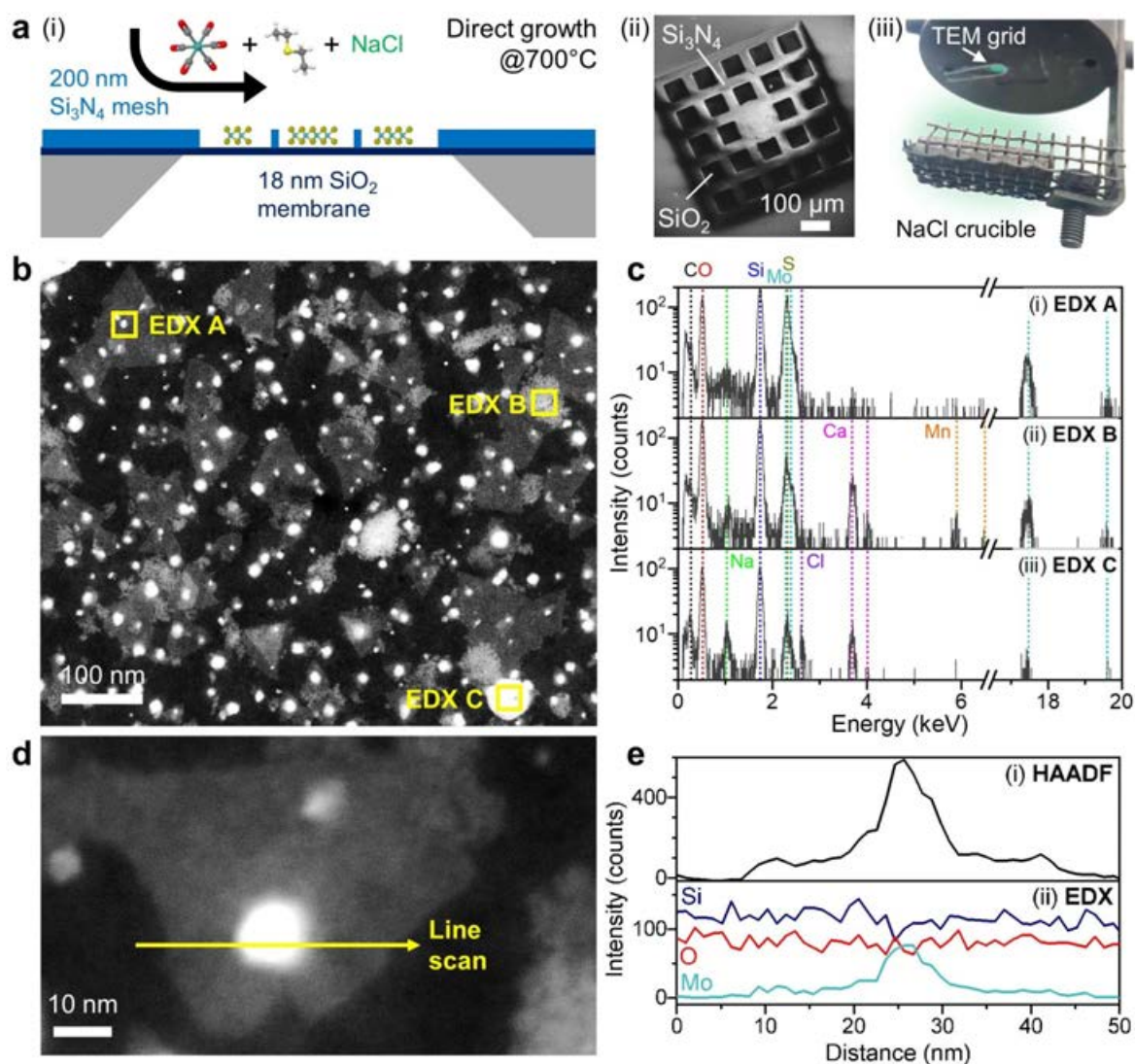
Figure 3.21 NaCl-assisted growth TEM study. **(a)** (i) Schematic illustration of the direct MOCVD growth of MoS$_2$ from Mo(CO)$_6$ and DES at 700 °C onto a SiO$_2$ membrane supported by a Si$_3$N$_4$ TEM grid. An SEM image of the TEM grid is shown in (ii), which is mounted face-down above the NaCl evaporation crucible in the growth setup. **(b)** STEM image with designated areas for **(c)** EDX analysis in the zones (i) A, (ii) B, and (iii) C. **(d)** STEM image of a MoS$_2$ domain with center particle, over which a line scan was performed with respective **(e)** (i) HAADF intensity and (ii) EDX spectra profiles.

compound. Nevertheless, based on the XPS results, it is reasonable to conclude that intermediate $Na_xMo_yO_z$ compounds play a dominant role in the here observed alkali-catalyzed reaction mechanism. This also raises the question about the source of O in the reaction environment, which could include $Mo(CO)_6$, the SiO_2 substrate, and more likely H_2O found in the vacuum background by the residual gas analyzer Fig. B7.

As a final note, it is remarked that even with extended growth time it was difficult to achieve coalesced thin films with the alkali-salt route, which may be related to the uncontrolled, excessive NaCl amounts inducing a surface poisoning effect and limiting nucleation and coverage, as previously reported [178]. Moreover, during the course of NaCl-evaporation experiments a whitish condensate from NaCl (confirmed by a powder XRD sample) and related reaction products was accumulated on the reactor walls, resulting in a memory effect and increased grain sizes in consecutive runs even when no additional NaCl was employed. Eventually, this required cleaning/replacement of the quartz tube for resetting to initial NaCl-free conditions. As observed for powder CVD approaches, adopting solid source approaches for scaled, and reproducible TMD growth is highly difficult.

3.4.1.2 Soda-lime glass substrate

Aiming at a more controlled introduction of alkali-elements, MoS_2 growth was performed on different, commercial alkali-containing soda-lime silicate glasses. This approach provides a promising route towards large-area, grain size enhanced MoS_2 synthesis with improved scalability potential and availability of low-cost wafers up to 6". The goal of the study was to get further insights into the alkali-catalyzed growth behaviour and to identify substrates yielding coalesced MoS_2 films with largest possible grain size.

The used substrates included a float-glass (Marienfeld Superior), and two types of crown-glasses (SCG 94 and B270i) with material properties and composition listed in the appendix (table A2). AFM images of the as-received glass surfaces are appended in Fig. B17, which show higher RMS roughnesses ($\gtrsim 0.8\,\text{nm}$) compared to the previously used thermally oxidized SiO_2/Si wafers ($\sim 0.2\,\text{nm}$) due to polishing grooves. As illustrated in Fig. 3.22, the soda-lime silicate glasses mainly composed of SiO_2 "silica", Na_2O "soda" (with additions of K_2O in modified crown-glasses), and CaO "lime", are suitable to catalyze the 2D lateral MoS_2 grain growth from Mo and S precursors on the surface due to substrate-controlled alkali (Na, K) supply from the bulk [268]. An essential factor for the growth-promoting effect is the surface concentration c_{alkali} of alkali catalyst species. In a simple model, c_{alkali} depends on the initial concentration

c_0 depending on glass composition and may change in time during synthesis due to migration processes from the bulk to the surface along z-direction, due to local accumulation along (x, y)-directions underneath or between growing MoS$_2$ domains [369], and depletion from the surface through evaporation of volatilized species [372, 213]. The growth temperature T plays an important role in the formation of intermediate compounds and as activation energy for diffusion processes close to the softening point in "molten" glass [268]. In addition, precursor trapping in the bulk can occur [266].

A comparative growth parameter study was carried out on the different soda-lime glasses at the previously optimized conditions for growth on SiO$_2$ at 700 °C, 0.02 sccm
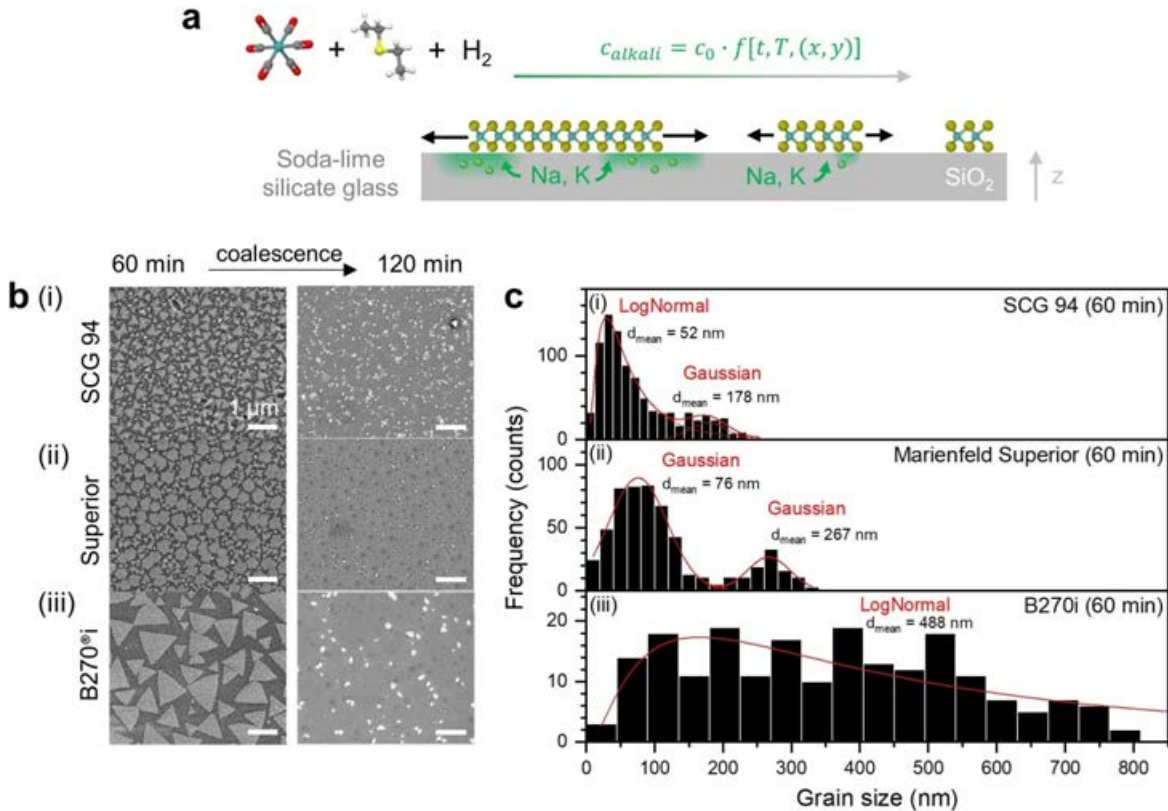
Figure 3.22 MoS$_2$ growth on different soda-lime glasses from 0.02 sccm Mo(CO)$_6$, 1.2 sccm DES flow, and 12.5 sccm H$_2$ at 700 °C. **a** Schematic illustration showing MoS$_2$ domain growth on alkali(Na,K)-containing soda-lime silicate (SiO$_2$) glass, the grain size depends on the alkali concentration c_{alkali} diffusing from the bulk to the surface, which is a function of time t, position (x, y) and, growth temperature T. **(b)** SEM images of sub-monolayer (60 min) and coalesced (120 min) MoS$_2$ thin films grown on different soda-lime silicate glasses: (i) Plan Optik SCG 94 crown-glass (ii) Marienfeld Superior float-glass, and (iii) Schott B270®i crown-glass. **(c)** Histograms of particle size distribution extracted from SEM images and designated fits, respectively, where the mean grain sizes d_{mean} are depicted.

$Mo(CO)_6$, and 1.2 sccm DES flow, and 12.5 sccm H_2. Growth times of 60 min were used for sub-monolayer films to evaluate the grain size distribution, and longer growth times (120 min) were used to demonstrate the growth of coalesced thin films. While the grain size enhancing effect of soda-lime glasses is clearly apparent from the 60 min samples on all the three tested surfaces (Fig. 3.22b) when comparing to alkali-free growth on SiO_2, the corresponding histograms in Fig. 3.22c reveal differences in grain sizes distributions depending on the glass composition. The achievable grain sizes increase along the order SCG 94, Superior, and B270i. For the latter, grain sizes approaching µm-scale could be obtained accounting for the majority of covered surface area. Additionally, some domains of several µm in size were evidenced with nucleation cluster still present or evaporated from the domain centers (see appendix, Fig. B21). Interestingly, bimodal grain size distributions of the 1L film are apparent from the histograms. Further growth time studies of sub-monolayer coverage films confirmed the dynamic evolution of two families of "large" (l-MoS_2) and "small" (s-MoS_2) grain size distributions emerging from the early nucleation phase, as shown in Fig. 3.23. The typical film morphology evolution towards the coalesced film is therefore determined by l-MoS_2 regions between which s-MoS_2 grains fill the gaps (also see appendix, Fig. B20). A similar, heterogeneous growth behaviour has been previously reported for NaCl-assisted MOCVD of MoS_2 thin films and has been explained by spatially varying alkali accumulation at the MoS_2/substrate interface evidenced by TOF-SIMS mapping [369]. Similar chemical analysis could help to further understand the role of temporally and locally changing c_{alkali} on the here used soda-lime glass surfaces.

The 120 min samples in Fig. 3.22b demonstrate growth of coalesced films (grey contrast) with onsetting bilayer nucleation (light grey/white contrast spots) preferentially occurring at grain boundaries of the underlying first layer, as illustrated in the schematic in Fig. 3.24a. Therefore, highest second layer nucleation densities can be observed on SCG 94 that exhibited the smallest 1L grain sizes [Fig. 3.22b(i)], and lowest second layer nucleation densities can be observed on B270i with largest 1L grain sizes [Fig. 3.22b(iii)], which suggests an increasingly self-limited growth behaviour in function of the 1L grain boundary density. The second- and multi-layer grain boundary nucleation behaviour was captured in more detail by magnified SEM (see appendix, Fig. B22), and topographic/phase AFM imaging in Fig. 3.24(b-c). The topographic images reveal heterogeneous particle formation, nucleated bilayers and few-layer pyramidal stacks on the coalesced primary layer. The phase images reveal intra-grain defect lines and grain boundaries of the primary layer and defect-induced bi- and few-layer domain nucleation on the primary layer. As a remark, as-grown,

coalesced microcrystalline MoS$_2$ films on soda-lime glass typically exhibited about an order of magnitude stronger PL signals than their nano-crystalline counterparts on SiO$_2$. However, dynamic PL intensity variation under laser irradiation combined with a SEM and XPS study hinted at residual, metastable and photo-catalytically transformed surface species, which is not discussed in further detail.

To further understand the time-dependent, nucleation-promoting effect due to varying c_{alkali}, MoS$_2$ thin films were grown for 15 min *with* (1 h) and *without* pre-annealing of soda-lime glass at 700 °C prior growth start (see appendix, Fig. B23). While the sample without pre-anneal shows the previously described bimodal nucleation behaviour (*s*-MoS$_2$: ∼26 nm, *l*-MoS$_2$: ∼90 nm), the annealed sample shows a more
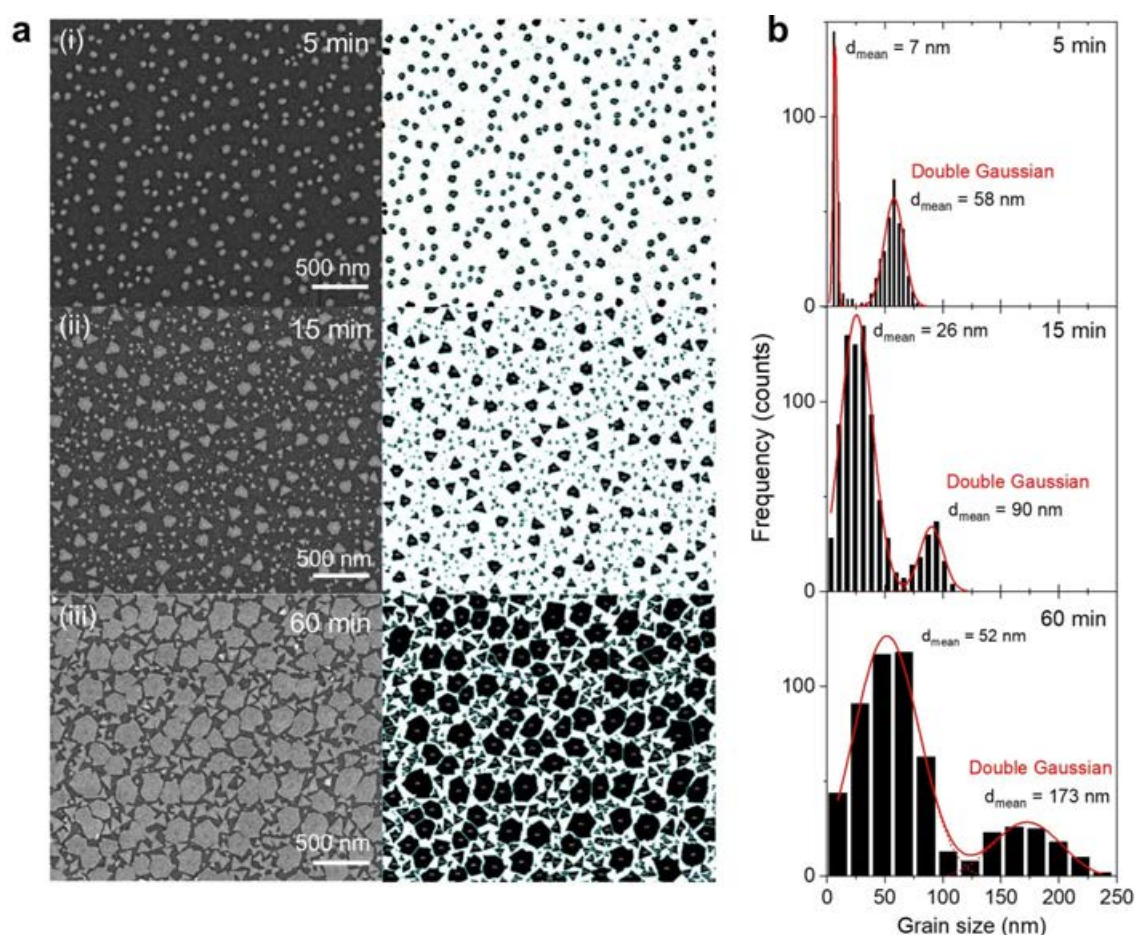
Figure 3.23 Time-dependent MoS$_2$ grain size evolution on soda-lime glass (Marienfeld Superior). MoS$_2$ thin films were grown at 700 °C. SEM images with corresponding binary images analyzed by ImageJ, and **(b)** respective grain size distribution are shown for growth times of (i) 5 min, (ii) 15 min, and (iii) 60 min. Histograms were fitted by double Gaussians for extraction of mean grain sizes d_{mean}.

pronounced difference in the bimodal grain size distribution with largely enhanced l-MoS$_2$ domains (s-MoS$_2$: $\sim$29 nm, l-MoS$_2$: $\sim$850 nm), suggesting an initially boosted growth rate of the l-MoS$_2$ family with an even more pronounced effect in case of substrate pre-annealing. Further growth tests with even shorter growth times of only 5 min revealed that the primary l-MoS$_2$ domains already had been formed within a few minutes at this very early growth stage, possibly promoted by an alkali-enriched c_{alkali} at growth start. After this initial grain size boosting effect, growth of l-MoS$_2$ slows down indicating that c_{alkali} depletes over time, as it has been observed for repeated growth on soda-lime glasses, where the grain size decreased in subsequent growth runs
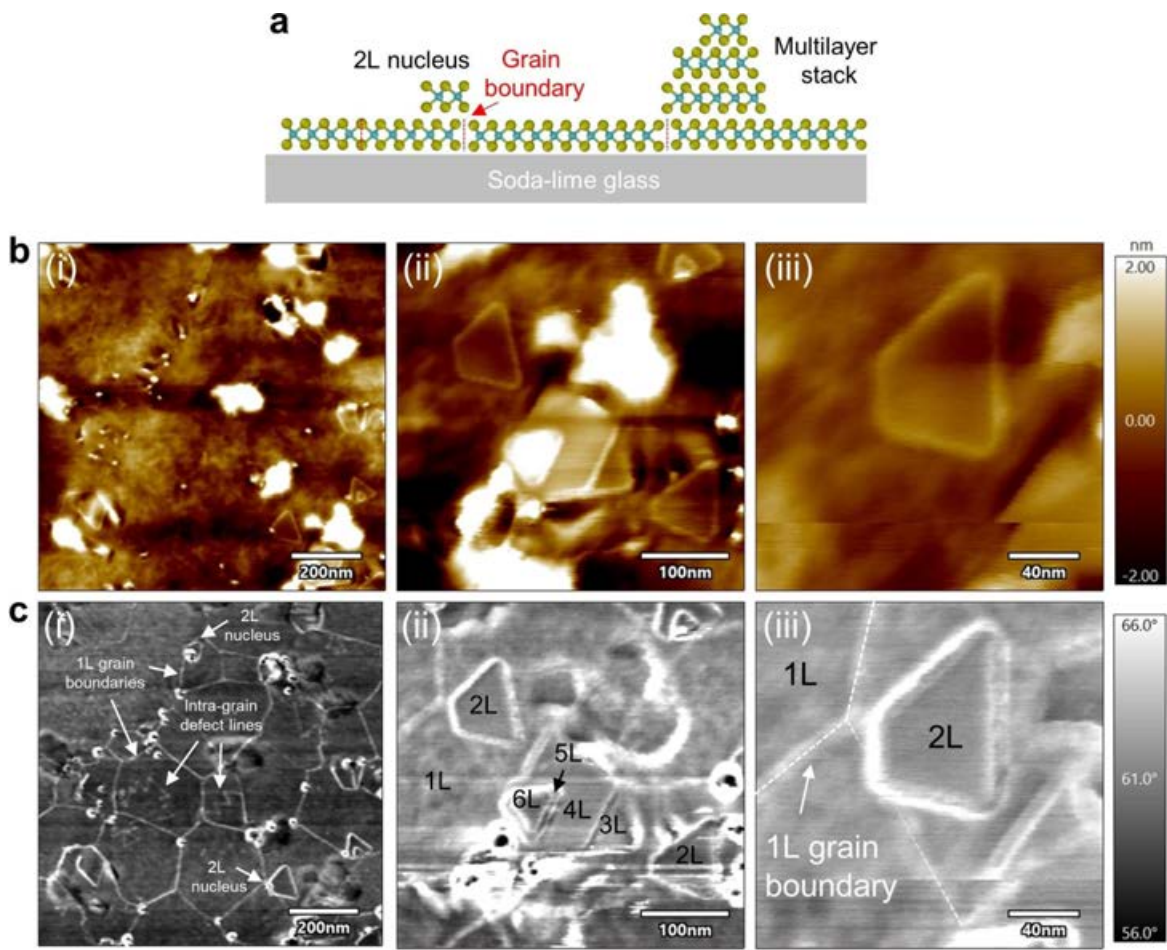
Figure 3.24 AFM of a 1L-MoS$_2$ thin film grown on soda-lime glass (SCG 94) at 700 °C (180 min). **(a)** Illustration of coalesced MoS$_2$ layer with grain boundaries acting as nucleation points for second layer and multi-layer stacks. **(b)** Topographic images and **(c)** phase images for scan sizes (i) 1×1 µm^2, giving an overview of grain structure with boundaries between stitched 1L grains, intra-grain defect lines, and 2L nucleation centers located at grain boundaries, (ii) 0.4×0.4 µm^2, showing a multi-layer stack, and (iii) 0.2×0.2 µm^2, 2L-domain nucleated on 1L grain boundary at high magnification.

on the same substrate [268]. XPS analyses of the Na 1s peak of as-received soda-lime glass substrates (see appendix, Fig. B18) and as-grown films (see appendix, Fig. B19) confirm a decrease in Na-surface concentration post-growth.

To test the temperature dependence of alkali-assisted grain size enhancement, growth temperature series for MoS$_2$ thin films grown at 550, 600, 650 and 700 °C were carried out both on soda-lime glass and on SiO$_2$ with NaCl-evaporation. In both cases, enlarged grain sizes were observed only for the 700 °C conditions (Fig. 3.25), indicating a temperature threshold to activate the catalytic effect. This is in agreement with a previous report [369, 379] and may be related with the melting point of intermediate alkali metal oxides Na$_x$Mo$_y$O$_z$, such as Na$_2$Mo$_2$O$_7$ (605 °C) or Na$_2$MoO$_4$ (687 °C) that mediate the vapor-liquid-solid (VLS) and vapor-solid (VS) mechanisms [370, 372]. The exact composition of intermediates within the ternary Na-Mo-O phase diagram was not determined here, but could be subject for detailed analysis in further X-ray diffraction studies [376, 213].
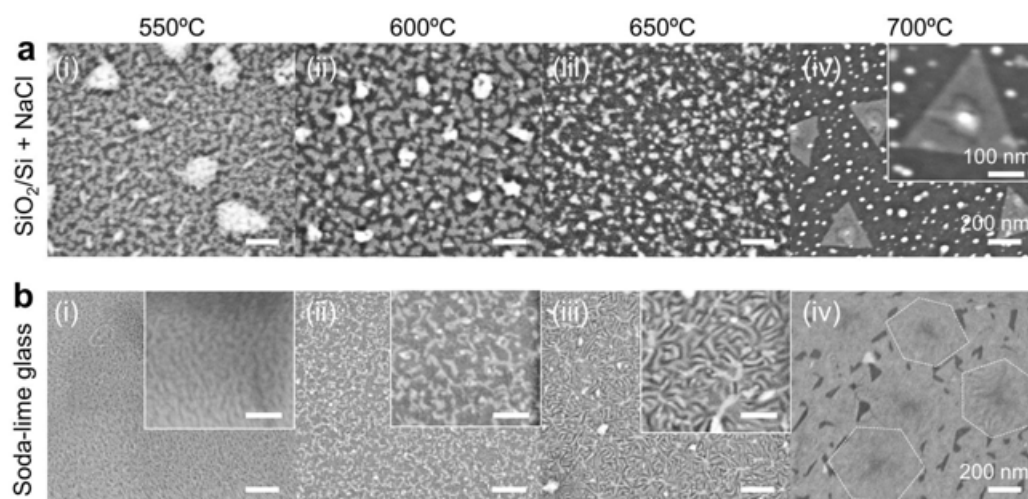
Figure 3.25 Growth temperature study of alkali-assisted growth in ICN2 reactor. SEM images of MoS$_2$ thin films grown from Mo(CO)$_6$ and DES on **(a)** SiO$_2$/Si using NaCl evaporated from a crucible upstream the substrate, and on **(b)** soda-lime float-glass "Superior" for growth temperatures of (i) 550 °C, (ii) 600 °C, (iii) 650 °C, and (iv) 700 °C. Scale bars are 200 nm and 100 nm for insets. The SEM images show that the grain-size-enhancing effect of alkali species is only achieved for temperatures of 700 °C.

Moreover, the carbon-reducing alkali effect [180] previously reported for organosulfide based MOCVD of MoS$_2$ thin films was examined. For this purpose, Raman analysis of a H$_2$ series carried out at 700 °C with 0, 5.5 and 12.5 sccm H$_2$ flows showed that the alkali-assisted growth in absence of H$_2$ does not avoid C formation (see appendix,

Fig. B24). This is probably because the presence of alkali species on the substrate surface have limited impact on the gas-phase pyrolysis reactions that were mainly found responsible for C incorporation in previous sections. Addition of H_2 is still required for the growth of low-carbon films with vanished carbon D and G Raman bands (see appendix, Fig. B24b). Importantly, enlarged grain growth was strongly hindered without H_2 in C-contaminated films (30 – 70 nm) compared to low-carbon films (several 100 nm) grown with 5.5 and 12.5 sccm H_2, which indicates that the combined H_2- and alkali-assisted process is key to C mitigation and grain size enhancement.

In summary, this study shows that alkali-assisted TMD synthesis is promising for the growth of films with enlarged grain sizes under the here optimized conditions at 700 °C. The substrate-controlled alkali supply by (Na,K)-containing soda-lime glass offers a more reproducible route compared to solid-source NaCl evaporation and yielded coalesced, cm-scale films with up to µm-sized domains. Both alkali approaches were observed to follow similar reaction mechanisms, involving low melting point, molten $Na_xMo_yO_z$ seeding clusters and lowered energy barriers promoting the growth dynamics and lowering nucleation densities above a certain temperature threshold. However, despite the undisputable benefit for grain size enhancement and grain boundary defect reduction, also a critical evaluation must be undertaken when considering the use of alkali-assisted approaches. First, heterogeneous film morphologies were commonly observed, including particle formation due to intermediate reaction products, spatial grain size variations, and occasional multi-layer-stack formation, which may result in non-uniform mechanical and (opto)electronic film properties. Secondly, residual alkali impurities raise concerns because alkali migration is well-known in the semiconductor industry to cause reliability and oxide leakage issues [380, 381], that is why the use of alkali elements is not tolerated in CMOS-compatible fabrication processes. Even if wet transfer from the growth substrate might help to wash out alkali impurities [178], the electrical performance of transistors might be degraded [369]. Finally, a closing remark concerns the practical applicability and use of soda-lime glass substrates at increased growth temperatures (i.e. 700 °C) required to activate the catalyzed growth. At these temperatures close to the glass softening point, the mechanical properties of glass turn highly viscous, which may lead to substrate deformation. In particular, in the vertical ICN2 reactor setup with down-facing, "hanging" substrate, bowing due to creep under gravitational force was observed at prolonged growth times. Although such bowing might be avoided in a "sitting" substrate configuration, it must be taken into account that any non-planar surfaces may complicate subsequent layer transfer steps required for MoS_2 device integration.

3.4.2   Low Mo flow growth rate controlled MOCVD

The following growth study was carried out in the horizontal, hot-wall Yonsei reactor, described in section 2.3.1. Aiming at enlarged MoS$_2$ domains and following the approach of Kang et al. [47], thin films were grown on SiO$_2$/Si with long growth times using ultra-low, growth-rate-controlling Mo(CO)$_6$ flows ($\sim 8.3 \times 10^{-5}$ sccm) in excess of DMS (~ 0.6 sccm), allowing a Mo-diffusion-limited regime under highly S-rich conditions (S:Mo ~ 4560), which is favorable for the 2D domain growth mode. Optionally, NaCl was placed at the low-temperature furnace entrance upstream the substrate for alkali-assisted growth, avoiding NaCl evaporation in the higher temperature zone, while still showing a grain size enhancing effect [47].

Figure 3.26 displays an optimization study, in which growth temperatures of 600 °C, 650 °C, and 700 °C were investigated. From the AFM images (Fig. 3.26a) it is apparent that the optimal growth regime for 2D domain growth can be found at 600 °C with average domain sizes around 158/280 nm (without NaCl) and 363/842 nm (with NaCl), as shown by the histograms in Fig. 3.26b. The bimodal grain size distribution typically observed for alkali-assisted growth in case of the NaCl-free process in Fig. 3.26b(i) is surprising, but might be explained by a memory effect of the reactor from prior NaCl-assisted growth runs. Growth temperatures above 600 °C resulted in decreased domain sizes and a more particulate-like 3D growth mode shown in the magnified AFM insets in Fig. 3.26a(iii) and (vi). A probable explanation for this behaviour can be the higher Mo partial pressure due to increased thermal Mo(CO)$_6$ decomposition along the hot-wall tube, resulting in reduced S:Mo ratios and Mo clustering [310] at elevated temperatures [47, 310], and/or increased C incorporation evidenced by the increased D and G bands seen in the corresponding Raman spectra (Fig. 3.26c). The PL spectra are shown in Fig. 3.26d). Variations in intensity and peak positions can be explained by differences in grain size, film coverage, carbon-induced quenching, and crystalline MoS$_2$ quality. The latter C incorporation likely correlates with DMS-pyrolysis-induced C contamination, which can be expected to onset above around 600 °C similar to the case of DES as per their almost identical, bond dissociation energies found in DFT-simulations (see appendix table A1), and consistent with explanations in section 3.2.4. Moreover, the Δ-widening above values of 20 cm^{-1} with increasing temperature and C incorporation suggests few-layer-stacked MoS$_2$ and hints at the previously observed, carbon-induced 2D-to-3D growth mode transition in agreement with studies carried out in the ICN2 reactor. A final important result is that NaCl helps lowering C incorporation, as seen in comparison of the Raman spectra of the 700 °C samples, and

in agreement with literature [180]. Further studies are required to understand this C-reducing effect in detail.
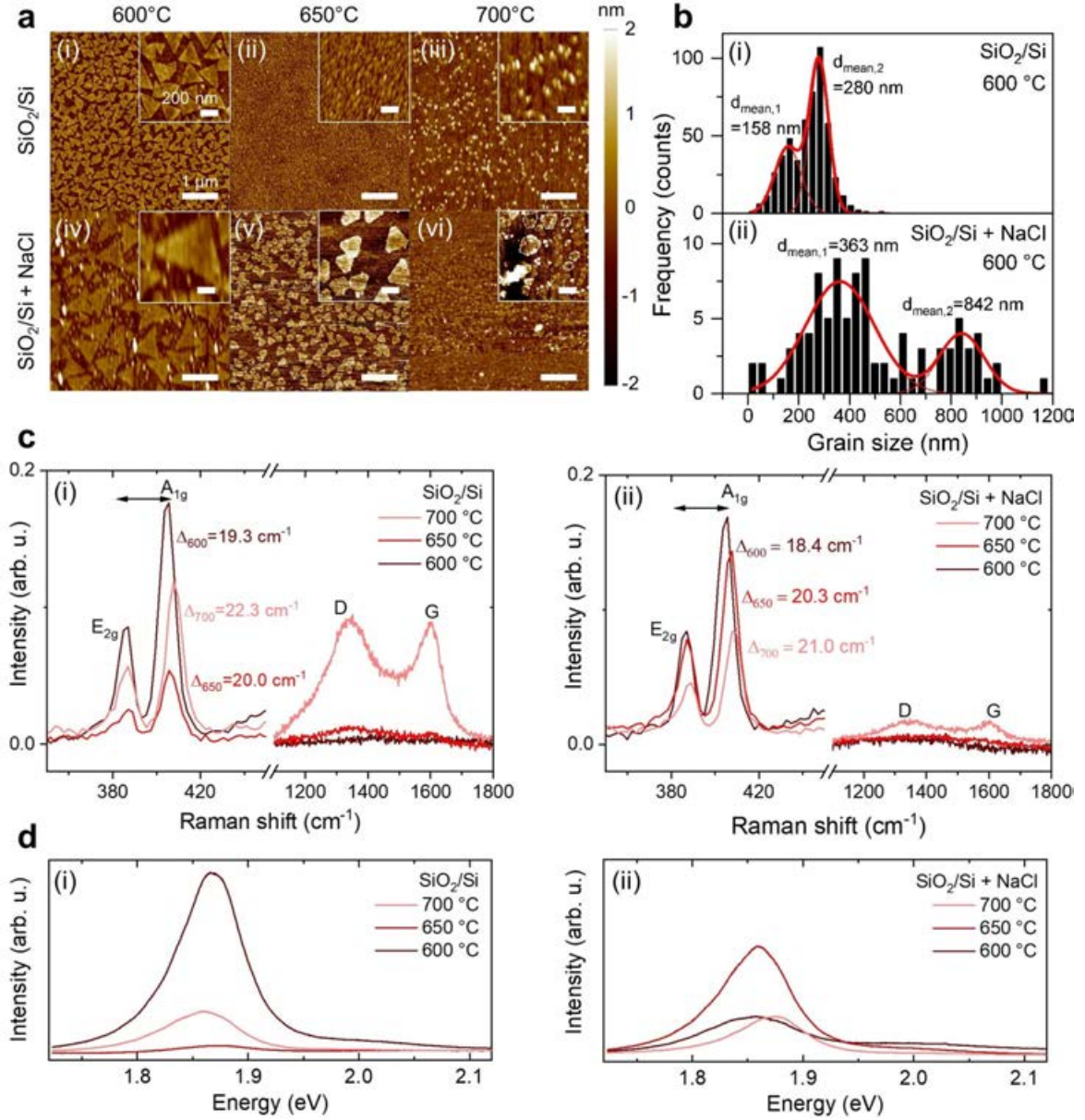
Figure 3.26 Low growth rate MOCVD. **(a)** AFM images for MoS_2 thin films grown on SiO_2/Si for 16 h from 8.3×10^{-5} sccm $Mo(CO)_6$ and 0.4 sccm DMS, 5 sccm H_2, 100 sccm Ar at varied growth temperatures of 600, 650, and 700 °C (i-iii) without, and (iv-vi) with NaCl placed at the furnace entrance upstream the substrate. Scale bars are 1 μm and 200 nm for magnified insets. **(b)** Histograms of grain size distribution for growth at 600 °C (i) without and (ii) with NaCl. The mean grain sizes d_{mean} are depicted. **(c)** Raman spectra were normalized to the Si peak (521 cm^{-1}). The frequency difference Δ between A_{1g} and E_{2g}^1 MoS_2-modes is given for the different growth temperatures. **(d)** PL spectra.

In conclusion, the low growth rate approach was found compatible with the alkali-assisted approach and largest 2D domain sizes could be obtained in the low-carbon 600 °C regime. Importantly, growth results were found consistent with previous studies in the ICN2 reactor, pointing at the universality of conclusions made for the organosulfide-based TMD synthesis. Although the Mo-flow-limited route was suitable for enhancing grain sizes, which will be helpful for benchmarking grain-size dependent transistor properties, the extended growth times are not attractive for high-throughput manufacturing from an industrial perspective.

3.5   Summary

In this chapter, large-area MOCVD of layer-thickness and grain size-controlled, poly-crystalline MoS$_2$ thin films from organosulfur precursors was demonstrated on cm^2-scale, amorphous substrates (i.e. SiO$_2$/Si and soda-lime silicate glass wafers). A systematic study was presented involving key growth parameters (growth time, temperature, Mo:S ratio, H$_2$ flow) and their effect on layer morphology, chemical composition, and (opto)electronic properties was clarified by using a large variety of film characterization methods (SEM, AFM, TEM, Raman, PL, EDX, XPS/UPS). In particular, the origin, effect and mitigation of C incorporation, including *in situ* gas-phase monitoring of the growth process, revealed the crucial role of organosulfide pyrolysis during MOCVD, resulting in undesired graphitic C(sp^2) impurities at elevated organosulfide concentration and growth temperatures. The carbon formation competes with MoS$_2$ growth, leads to a 2D-to-3D growth mode transition and interrupted film morphologies, and may introduce unintentional doping and interface trap states. By adding optimized flows of H$_2$ to the growth process the C contamination may be reduced significantly, which is expected to be favorable for the preparation of low-impurity, continuous films that are suitable for transistor application.

Furthermore, alkali-assisted growth approaches by the use of NaCl and (Na,K)-containing soda-lime glass substrates were explored to reduce nucleation densities by more than two orders of magnitude with enhanced MoS$_2$ grain sizes up to ∼µm, involving a mechanism of intermediate, low melting point alkali metal oxide compounds. Growth modes, introduced film heterogeneities and alkali impurities through such route were critically discussed. Finally, grain size enhancement was explored on various SiO$_2$-composed substrates comparing growth at optimized conditions in the two different hot-wall reactors, with alkali-assisted and low growth rate equilibrium approaches,

Table 3.2 Overview of MoS$_2$ grain size enhancement studies. Thin films were grown in the ICN2 and Yonsei reactors at high and low growth rates on different substrates with/without alkali-assisted approaches. Nucleation densities N and average grain sizes d_{mean} are extracted from previously shown SEM images (for bimodal grain size distributions the given values correspond to the two distribution peaks).

Reactor	Growth time (h)	Substrate	NaCl	N (µm^{-2})	d_{mean} (nm)
ICN2	1	SiO$_2$	no	929	30
ICN2	1	SiO$_2$	yes	35	84
ICN2	1	Soda-lime SCG 94	no	121	52, 178
ICN2	1	Soda-lime Marienfeld Superior	no	75	76, 267
ICN2	1	Soda-lime B270™i	no	2	488
Yonsei	16	SiO$_2$	no	16	258, 288
Yonsei	16	SiO$_2$	yes	3	363, 842

summarized in table 3.2 (the complete set of histograms is shown in the appendix Fig. B25). MoS$_2$ domain size control opens opportunities for applications from catalysis to electronics [382]. A proof-of concept of the hydrogen evolution reaction catalyzed by nanocrystalline MoS$_2$ thin films is shown in the appendix in Fig. B26, development of a MoS$_2$ transistor technology as the main objective of this thesis will be discussed in chapter 5.

In conclusion, this chapter presents important insights into gas-phase chemistry and growth parameter control in the scalable MOCVD of 2D semiconductors. The highly relevant issues of controlling impurity levels and reduced grain boundary defect densities have been addressed. The findings underline the challenges of high-quality 2D TMD growth from low-cost, low-toxicity organic chalcogen precursors and highlight opportunities to engineer film properties by a fine-tuned growth process, which has wider implications for the development of high-performance (opto)electronic devices.

As an outlook, and in face of C incorporation still being a major hurdle for MOCVD of 2D TMD grown from organosulfides, the use of chalcogen hydrides may be a viable solution. However, the use of these highly toxic precursors might not be an option under certain circumstances due to safety concerns. Future efforts could be directed to adding trace amounts of oxidizers to the growth process, such as H$_2$O [199, 170] or O$_2$ [213, 383], for improved carbon and defect elimination and using growth-etch cycles [199]. While still relying on external, volatile precursors and the advantages of controlled MOCVD gas supply, the introduction of an oxidative environment also opens a reaction path towards enlarged grain sizes: this is due to the volatile, intermediate Mo^{VI} oxide adatom species with higher surface diffusivities compared to elemental Mo^0

from Mo(CO)$_6$ decomposition when working in a reductive H$_2$ atmosphere. Further advances of controlled alkali-assisted growth via MOCVD-compatible, gaseous alkali precursors [213] might be promising, although concerns about alkali contamination must be considered [369]. Alternatively, (oxy)halide-based growth promotors [368, 375] and vapor-pressure-controllable, inorganic molecular halide-based metal precursors may provide another promising route [315, 384]. It is clear though that developing and identifying optimal precursors will be of upmost importance in the scalable, fast growth rate synthesis of high-quality TMD thin films in the future.

Chapter 4

MOCVD of epitaxial MoS$_2$ thin films

Combining the scaling benefits of MOCVD with the concept of van der Waals (vdW) heteroepitaxy on crystalline wafer templates provides a promising route for synthesis of pristine 2D TMD thin films over large areas. In this context, single-crystal sapphire is a widely used substrate owing to its commercial availability at relatively low cost and its industrial relevance. It is particularly attractive for TMD epitaxy thanks to its crystallographic compatibility and stability in harsh growth conditions. Recent studies have highlighted surface step topography to be key for controlling edge-guided nucleation of unidirectionally aligned domains as a route towards single-crystalline TMDs by using sapphire wafers with customized miscuts [176] and by an optimized MOCVD process [48]. Furthermore, sapphire surface chemistry [259, 257, 384] and surface crystal structure, such as (1×1) and $(\sqrt{31} \times \sqrt{31})\pm R9°)$ reconstructions [385], have a great influence on TMD crystallinity, namely the in-plane heteroepitaxial relationship and domain orientation. However, the control and impact of sapphire surface preparation on the epitaxial relation and orientation dispersion has not been studied in a systematic fashion so far. Moreover, TMD epitaxy using organic chalcogen precursor chemistry [310, 190] has been challenging due to C incorporation and the complex interplay of surface and reaction conditions [386]. Therefore, better understanding of the popular TMD-sapphire heteroepitaxy is desired, including optimized sapphire surface preparation and MOCVD conditions for orientation-selective, domain growth with low in-plane mosaic spread.

4.1   Review of TMD epitaxy on sapphire

TMD growth on amorphous substrates, such as SiO$_2$, leads to randomly oriented domains; they form grain boundaries upon thin film coalescence, which alter the electrical film properties [387, 388] due to the misorientation-angle-dependent electrical transport [389]. In contrast, epitaxial growth on single-crystalline substrates may yield aligned domains that merge seamlessly, thus, avoiding high-angle grain boundary defects. In particular, when coupled with MOCVD – in this context often referred to as "metal-organic vapor phase epitaxy" (MOVPE) [177, 83] – this strategy has great potential to enable wafer-scale, electronic-grade, single-crystal 2D TMD thin films [82, 239, 48]. For lattice-guided TMD epitaxy a suitable crystalline template with crystallographic compatibility is required; several 2D and 3D substrates with hexagonal symmetry have been considered. While 2D material vdW substrates, including graphene [310, 192, 390, 391], hBN [251, 392], and combinations of various TMDs (MoS$_2$, WS$_2$, MoSe$_2$, WSe$_2$) [254, 195] have been employed, single-crystalline 2D substrates typically cannot be easily obtained over large areas; thus, "quasi" vdW epitaxy of TMDs on commercially available 3D bulk substrates has become a preferred approach. Conventional 3D bulk substrates include mica [151, 393, 244], Au(111) [193, 255, 394], GaN(0001) [395], and α-Al$_2$O$_3$(0001) [163, 258, 239, 48]. From the latter, insulating Al$_2$O$_3$(0001) wafers are the most common choice because of their (1) commercial, large-diameter availability at relatively low cost and their wide application in practical (opto)electronic applications, (2) thermal and chemical stability at high temperatures required for high-quality TMD growth [396, 48], (3) atomically flat surface that may be custom-manufactured by wafer cutting and thermal annealing [176, 191], (4) prospective compatibility with industry-scale integration processes [191, 53, 46], and importantly (5) hexagonal lattice favoring c-axis oriented vdW epitaxy of three-fold symmetry TMDs [82, 253].

The interplay of substrate and film symmetry plays a critical role for the rotationally commensurate vdW heteroepitaxy. As a general rule, the high symmetry in-plane directions of the 2D film tends to align with the high symmetry direction(s) of the substrate surface [253], which are the $\{11\bar{2}0\}$ and $\{10\bar{1}0\}$ directions in case of Al$_2$O$_3$(0001). As illustrated in Fig. 4.1, this results in the R0° and R30° heteroepitaxial relationships with each two anti-parallel 0°/60° and $-30°/30°$ energetically stable MoS$_2$ domain configurations [252, 176, 253] forming (3×3)-on-(2×2) and (5×5)-on-(3×3) unit cell coincidence lattices [175], respectively. In symmetry terms, the two anti-parallel domain alignment directions arise from the non-centrosymmetric MoS$_2$ lattice and C$_{2v}$ symmetry of the c-sapphire surface [397, 253, 242, 314]. Merging of
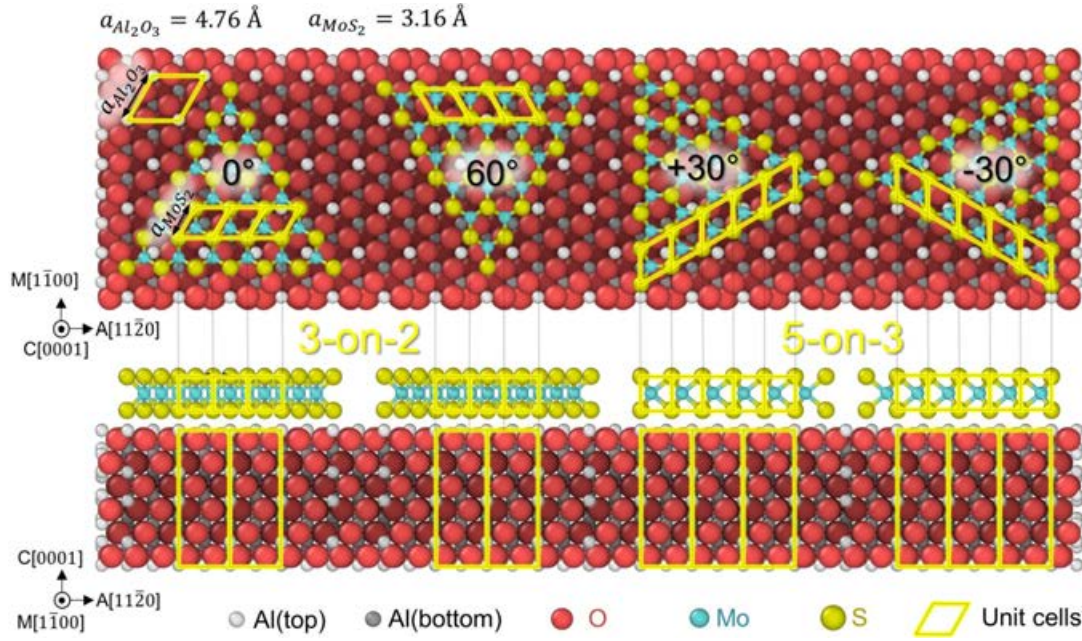
Figure 4.1 $MoS_2/\alpha-Al_2O_3(0001)$ heteroepitaxy model. Top- and side-view of rotationally aligned $MoS_2(0\,0\,0\,1)$ on $Al_2O_3(0\,0\,0\,1)$. The mismatch of $\sim34\%$ between the in-plane lattice parameters a_{MoS_2} and $a_{Al_2O_3}$ is effectively reduced either by 0°/60° oriented domains forming a 3-on-2 superstructures (R0° configuration, $\sim0.4\%$ mismatch), or by $-30°/30°$ oriented domains forming a 5-on-3 superstructure (R30° configuration, $\sim4\%$ mismatch)), as highlighted by the yellow unit cells.

60°-rotated and 30°-rotated domains has been observed experimentally for MoS_2 grown on sapphire [163, 252, 322]. Stitched anti-parallel domains lead to the formation of grain boundary defects [82] that are referred to as "anti-phase", "inversion" or "mirror twin" grain boundaries in the literature [398, 388, 399]. These grain boundaries show metallic character and form conducting 1D nanowire channels within the semiconducting 2D TMD layer, which affect the electrical and optical film properties [400, 401, 402, 403, 398]. Therefore, it is desired to obtain orientation-selective TMD epitaxy with – in the ideal case – unidirectionally aligned domains that smoothly stitch together without forming any domain boundaries (translational grain boundaries not discussed here [261]). To achieve this goal orientation-controlled growth must ensure (1) selection of domains with a preferred R0°-only or R30°-only epitaxial relationship, (2) selection of domains with a single preferred direction within the R0° (either 0° or 60°) or R30° system ($-30°$ or 30°), and (3) ideally zero azimuthal mosaic spread. Recent strategies to address these challenges of domain orientation control have focused on sapphire surface engineering and growth condition optimization.

Sapphire surface engineering – such as by thermal annealing, reconstruction, passivation, and wafer manufacturing – has a fundamental impact on long-range, commensurate vdW epitaxy and is key on the roadmap to electronic grade, synthetic 2D semiconductors [128, 203, 314]. Several reports have pointed out that annealing sapphire at temperatures $\gtrsim 975\,°C$ and obtaining stepped surfaces with atomically-flat terraces is required for uniform, epitaxial domain registry [163, 239, 385, 258, 397]. Sapphire pre-baking at $1050\,°C$ in H$_2$-rich atmosphere has been reported to decrease nucleation density and C incorporation in organosulfide based MOCVD [177]. Furthermore, sapphire annealing at even higher temperatures $\gtrsim 1150\,°C$ reconstructs the sapphire surface into an Al-rich $(\sqrt{31} \times \sqrt{31})\pm R9°$ surface providing a means to select the R30° relationship for epitaxial MoS$_2$ [385, 150] and WS$_2$ films [404]; however, the evolution of sapphire surface termination under MOCVD reaction conditions has still not been fully understood [405]. Terrace-selective nucleation due to non-homogeneous sapphire surface termination has been reported [191, 406]; chalcogen surface passivation [239, 249, 248] may favor the R30° over the R0° configuration according to theoretical simulations [407, 259], while other calculations predict the R0° to be more stable [252]. Recently, also an important role of the OH-groups terminating the sapphire surface was found with regard to domain selectivity and dispersion. OH-terminated sapphire shows R0° and R30° and large mosaic spread due to orientation-independent MoS$_2$ adsorption energies; in contrast, half-Al-terminated surfaces after $\gtrsim 500\,°C$ annealing and OH-removal showed preferential selectivity of the energetically favorable R0° epitaxial relationship with a low mosaicity [384]. Furthermore, the step morphology of the sapphire surface allows growth control by edge-guided nucleation due to strong interaction of the triangle domain and step edges [239, 397], which may impart a preferred domain orientation [408, 48, 176, 256]. In this context, appropriate sapphire step height in relation to TMD layer thickness seems to be an important criterium to enable and control mono- to few-layer TMD nucleation [407, 248]. Moreover, engineering the step direction by custom-manufactured miscuts off the A[$1\,1\,\overline{2}\,0$]-axis [176, 248] and M[$1\,0\,\overline{1}\,0$]-axis [48, 259] has enabled unidirectional domain growth by breaking the degeneracy of anti-parallel domain nucleation energies within the R30° and R0° systems, respectively. However, recent reports have been ambiguous; while using sapphire with a defined miscut direction did not necessarily yield unidirectional growth [404], another work has reported unidirectional growth independent of miscut direction [397]. It has also been of controversial debate if step shape, i.e. curved steps opposed to parallel steps, affects domain orientation and their angular dispersion. While sapphire step meandering with activated kinetics during MOCVD at high temperatures ($1000\,°C$) has

been reported to induce mosaic spread [48, 409], inclined step directions off the high-symmetry sapphire directions did not disturb the preferred domain orientation [259]. Atomistic modelling supported the latter observation by the argument that steps appearing curved at the macro-scale actually consist of discrete kinks to which nuclei can still dock in an aligned fashion while maintaining their epitaxial relationship to the substrate lattice [410]. Besides the step morphology also the role of step chemistry has been recently discussed with respect to domain nucleation and orientation selection, which is strongly linked to the growth conditions [411, 259, 412].

The growth conditions – such as precursor chemistry, gas-phase composition, use of alkali-catalyst, pressure, and temperature – have a major impact on the in-plane domain orientation. A chalcogen-rich growth environment was found to be a critical factor not only to enable aligned domain growth [258, 176], but also to switch from a R0° to R30° configuration upon increasing the chalcogen supply [257]. There are three hypotheses to explain this phenomenon. First, chalcogen-rich conditions might lead to chemical reduction of the sapphire surface by oxygen removal and formation of an Al-rich termination, favoring the R30° configuration [257]. Second, chalcogen-rich conditions may result in chalcogen surface passivation that stabilizes the enhanced film-substrate coupling of the R30° configuration [407, 259]. Third, the chalcogen chemical potential determines the TMD domain edge termination and its coupling with sapphire step edges; for instance, in MoS_2 synthesis, S-rich conditions energetically favor fully S-dimer-saturated Mo edges coupling with $[1\,0\,\bar{1}\,0]Al_2O_3$-edges [176]. The availability and controllability of chalcogen concentration might also explain the preferential epitaxial relationships observed in different vapor phase growth techniques. While in CVD using solid precursors [176, 248] the R30° epitaxial relationship has been commonly observed, in MOCVD [48, 259] and MBE [413, 149] the R0° relationship has been predominantly observed. This may be related to the facilitated chalcogen supply by elemental powder evaporation in CVD opposed to precursor-decomposition-limited chalcogen supply in MOCVD and high chalcogen desorption rates in high vacuum conditions in MBE. The use of alkali-catalysts has been reported to result in a loss of epitaxial registry due to ion intercalation [369]. Moreover, carefully added O_2 to the gas-phase for growth-etch balance has allowed control over R0° and R30° selection [175, 176] and H_2-addition has played an important role in the activation of oriented and step-edge guided nucleation [411, 177, 199, 412, 414]. Zhu et al. have recently shown that the increased hydrogen chemical potential at increased reactor pressure modifies sapphire step chemistry by removing O-remnants, which allows pressure-controlled switching between top and bottom step nucleation with opposed 0°/60° domain orientations [259].

Furthermore, it was found that increased growth temperatures improves selectivity towards unidirectional domain alignment and low mosaic spread [259, 384].

These recent advances of improved domain orientation control encourage further research into the underlying mechanisms of TMD epitaxy on sapphire and the complex interplay between substrate and growth conditions [386]. For example, MOCVD from organic chalcogen precursor has shown particularly challenging compared to hydride based processes [190, 49]. A series of questions arises:

- How do wafer miscut manufacturing and thermal annealing affect TMD epitaxy?

- Can engineered sapphire surface reconstructions be used to control the epitaxial relationship?

- Does the sapphire surface termination/reconstruction get modified under growth conditions?

- Does the step morphology (height, shape, density) affect the domain orientation?

- Does the sapphire surface preparation have an impact on C incorporation in organosulfide based MOCVD?

- Is the epitaxial film registry preserved in alkali-assisted growth?

- Can the S:Mo ratio be used for selecting the epitaxial relationship?

- Does high growth temperature improve epitaxial quality?

- How does the in-plane domain dispersion evolve with growth time and during monolayer coalescence and layer-by-layer nucleation?

To be able to answer these questions, it demands to establish accurate control over sapphire starting surfaces, as well as growth conditions that allow systematic study of their impact on TMD epitaxy. TMD epitaxy is dominated by the two R0°/R30° epitaxial relationships and typically shows mosaic spread of oriented domains due to the relatively weak out-of-plane vdW film-substrate interaction [385, 149, 83, 249]; thus, precise determination of the domain orientation by suitable characterization methods is essential to assess epitaxial quality, which makes the use of diffraction and microscopy techniques indispensable. TEM is a powerful tool combining selected-area diffraction with atomic-resolution imaging [261]; yet, it only provides local, nanoscopic information, with the addded drawback of potentially losing the link to the growth

substrate during typical sample preparation by layer transfer. In contrast, grazing incidence surface diffraction methods based on electrons (RHEED) [249, 409, 149, 176] or X-rays (GIXRD) [415, 48, 176, 248] are able to detect long-range order with statistical information from macroscopic, as-grown samples over wafer-scale areas. RHEED is a highly surface sensitive method that can provide real-time diffraction pattern feedback due to the strong electron-matter interaction. Although X-ray-matter interaction is relatively lower, GIXRD using high-brilliance synchrotron radiation compensates for fast data aquisition and a full picture of surface reconstructions [416, 417] and film-substrate registry by reciprocal space mapping [418, 391]. Common X-ray tubes in lab instruments provide orders of magnitude lower intensities, but fortunately, TMD's heavy element constituents exhibit a high electron density and X-ray scattering cross-section making 2D TMD diffractometry feasible [415]. Therefore, laboratory GIXRD allows routine analysis of epitaxial relationships and in-plane, azimuthal domain distributions. It is emphasized that surface diffraction analyses should be complemented by microscopic imaging (AFM/SEM) and domain orientation statistics because diffraction experiments cannot distinguish between symmetry-equivalent, anti-parallel domains [415, 322].

In this work, MOCVD of epitaxial MoS_2 thin films grown from $Mo(CO)_6$ and dimethyl sulfide $(CH_3)_2S$ on surface-engineered $Al_2O_3(0001)$ is investigated, consisting of two main parts: First, distinct Al_2O_3 surfaces (reconstruction, step morphology) are prepared by miscut and thermal annealing treatments to subsequently study their impact on MoS_2 epitaxy; Second, the influence of growth parameters (with/without NaCl, S:Mo ratio, temperature, time) is explored. Vicinal Al_2O_3 surfaces, domain morphology and orientation of rotationally commensurate MoS_2 films are characterized by microscopic analysis (AFM, SEM), and by electron (RHEED), laboratory and synchrotron X-ray (GIXRD) surface diffraction techniques. Furthermore, Raman and photoelectron spectroscopies are applied. Al_2O_3 substrates with $\pm 0.2°$ and $\pm 0.05°$ miscut angles are compared after thermal annealing at 1050–1350 °C, resulting in atomically-smooth, stepped surfaces with defined step shapes, heights and terrace widths. Moreover, the surface termination is controlled in O_2- and H_2-annealing atmosphere to obtain (1×1) and Al-rich $(\sqrt{31} \times \sqrt{31}) \pm R9°$ surface reconstructions, respectively.

4.2   Sapphire surface preparation

Accurate control over the sapphire surface topography, reconstruction and chemistry is an essential prerequisite to investigate the potential impact of distinct surface conditions on TMD epitaxy. Surface engineering can be realized by 1) customized wafer cutting from the sapphire ingot at defined miscut angles towards specific crystalline planes (e.g. c-, a-, m-, r-planes) [269, 419] and towards specific crystalline directions (e. g. A-, or M-axes) [176], and by 2) thermal annealing treatments at defined temperature and in controlled atmospheres [270]. Among the stable surface orientations, the c-plane sapphire, or simply "c-sapphire" Al$_2$O$_3$(0001), is chosen for this study. Figure 4.2 displays c-sapphire surfaces as-received and after a typical annealing treatment. While the as-received surface exhibits a relatively rough, groovy surface from wafer cutting and polishing processes, the conditioned "epi-ready" surface after thermal annealing shows the characteristic, stepped morphology with atomically-smooth terraces desired for TMD epitaxy [163, 239, 385].
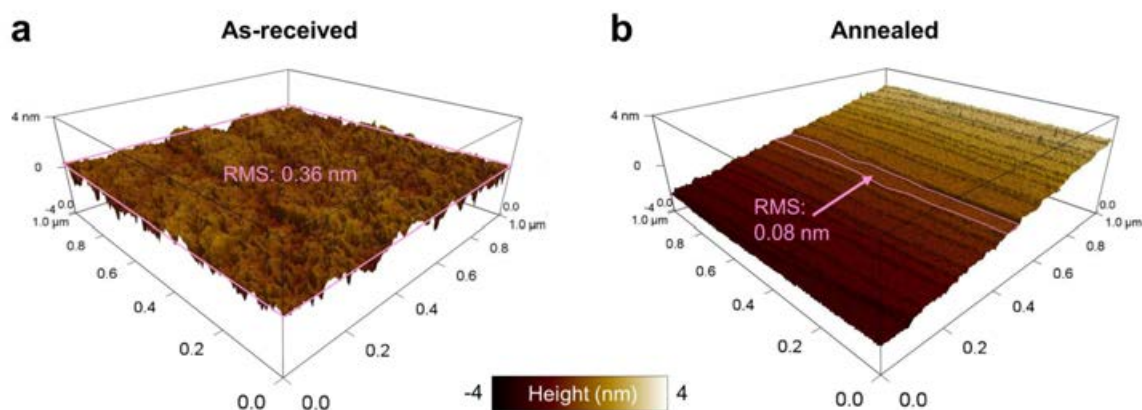
Figure 4.2 Surface morphology of c-sapphire measured by AFM. **(a)** As-received **(b)** Thermally annealed in O$_2$-rich atmosphere at 1200 °C (2 h).

In this section, sapphire wafers with defined 0.2° and 0.05° miscut angles off the C(0 0 0 1)-plane are treated under variation of annealing parameters to investigate the evolution and preparation of distinct surface morphologies and reconstructions. The studied parameters include annealing time, temperature and gas environment under O$_2$-rich or H$_2$-rich atmosphere.

4.2.1   Miscut

The characteristic step morphology of annealed c-sapphire is a consequence of its crystal structure [420]. In its thermodynamically most stable form sapphire crystallizes in the so-called corundum structure, belonging to the space group $R\bar{3}c$ (#167) [270, 269]. Figure 4.3a shows a perspective view of the hexagonal crystal, in which the conventional unit cell with lattice constants $a = 4.76\,\text{Å}$ and $c = 12.99\,\text{Å}$ is highlighted in yellow. The atomic arrangement along the $C[0\,0\,0\,1]$-direction consists of periodic stacking of $\cdots Al-O_3-Al-Al-O_3-Al-Al-O_3-Al\cdots$ atomic layer units with an $O-O$ interlayer distance of $c/6 = 2.16\,\text{Å}$ [270]. Figure 4.3b shows a schematic side view of the crystal, whose vicinal surface is inclined to the low index $(0\,0\,0\,1)$-plane at an angle α introduced by the manufactured miscut. This miscut angle α defines the terrace width w for a given step height h, where h is typically a multiple of $c/6$ that depends on the annealing conditions [420, 269, 421]. The relation between α, h, and w follows
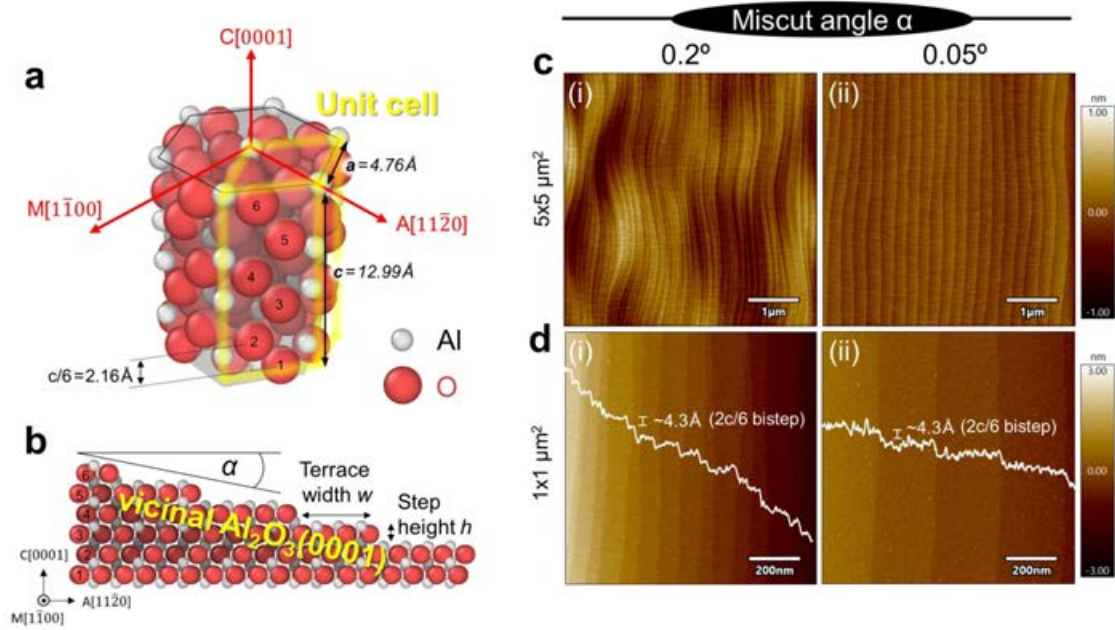
Figure 4.3 Sapphire crystal structure, vicinal surface and miscut angle. **(a)** α-Al_2O_3 corundum crystal structure with highlighted, conventional unit cell (yellow) and crystallographic axes (red). **(b)** Side-view showing the stepped surface where the step height h is typically a multiple of the Al-O-Al distance $c/6$. The terraces width w depends on the manufactured miscut angle α (bottom). **(c)** Flattened AFM images for nominal miscuts of (i) α=0.2° and (ii) α=0.05° annealed at 1200 °C (2 h). Corresponding **(d)** plane-fitted AFM images with overlayed line profiles and indicated step heights.

eq. (4.1):

$$tan(\alpha) = \frac{h}{w} \qquad (4.1)$$

Figure 4.3c shows flattened AFM images of annealed sapphire surfaces (1200 °C, 2 h) for wafers with nominal miscuts of 0.2° and 0.05°. The step undulations depend on the annealing conditions, as discussed below, and from anisotropy caused by the non-specified miscut orientation [422, 423, 424] of the wafers (wafers with specified miscut orientation along the A- or M-axes show parallel steps, see appendix Fig. C1). The AFM images in Fig. 4.3d show a zoomed-in view of the periodic terrace-step morphology. After plane-fitting on the terraces line profiles (overlaid, white lines) perpendicular to the steps can be extracted. For the here used annealing conditions of 1200 °C, predominantly bisteps with $h = 2c/6 \sim 4.3$ Å can be observed, consistent with literature [422, 421]. The terrace widths are of the order of $w = 60\pm25$ nm and $w = 230\pm23$ nm, from which the miscut angles can be calculated to be $\alpha = 0.21 \pm 0.05°$ and $0.05 \pm 0.005°$, respectively, in good agreement with the nominal values. Custom-defined miscut angles can therefore be used to produce templates with controlled densities of surface steps that have been reported to play an important role for edge-guided TMD nucleation [408, 176, 48, 412]. On the one hand, reducing the step density and increasing the terrace size may reduce dispersion from domains nucleating at meandering steps [409]; on the other hand, nucleation at parallel steps along A[$1\,1\,\bar{2}\,0$] and M[$1\,\bar{1}\,0\,0$] can break the degeneracy of anti-parallel TMD domains [48, 176].

4.2.2 Annealing time

As the surface rearrangement is a diffusion-controlled process, time is an important factor for the evolution of the step morphology towards the equilibrium state. The time scale for reaching this state is typical of the order of several hours. Figure 4.4a shows flattened AFM images for annealing at 1050 °C and annealing times of 2 h, 6 h, and 12 h. Straightening of the step morphology with increasing time can be observed due to the advancing surface rearrangement. Furthermore, as visible from the magnified, plane-fitted images (Fig. 4.4b), step bunching phenomena can merge multiple $c/6$-monosteps to form increased step height junction points with enlarged facets [425, 269, 426]. The sample annealed for an extended time of 12 h suggests that the thermal energy at the 1050 °C condition is not sufficient to coalesce monosteps at full length. To avoid these multiple step points that might act as randomly dispersed nucleation points for TMD growth, the annealing temperature was further increased.
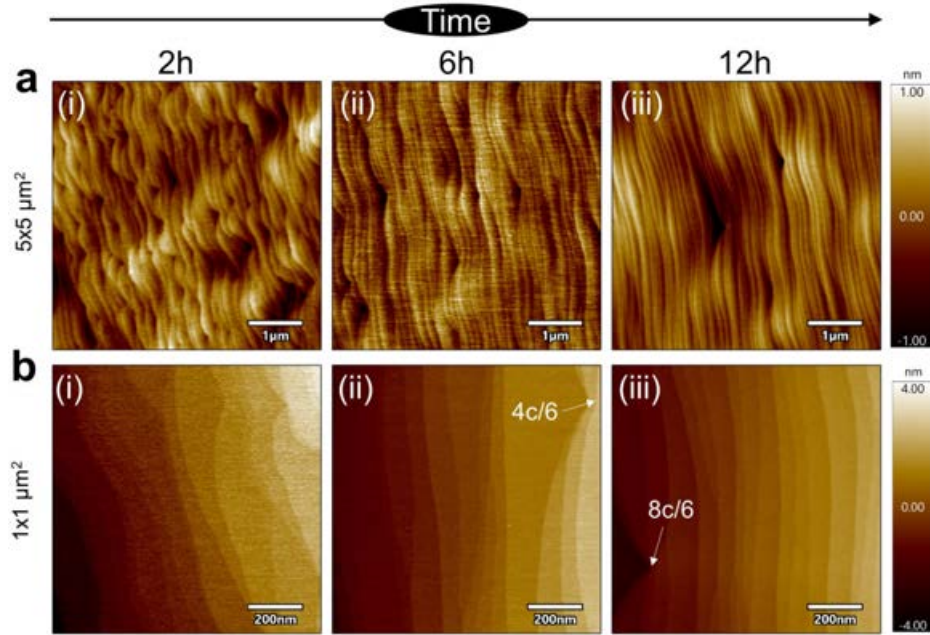
Figure 4.4 Sapphire annealing time. **(a)** Flattened AFM images of $Al_2O_3(0001)$ surfaces after annealing in O_2-rich atmosphere at $1050\,°C$ for (i) $2\,h$, (ii) $6\,h$, and (iii) $12\,h$. Corresponding **(b)** plane-fitted images.

4.2.3 Annealing temperature

Increasing the annealing temperature accelerates surface kinetics during sapphire annealing, and, therefore, equilibrium step morphology is obtained at a faster rate. While at the $1050\,°C$ condition after $2\,h$ the sapphire steps still shows many undulations with predominantly monosteps, the $1200\,°C$ annealed sample exhibits straightened, more parallel step morphology (Fig. 4.5a). Furthermore, as can be seen in Fig. 4.5b, the additionally provided thermal energy enables step pairing of closely approaching monosteps [270, 422] and higher tendency to overcome the energy barriers for bistep formation (Fig. 4.5b), consistent with literature [425, 422]. If temperature is further elevated to $1350\,°C$, step bunching and formation of steps with multiple $c/6$ height and enlarged terraces can be observed. However, for this specific sample particle formation of non-identified origin was observed, which has also been occasionally observed in other reports [425, 427]. They may be caused by redeposition and compound formation of common impurities (Na, Ca, Si) stemming from the furnace environment or the alumina annealing crucibles (see XPS analysis in appendix, Fig. C8), or may be explained by segregation effects from sapphire bulk impurities [425, 428]. Substrates that showed such particle contamination were discarded for subsequent TMD growth.
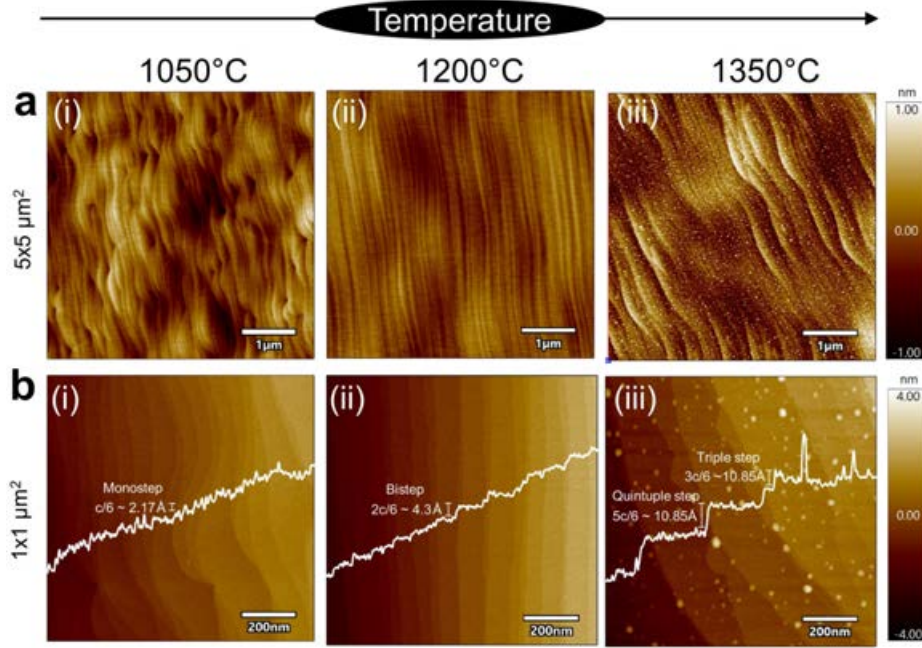
Figure 4.5 Sapphire annealing temperature.**(a)** Flattened AFM images of Al$_2$O$_3$(0001) surfaces after O$_2$-annealing for 2 h at (i) 1050 °C, (i) 1200 °C, and (iii) 1350 °C. Corresponding **(b)** plane-fitted images with selected line profiles.

Nevertheless, these results show that increased annealing temperatures enable step height engineering, which may have important implications for edge-guided nucleation of TMD thin films with controlled layer number. Previously it has been shown that 1200 °C-annealed sapphire with 2c/6 bisteps yielded MoS$_2$ monolayer nucleation [176], 1350 °C-annealed sapphire with substantially higher 6c/6 steps yielded bilayer MoS$_2$ nucleation [248]. Other works reported monolayer nucleation of WSe$_2$ at c/6 steps [408] and MoS$_2$ at 2c/6 – 4c/6 steps [191], the latter of which are below the critical height of $\gtrsim$ 6c/6 predicted for bi- and few layer nucleation according to theoretical studies [407].

4.2.4 Annealing atmosphere

In a next step, the influence of the annealing atmosphere was investigated. Figure 4.6(a-b) shows a series of sapphire surfaces annealed at 1050 °C (2 h) in pure H$_2$, 5 % H$_2$/Ar, inert Ar, in air ($\sim$21 % O$_2$/N$_2$), and pure O$_2$ flow. While the surfaces annealed in H$_2$-rich atmosphere show almost no modification and still exhibit polishing damage from the as-received state, gradual change from reductive over inert to oxidative conditions promote the gradual evolution towards step-terrace morphology. This is due to faster oxygen ion diffusion kinetics in O$_2$-rich than in H$_2$-rich conditions,

facilitating surface reorganization to reach the equilibrium stepped surface state [270]. Annealing in air or pure O_2 are similarly suitable to obtain atomically smooth, stepped surfaces. Furthermore, corresponding water contact angle measurements (Figure 4.6c) show wetting behaviour for the reorganized surfaces, while a contact angle of 36° was measured for the purely H_2-annealed sample. This is related with the surface morphology and differences in surface chemistry with more hydrophobic tendency for the H_2-annealed sample. Previous reports found Al-rich surface composition [270, 385] in H_2-annealed sapphire that may explain hydrophobic nature compared to O-rich, hydrophilic sapphire surfaces.
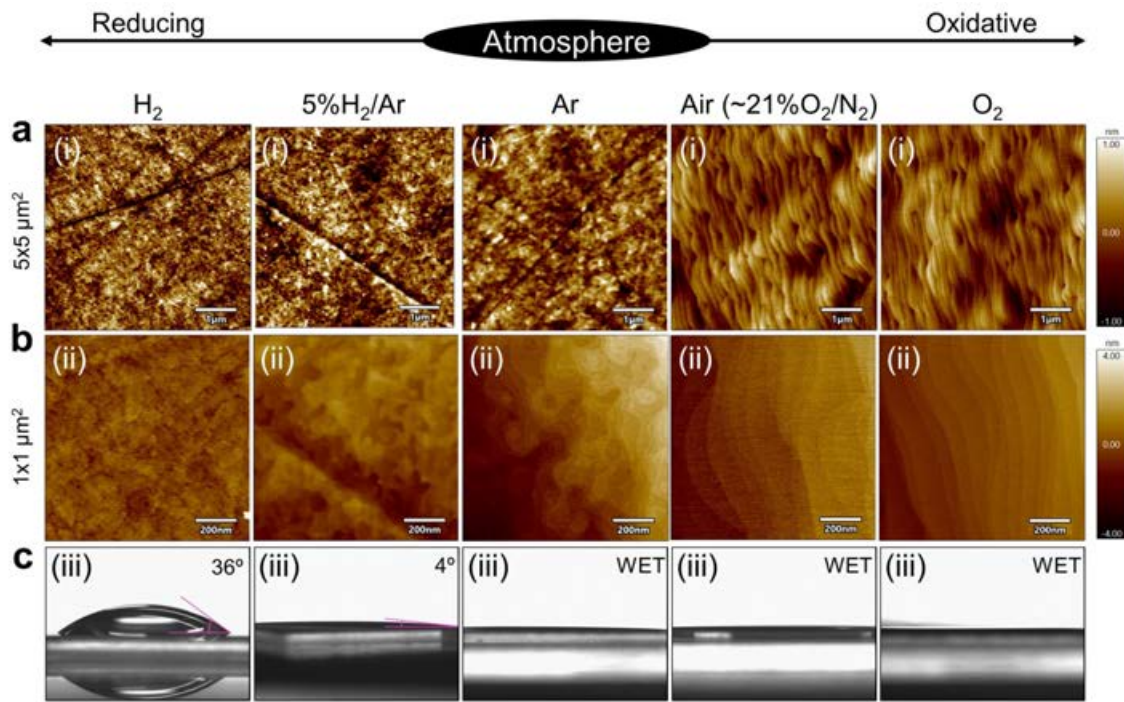
Figure 4.6 Sapphire annealing atmosphere. **(a)** Flattened AFM images of $Al_2O_3(0001)$ surfaces annealed at 1050 °C and 2 h for varying annealing atmosphere from reducing to oxidative: (i) 50 sccm H_2 at 10 mbar, and annealing at atmospheric pressure in (ii) 50 sccm 5 % H_2/Ar (iii) inert Ar, (iv) air ∼21 % O_2/N_2, (v) and 50 sccm O_2. Corresponding **(b)** plane-fitted AFM images, and **(c)** static water contact angle measurements.

4.2.5 Surface reconstruction

The template properties of c-sapphire for heteroepitaxy are not only depending on the surface morphology, but also strongly determined by the crystal structure of the outermost surface atoms – the so-called surface reconstruction. Various reconstructions

of c-sapphire surface have been reported in the literature following a sequence of thermally induced transformations, starting from the simple (1×1) surface [429] to the intermediate reconstructions $(\sqrt{3} \times \sqrt{3})$R30° at $\gtrsim$1100 °C [429], $(2\sqrt{3} \times 2\sqrt{3})\pm$R30° at $\gtrsim$1100 °C and $(3\sqrt{3} \times 3\sqrt{3})\pm$R30° at $\gtrsim$1150 °C [417], and finally $(\sqrt{31} \times \sqrt{31})\pm$R9° above around 1200–1250 °C [429, 416, 430, 431, 432]. These transformations are triggered by a change of surface composition in form of oxygen loss and therefore imply transformation towards a more Al-rich surface, which is facilitated by annealing in vacuum conditions or reducing H$_2$ atmosphere [429, 385, 433]. Aiming to produce the highly stable $(\sqrt{31} \times \sqrt{31})\pm$R9° reconstruction [416], sapphire samples were first O$_2$-annealed at 1200 °C to obtain regularly straight stepped morphology (Fig. 4.7a), which is difficult to obtain by direct annealing in H$_2$-atmosphere even at increased temperature (see Fig. 4.6 and appendix Fig. C3). In a second step, the step-conditioned surface undergoes another 1200 °C annealing in 5 %/H$_2$, in the following just referred to as "H$_2$-annealed", and produces a ragged step morphology consistent with literature [385]. While AFM phase images show a rather homogeneous phase contrast for the O$_2$-annealed surface, the patchy phase contrast on the H$_2$-annealed sample suggests
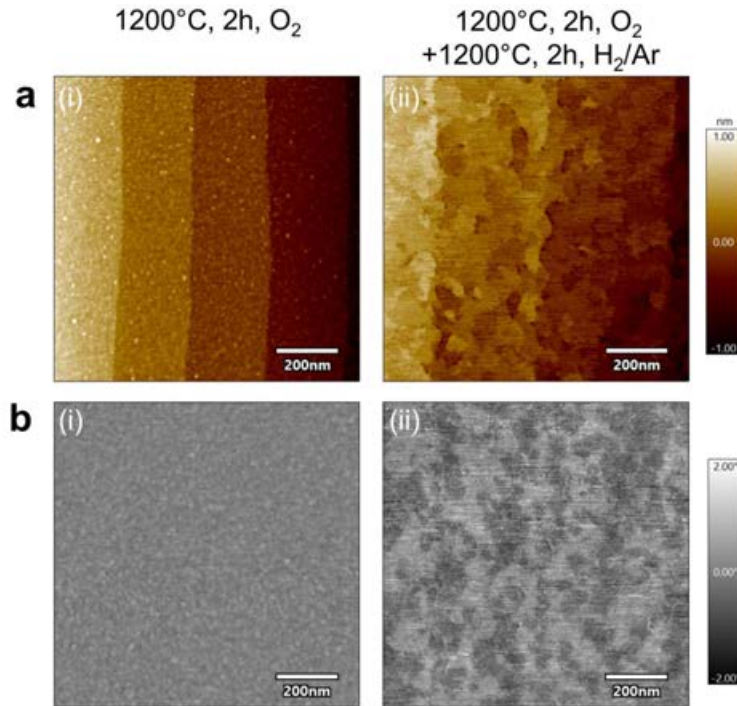
Figure 4.7 Topography and composition of reconstructed sapphire surface. **(a)** Plane-fitted, AFM images of Al$_2$O$_3$(0001) surfaces annealed at 1200 °C (2 h) in (i) O$_2$ for "O-rich" (1×1) reconstruction, and subsequently in (ii) H$_2$ for Al-rich $(\sqrt{31} \times \sqrt{31})\pm$R9° reconstruction. Corresponding **(b)** flattened AFM phase images.

local variations in chemical composition on the surface (Fig. 4.7b), as will be further discussed below. This was confirmed on both 0.05° and 0.2° miscut surfaces (see appendix, Fig. C6).

For surface crystallographic analysis both the O_2- and H_2-annealed samples were measured by RHEED (Fig. 4.8a). Based on reference literature data [434] the characteristic diffraction patterns recorded along the $[1\bar{1}00]$ zone axes were identified, revealing
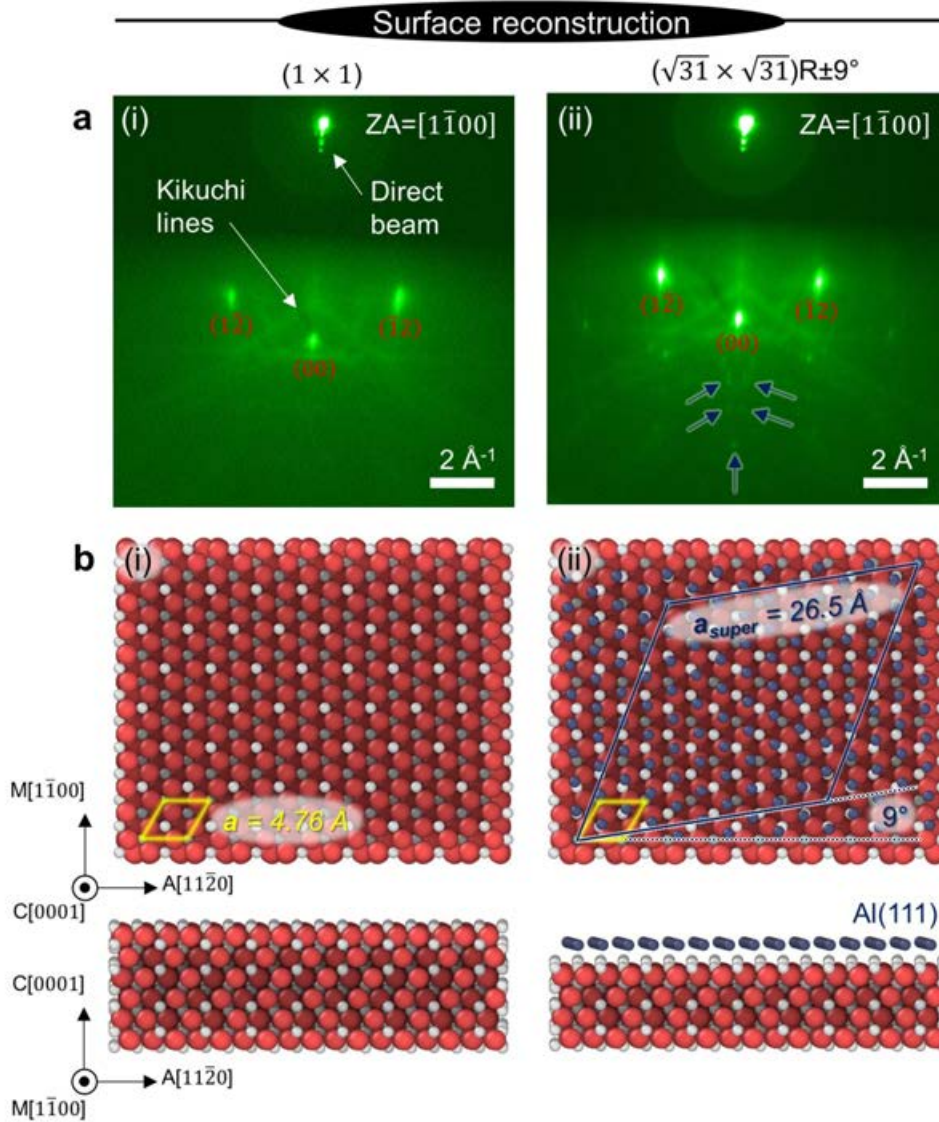
Figure 4.8 Sapphire surface reconstruction. **(a)** RHEED patterns seen along $[1\bar{1}00]$ zone axis (ZA) of $Al_2O_3(0001)$ surfaces annealed at $1200\,°C$ ($2\,h$) in (i) O_2 for "O-rich" (1×1) reconstruction, and subsequently (ii) in H_2 for Al-rich $(\sqrt{31} \times \sqrt{31})\pm R9°$ reconstruction. **(b)** Surface models illustrate the two reconstructions in top and side views.

the dominant (1×1) and $(\sqrt{31} \times \sqrt{31})\pm$R9° reconstructions for O$_2$- and H$_2$-annealed samples, respectively. Moreover, typical Kikuchi lines due to inelastic scattering events are observed [435]. As illustrated by the top and side views of the crystal models in Fig. 4.8b, the (1×1) surface can be visualized by slicing a corundum bulk crystal between the Al–Al layers in the $(0\,0\,0\,1)$-plane forming an Al-terminated surface. For simplicity, and despite the actual Al-termination, this surfaces will be referred to as "O-rich" surface in the following. On the other hand, the Al-rich $(\sqrt{31} \times \sqrt{31})\pm$R9° surface has been described as an Al lattice (dark blue-colored atoms) stacked on top of bulk Al$_2$O$_3$(0001) ($a_{bulk} = 4.78\,\text{Å}$, yellow unit cell), from which the two outermost oxygen layers have been desorbed during high temperature annealing [416, 430]. The remaining Al atoms arrange into a hexagonal structural resembling a closely-packed Al$(1\,1\,1)$ lattice with constant $\sim$3.01 Å that is rotated by 32° with respect to the underlying Al$_2$O$_3$ bulk [431]. This configuration creates a rhombic superstructure (blue supercell, $a_{super} = a_{bulk}\sqrt{31} = 26.5\,\text{Å}$) that is rotated by 9° with respect to the bulk and producing the characteristic RHEED pattern marked by the blue arrows in Fig. 4.8a(ii). Although, the $(\sqrt{31} \times \sqrt{31})\pm$R9° reconstruction is unequivocally present on the sapphire surface, at this point it is not clear though to which extent the surface has transformed from the (1×1) starting surface and if other, low-intensity intermediate reconstructions are present. The here used annealing time and temperature may not have fully transformed the whole surface towards the $(\sqrt{31} \times \sqrt{31})\pm$R9° surface during the treatment. Similar doubts were also expressed in another report using an annealing temperature of 1175 °C [405]. Nevertheless, even after four months of storage in ambient conditions the reconstructed surface still showed the characteristic $(\sqrt{31} \times \sqrt{31})\pm$R9° RHEED pattern (see appendix, Fig. C7), proving the high stability of this reconstruction in agreement with literature [416]. Therefore, *ex situ* H$_2$-annealed sapphire surfaces are preserved until subsequent use for epitaxial MoS$_2$ growth.

4.3 MoS$_2$ epitaxy on sapphire

In this section MOCVD of epitaxial MoS$_2$ thin films grown on the annealed c-sapphire surfaces is investigated. The study consists of two main parts: First, it is aimed at studying the impact of distinct sapphire surface conditions prepared in the previous section, including surface reconstructions and step morphology shaped by the wafer miscut and annealing treatment. Regarding the influence of surface morphology, it is reasonable to assume that the *ex situ* annealed starting surfaces maintain their

as-prepared step topography during MOCVD, as the here used growth temperatures of ∼600–700 °C are far below temperatures at which the kinetics of sapphire surface rearrangement are active [48, 269]. However, it is one aim of this study to investigate if surface reconstructions are stable or modified under MOCVD reaction conditions and how they impact the domain orientation. The second part of the study is focused on the influence of certain growth parameters on the heteroepitaxy, including the use of an NaCl-assisted process, the S:Mo ratio, growth temperature, and extended growth times for monolayer coalescence and second layer nucleation.

MoS$_2$ thin films were grown in the horizontal, hot-wall "Yonsei reactor" (see section 2.3.1) during a limited five weeks research stay time frame using sapphire substrates that had been previously prepared at ICN2. A simplified illustration of the MOCVD
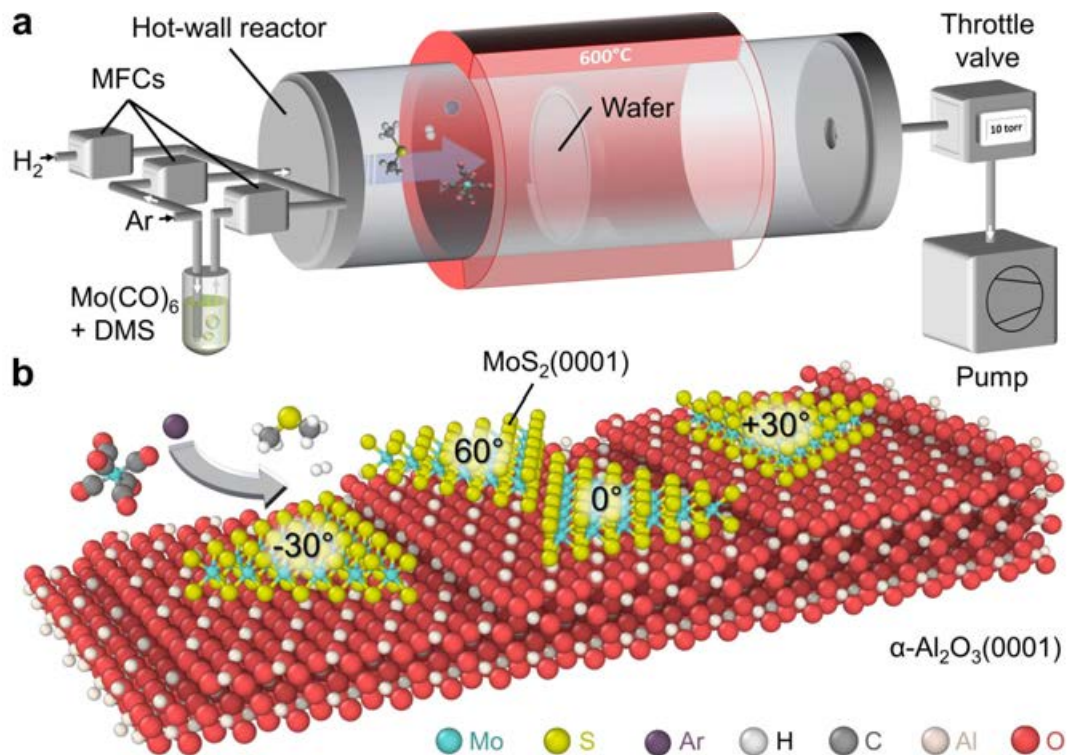
Figure 4.9 MOCVD reactor and epitaxial growth model. **(a)** Schematic illustration of the horizontal, hot-wall reactor for wafer-scale MoS$_2$ growth. Mass flow controllers (MFCs) regulate the precursor flow coming from a single, external canister filled with a solution of molybdenum hexacarbonyl [Mo(CO)$_6$] dissolved in dimethyl sulfide [DMS; ((CH$_3$)$_2$S)]; precursors are injected into the reaction chamber by Ar carrier gas together with H$_2$ at a standard growth temperature of 600 °C and a pressure of 10 Torr, controlled by an automatic throttle valve upstream the vacuum pump. **(b)** Simplified MOCVD model of epitaxially oriented MoS$_2$ domains grown from Mo(CO)$_6$ and DMS on the vicinal surface of stepped, c-plane sapphire [α-Al$_2$O$_3$(0001)].

reactor and growth process is shown in Fig. 4.9. Briefly, precursors are vaporized from a Mo(CO)$_6$/DMS solution of defined concentration setting the S:Mo ratio; they are transported by Ar carrier gas into the reactor chamber, which is kept at a standard pressure of 10 Torr and growth temperature of 600 °C, if not otherwise indicated. A 2" c-sapphire wafer or quarter-cut pieces (together with SiO$_2$ reference chips) are placed on a vertical quartz holder at an optimized distance from the furnace entrance. Optionally, NaCl is put at the furnace entrance for study of salt-assisted growth. Ar/H$_2$ is injected for reductive atmosphere and minimizing C incorporation stemming from the organosulfide precursor. For post-growth film characterization microscopy (AFM, SEM) is used to detect domain shape and orientation. Upon return to ICN2, the MoS$_2$ thin films were analyzed over cm-scale by grazing incidence electron and X-ray surface diffraction, including *ex situ* RHEED, laboratory and synchrotron GIXRD. Main metrics for the assessment of registry and epitaxial quality are the in-plane epitaxial relationship (R0°/R30°) and the azimuthal domain dispersion (mosaic spread) determined by the FWHM of ϕ-scans.

4.3.1   Heteroepitaxial relationship

This section will explain how to determine the heteroepitaxial film-substrate registry. Figure 4.10a shows an exemplary AFM image of MoS$_2$ thin film grown on 1200 °C, O$_2$-annealed, 0.05°-miscut Al$_2$O$_3$. The growth time (14 h) was chosen to produce a sub-monolayer coverage film consisting of isolated, easily distinguishable domains, as visible in the magnified inset. In this case of triangular-shaped domains, the epitaxial orientation of the film with respect to the Al$_2$O$_3$ substrate can be deduced by microscopic inspection. In this procedure, the orientation of the Al$_2$O$_3$ substrate must be known (e.g. from the wafer flat) to assume to which crystalline direction the MoS$_2$ triangle edges are parallel. Here, the AFM image is oriented according to the photographed wafer. The histogram in Fig. 4.10a shows the percentage distribution of domain orientations relative to the A[1 1 $\overline{2}$ 0]-axis of Al$_2$O$_3$ (see also appendix, Fig. C12c). For this sample a preferential R0° epitaxial relation can be observed with predominantly 0°-oriented domains ($\sim$63.8 % of triangles pointing upwards) and 60°-oriented domains ($\sim$16 % of triangles pointing downwards). The remaining domains consist of a minor R30° fraction of $-30°/30°$-oriented domains (4.3 % and 5.2 % triangles pointing left and right, respectively) and randomly aligned domains not following any high symmetry direction of sapphire (10.7 %). An additional way of visualizing the directionality of aligned domains on the crystalline Al$_2$O$_3$ substrate is to apply fast Fourier-transform

on the binarized AFM image, which reveals a six-fold symmetry pattern as opposed to the round blur for the case of randomly aligned domains grown on an amorphous SiO$_2$ reference substrate [436] (see appendix, Fig. C11). The microscopic inspection is benefitial to distinguish between the different domain orientations, including the anti-parallel domains with the same epitaxial relationship caused by the three-fold symmetry of MoS$_2$. However, the image analysis is a local and indirect method that requires an assumption for the substrate orientation and that is highly dependent on image quality for precise edge detection. Moreover, it relies on the assumption that the outer domain shape (" 2D crystal tracht") reflects the lattice orientation of a given domain and alignment with the underlying substrate. This might not always be true for slanted or irregular domain edge shapes and may result in misinterpretation; for instance in cases where an inclined domain edge seemingly points at misalignment, the actual domain lattice orientation may be in perfect registry with the substrate, and in cases where the edge is seemingly aligned the actual domain lattice may be incommensurate. Moreover, this method only works for thin films with uncomplete layer coverage with well-differentiable domains. Therefore, additional characterization by diffraction experiments is desired for the verification of domain orientation.

RHEED allows to detect long-range crystalline order and surface symmetry in monolayers over large-areas ($\sim$ cm^2) and is well-suited for *ex situ* analysis of MOCVD-grown MoS$_2$ thin films [437, 409]. By measurement of reciprocal distances in the RHEED patterns, the interplanar lattice distances of MoS$_2$ and sapphire can be determined and the heteroepitaxial orientation of the MoS$_2$ crystal on the underlying sapphire substrate can be deduced. Figure 4.10b shows RHEED patterns along the M[1$\bar{1}$0 0] and A[1 1 $\bar{2}$ 0] zone axes of the Al$_2$O$_3$ crystal. Intense diffraction spots from the (1×1)-reconstructed Al$_2$O$_3$ surface are obtained and indexed by the red labels [also see Fig. 4.8a(i) for bare Al$_2$O$_3$]. Additionally, the superposed streaks indexed in turquoise from the MoS$_2$ domains can be simultaneously detected on the RHEED screen thanks to the controlled sub-monolayer coverage (mono- to few layer coverage would obscure the sapphire pattern and not allow to determine the TMD/sapphire epitaxial relationship [413, 149, 291]). Their rather low intensity and broadened, blurry signal may be explained by the sub-monolayer coverage, finite-size, crystalline quality, and in-plane, mosaic spread [291], which will be further discussed throughout this chapter. The streaky patterns imply a smooth surface and it is noted that the streaks appear rotation-dependent with maximum intensity along the high-symmetry axes of the sapphire crystal when turning the sample around its azimuth, which means that the domains have a preferred, epitaxial in-plane orientation. The scale bars on the bottom-

right corners in Fig. 4.10b had been previously calibrated with the well-known lattice constant of the bare Al$_2$O$_3$ reference. The reciprocal space coordinate axes are denoted on the bottom-left corners of each RHEED pattern, where $k_\parallel$ and $k_\perp$ are the momentum transfers parallel and perpendicular to the surface, respectively. Here it is focused on the parallel, in-plane component, for which the respective line profiles of dominant Al$_2$O$_3$ (red) and MoS$_2$ (turqoise) peak intensities have been extracted and are shown below the
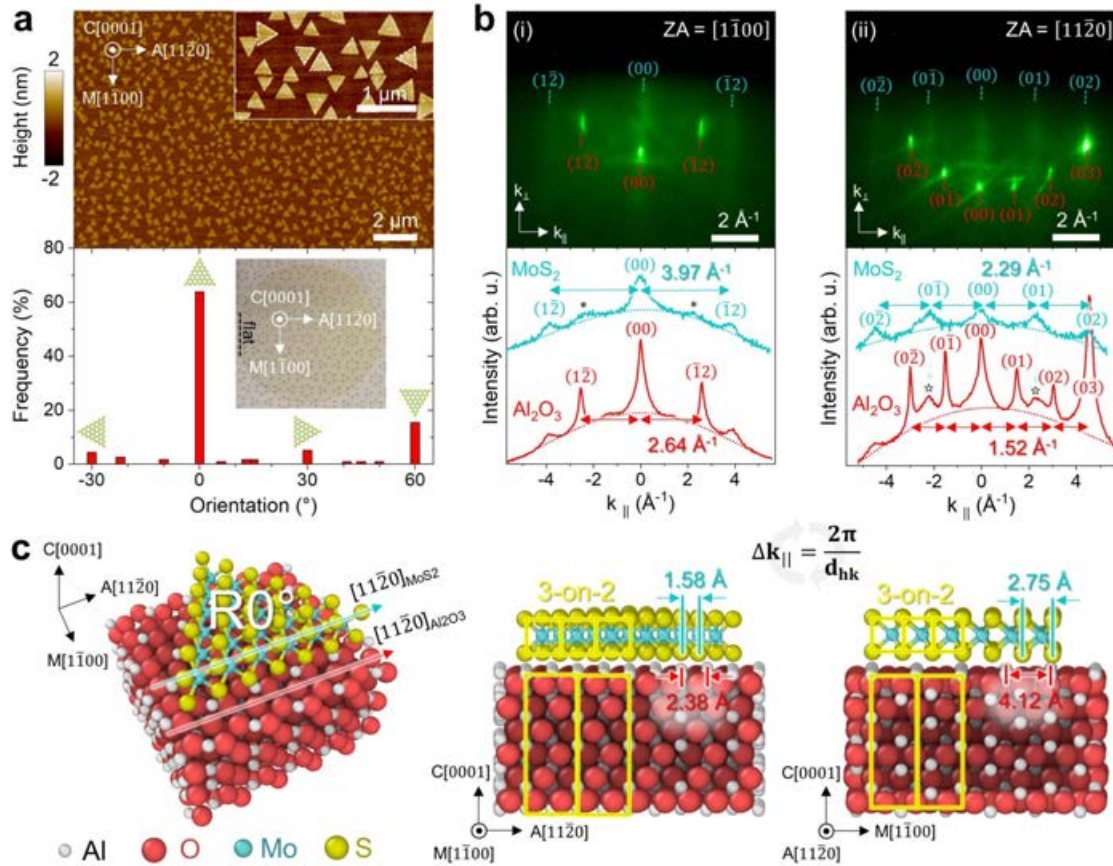
Figure 4.10 MoS$_2$/Al$_2$O$_3$ in-plane heteroepitaxial relationship. **(a)** AFM analyis of MoS$_2$ domains grown at 600 °C on O-rich Al$_2$O$_3$ surface, showing the AFM micrograph with a magnified inset (top) and statistical analysis of domain orientation relative to A[1 1 $\overline{2}$ 0]-axis of Al$_2$O$_3$ (bottom). The inset shows as-grown MoS$_2$ on a 2" sapphire wafer with the flat indicating the A-plane. **(b)** RHEED patterns seen along the zone axes (ZA) (i) ZA=[1 $\overline{1}$ 0 0], and (ii) ZA=[1 1 $\overline{2}$ 0]. Diffraction patterns from the Al$_2$O$_3$ substrate (red) and MoS$_2$ film (turquoise) are indexed. Integrated line profiles for momentum transfer $k_\parallel$ are given below with averaged peak-to-peak reciprocal lattice distances. **(c)** Illustration of the R0° heteroepitaxy model. From left to right: Perspective view, and side views seen along M-axis and A-axis of Al$_2$O$_3$, respectively, with slight out-of-plane tilt along viewing direction for better visualization of atomic columns. Real space interplanar lattice distances are obtained from the reciprocal space distances of the RHEED patterns.

RHEED patterns. Nevertheless, some intensity contributions related to Kikuchi lines crossing the MoS$_2$ line profile ($*$) and MoS$_2$ streaks crossing the Al$_2$O$_3$ line profile ($\star$) can be noted. The reciprocal distances $\Delta k_{\parallel}$ between intensity peaks over the arching background (dotted line) have been extracted and the average peak-to-peak distances are indicated next to the line profiles. The reciprocal distances have been converted into the inversely proportional real space interplanar distances d_{hk}, which are depicted in the heterostructure models in Fig. 4.10c. For diffraction patterns seen along the $[1\,\bar{1}\,0\,0]$ zone axis, the perpendicular interplanar distances along A$[1\,1\,\bar{2}\,0]$ direction for Al$_2$O$_3$ and MoS$_2$ are determined to be $d_{(1\,\bar{2})}$(Al$_2$O$_3$) = 2.38$\pm$0.02 Å and $d_{(1\,\bar{2})}$(MoS$_2$) = 1.58$\pm$0.02 Å, respectively. For diffraction patterns seen along the $[1\,1\,\bar{2}\,0]$ zone axis, the perpendicular interplanar distances along M$[1\,\bar{1}\,0\,0]$ direction for Al$_2$O$_3$ and MoS$_2$ are determined to be $d_{(0\,1)}$(Al$_2$O$_3$) = 4.12 $\pm$ 0.07 Å and $d_{(0\,1)}$(MoS$_2$) = 2.75 $\pm$ 0.07 Å, respectively. From the Al$_2$O$_3$-related interplanar distances the Al$_2$O$_3$ lattice constant can be calculated to be $a_{Al_2O_3} = 2 \cdot 2.38$ Å $= 2/\sqrt{3} \cdot 4.12$ Å $= 4.76$ Å, as expected from the calibration with a bare sapphire reference sample. From the MoS$_2$-related interplanar distances the MoS$_2$ lattice constant can be calculated to be $a_{MoS_2} = 2 \cdot 1.58$ Å $= 3.17 \pm 0.1$ Å and $2/\sqrt{3} \cdot 2.75$ Å $= 3.17 \pm 0.1$ Å. This is in good agreement with the bulk value for MoS$_2$ within the experimental uncertainty ($a_{MoS_2} = 3.16$ Å [80], see also section 2.1.1). The obtained interplanar distances match the 3-on-2 superstructure along the A-($3 \cdot 1.58$ Å $\approx 2 \cdot 2.38$ Å) and M-axes ($3 \cdot 2.75$ Å $\approx 2 \cdot 4.12$ Å), as highlighted by the yellow unit cells in Fig. 4.10c. This unequivocally reveals the preferential R0° heteroepitaxial relationship with $[1\,1\,\bar{2}\,0]$MoS$_2$ $\parallel$ $[1\,1\,\bar{2}\,0]$Al$_2$O$_3$, consistent with AFM analysis. R30° domains seen in AFM could not be detected due to their low domain fraction and low intensity on the RHEED screen, which is a limitation of the used setup and manipulation.

Further out-of-plane ($k_{\perp}$) analysis would allow determination of vertical interlayer distances in the MoS$_2$/Al$_2$O$_3$ model, such as determination of the vdW gap between film and substrate. Unfortunately, the signal-to-noise ratio was not sufficiently high to extract useful information from the obtained data. However, in a previous work Xiang et al. were able to determine the vdW gap of 3.02 Å from highly-resolved RHEED patterns [437]. Their interface model further included an interfacial buffer layer in form of a sulfur-passivated sapphire surface. Further evidence for such chalcogen termination at the TMD/sapphire interface has been provided by cross-sectional TEM analyses of solid powder evaporation CVD- and MOCVD-grown MoS$_2$ [249, 248] and MOCVD-grown WSe$_2$ [239, 259]. Nevertheless, the refined interface chemistry has

not been included in the here shown, simplified representation in Fig. 4.10c mainly focusing on the aspect of epitaxial registry.

4.3.2 Impact of sapphire surface condition

In this section the effect of distinct sapphire surfaces on MoS$_2$ domain epitaxy is studied. To investigate the role of Al$_2$O$_3$ reconstruction on the in-plane film-substrate registry GIXRD mapping data was obtained during a synchrotron experiment at the beamline BM32 dedicated to surfaces and interfaces at the ESRF (Grenoble).[1]

4.3.2.1 Surface reconstruction

The effect of sapphire reconstruction on MoS$_2$ epitaxy was studied using low 0.05° miscut wafers exhibiting wide terraces and reduced step density intending to induce pronounced surface- over potential step edge nucleation effects. Figure 4.11 shows
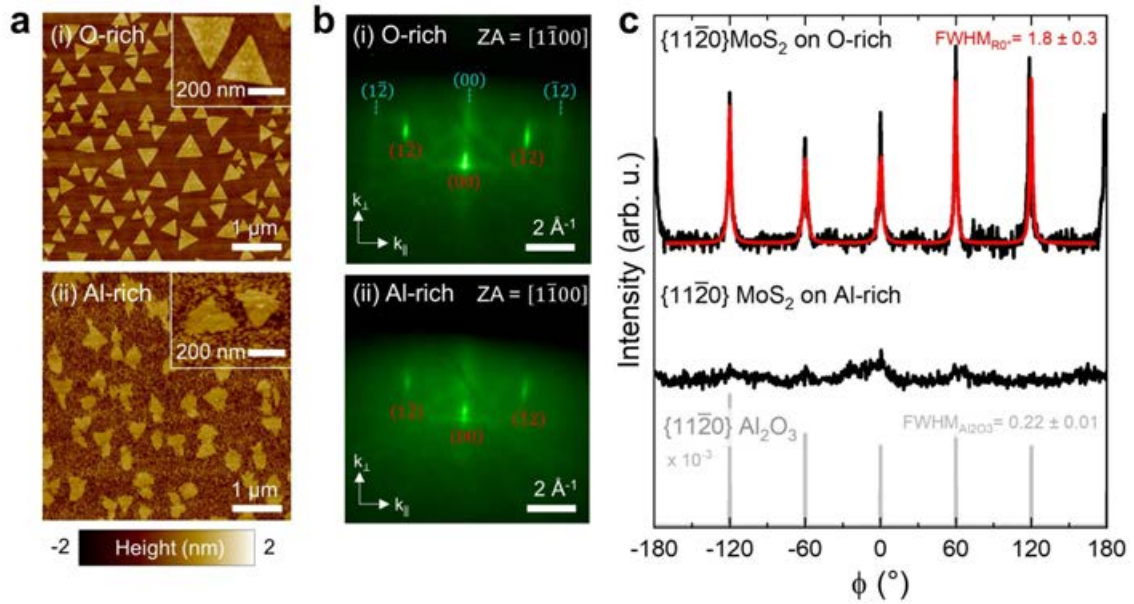
Figure 4.11 Impact of sapphire surface reconstruction on MoS$_2$ epitaxy. **(a)** AFM images of MoS$_2$ grown on 1200 °C-annealed, 0.05° miscut sapphire with (i) O-rich (1 × 1), and (ii) Al-rich ($\sqrt{31} \times \sqrt{31}$)±R9° surfaces. **(b)** RHEED patterns seen along [1$\bar{1}$00] zone axis (ZA). **(c)** GIXRD in-plane, azimuthal ϕ-scans of the MoS$_2$(11$\bar{2}$0) and Al$_2$O$_3$(11$\bar{2}$0) reflections.

comparative AFM, RHEED and GIXRD analyses for MoS$_2$ thin films deposited in the same growth run on 1200 °C-annealed Al$_2$O$_3$ with O-rich (1 × 1) and Al-rich ($\sqrt{31} \times \sqrt{31}$)±R9° surfaces, respectively. The O-rich sapphire reveals the growth of triangular, epitaxially aligned domains with hundreds of nanometers in size – in contrast to the growth on the Al-rich surface. Although there exist hundreds of nanometer sized domains on the Al-rich surface, the domains have irregular, fractal edge shape and the space between the large domains is filled by finely dispersed, smaller domains down to few tens of nanometers in size. The disrupted and non-uniform growth behaviour on Al-rich sapphire was confirmed in three additional growth runs in which sapphire substrates with the two different surface reconstructions were placed, followed by post-growth, microscopic shape analysis (see appendix Fig. C14). The distinct growth behaviour was observed regardless of miscut angles (0.2° or 0.05°) and miscut directions (off-angle towards M or A-axes), including sapphire wafers from different manufacturers, strongly suggesting that the perturbed domain epitaxy is a consequence of the H$_2$-annealed, Al-rich surface. To characterize the structural film quality and examine the reason for the distinct growth behaviours, further diffraction studies were carried out. RHEED analysis for MoS$_2$ on the O-rich surface shows the previously discussed diffraction pattern with preferential R0° epitaxial relationship (section 4.3.1), while the pattern of MoS$_2$ on the Al-rich surface is highly blurred, indicating a more disordered film (Fig. 4.11)b(ii). Due to the fuzzy pattern it is difficult to clearly evaluate the presence and evolution of the Al-rich surface reconstruction after MoS$_2$ growth.

Laboratory GIXRD setup confirms the preferential R0° domain alignment on the O-rich surface. This is evidenced by the in-plane MoS$_2$ diffraction signal for 360° azimuthal sample rotation around the surface normal showing periodical 60°-separated MoS$_2(11\overline{2}0)$ film peaks aligned with the Al$_2$O$_3(11\overline{2}0)$ substrate reference peaks. Pseudo-Voigt peak fitting reveals the low mosaic spread of 0/60°-oriented domains with an average FWHM of 1.8±0.3°. The intensity variations of the R0° peaks can be attributed to the sample geometry with direction-dependent probe volume contributing to the diffracted intensities. Intensity contributions appearing between the R0° peaks point at a secondary R30° domain fraction shifted by 30° with respect to $(11\overline{2}0)$Al$_2$O$_3$ peaks and signal contribution of minor fraction of randomly misoriented domains; however, their low intensity and signal-to-noise-ratio did not allow reliable fitting. On the other hand, the MoS$_2$ film grown on Al-rich sapphire exhibits a diffuse diffraction signal from which R0°- and R30°-related peaks and higher disorder can be suspected, but the low signal intensity complicates proper fitting and interpretation of the data.

Further characterization was carried out by synchrotron GIXRD (at this point samples stored in a vacuum desiccator were $\sim$ 10 months old). The use of high intensity synchrotron radiation is a powerful tool for rapid and high-resolution reciprocal space mapping of the film-substrate lattice registry and surface reconstruction, which is not possible to achieve within a reasonable amount of time with a laboratory setup. Figure 4.12a and Fig. 4.13a show the in-plane $(h\,k\,i\,0)$ reciprocal space maps of MoS$_2$ thin films grown on (1×1) and $(\sqrt{31} \times \sqrt{31})\pm$R9° reconstructed c-sapphire. Azimuthal sectors of 80° capture the six-fold, in-plane surface symmetry of MoS$_2$ and Al$_2$O$_3$ diffraction patterns and reveal up to third order Bragg reflections indexed by underlined and non-underlined labels in the graphs. The $[1\,1\,\overline{2}\,0]$ and $[1\,0\,\overline{1}\,0]$ crystallographic directions of the Al$_2$O$_3$ crystal substrate surface serve as the reference coordinate system. For the (1×1) sample the reflections from the MoS$_2$($1\,1\,\overline{2}\,0$) planes are dominant along the $[1\,1\,\overline{2}\,0]$, whereas those from the MoS$_2$($1\,0\,\overline{1}\,0$) planes are dominant along the $[1\,0\,\overline{1}\,0]$ direction, corroborating the preferential R0° epitaxial relationship found in the RHEED and GIXRD analysis discussed before. For MoS$_2$ on $(\sqrt{31} \times \sqrt{31})\pm$R9°-Al$_2O_3$ R0°-related intensities are less intense and intensities of $[1\,1\,\overline{2}\,0]$MoS$_2$||$[1\,0\,\overline{1}\,0]$Al$_2$O$_3$ reflections marking R30° relationship are relatively enlarged, which will be discussed in more detail below. Characteristic for the R0° MoS$_2$/sapphire heteroepitaxy are the nearly coinciding MoS$_2$($2\,2\,\overline{4}\,0$) and Al$_2$O$_3$($3\,0\,\overline{6}\,0$) reflections along the $[1\,1\,\overline{2}\,0]$ direction and MoS$_2$($2\,0\,\overline{2}\,0$) and Al$_2$O$_3$($3\,0\,\overline{3}\,0$) reflections along $[1\,0\,\overline{1}\,0]$ direction highlighted by the yellow-dotted circles, marking the nearly lattice-matched 3-on-2 superstructure coincidence of MoS$_2$/Al$_2$O$_3$ unit cells. Some streaky, bent features appear in both maps, which were found to be constant within a $\delta - \omega$ plot (see appendix, Fig. C16). These might be related with artifact reflections coming from the Be window used in this experiment. Moreover, some spurious signals between the first order MoS$_2$ and Al$_2$O$_3$ reflections were detected in both samples, which will require further analysis for identification.

Next, detailed analysis of features related to the sapphire surface reconstruction is discussed for which the synchrotron GIXRD signal allows more precision than the previous RHEED analysis. The regions marked in Fig. 4.13a by the green and orange boxes close to the Al$_2$O$_3$($1\,1\,\overline{2}\,0$) and ($3\,0\,\overline{3}\,0$) were rescanned and magnified by higher resolution maps on the right of Fig. 4.13a. Reflections of $\pm$9° rotated rhombic patterns are observed and calculation of lattice constants (see appendix Fig. C15) clearly reveals the presence of the $(\sqrt{31} \times \sqrt{31})\pm$R9° reconstruction. Therefore, it is demonstrated that the Al$_2$O$_3$ surface reconstruction is preserved during MoS$_2$ growth at 600 °C, corroborating previous findings on the stability of the reconstruction under S-rich

MOCVD conditions below a certain temperature threshold [405]. This high stability and chemical inertness of the $(\sqrt{31} \times \sqrt{31})\pm$R9° reconstruction may prevent evolution towards a desirable S-passivated surface at the TMD/sapphire heterointerface [49, 249, 248], similar as it has been observed to prevent surface passivation by nitridation [439, 432]. In contrast, the (1×1)-surface allows S-passivation [49, 249, 248] and N-passivation [439, 432]. Previous reports [405, 417] raised doubts about composition uniformity and completeness of the surface reconstruction after annealing, i.e. other reconstructions than the $(\sqrt{31} \times \sqrt{31})\pm$R9° may possibly be present. Indeed, a careful look at the small map around the Al$_2$O$_3$(1 1 $\bar{2}$ 0) peak (orange framed high-resolution map in Fig. 4.13a) suggests a shallow detail marked with the white arrow close to the MoS$_2$(1 1 $\bar{2}$ 0) diffraction ring. If this feature was related to a Al$_2$O$_3$ reconstruction, it would be part of a pattern going beyond the measured regions of the higher resolution map, which unfortunately cannot be distinguished in the large, lower resolution map. Nevertheless, the feature's position matches the $(3\sqrt{3} \times 3\sqrt{3})\pm$30° reconstruction [417] given its distance from the Al$_2$O$_3$(1 1 $\bar{2}$ 0) spot in the reciprocal space within $1\,\%$ error [see appendix for detailed analysis, Fig. C15a; distance $d_{EF} = 0.19\,\text{nm}^{-1} \approx 1/(3\sqrt{3})$]. Its intensity is weaker than that of the $(\sqrt{31} \times \sqrt{31})\pm$R9°-related spots; this suggests that a residual, low fraction of the $(3\sqrt{3} \times 3\sqrt{3})\pm$R30° reconstruction may coexists for the used annealing procedure, which is consistent with the reported series of intermediate reconstructions in the temperature range of $1100 - 1250\,°\text{C}$ [417, 416]. For confirmation, the synchrotron experiment could be repeated within a larger high-resolution window that may reveal the whole $(3\sqrt{3} \times 3\sqrt{3})\pm$R30° pattern.

The radial line profiles along the [1 1 $\bar{2}$ 0] and [1 0 $\bar{1}$ 0] are shown in Fig. 4.12b and Fig. 4.13b for the MoS$_2$ films grown on (1×1)- and $(\sqrt{31} \times \sqrt{31})\pm$R9°-reconstructed Al$_2O_3$, respectively. MoS$_2$-related (underlined labels) and Al$_2$O$_3$-related (non-underline labels) peaks appear at similar positions for both samples, while differences in the intensity ratios of MoS$_2$ peaks along the [1 1 $\bar{2}$ 0] and [1 0 $\bar{1}$ 0] are apparent due to different R0° and R30° domain fractions between both surfaces (a quantitative analysis will be given for the azimuthal (1 1 $\bar{2}$ 0)MoS$_2$ peak scan below). The radial scans allow precise determination of peak positions, from which the lattice constants can be extracted. Figure 4.13d shows the MoS$_2$ lattice constant a_{MoS2} extracted from the first to third order reflections over the reciprocal, in-plane wave vector $q_\parallel$. As any source of systematic error in the position of the reflections is larger at lower angles and reduces with $q_\parallel$ and the detector angle (here 2δ), extraction of the lattice constant from higher order reflections at larger angles minimizes the error. Consequently, the (3 0 $\bar{3}$ 0) peaks should deliver the best value.
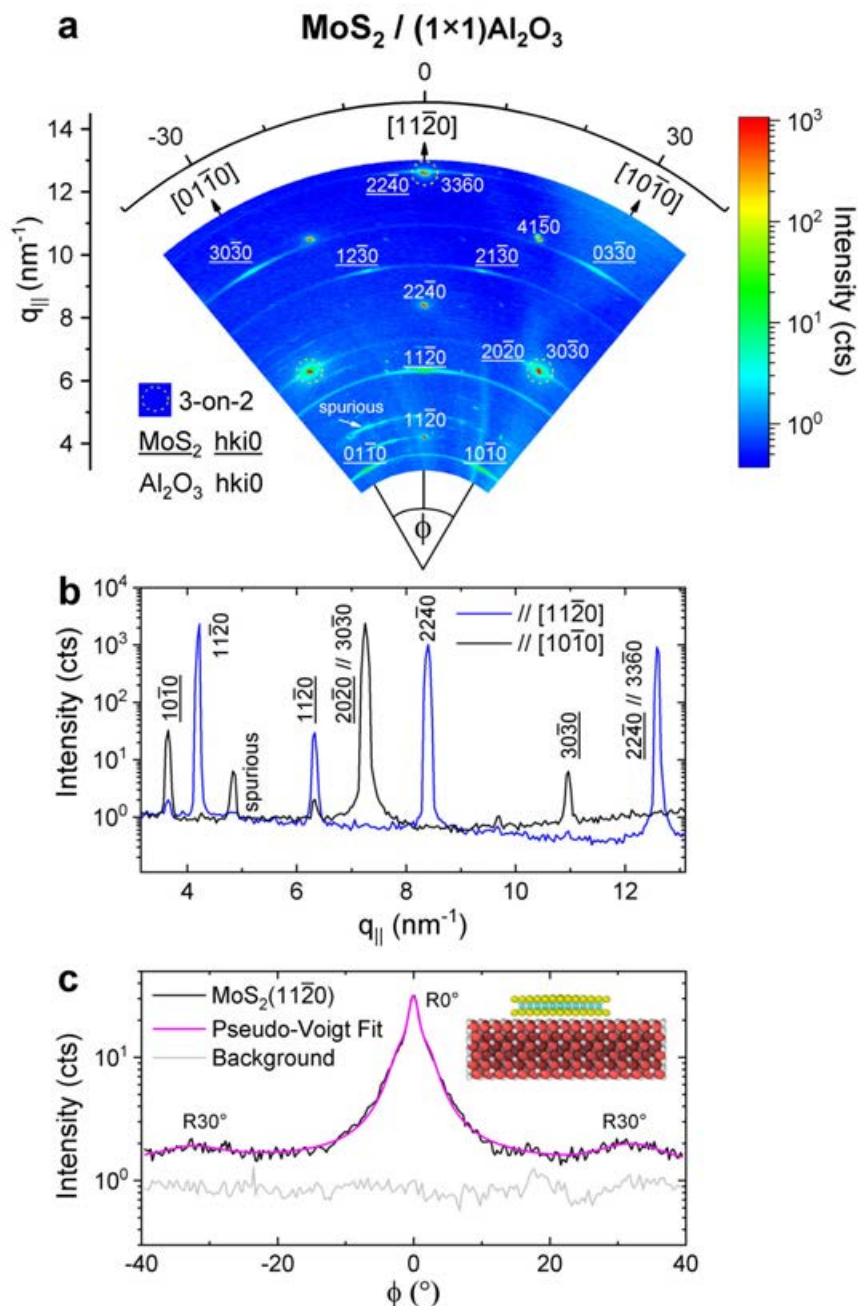
Figure 4.12 In-plane, synchrotron GIXRD of MoS$_2$(0001)/(1 × 1)Al$_2$O$_3$(0001) heteroepitaxy. MoS$_2$ thin films were grown at 600 °C on 1200 °C-O$_2$-annealed O-rich, 1 × 1 Al$_2$O$_3$. **(a)** Reciprocal space map. **(b)** Radial scans along [1 1 $\overline{2}$ 0] and [1 0 $\overline{1}$ 0] directions. **(c)** Azimuthal scan around (1 1 $\overline{2}$ 0) MoS$_2$ peak. The inset shows a heterostructure model with R0°-oriented MoS$_2$ on the O-rich Al$_2$O$_3$ surface.

However, as a collection of peaks is available extrapolating the linear trendline to $q^{-1} = 0$ may give a more reliable result for the experimentally non-accessible
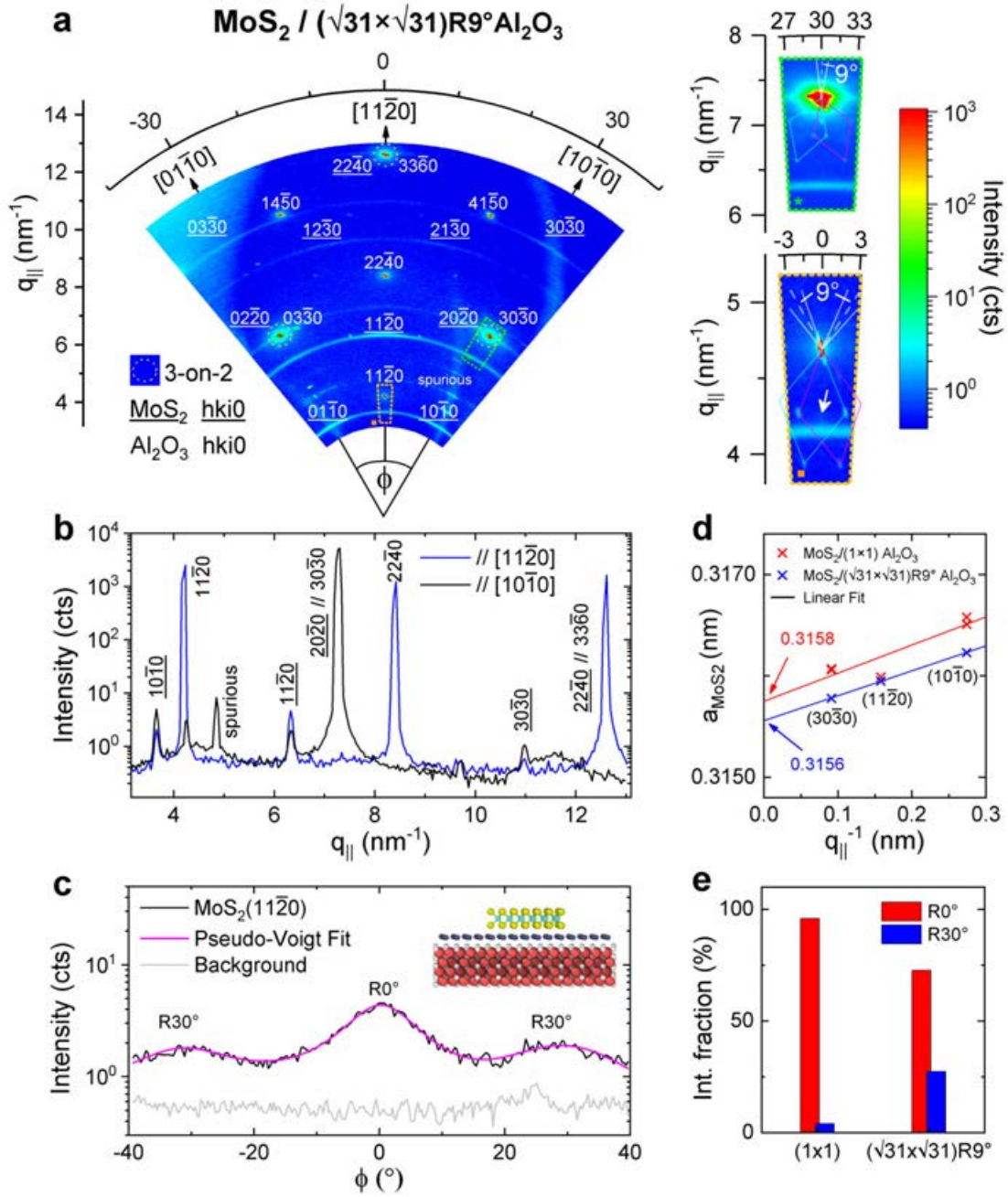
Figure 4.13 In-plane, synchrotron GIXRD of MoS$_2$(0001)/($\sqrt{31} \times \sqrt{31}$)$\pm$R9°Al$_2O_3$(0001) heteroepitaxy. MoS$_2$ thin films were grown at 600 °C on 1200 °C-H$_2$-annealed Al-rich Al$_2$O$_3$. **(a)** Reciprocal space map. Insets show diffraction patterns of the $\sqrt{31} \times \sqrt{31}$R9° surface reconstruction around Al$_2$O$_3$ peaks according to the color-coded frames. **(b)** Radial scans along $[11\bar{2}0]$ and $[10\bar{1}0]$ directions. **(c)** Azimuthal scan around $(11\bar{2}0)$ MoS$_2$ peak. The inset shows a heterostructure model with R30°-oriented MoS$_2$ on the Al-rich Al$_2$O$_3$ surface. **(d)** Extraction of lattice constant a_{MoS_2} for MoS$_2$ grown on O-rich and Al-rich sapphire. **(e)** Integrated intensity fractions of R0°/R30° domains.

$q_\parallel \to \infty$ limit. Using this method, a_{MoS_2} can be extracted as 3.1556±0.0001 Å and 3.158±0.001 Å for MoS$_2$ thin films grown on the (1×1)- and $(\sqrt{31} \times \sqrt{31})$±R9°-reconstructed surfaces, respectively, which is in agreement with reported bulk values in the range of 3.15–3.16 Å [80, 391]. This indicates negligible strain in the MoS$_2$ film in heterostructures on both (1×1) and $(\sqrt{31} \times \sqrt{31})$ surfaces, which has previously been observed for epitaxial MoS$_2$ films on c-sapphire [437] and graphene [391], and which is typical for weakly coupled vdW heterostructures [83]. Another interesting feature to analyze is the MoS$_2$ peak shape, and in particular, the peak broadening, which can depend on instrumental factors, film-related microstrain and crystal domain size [280]. The instrument-related broadening is negligible here, as indicated by the narrow FWHM of substrate-related Al$_2$O$_3$ peaks (note the logarithmic scale in Fig. 4.12b and Fig. 4.13b). A way to differentiate between strain and domain size broadening is possible by the Williamson-Hall plot (see appendix Fig. C17). In the case of strain a slope should be visible when fitting the peak collection; however, no such trend is apparent. Therefore, it can be concluded that no significant microstrain is present in the MoS$_2$ films and that the broadening can be attributed to the crystallite size L_a. L_a can be determined from the Williamson-Hall plot intercept and the Scherrer equation (see appendix Fig. C17) to be 23.4±2.5 nm and 25.2±3.5 nm for MoS$_2$ grown on (1×1)- and $(\sqrt{31} \times \sqrt{31})$±R9°-surfaces, respectively. This is smaller than the domain sizes detected by AFM (several tens to hundreds of nm) and could point at sub-domains and/or intragrain defects being present, as suggested in previous reports on MBE-grown MoS$_2$ [418] and MOCVD-grown WS$_2$ [406].

The ring-like patterns seen in the reciprocal space maps in azimuthal directions around MoS$_2$ related peaks point at the in-plane, angular dispersion of MoS$_2$ domains across the sapphire surfaces. Exemplary azimuthal scan profiles around $(1\,1\,\overline{2}\,0)$ MoS$_2$ peaks in Fig. 4.12c and Fig. 4.13c show the signal distribution over background (gray), for which the latter has been extracted from the "blue background" in the reciprocal space map along azimuthal direction at a radial increment close to the $(1\,1\,\overline{2}\,0)$ MoS$_2$ rings. MoS$_2$ domains grown on the O-rich (1×1) surface show overall lower, mosaic spread with the lowest FWHM being ∼2.5° for the preferred R0° domain fraction, in good agreement with the measurements of the laboratory GIXRD setup. A dominant intensity contribution of domains with R0° epitaxial relationship (0/60°-oriented domains) compared to R30° (−30/30°-oriented domains) can be observed on both surfaces. However, it is evident that the fraction of R30° compared to R0° domains is relatively higher on the $(\sqrt{31} \times \sqrt{31})$±R9° surface. This is represented in Fig. 4.13e by the relative fractions of integrated peak intensities compared to the

total intensities, following the analysis procedure of Liu et al. [391]. Therefore, this result suggests that the $(\sqrt{31} \times \sqrt{31})\pm$R9° surface induces a preferential R30° epitaxial relationship, consistent with previous reports [385, 405, 150]. This can be explained by MoS$_2$ domains epitaxially following the symmetry of the Al(111) termination plane that is rotated approximately by 30° with respect to the underlying Al$_2$O$_3$ bulk in the stacked $(\sqrt{31} \times \sqrt{31})\pm$R9° surface model (Fig. 4.8b). However, the R30° fraction does not become the dominant one, which is likely related to the only partial surface reconstruction during 1200 °C-H$_2$-annealing, as previously discussed. It is expected that sapphire annealing at higher temperatures results in a more complete $(\sqrt{31} \times \sqrt{31})\pm$R9° reconstruction across the surface and, thus, higher controllable R30° fraction [385].

The detailed GIXRD analysis allows a first hypothesis for explaining the non-uniform, morphologically disturbed MoS$_2$ growth on the H$_2$-annealed, Al-rich surface. From a crystallographic point of view the non-uniform Al$_2$O$_3$ surface crystal structure with various coexisting reconstructions creates competition between dominant R0°/R30° film-substrate registries, which induces spatially non-uniform commensurability. Evidence of the patchy AFM phase contrast of the as-annealed, starting surface may indirectly support this hypothesis (Fig. 4.7b, Fig. C6). Recently, such non-homogeneous, terrace-selective TMD growth behaviour and layer properties have been characterized by correlated conductive AFM and time-of-flight secondary ion mass spectroscopy in other works [191, 406].Moreover, out-of-plane data obtained by X-ray reflectivity during this synchrotron experiment [438] could give further insights of the MoS$_2$/sapphire heterostructure interface on the distinct surfaces. This will require further analysis and building an electron density model [418, 440].

Secondly, comparative Raman analysis of MoS$_2$ thin films grown on the O-rich and Al-rich surfaces offers more insights to explain the disturbed growth behaviour (Fig. 4.14), as discussed in the following. Total average spectra and Raman mapping from a 5×5 µm surface area reveal the presence of increased C incorporation homogeneously distributed over the Al-rich surface, as evidenced by characteristic D and G bands; in contrast, Raman mapping of the O-rich surface does not show pronounced C incorporation. Additionally, XPS analysis was performed, suggesting incorporation of graphitic C(sp^2) with higher C content on the Al-rich than the O-rich surfaces (see appendix, Fig. C9); however, the result is not as clear as the Raman analysis and no *in situ* annealing for adventitious carbon removal was performed, as described in section 3.2.3. It can be speculated that the surface chemistry of the $(\sqrt{31} \times \sqrt{31})\pm$R9° reconstruction renders the Al-rich surface active towards graphitic C formation. This may be due to the metallic character [430] and surface-catalytic

Lewis acid behaviour of the $(\sqrt{31} \times \sqrt{31})\pm R9°$ surface that has enabled direct graphene growth from methane [441, 433], and might catalyze in a similar way C contamination stemming from the Dimethyl sulfide source.
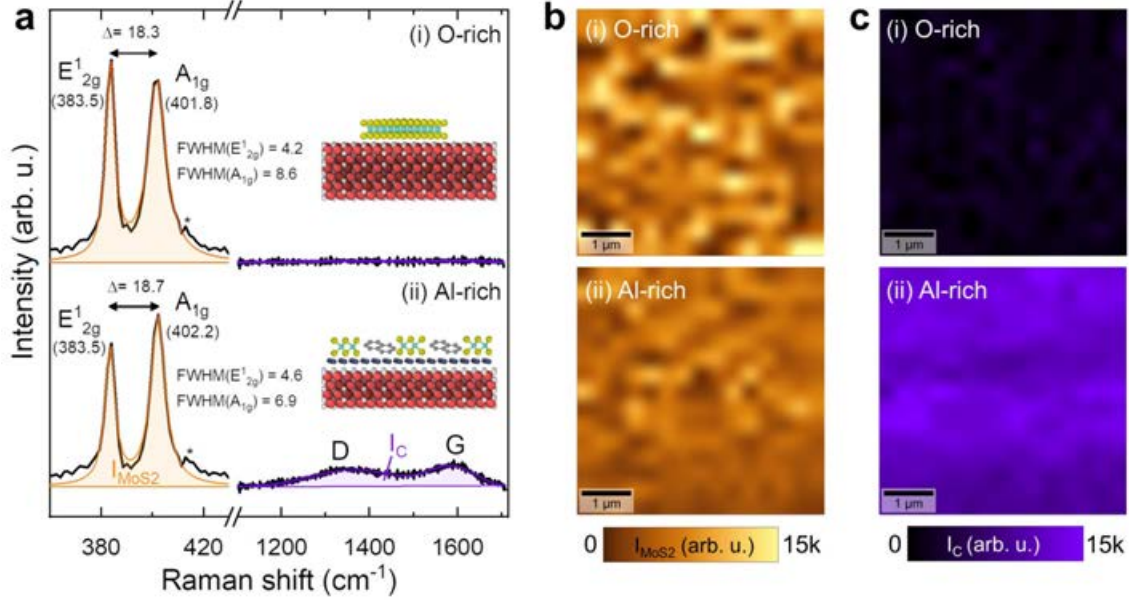
Figure 4.14 Raman spectroscopy of MoS$_2$ thin films grown at 600 °C on O-rich (1×1) and Al-rich $(\sqrt{31} \times \sqrt{31})\pm R9°$ surfaces. **(a)** Total average Raman spectra extracted from 225 points of a 5×5 µm map, showing the characteristic in- and out-of-plane E_{2g}^1 and A_{1g} MoS$_2$ modes and carbon-related D and G bands. The substrate-related sapphire peak is marked by the asterisk (*). Insets show hypothesized heterostructure models. 5×5 µm mappings of the **(b)** $I_{MoS2} = E_{2g}^1 + A_{1g}$ peaks integral, and **(c)** $I_C = I_D + I_G$ for both surfaces.

Consequently, the O-rich (1×1)Al$_2$O$_3$ surface is a favorable choice for the here used conditions and precursor chemistry, which highlights the implications of engineering the substrate surface termination for the MOCVD process. Further Raman analysis of the MoS$_2$-related E_{2g}^1 and A_{1g} modes in Fig. 4.14a with $\Delta = 18.3\,\text{cm}^{-1}$ and $\Delta = 18.7\,\text{cm}^{-1}$ for films grown on O-rich and Al-rich sapphire, respectively, confirm the presence of monolayer MoS$_2$. While the mapping of integrated MoS$_2$ intensity may not resolve the isolated $\sim$200 nm-sized domains of the O-rich sample due to the larger laser spot size of ~ 1 µm, the more finely dispersed domain growth on the Al-rich sample is reflected in an apparently more uniform intensity distribution (Fig. 4.14b). Differences in position and FWHM of the A_{1g} mode averaged from the 225 measurement points can be observed between the two samples, i.e. redshift and broadening suggesting relative n-doping of MoS$_2$ on O-rich sapphire. This may be related to differences in the heterostructures [442] and substrate-induced doping effects [443, 444, 128], and/or structural film quality [445, 248]. Due to possible doping effects, structural quality and

low coverage of the films a low-intensity PL response was observed for both samples (Fig. C18), similar to a previous report of MOCVD MoS$_2$ films grown on sapphire at relatively low temperature of 700 °C [405].

4.3.2.2 Step morphology

The impact of sapphire surface steps (e.g. height, density, shape) and their role in edge-guided TMD nucleation imparting a preferred domain orientation is currently an actively debated topic. Here, growth on sapphire wafers with 0.2° and 0.05° miscut angle O$_2$-annealed at 1050 °C (2 h) with distinct step morphologies were compared (see appendix Fig. C4 and Fig. C5). The 1050 °C-annealed surfaces exhibit predominantly $c/6$ monosteps ($h \sim 0.2$ nm) and a more wavy step shape compared to the previous 1200 °C-annealed substrates with higher portion of $2c/6$ bisteps ($h \sim 0.4$ nm, see section 4.2.3, Fig. 4.5). Examining the AFM images of as-grown MoS$_2$ thin films in Fig. 4.15a, despite the higher step density (smaller terrace size) the nucleation density of MoS$_2$ domains on the 0.2° miscut sample (~ 5.9 μm^{-2}) is even slightly lower than on the 0.05° miscut sample (~ 5.0 μm^{-2}), suggesting that there is no significant impact of the step edges on the nucleation density. Although the step structure is only vaguely discernible below the MoS$_2$ domains due to image quality [Fig. 4.15a(ii) for better visibility], it can be assumed that the MoS$_2$ domain edges are neither nucleated at the step edges nor strictly following edge alignment along them.

The triangular domains lie across the steps while their orientation is dictated by the sapphire surface's crystallographic orientation and not by the inclined steps. Therefore, domain orientation is surface lattice-guided rather than step-guided, similar to a previous reports [175, 404]. The statistical orientation analysis from microscopic inspection in Fig. 4.15 (see also appendix, Fig. C12) evidences a primary R0° epitaxial relationship (0/60°-oriented domains) and secondary R30° domain fraction with similar distributions for both surfaces, with lower tendency towards unidirectional domain selection compared to the previously discussed 1200 °C-annealed sample (Fig. 4.10). However, orientational classification is complicated due to irregular triangle shapes and AFM allows only local domain inspection. Therefore, further GIXRD was carried out for reliable, large-area quantification of the epitaxial relationship and in-plane angular dispersion (Fig. 4.15c). The preferential R0° relationship is revealed and the mosaic spread of 5.2±0.3° and 4.9±0.7° is similar for 0.05° and 0.2° miscut wafers, respectively. The same trend was also confirmed for these miscuts in the case of NaCl-assisted growth (see appendix, Fig. C19), which will be further discussed in the next section.

The apparent lack of edge-imparted, orientational nucleation control of the here used 1050 °C-annealed Al$_2$O$_3$ surfaces could be discussed as follows. A first aspect might be the role of step height in reducing the free energy and increasing the probability for step edge nucleation events. A "proper" step height in relation to TMD layer thickness has been pointed out by theoretical [407] and experimental [248] studies. Possibly, monosteps are not high enough to efficiently induce edge nucleation, although under certain conditions TMD nucleation at monosteps has been observed [408]. A second criterium might involve the step direction for minimizing the free energy of edge nucleation in interplay with domain edge termination (zigzag or armchair) [176, 407, 386], which might not be fulfilled due to the unspecified miscut and step direction of the here used wafers and growth conditions affecting the domain edges. A third aspect might be appropriate growth conditions to activate edge nucleation, such as by an optimized H$_2$ partial pressure [411, 259], and, as speculated, by a minimum growth temperature threshold [404]. To address the first two aspects, 1200 °C-O$_2$-annealed, straight-stepped surfaces with defined wafer miscuts along A- and M-directions were compared (Fig. C1). While a stripe-like domain growth behaviour along the parallel step edges could be observed (Fig. C20), the MoS$_2$ thin films exhibited relatively high mosaic spreads beyond ∼13.9°. More research into the nucleation criteria is required
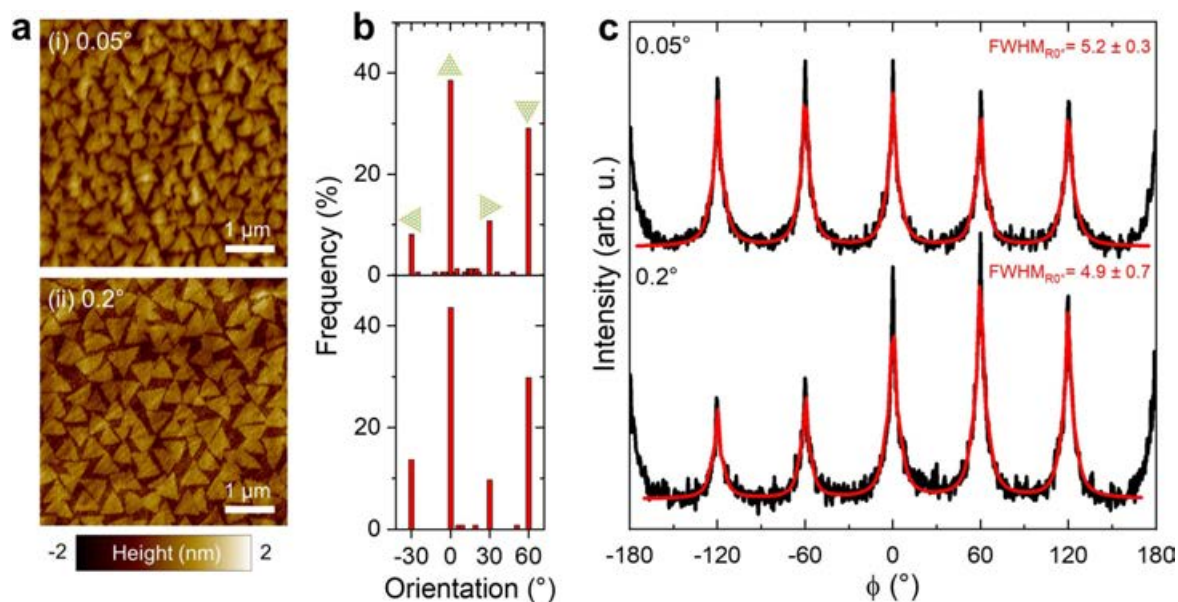
Figure 4.15 Impact of sapphire miscut angle on MoS$_2$ epitaxy. **(a)** AFM images of MoS$_2$ grown on 1050 °C-annealed sapphire with miscut angle (i) 0.05°, and (ii) 0.2°, and corresponding **(b)** statistical domain orientation analysis. **(c)** GIXRD in-plane, azimuthal ϕ-scans around the MoS$_2\{1\,1\,\overline{2}\,0\}$ reflections.

towards unidirectional domain growth, which may be achieved by a combination of morphological step engineering (height, shape and direction) [248, 407], chemical activation and adapted growth conditions [411, 259, 412, 404].

4.3.3 Impact of growth conditions

In this section the effect of various growth parameters on MoS$_2$ epitaxy will be explored, including the use of NaCl to test alkali-assisted epitaxy, variation of growth temperature, S:Mo ratio, and prolonged growth times for layer coalescence and layer nucleation.

4.3.3.1 NaCl – Grain size enhanced epitaxy

In the ideal case of unidirectionally aligned, seamlessly merging domains the domain size would not matter for single-crystal coalescence – translational grain boundaries taken aside [261]. However, in real case scenarios of non-perfect epitaxial registry, in-plane mosaic spread may result in low-angle grain boundaries. Therefore, increasing the grain size is still an important factor to reduce the grain boundary defect density [446]. This raises the question if grain-size enhancing methods, such as alkali-assisted growth, are compatible with TMD epitaxy. Previous reports have suggested that alkali ion intercalation results in film/substrate decoupling [418] and that the epitaxial TMD/sapphire registry is lost during NaCl-assisted growth [369].

To investigate the possibilities of alkali-assisted growth, MoS$_2$ thin films were deposited in comparative growth runs with and without NaCl on annealed sapphire and SiO$_2$ reference substrates. The grain size enhancing effect of NaCl could be observed on both substrates (for an overview see appendix, Fig. C13). MoS$_2$ thin films grown on 1050 °C-annealed, 0.05° miscut sapphire are compared in Fig. 4.16. While the AFM images clearly demonstrate the increase in domain size with the use of NaCl, the apparent domain shape and indirect optical inspection may leave doubts about the epitaxial alignment. However, GIXRD analysis clearly reveals a preferential R0° epitaxial relationship and decreased mosaic spread from 5.2±0.3° to 4.2±0.5° when NaCl is employed. This demonstrates the possibility of grain-size enhanced, alkali-assisted epitaxy, for certain alkali concentrations and film coverages. This was further confirmed on sapphire substrates with different miscuts (see appendix, Fig. C19). The result also emphasizes the benefit of diffraction as a direct technique to confirm epitaxy of seemingly non-aligned domains upon optical inspection of their outer shape.
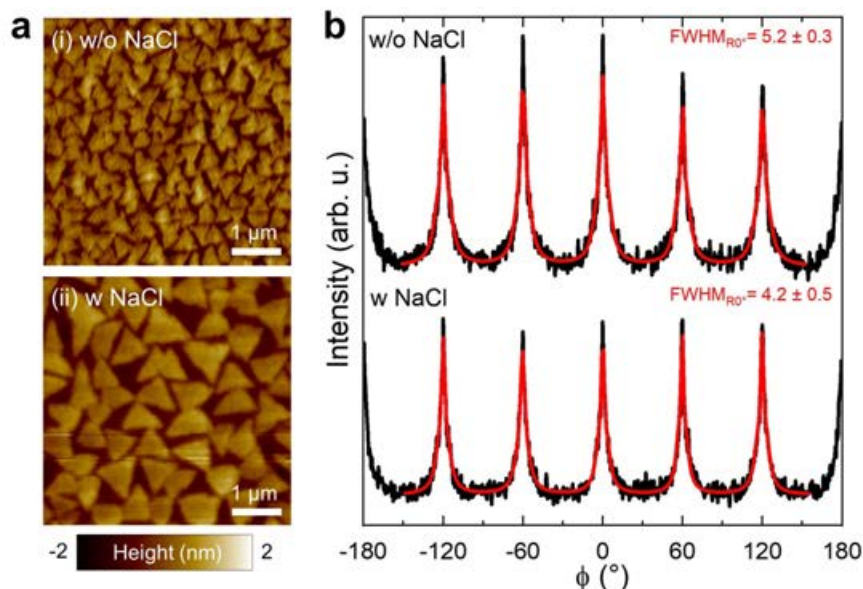
Figure 4.16 NaCl effect on MoS$_2$ epitaxy.**(a)** AFM images of MoS$_2$ grown on 1050 °C-annealed, 0.05° miscut sapphire (i) without NaCl, and (ii) with NaCl. **(b)** GIXRD in-plane, azimuthal ϕ-scans around the MoS$_2\{1\,1\,\overline{2}\,0\}$ reflections.

4.3.3.2   S:Mo ratio – R0°/R30° switching

Chalcogen-rich growth conditions are widely reported to be a prerequisite for TMD epitaxy [258, 176, 82] and may further enable control over domain orientation [257, 258]. To this end, the Mo(CO)$_6$/DMS concentration of the single-bubbler precursor solution was varied. Lowering the concentration of dissolved Mo(CO)$_6$ effectively decreases the Mo supply and consequently the Mo-controlled growth rate [196], which results in the decreased domain coverage seen in the AFM images in Fig. 4.17a. At the same time, the reduced Mo supply effectively increases the S:Mo ratio, which induces a change of preferred domain orientation and epitaxial relationship from R0° to R30°. The here used S:Mo ratio produces a transition regime with both domain families being present, which is also reflected by the 30° periodically shifted diffraction signals appearing in the GIXRD measurement (Fig. 4.17b). Notably, the mosaic spread of the R0° fraction is significantly narrowed from 4.2±0.5° to 0.6±0.3° in the S-rich condition, while the newly formed R30° fraction exhibits an increased mosaic spread of 8.5±2.3°. Therefore, the S potential not only affects the R0°/R30° epitaxial relationship, but also the mosaic spread of these domain families. This may be related with the modified sapphire surface chemistry [248, 407, 259] and/or modified MoS$_2$ edge termination in interaction with surface steps [176]. The AFM data further suggests two sequential nucleation phases. This is highlighted by the inset in Fig. 4.17a(ii) showing supposedly R0°-oriented
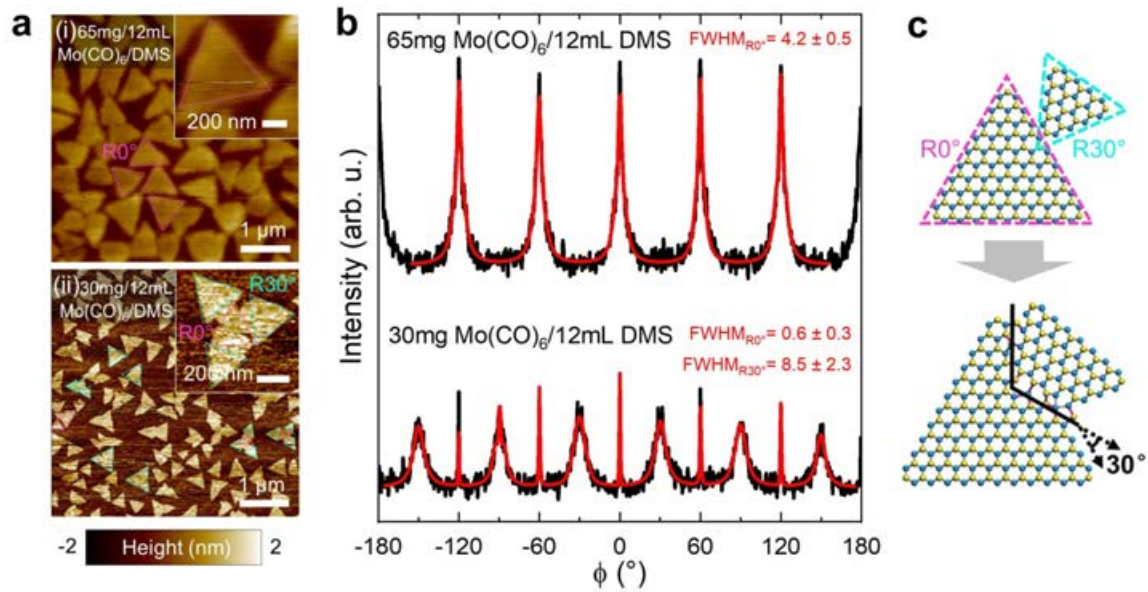
Figure 4.17 S:Mo ratio effect on MoS$_2$ epitaxy. **(a)** AFM images MoS$_2$ thin films grown at 600 °C (with NaCl) on 1050 °C-annealed, 0.05° miscut sapphire for Mo(CO)$_6$:DMS concentrations of (i) 65 mg/12 mL, and (ii) 30 mg/12 mL. Insets for magnified views. **(b)** GIXRD in-plane, azimuthal ϕ-scans around the MoS$_2\{1\,1\,\bar{2}\,0\}$ reflections. **(c)** Illustration of coalescence between 0° and 30° rotated domains. Adapted with permission from Ji et al. [252] © 2015 American Chemical Society.

nucleation cores transitioning into the R30°-oriented peripheral domain parts. The results indicate that the S:Mo ratio allows control over R0°/R30° domain selection; however, these conditions result in the presence of both domain families (0°/60° and −30°/30°), which are prone to domain boundary formation not only by anti-parallel domains within a family but also between the families in form of 30°-angled boundaries (Fig. 4.17c) [163, 252]. This can alter the electronic film properties. Therefore, growth conditions need tuning towards selection of a single domain family to exclude 30°-angled boundaries. Further studies are required to exploit the S:Mo ratio to select domain orientation and narrow mosaic domain spread. Independent S and Mo sources could allow enhanced control over precursor supply and gas-phase composition.

4.3.3.3 Growth temperature – Reduction of mosaic spread

Growth temperature is a determining factor in promoting the epitaxial alignment of TMD epilayers and improving their crystalline film quality by defect reduction [49, 82, 447]. Here, a temperature study by stepwise increase from 600 °C, to 650 °C, and 700 °C is presented in Fig. 4.18.

As shown in the AFM images, clearly discernible, triangular domains could only be observed at the 600 °C condition, while elevated temperatures lead to disrupted film morphology, including smaller domain size and particle formation. The particle formation can be explained by a 2D-to-3D growth mode transition (see also section 3.3.1) induced by increased C incorporation stemming from the onsetting DMS pyrolysis (see also section 3.2.4section 3.4.2), or could be related to metal-rich clusters due to increased $Mo(CO)_6$ decomposition and S surface desorption at elevated temperatures [310, 148]. The observation of truncated domains upon temperature increase deposited on SiO_2 reference substrates in the same growth runs (see section 3.4.2 and appendix, Fig. C21) hints at a modified domain edge termination caused by the S:Mo gas-phase and locally effective surface concentration ratio, such as due to increased chalcogen desorption at elevated temperatures [322, 119] (see also section 2.1.4). Notably, the temperature increase alters domain morphology more sensitively on sapphire than on SiO_2 substrates.
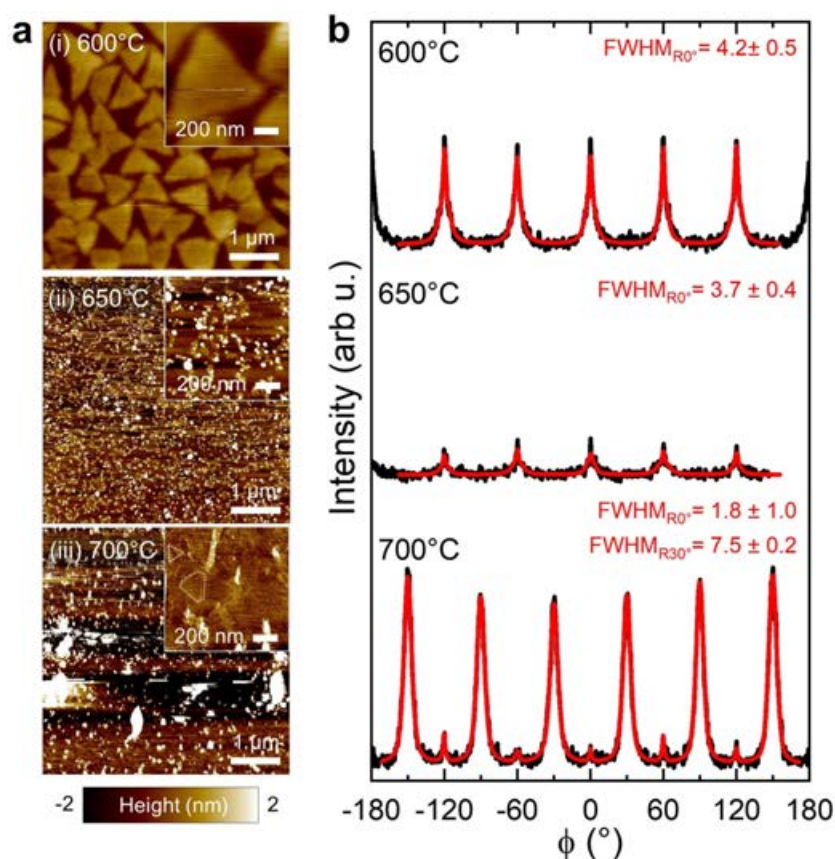
Figure 4.18 Growth temperature effect on MoS₂ epitaxy. **(a)** AFM images of MoS₂ grown on 1050 °C-annealed, 0.05° miscut sapphire for growth temperatures of (i) 600 °C, (ii) 650 °C, and (iii) 700 °C. Insets for magnified views. **(b)** GIXRD in-plane, azimuthal ϕ-scans around the MoS₂$\{1\,1\,\bar{2}\,0\}$ reflections.

More detailed TEM and XPS analysis could give further insights. In the GIXRD measurements a trend of decreasing mosaic spread for the R0° domain fraction can be observed pointing at improved epitaxial alignment (Fig. 4.18b), which is consistent with previous works reporting significant improvements in TMD crystalline quality by elevating temperature in the range from 600 to 900 °C [49, 195, 259, 384]. Interestingly, at 700 °C a dominant R30° domain fraction appears. This may be a consequence of the aforementioned, temperature-induced changes in the effective S:Mo ratio affecting epitaxial R0°/R30° selection (see previous section 4.3.3.2); however, further growth studies are required to understand this observation.

By using the in-plane, angular domain dispersion as a metric for epitaxial film quality, the synthesized films can be benchmarked to literature values, as shown in Fig. 4.19. For a fair comparison, all data points correspond to TMD thin films (MoS$_2$, WSe$_2$) heteroepitaxially grown by MOCVD on c-sapphire, and characterized by surface diffraction techniques (either GIXRD or RHEED) for large-area, statistically reliable data. In fact, only few published work meeting these criteria is currently available for comparison despite the popularity of the TMD/sapphire system. The reference sources include data from the 2D crystal consortium at Pennsylvania State University (USA),
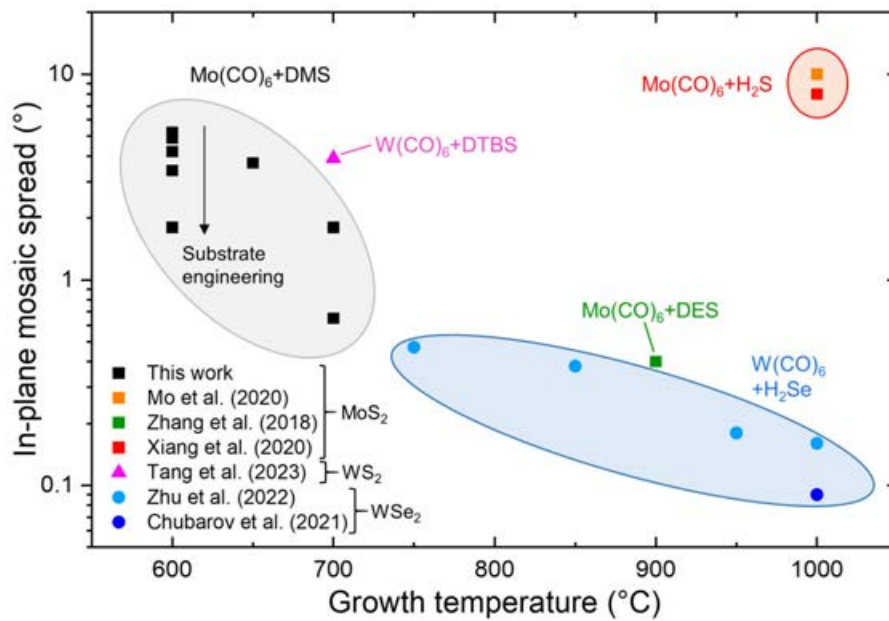
Figure 4.19 Quality benchmark of wafer-scale MOCVD TMD epitaxy on sapphire. In-plane, mosaic spread of MoS$_2$, WS$_2$ and WSe$_2$ thin films as a function of growth temperature obtained for different precursor chemistries. The domain dispersion has been characterized by large-area surface diffraction methods in various literature reports: Mo et al. [405], Xiang et al. [249], Zhang et al. [369], Tang et al. [404], Zhu et al. [259], Chubarov et al. [48].

imec (Belgium), and Aixtron (Germany). The benchmark suggests a general trend of lower, in-plane domain dispersion (i.e. improved epilayer alignment) for increasing growth temperatures, although outliers exist for non-optimized conditions at 1000 °C. The current state-of-the-art for TMD epitaxy on sapphire in terms of mosaic spread is defined by the work of Chubarov et al. with the lowest reported value of 0.09° [48] for MOCVD WSe$_2$ thin films grown at 1000 °C. Another notable recent result, although achieved by the solid evaporation CVD method (not listed in Fig. 4.19), was obtained by Liu et al. [448] for bilayer MoS$_2$ thin films grown at 1050–1080 °C, with a mosaic spread of 0.26±0.17°[2]. As a reference to these values, mosaic spreads of $\lesssim 0.1°$ are typical for conventional III-V semiconductor heteroepitaxy [280, 449]. The precursor chemistry plays an important factor in the achievable film quality plays: organic chalcogen precursor chemistry complicates the epitaxy at high temperatures compared to carbon-free hydrides due to the challenges of C incorporation [190, 310, 404] (see chapter 3). Furthermore, results may also be impacted by different growth [48, 259, 404] and sapphire surface conditions [191, 384, 406] and the nature of TMD constituents (Mo, W, S, Se etc.) exhibiting different surface kinetics [320], reaction chemistries, and phase diagrams (see also section 2.1.5).

4.3.3.4 Time – 1L coalescence and 2L nucleation

The previous sections have focused on sub-monolayer coverage thin films to facilitate the optical inspection of isolated, epitaxial MoS$_2$ domains. For transistor applications, the growth of a coalesced, mono- to few layer thin films is desired [248]. Therefore, the growth time was extended to study the structural properties of the coalesced film. Furthermore, understanding nucleation and epitaxy on subsequently stacked layers is of interest, where the layer-by-layer growth implies an essential change from heteroepitaxy on sapphire to homoepitaxy on MoS$_2$ [254, 195]. Figure 4.20 shows AFM and GIXRD data for MoS$_2$ thin films for growth times of 16 h and 16+6 h. The first layer exhibits preferential R0° epitaxial relationship with both 0°/60°-oriented domains being present with a mosaic spread of 5.2±0.3°. This inherently results in defect formation upon coalescence of the primary layer by twin grain boundaries between the anti-parallel domains, and twist grain boundaries between inclined domains with dispersed orientations around the high-symmetry directions (mistwist angle δ, Fig. 4.20d). For the extended growth time, second layer nucleation of small-grained

---

[2]The mosaic spread was determined from the FWHM of fitted GIXRD source data [248] of Fig.4 provided online by Nature (2022)
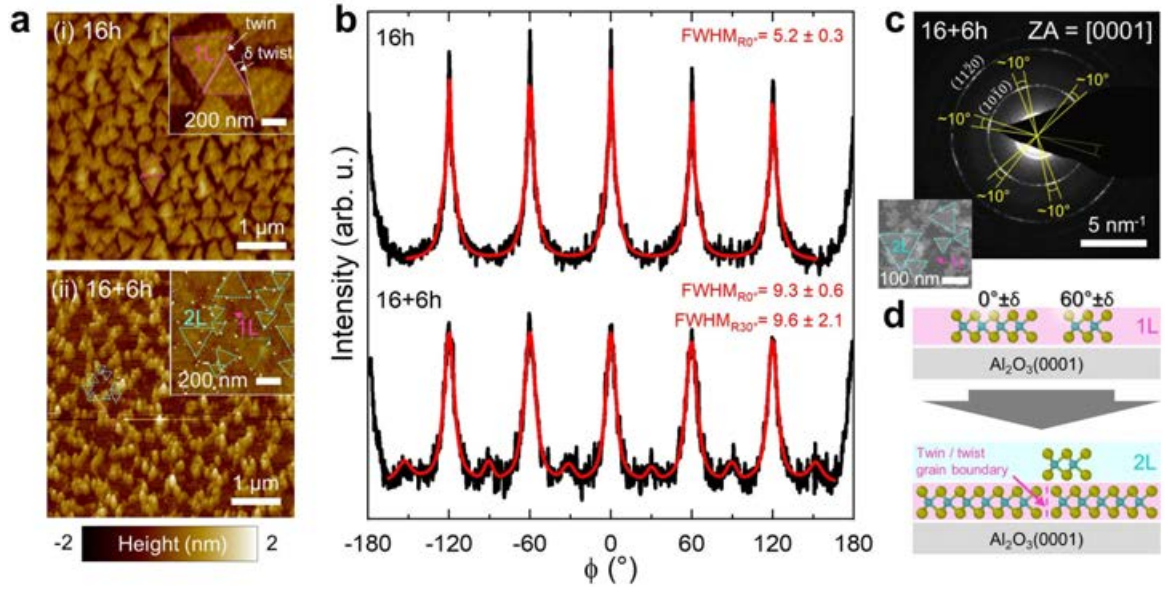
Figure 4.20 Growth time effect on MoS$_2$ epitaxy – coalescence and 2L nucleation. **(a)** AFM images of MoS$_2$ grown on 1050 °C-annealed, 0.05° miscut sapphire for growth times of (i) 16 h, and (ii) 16+6 h. Insets for magnification. **(b)** GIXRD in-plane, azimuthal ϕ-scans around the MoS$_2\{1\,1\,\bar{2}\,0\}$ reflections. **(c)** TEM diffraction pattern seen along C[0 0 0 1] zone axis. **(d)** Top: Schematic of 1L-MoS$_2$ with sub-monolayer coverage. Bottom: 1-2L-MoS$_2$ film, where defect-driven 2L domains nucleate at grain boundaries of anti-parallel/twisted 1L domains.

domains is observed to preferentially occur on the primary layer grain boundaries, consistent with the work of Jin et al. [195]. The mosaic spread of the R0° domain family seen by GIXRD broadens to 9.3±0.6° and a second minor R30° contribution with similar angular spread becomes apparent, indicating higher in-plane disorder with increasing growth time, layer coalescence and defect-mediated epilayer nucleation. The homoepitaxy is prone to nucleation of anti-parallel domains, stacking faults and reduction in domain size due to increased density of the defect-mediated nucleation [446, 195] (see another clear example of grain boundary nucleation in appendix Fig. 3.24). Top-view TEM imaging in Fig. 4.20c after transfer of the 1-2L film onto a TEM grid shows irregular 2L domains deviating from triangular shape (grey) on top of the 1L (black). Electron diffraction along the [0 0 0 1] zone axis reveals the patterns of the $(1\,0\,\bar{1}\,0)$ and $(1\,1\,\bar{2}\,0)$ MoS$_2$ lattice planes with six-fold symmetry and ring-like structure confirming the in-plane rotational disorder. The intensity distribution (FWHM) around high-symmetry directions, with mosaic spread of around ∼10°, is consistent with the GIXRD result.

The result confirms the challenge of defect-free and layer-controlled TMD epitaxy. Monolayer heteroepitaxy on sapphire requires further research into tuned growth and

substrate conditions towards the unidirectional growth and single-crystal coalescence. Entering into bi- and few layer homoepitaxy creates more complexity, as mirror symmetry and stacking fault issues pile up with imperfections translating from the primary into added epilayers, in particular for time-controlled growth in a layer-by-layer fashion. Promising strategies for layer thickness controlled TMD synthesis could involve time- and flux-controlled ripening [197, 320] or temperature-controlled, hydrogen- or chlorine-based etching approaches [450, 291, 323] to remove superficial bilayer islands. Alternatively, edge-guided nucleation may control few layer growth by step height engineered sapphire surfaces [248, 407].

4.3.4   Wafer-scale epitaxy of coalesced MoS$_2$ thin film

To demonstrate the wafer-scale synthesis of coalesced MoS$_2$ thin films, growth was carried out at $600\,°C$ for 16+6 h on a $1050\,°C$, O$_2$-annnealed, 0.05°, uniformly stepped 2" sapphire wafer, as shown in Fig. 4.21. Optical inspection of the wafer after growth shows yellow coloration over the 2" wafer area, although a slight color gradient with increasing intensity from bottom to top is apparent (from position "3" to "1" in Fig. 4.21). Uniformity was checked in the marked wafer positions by AFM and Raman/PL spectroscopies. AFM images show a fine-grained structure due to the high-density, defect-mediated second layer nucleation (section 4.3.3.4); in position "3" the apparently lowest second layer nucleation is visible, where grain boundary contours of the primary layer are better discernible, consistent with the deposition gradient. Notably, particle formation can be observed, resulting in increased RMS roughnesses around $0.7\,nm$. These particles of currently undetermined composition may be attributed to an aging effect, potentially caused by air exposure, evidenced by the AFM measurement taken a few days after the growth. The particle formation was also observed for sub-monolayer coverage thin films that were measured five days after growth (Fig. C22). In comparison, the particles had not been present immediately after growth (e.g. Fig. 4.11a). Although these samples had been vacuum-packaged or stored in a vacuum desiccator most of the time, they had been air-exposed after reactor take-out and during AFM measurement. The signal intensity of PL and Raman spectra are typically used as a measure for the spatial uniformity of TMD thin films over wafer areas [47, 176, 170]. The intensity variations seen in PL and Raman spectra [Fig. 4.21(b-c)] are consistent with the optically visible deposition gradient; the Raman frequency difference around $\Delta = 21\,cm^{-1}$ proves the 1-2L nature of the film [169].
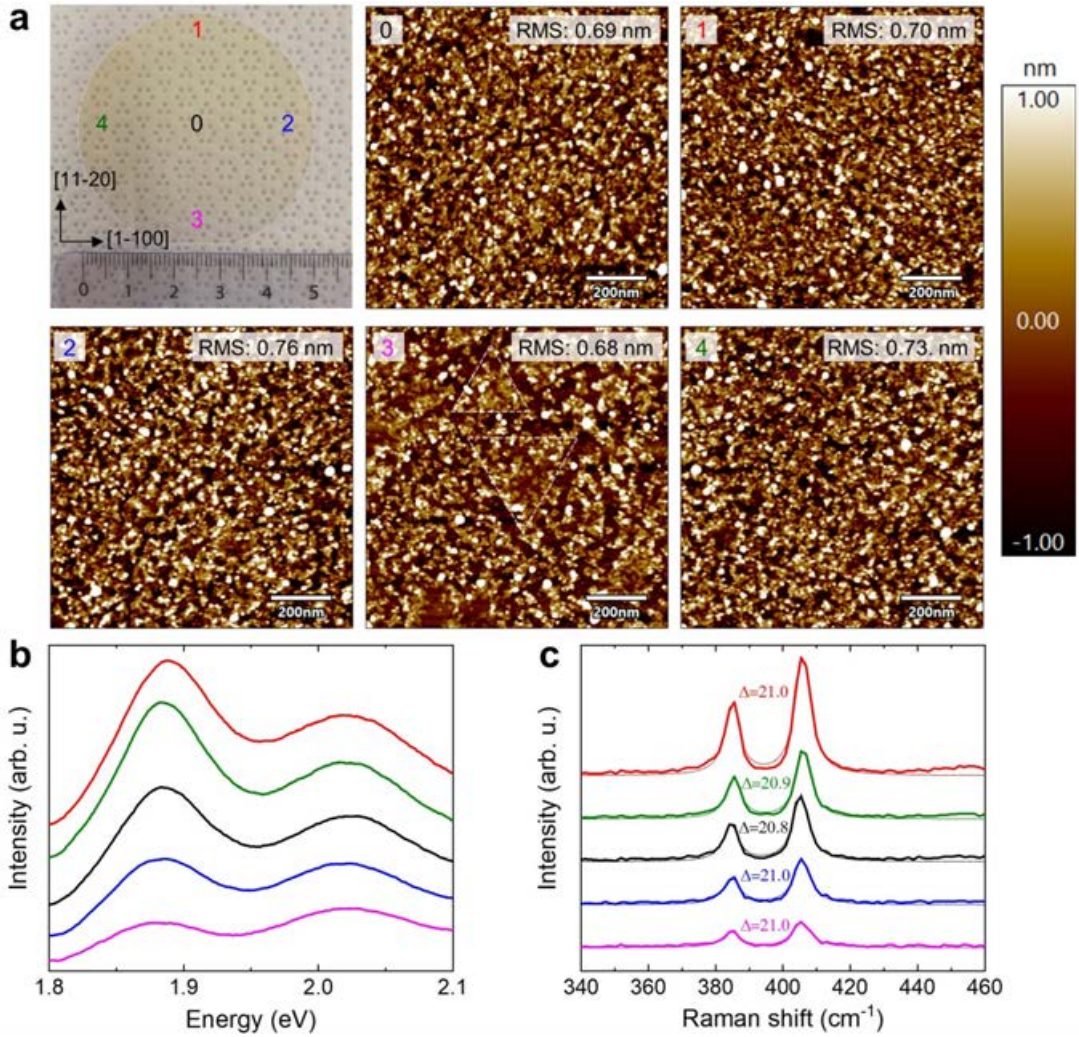
Figure 4.21 Wafer-scale MoS$_2$ epitaxy on sapphire. 1-2L MoS$_2$ thin film grown at 600 °C for 16+6 h on 0.05° miscut, 1050 °C-ambient-annealed 2″ sapphire. **(a)** Photograph of wafer after growth and AFM images recorded in the corresponding marked wafer positions. **(b)** PL spectra corresponding to the different locations shown in (a), and corresponding **(c)** Raman spectra of MoS$_2$-related E$_{2g}^1$ and A$_{1g}$ modes with depicted frequency differences $\Delta = A_{1g} - E_{2g}^1$.

The observed deposition gradients are not surprising. They may arise from inhomogeneities in gas flow dynamics, depletion and buoyancy effects due to thermal convection, which are common challenges in horizontal reactor designs [451, 452, 235] – and sometimes accounted for by using tilted substrate holders [169]. However, it is emphasized that TMD growth using metal hexacarbonyls in a hot-wall reactor is prone to strong thermal decomposition gradients along the tube axis (see section 2.2.2, Fig. 2.10), making the vertical wafer positioning perpendicular to the flow direction

a preferred choice in case of stationary wafer placement. Substantial improvements in film uniformity can be obtained by the introduction of rotatable substrate holders/susceptors, such as by gas foil rotation [48, 236], helping to average out deposition gradients, which is standard in modern, industrial-scale MOCVD reactors [453]. Furthermore, vertical reactor designs with showerhead-type injectors may result in a more uniform gas injection [197, 170, 454] and cold-wall systems with actively-cooled shower head technologies should be considered. Therefore, improving reactor design is key to enabling industry-scale, homogeneous MOCVD of 2D TMDs in the future. From this perspective, predictive, computational modelling of reaction dynamics will be a relevant toolkit to guide this development [452, 235, 236, 318].

4.4   Summary

In this chapter, the rotationally commensurate vdW epitaxy of large-area 2D MoS$_2$ thin films by MOCVD has been demonstrated on industrially relevant c-sapphire wafers. The work has been focused on the preparation of distinct sapphire surfaces engineered by wafer manufacturing and thermal annealing, and the study of growth parameters to broadly explore their impact on the orientation-selective 2D-on-3D MoS$_2$/sapphire heteroepitaxy. A summary of all this work is provided by Fig. 4.22. For this purpose, a framework of combined diffractometry and microscopy methods has been established to analyze sapphire surface morphology and reconstruction, and to assess as-grown films by their in-plane epitaxial relationship and mosaic spread. While synchrotron GIXRD allowed comprehensive reciprocal space mapping, laboratory GIXRD and RHEED enabled routine analysis of epitaxial film quality. This was complemented by microscopic inspection by AFM/SEM to obtain a complete picture of film morphology and texture because diffraction techniques alone are not able to differentiate between symmetry-equivalent, anti-parallel domain orientations. The latter pose an inherent challenge upon layer coalescence due to the formation of twin grain boundary defects. It was found that the sapphire surface reconstruction plays an important role in the orientation-selective MoS$_2$ domain growth and the reaction product-selective MoS$_2$ film purity. For instance, the O-rich (1×1) surface led to triangular domain growth with preferential R0° epitaxial relationship, while the Al-rich $(\sqrt{31} \times \sqrt{31}) \pm R9°$ surface showed the tendency to induce the R30° epitaxial relationship and increased C contamination, resulting in disperse domain epitaxy. Complementary synchrotron GIXRD and AFM studies suggest that the uniformity of sapphire surface reconstruction and passivation may

be important requirements for large-area, uniform heteroepitaxial commensurability; GIXRD suggested various sapphire surface reconstructions present on H_2-annealed, Al-rich surfaces and AFM images showed a patchy phase contrast that may be related with the spatial uniformity and selectivity of the R0°/R30° heteroepitaxy. Furthermore, the surface step morphology (step density, shape, height, direction) controllable by miscut and thermal annealing influences the preferential domain alignment (observed up to an extent of ~64 % of 0°-oriented domains) under certain conditions; yet, a strong tendency of anti-parallel domain alignment along the high-symmetry Al_2O_3 surface directions, rather than step-guided unidirectional nucleation, has been observed. The MoS_2 thin films have been benchmarked to literature data by comparing the routinely measured mosaic spread as a figure of merit. Best results of domain epitaxy have been obtained on 1200 °C, O_2-annealed, straight stepped (1×1) surfaces at growth temperatures of 600 °C, exhibiting R0° preferential relationship and mosaic domain spread below 2°. Increased growth temperatures and S:Mo ratios allow switching the R0°/R30° epitaxial relationships and further reduction of mosaic spread, although at the cost of adverse effects, such as the higher C incorporation stemming from
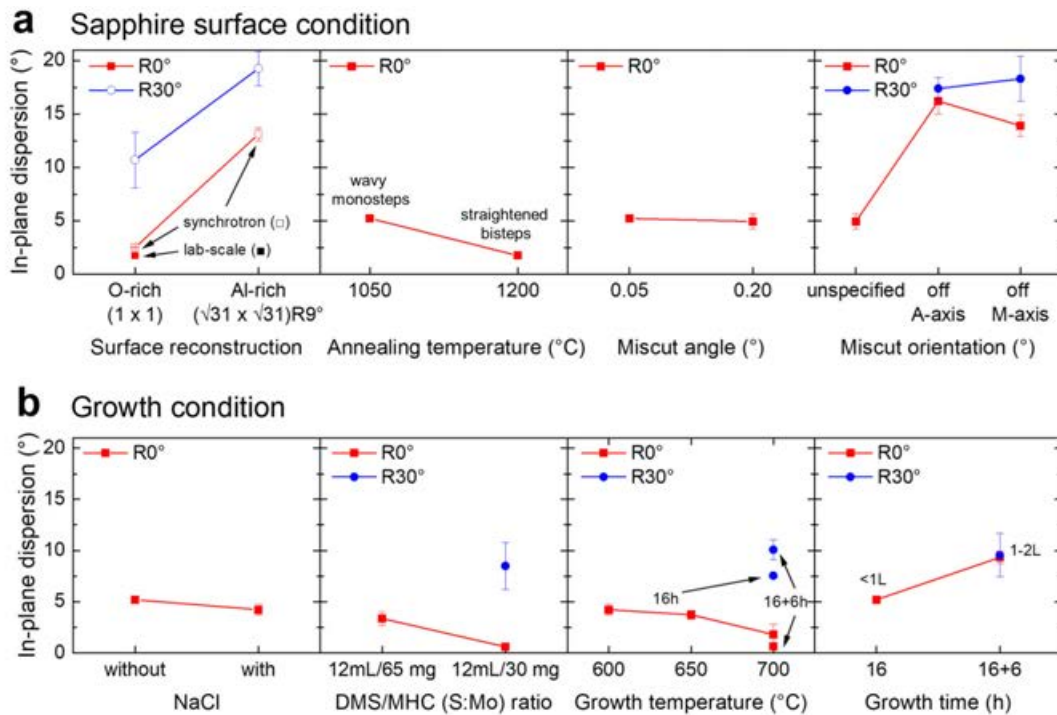
Figure 4.22 Overview of structural analysis of epitaxial MoS_2 thin films by GIXRD. In-plane angular dispersion (mosaic spread) of R0° and R30° domains due to the impact of the **(a)** sapphire substrate, and **(b)** growth parameters.

the organosulfide precursor chemistry. In contrast to a previous report [369], the use of NaCl did not inhibit epitaxial registry while enhancing domain size. For further comparison of this work with literature, the interested reader is referred to the appendix (table C1). As an outlook, statistical validation of results is necessary and further research into unidirectional, low-mosaicity TMD films needs to be pursued. Breaking the symmetry of anti-parallel domains by sapphire edge-guided nucleation remains a promising strategy, although engineered step morphology and chemistry in interplay with the growth conditions (temperature, pressure, S:Mo:H$_2$ gas-phase composition) require optimization. From a crystallographic perspective, low-symmetry substrate surfaces [253, 242], such as two-fold A-plane sapphire [419, 455, 456] may provide another promising route to reduce domain boundaries, lowering the number of energetically degenerate domain configurations.

In conclusion, by laying out the opportunities and limitations of orientation-selective domain epitaxy via optimized substrate engineering and growth conditions, this work has provided essential understanding towards the wafer-scale synthesis of single-crystal 2D semiconductors from low cost, low toxicity organic precursors on commercial substrates. This is of paramount importance for large-area device integration and high-performance electronic applications.

Chapter 5

MoS$_2$ integration and transistor technology for flexible electronics

Field-effect transistors are arguably the most important element of logic circuits and form the backbone of modern electronics today. Novel materials, such as 2D semiconductors, offer opportunities complementing conventional Si technology or even replacing elements beyond CMOS in ultra-scaled "more Moore" devices and implementing "more than Moore" functionalities for further diversification in future, hybrid electronics [14]. A strong advantage of 2D semiconductors relies on their combination of excellent mechanical and electronic properties that enables to build flexible electronic circuitry [38, 42] that can not be realized with classical, rigid materials. This opens prospects for bendable, stretchable and wearable devices for multifunctional sensors, bioelectronics and medical applications, such as implantable neuroprostheses that require adaptability to soft tissues.

To realize the full potential of 2D semiconductors for flexible electronics, integration challenges must be overcome, such as the large-area synthesis of low-defect, crystalline transistor channel material addressed in previous chapters, optimized device manufacturing processes and interface engineering. This requires accompanying metrology, electrical device testing and thin film quality benchmarking. The refinement of fabrication protocols must include great attention to interface quality by clean and residue-free 2D processing, reduction of impurity and trap densities because 2D materials are highly sensitive to heterogeneities and perturbations in their surrounding environment, which can alter device functionality.

In this chapter, the technological processes for implementing large-area, cm^2-scale MOCVD-grown MoS$_2$ thin films into transistors are developed and monitored along the process chain by morphologic, spectroscopic, and electrical analyses. This includes the development of a suitable 2D layer transfer method, focusing on residue-free removal of polymer support layers to preserve clean MoS$_2$ interfaces. It also involves AlO$_x$ oxide dielectric integration and passivation through a seeded ALD-encapsulation route aiming at enhanced MoS$_2$ channel properties. Standard clean room processes are used to fabricate liquid and solid-gated MoS$_2$-FETs for benchmark studies of different MOCVD-grown MoS$_2$ thin films. Finally, the solid-gate MoS$_2$-FET technology is translated from rigid to flexible substrates and prototypes of flexible, 2D material-based neuroprosthetic devices are realized to demonstrate the proof-of-concept of MoS$_2$-FETs on-site multiplexing of graphene neural sensor arrays.

5.1   MoS$_2$ transfer

Fabrication of 2D FETs requires a step, in which the 2D semiconductor is implemented into the device. In principle, there are at least two ways to achieve this, either by direct growth onto the device or by growth on an external template followed by layer transfer onto the device. As the direct growth process typically involves temperature-activated reactions, it must comply with the inherent thermal stability limits of the underlying device structures at BEOL-compatible temperatures. Although there have been numerous efforts in the low-temperature TMD growth by MOCVD around 450 – 475 °C [457, 458] for rigid devices and even down to 250 °C at polymer-compatible temperatures for flexible devices [459, 237], the thermal budget, process compatibility and achievable film quality remain a major hurdle for direct growth approaches. Moreover, ongoing advances in the direction of single-crystal van der Waals epitaxy for high quality films rely on elevated process temperatures and growth substrates that are not compatible with direct synthesis on arbitrary substrates, in particular not the here targeted polymer substrates for flexible integration. For the latter reasons, a large-area transfer from the growth substrate to the target device preserving 2D layer properties is desired.

5.1.1   Transfer method assessment

To identify a suitable transfer process, reported methods were compared, practically assessed and adapted to the here developed MoS$_2$ technology. As reviewed by Watson et al. [460], different 2D layer transfer methods can be found in literature, generally categorized into wet and dry transfer methods. Wet techniques may involve chemical etchants, such as NaOH or KOH, to facilitate intercalation and layer delamination from the growth substrate, and liquid media, in many cases water [461, 462, 169], from which the floating layer can be scooped in the main transfer step. Dry techniques avoid any liquid contact and may involve visco-elastic stamps, such as PDMS [133, 463], metallic spalling layers [464, 465], hot-pressing wafer bonding-debonding approaches [51], or lamination by thermal release tapes (TRT) [466, 197, 467, 291]. The latter TRTs are based on the principle of adhesive layer pick-up and thermally controlled detachment after transfer. In practice, many transfer methods combine wet and dry strategies. For instance, liquids may be used in an intercalation step, while the transfer onto the target substrate is a dry step. In both wet and dry techniques, often sacrificial support layers are used to preserve the mechanical integrity of the transferred film, which are dissolved after transfer. For this, spin-coatable polymers, such as poly(methyl methacrylate) (PMMA) are frequently chosen due to their favorable mechanical properties and tight adhesive contact [460]. In the following, wet fishing and a semi-dry TRT transfer procedures are described (for more details see appendix, section D.1).

The wet transfer process is illustrated in Fig. 5.1. First, a sacrificial PMMA polymer support layer is spin coated onto the MoS$_2$ sample and hard-baked. Then, a blade is used to scratch away PMMA/MoS$_2$ around the edges of the substrate to make the MoS$_2$/substrate interface accessible for liquid intercalation. The edge of the sample is dipped into NaOH(aq) and moved in and out to detach the PMMA/MoS$_2$ stack from the substrate. From experience, initiating the detachment by only dipping into H$_2$O [462] typically does not work or only at unefficiently slow rate. Once a broad detachment front has been created, the process can be continued in a water bath where further water intercalation by capillary force aids the complete sheet detachment until the PMMA/MoS$_2$ stack floats freely on the water surface. Next, the PMMA/MoS$_2$ sheet is transferred into two subsequent water baths to wash off NaOH residues. The PMMA/MoS$_2$ sheet is fished onto an arbitrary target substrate and put onto a hotplate to dry, dewrinkle and promote adhesion of the transferred film. Finally, the PMMA/MoS$_2$/target substrate is immersed into a suitable solvent (e.g. acetone, Remover PG) for dissolution of the PMMA support layer.
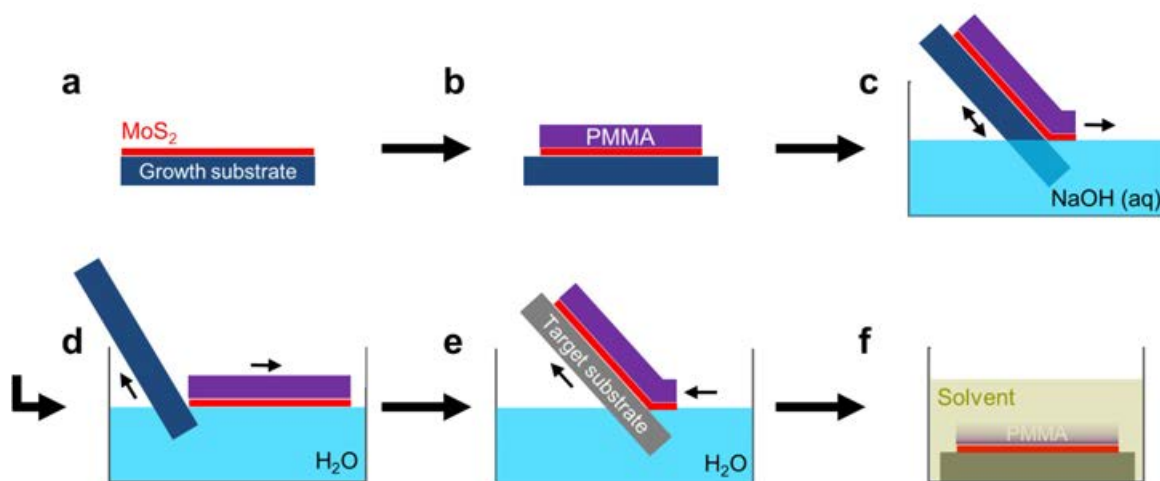
Figure 5.1 Wet fishing transfer procedure. **(a)** As-grown MoS$_2$ thin film **(b)** PMMA spin-coating and scratching of PMMA/MoS$_2$ at the sample edges. **(c)** Initiation of PMMA/MoS$_2$ delamination by edge dipping into NaOH(aq) bath. **(d)** Release and floating of PMMA/MoS$_2$ in H$_2$O bath. **(e)** Fishing of PMMA/MoS$_2$ onto target substrate. **(f)** PMMA dissolution.

The semi-dry thermal release tape (TRT) transfer process is schematically illustrated in Fig. 5.2. Further information and photos of each step can be found in the appendix (Fig. D2). Similarly to the wet transfer, a sacrificial PMMA layer is spin coated onto the MoS$_2$ sample and hard-baked. Then, a blade is used to scratch away PMMA/MoS$_2$ around the border edges of the substrate to later facilitate water intercalation for MoS$_2$ detachment. Next, a TRT is placed onto the PMMA/MoS$_2$ and gently applied by a roller to push out potentially trapped air bubbles. A water droplet is placed on top and covered with an overlapping polydimethlysiloxane sheet (PDMS) that spreads out the droplet and acts as a compliant layer in the next step. The stack is placed into a pressing dye to apply uniaxial pressure and squeeze the water sideways to the edges of the layer stack, where it intercalates at the MoS$_2$/substrate interface by capillary force [461]. The layer stack is unmounted from the dye, the PDMS is removed, and the TRT/PMMA/MoS$_2$ stack is slowly detached from the growth substrate. The TRT/PMMA/MoS$_2$ is gently transferred onto the target substrate, making this step essentially a dry process. Then, the sample is placed onto a hotplate and ramped to 155 °C to enhance MoS$_2$/target substrate adhesion. The TRT is peeled off from the PMMA/MoS$_2$/target substrate when the TRT loses its adhesion strength at around 155 °C [291]. Finally, the protective PMMA layer is dissolved in a suitable solvent (e.g. acetone, Remover PG, see section 5.1.2).
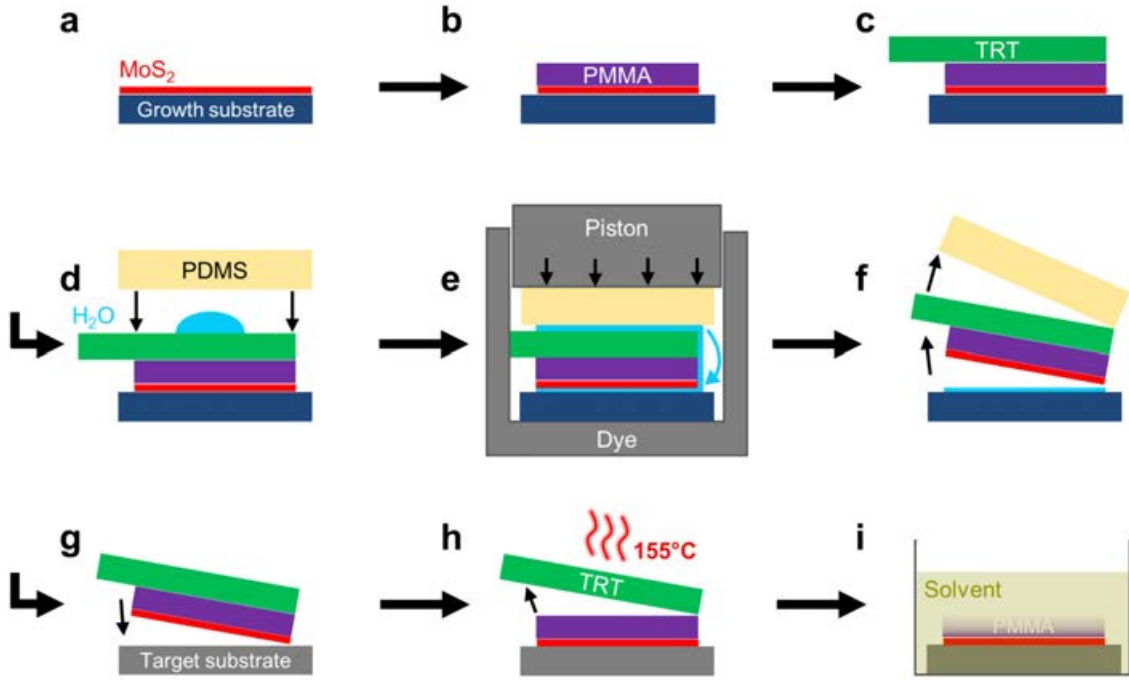
Figure 5.2 TRT transfer procedure. **(a)** As-grown MoS$_2$ thin film **(b)** PMMA spin-coating and scratching of PMMA/MoS$_2$ at the sample edges. **(c)** Application of TRT. **(d)** Adding of water droplet and PDMS. **(e)** Pressing of layer stack, spreading of droplet and water intercalation at MoS$_2$/substrate interface. **(f)** Dismounting. **(g)** Removal of PDMS and TRT/PMMA/MoS$_2$ stack. **(h)** Transfer of TRT/PMMA/MoS$_2$ stack onto target substrate. **(i)** TRT release on hotplate at 155 °C. **(j)** PMMA dissolution.

The microscopy images in Fig. 5.3 show the MoS$_2$ transfer to SiO$_2$ substrates, comparing the wet fishing and TRT method. Based on practical experience from repeated transfers and literature research, the advantages and challenges of each method are listed in table 5.1 by considering three main aspects: applicability, scalability and preservation of sheet integrity. In terms of applicability both methods are suited for MoS$_2$ transfer from the typical oxide growth substrates (SiO$_2$, glass, sapphire) used in this work, exploiting layer detachment by water intercalation at the hydrophobic/hydrophilic MoS$_2$/substrate interface. The flatness of the substrate is critical for the TRT method; For glass substrates that had deformed during high temperature MoS$_2$ growth, it was observed that the relatively rigid TRT may not conformally adhere during layer pick-up, which may cause untransferred regions and lowered yield. On the other hand, the TRT method is advantageous for precise target placement, which makes the TRT transfer step more controllable than scooping. The target substrates can be SiO$_2$ or AlO$_x$/PI relevant for this work, but in principle both methods can be applied to arbitrary substrates [461, 466] and layer-by-layer assembly [468, 467].
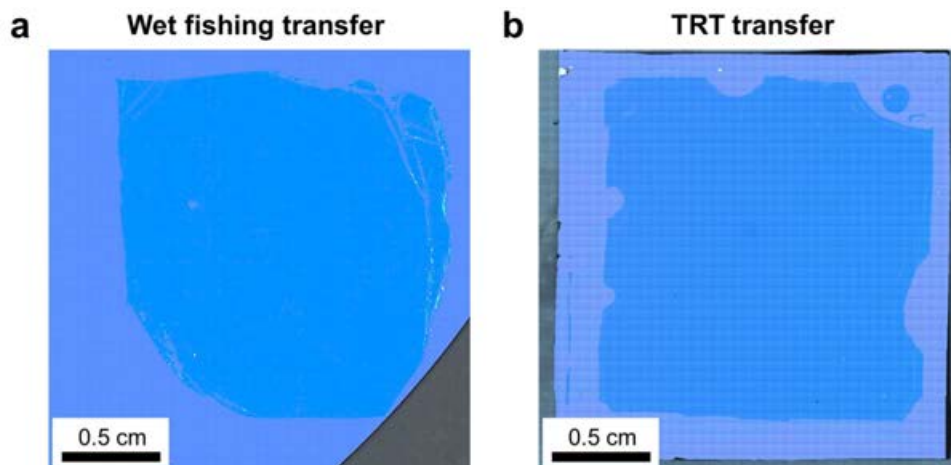
Figure 5.3 Centimeter-scale MoS$_2$ transfer. Microscope images of MoS$_2$ thin films after transfer onto a SiO$_2$ chip via **(a)** wet fishing, and **(b)** TRT method.

The microscopy images in Fig. 5.3 demonstrate that at least $\sim 1.5 \times 1.5\,\mathrm{cm}^2$ sheets can be succesfully transferred, which fulfills the minimum area requirements for devices fabricated in this work, and with the potential to be further extended up to 4" wafer-scale areas [169, 197]. Although both methods allow large-area transfer, the TRT method is expected to have higher scalability and automatization potential by use of semiconductor fabrication compatible pressing and bonding-debonding tools [52, 53, 51]. Regarding the preservation of layer integrity, process-specific challenges were identified. The wet transfer is typically prone to sheet defects caused by wrinkles and bubbles (see appendix Fig. D1) difficult to avoid by manual handling. Moreover, the use of harsh etching chemicals may result in chemical modifications, residues and domain boundary etching [460, 259]. The latter can be avoided by the (semi)dry TRT method; however, mechanical instabilities and tensile strain pose a challenge for damage-free TRT transfer [54]. This was addressed here by process optimization, such as the here used uniaxial pressing step to prevent shear forces. Moreover, it is crucial to avoid particles at the PMMA/MoS$_2$ and TRT/PMMA interfaces to guarantee seamless layer lamination because particle inclusions cause stress concentration and non-adhered TRT zones (see appendix, Fig. D3)). Therefore, the process was moved to a cleanroom environment to minimize particle load, which may be further improved by stacking in a controlled atmosphere [52] or vacuum [467] for improved interface control. Lastly, due to the use of sacrificial polymer support layers, minimization of polymer residues is essential to preserve layer properties, which will be addressed in the next section.

Table 5.1 Qualitative comparison of transfer methods.

Criterium	Wet fishing transfer	(Semi-)dry TRT transfer
Applicability	+ Any water-compatible target substrate + Layer-by-layer (hetero)assembly [468] − Fishing complicates precise placement	− Flatness pick-up and target substrate critical + Layer-by-layer (hetero) assembly [467] + Deterministic placement onto target
Scalability/ reproducibility	+ cm-scale to wafer-scale [468, 169, 52] − Variations due to manual scooping − More difficult to automatize	+ cm-scale to wafer-scale [197] + Automatable roll-to-roll/plate processes [54, 469] + Manual handling avoidable by wafer (de)bonding approaches and existing fab-compatible tools [466, 197, 51, 53, 52]
Structural/ chemical integrity	− Crumpling, wrinkles, bubbles are common − Potential support layer residues − Typically harsh etchants required − Interface adsorbants, ion/etchant impurities	− Tensile stresses/sheet cracking [54] − Voids in zones of non-adhered TRT − Potential support layer/adhesive residues + Etchant-free, water-assisted or fully dry process [197] + Clean interfaces by controlled atmosphere [52]/vacuum [467]

In conclusion, transfer via wet fishing and semi-dry TRT transfer have been explored, making both methods viable candidates for centimeter-area, research-scale transfer. Nevertheless, the TRT-based method was selected to be further pursued for the fabrication of FET devices because it is believed to be the prospectively more promising approach in terms of transfer precision, reliability and scalability potential [52]. As an outlook, development of automatized transfer processes compatible with high-volume manufacturing apparatus typically used in semiconductor fabrication processes are expected to guide future efforts for large-scale 2D integration. Recently, promising examples include wafer bonding [51, 52] and laser-debonding techniques [16, 53, 46] were established at 300 mm wafer level.

5.1.2 Residue-free removal of polymer support layer

Polymer residues stemming from device fabrication, such as transfer using sacrifical support layers [55, 470] or lithography using photoresists [341, 471], are well-known to degrade the electrical performance of MoS$_2$-FETs. These residues result in unintentional doping and reduced charge carrier mobility of the MoS$_2$ channel [341] and increased contact resistance at source and drain [472, 473]. Therefore, efficient, large-area and damage-free residue removal during fabrication is required to ensure clean interfaces for devices with high yield, high uniformity and high performance [55]. While enhanced electrical performance could be proven by mechanical, tip-based cleaning approaches, these procedures are not practical for wafer batch processing. For the latter purpose, O$_2$-plasma [474, 472] and UVO treatments [475, 473] may provide efficient, scalable cleaning options, but bear the risk of damaging the TMD sheet through chemical modification by oxidation [476]. Furthermore, residue removal by annealing treatments in various atmospheres (vacuum, N$_2$, H$_2$) has been employed [477, 478], but thermal budgets

must be considered to preserve stability of the device and the performance of metal contact interfaces [479, 480]. Wet cleaning techniques are widely used in semiconductor industry providing controllable protocols for specific removal of surface contaminants and residues by tailored chemistry, a concept which requires more attention in 2D material processing. For example, for 2D material transfer, PMMA is usually employed because of its common availability in research laboratories, although several studies have pointed at the issue of excessive PMMA residues remaining on the 2D surface after acetone removal and even after additional thermal annealing steps [478, 481, 55, 470]. Therefore, to minimize polymer residues investigation of alternative, better suitable polymer-solvent pairs are desired for efficient surface cleaning [470].

In this study, various polymers and solvents are assessed to identify promising options for residue-free MoS$_2$ transfer. The assessment is based on AFM analysis of transferred MoS$_2$ layer step edges and surface roughness analysis. Poly(methyl methacrylate) (PMMA A4 950K, MicroChem, USA) and methyl methacrylate [MMA (8.5) MAA EL6 copolymer, MicroChem, USA] are tested, which are widely used as sacrificial transfer support layers, protective masks, and photoresists [482]. PMMA and MMA were applied onto 2L MOCVD MoS$_2$/SiO$_2$ by spin-coating at controlled rotation speed (3000 and 1300 rpm) to obtain films with comparable thickness ($\sim$ 220 nm), followed by hard-baking (180 °C, 30 s). Then, the removal of polymers is examined by using acetone (extra pure, Fisher), Remover PG (Kayaku Advanced Materials, Japan), and TechniStrip NI555 (MicroChemicals GmbH, Germany) for dissolution at 50 °C (1 h), followed by IPA rinse to remove resist-contaminated solvent and to avoid striation. Acetone serves as a standard reference in this study due to its common use, although it is expected not to be an optimal stripper. This is due to the aforementioned, limited residue removal capabilities and its physicochemical properties, such as high vapor pressure and risk of use at high solvent temperatures. Remover PG is a powerful, stripper based on N-methyl-2-pyrrolidone (NMP) [483] for universal removal of a wide range of polymers and photoresists. Its low vapor pressure allows heating up to 80 °C to efficiently dissolve cross-linked photoresists and has previously been used for wet cleaning during MoS$_2$-FET fabrication [55]. Since NMP has been classified as a toxic chemical, alternatives should also be considered [484]. TechniStrip NI555 (MicroChemicals GmbH, Germany) is an acidic-based, non-alkaline stripper for fast and complete dissolution of cross-linked resist films avoiding insoluble resist debris deposition, and was chosen for its relatively low toxicity (NMP-, TMAH-, and hydroxylamine-free composition [485]). Furthermore, vacuum annealing treatment ($\sim$1 × 10^{-8} mbar, 350 °C, 1 h) was tested for additional, post-dissolution residue removal.

In a first experiment illustrated in Fig. 5.4a, 2L MoS$_2$ thin films were transferred by the PMMA-assisted TRT method (section 5.1) from the SiO$_2$/Si growth substrate to another SiO$_2$/Si substrate, PMMA was dissolved by either acetone or Remover PG, and samples were subsequently thermally annealed in vacuum. The comparison of AFM scans performed over the step edges of the transferred bilayer sheets [Fig. 5.4(a-b)] reveals excessive organic residues for the acetone cleaning procedure. Although the residues can be further removed by the annealing step, an excess of remaining residues is evidenced in the topographical AFM image taken in the same sample location. In contrast, a relatively smooth and clean MoS$_2$ (and SiO$_2$) surface is already obtained after the solvent cleaning step with Remover PG. Thanks to this, only a
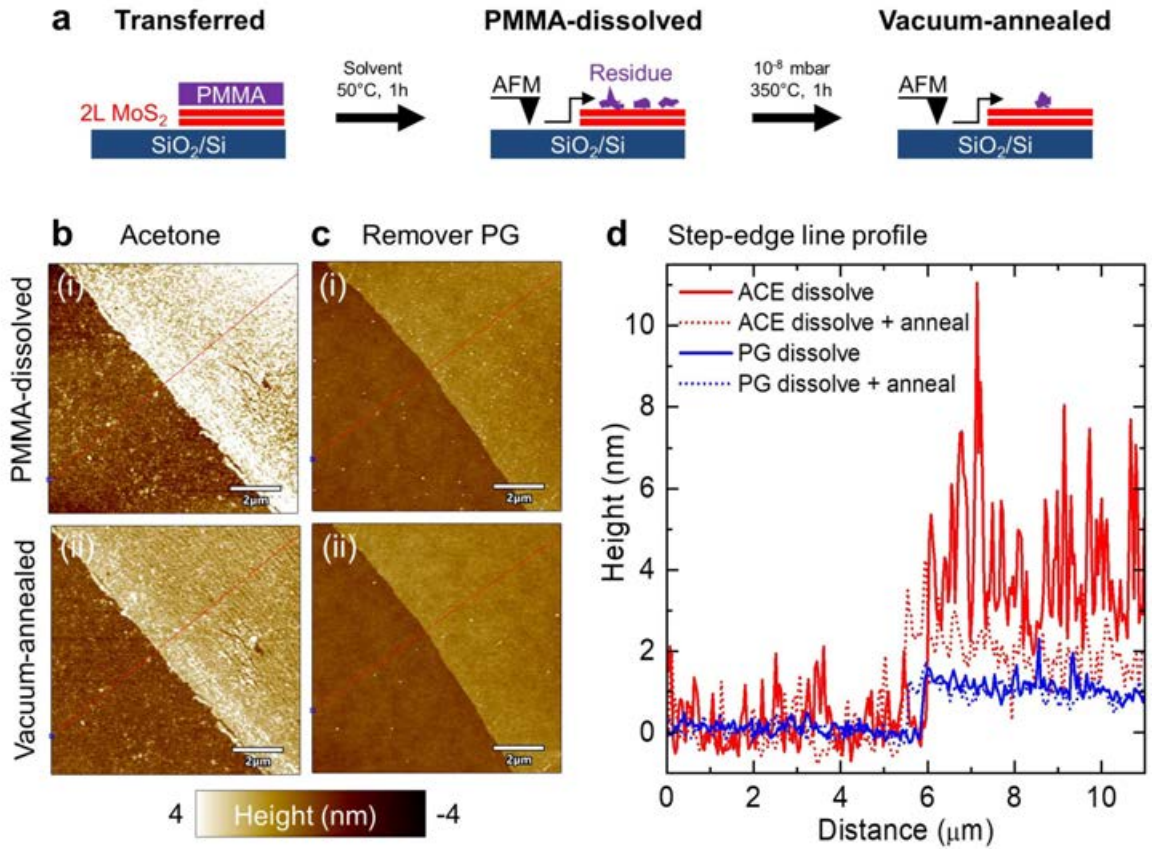
Figure 5.4 MoS$_2$ transfer PMMA residue characterized by step-edge analysis. **(a)** Schematic illustration of the experimental sequence of 2L-MoS$_2$ transferred onto a SiO$_2$ substrate, removal of the PMMA support layer in organic solvent, and subsequent thermal annealing in high vacuum. AFM scans over the step edge are used to detect PMMA residues. **(b-c)** AFM images around the step edge of the transferred MoS$_2$ sheet (i) after dissolving PMMA with either acetone or Remover PG, and (ii) after subsequent 350 °C vacuum annealing. AFM images were plane-fitted by setting the averaged SiO$_2$ substrate level as zero plane. **(d)** Height profiles extracted from the red lines marked in (b-c).

slight further reduction of surface residues (disappearing white particles) is observed in the topographical image after the annealing step. The superior PMMA-dissolution capability of Remover PG compared to acetone and the thermal annealing effect is further visualized by the corresponding line profiles across the 2L MoS$_2$ step ($\sim$ 1.4 nm bilayer height), confirming PMMA/Remover PG as the more suitable polymer-solvent pair of the two investigated here.

To further extend the polymer-solvent pair study, additional experiments were carried out by simply coating and removing polymers onto MoS$_2$/SiO$_2$ films while omitting the actual transfer step; the surface roughness was determined from 1×1 μm^2 AFM scans to quantify the residue amount (Fig. 5.5a). Figure 5.5b shows the AFM images with references for SiO$_2$ and as-grown MoS$_2$/SiO$_2$ for different combinations of MMA- and PMMA-coated surfaces after solvent cleaning with acetone, Remover PG or NI555, and subsequent vacuum annealing. As a general trend, the MMA films show higher density of residue particles and surface roughness compared to the PMMA film. Furthermore, for the series of NI555, acetone, and Remover PG, the density and size of remaining residue particles decreases monotonically after the dissolution step. These trends are quantitatively shown in the RMS roughness plot as function of the process step (Fig. 5.5). The graph displays a systematic reduction of RMS roughness from the dissolving to the annealing step, except for the case of PMMA/Remover PG, which exhibits a virtually unchanged roughness of around $\sim$0.36 nm due to the efficient dissolution step, only slightly above the measured reference value of as-grown MoS$_2$. The RMS roughness level of as-grown MoS$_2$ is not fully recovered; however, from topographical roughness data alone, and considering typically achievable AFM height resolution in the range of $0.05 - 0.1$ nm [486, 487], it is difficult to judge about the complete residue removal after Remover PG dissolution and annealing. Further surface metrology may involve chemical and spatial analysis of possibly remaining residues, such as by XPS [478] and secondary ion mass spectroscopy [488]. Also Raman and PL spectroscopy may indirectly probe changes in residue-induced doping. Overall, PMMA/Remover PG results in the lowest RMS values and can be identified as the most promising of all tested polymer-solvent pairs. Three additional MoS$_2$ samples were independently coated and cleaned, and RMS values were extracted and averaged from three randomly chosen regions of the 1×1 cm^2-sized samples after each process step (Fig. 5.5d; respective AFM images not displayed). The previously shown trends are confirmed, which attests repeatability and homogeneity of the PMMA/Remover PG cleaning protocol.

In summary, by comparing various polymer-solvents pairs, PMMA/Remover PG was identified as the most promising combination for MoS$_2$ transfer with minimized
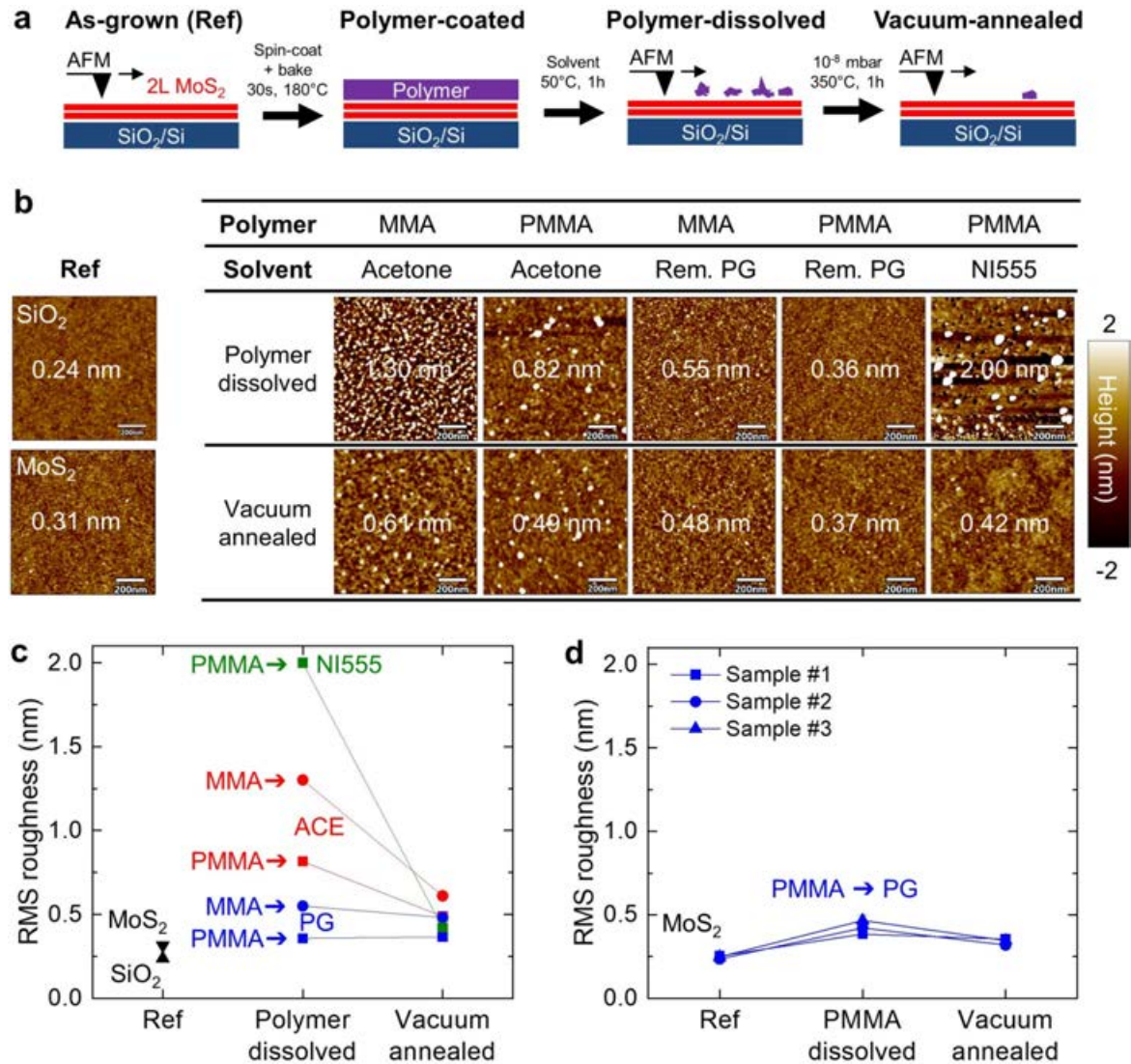
Figure 5.5 Polymer-solvent pair residue study. **(a)** Schematic illustration of the experimental sequence of measuring the AFM surface roughness of the as-grown MoS$_2$ starting surface, after polymer-coating and -dissolving (without layer transfer), and after vacuum annealing. **(b)** AFM images of SiO$_2$ and 2L MoS$_2$ reference surfaces and after polymer-dissolving and vacuum annealing for different polymer-solvent pairs. RMS roughness values are given in the center of each image. **(c)** Evolution of surface roughness for the different sample conditions extracted from the AFM images in (b). **(d)** Evolution and reproducibility of the MoS$_2$ surface roughness of the as-grown reference surface, after polymer-dissolving, and annealing for the PMMA-PG polymer-solvent pair measured on three independent samples. Each RMS data point was averaged from three $1 \times 1\,\mu m^2$ AFM images from randomly measured spots on $1 \times 1\,cm^2$-sized samples. Standard deviations are given as error bars.

organic residues based on morphological AFM analyses, highlighting the importance of surface metrology for monitoring and optimizing interface cleanliness. The results have shown that wet chemical cleaning by tailored selection of the solvent system allows a simple yet effective way to reduce residues during semiconductor-compatible device fabrication. Furthermore, it could be shown that thermal annealing may be helpful for further residue removal after solvent cleaning. In this context, it is remarked that appropriate cleaning methods are of general importance not only for the transfer step, but should be optimized in other fabrication steps directly involving the MoS$_2$ interfaces, such as surface preparation prior transfer and contact photolithography on top of MoS$_2$. So far, the direct impact of the optimized polymer-solvent system on electrical FET device performance remains to be demonstrated; however, literature studies suggest that improvements in FET mobility by a factor of two to three can be expected by optimized PMMA-removal compared to a standard acetone protocol [55]. As a final remark, it is mentioned that Remover PG as a NMP-based solvent is classified as toxic and teratogenic, and its handling requires appropriate safety precautions and disposal measures [489]. Safer solvent substitutes with similar stripping performance as NMP, such as dimethyl sulfoxide (DMSO), may be considered for future studies [484].

5.2 Dielectric integration and encapsulation

Dielectric integration and passivation are essential to transistor technology. While the gate dielectric is an integral building block of transistors, the passivation ensures hermetic encapsulation from the ambient and reliable device functionality. This is essential due to the high sensitivity of 2D transistor channels to adsorbates and environmental impurities [490, 491, 63]. Frequently, high-κ oxides (e.g. Al$_2$O$_3$, HfO$_2$) are chosen for the dielectric due to their high capacitance for efficient, low-voltage switching, their low gate leakage and because of the availability of established fabrication processes for wafer-scale, conformal dielectric integration, such as atomic layer deposition (ALD). Optimized AlO$_x$ ALD integration has enabled MoS$_2$-FETs with hysteresis-improved switching behaviour [63, 58, 492], reduced interface traps and steep subthreshold slopes [493]. Furthermore, the performance of MoS$_2$ channels can be enhanced by the AlO$_x$ n-doping [493] and screening effect [494] due to the high dielectric mismatch of MoS$_2$ with the oxide environment, which can effectively dampen Coulomb scattering of charged impurities at the interface. This allowed the scaled integration of AlO$_x$-sandwiched MOCVD-MoS$_2$-FETs with mobilities of $\sim 17\,\mathrm{cm^2\,V^{-1}\,s^{-1}}$ [41].

However, ALD oxide encapsulation of 2D materials is challenging due to the fact that the inert, dangling-bond-free 2D basal planes do not provide the necessary nucleation sites for conformal ALD [495, 496], and may result in pin-hole formation and unreliable oxide quality. It has been tried to circumvent this issue by modifying the ALD process towards shorter inert gas purges deviating from ideal ALD behaviour, aiming at physisorbed precursor surface species as nucleation sites for subsequent ALD cycles. However, such process adaptation results in H and C impurities and higher oxide leakage [496]. Furthermore, MoS_2 surface pre-treatment by ultra-violet ozone (UVO) prior to ALD [497, 498], utilization of ozone instead of H_2O as oxidant precursor [499], or plasma-enhanced ALD using low-energy O_2-remote plasma [500] have provided routes for improved nucleation and sub-$10\,nm$, pinhole-free encapsulation; yet, these strategies require careful optimization because of concerns of damaging the TMD sheet through oxidation [476]. Seeding approaches using a buffer layer prior ALD have also been pursued, such as non-covalent organic seed molecules [501], SiO_2 [502] or AlO_x [503, 493] seed layers. The latter AlO_x seed layer can be deposited by e-beam evaporation of a nm-thin Al layer that immediately oxidizes upon air exposure to form sub-stoichiometric AlO_x [493], which is expected not to react with or damage the underlying MoS_2 layer [480]. This integration procedure has led to stable *n*-doping and excellent FET transfer characteristics [493]. Nevertheless, such a buffer layer adds complexity to the dielectric stack and bears the risk of introducing trap states at the newly formed interfaces, which can result in poor on/off-current ratios and subthreshold swings [493]. Therefore, good understanding of the impact of AlO_x capping on the (opto)electronic properties of the MoS_2 film is required. The following section will describe the technological implementation of the seeded AlO_x encapsulation route monitored by morphological (AFM, TEM) and spectroscopic analyses (Raman, PL, XPS and valence band analysis).

5.2.1 AlO$_x$ oxide encapsulation

This section will describe the realization of thickness-controlled AlO_x seed layer deposition, followed by smooth ALD encapsulation of MoS_2 thin films, including morphological characterization by AFM and cross-sectional TEM. To provide a simple testing platform, the AlO_x capping is carried out on as-grown MOCVD MoS_2 films on SiO_2/Si chips to avoid complex device structures; this strategy allows detailed Raman, PL and XPS spectroscopic analyses of the AlO_x/MoS_2 interface.
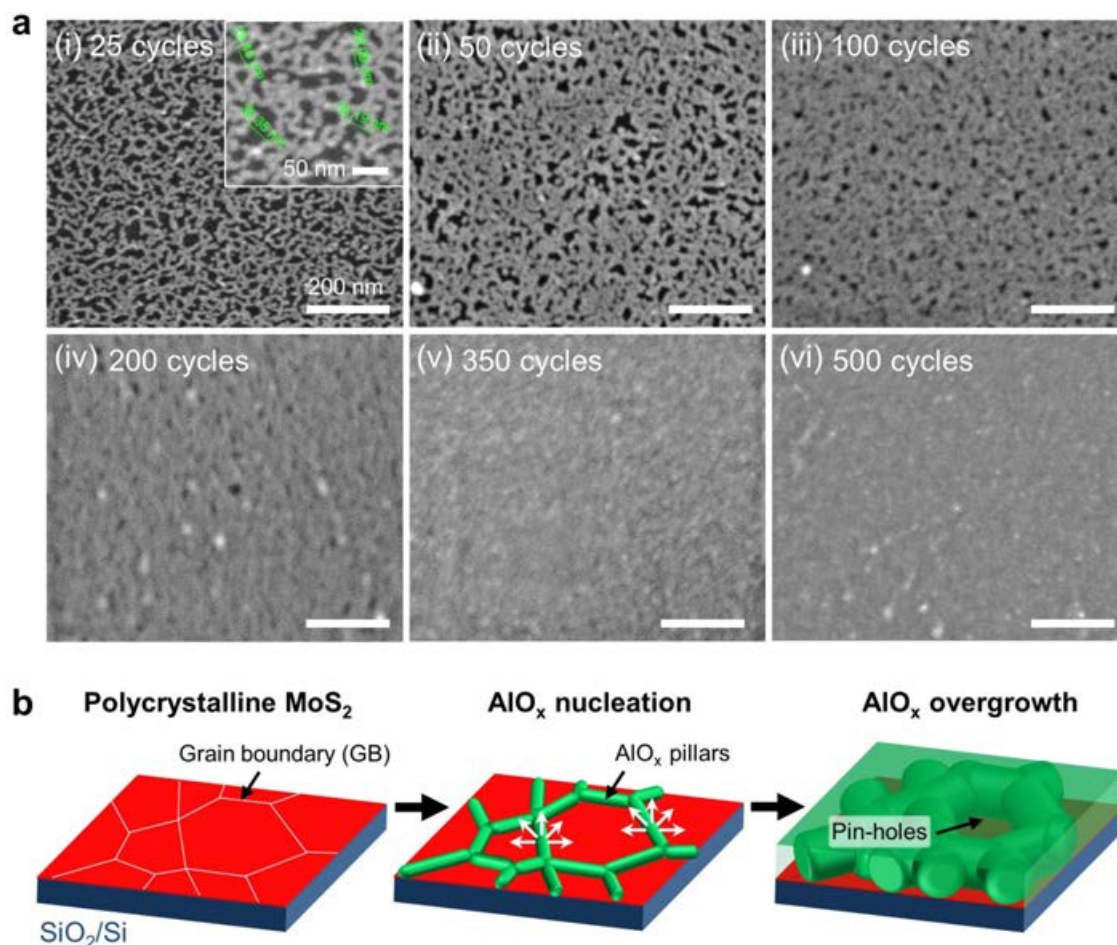
Figure 5.6 Direct ALD of AlO$_x$ on polycrystalline MoS$_2$. **[(a)(i-vi)]** SEM images for 25, 50, 100, 200, 350, and 500 ALD cycles. The regions of light contrast are AlO$_x$, whereas the dark regions are uncovered MoS$_2$ (pinholes in the AlO$_x$ film). **(b)** Schematic illustration of ALD process on polycrystalline MoS$_2$ starting surface on which AlO$_2$ nano-pillars nucleate at the MoS$_2$ grain boundaries, and laterally grow over MoS$_2$ until formation of a thin film. Due to this anisotropic overgrowth the AlO$_x$ layer is expected to be inhomogeneous and prone to pinholes.

5.2.1.1 Direct ALD onto polycrystalline MoS$_2$ film

Serving as reference and to highlight the challenge of ALD encapsulation of 2D materials, AlO$_x$ layers were grown *directly* by a standard TMA/H$_2$O ALD process onto polycrystalline MOCVD MoS$_2$ thin films with grain size ~ 30 nm. Figure 5.6a displays a sequence of SEM images, following increasing ALD cycle numbers, showing the evolution of deposited AlO$_x$ (light gray contrast) on the MoS$_2$ film (black contrast). The images suggest that the AlO$_x$ nucleation is inhibited on the inert MoS$_2$ basal

planes and occurs predominantly at the MoS$_2$ grain boundary defects by decorating and visualizing the grain structure of the underlying MoS$_2$ film. With increasing ALD cycle number, these AlO$_x$ seeds form a network of 3D-nucleated, elongated pillars along the grain boundaries, consistent with literature [369]. Eventually, the lateral overgrowth forms a coalesced oxide layer, as illustrated in the model in Fig. 5.6b. However, after extended cycles, at a growth-per-cycle of $\sim$1.3 Å/cycle averaged from profilometry thickness measurements, of 350 ($\sim$43 nm) and 500 ($\sim$70 nm) cycles, the oxide layer still shows signs of uncovered MoS$_2$ areas based on SEM inspection. For the case of larger grain size MoS$_2$ thin films, therefore, reduced AlO$_x$ grain boundary nucleation density, an even higher minimal oxide thickness can be expected for complete overgrowth. Therefore, this non-conformal nucleation behaviour renders direct ALD unsuitable for pinhole-free oxide films of typical gate dielectric thicknesses $\lesssim$50 nm.

5.2.1.2 Seed layer approach

As direct ALD of AlO$_x$ on MoS$_2$ does not yield satisfying results, a seed layer strategy was adopted prior ALD, as shown in Fig. 5.7a. The seeding consisted in physical vapor deposition (PVD) of three subsequent 1 nm Al layers by e-beam evaporation at deposition rates of 0.2 to 0.3 Å s^{-1} in high vacuum at $<5 \times 10^{-7}$ Torr, monitored by a quartz crystal balance. Between subsequent seeding steps, the Al layers are left in ambient air for $\sim$1 h to oxidize [504, 493, 505]. Although previous reports have shown that 1 nm may be sufficient for uniform seeding prior ALD in planar device structures [503, 493, 506], in a conservative approach and anticipating the fabrication of more complex devices (section 5.4), deposition of three 1 nm layers with 120° wafer rotation between consecutive steps was chosen. This accounts for potential non-planarities or shadowing effects, such as in interdigitated contact regions, that might arise due to the directional nature of the PVD process. Besides, the stepwise deposition allows to study the evolution of (opto)electronic MoS$_2$ properties as function of oxide layer thickness.
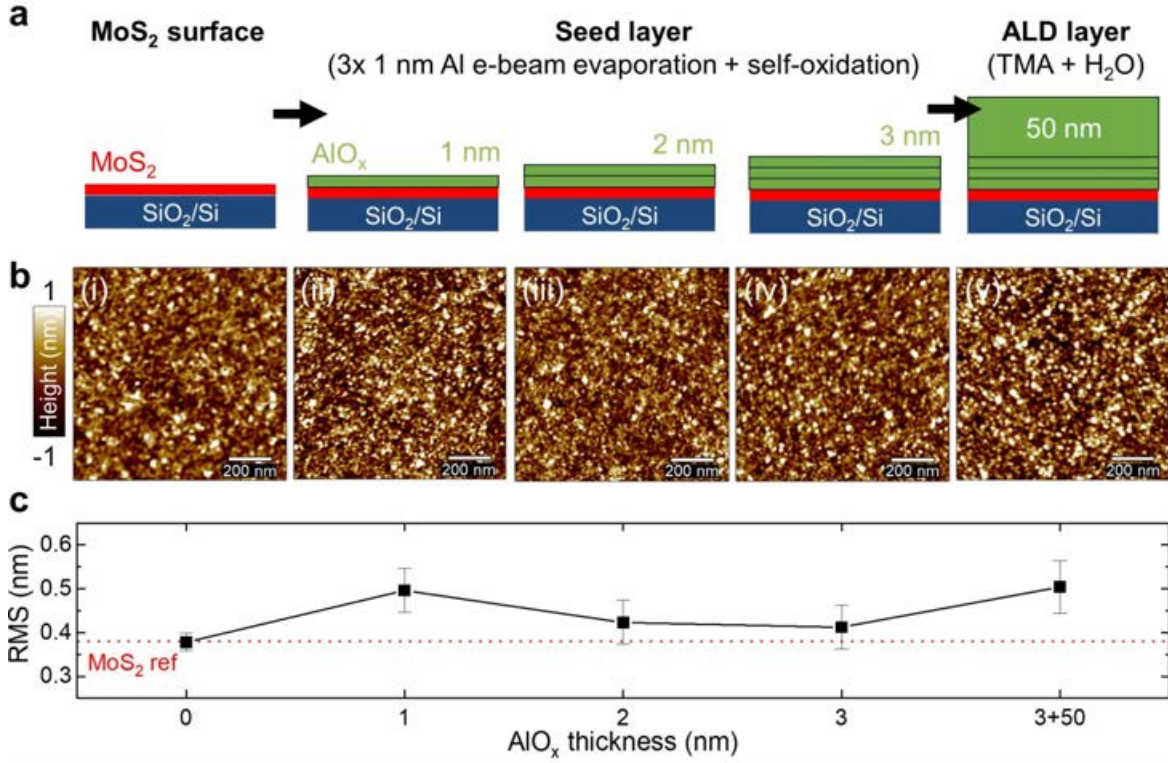
Figure 5.7 MoS$_2$ encapsulation by AlO$_x$ seed layer and ALD. **(a)** Schematic illustration of exposed MoS$_2$ starting surface, AlO$_x$ seed layer deposition of 3×1 nm Al by e-beam evaporation and subsequent self-oxidation in ambient atmosphere, and ALD encapsulation. **[(b)(i-v)]** AFM images of the surfaces after each step, and **(c)** corresponding RMS roughness after each deposition step.

Topographical AFM analysis after each seed layer step and final ALD of 50 nm AlO$_x$ shows the conformal and smooth oxide encapsulation [Fig. 5.7b], where the RMS roughness $\lesssim 0.5$ nm remains only marginally above the MoS$_2$ reference value (Fig. 5.7c). To verify seed layer thickness control, AFM scans were performed over the step edge of AlO$_x$/2L MoS$_2$ layer stacks after nominally 1, 2, and 3 nm AlO$_x$ deposition and self-oxidation, as shown in Fig. 5.8[a-c(i)]. From the corresponding line profile scans in Fig. 5.8[a-c(ii)], and assuming a MoS$_2$ bilayer thickness of 1.4 nm, subsequent deposition of $\sim 0.90 + 1.15 + 1.15$nm result in a total overlayer thickness of ~ 3.2 nm. The 7 % deviation from the target value can be explained by thickness variations due to the step edge creation, the manual shutter operation during PVD, and layer thickness changes upon oxidation. Cross-sectional TEM analysis of the nominal 3 nm AlO$_x$ seed layer in Fig. 5.8e shows an averaged thickness of 2.4 ± 0.3 extracted from 20 measurement points, which is lower than the thickness value extracted by AFM. The deviation can be explained by the FIB sample preparation and/or spatial thickness variations over

the different samples. It is remarkable, however, that the metal evaporation/oxidation route yields such smooth, conformal capping layer because previous work discussed non-continuous island formation for deposition of thin metal layers on the $MoS_2(0001)$ surface [507]. The EDX line profile scan confirms the expected elemental composition of the layer stack (Fig. 5.8e), including Si from SiO_2 substrate, Mo from MoS_2, and Al from
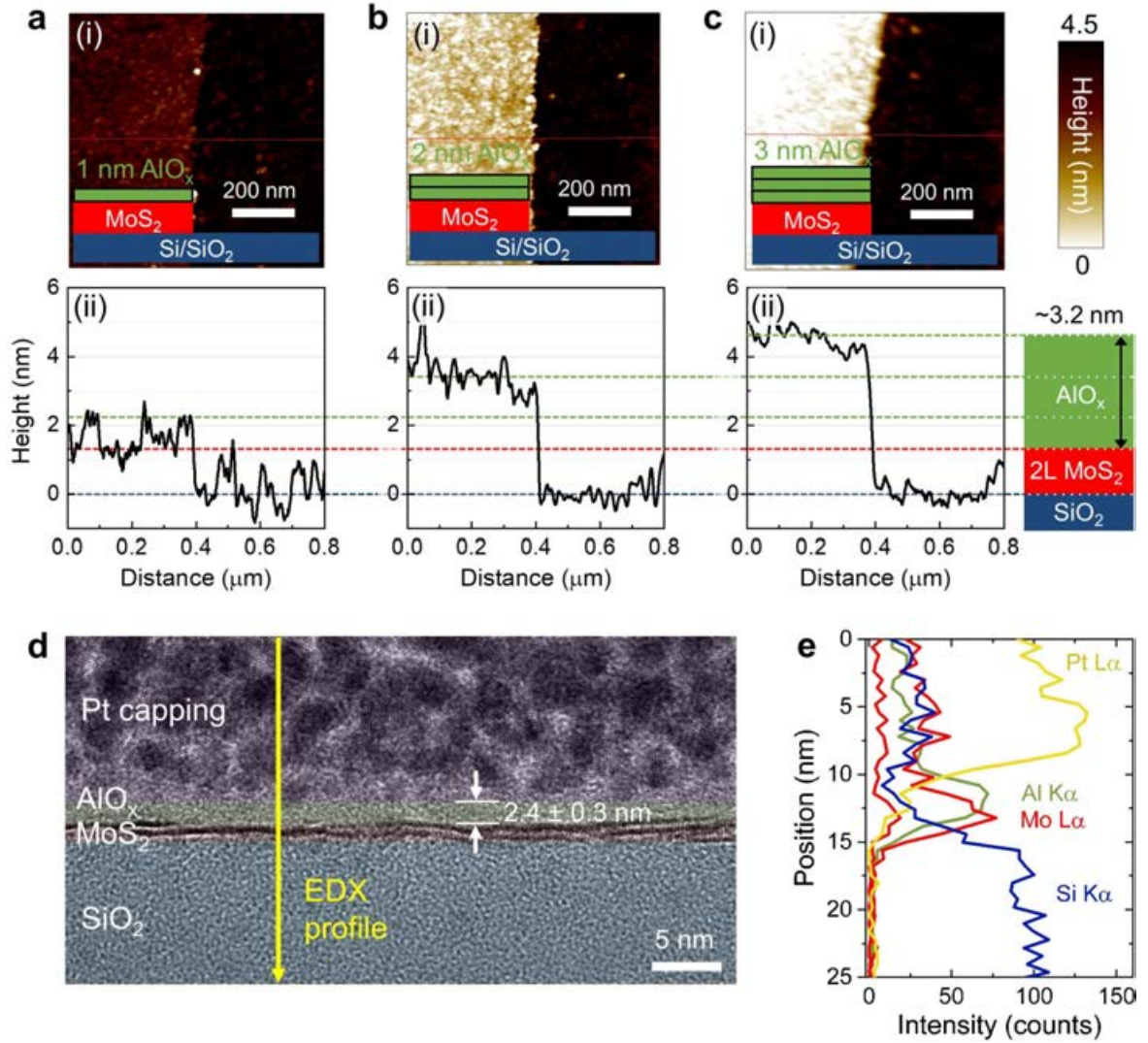
Figure 5.8 AlO_x seed layer thickness analysis. **(a-c)** (i) AFM images of three subsequently deposited 1 nm seed layers grown onto MoS_2/SiO_2. An intentional scratch was made to measure the layer thickness over the step-edge, and (ii) corresponding height profiles are marked in the AFM images in (a-c). Schematic illustrations show the AlO_x(green)/MoS_2(red)/SiO_2(blue) stacks for different AlO_x thicknesses. **(d)** False-colored, cross-sectional TEM image of a nominal 3×1 nm AlO_x seed layer on the 2L MoS_2 thin film. A Pt capping layer was deposited for FIB lamella preparation. **(d)** EDX line profile scan confirming the chemical composition across the $Pt/AlO_x/MoS_2/SiO_2$ interface.

AlO$_x$. The Pt capping layer used for sample preparation contains C-contamination due to the deposition from metal-organic precursors, but the limited spatial resolution and low signal-to-noise ratio do not allow reliable determination of potential C contamination from the MOCVD MoS$_2$ film at the AlO$_x$/MoS$_2$ interface. The morphological analysis demonstrates the successful implementation of a thickness-controlled AlO$_x$ seeding process for subsequent, conformal ALD encapsulation.

5.2.2 Spectroscopic analysis of AlO$_x$-encapsulated MoS$_2$

The statement "*the interface is the device*"[508] is especially true for 2D semiconductor devices; thus, interface quality and interactions of the 2D channel region with the surrounding dielectric are crucial to determine FET device performance. For example, the AlO$_x$ encapsulation of MoS$_2$ can result in at least two distinct charge transfer mechanisms depending on both the energetic position and spatial position of defects and fixed charges at or near the AlO$_x$/MoS$_2$ interface [493]: First, *trapping* of charges can occur due to "interface traps" *at* the interface, or due to "border traps" *near* the interface within ∼3 nm proximity [509, 510, 286] via tunneling [511]. Both these interface and border trap states are energetically situated within the MoS$_2$ bandgap and can eventually lower transistor performance (e.g. by altering mobility μ_{FE} and subthreshold swing SS). Second, *modulation doping* by electron (hole) transfer from donor (acceptor) states not overlapping with the MoS$_2$ bandgap can induce *n*-type (*p*-type) charge carriers from above (below) the conduction (valence) band. Theoretical and experimental studies have shown that MoS$_2$ encapsulation with O-deficient, substoichiometric oxide induces modulation-like *n*-doping of MoS$_2$ through donor states from fixed charges in the oxide [512]. Ideally, such modulation doping may exploit the electrostatic dipole formation for threshold voltage tuning [513] while not degrading μ_{FE} and SS, and allowing stable and improved device performance, if at the same time detrimental interface trapping can be avoided [493, 66]. Therefore, understanding of possible trapping and doping effects at and near the oxide/2D channel interface is important.

For this purpose electrical and/or spectroscopic characterization can be performed. $I - V$ transfer curves of the final transistor devices can provide key figures of merit (I_{ON}/I_{OFF}, μ_{FE}, SS, V_T, D_{IT}) linked to interface defects; however, their discrimination, e.g. between interface and border traps is more difficult [63, 61], and can be more efficiently evaluated by $C - V$ characteristics of capacitors [514, 471, 515]. This electrical characterization, though, requires manufacturing device structures. On the other hand, analysis by spectroscopic methods, such as Raman, PL and XPS, allow for

quick and non-destructive interface monitoring of as-grown layer stacks without the effort of complete device integration. Raman spectroscopy can detect doping through electron-phonon interaction affecting peak positions and widths [516, 512, 517]; PL spectroscopy can detect interface traps by intensity quench through non-radiative recombination [516, 517] and doping by modulation of the trion-to-exciton ratio [357, 355, 353]. XPS allows to study doping and band alignment by valence band shifts relative to the Fermi level [518]. In the following, these spectroscopic techniques are used to investigate oxide thickness dependent trapping and doping [504] at and near the AlO_x/MoS_2 interface during the seed layer capping steps. The findings will support the later discussion of AlO_x-integrated MoS_2 transistor device performance.

Figure 5.9a(i) shows the in-plane (E_{2g}^1) and out-of-plane A_{1g} MoS_2 Raman modes of as-grown MoS_2 and after deposition of 1, 2, and 3 nm AlO_x, as illustrated by the schematics. Peak positions and width (FWHM) were extracted as function of AlO_x thickness [Fig. 5.9b(ii)]. With increasing thickness a slight, gradual blueshift (stiffening) of the A_{1g}-mode and separation from the rather unaltered E_{2g}^1-mode position can be observed, and both Raman modes show an overall FWHM increase. Before evaluating this result, it has to be mentioned that modulation of the Raman-active MoS_2 modes might be influenced by various factors, such as strain, defects, doping, and dielectric screening [519, 520, 480]. Due to possibly superimposed and/or compensating effects one must be cautious with interpretation of the origin of oxide capping induced changes [521]. Although it was commonly claimed from indirect measurements that encapsulation may induce strain on the underlying MoS_2 layer [521, 516, 500], Schauble et al. excluded the strain argument by direct MoS_2 lattice constant GIXRD measurements after e-beam deposition (and oxidation) of several metal thin films onto MoS_2 [480]. Therefore, modulation of the Raman-active MoS_2 modes is more likely related with doping and/or screening effects. In case of n-doping, and as consequence of electron-phonon interactions, the doping-sensitive A_{1g}-mode has been predicted to redshift and broaden [443] due to phonon mode softening or the vibrational Stark effect [521, 522], whereas the E_{2g}^1-position remains largely unaffected. Considering that a A_{1g}-redshift correlates with increased electron density of $\sim 4.5 \pm 0.5 \times 10^{12}\,cm^{-2}$ electrons per cm^{-1} peak shift [443], n-doping of MoS_2 upon AlO_x-encapsulation has been reported to result in A_{1g}-shifts (electron density increase) of $-1.4\,cm^{-1}$ ($6.3 \times 10^{12}\,cm^{-2}$) [493] and $-1.9\,cm^{-1}$ ($8.55 \times 10^{12}\,cm^{-2}$) [512]. Furthermore, asymmetric Fano line shape of the E_{2g}^1-mode has been reported to indicate n-doping [480, 493].
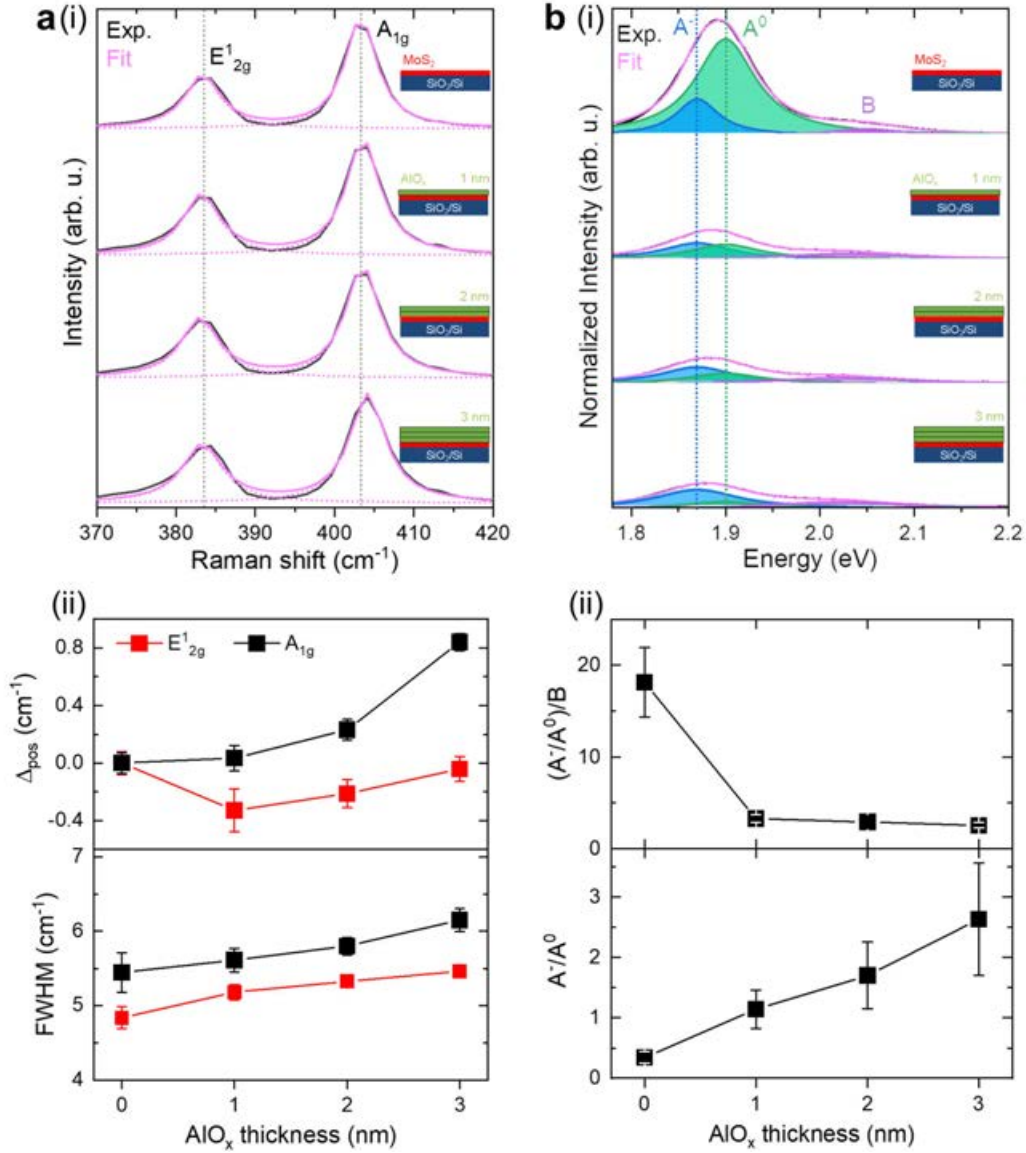
Figure 5.9 Raman and PL study of AlO$_x$-encapsulated MoS$_2$. **(a)**(i) Experimental Raman spectra (black lines) of MoS$_2$-related in-plane (E_{2g}^1) and out-of-plane (A_{1g}) modes fitted by double-Lorentzians (pink lines) for as-grown MoS$_2$ and after seed layer capping with 1, 2, 3 nm AlO$_x$, as illustrated by the schematics; (ii) Analysis of absolute Raman peak position shift Δ_{pos} and FWHM of E_{2g}^1 and A_{1g} modes. **(b)** Experimental PL spectra (black lines) fitted by Gaussians (pink lines) and deconvoluted into trion A^- (blue), neutral exciton A^0 (green), and B exciton (purple) contributions. Spectra are normalized to the B exciton intensity; (ii) Analysis of PL integral ratio $(A^- + A^0)/B$ and trion-to-exciton ratio A^-/A^0. Both Raman and PL data show total average spectra extracted from 30×30 µm^2 maps from 225 measurement points. Error bars are standard deviations. Connection lines are drawn to guide the eye.

Here, while the rather unaffected E_{2g}^1-position, and the increasing FWHM and asymmetric peak shape of the A_{1g}-mode do suggest n-doping with increasing AlO_x thickness, in contrast, the A_{1g}-position remains relatively unaltered yet slighty blueshifting up to $0.7\,\mathrm{cm}^{-1}$ ($3.2 \times 10^{12}\,\mathrm{cm}^{-2}$ electron density decrease) for the $3\,\mathrm{nm}$ sample. Although unaltered MoS_2 Raman positions after oxide encapsulation have been reported, n-doping by a negative threshold voltage shift in FET transfer curves could be observed in these works [506, 516], which highlights the ambiguity of Raman analysis. The results can be explained by an increased interlayer distance and weakened MoS_2-AlO_x coupling. This may be caused by a high density of interfacial impurities, adsorbates and dangling bonds [516, 506], and a more pronounced charge screening effect due to the AlO_x high-κ dielectric environment [523]. The latter results in splitting of A_{1g} and E_{2g}^1 modes by opposite blue- and redshifts, as it is evidenced in Fig. 5.9b(ii). Nonetheless, deriving screening or doping effects from Raman spectra alone remains elusive and requires further evidence from complementary experiments.

The PL analysis in Fig. 5.9b(i) shows the corresponding spectra composed of negative trions A^-, neutral excitons A^0, and B excitons. The as-grown, uncapped MoS_2 shows an intense PL signal of $(A^- + A^0)/B \sim 18$ and a typical trion contribution of $A^-/A^0 \sim 0.3$ because of doping from charged impurities of the SiO_2 substrate [353]. Since the bottom MoS_2/SiO_2 interface is not expected to change upon AlO_x seed layer capping, any alteration of the PL signal can be ascribed to the top-encapsulation effect. After adding the first AlO_x layer a clear PL quench with a six-fold intensity drop to a level of $(A^- + A^0)/B < 3$ is evident, which stays rather constant upon adding consecutive AlO_x layers. This indicates that trap states have formed *at* the AlO_x/MoS_2 interface acting as non-radiative recombination centers during laser illumination [517, 516, 493]. While the intensity drop is abruptly dropping only upon first interface formation, a monotonic increase of the A^-/A^0 with increasing AlO_x thickness can be observed. The A^-/A^0 ratio, an indicator of electron charge density, suggests gradually increasing n-doping, possibly through the increased number of border traps and fixed charges added *near* the AlO_x/MoS_2 interface with consecutive seed layer steps. The mechanism behind this n-doping has been previously explained by hole trapping by using photoconductivity measurements [517], electrostatic doping by fixed, positive oxide charges [524, 516], and/or modulation-like doping of MoS_2 by negative charge transfer from donor states inside the bandgap of O-deficient AlO_x [512]. Therefore, the PL results with AlO_x overlayers suggest that both interface trapping and doping effects are present.
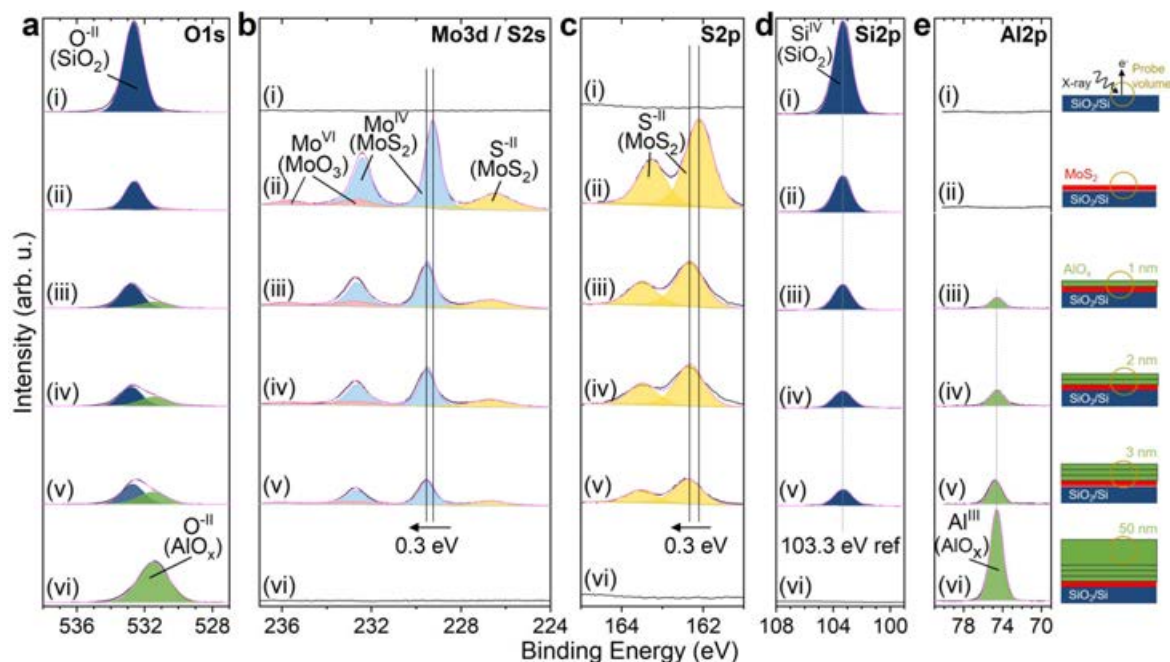
Figure 5.10 XPS study of AlO$_x$-encapsulated MoS$_2$. The following core level spectra are shown: **a** O 1s, **b** Mo 3d / S 2s, **c** S 2p, **d** Si 2p, and **e** Al 2p. The schematics on the right illustrate the analyzed samples: (i) SiO$_2$/Si substrate reference, (ii) MoS$_2$/SiO$_2$ as-grown, after seed layer deposition of (iii) 1 nm AlO$_x$, (iv) 2 nm AlO$_x$, (v) 3 nm AlO$_x$, and after final (vi) 50 nm AlO$_x$ encapsulation. Black lines correspond to the measured spectra, colored areas under singlet/doublets represent fits assigned to the same chemical species, as exemplarily designated in each graph (a-e), and pink lines show the synthetic fitting envelopes of summed peaks. Spectra are calibrated to the SiO$_2$ substrate peak at Si 2p 103.3 eV [276], except sample (vi) where the thick AlO$_x$ layer does not allow to transmit substrate signal and is referenced to Al 2p 74.6 eV found in the seed layer samples. For comparison spectra are plotted with the same intensity scale for each respective core level graph (a-e).

Figure 5.10 presents XPS core level spectra of as-grown MoS$_2$ thin films, after each AlO$_x$ seeding step and after the final ALD encapsulation; the corresponding survey spectra can be found in the appendix (Fig. D6). For extraction of useful depth information, the XPS sampling depth is determined by the inelastic mean free path λ_{IMFP} of photoelectrons that escape from a given material [525]. Considering Al$_2$O$_3$ and the used Kα X-ray energy of 1486.6 eV, a mean free path of $\lambda_{IMFP} \approx 3$ nm [526] and a resulting sampling depth of around $3\lambda_{IMFP} \approx 9$ nm can be estimated. As illustrated by the schematics in Fig. 5.10, it was therefore possible to obtain depth signal from "buried" components of the AlO$_x$/MoS$_2$/SiO$_2$ stacks. These show increasingly attenuated intensities of MoS$_2$- and SiO$_2$-related peaks for increasing AlO$_x$ seed layer thickness, but importantly, energy calibration could be performed on the common Si 2 p substrate reference peak at 103.3 eV (except for the 50 nm-encapsulated sample

for which only the ALD oxide top surface could be probed and which was referenced at the Al 2 p position of seed layer samples at 74.6 eV [527, 277]). The MoS_2 film shows the assigned color-coded Mo 3 d/S 2 s and S 2 p core level features already described in previous XPS analysis (see section 3.2.3). Chemical analysis of the seed layer shows no signs of a peak corresponding to the metallic Al^0 2 p oxidation state that would appear at 2.7 eV [527] below the observed peak of the Al^{III} 2 p oxidation state, although sub-stoichiometric AlO_x cannot be excluded. Stoichiometry quantification of samples with different AlO_x thicknesses from RSF-corrected, relative peak intensity ratios $(O^{-II}$ 1 s):(Al^{III} 2 p) yielded $\sim 1.5 \pm 0.1$ (1 nm), $\sim 1.5 \pm 0.1$ (2 nm), $\sim 1.4 \pm 0.1$ (3 nm), and $\sim 1.4 \pm 0.1$ (3+50 nm), respectively, suggesting that substoichiometric AlO_x might be present within experimental error; however, assuming a 5 %-error best case scenario for a routine XPS measurement, the accurate determination of oxide stoichiometry is difficult without RSF derivation through calibrated standards [528] (the same holds for the often claimed absolute TMD stoichiometries from XPS analysis [381]).

The most remarkable feature of the set of spectra is a 0.3 eV shift of MoS_2-related Mo 3 d and S 2 s and S 2 p core levels *after* AlO_x encapsulation. A shift in XPS may correspond to a chemical shift, suggesting a change in the bonding environment and chemical composition, or may indicate a rigid band shift, suggesting movement of the Fermi level relative to the valence band and core levels. A closer look clarifies that the difference in shifts between Mo 3 d and S 2 p doublets is essentially zero within experimental error, meaning that both doublets shift collectively, while neither in the Al 2 p, Mo 3 d nor S 2 p spectra any new doublets arise that could account for chemical modifications, such as MoS_2 desulfurization or formation of an AlS phase. Therefore, chemical shifts and reaction of Al with S from MoS_2 upon seeding can be excluded, coinciding with the intact MoS_2 sheet seen in cross-sectional TEM and in agreement with previous reports [480, 500]. In view of the negative Gibbs free energy of the exergonic, spontaneous reaction of MoS_2 with Al [529, 507], the observed inertness may be surprising, but agrees well with previous reports that have explained this finding by kinetic limitations and the layered MoS_2 structure [480, 529, 507]. Therefore, the Al seeding does not seem to physically react with or damage MoS_2, and, consequently, the 0.3 eV shift can be interpreted as a Fermi level upshift away from the valence band upon AlO_x capping. This might be related with charge transfer doping, or Fermi level pinning at AlO_x-related midgap defects states [512], which will be further discussed by valence band analysis and a band diagram model.
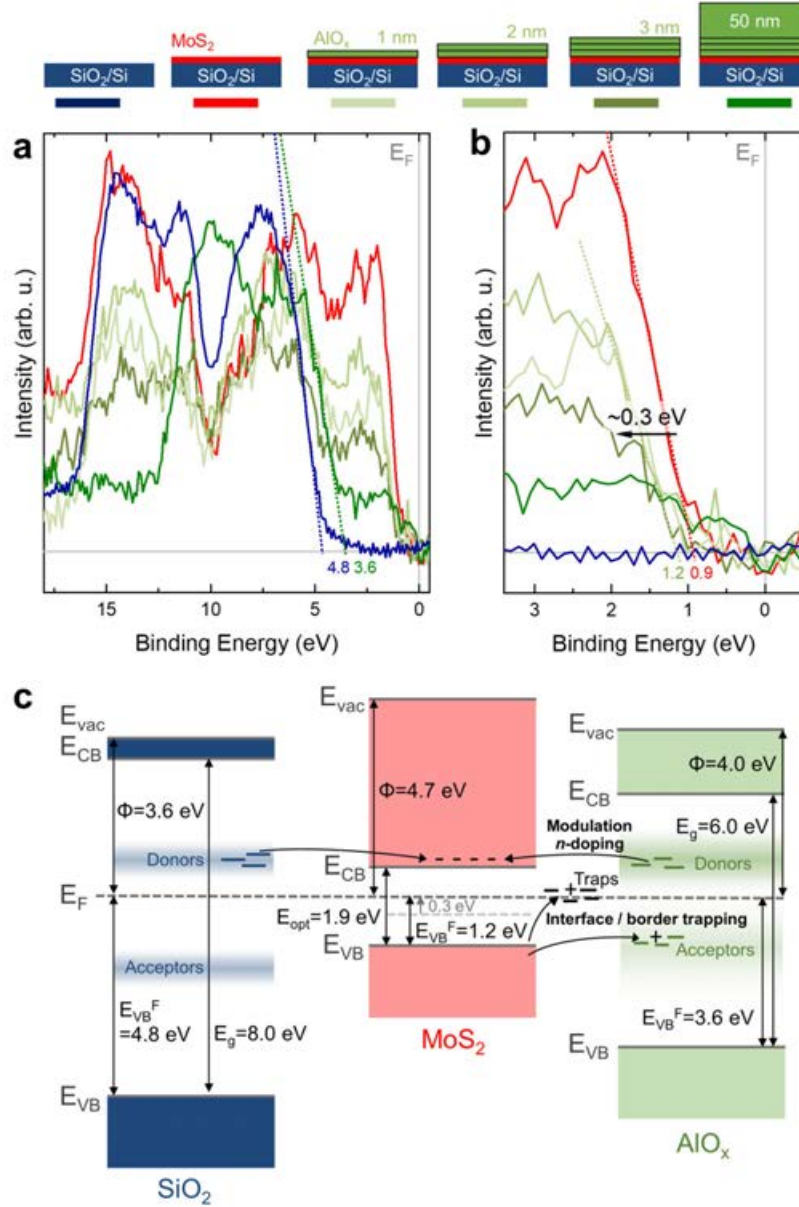
Figure 5.11 Valence band study and interface model of AlO$_x$-encapsulated MoS$_2$/SiO$_2$. Schematics on top serve as legend: SiO$_2$/Si substrate reference (blue), MoS$_2$/SiO$_2$ as-grown (red), after seed layer deposition of 1 nm AlO$_x$, 2 nm AlO$_x$, 3 nm AlO$_x$, and after final 50 nm AlO$_x$ ALD-encapsulation (various green tones). **(a)** Overview valence band spectra. **(b)** Zoom of MoS$_2$ valence band edge region. **(c)** Band model of the AlO$_x$/MoS$_2$/SiO$_2$ interface, including vacuum levels E_{vac}, conduction band minima E_{CB}, valence band maxima E_{VB}, and Fermi level E_F. Bands were constructed from work functions Φ, valence band edge energies E_{VB}^F, the MoS$_2$ optical bandgap E_{opt} extracted by PL/XPS/UPS data in this and previous section 3.3.2.2, and literature values were used for the AlO$_x$ work function [530], and SiO$_2$ [361] and AlO$_x$ [58] bandgaps, including prominent in-gap defect bands (blurred donor and acceptor regions) of SiO$_2$ [61] and AlO$_x$ [531]. Electron (-) transfer from donor states of O-vacancies defects [531, 512] is proposed to explain n-type modulation doping and Fermi-level upshift. Additionally, interface trap and border trap states energetically located within the MoS$_2$ bandgap and physically located *at* and *near* the AlO$_x$/MoS$_2$ interface result in charge trapping, such as by hole (+) capture in acceptor states [517].

The valence band regions of the different samples were analyzed by XPS, including a SiO$_2$ substrate reference, as illustrated in Fig. 5.11. Overview spectra display the (superimposed) valence band structures of SiO$_2$, MoS$_2$, and AlO$_x$, whose spectral hybridization features have been described elsewhere [532, 518, 533, 518, 534, 535]. The energies of valence band maxima E_{VB}^F with regard to the Fermi level are extracted at the intersection points of the valence edge tangents with the baseline. The valence band maxima of SiO$_2$ (4.8±0.1 eV) [365, 361] and the amorphous AlO$_x$ ALD layer (3.6±0.1 eV) [534, 536] are in agreement with literature values. Figure 5.11b shows a magnified view of the MoS$_2$ valence edge region. While the increasing thickness of the AlO$_x$ overlayer attenuates the MoS$_2$-related valence features, the ∼0.3 eV upshift of the 1, 2, and 3 nm AlO$_x$-capped MoS$_2$ (1.2±0.1 eV) with regard to the uncapped MoS$_2$ (0.9±0.1 eV) is evident. Interestingly, all AlO$_x$-capped films show the same upshift regardless of oxide thickness, consistent with the previously described XPS core level shifts (Fig. 5.10); no gradual thickness-dependent effect can be observed, as it was the case for the trion-to-exciton ratio in previous PL studies (Fig. 5.9b). Although there may be an overlaid charge transfer doping effect, this suggests the Fermi-level position to be pinned at midgap interface traps after AlO$_x$ capping. The ALD-encapsulated 3 + 50 nm AlO$_x$ sample shows an extension of states beyond the valence band edge up to the Fermi level, which must be associated to AlO$_x$-related features because of the fully attenuated MoS$_2$ signal at this oxide thickness. According to previous reports, and analyzed by extensive X-ray photoemission and absorption, electron energy loss spectroscopy, and electrical CV-measurements, these defect states typical for ALD layers can be attributed to charged oxygen-vacancies [535, 531] and intrinsic localized excitonic, polaronic, and charge transfer band states [534] reaching into the AlO$_x$ bandgap above the valence band maximum E_{VB}. Such states are also expected below the conduction band minimum E_{CB}, but they cannot be accessed here by XPS). Similar defect states might be present for the AlO$_x$ seed layers affecting the AlO$_x$/MoS$_2$ interface, but the overlapped MoS$_2$ states and low signal intensity do not allow more refined analysis of the valence band data of Fig. 5.11.

A schematic band diagram is drawn in Fig. 5.11c summarizing the findings of the PL/XPS analysis and previous XPS/UPS data from section 3.3.2.2, and adding bandgaps and oxide defect levels from literature. Bands are drawn before vacuum level alignment and band bending due to the possibility of Fermi level pinning and possible dipole heterostructure effects beyond the Anderson rule [537]. The SiO$_2$ band is added for completeness, contributing to substrate doping effects through oxide defect bands and charged impurities [353]; however, the straddling gap MoS$_2$/AlO$_x$ heterostructure

band alignment (type I) is the main focus of this analysis. As qualitatively discussed and supported by spectroscopic analysis (Raman, PL, XPS), the AlO$_x$/MoS$_2$ interface is affected by traps physically located *at* the interface (adsorbates, AlO$_x$ termination, dangling bonds) and border traps *near* the interface within the AlO$_x$ capping layer (fixed charges, O-vacancies). The gradual trion-to-exciton PL ratio increase with oxide thickness suggested that oxide donor states by electron transfer from O-vacancies energetically located above the MoS$_2$ conduction band and oxide may contribute to modulation-like *n*-doping [58, 512, 531]. However, the relatively unaltered Raman A_{1g}-mode shifting behaviour suggested that interface traps and adsorbates might dominate the current interface characteristics. This is also suggested by the strong PL quenching via non-radiative transitions and oxide-thickness independent, constant valence band shift pointing at Fermi level pinning at traps of the defective AlO$_x$/MoS$_2$ interface. These interface traps energetically located within the MoS$_2$ midgap [517] are likely to degrade MoS$_2$ transistor channel performance. Further quantification by determining the interface trap density D_{IT} will be achieved by electrical characterization of field-effect transistors in the following section. While oxide donor states by electron transfer from O-vacancies energetically located above the MoS$_2$ conduction band and oxide may contribute to modulation-like *n*-doping [58, 512, 531], as suggested by the gradual trion-to-exciton PL ratio increase with oxide thickness, interface traps and adsorbates might dominate the current interface characteristics, as suggested by the relatively unaltered Raman A_{1g}-mode shifting behaviour, strong PL quenching via non-radiative transitions and oxide-thickness independent, constant valence band shift pointing at Fermi level pinning at traps and defects at the AlO$_x$/MoS$_2$ interface.

In summary, working hypotheses for the involved doping and trapping mechanisms of the AlO$_x$/MoS$_2$ heterointerface model were established by employing non-destructive spectroscopic analysis accompanying the development of an oxide seeding and ALD-route for MoS$_2$ channel encapsulation. This allowed monitoring interface quality and the impact of oxide encapsulation on the (opto)electronic MoS$_2$ properties, suggesting that the current technology is dominated by high trap densities in the MoS$_2$ channel and at the AlO$_x$ dielectric interface. More in-depth X-ray photoemission/absorption [534], internal electron photoemission [58], photo de-population [531] specific trap spectroscopies [538], and deep level transient spectroscopy [539] could help to further clarify defect types, their exact energetic location within the insulator bandgap and their role in charge transfer with the MoS$_2$ channel. Prospectively, aiming to mitigate ambient exposure effects and adsorbate inclusion, and reducing interface trap densities to enable the full potential of previously reported AlO$_x$ *n*-doping of MoS$_2$ [493], it is proposed to

investigate thermal annealing before [540] and after seeding and ALD encapsulation steps [493, 534] monitored by spectroscopic studies. Furthermore, the insertion of dangling-bond free interlayers, such as hBN [516], before AlO$_x$ capping may reduce interface trap states by improved 2D-2D van der Waals channel interfaces. Further improvement in interface quality is essential for the development of high-performance 2D semiconductor devices.

5.3 MoS$_2$ transistor technology

Building on the previously developed transfer and encapsulation processes, this section gives an overview of device fabrication and MoS$_2$ technology of several generations of FET-architectures, starting from simple-to-build, liquid-gated devices over more complex, encapsulated AlO$_x$-solid-back-gated devices on rigid substrates, and towards the final goal of monolithically integrated MoS$_2$-FETs on flexible polyimide substrates for multiplexed neuroprosthetic applications. This includes benchmarking the impact of different MoS$_2$ thin film channel materials linked to MOCVD optimization studies presented in chapter 3 (reduction of C incorporation, grain size enhancement), evaluated by key figures of merit (I_{ON}/I_{OFF}, μ_{FE}, SS, V_T, D_{IT}) obtained from electrical device characterization.

5.3.1 EDL-gated MoS$_2$ FETs

As a first generation of FET devices, ionic liquid/gel-gated MoS$_2$ FETs were fabricated. While this device architecture may eventually provide a route towards low-cost, inkjet-printed electronic devices [136] and a versatile platform to study novel properties and functionalities of 2D materials [287], the main motivation is to achieve rapid and facile electrical FET testing thanks to minimized device fabrication efforts. Further, this fabrication strategy allows exploiting the excellent gating properties of electric double layers (EDL), which enables to study the performance limits of different 2D channel materials.

Figure 5.12 shows the schematic device structure of a liquid-gated FET in which the (top-)gate dielectric is formed by an ionic liquid (or gel) instead of a conventional, solid metal oxide. The ionic liquid/gel is electrically insulating, but ionically conductive, and mobile ions can undergo drift diffusion in response to an electric field caused by the gate voltage V_G, which can be applied inside the liquid by a simple wire
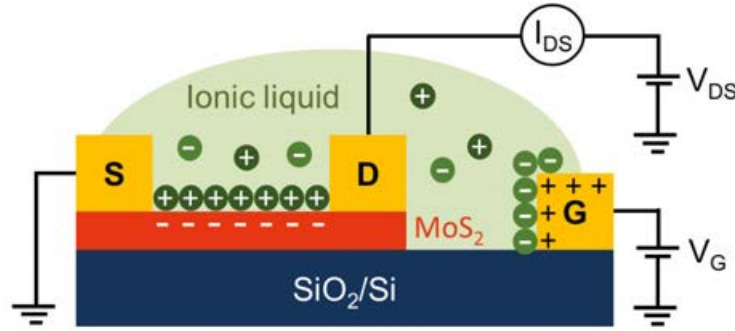
Figure 5.12 Schematic of EDL-gated MoS$_2$ FET device architecture in side-gate configuration. The MoS$_2$ channel is contacted by source (S) and drain (D) electrodes through which the S-D voltage V_{DS} applies the S-D current I_{DS} that can be modulated and switched by the gate (G) bias V_G by electrostatic doping via an electric double layer (EDL) at the ionic liquid/MoS$_2$ interface.

electrode or a lithographically defined side gate. Under bias conditions, an EDL forms at the 2D channel interface and the electrostatic field-effect doping induces high charge carrier densities ($\sim 1 \times 10^{13}$ – $1 \times 10^{14}\,\mathrm{cm}^{-2}$) [287, 541]. As the EDL thickness is only $\sim$1 nm, large gate capacitances on the order of 1 to $4\,\mu\mathrm{F\,cm}^{-2}$ can be achieved by commonly used ionic liquids, such as DEME:TFSI [541, 542], or gels, such as PEO:BMIM [543], exceeding conventional high-κ oxide dielectrics by more than an order of magnitude [239, 287, 544]. Therefore, gating of the 2D channel is extremely effective and allows low switching voltages. Moreover, in contrast to oxide dielectrics typically deposited by ALD, ionic liquids/gels, can be easily applied by simple spin-coating or drop-casting while creating dangling bond-free interfaces. This route enables transistor characteristics with subthreshold slopes close to the ideal value of $60\,\mathrm{mV\,dec}^{-1}$ [545] and mainly limited by the channel quality and impurities [369, 239], contacts [541, 542] and substrate effects [544, 239].

As shown in Fig. 5.13, the fabrication of interdigitated EDL-gated FETs is relatively simple and was utilized to benchmark two sets of MoS$_2$ films grown in previous MOCVD optimization studies; in particular, it was compared:

- **C-contaminated versus C-reduced MoS$_2$ films** with nm-grain size as-grown on SiO$_2$ at 700 °C without and with 10 sccm H$_2$ (see also section 3.3.1)

- **nm-grain size versus μm-grain-size MoS$_2$ films** grown at optimized 700 °C/H$_2$ conditions on SiO$_2$ and B270i soda-lime glass (see also section 3.4)
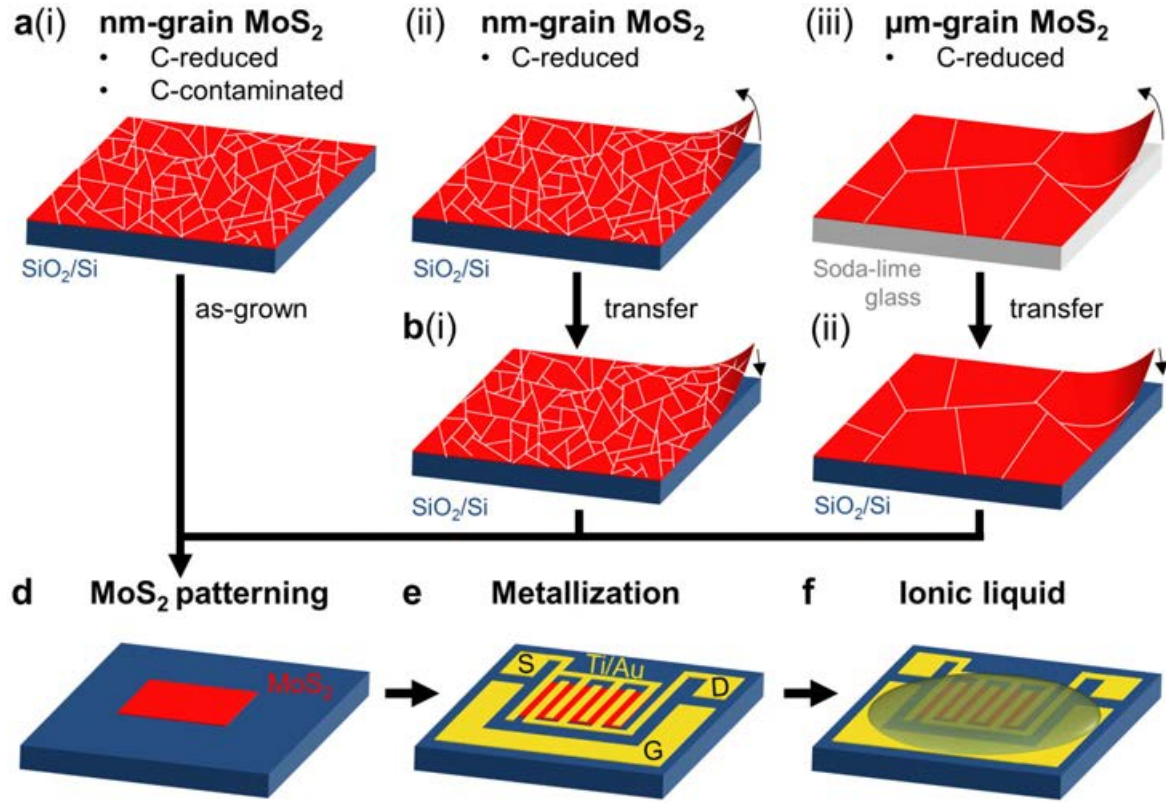
Figure 5.13 Liquid-gate MoS$_2$-FET fabrication and study overview. Schematic illustration of process sequence, following **(a)** selection of MoS$_2$ samples with small domain size (30 nm grown on SiO$_2$ and large domain size (up to μm) grown on soda-lime glass, **(b)** transfer of small and large domain films onto SiO$_2$ chip for comparison, **(d)** MoS$_2$ patterning by photolithography and RIE. **(e)** Metallization with Ti/Au deposition for source (S), drain (D), and gate (G) contacts, and **(f)** drop-casting of ionic gel/liquid.

The MoS$_2$ films were used as-grown on SiO$_2$ or films were transferred to SiO$_2$ via the TRT-method (section 5.1). The device fabrication, performed on $2 \times 2 \text{cm}^2$ SiO$_2$/Si chips, consisted in the following steps: First, the MoS$_2$ channels were patterned by photolithography and RIE etching (Fig. 5.13d); subsequently, Ti/Au source (S), drain (D) and gate (G) were metallized by e-beam evaporation using a photoresist mask (Fig. 5.13e). It is noted that the photolithography developing step of interdigitated S-D contacts, due to the use of water- and TMAH-based developers (Tetramethylammonium hydroxide), required strict process optimization (developing time, careful water rinse) because of the risk of layer delamination due to etching and intercalation at the MoS$_2$/SiO$_2$ interface. After metallization, metal lift-off in acetone and vacuum annealing of contacts at 250 °C were performed. Finally, ionic liquid/gel (either DEME-TFSI

or PEO:BMIM:TFSI, as will be indicated) was drop-casted (Fig. 5.13f). A protocol including more detailed processing parameters is given in the appendix (section D.4).

The FET design uses highly interdigitated S-D contacts with a W/L ratio of 17000 for increased output current, channel length of 3 µm and co-planar side-gate configuration, as shown in the microscopy images in Fig. 5.14a. An exemplary device measured in the tip station under ambient conditions is shown in Fig. 5.14b. The side-gate-to-channel area ratio is 14 ensuring sufficient charge accumulation for EDL formation in the channel area during gate biasing [545, 546].
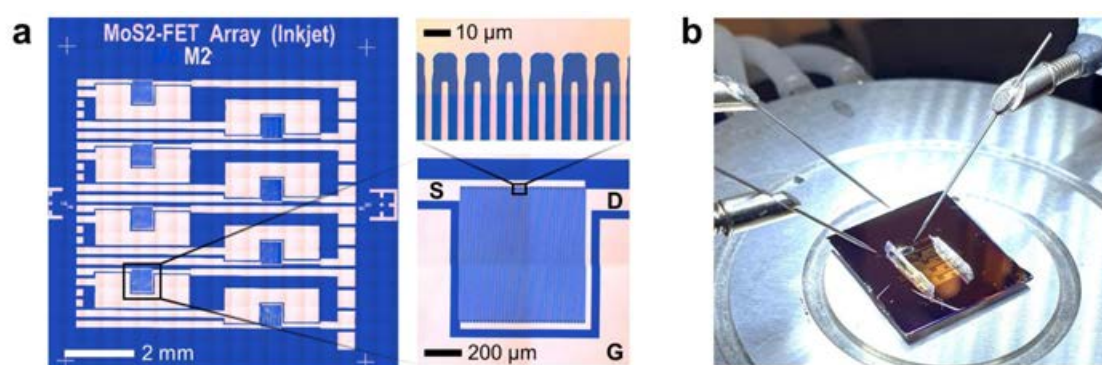
Figure 5.14 EDL-gated MoS$_2$ FET device design and electrical measurement setup. **(a)** Microscopy images showing a chip containing eight FET devices with highly interdigitated source-drain structure with contact width of 600 µm and 3 µm channel length (W/L=17000) in side-gate configuration. **(b)** Photograph of a device during electrical testing under ambient conditions in the probe station. PDMS is used to create a pool for the ionic liquid and to keep the contact pads dry.

During transfer curve measurements, bias voltages must stay within a certain electrochemical window to avoid electrochemical reactions, such as of the ionic liquid. DEME-TFSI was chosen for its stability and large potential window of ± 3 V at room temperature [547]. However, as ionic liquids are well-known to be hygroscopic, during the measurements under ambient conditions certain exposure to ambient humidity cannot be avoided and water electrolysis might compromise FET stability and performance [545]. Therefore, maximum sweep gate voltages were typically kept below ± 1–1.5 V) and measurement times were minimized to avoid chemical reactions. Moreover, to avoid water uptake ionic liquid was stored in a vacuum desiccator and small volumes for experimental use were extracted in an inert gas filled glovebox.

Impact of C incorporation on MoS$_2$-FET performance

The previous chapter chapter 3 discussed in detail the importance of MOCVD growth parameter optimization to control C impurity level and film morphology and to obtain coalesced, mono- to few layer MoS$_2$ thin films suitable for transistor channel application. It has been shown that the C incorporation could be avoided by addition of hydrogen to the growth process, yielding virtually carbon-free films. Here, the C-contaminated MoS$_2$ film with disrupted channel [Fig. 5.15a(i)] and C-reduced MoS$_2$ films with continuous channel [Fig. 5.15b(i)] their $I_{DS} - V_G$ transfer and $I_{DS} - V_{DS}$ output characteristics are compared in Fig. 5.15(a-b)(ii-iii).

The C-contaminated MoS$_2$-FET shows ambipolar switching behaviour under gate bias V_G characteristic of low-quality, solution-gated graphene [12] with a low on/off-current ratio of $I_{ON}/I_{OFF} \sim 3$ [Fig. 5.15a(ii)]. The charge neutrality point (CNP, see inset) is located at positive bias voltages, which may be due to p-doping from charge transfer at the MoS$_2$/C($sp2$)/SiO$_2$ interface (section 3.3.2) and processing residue [12, 548]. Also, it shows dynamic drift upon sweeping between around 0.35 V and 65 V, which may be caused by dynamic ion intercalation and doping effects at the layered interface [548]. The rather linear $I_{DS} - V_{DS}$ output characteristic in Fig. 5.15a(iii) shows a highly resistive film; considering $V_G = 0$, $I_{DS} \sim 15$ µA at $V_{DS} = 0.5$ V and sheet resistance of $R_{SH} \sim 33$ kΩ, further using the formula $\sigma_{DS} = 1/(R_{SH} \cdot t_{CH})$ [286], and assuming a graphene channel thickness of $t_{CH} = 0.4$ nm, a corresponding conductivity on the order of $\sigma \sim 8 \times 10^4$ S m^{-1} can be extracted. This conductivity agrees well with reported values for sub-10 nm grain size graphene [362] and is also consistent with the sub-10 nm grain size L_a estimated from the Raman I_D/I_G-ratio (see section 3.2.1). Therefore, it is speculated that the electrical behaviour of the C-contaminated device is dominated by the resistive, nano-crystalline graphitic C($sp2$) layer; the interrupted, non-percolated MoS$_2$ film cannot provide semiconducting switching operation. In contrast, the C-reduced FET with continuous 2-3L channel MoS$_2$ exhibits the desired on/off switching behaviour with $I_{ON}/I_{OFF} > 1 \times 10^4$ [Fig. 5.15b(ii)]. The estimated field-effect mobility from the maximum slope of this device is ~ 0.29 cm^2 V^{-1} s^{-1}, assuming an EDL-capacitance of 2 µF cm^{-2}. The subthreshold slope is $SS = 112$ mV dec^{-1} and the device shows a positive threshold voltage of $V_T \sim 0.8$ V with an uncertainty of $\Delta V_T \sim 0.08$ V due to the hysteresis observed in forward and backward gate voltage sweeps. The hysteresis can be attributed to bias instabilities [511] from defects and traps induced at the MoS$_2$/SiO$_2$ bottom-interface. Hole (electron) trapping is thus suggested to be responsible for the negative (positive) shift of the transfer curve in

the forward (backward) sweep; the time constant for charge trapping/detrapping is comparable to the used sweep times of 1 min (0.05 V s^{-1} sweep rate). Also, the measurement under ambient conditions may explain the hysteresis observation [549];
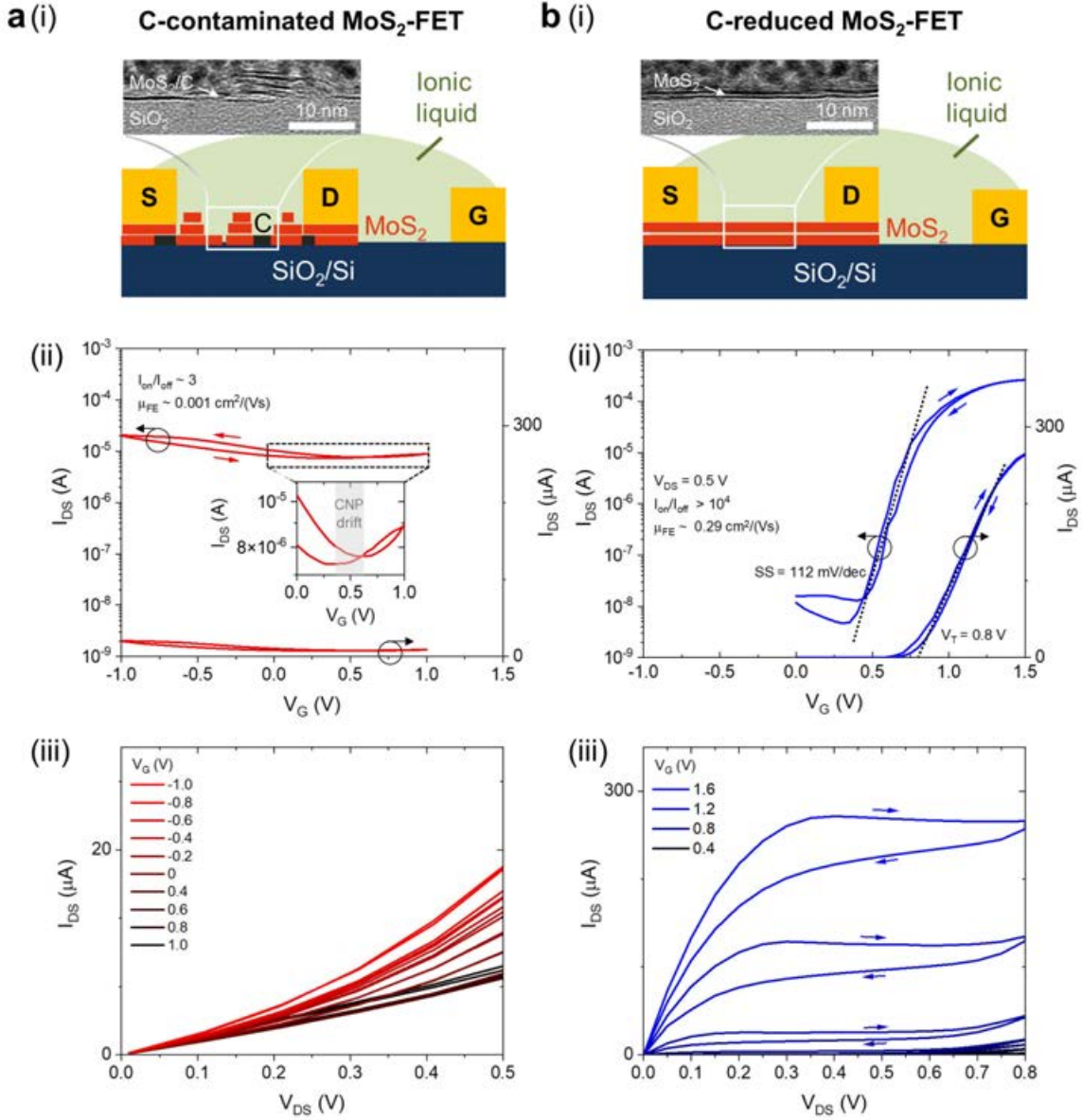
Figure 5.15 Impact of C incorporation on few-layer EDL-gated MoS$_2$-FETs. **(a)** C-contaminated MoS$_2$-FET and **(b)** C-reduced MoS$_2$-FET; with (i) schematic illustrations of both devices and exemplary cross-sectional TEM images. (ii) $I_{DS} - V_G$ transfer curves in logarithmic scale (left axis) and linear scale (right axis) measured at $V_{DS} = 0.5$ V. Extracted FET characteristics (subthreshold swing SS, threshold voltage V_T, and mobility μ_{FE}) are indicated. (iii) $I_{DS} - V_{DS}$ current output measured for several gate biases V_G. DEME:TFSI ionic liquid was used as dielectric. Channel width was $W = 51\,000$ µm and length $L = 3$ µm.

it can also be affected by water uptake of the ionic liquid [545]. Nonetheless, as an important intermediate conclusion, the drastically different electrical behaviour of the two compared films highlights the importance of optimized growth parameters for MoS$_2$ films with reduced C incorporation and continuous channel properties to obtain functional, switchable FET devices with high on/off-current ratio.

Impact of grain size on MoS$_2$-FET performance

As a grain boundary-rich MoS$_2$ channel is likely limiting transistor performance, such as the field-effect mobility μ_{FE}, a comparison between MoS$_2$ channels with "small" ($\sim$30 nm) versus "large" (up to $\sim$µm) grain sizes was conducted, taking advantage of alkali-assisted, growth on soda-lime glass (Fig. 5.16). As growth on soda-lime glass showed tendency of self-limiting growth behaviour, $\sim$1L MoS$_2$ films were used for this study and both films were transferred to SiO$_2$ to ensure comparability.

From the comparison of transfer curves in Fig. 5.16b both devices yield desired *on/off* switching behaviour with a high on/off-ratio $I_{ON}/I_{OFF} > 10^5$ for the large grain device. Subthreshold slopes of both devices were very similar (115 and 110 mV dec) suggesting that both devices have a comparable interface defect densities; it also indicates that the transfer process does not degrade performance compared to the as-grown devices (Fig. 5.15). The gate sweeping at different V_{DS} demonstrates device operation with tunable output current level [Fig. 5.16(a-b)(iii)], revealing a pronounced hysteresis for the large-grain, alkali-assisted MoS$_2$ film. Notably, the large-grain device yields about a factor of ~ 8 higher output current; this can be explained by fewer grain boundary defects and higher channel conductivity, which is also reflected in a higher mobility of $\sim 0.23\,\text{cm}^2\,\text{V}^{-1}\,\text{s}^{-1}$ for the large grain device compared to $\sim 0.04\,\text{cm}^2\,\text{V}^{-1}\,\text{s}^{-1}$ for the small grain device. However, despite the mobility improvement, the transistor performance still lies about an order of magnitude below previously reported μ_{FE} values (1 to $10\,\text{cm}^2\,\text{V}^{-1}\,\text{s}^{-1}$) of MOCVD-grown MoS$_2$ in EDL-gated devices [369, 239]. It is remarked that the film quality is not only determined by grain size/boundaries, but also other line and point defects. Indeed, when analyzing MoS$_2$ thin films grown on soda-lime glass by AFM phase images, intragrain defects and pyramidal multilayer defects are apparent (see also Fig. 3.24. Furthermore, film heterogeneities (clusters formation, grain size variations, residual alkali- or intermediate catalyst impurities) were observed in alkali-assisted growth (section 3.4.1), which is very likely degrading transistor performance [369]. Moreover, Ti/Au contacts are not optimal due to possible reactions and Schottky barriers with MoS$_2$ [480, 550, 479], which may be improved by

Ni, Pd or pure Au [239] (although pure Au contacts may not be practical due to poor adhesion). Despite these limitations, enhanced on-current and mobility performance could be shown by increasing MoS$_2$ grain size controlled by the optimized MOCVD process.
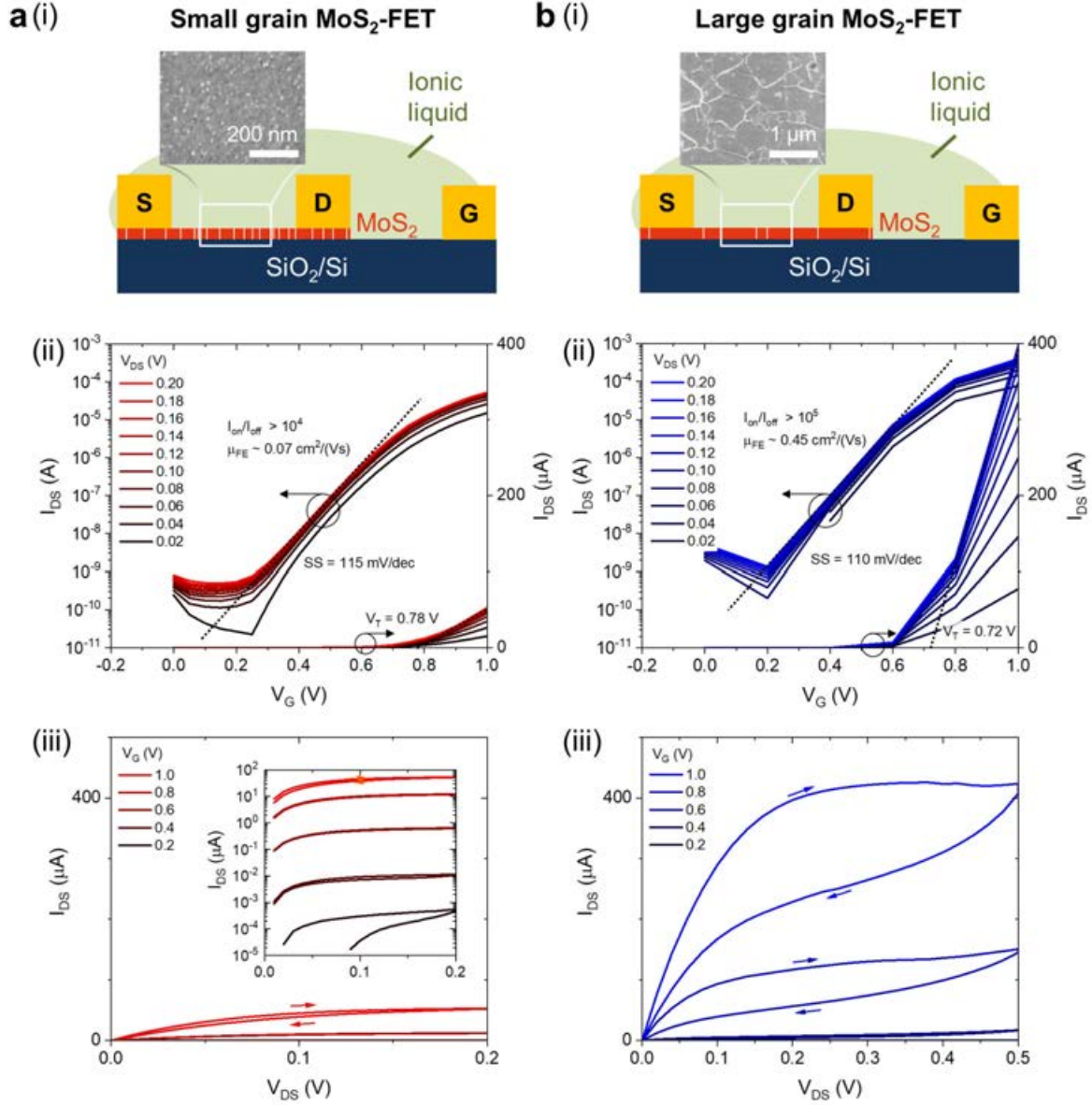
Figure 5.16 Impact of grain size on 1L MoS$_2$-FETs. **(a)** Small grain size MoS$_2$-FETs and **(b)** Large grain size MoS$_2$-FETs with (i) schematic illustrations of the devices and top-view SEM images. (ii) $I_{DS} - V_G$ transfer curves in logarithmic scale (left axis) and linear scale (right axis) for different drain-source biases V_{DS}, as indicated. Extracted FET characteristics (subthreshold swing SS, threshold voltage V_T, and mobility μ_{FE}) are indicated. (iii) $I_{DS} - V_{DS}$ current output measured for several gate biases V_G. PEO:BMIM:TFSI ionic gel was used as dielectric. Channel width was $W = 51\,000\,\mu m$ and length $L = 3\,\mu m$.

5.3.2 Solid-gated MoS$_2$ FETs

While EDL-gated FETs provide a convenient testing platform, a more advanced technology towards the goal of developing flexible electronics is desired, in particular for MoS$_2$-multiplexed neuroprosthetic devices. As a first building block, solid-gated MoS$_2$-FETs are developed that can later serve as integrated switching elements for multiplexing purposes. A back-gated FET device structure is shown in Fig. 5.17 with the MoS$_2$ channel sandwiched between 50 nm AlO$_x$ oxide layers and top-contacted by Ti/Au source (S) and drain (D) contacts, as shown in Fig. 5.17a. This architecture allows switching by the gate (G) electrode and bottom AlO$_x$ dielectric, while the top AlO$_x$ encapsulation protects the sensitive MoS$_2$ channel from the environment. For step-by-step technology validation, the transistor devices were first fabricated on rigid substrates (SiO$_2$) and then adapted to a flexible design by simply adding a polymer layer (e.g. polyimide) between the SiO$_2$ carrier substrate and the bottom-gate structure. In this way, the polymer serves as the new, flexible substrate that can be easily peeled off the rigid carrier wafer. Details on the fabrication protocol are given in the appendix (section D.4).

The electrical characterization of AlO$_x$-encapsulated MoS$_2$-FETs, including translation from rigid to flexible substrates is shown in Fig. 5.17(b-c), which compares the transfer and output characteristics of devices fabricated on SiO$_2$ and polyimide substrates. The devices perform almost identically, proving that implementing the polyimide substrate does not alter the performance of the AlO$_x$/MoS$_2$/AlO$_x$ stack. The transfer curves show on/off-current ratios $> 10^3$, relatively low hysteresis ($\Delta V_T \sim 0.4$ V) and positive threshold voltages. This is benefitial for enhancement mode operation, which satisfies basic multiplexing requirements; however, the required ± 8 V-switching window between *on-* and *off*-state is wide due to the shallow subthreshold slopes of $SS \gtrsim 3500$ mV dec; this SS points to low channel and interface quality of the current technology limited by interface traps [61], consistent with previous spectroscopic studies (section 5.2.2). The interface trap densities extracted from the transfer curves are on the order of $D_{IT} \sim 6 \times 10^{13}$ eV^{-1} cm^2, comparable to results obtained from frequency-dependent capacitance measurements of metal-insulator-semiconductor-metal capacitor test structures (Fig. D7) fabricated in the same run. This high interface defect density is responsible for charge scattering and limited transport properties [288] resulting in a comparatively low field-effect mobility of $\mu_{FE} \sim 0.04$ cm^2 V^{-1} s^{-1}. Therefore, further technology improvements are demanded, including optimization of the oxide encapsulation protocol for reduced charge trapping. Moreover, there is potential for

enhanced MoS$_2$ channel quality, which can be addressed by further growth optimization, as highlighted by the study summarized in Fig. 5.18. The SEM images show sub-monolayer covered MoS$_2$ films with increasing grain sizes of ~ 30 nm (ICN2 reactor,
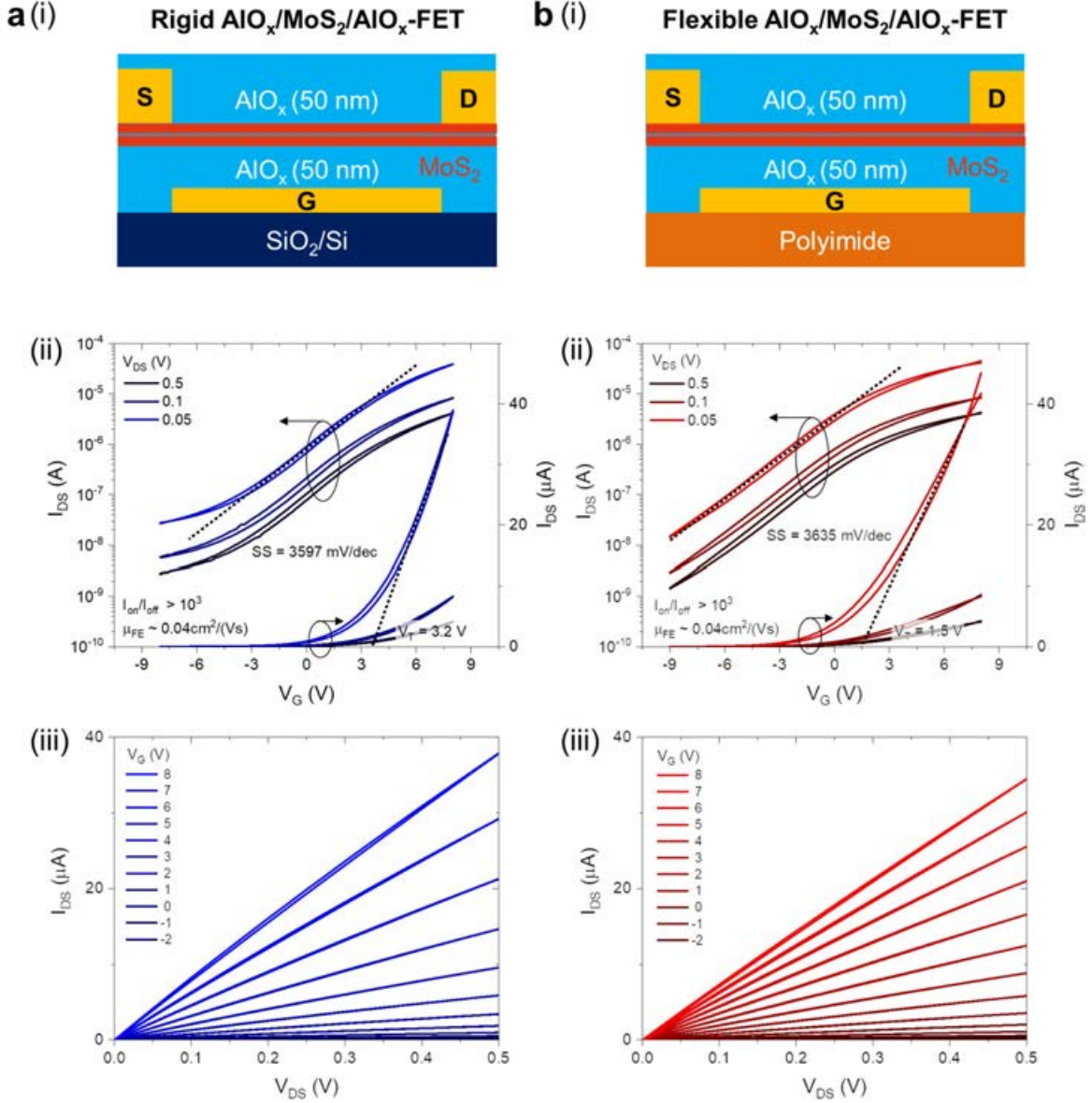
Figure 5.17 Solid-gated MoS$_2$-FETs and technology translation from rigid to flexible substrates. **(a)** Rigid AlO$_x$/MoS$_2$/AlO$_x$-FET and **(b)** Flexible AlO$_x$/MoS$_2$/AlO$_x$-FET with (i) schematic illustrations of both devices. (ii) $I_{DS} - V_G$ transfer curves in logarithmic scale (left axis) and linear scale (right axis) for different drain-source voltages V_{DS}. Extracted FET characteristics (subthreshold swing SS, threshold voltage V_T, and mobility μ_{FE}) are indicated. (iii) $I_{DS} - V_{DS}$ output curves measured in linear regime before pinch-off for several gate biases V_G. Channel width was $W = 6000$ µm and length $L = 2$ µm. Transfer curves were measured at $V_{DS} = 0.5$ V.

Mo(CO)$_6$+DES, without NaCl) and $\sim 850\,$nm (Yonsei reactor, Mo(CO)$_6$+DMS, with NaCl). Despite the enhanced *on*-current and mobility improvement for devices with large grain sizes, specific drawbacks depending on the growth process can be noted. The film grown by alkali-assisted MOCVD shows an increased hysteresis ($\Delta V_T \sim 2.4\,$V), which might be explained by the film heterogeneities seen in the SEM images, such as impurity particles and intermediate reaction products related to the use of NaCl.
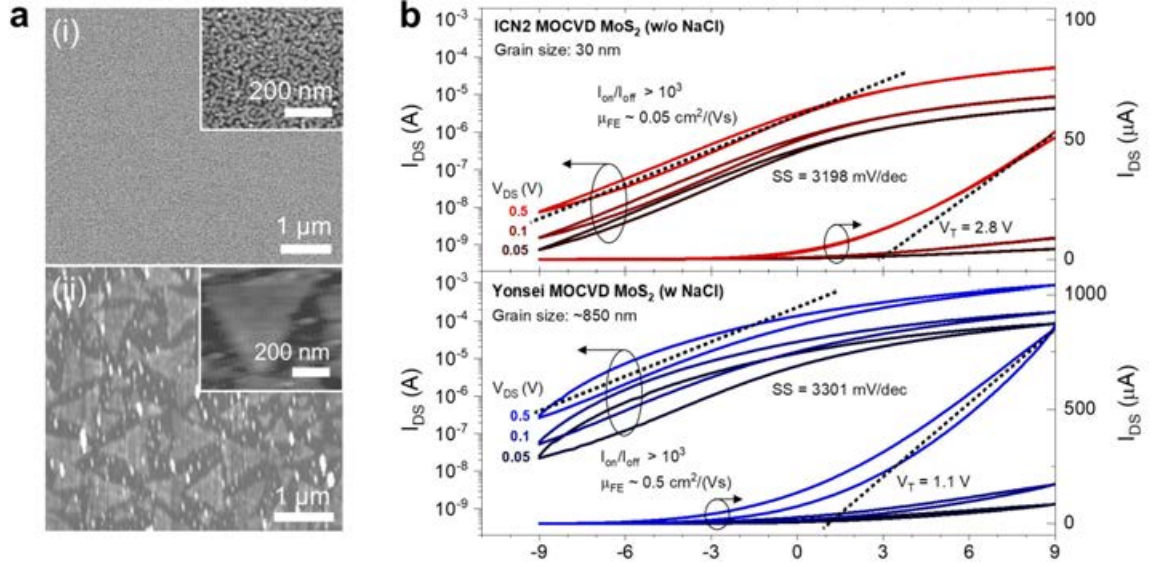
Figure 5.18 Impact of MoS$_2$ grain size in AlO$_x$-encapsulated MoS$_2$-FET devices on flexible polyimide substrates. **(a)** Exemplary SEM images of MoS$_2$ thin films (i) grown in ICN2 reactor on SiO$_2$ (without NaCl), and (ii) grown in Yonsei reactor on SiO$_2$ (with NaCl). For the micrographs the growth was intentionally stopped at sub-monolayer coverage to reveal the grain size, but was extended to $\sim$1-2L coverage for device fabrication. Insets show the magnified grain structure. **(b)** $I_{DS} - V_G$ characteristics of devices fabricated with the corresponding MoS$_2$ films. Transfer curves are shown in logarithmic scale (left axis) and linear scale (right axis) for different drain-source voltages V_{DS}. Extracted FET characteristics (subthreshold swing SS, threshold voltage V_T, and mobility μ_{FE}) are indicated. Channel width was $W = 6000\,$µm and length $L = 2\,$µm.

5.3.3 Evaluation of MoS$_2$-FET results

The fabrication and characterization of MoS$_2$-FETs with different architectures and benchmarking of different MoS$_2$ films allows a summary and assessment of the current status of the MoS$_2$ FET technology. Table 5.2 shows an overview of the presented architectures, integration schemes and their figures of merit from electrical analysis. Conclusions developed in this work about performance limitations are drawn and mitigation strategies are proposed for technology maturation.

Compared to the solid-gated FETs using comparatively thick 50 nm AlO$_x$ [and 285 nm back-gated SiO$_2$ dielectrics as an additional reference, Fig. D13], the nm-thin EDL-gated FETs allowed to obtain orders of magnitude greater gate capacitances C_G, and thereby superior gating control over the channel. Therefore, increased $I_{ON}/I_{OFF} > 10^5$ within reduced ± 1 V switching windows could be obtained. Furthermore, the EDL architecture allows to obtain FET devices, for which performance is limited by intrinsic channel properties instead beeing limited by the oxide interface trap contributions characteristic of the AlO$_x$-encapsulated devices. In the case of the EDL-gated devices, this is reflected in the significantly lowered $SS \sim 110$ mV dec obtained from eq. (2.6) (section 2.3.4) due to the increased C_G and reduced D_{IT}, contributing to lower body factors of $m \sim 4$ closer to the ideal value of $m = 1$ ($SS \sim 60$ mV dec) as compared to the solid-gated devices. The value of $SS \sim 110$ mV dec lies in the typical range for MOCVD-grown MoS$_2$ [61, 282]; to obtain near-ideal SS would therefore require to further reduce channel defects [539] to approaching a near-ideal SS that has been demonstrated in devices using exfoliated MoS$_2$ [61]. Interestingly, there is no significant difference between the D_{IT} of 30 nm and 488 nm MoS$_2$ grain size films; this suggests that MoS$_2$/SiO$_2$ interface defects dominate over grain boundary defects; alternatively, it could be that any additionally introduced defects (impurities, particle formation) by the alkali-assisted approach compensate the reduction of defect density resulting from the grain size enhancement. On the other hand, the enlarged grain sizes clearly showed a trend towards higher mobilities and *on*-currents for both EDL- and AlO$_x$-gated devices. Importantly, device performance seems not to be affected by the transfer process that is required for the solid-back-gated devices, which is reflected in the almost identical SS and D_{IT} values for as-grown and transferred EDL-devices. Moreover, all devices with the here used MOCVD-grown MoS$_2$ films show a positive V_T, which is benefitial for enhancement mode devices and multiplexing, although the control of V_T position has not been intentionally tailored here. The V_T positions may be fixed by interfacial traps and channel defects, such as S vacancies [551, 552, 553, 250]. The main limitations of the current AlO$_x$-gated FET technology are manifested by the high $D_{IT} > 6 \times 10^{13}$ eV^{-1} cm^2 and correlated $SS > 3500$ mV dec^{-1}, revealing large improvement potentials towards the ideal value of ~ 60 mV dec. The D_{IT} is contributed by MoS$_2$ channel defects and interface defects resulting in charge trapping and deteriorated transport properties [61, 539]. Therefore, based on these presented data, the alleviation of these two defect contributions by appropriate mitigation measures should be prioritized in further efforts of technology improvement, as proposed in the following.

Table 5.2 Overview of MoS$_2$-FET device characteristics and figures of merit for different MoS$_2$ films (growth reactor, layer number, average grain size, C content) and transistor architectures, including gate capacitance C_G, channel width-to-length ratio W/L, on/off-current ratio I_{ON}/I_{OFF}, subthreshold slope SS, threshold voltage V_T, interface trap density D_{IT}, field-effect mobility μ_{FE}.

FET/gate-type	C_G (µF cm^{-2})	MoS$_2$ film	Transfer	W/L	I_{ON}/I_{OFF}***	SS (mV dec^{-1})	D_{IT} (eV^{-1} cm^{-2})	V_T (V)	μ_{FE} (cm^2 V^{-1} s^{-1})
EDL-topgate									
DEME:TFSI	$\sim$2*	ICN2, few-L, 30 nm, C-cont.	no	17000	$\sim$3	-	-	-	0.001
DEME:TFSI	$\sim$2*	ICN2, $\sim$2-3L, 30 nm, C-red.	no	17000	$>10^4$	112	3.6×10^{13}	0.8	0.29
PEO:BMIM:TFSI	$\sim$2*	ICN2, $\sim$1L, 30 nm, C-red.	yes	17000	$>10^4$	113 ± 3	$3.6 \pm 0.1 \times 10^{13}$	0.71 ± 0.03	0.03 ± 0.01
PEO:BMIM:TFSI	$\sim$2*	ICN2, $\sim$1L, 488 nm, soda-lime, C-red.	yes	17000	$>10^5$	116 ± 8	$3.7 \pm 0.2 \times 10^{13}$	0.73 ± 0.04	0.11 ± 0.09
Solid-backgate									
285 nm SiO$_2$/Si^{++}	$\sim$0.01**	ICN2, $\sim$2-3L, 30 nm, C-red.	no	17000	$>10^5$	8915	2.2×10^{13}	41	0.003
50 nm Al$_2$O$_3$ (rigid SiO$_2$)	0.14	ICN2, $\sim$2-3L, 30 nm, C-red.	yes	4000/7200/10000	$>10^3$	3426 ± 99	$6.3 \pm 0.2 \times 10^{13}$	2.6 ± 0.8	0.02 ± 0.01
50 nm Al$_2$O$_3$ (flex. PI)	0.14	ICN2, $\sim$2-3L, 30 nm, C-red.	yes	3000/6000	$>10^3$	3463 ± 398	$6.4 \pm 0.6 \times 10^{13}$	1.8 ± 1.7	0.06 ± 0.05
50 nm Al$_2$O$_3$ (flex. PI)	0.14	Yonsei, $\sim$1-2L, 850 nm, NaCl	yes	3000	$>10^3$	3301	6.1×10^{13}	1.1	0.47

all values for V_{DS} = 0.5 V, except * V_{DS} = 0.2 V for transferred liquid-gated devices
* C_{EDL} was not determined experimentally; typical values are in the range 1 – 4 µF cm^{-2} [287] [136]
** estimated value based on used device geometry, 285 nm oxide thickness and ϵ_r = 3.9 [554]
*** due limited sweep ranges not fully saturating (depleting) the channel, true on/off-ratios are higher than listed

First, MoS$_2$ channel defects (impurities, grain boundaries, point defects) must be addressed by further growth optimization or post-growth treatments. Impurity reduction, such as mitigating C incorporation through MOCVD-optimization has turned out to be essential to guarantee channel functionality and high on/off switching capabilities, and could be progressed by advanced precursor selection and purity towards electronic-grade 2D films [190, 239]. The use of alkali-assisted processes must be carefully reconsidered due to impurities and particles from reaction intermediates that may result in heterogeneous film properties and switching instabilities [369], as evidenced by the pronounced hysteresis behaviour for the alkali-assisted MoS$_2$ films. The impact of grain boundary defects has been investigated and the general trends seen for both EDL- and solid-gated FET devices demonstrated mobility (up to $0.9\,\mathrm{cm}^2\,\mathrm{V}^{-1}\,\mathrm{s}^{-1}$) and *on*-current (up to $0.6\,\mathrm{mA}\,\mathrm{\mu m}^{-1}$) improvements that encourage further efforts in grain size enhancement and 2D defect reduction. As a next step, integration of epitaxial, single-crystal MoS$_2$ films grown on sapphire is recommended that may enable further FET performance gains with mobilities $>30\,\mathrm{cm}^2\,\mathrm{V}^{-1}\,\mathrm{s}^{-1}$ [48, 282, 248] and *on*-currents approaching or even exceeding [493, 248] IRDS 2028 targets[1] for optimized device integration. Foundations of domain-aligned, large-area MOCVD synthesis towards single-crystalline films were laid in previous chapter 4, but these films have not been integarted into devices yet. Lastly, tailoring point defects [555, 250, 539] like S vacancies may provide enhanced mobilities and threshold voltage tuning via post-growth surface engineering by vacancy creation and/or passivation, such as thermal annealing and post-sulfurization [552, 250], and chemical treatments using super-acids [556, 557, 558] or thiol chemistries [559, 560, 561]. Further studies on channel defects may be supported by advanced atomistic defect monitoring and quantification, such as by conductive AFM [159, 562], non-contact CO-tip AFM and scanning tunneling microscopy/specroscopy [563, 564, 555, 565, 566, 567].

Second, MoS$_2$/AlO$_x$ interface defects (processing residues, adsorbates, dangling bonds) must be alleviated by adapting the oxide integration and device manufacturing process. Fabrication steps directly involving the MoS$_2$ interfaces, such as transfer using sacrifical (polymer) support layers or photolithography using photoresists, ideally, should all guarantee residue-free processing. The concept of tailored polymer/solvent pairs for wet cleaning demonstrated in section 5.1.2 should be further extended to the optimization of photoresist removal in the MoS$_2$ photolithography steps for the S-D contact step. Additionally, carefully optimized, soft UVO- [497, 498, 476] or low-energy

---

[1]International Roadmap for Devices and Systems (IRDS™), high-performance (HP) drive current: $I_{ON} = (924\,\mathrm{\mu A}\,\mathrm{\mu m}^{-1})$ [22]

plasma-treatments [568, 569] may support improved interface cleanliness prior AlO$_x$-encapsulation. Although the AlO$_x$ seeding and ALD route has succesfully enabled conformal encapsulation of MoS$_2$, especially the top AlO$_x$/MoS$_2$ interface capping is critical [516], and prone to adsorbate trapping (H$_2$O, adventitious carbons) in the current process due to multiple seeding and ambient exposure steps [493]. While a high-level solution to this issue may consist in carrying out the complete encapsulation process in the controlled vacuum environment of a multi-chamber PVD/(PE)ALD cluster coating tool, this may not be accessible in an academic research facility. Pragmatically, the number of seeding steps and serial interfaces prone to adsorbate trapping could be reduced (under verification of preserved conformal coating) and the oxidation step could be performed in a more controlled environment, such as a UVO cleaner, while reducing ambient exposure time and providing a clean interface by an immediately followed ALD capping step. Moreover, adapting the ALD process by tuning of H$_2$O exposure cycles [570] and lowered growth temperatures of 150 °C [41, 493] have shown promising results in other works. The currently used ALD temperature of 200 °C may result in uncontrollable thermal diffusion into the defective MoS$_2$ films at elevated temperatures [571]. Optionally, dedicated thermal (vacuum) annealing steps implemented right before [540] or after [570] oxide encapsulation for removal of interface adsorbates and traps could be implemented. Inert or forming gas post-encapsulation annealing may tune oxide defects to unleash intended modulation n-doping by the high-κ dielectric sandwiching [493, 41, 572] that has been so far interfered by detrimental trapping mechanisms. By adding an optimized annealing step reduction of interface traps by $\Delta D_{IT} = 5 \times 10^{13}\,\mathrm{cm^{-2}\,eV}$ has been reported [493]. Alternatively, to overcome the well-known dangling bond issue from conventional 3D amorphous oxide at the 2D material interface [59, 64], oxide passivation [573, 574] or improved material selection, for example a hBN buffer layer [516, 289], may ensure improved, dangling-bond-free van der Waals interfaces to the MoS$_2$ channel. Preliminary results for MoS$_2$/hBN heterostack formation by direct MOCVD growth of MoS$_2$ onto large-area MOCVD hBN available on 2" sapphire wafers [575] are shown in the appendix Fig. D8, Fig. D9). Such MoS$_2$/hBN structures could be implemented into FET devices by transferring the layer stack, followed by a hBN transfer on top for hBN/MoS$_2$/hBN sandwich encapsulation. In the future, 3D ionic crystal insulators like ultra-thin CaF$_2$ [576, 60] or high-κ perovskite membranes [577, 578, 579] by van der Waals heterostacking may be promising owing to their well-defined interfaces with 2D materials; yet, wafer-scale integration processes of novel insulators for 2D electronics and compatibility with flexible technologies are to be demonstrated.

5.4 Towards flexible, MoS$_2$-multiplexed/graphene neural sensing devices

Advances in neuroscience and further understanding of the brain heavily rely on the material-driven, technological development of novel transducers for neural interfacing tools [43, 580]. Flexible, active devices, such as solution-gated graphene field-effect transistors (Gr-SGFETs) combine outstanding features for surface-conformal, high-fidelity and wide frequency band neural sensing and enable large-area and high-density mapping of brain activity through arrangement into high channel count arrays [13, 581, 44, 582]. The signal read-out from thousands of recording sites requires multiplexing to reduce the connector footprint; However, current switching approaches by device-external CMOS electronics are limited by the intersite cross-talk [473, 583]. This inherent challenge can be solved by a thin film transistor (TFT) matrix providing device-internal, on-site switches to each pixel of the SGFET sensor array. In this proof-of-concept study, a TFT formed by MOCVD MoS$_2$-FETs is monolithically integrated with Gr-SGFETs in flexible, polyimide-supported, electrocortigraphy (ECoG) probes in an 1×8 pixel arrangement produced by a microfabrication process on 4" wafer-scale. The pixel on/off-switching operation and detection of an external electrical bias of such MoS$_2$/Gr-SGFET hybrid devices is demonstrated *in vitro* and time-division multiplexing of recording sites is performed. This 2D material based technology aims at providing the basis for a new generation of flexible, actively addressable and cross-talk-reduced neural sensing ECoG devices with channel counts scaled beyond the state-of-the-art.

As shown in Fig. 5.19, the adoption of time-division multiplexed readout requires switching elements that are either external or internal to the sensor device on which the recording sites are located. The external switching has the advantage that it can be relatively easy realized by established CMOS electronics [584, 581], therefore allowing simpler architecture and fabrication of the sensor probe itself. However, in practical scenarios during probe implantation the externalization bears the drawback of requiring long cable connections with large track resistances that inevitably compromise recording fidelity by so-called intersite cross-talk [581], which poses a major scaling limitation of multi-channel recording devices [583]. This cross-talk arises from current contributions of non-activated sites adjacent to activated sites and results in increased contamination of the recorded signal scaling with track resistance and array size. A solution to this problem is the integration of on-site semiconductor switches with large on/off-ratio
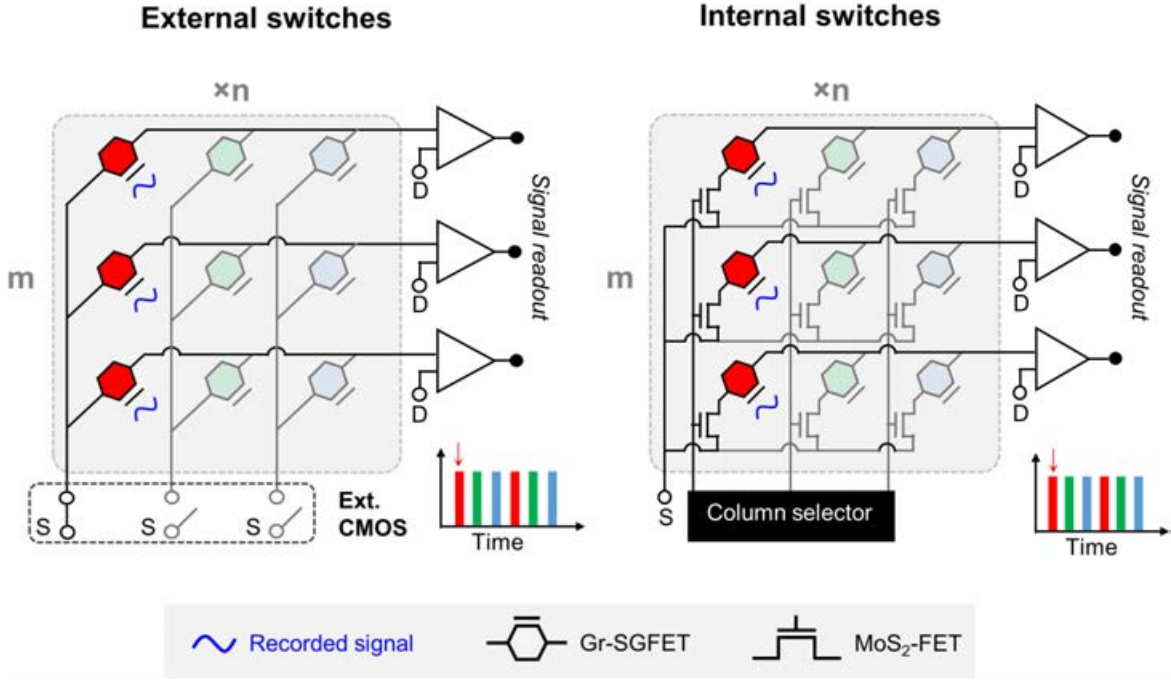
Figure 5.19 Time-division multiplexing for a sensor matrix arranged into $m \times n$ rows and columns. Active recording sites depicted with dark blue wave symbols can be addressed column-wise (red, green, light blue sensor elements) in sequential time windows according to the schematic graphs on the bottom-right of the matrices. Active read-out branches are highlighted, while deactivated branches are shaded. The multiplexing can be either realized by external switches, e.g. via external CMOS electronics (left), or internal switches formed by an integrated FET array (right).

directly on the sensor array that can effectively silence non-addressed sites by a large, serial impedance in the *off*-state, thus, avoiding alternate current pathways impairing the recordings [580]. These local switches connected in series to each sensor element can be provided by an integrated TFT-matrix controlled by a column selector applying on/off gate bias to each transistor element. The realization of such complex monolithic integration in flexible ECoG devices was already demonstrated by thin film silicon CMOS technology in combination with high-density platinum electrode arrays [585, 586, 587]. Although crystalline silicon, being a rigid and brittle semiconductor in its bulk form, can be made flexible by thinning it to a few hundreds of nm, it has limits to deformation tolerance and durability [588] due to a comparatively low fracture strain (strength) of about $\sim 1\,\%$ ($\sim 6\,$GPa) [589, 92, 93, 94]. Here, the properties of 2D semiconductors offer an advantage for flexible electronics both in thickness and elastic limit [38], taking the example of 1L MoS$_2$ with a superior fracture strain (strength) of $\sim 6 - 11\,\%$ ($\sim 24\,$GPa) [90] and excellent device endurance under repeated bending

for radii as low as 0.7 mm [41, 590, 591]. Previous examples show that 2D MoS$_2$-FETs combine ideal mechanical and electronic properties for integration into flexible, active-matrix-addressed devices [42] for applications in photodetector arrays [592], gas sensor arrays [593], on-skin, tactile pressure sensors [594], and flexible OLED displays [41]. So far, MoS$_2$-switched arrays for flexible neural interface devices have not been demonstrated. In the following, it is discussed how prototypes of multiplexed ECoG devices using monolithically integrated MoS$_2$-FETs as on-site switches to Gr-SGFET sensor elements are fabricated and electrically tested.

5.4.1   MoS$_2$-FET/Gr-SGFET hybrid devices

Figure 5.20 shows the cross-sectional structure of an elementary pixel unit of the MoS$_2$/Gr hybrid device. The pixel is built by a coplanar cascode configuration of a MoS$_2$-FET switch connected in series to a Gr-SGFET sensor on polyimide polymer substrate and passivated by SU-8 polymer. The total device thickness is of 13 μm to ensure the desired flexibility. The back-gated MoS$_2$-FET is formed by the MoS$_2$ channel sandwich-encapsulated inside AlO$_x$ oxide islands, which are on their part embedded between the polymer layers. Via-holes are etched through the oxide stack for contacting the Ti/Au metal back-gate and interdigitated Ti/Au source and drain MoS$_2$ top-contacts. The MoS$_2$-FET can be switched between the *on* and *off*-state by the gate bias V_{G,MoS_2}, delivering the source-drain current I_{DS} to the active Gr-SGFET sensing channel driven by the voltage V_{DS}. An opening in the SU-8 passivation layer brings the graphene channel in direct contact to the biological environment that can be simulated by an electrolyte solution closely matching the extracellular fluid in the human body, such as phosphate buffered saline (PBS) [595]. A Ag/AgCl reference electrode is immersed into the electrolyte to apply a solution-gate potential $V_{G,Gr}$, which is used to modulate the I_{DS} current in the graphene channel; this is induced through the electric double layer capacitance at the graphene-electrolyte interface and the quantum capacitance of graphene [596, 12].

The MoS$_2$/Gr hybrid probes are fabricated by standard microfabrication and photolithography processes. The fabrication flow is schematically illustrated in Fig. 5.21 and described in the following. The detailed fabrication protocol can be found in the Appendix (section D.4), including process parameters, chemicals and equipment used for each step. Nanocrystalline (30 nm grain size) 2-3L MoS$_2$ grown in the ICN2 reactor was chosen for MoS$_2$-FET device fabrication due to steady, in-house availability, more reliable transfer compared to MoS$_2$ grown on soda-lime glass, and favorable electrical
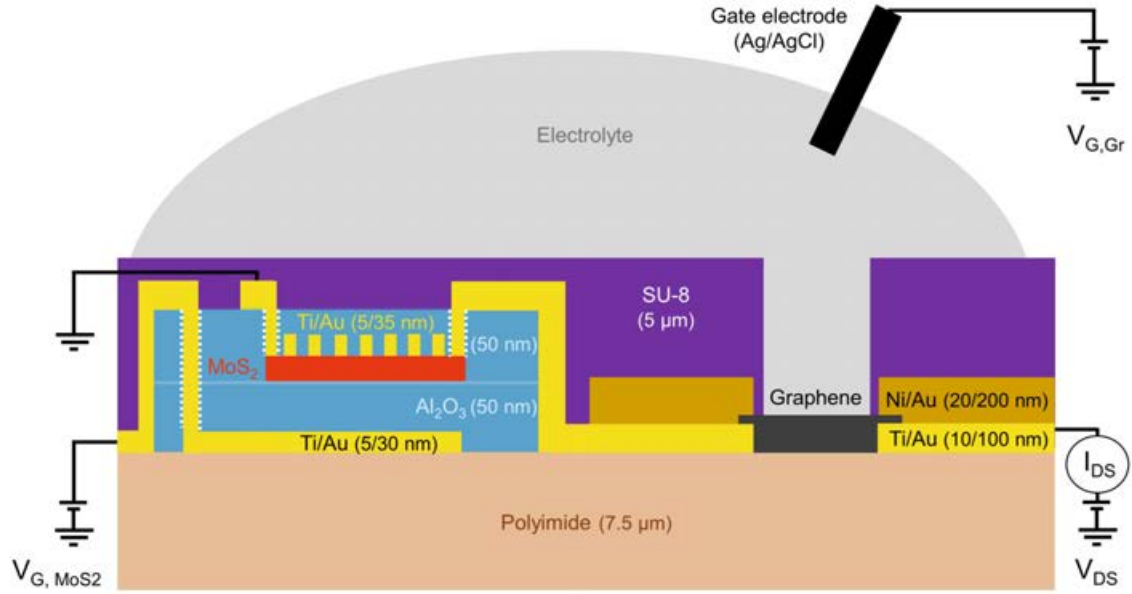
Figure 5.20 MoS$_2$/Gr hybrid device architecture, showing the device cross-section of a MoS$_2$-FET switch connected in series with a Gr-SGFET sensor forming a pixel. The pixel can be switched *on* or *off* by the gate voltage V_G applied to the MoS$_2$ gate. The drain-source current I_{DS} can be modulated in the SGFET channel in presence of a solution-gate potential $V_{G,Gr}$ induced from an electrode inside the electrolyte as *in vitro* simulation of a neural activity field potential. Layer thickness proportions are not at scale for illustration purposes.

performance of 2-3L films compared to 1L films [291, 248, 333]. For the Gr-SGFETs single-layer CVD graphene is used; more information about the CVD growth on copper foil and transfer is given in the appendix (section D.2).

Devices are fabricated on 4 inch SiO$_2$/Si support wafers. In a first step 7.5 μm biocompatible polyimide is applied by spin coating and curing, which serves as the flexible substrate. Then, MoS$_2$-FETs are fabricated with a bottom-gate design: Ti/Au (3 nm/30 nm) gate metal is deposited by e-beam evaporation using a photolithography mask and lift-off. The gate dielectric of nominally 50 nm AlO$_x$ is deposited by ALD at 200 °C onto the full wafer and the areas for the MoS$_2$-FET devices and via-hole openings to the gate metal are defined by RIE and Al wet etch. Next, the surface is prepared by an UVO treatment step; a ∼ 2 × 2 cm^2 sheet of MOCVD-grown MoS$_2$ is transferred by the PMMA-assisted TRT method (see section 5.1) and vacuum annealed (180 °C) for improved layer adhesion. Then, the PMMA support layer is dissolved and PMMA is respun over the whole wafer serving as protection for the underlying polyimide during the subsequent MoS$_2$ channel patterning step.
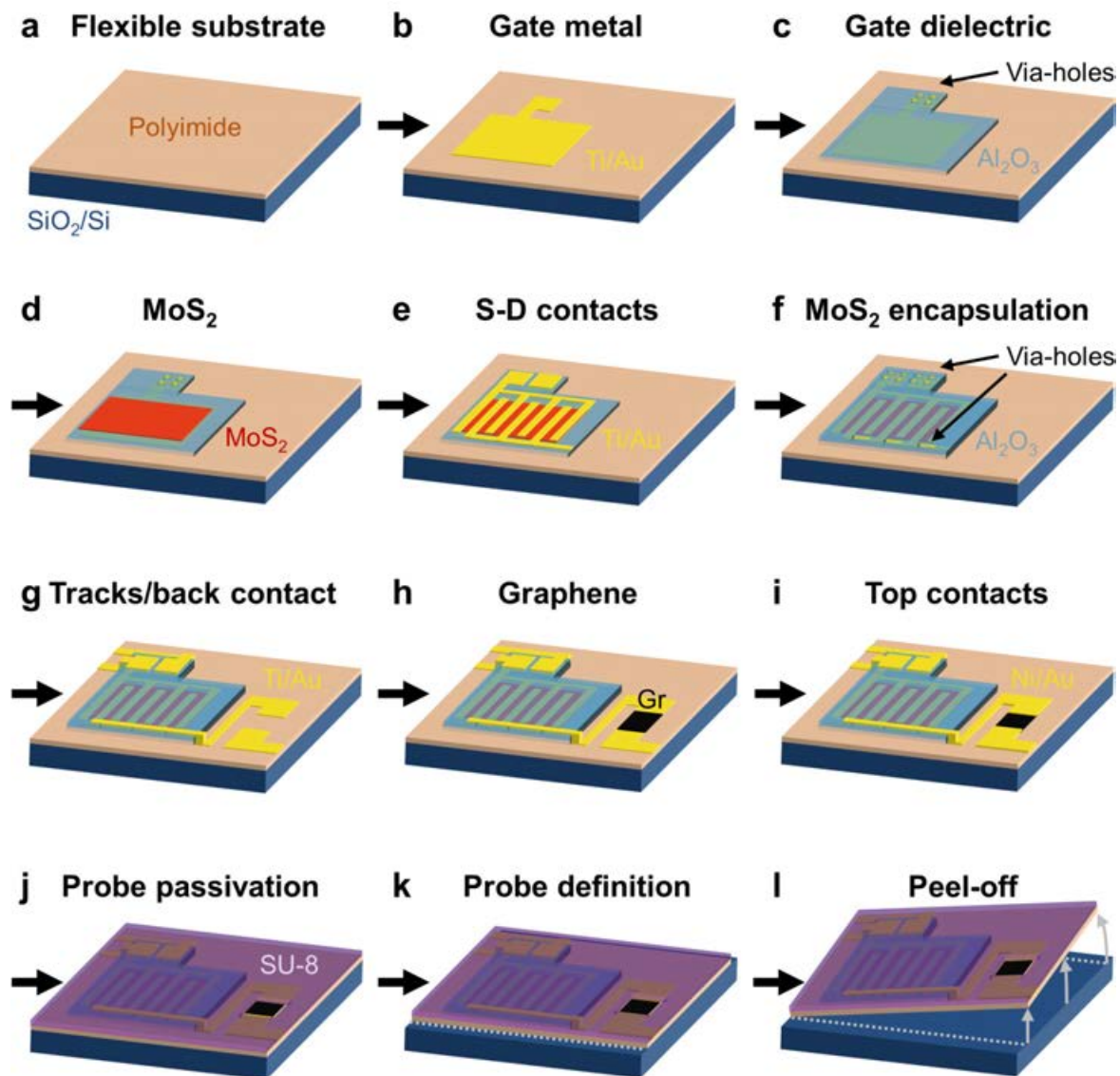
Figure 5.21 Microfabrication of flexible, monolithically integrated MoS$_2$-FET/Gr-SGFET hybrid devices. Schematic illustration of fabrication process sequence shown for a MoS$_2$/Gr pixel: **(a)** polyimide deposition by spin-coating and curing on 4 inch SiO$_2$/Si support wafer, **(b)** Ti/Au gate metal deposition by e-beam and lift-off process, **(c)** AlO$_x$ bottom-gate dielectric deposition by ALD, followed by Al wet etch for area definition and via-holes, **(d)** MoS$_2$ transfer and channel definition by RIE, **(e)** deposition of interdigitated Ti/Au source-drain (S-D) top contacts by e-beam and lift-off, **(f)** MoS$_2$ passivation by AlO$_x$ deposition via self-oxidized, e-beam Al seed layer and ALD top-encapsulation, followed by RIE/Al wet etch for area definition and via-holes, **(g)** Ti/Au deposition for metal tracks and graphene bottom-contacts, **(h)** graphene wet transfer and Gr-SGFET sensor area definition by RIE, **(i)** Ni/Au deposition for graphene top-sandwich-contact, **(j)** probe passivation by spin-coating and curing of SU-8, **(k)** probe definition by deep RIE, and **(l)** peeling of finalized device from the support wafer.

MoS$_2$ is patterned using a photolithghraphy mask on top of PMMA and RIE-etching fully through the PMMA/MoS$_2$ stack in regions next to the channel areas to be defined. In this way, the photoresist/PMMA can be efficiently removed from the MoS$_2$ channel regions by using appropriate solvents (see section 5.1.2). Ti/Au (5 nm/35 nm) source-drain transistor terminals with a highly interdigitated top-contact design ($W/L = 3000$ and 6000) are deposited by e-beam evaporation and lift-off step using a photolithography mask. For high resolution in the interdigitated regions an invertible photoresist is used, allowing for an undercut profile and facilitating the metal lift-off. Then, vacuum annealing at 250 °C is carried out, which may improve contacts to few layer MoS$_2$ [472, 490, 597, 479]. Top-passivation of the MoS2-FETs is realized by an AlO$_x$ seed layer followed by 50 nm ALD-deposited AlO$_x$, as described in section 5.2.1. The oxide passivation layer is patterned and via-holes are opened by RIE and Al wet etch. Ti/Au metal track lines (10 nm/100 nm) are deposited to contact the gate, source and drain of the MoS$_2$-FET and serving as the bottom-contact for the subsequent, coplanar integrated graphene technology level. After preparing the surface by UVO treatment, graphene is transferred by a PMMA-supported wet transfer (see appendix, section D.2), and vacuum annealed at 180 °C for improved adhesion. Then, the graphene channel is patterned by photolithography and O$_2$-plasma etch. A top Ni/Au (20 nm/200 nm) metal layer is added for graphene sandwich contacts onto the existing bottom metal tracks. SU-8 is applied by spin-coating and curing. Finally, the probes are defined by deep reactive ion etching using a photoresist etching mask and the flexible probes can be carefully peeled off the support wafer with a tweezer.

The finalized MoS$_2$-FET/Gr-SGFET ECoG flex probes consist of a broad base with source, drain and gate contact pads for insertion into a ZIF-connector on a printed circuit board (PCB), a long shank with metal tracks, and the probe head with sensor pixels (Fig. 5.22). At this proof-of-concept stage, a 1×8 array arrangement was chosen as technology platform for individual addressing of MoS$_2$ gate and source-drain voltages in the probe head. This design allows to test single pixels and to externally connect functioning pixels from several probes to form larger $m \times n$ arrays, while improvement of device yield during batch production is still under development. Figure 5.22a depicts the highly interdigitated S-D design of the MoS$_2$-FET with $W/L = 6000$ (also $W/L = 3000$ are included on the 4" wafer design) with fingers of 4 μm width and 2 μm pitch shown in the further magnified inset. The AlO$_x$/MoS$_2$/AlO$_x$ islands are pocketed within the flexible probe, as previously shown for flexible graphene devices [598, 38], which was a design choice made after experiencing polymer-oxide probe delamination issues with continuous oxide layers throughout the entire probe area. The graphene
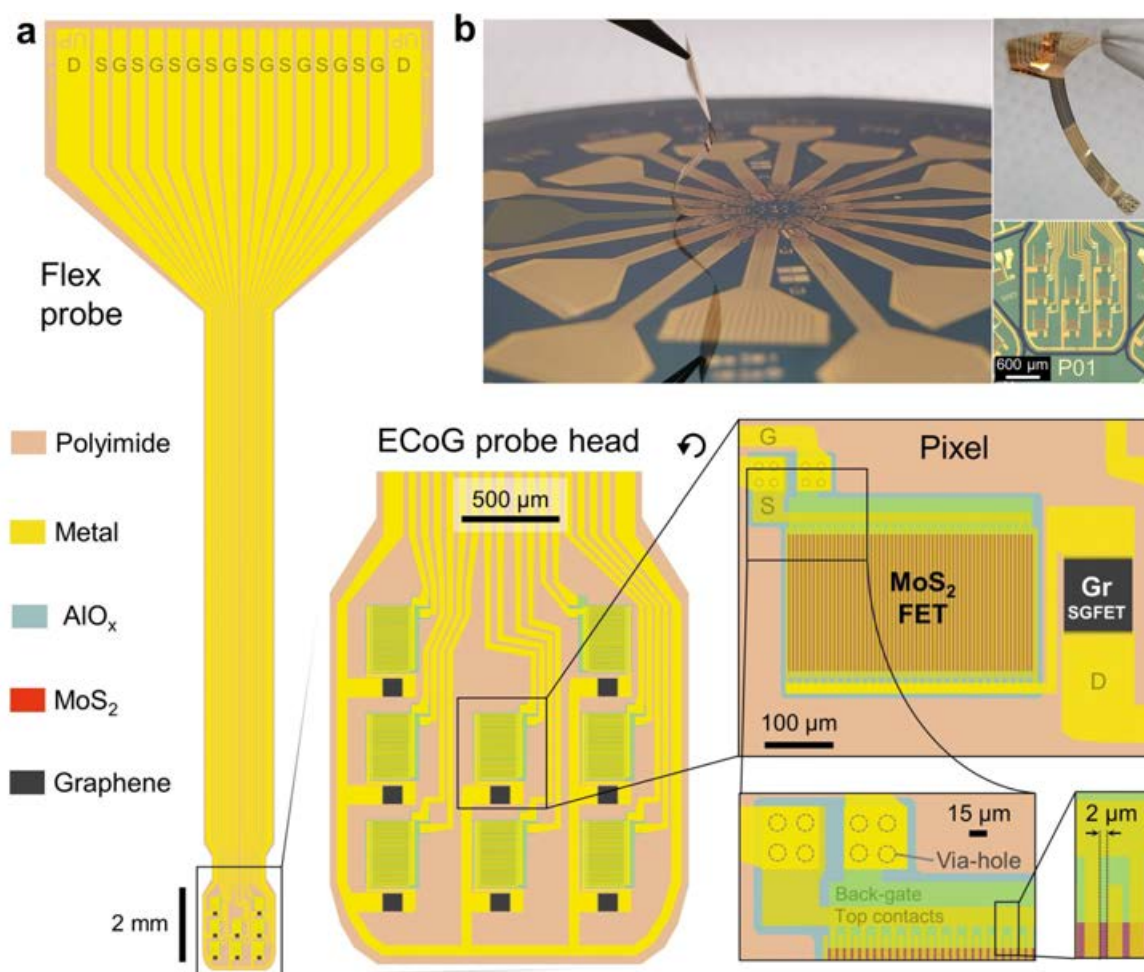
Figure 5.22 Design of flexible MoS$_2$-FET/graphene hybrid probes. **(a)** Schematic illustration of the device design: full probe with connecting part and contacts for source (S), drain (D) and gate (G), ECoG probe head with 8 pixel elements in 1×8 arrangement connected by source/gate tracks and a common drain; pixel composed of a Gr-SGFET neural sensor switched by a MoS$_2$-FET; via-hole region for interconnections of the back-gate and source-drain contacts through the oxide encapsulation of the MoS$_2$-FET, and interdigitated source-drain contact fingers for *on*-current enhancement. **(b)** Flexible probes fabricated on a 4" carrier wafer and probe peel-off. The insets show a peeled-off probe (top) and a magnified view of the probe head (bottom).

microtransistor is formed by a $100 \times 100 \, \mu m^2$ channel area. The overlaying SU-8 passivation layer (with openings at Gr sensors) is omitted for clarity.

Figure 5.22b displays a photograph of the 4" carrier wafer with 18 finalized ECoG devices with their probe heads concentrically grouped around the wafer center within a $\sim 1.5 \times 1.5 \, cm^2$ area. This design was chosen for efficient space use and for optimized yield of covered devices by a single $2 \times 2 \, cm^2$ MoS$_2$ sheet transfer. The photo captures

the peeling process of a probe with a tweezer, highlighting its flexibility, and the eventually released probe shown in the top right inset. The bottom right inset shows an optical microscopy image of a probe head surrounded by MoS$_2$-FET/Gr-SGFET cascode test structures for on-wafer testing.

Figure 5.23 represents cross-sectional TEM images of an AlO$_x$-encapsulated MoS$_2$-FET device on polyimide. The overview image in Figure 5.23a shows a region between source (S) and drain (D) contact fingers with the 2 µm long MoS$_2$ channel. The further magnified images [Fig. 5.23(b-c)] display the layer stack in agreement with the chemical profile measured by EDX (Fig. 5.23d). Insets in Fig. 5.23b show the intact ∼3L MoS$_2$ film, but also reveal delaminated MoS$_2$ layers in some regions.
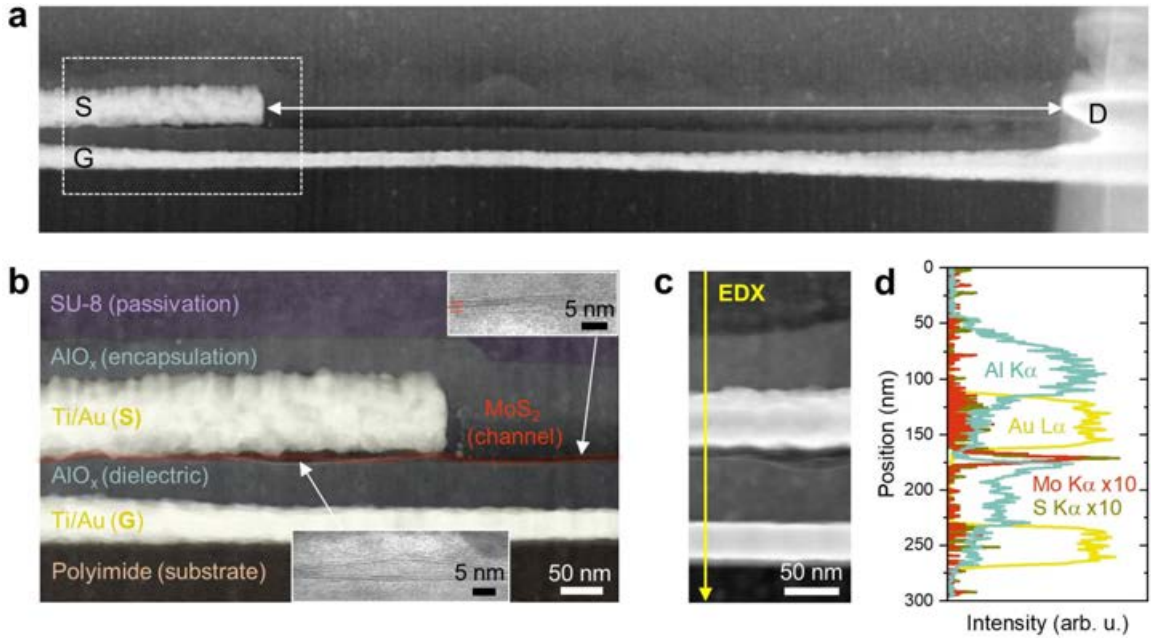
Figure 5.23 TEM cross-section of AlO$_x$-encapsulated MoS$_2$-FET on polyimide. **(a)** STEM overview image of FIB-prepared lamella showing the back-gated FET structure between source (S) and drain (D) contact fingers. **(b)** Magnified, false-colored STEM image of the source contact region with all layers. Insets show magnified regions of intact and partly delaminating ∼3L MoS$_2$ in a void underneath the Ti/Au contact. **(c)** Magnified image of the SU-8/AlO$_x$/Au/Ti/MoS$_2$/AlO$_x$/Au/Ti/polyimide stack region with corresponding **(d)** chemical analysis line profile by EDX.

5.4.2   Proof-of-concept of pixel and multiplexed operation

For validation of single pixel operation of the MoS$_2$-FET/Gr-SGFET cascode, on-wafer test structures were initially measured in dry conditions without applying a solution

gate voltage ($V_{G,Gr}$ floating) of the Gr-SGFET for characterization of the MoS$_2$-FET transfer curve and *on*-current level validation of the cascode. For this purpose, separate drain contact pads allow current measurement through the MoS$_2$-FET without and with the graphene channel in series, as shown in Fig. 5.24a. The resulting MoS$_2$ transfer curves measured at a typical Gr-SGFET source-drain operation voltage of $V_{DS} = 0.05\,\text{V}$ [12] exhibit low *off*-current levels in the nA range and sufficiently high *on/off*-ratios $> 10^3$ for switching operation. The transfer curves are fairly similar except for the deviation in the on-state region (Fig. 5.24b), where the *on*-current (resistance) at +9V decreases (increases) from $15\,\mu\text{A}$ ($3.3\,\text{k}\Omega$) to $7\,\mu\text{A}$ ($7.5\,\text{k}\Omega$) with the added graphene channel. This shows that despite the high intrinsic resistivity of the nanocrystalline MoS$_2$-FET channel ($\sim 9.9\,\text{M}\Omega\,\mu\text{m}$), the implementation of a highly interdigitated source-drain design ($W/L = 3000$) allows the MoS$_2$-FET to drive sufficiently high *on*-currents. The cascode device shown in Fig. 5.24 is limited by the resistivity of the graphene channel. From a device perspective, suitable current levels of typically tens of µA required for Gr-SGFET neural sensing operation [12, 581, 599] can be achieved with the current MoS$_2$ technology. Nevertheless, from a material perspective, the MoS$_2$-FET performance towards higher *on*-state conductivity and steeper SS for lower voltage switching can be enhanced by, for instance, improving the MoS$_2$ channel/interface quality as well as by contact engineering; this will also enable a further reduced area footprint of the MoS$_2$-FETs for high-density ECoG integration.

Furthermore, pixel on/off operation and *in vitro* solution-gated I_{DS}-current modulation of a flexible MoS$_2$-FET/Gr-SGFET hybrid sensor was characterized, for which an ECoG probe was inserted into a ZIF-connector on a rigid PCB and wired to custom-built electronics and a commercial measurement system (National Instruments USB-6363) for MoS$_2$ gate bias control and data acquisition. The pixel was switched between *on*- and *off*-state by $V_{G,MoS2} = \pm 9\,\text{V}$, from which a switching time of $\sim 4\,\mu\text{s}$ could be extracted from the stabilization time of the voltage drop measured across the MoS$_2$-FET in its *off*-state (Fig. 5.24d). From this switching time a maximum single pixel on/off cycle sampling frequency of $125\,\text{kHz}$ is expected allowing typical kHz sampling frequencies required for multiplexed operation. This fast response is expected to be further improved with better MoS$_2$ quality, as it was shown for pulse-switched, flexible devices using exfoliated MoS$_2$ with switching times even down to $\sim 0.25\,\mu\text{s}$ [600], which would theoretically allow $2\,\text{MHz}$ single pixel on/off sampling. For testing the sensor function *in vitro* the ECoG probe head was placed into $10\,\text{mM}$ PBS electrolyte solution on an agar medium and Gr-SGFETs were gated by a wire electrode (Fig. 5.24c). While in the pixel *off*-state no signal is measured (black flatline in Fig. 5.24e), in

the *on*-state the graphene $I_{DS} - V_{G,Gr}$ transfer curve (blue line, Fig. 5.24e) can be modulated by sweeping the liquid-gate potential. Typical ambipolar behaviour of the graphene channel can be observed with a minimum of free charge carriers, thus minimum of conductivity, where the gate voltage reaches the so-called charge neutrality point (CNP).
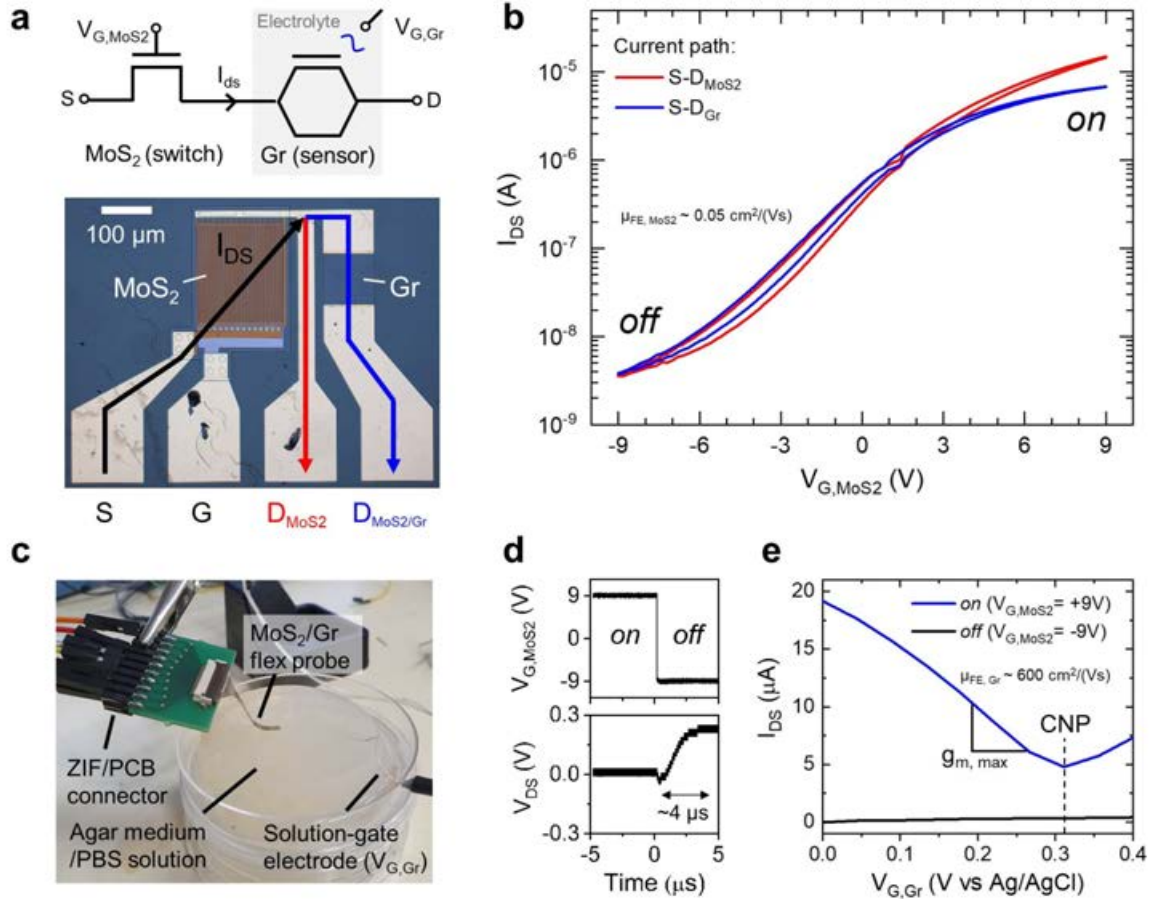
Figure 5.24 Pixel operation of MoS$_2$-FET/Gr-SGFET hybrid sensor. **(a)** Schematic of a MoS$_2$-FET/Gr-SGFET pixel and microscope image of a test structure ($W/L = 3000$) containing contact pads for source (S), MoS$_2$ gate (G), and drain allowing a I_{DS} current path without (D_{MoS2}, red) or with a serially connected Gr-SGFET ($D_{MoS2/Gr}$, blue). **(b)** Transfer curve of MoS$_2$-FET showing switching behaviour with on/off-current ratio $> 10^3$ within the characterized $\pm 9V$ working range. Transfer curves were measured for $V_{DS} = 0.05\,\text{V}$ at a sweeping rate of $0.2\,\text{V s}$. **(c)** Photograph of measurement setup for *in vitro* device testing on agar medium/phosphate buffer saline (PBS), where a potential $V_{G,Gr}$ can be applied by a solution-gate electrode. **(d)** Transient response of MoS$_2$-FET switching from *on* to *off*-state, showing a V_{DS}-stabilization time of around $4\,\mu\text{s}$. e) I_{DS}-current modulation by sweeping the solution-gate voltage $V_{G,Gr}$. The pixel can be switched *on* (blue curve) or *off* (black curve) by the MoS$_2$-FET. The charge neutrality point (CNP) and slope of maximum transconductance are indicated.

The CNP corresponds to a bias point where the Fermi level is at the Dirac point, which is the meeting point of the valence and conduction band in the cone-like graphene band structure. A $V_{G,Gr}$-controlled Fermi level shift with respect to the Dirac point induces an increased electron (hole) charge carrier density and increased n-type (p-type) conductivity [12]. The measured CNP position around $0.3\,\text{V}$ (Fig. 5.24e) depends on various factors, such as the graphene doping level from sheet defects, graphene–substrate interactions, microfabrication residues [601], the electrochemical potential of the reference electrode, and the electrolyte properties [12]. The maximum transconductance is $g_m \sim 6 \times 10^{-5}\,\text{S}$ from which a field-effect mobility of $\mu_{FE,Gr}$ $\sim 600\,\text{cm}^2\,\text{V}^{-1}\,\text{s}^{-1}$ can be estimated by assuming a EDL-capacitance of $2\,\mu\text{F}\,\text{cm}^{-2}$, which is in the typical order of magnitude for CVD-graphene SGFETs on polyimide substrate with non-optimized contacts [12, 473]. In summary, fast on/off pixel switching and sensing operation by an external electric field potential has been demonstrated *in vitro*.

In a next step, sequential switching between pixels on the ECoG probe is performed to show time-division multiplexed operation at baseline current ($V_{DS} = 50\,\text{mV}$). Although the probe contains 8 pixels per probe, due to fabrication yield issues, only 5 functional pixels are represented here to demonstrate switching in a 1×5 configuration (Fig. 5.25a), in which the 5 selected columns were successively addressed by the column selector in a cyclic manner at a sampling rate of $500\,\text{kHz}$ and taking 100 samples per column, as illustrated in Fig. 5.25b. Figure 5.25c shows the sequentially switched on/off column selector bias (upper panel) and the corresponding, temporal I_{DS} current read out for sequential, discrete periods of $20\,\mu\text{s}$ (bottom panel). The transient *on*-switching response for columns #1 and #7 can be explained by switching through non-functional pixels on the 8-pixel probe and re-establishing the *on*-current, whereas the columns #2/#3/#4 succesively addressed in the row show quickly recovering blips upon channel switching and then maintain a constant drive current. Each column shows repeated channel recordings for 100 multiplexing cycles (identical curves are overlaid in the graph), proving reliable and reproducible switching behaviour. The "extraction interval" (highlighted in grey) in the current-stabilized regions is defined for data recording. In Fig. 5.25d the five active channels were continuously sampled by recording the averaged signal from the extraction intervall at an effective sampling frequency of $0.5\,\text{kHz}$ during $90\,\text{s}$. Although small variations ($< 5\,\mu\text{A}$) can be observed in the *on*-current levels between different pixel columns, explainable by variations in MoS$_2$ or Gr sheet conductivity from the device fabrication process [581], overall, constant currents over time in absence of external stimulation provide a stable baseline signal for reliable, active neural recordings. Furthermore, the internally multiplexed,

on-site MoS$_2$/Gr-SGFET array configuration showed reduced floor noise compared to an externally multiplexed Gr-SGFET array configuration, as shown by power spectral density measurements in a range from $1 - 200$ Hz (see appendix, Fig. D18). Reduction of noise sources is important for high-fidelity recordings.
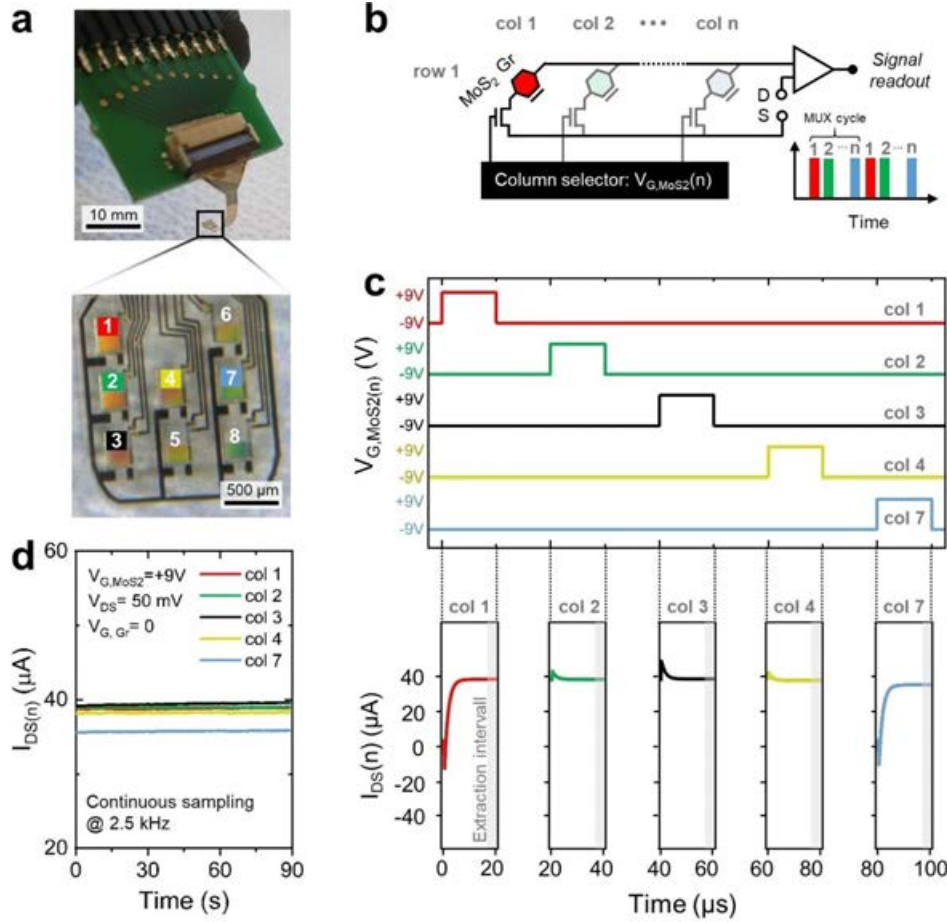
Figure 5.25 Multiplexed operation of flexible MoS$_2$-FET/Gr-SGFET hybrid sensor array. **(a)** Photograph of flexible probe with and magnified image of the probe head from which five pixel columns are selected as devices under test (#1, #2, #3, #4, #7; highlighted by colors). **(b)** Schematic of a generalized MoS$_2$-FET/Gr-SGFET sensor array in $1 \times n$ arrangement; Gr-SGFETs arranged in a single row of pixel columns are individually addressed by on-site MoS$_2$-FET switching via $V_{G,MoS2(n)} = \pm 9$ V gate biasing and connected by a common drain (D) with continuous row signal read-out. **(c)** Time-division multiplexing by sequential on/off-switching of five selected column pixels (upper panel) and continuous $I_{DS}(n)$ readout in each channel shown over 100 repeated multiplexing cycles at an effective sampling rate of 0.5 kHz per channel for the 100 samples. Readout curves are overlaid in the graphs. Extraction intervals are highlighted in grey from which a stable, averaged signal can be picked for data acquisition. **(d)** Current output from continuous sampling of the averaged signal of the extraction intervals of the five selected columns.

The above discussed multiplexed operation was carried out in dry conditions (in air), as shown in the photograph (Fig. 5.25b) because rapid device degradation within seconds to minutes could be observed for device operation in PBS solution. Current stability issues may arise from pin-holes and interfacial delamination in the polymeric probe passivation, polymers prone to water-uptake and soaking along weakened interfaces, and accelerated failure due to voltage differential between powered metal tracks, such as the high $\pm 9\,$V potential supplied to MoS$_2$ gate tracks exposed to penetrating liquid [602]. Failure mode assessment by cross-sectional SEM and TEM analysis showed that even dry-tested probes revealed interfacial delamination in certain probe areas (see Fig. 5.23 and appendix, Fig. D17). It is suspected that layer detachment might happen during the probe peel-off from the carrier wafer due to induced stress/strain, which has been previously reported for on-wafer produced and peeled-off flexible MoS$_2$ devices [603]. Moreover, cross-sectional TEM images revealed buckling and separation of few layer MoS$_2$ beneath source-drain contacts Fig. 5.23. Although the FIB sample preparation may have caused these defects [46], the observation of these defects may explain performance degradation and yield of functional devices per probe/wafer of $\sim 55\,\%$.

At this point, fabrication yield issues and common engineering challenges of flexible electronic devices must be overcome [588, 604], for which a list of suggested mitigation strategies to currently occuring problems can be found in the appendix (table D6). This roadmap includes further improvements of the device design, fabrication process and interface engineering, aiming at a technology for low-voltage switchable MoS$_2$-FETs, high interfacial toughness flexible devices with hermetic, long-term biostable packaging. This technology can be used for *in vivo* testing of scaled, MoS$_2$ on-site multiplexed Gr-SGFET microtransistor ECoG probes.

5.5   Summary

This chapter has summarized the intensive efforts on the technology development for scaled fabrication of high-performance, flexible 2D FETs produced from MOCVD-grown MoS$_2$ thin films. By using spectroscopic and electrical analysis to monitor material interface quality along the fabrication sequence and electrical performance of finalized devices, manufacturing processes were established for the fabrication of various FET architectures, such as residue-free MoS$_2$ layer transfer and AlO$_x$-oxide dielectric integration. Liquid-gated FETs were initially presented as an efficient platform for MoS$_2$ thin film benchmarking, helping to assess the importance of an optimized MOCVD

process yielding continuous MoS_2 channels with reduced C incorporation and enhanced grain sizes. Afterwards, more complex solid-gated FETs and their translation from Si to polyimide substrates have been presented to demonstrate the realization of flexible MoS_2-FETs. Despite the currently still improvable device performance limited by MOCVD MoS_2 channel and oxide interface quality, this technology has potential to be used in a variety of electronic applications requiring flexible, integrated switching circuitry, such as high channel count neural sensing devices. As a proof-of-concept, MoS_2-TFT matrices were monolithically integrated as on-site switches to graphene neural sensor arrays on wafer-scale, flexible polymide-supported ECoG probes; basic pixel multiplexing and current modulation in Gr-SGFETs by an external electrical bias were demonstrated *in vitro*. Current challenges of device stability were highlighted and mitigation strategies were discussed, providing a technological roadmap for conformal, flexible electronics with prospective *in vivo* applications. Despite the need for further technology maturation and robustness, this proof-of-concept lays the foundation for a new generation of actively addressable, crosstalk-reduced, high density and high channel count neural interface devices based on 2D materials.

Chapter 6

Conclusions & Outlook

6.1 Main outcomes and accomplishments

This thesis has contributed to the development of a 2D MoS$_2$ thin film technology, covering from the scalable synthesis by MOCVD, over the characterization of film properties by extensive metrology (SEM, AFM, TEM, Raman, PL, XPS, EDX, RGA, GIXRD, RHEED) to the final integration into flexible, proof-of-concept electronic devices. This work has significant implications for the future development of 2D semiconductor-based technologies and their applications.

The following is a list of this dissertation's main achievements and conclusions:

- **Parameter study and optimization of the MOCVD of MoS$_2$ thin films.** The growth of MoS$_2$ thin films was investigated from the nucleation of isolated domains, their lateral growth, until final coalescence and formation of mono- to few layer thin films. In a systematic, empirical optimization process, this involved studying the influence of growth parameters (time, temperature, gas composition, H$_2$ flow etc.) on the thin film morphology (nucleation density, grain size, shape, layer thickness/number), chemical composition, stoichiometry, and the resulting (opto)electronic properties. This has implications for better understanding the complex synthesis-property correlations in 2D TMD systems.

- **The origin, effect and mitigation of carbon incorporation.** The use of organosulfide precursors in the MOCVD of MoS$_2$ thin films enables a less harmful alternative to hydrogen sulfide, but complicates their growth due to possible introduction of carbon impurities stemming from pyrolysis processes

under certain growth conditions. Carbon incorporation poses a challenge for the synthesis of high-quality films, as it can alter their morphology by disturbing the lateral 2D film growth mode, which impacts on their (opto)electronic properties. Use of H_2 was found key to mitigate carbon impurities and to enable the growth of continuous mono- to few layer MoS_2 thin films with improved properties for transistor applications.

- **Grain size enhancement.** Strategies of grain size controlled/enhanced MoS_2 thin films by alkali-assisted growth (use of NaCl and catalytic soda-lime glass substrates) and by using low growth rates were investigated. While the alkali-assisted approach provides a reaction route through volatile $Na_xMo_yO_z$ reaction intermediates with increased diffusivity [], the low growth rate approach controlled by ultra-low Mo precursor supply enables longer Mo adatom diffusion length on the substrate surface. Both methods have implications for the reduction of nucleation density and grain size defect densities in polycrystalline MoS_2 thin films.

- **Understanding the role of the growth substrate and epitaxy.** The use of technologically relevant and commercially available wafer substrates is important when developing a scalable thin film manufacturing process. The growth on amorphous substrates (e.g. SiO_2, soda-lime glass) results in polycrystalline MoS_2 films prone to induce mis-orientation grain boundaries; the choice of crystalline substrates (e.g. sapphire) on the other hand, can enable substrate-aligned domain epitaxy. A characterization framework combining microscopic and grazing angle diffraction techniques was established. This allowed to determine in-plane, film-substrate orientational relationships and dispersion as figures of merit for epitaxial film quality. The crystal-symmetry-related formation of anti-parallel domains resulting in anti-phase boundaries upon coalescence was identified as a major challenge for epitaxial growth. Notably, substrate surface preparation and growth conditions were found to play an important role in controlling the orientation-selective van der Waals heteroepitaxy as a route towards wafer-scale, single-crystalline thin films.

- **Residue-free layer transfer.** Wet and semi-dry manual transfer techniques were compared and a process based on a sacrifical polymer support and thermal release tape (TRT) was studied for the cm-scale transfer from growth to target wafers. As interface cleanliness of 2D semiconductors is critical to preserve their layer properties, the removal of processing residues is of paramount importance. Polymer-solvent pairs for sacrificial polymer and its removal were studied;

PMMA/Remover PG was identified as a more promising combination than the widely used PMMA/acetone pair, according to morphological characterization.

- **MoS$_2$ integration and oxide encapsulation through seed layer strategy.** The industry-compatible, standard dielectric integration by ALD applied to 2D materials poses a challenge due to the inert nature of 2D material basal planes. Therefore, deposition of a few nm-thick seed layer prior ALD was studied for integration of AlO$_x$ back-gated and encapsulated MoS$_2$-FETs. Nevertheless, it was shown that the current technology is affecting the optical and electronic properties of MoS$_2$ by high interfacial trap densities ($D_{IT} > 10^{13}$ cm^{-2} eV^{-1}), for which a hypothetical band diagram model was developed based on spectroscopic analyses.

- **Development and benchmark of MoS$_2$ transistors.** Several MoS$_2$ FET generations of liquid and solid-gated architectures were fabricated, including the successful translation from rigid to flexible substrates. Electrical transfer curve characterization and benchmark of transistors using MoS$_2$ with different film properties were performed.

- **Proof-of-concept of MoS$_2$-multiplexed, flexible neural interface devices.** MoS$_2$-FET-switches monolithically integrated into a 1×8 matrix of graphene-based neural sensor on polymide-based ECoG arrays were fabricated in a wafer-scale, clean room batch process. The pixel and multiplexed device operation was validated in dry and *in vitro* conditions.

6.2   Outlook for 2D electronics

The large-area synthesis and integration of atomically-thin 2D TMD semiconductors, such as MoS$_2$, has enabled unprecedented opportunities in the field of nanoelectronics. This includes the promise of ultra-thin, high on/off, low-power transistors for continued feature size downscaling to the atomic limit in integrated circuits beyond conventional Si CMOS. Furthermore, ultra-thin 2D TFT pixel addressing matrices may provide benefit for various sensing or display applications, with the additional attribute of mechanical flexibility for foldable and wearable devices. The presented proof-of-concept of an integrated MoS$_2$-TFT matrix applied in a multiplexed neural interface technology can pave the way for future development of high-density, high channel count neural interface devices [581, 583, 605].

Despite the remarkable progress already achieved for 2D TMDs in electronic devices, they are still lacking behind their predicted performance potential, such as reaching the theoretical field-effect mobility of $\sim 400\,\mathrm{cm^2\,V^{-1}\,s^{-1}}$ [102] in the case of monolayer MoS$_2$. Ultimately, from an applied research and commercializaton perspective, the success of 2D semiconductors and their widespread implementation in commercial, next-generation electronic devices will critically depend on maturation of scalable synthesis, such as by MOCVD and epitaxy, and improved device integration.

In terms of large-area MOCVD of TMDs, challenges to overcome include:

- Controlling layer thickness/number and layer-by-layer epitaxy. In particular, difficulties arise from bilayer nucleation before closure of the primary layer [404, 197, 48, 234] and at the frontier between first layer heteroepitaxy and few layer homoepitaxy, where stacking faults become prominent defects [446, 254]. Strategies to address these issues may include time- and precursor-flux-controlled ripening [197, 322, 320], temperature- and etching gas-controlled island layer back-etching [291, 323, 450], or substrate step-height-guided layer number control [248, 407].

- Improving crystal quality by avoiding undesired grain boundary defects that impair transport properties. This can be achieved by enhancing grain size in polycrystalline thin films or by single-crystal heteroepitaxy on crystalline wafer substrates. In the heteroepitaxy approach, the great challenge is to break the symmetry of equivalent anti-parallel orientations of the non-centrosymmetric MoS$_2$ domains [397]; this may include the use of low-symmetry substrates [253, 242] and/or step-edge guided epitaxy [48, 248, 407]. In this context, the optimal growth and substrate surface conditions affecting the orientation-selective van der Waals epitaxy still must be better understood [259]; in particular, the exact criteria inducing step-guided nucleation for controlled unidirectional growth are still to be fully harnessed [259, 397, 407, 248]. Further research into hydrogen-activated TMD-edge coupling may be promising in this direction [259, 414, 411]. It is clear that the control of surface morphology, termination, passivation and step engineering are key to substrate preparation and wafer-scale epitaxy [241, 384, 406, 606, 259, 314]. For the case of unidirectional domain growth, the problem of slightly offset domains creating translational grain boundary defects remains to be addressed [48, 261].

- Improving crystal quality by engineering point defects [607, 304, 539, 324, 383, 250] that are highly dependent on the growth conditions, such as temperature, pressure and precursor ratio [310, 354, 608].

- Gaining advanced control over multiple-source heterostructure and superlattice growth [195], alloying [292] and substitutional doping [72, 293, 609, 610] to tune TMD thin films by benefiting from MOCVD's outstanding process control and versatility [203]. This may allow to tailor bandgaps [292] and FET characteristic, such as the threshold voltage or n/p-type behaviour [73, 609, 610, 611]

- Developing and finding optimal (volatile, thermally stable, non-contaminating, etc., see section 2.2.2) precursors, which will requiring intensified efforts of chemists and MOCVD engineers. For example, for high temperature MOCVD processes, research into novel, volatile, chelated transition-metal precursors with suitable decomposition pathways [612, 613] that provide higher thermal stability than the widely used hexacarbonyls may be desirable.

- Improving film purity for electronic-grade 2D semiconductors, which is highly dependent on the precursor selection, purity and growth conditions [239, 234].

- Advancing reactor technology for industry-scale and high throughput TMD production, such as in showerhead and planetary type reactors [167, 197, 170, 404, 296]. Cold-wall reactors may be preferred compared to hot-wall reactors to handle issues arising from early precursor decomposition and concentration gradients [190, 237, 236]. Wafer-scale uniformity can be addressed by wafer rotation to average out deposition gradients and may be guided by simulation of reactor flow dynamics [236, 453]. Notably, reactor technology has seen a clear push from thin film deposition equipment manufacturers in recent years, such as AIXTRON, CVD EQUIPMENT CORPORATION/FIRSTNANO or OXFORD INSTRUMENTS, signaling fast adoption and industry interest.

- Low-temperature synthesis avoiding transfer processes for back-end of line TMD integration [614, 457, 458] and direct growth onto flexible substrates [459, 237], in particular in the realm of flexible electronics. This remains to be a very challenging task as thermal energy is involved in chemical dissociation processes and required for accelerated surface kinetics during crystallization of high-quality films. Plasma-enhanced growth approaches [615, 616, 617, 618], reaction routes involving high-volatility/diffusivity precursors [213] and non-contaminating, catalytic growth promotors [614, 368, 375] may be subject of further research in this direction.

In terms of integration for high-performance nanoelectronic devices, challenges to overcome include:

- Ensuring high-quality, dangling-bond-free van der Waals interfaces to 2D semiconductors. This includes the quest of finding scalable encapsulation approaches and compatible dielectric materials [59, 64, 61]. The latter demands high-quality insulators with stringent requirements, including low gate leakage currents ($\lesssim 10^{-2}$ A cm^{-2}), low density of interface traps ($D_{IT} \lesssim 10^{10}$ cm^{-2} eV^{-1}) and border traps ($D_{OT} \lesssim 10^{17}$ cm^{-3} eV^{-1}), and high dielectric strength ($\gtrsim 10$ MV cm^{-1}) [61].

- Contact engineering by finding suitable contact materials with reduced Fermi-level pinning and (ideally zero-height) Schottky barriers, as well as non-damaging, clean integration processes [66, 68] for ultra-low contact resistance ($\lesssim 100$ Ω μm [285, 17]). Promising result approaching these values have been recently achieved by ohmic bismuth contacts [69] and thermally stable Sb_2Te_3 contacts [619]. Furthermore, contact engineering has allowed *n*- [68] and *p*-type [620] doping enabling inverter designs necessary for 2D digital logic.

- Developing scalable, 2D materials-adapted fabrication routes for automatized, reliable layer transfer [16, 51, 53, 46, 52] and ensuring clean interfaces during lithography by suitable solvents [55], and innovative fabrication routes [56].

- Mechanical device integrity arising from weakly van der Waals coupled material systems requires to mitigate their tendency for delamination [46, 621]. This ease of delamination creates a major challenge not only during the course of material processing and device fabrication, but also for the long-term stability and reliability of the final device; in particular, the endurance of flexible devices under repeated bending stress needs critical validation. Device engineering for improved interlayer adhesion and toughened 2D interfaces by novel encapsulation strategies and material innovation is needed [622] (also see appendix, table D6)

Due to these manifold challenges the path to commercialization of 2D semiconductors is still hard to predict. Nevertheless, it is important to consider the perspective that the progress from the discovery of new materials to their final product implementation is typically a lengthy process. As for silicon electronics, whose success story has been to a great extent thanks to controlling its excellent interface formed with SiO_2 ($D_{IT} \sim 10^{10}$ cm^{-2} eV^{-1} [286]), the capability of heterogeneous 2D integration with engineered van der Waals interfaces will inevitably decide over realization of practical, high-performance 2D electronic devices. While devices fabricated from MOCVD-grown TMDs are still in an early stage, the MOCVD technique will certainly continue to

play a leading role in wafer batch fabrication and further development of large-area 2D integrated circuits. Its industry-compatible manufacturing aspect is key on the roadmap of establishing 2D semiconductors complementary to and beyond conventional Si CMOS technology [17, 14]. Finally, for the specific target of bioelectronic and medical applications, such as neural interface devices, further advances to ensure their biocompatibility, hermeticity, mechanical integrity and reliable function will be indispensible for safe translation to *in vivo* environments.

6.3 Alternative and new directions

The tunable MoS_2 growth yielding nano- to micron-sized grains (see appendix, Fig. B25) opens various directions for future research and applications [382]. The primary objective of this thesis was to develop MoS_2 transistors for electronics, with a focus on large-grain, single-crystalline thin films with low defect densities for improved electrical transport properties. However, alternative application fields apart from electronics can be thought of. Moreover, small grain size and defect-tailored thin films may be taken advantage of in new ways for data processing in the targeted neural interface devices based on fundamentally different function principles.

Following alternative applications to electronics, MoS_2 is a promising candidate material for heterogeneous (photo)catalysis [109, 110], such as the hydrogen evolution reaction (HER) for water-splitting [111] and sustainable solar-to-hydrogen conversion [623, 624, 625]. This is because MoS_2 has high catalytic activity at its edge and sheet defects [626]. The catalytic activity of synthetic MoS_2 can be further enhanced by increasing the coverage and active edge perimeter in form of nanocrystalline domains [627] and by activating the basal planes via H_2-induced defect creation during growth [628] or via plasma post-treatments [629]. In this context, MOCVD may provide uniform, highly active MoS_2 catalysts on wafer-scale [629, 630, 631]. A preliminary result for demonstration of HER catalysis by MOCVD-grown, nanocrystalline MoS_2 thin films can be found in the appendix in Fig. B26. Furthermore, direct-grown MoS_2 nanocatalysts on graphene (see appendix Fig. B16, Fig. B15) could be investigated as an efficient, noble-metal-free 2D heterostructure catalyst, where graphene acts as the conductive substrate [632, 633, 631].

Following a new direction for application in neural interface devices apart from a TFT-addressing matrix, MoS_2 has been considered for next-generation, neuromorphic computing applications that may enable a paradigm shift in the future of electronics [36,

14]. In contrast to the classical von-Neumann approach, where memory and logic are seperated at the hardware level, the neuromorphic approach merges the memory and logic units for highly energy-efficient and responsive in-memory data processing; it makes use of memristive systems that are bio-inspired, artificial neural networks mimicking the synaptic connectivity of the brain composed of neurons in the brain. The building blocks of these systems are non-volatile, resistive elements switchable between low and high resistive states, so-called "memristors". Several 2D TMD memristive devices [634], including MoS_2 memristors, have been demonstrated and their working principle mediated by structural [635] and grain boundary defects [636] has been explained by filament formation [637, 638], phase change effects [639, 640], and ion-migration-based plasticity [640, 641]. Nanocrystalline MoS_2 memristors based on ion migration have been reported [641] and have shown enhanced resistive switching ratios for monolayer MoS_2 with increased defect densities [642]. Defect-engineered MoS_2 memristors, in which the switching voltage range approaches biological action potentials, will open the possibility of directly interfacing neuromorphic systems with the biological nervous system [637, 643]. Prospectively, MoS_2 memristors patterned into crossbar arrays [644, 645, 35] may therefore have a disruptive potential for hybrid sensing and on-device data processing of neural activity in flexible, energy-efficient, high-density brain-computer-interfaces.

In conclusion, this work not only contributes to the fundamental understanding of scaled crystal growth and device integration of MoS_2 thin films, but also offers a first look to vast and unexplored opportunities for MoS_2 applications in various fields spanning from (opto)electronics, catalysis, energy conversion, neuromorphic computing to neuroprosthetics; which can create the potential of multiple, pivotal technology advancements in the future.

"God made the bulk; surfaces were invented by the devil."

– **WOLFGANG PAULI**

Publications

The work presented in this dissertation has resulted in the following publications.

Peer-reviewed journal contribution:

- **Schaefer, C. M.**; Caicedo Roque, J. M.; Sauthier, G.; Bousquet, J.; Hébert, C.; Sperling, J. R.; Pérez-Tomás, A.; Santiso, J.; del Corro, E.; Garrido, J. A., Carbon Incorporation in MOCVD of MoS2 Thin Films Grown from an Organosulfide Precursor. Chem. Mat. 2021, 33 (12), 4474-4487.

Conference contributions:

- **Schaefer, C. M.**; Hoang, A. T.; Caicedo Roque, J.; Santiso, J.; Ahn, J.-H.; Garrido, J. A. Impact of sapphire surface preparation on the MOCVD of epitaxial MoS2 thin films. **Oral presentation**, Graphene Conference, 12th edition, 5-8 July 2022, Aachen, Germany

- **Schaefer, C. M.**, Hoang, A. T.; Caicedo Roque, J.; Santiso, J.; Ahn, J.-H.; Garrido, J. A., MOCVD of epitaxial MoS2 thin films on c-sapphire, **Poster presentation**, OPERA Training School — Modern directions in epitaxy, 21-24 June 2022, DTU, Lyngby, Denmark

- **Schaefer, C. M.**, Hoang, A. T.; Caicedo Roque, J.; Santiso, J.; Ahn, J.-H.; Garrido, J. A., Sapphire template preparation for epitaxial growth of MoS2 thin films. **Oral presentation**, JPhD Conference – 6th scientific meeting of BNC-b students, 25-26 Nov 2020, Bellaterra, Spain

- **Schaefer, C. M.**, Remacha, L.; Caicedo Roque, J.; Sperling, J. R.; Pérez-Tomás, A.; Santiso, J.; Garrido, J. A., Impact of carbon incorporation on the electronic properties of MOCVD MoS2 transistors. **Oral presentation**, RPGR conference, 12th edition, 10-14 October 2021, Seoul, Rep. of Korea

- **Schaefer, C. M.**, Caicedo Roque, J.; Sauthier, G.; Sperling, J. R.; Pérez-Tomás, A.; Santiso, J.; Del Corro, E.; Garrido, J. A., In situ gas-phase monitoring of pyrolysis and ex situ assessment of carbon contamination in MOCVD grown MoS2 films. **Poster presentation**, Graphene Conference, 10th edition, 19-23 October 2020, Online event

- **Schaefer, C. M.**, Caicedo Roque, J.; Sauthier, G.; Sperling, J. R.; Pérez-Tomás, A.; Santiso, J.; Del Corro, E.; Garrido, J. A., In situ and ex situ assessment of carbon contamination in MoS2 thin films grown by MOCVD. **Oral presentation**, JPhD Online Conference – 5th scientific meeting of BNC-b students, 17-18 Sept 2020, Bellaterra, Spain

- **Schaefer, C. M.**, Caicedo Roque, J.; Del Corro, E.; Bousquet, J.; Santiso, J.; Garrido, J. A., MOCVD-grown MoS2: assessment and reduction of carbon contamination. **Poster presentation**, Graphene Conference, 9th edition, 25-28 June 2019, Rome, Italy

- **Schaefer, C. M.**, Caicedo Roque, J.; Del Corro, E.; Bousquet, J.; Sauthier, G.; Santiso, J.; Garrido, J. A., MOCVD-grown MoS2: assessment and reduction of carbon contamination. **Oral presentation**, JPhD – 4th scientific meeting of BNC-b students, 6-7 June 2019, Bellaterra, Spain

- **Schaefer, C. M.**, Caicedo Roque, J.; Del Corro, E.; Bousquet, J.; Sauthier, G.; Santiso, J.; Garrido, J. A., NaCl-assisted, low pressure MOCVD growth of mono-to few layer MoS2. **Poster presentation**, Graphene Conference, 8th edition, 26-29 June 2018, Dresden, Germany

References

[1] N. Mounet et al. "Two-dimensional materials from high-throughput computational exfoliation of experimentally known compounds". *Nature Nanotechnology* 13.3 (2018), 246–252. DOI: 10.1038/s41565-017-0035-5.

[2] X. M. Li et al. "Graphene and related two-dimensional materials: Structure-property relationships for electronics and optoelectronics". *Applied Physics Reviews* 4.2 (2017), 31. DOI: 10.1063/1.4983646.

[3] J. F. Sierra et al. "Van der Waals heterostructures for spintronics and opto-spintronics". *Nature Nanotechnology* 16.8 (2021), 856–868. DOI: 10.1038/s41565-021-00936-x.

[4] J. R. Schaibley et al. "Valleytronics in 2D materials". *Nature Reviews Materials* 1.11 (2016), 16055. DOI: 10.1038/natrevmats.2016.55.

[5] Y. Cao et al. "Unconventional superconductivity in magic-angle graphene superlattices". *Nature* 556.7699 (2018), 43–50. DOI: 10.1038/nature26160.

[6] W. Cao et al. "2-D Layered Materials for Next-Generation Electronics: Opportunities and Challenges". *Ieee Transactions on Electron Devices* 65.10 (2018), 4109–4121. DOI: 10.1109/ted.2018.2867441.

[7] F. Xia et al. "Two-dimensional material nanophotonics". *Nature Photonics* 8.12 (2014), 899–907. DOI: 10.1038/nphoton.2014.271.

[8] D. Deng et al. "Catalysis with two-dimensional materials and their heterostructures". *Nature Nanotechnology* 11.3 (2016), 218–230. DOI: 10.1038/nnano.2015.340.

[9] Z. Meng et al. "Electrically-Transduced Chemical Sensors Based on Two-Dimensional Nanomaterials". *Chemical Reviews* 119.1 (2019), 478–598. DOI: 10.1021/acs.chemrev.8b00311.

[10] G. M. Marega et al. "Logic-in-memory based on an atomically thin semiconductor". *Nature* 587.7832 (2020), 72–77. DOI: 10.1038/s41586-020-2861-0.

[11] G. Cao et al. "2D Material Based Synaptic Devices for Neuromorphic Computing". *Advanced Functional Materials* 31.4 (2021), 2005443. DOI: https://doi.org/10.1002/adfm.202005443.

[12] C. Hébert et al. "Flexible Graphene Solution-Gated Field-Effect Transistors: Efficient Transducers for Micro-Electrocorticography". *Advanced Functional Materials* (2017), 1703976–n/a. DOI: 10.1002/adfm.201703976.

[13] E. Masvidal-Codina et al. "High-resolution mapping of infraslow cortical brain activity enabled by graphene microtransistors". *Nature Materials* 18.3 (2019), 280–288. DOI: 10.1038/s41563-018-0249-4.

[14] M. C. Lemme et al. "2D materials for future heterogeneous electronics". *Nature Communications* 13.1 (2022), 1392. DOI: 10.1038/s41467-022-29001-4.

[15] D. A. Antoniadis and J. E. Chung. "Physics and technology of ultra short channel MOSFET devices". *International Electron Devices Meeting 1991 [Technical Digest]*. 1991, 21–24. DOI: 10.1109/IEDM.1991.235433.

[16] C. Huyghebaert et al. "2D materials: roadmap to CMOS integration". *2018 IEEE International Electron Devices Meeting (IEDM)*. 2018, 1–22. DOI: 10.1109/IEDM.2018.8614679.

[17] D. Akinwande et al. "Graphene and two-dimensional materials for silicon technology". *Nature* 573.7775 (2019), 507–518. DOI: 10.1038/s41586-019-1573-9.

[18] B. Radisavljevic et al. "Single-layer MoS2 transistors". *Nature Nanotechnology* 6.3 (2011), 147–150. DOI: 10.1038/nnano.2010.279.

[19] B. Radisavljevic and A. Kis. "Reply to 'Measurement of mobility in dual-gated MoS2 transistors'". *Nature Nanotechnology* 8.3 (2013), 147–148. DOI: 10.1038/nnano.2013.31.

[20] C. D. English et al. "Approaching ballistic transport in monolayer MoS2 transistors with self-aligned 10 nm top gates". *2016 IEEE International Electron Devices Meeting (IEDM)*. 2016, 1–5. DOI: 10.1109/IEDM.2016.7838355.

[21] Y.-Y. Chung et al. "First Demonstration of GAA Monolayer-MoS2 Nanosheet nFET with $410\mu A$ μ m ID 1V VD at 40nm gate length". *2022 International Electron Devices Meeting (IEDM)*. 2022, 1–34. DOI: 10.1109/IEDM45625.2022.10019563.

[22] T. More Moore Team. "International Roadmap for Devices and Systems (IRDS™) 2020 Edition". *IEEE* 2020 Update (2020). DOI: https://irds.ieee.org/images/files/pdf/2020/2020IRDS{_}MM.pdf.

[23] X. Huang, C. Liu, and P. Zhou. "2D semiconductors for specific electronic applications: from device to system". *npj 2D Materials and Applications* 6.1 (2022), 51. DOI: 10.1038/s41699-022-00327-3.

[24] Y. Liu, Y. Huang, and X. F. Duan. "Van der Waals integration before and beyond two-dimensional materials". *Nature* 567.7748 (2019), 323–333. DOI: 10.1038/s41586-019-1013-x.

[25] M. Romagnoli et al. "Graphene-based integrated photonics for next-generation datacom and telecom". *Nature Reviews Materials* 3.10 (2018), 392–414. DOI: 10.1038/s41578-018-0040-9.

[26] N. Goel and M. Kumar. "2D Materials for Terahertz Application". *Nano Express* 2.3 (2021), 31001. DOI: 10.1088/2632-959X/ac0d56.

[27] D. Schall et al. "50 GBit/s Photodetectors Based on Wafer-Scale Graphene for Integrated Silicon Photonic Communication Systems". *ACS Photonics* 1.9 (2014), 781–784. DOI: 10.1021/ph5001605.

[28] G. Konstantatos et al. "Hybrid graphene–quantum dot phototransistors with ultrahigh gain". *Nature Nanotechnology* 7.6 (2012), 363–368. DOI: 10.1038/nnano.2012.60.

[29] M. Liu et al. "A graphene-based broadband optical modulator". *Nature* 474.7349 (2011), 64–67. DOI: 10.1038/nature10067.

[30] Y. Yu et al. "Recent advances in wide-spectrum photodetectors based on low-dimensional semiconductors". *Materials Today Electronics* 2 (2022), 100013. DOI: https://doi.org/10.1016/j.mtelec.2022.100013.

[31] S. Parhizkar et al. "Two-Dimensional Platinum Diselenide Waveguide-Integrated Infrared Photodetectors". *ACS Photonics* 9.3 (2022), 859–867. DOI: 10.1021/acsphotonics.1c01517.

[32] D. S. Schneider et al. "Highly Responsive Flexible Photodetectors Based on MOVPE Grown Uniform Few-Layer MoS2". *ACS Photonics* 7.6 (2020), 1388–1395. DOI: 10.1021/acsphotonics.0c00361.

[33] C. Anichini et al. "Chemical sensing with 2D materials". *Chemical Society Reviews* 47.13 (2018), 4860–4908. DOI: 10.1039/C8CS00417J.

[34] M. C. Lemme et al. "Nanoelectromechanical Sensors Based on Suspended 2D Materials". *Research* 2020 (2023). DOI: 10.34133/2020/8748602.

[35] M. Lanza et al. "Resistive Switching Crossbar Arrays Based on Layered Materials". *Advanced Materials* n/a.n/a (2022), 2205402. DOI: https://doi.org/10.1002/adma.202205402.

[36] M. A. Zidan, J. P. Strachan, and W. D. Lu. "The future of electronics based on memristive systems". *Nature Electronics* 1.1 (2018), 22–29. DOI: 10.1038/s41928-017-0006-8.

[37] D. Akinwande et al. "A review on mechanics and mechanical properties of 2D materials-Graphene and beyond". *Extreme Mechanics Letters* 13 (2017), 42–77. DOI: 10.1016/j.eml.2017.01.008.

[38] D. Akinwande, N. Petrone, and J. Hone. "Two-dimensional flexible nanoelectronics". *Nature Communications* 5 (2014), 12. DOI: 10.1038/ncomms6678.

[39] Y. Lee et al. "Graphene-based stretchable/wearable self-powered touch sensor". *Nano Energy* 62 (2019), 259–267. DOI: 10.1016/j.nanoen.2019.05.039.

[40] M. Park et al. "MoS2-Based Tactile Sensor for Electronic Skin Applications". *Advanced Materials* 28.13 (2016), 2556–+. DOI: 10.1002/adma.201505124.

[41] M. Choi et al. "Flexible active-matrix organic light-emitting diode display enabled by MoS2 thin-film transistor". *Science Advances* 4.4 (2018), 7. DOI: 10.1126/sciadv.aas8721.

[42] E. Singh et al. "Flexible Molybdenum Disulfide (MoS2) Atomic Layers for Wearable Electronics and Optoelectronics". *ACS Applied Materials & Interfaces* 11.12 (2019), 11061–11105. DOI: 10.1021/acsami.8b19859.

[43] X. Tang et al. "Flexible brain–computer interfaces". *Nature Electronics* (2023). DOI: 10.1038/s41928-022-00913-9.

[44] A. Bonaccini Calia et al. "Full-bandwidth electrophysiology of seizures and epileptiform activity enabled by flexible graphene microtransistor depth neural probes". *Nature Nanotechnology* 17.3 (2022), 301–309. DOI: 10.1038/s41565-021-01041-9.

[45] S. Das et al. "Transistors based on two-dimensional materials for future integrated circuits". *Nature Electronics* 4.11 (2021), 786–799. DOI: 10.1038/s41928-021-00670-1.

[46] T. Schram et al. "Challenges of Wafer-Scale Integration of 2D Semiconductors for High-Performance Transistor Circuits". *Advanced Materials* n/a.n/a (2022), 2109796. DOI: https://doi.org/10.1002/adma.202109796.

[47] K. Kang et al. "High-mobility three-atom-thick semiconducting films with wafer-scale homogeneity". *Nature* 520.7549 (2015), 656–660. DOI: 10.1038/nature14417.

[48] M. Chubarov et al. "Wafer-Scale Epitaxial Growth of Unidirectional WS2 Monolayers on Sapphire". *ACS Nano* (2021). DOI: 10.1021/acsnano.0c06750.

[49] Z. Lin et al. "Research Update: Recent progress on 2D materials beyond graphene: From ripples, defects, intercalation, and valley dynamics to straintronics and power dissipation". *Apl Materials* 6.8 (2018), 20. DOI: 10.1063/1.5042598.

[50] S. M. Shinde et al. "Surface-Functionalization-Mediated Direct Transfer of Molybdenum Disulfide for Large-Area Flexible Devices". *Advanced Functional Materials* 28.13 (2018), 11. DOI: 10.1002/adfm.201706231.

[51] A. Quellmalz et al. "Large-area integration of two-dimensional materials and their heterostructures by wafer bonding". *Nature Communications* 12.1 (2021), 917. DOI: 10.1038/s41467-021-21136-0.

[52] S. Wittmann et al. "Assessment of Wafer-Level Transfer Techniques of Graphene with Respect to Semiconductor Industry Requirements". *Advanced Materials Technologies* n/a.n/a (2023), 2201587. DOI: https://doi.org/10.1002/admt.202201587.

[53] A. Phommahaxay et al. "The Growing Application Field of Laser Debonding: From Advanced Packaging to Future Nanoelectronics". *2019 International Wafer Level Packaging Conference (IWLPC)*. 2019, 1–8. DOI: 10.23919/IWLPC.2019.8914124.

[54] C. Kim et al. "Damage-free transfer mechanics of 2-dimensional materials: competition between adhesion instability and tensile strain". *NPG Asia Materials* 13.1 (2021), 44. DOI: 10.1038/s41427-021-00311-1.

[55] P.-C. Chen et al. "Effective N-methyl-2-pyrrolidone wet cleaning for fabricating high-performance monolayer MoS2 transistors". *Nano Research* 12.2 (2019), 303–308. DOI: 10.1007/s12274-018-2215-5.

[56] A. Daus et al. "High-performance flexible nanoscale transistors based on transition metal dichalcogenides". *Nature Electronics* 4.7 (2021), 495–501. DOI: 10.1038/s41928-021-00598-6.

[57] A. Leonhardt et al. "Improving MOCVD MoS2 Electrical Performance: Impact of Minimized Water and Air Exposure Conditions". *Ieee Electron Device Letters* 38.11 (2017), 1606–1609. DOI: 10.1109/led.2017.2752424.

[58] A. Leonhardt et al. "Material-Selective Doping of 2D TMDC through AlxOy Encapsulation". *ACS Applied Materials & Interfaces* 11.45 (2019), 42697–42707. DOI: 10.1021/acsami.9b11550.

[59] T. Knobloch et al. "Improving stability in two-dimensional transistors with amorphous gate oxides by Fermi-level tuning". *Nature Electronics* 5.6 (2022), 356–366. DOI: 10.1038/s41928-022-00768-0.

[60] Y. Y. Illarionov et al. "Ultrathin calcium fluoride insulators for two-dimensional field-effect transistors". *Nature Electronics* 2.6 (2019), 230–235. DOI: 10.1038/s41928-019-0256-8.

[61] Y. Y. Illarionov et al. "Insulators for 2D nanoelectronics: the gap to bridge". *Nature Communications* 11.1 (2020), 3385. DOI: 10.1038/s41467-020-16640-8.

[62] M. Rostami Osanloo et al. "Transition-metal nitride halide dielectrics for transition-metal dichalcogenide transistors". *Nanoscale* 14.1 (2022), 157–165. DOI: 10.1039/D1NR05250K.

[63] Y. Y. Illarionov et al. "Improved Hysteresis and Reliability of MoS2 Transistors With High-Quality CVD Growth and Al2O3 Encapsulation". *IEEE Electron Device Letters* 38.12 (2017), 1763–1766. DOI: 10.1109/LED.2017.2768602.

[64] M. Waltl et al. "Perspective of 2D Integrated Electronic Circuits: Scientific Pipe Dream or Disruptive Technology?" *Advanced Materials* n/a.n/a (2022), 2201082. DOI: https://doi.org/10.1002/adma.202201082.

[65] M. Lanza et al. "Yield, variability, reliability, and stability of two-dimensional materials based solid-state electronic devices". *Nature Communications* 11.1 (2020), 5689. DOI: 10.1038/s41467-020-19053-9.

[66] A. Rai et al. "Air Stable Doping and Intrinsic Mobility Enhancement in Monolayer Molybdenum Disulfide by Amorphous Titanium Suboxide Encapsulation". *Nano Letters* 15.7 (2015), 4329–4336. DOI: 10.1021/acs.nanolett.5b00314.

[67] Y. Wang et al. "Van der Waals contacts between three-dimensional metals and two-dimensional semiconductors". *Nature* 568.7750 (2019), 70–+. DOI: 10.1038/s41586-019-1052-3.

[68] Y. Wang and M. Chhowalla. "Making clean electrical contacts on 2D transition metal dichalcogenides". *Nature Reviews Physics* 4.2 (2022), 101–112. DOI: 10.1038/s42254-021-00389-0.

[69] P.-C. Shen et al. "Ultralow contact resistance between semimetal and monolayer semiconductors". *Nature* 593.7858 (2021), 211–217. DOI: 10.1038/s41586-021-03472-9.

[70] H. Sun et al. "Etching of two-dimensional materials". *Materials Today* 42 (2021), 192–213. DOI: https://doi.org/10.1016/j.mattod.2020.09.031.

[71] A. Nipane et al. "Damage-Free Atomic Layer Etch of WSe2: A Platform for Fabricating Clean Two-Dimensional Devices". *ACS Applied Materials & Interfaces* 13.1 (2021), 1930–1942. DOI: 10.1021/acsami.0c18390.

[72] H. Gao et al. "Tuning Electrical Conductance of MoS2 Monolayers through Substitutional Doping". *Nano Letters* 20.6 (2020), 4095–4101. DOI: 10.1021/acs.nanolett.9b05247.

[73] F. Zhang et al. "Carbon doping of WS2 monolayers: Bandgap reduction and p-type doping transport". *Science Advances* 5.5 (2019), 8. DOI: 10.1126/sciadv. aav5003.

[74] D. Wang, X.-B. Li, and H.-B. Sun. "Modulation Doping: A Strategy for 2D Materials Electronics". *Nano Letters* 21.14 (2021), 6298–6303. DOI: 10.1021/acs. nanolett.1c02192.

[75] Q. H. Wang et al. "Electronics and optoelectronics of two-dimensional transition metal dichalcogenides". *Nature Nanotechnology* 7.11 (2012), 699–712. DOI: 10. 1038/nnano.2012.193.

[76] S. Das et al. "Beyond Graphene: Progress in Novel Two-Dimensional Materials and van der Waals Solids". *Annual Review of Materials Research* 45.1 (2015), 1–27. DOI: 10.1146/annurev-matsci-070214-021034.

[77] M. Chhowalla et al. "The chemistry of two-dimensional layered transition metal dichalcogenide nanosheets". *Nature Chemistry* 5.4 (2013), 263–275. DOI: 10.1038/nchem.1589.

[78] A. A. Opalovskij and V. E. Fedorov. "Mixed molybdenum chalcogenides". *Doklady Akademii Nauk SSSR* 163 (1965), 1163–1164.

[79] M. Samadi et al. "Group 6 transition metal dichalcogenide nanomaterials: synthesis, applications and future perspectives". *Nanoscale Horizons* 3.2 (2018), 90–204. DOI: 10.1039/c7nh00137a.

[80] A. Jain et al. "The Materials Project: A materials genome approach to accelerating materials innovation". *APL Materials* 1.1 (2013), 11002. DOI: 10.1063/1. 4812323.

[81] A. Stukowski. "Visualization and analysis of atomistic simulation data with OVITO-the Open Visualization Tool". *Modelling and Simulation in Materials Science and Engineering* 18.1 (2010). DOI: 10.1088/0965-0393/18/1/015012.

[82] T. H. Choudhury et al. "Epitaxial Growth of Two-Dimensional Layered Transition Metal Dichalcogenides". *Annual Review of Materials Research, Vol 50, 2020*. Ed. by D. R. Clarke. Vol. 50. Annual Review of Materials Research. Annual Reviews, 2020, 155–177. DOI: 10.1146/annurev-matsci-090519113456.

[83] W. Mortelmans et al. "Epitaxy of 2D chalcogenides: Aspects and consequences of weak van der Waals coupling". *Applied Materials Today* 22 (2021), 100975. DOI: https://doi.org/10.1016/j.apmt.2021.100975.

[84] A A Opalovskii and V E Fedorov. "MOLYBDENUM CHALCOGENIDES". *Russian Chemical Reviews* 35.3 (1966), 186. DOI: 10.1070/RC1966v035n03ABEH001439.

[85] A. K. Geim and I. V. Grigorieva. "Van der Waals heterostructures". *Nature* 499.7459 (2013), 419–425. DOI: 10.1038/nature12385.

[86] W. Li et al. "Gas Sensors Based on Mechanically Exfoliated MoS2 Nanosheets for Room-Temperature NO2 Detection". *Sensors* 19.9 (2019). DOI: 10.3390/ s19092123.

[87] J. P. Oviedo et al. "In Situ TEM Characterization of Shear-Stress-Induced Interlayer Sliding in the Cross Section View of Molybdenum Disulfide". *ACS Nano* 9.2 (2015), 1543–1551. DOI: 10.1021/nn506052d.

[88] D.-M. Tang et al. "Nanomechanical cleavage of molybdenum disulphide atomic layers". *Nature Communications* 5.1 (2014), 3631. DOI: 10.1038/ncomms4631.

[89] G. Casillas et al. "Elasticity of MoS2 Sheets by Mechanical Deformation Observed by in Situ Electron Microscopy". *The Journal of Physical Chemistry C* 119.1 (2015), 710–715. DOI: 10.1021/jp5093459.

[90] S. Bertolazzi, J. Brivio, and A. Kis. "Stretching and Breaking of Ultrathin MoS2". *ACS Nano* 5.12 (2011), 9703–9709. DOI: 10.1021/nn203879f.

[91] M. Sledzinska et al. "Fracturing of Polycrystalline MoS2 Nanofilms". *ACS Applied Electronic Materials* 2.4 (2020), 1169–1175. DOI: 10.1021/acsaelm.0c00189.

[92] D.-H. Kim et al. "Stretchable and Foldable Silicon Integrated Circuits". *Science* 320.5875 (2008), 507–511. DOI: 10.1126/science.1154367.

[93] J. Viventi et al. "A Conformal, Bio-Interfaced Class of Silicon Electronics for Mapping Cardiac Electrophysiology". *Science Translational Medicine* 2.24 (2010), 22–24. DOI: 10.1126/scitranslmed.3000738.

[94] U. Bhaskar et al. "On-chip tensile testing of nanoscale silicon free-standing beams". *Journal of Materials Research* 27.3 (2012), 571–579. DOI: 10.1557/jmr.2011.340.

[95] J. M. Gere and B. J. Goodno. *Mechanics of materials*. Cengage learning, 2012.

[96] D. Armani, C. Liu, and N. Aluru. "Re-configurable fluid circuits by PDMS elastomer micromachining". *Technical Digest. IEEE International MEMS 99 Conference. Twelfth IEEE International Conference on Micro Electro Mechanical Systems (Cat. No.99CH36291)*. 1999, 222–227. DOI: 10.1109/MEMSYS.1999.746817.

[97] C. Lee et al. "Measurement of the Elastic Properties and Intrinsic Strength of Monolayer Graphene". *Science* 321.5887 (2008), 385–388. DOI: 10.1126/science.1157996.

[98] M. Chhowalla et al. "The chemistry of two-dimensional layered transition metal dichalcogenide nanosheets". *Nature Chemistry* 5.4 (2013), 263–275. DOI: 10.1038/nchem.1589.

[99] A. Splendiani et al. "Emerging Photoluminescence in Monolayer MoS2". *Nano Letters* 10.4 (2010), 1271–1275. DOI: 10.1021/nl903868w.

[100] K. F. Mak et al. "Atomically Thin MoS2: A New Direct-Gap Semiconductor". *Physical Review Letters* 105.13 (2010), 4. DOI: 10.1103/PhysRevLett.105.136805.

[101] K. F. Mak et al. "Control of valley polarization in monolayer MoS2 by optical helicity". *Nature Nanotechnology* 7.8 (2012), 494–498. DOI: 10.1038/nnano.2012.96.

[102] X. Li et al. "Intrinsic electrical transport properties of monolayer silicene and MoS2 from first principles". *Phys. Rev. B* 87.11 (2013), 115418. DOI: 10.1103/PhysRevB.87.115418.

[103] G.-H. Lee et al. "Highly Stable, Dual-Gated MoS2 Transistors Encapsulated by Hexagonal Boron Nitride with Gate-Controllable Contact, Resistance, and Threshold Voltage". *ACS Nano* 9.7 (2015), 7019–7026. DOI: 10.1021/acsnano.5b01341.

[104] J. A. Robinson. "Perspective: 2D for beyond CMOS". *APL Materials* 6.5 (2018), 58202. DOI: 10.1063/1.5022769.

[105] A. Bruix et al. "In Situ Detection of Active Edge Sites in Single-Layer MoS2 Catalysts". *ACS Nano* 9.9 (2015), 9322–9330. DOI: 10.1021/acsnano.5b03199.

[106] A. V. Mashkina and L. N. Khairulina. "Selective Hydrogenation of Diethyl Disulfide to Ethanethiol in the Presence of Sulfide Catalysts". *Kinetics and Catalysis* 43.2 (2002), 261–267. DOI: 10.1023/A:1015380814044.

[107] J. V. Lauritsen et al. "Atomic-scale insight into structure and morphology changes of MoS2 nanoclusters in hydrotreating catalysts". *Journal of Catalysis* 221.2 (200), 510–522. DOI: 10.1016/j.jcat.2003.09.015.

[108] R. V. Mom et al. "In situ observations of an active MoS2 model hydrodesulfurization catalyst". *Nature Communications* 10 (2019), 8. DOI: 10.1038/s41467-019-10526-0.

[109] Q. Fu et al. "2D Transition Metal Dichalcogenides: Design, Modulation, and Challenges in Electrocatalysis". *Advanced Materials* (2020), 24. DOI: 10.1002/adma.201907818.

[110] X. D. Sun et al. "Thin-Layered Photocatalysts". *Advanced Functional Materials* 30.22 (2020), 43. DOI: 10.1002/adfm.201910005.

[111] J. Kibsgaard et al. "Engineering the surface structure of MoS2 to preferentially expose active edge sites for electrocatalysis". *Nature Materials* 11.11 (2012), 963–969. DOI: 10.1038/nmat3439.

[112] J. D. Benck et al. "Amorphous Molybdenum Sulfide Catalysts for Electrochemical Hydrogen Production: Insights into the Origin of their Catalytic Activity". *ACS Catalysis* 2.9 (2012), 1916–1923. DOI: 10.1021/cs300451q.

[113] J. Kibsgaard. "Atomic-scale investigation of MoS2-based hydrotreating model catalysts. A scanning tunneling microscopy studye" (2008).

[114] S. S. Grønborg et al. "Visualizing hydrogen-induced reshaping and edge activation in MoS2 and Co-promoted MoS2 catalyst clusters". *Nature Communications* 9.1 (2018), 2211. DOI: 10.1038/s41467-018-04615-9.

[115] A. Tuxen et al. "An atomic-scale investigation of carbon in MoS2 hydrotreating catalysts sulfided by organosulfur compounds". *Journal of Catalysis* 281.2 (2011), 345–351. DOI: 10.1016/j.jcat.2011.05.018.

[116] H. G. Fuchtbauer et al. "Morphology and Atomic-Scale Structure of MoS2 Nanoclusters Synthesized with Different Sulfiding Agents". *Topics in Catalysis* 57.1-4 (2014), 207–214. DOI: 10.1007/s11244-013-0176-1.

[117] S. Cristol et al. "Theoretical study of the MoS2 (100) surface: A chemical potential analysis of sulfur and hydrogen coverage. 2. Effect of the total pressure on surface stability". *Journal of Physical Chemistry B* 106.22 (2002), 5659–5667. DOI: 10.1021/jp0134603.

[118] A. G. Rajan et al. "Generalized Mechanistic Model for the Chemical Vapor Deposition of 2D Transition Metal Dichalcogenide Monolayers". *ACS Nano* 10.4 (2016), 4330–4344. DOI: 10.1021/acsnano.5b07916.

[119] H. A. Li et al. "Epitaxial Growth of Two-Dimensional Layered Transition-Metal Dichalcogenides: Growth Mechanism, Controllability, and Scalability". *Chemical Reviews* 118.13 (2018), 6134–6150. DOI: 10.1021/acs.chemrev.7b00212.

[120] F. A. Rasmussen and K. S. Thygesen. "Computational 2D Materials Database: Electronic Structure of Transition-Metal Dichalcogenides and Oxides". *The Journal of Physical Chemistry C* 119.23 (2015), 13169–13183. DOI: 10.1021/acs.jpcc.5b02950.

[121] J. Gao et al. "Aging of Transition Metal Dichalcogenide Monolayers". *ACS Nano* 10.2 (2016), 2628–2635. DOI: 10.1021/acsnano.5b07677.

[122] S. Park et al. "Operando Study of Thermal Oxidation of Monolayer MoS2". *Advanced Science* 8.9 (2021), 2002768. DOI: https://doi.org/10.1002/advs.202002768.

[123] S. Pace et al. "Thermal stability of monolayer WS2 in BEOL conditions". *Journal of Physics: Materials* 4.2 (2021), 24002. DOI: 10.1088/2515-7639/abd4f2.

[124] G. Mirabelli et al. "Air sensitivity of MoS2, MoSe2, MoTe2, HfS2, and HfSe2". *Journal of Applied Physics* 120.12 (2016), 9. DOI: 10.1063/1.4963290.

[125] P. Chen et al. "Thermal Degradation of Monolayer MoS2 on SrTiO3 Supports". *The Journal of Physical Chemistry C* 123.6 (2019), 3876–3885. DOI: 10.1021/acs.jpcc.8b11298.

[126] ASM International. *ASM alloy phase diagram database.* Materials Park, OH (USA), 2006.

[127] F. Reale, K. Sharda, and C. Mattevi. "From bulk crystals to atomically thin layers of group VI-transition metal dichalcogenides vapour phase synthesis". *Applied Materials Today* 3 (2016), 11–22. DOI: https://doi.org/10.1016/j.apmt.2015.12.003.

[128] N. Briggs et al. "A roadmap for electronic grade 2D materials". *2d Materials* 6.2 (2019), 23. DOI: 10.1088/2053-1583/aaf836.

[129] P. Joensen, R. F. Frindt, and S. Morrison. "Single-layer MoS2". *Materials Research Bulletin* 21.4 (1986), 457–461. DOI: https://doi.org/10.1016/0025-5408(86)90011-5.

[130] J. N. Coleman et al. "Two-Dimensional Nanosheets Produced by Liquid Exfoliation of Layered Materials". *Science* 331.6017 (2011), 568–571. DOI: 10.1126/science.1194975.

[131] C. Backes, et., and al. "Production and processing of graphene and related materials". *2d Materials* 7.2 (2020), 282. DOI: 10.1088/2053-1583/ab1e0a.

[132] K. S. Novoselov et al. "Two-dimensional atomic crystals". *Proceedings of the National Academy of Sciences of the United States of America* 102.30 (2005), 10451 LP –10453. DOI: 10.1073/pnas.0502848102.

[133] A. Castellanos-Gomez et al. "Deterministic transfer of two-dimensional materials by all-dry viscoelastic stamping". *2d Materials* 1.1 (2014), 8. DOI: 10.1088/2053-1583/1/1/011002.

[134] S. E. Skrabalak and K. S. Suslick. "Porous MoS2 Synthesized by Ultrasonic Spray Pyrolysis". *Journal of the American Chemical Society* 127.28 (2005), 9990–9991. DOI: 10.1021/ja051654g.

[135] X. X. Gao, G. Bian, and J. Zhu. "Electronics from solution-processed 2D semiconductors". *Journal of Materials Chemistry C* 7.41 (2019), 12835–12861. DOI: 10.1039/c9tc03935j.

[136] S. Ippolito et al. "Covalently interconnected transition metal dichalcogenide networks via defect engineering for high-performance electronic devices". *Nature Nanotechnology* 16.5 (2021), 592–598. DOI: 10.1038/s41565-021-00857-9.

[137] J. Mercier. "Recent developments in chemical vapor transport in closed tubes". *Journal of Crystal Growth* 56.2 (1982), 235–244. DOI: https://doi.org/10.1016/0022-0248(82)90439-0.

[138] A. A. Al-Hilli and B. L. Evans. "The preparation and properties of transition metal dichalcogenide single crystals". *Journal of Crystal Growth* 15.2 (1972), 93–101. DOI: https://doi.org/10.1016/0022-0248(72)90129-7.

[139] M. K. Agarwal, H. B. Patel, and K. Nagireddy. "Growth of single crystals of WSe2 by sublimation method". *Journal of Crystal Growth* 41.1 (1977), 84–86. DOI: https://doi.org/10.1016/0022-0248(77)90099-9.

[140] H. Hadouda et al. "MoS2 thin film synthesis by soft sulfurization of a molybdenum layer". *Materials Chemistry and Physics* 42.4 (1995), 291–297. DOI: https://doi.org/10.1016/0254-0584(96)80017-4.

[141] Y. Lee et al. "Synthesis of wafer-scale uniform molybdenum disulfide films with control over the layer number using a gas phase sulfur precursor". *Nanoscale* 6.5 (2014), 2821–2826. DOI: 10.1039/C3NR05993F.

[142] C.-R. Wu et al. "The Growth Mechanism of Transition Metal Dichalcogenides by using Sulfurization of Pre-deposited Transition Metals and the 2D Crystal Hetero-structure Establishment". *Scientific Reports* 7.1 (2017), 42146. DOI: 10.1038/srep42146.

[143] Y.-C. Lin et al. "Wafer-scale MoS2 thin layers prepared by MoO3 sulfurization". *Nanoscale* 4.20 (2012), 6637–6641. DOI: 10.1039/C2NR31833D.

[144] R. I. Romanov et al. "Synthesis of Large Area Two-Dimensional MoS2 Films by Sulfurization of Atomic Layer Deposited MoO3 Thin Film for Nanoelectronic Applications". *ACS Applied Nano Materials* 2.12 (2019), 7521–7531. DOI: 10.1021/acsanm.9b01539.

[145] G. Kim et al. "New Approaches to Produce Large-Area Single Crystal Thin Films". *Advanced Materials* n/a.n/a (2022), 2203373. DOI: https://doi.org/10.1002/adma.202203373.

[146] X. Xu et al. "Enhanced Quality of Wafer-Scale MoS2 Films by a Capping Layer Annealing Process". *Advanced Functional Materials* 30.11 (2020), 1908040. DOI: https://doi.org/10.1002/adfm.201908040.

[147] F. S. Ohuchi et al. "Growth of MoSe2 thin films with Van der Waals epitaxy". *Journal of Crystal Growth* 111.1 (1991), 1033–1037. DOI: https://doi.org/10.1016/0022-0248(91)91127-V.

[148] R. Y. Yue et al. "Nucleation and growth of WSe2: enabling large grain transition metal dichalcogenides". *2d Materials* 4.4 (2017), 10. DOI: 10.1088/2053-1583/aa8ab5.

[149] M. Nakano et al. "Layer-by-Layer Epitaxial Growth of Scalable WSe2 on Sapphire by Molecular Beam Epitaxy". *Nano Letters* 17.9 (2017), 5595–5599. DOI: 10.1021/acs.nanolett.7b02420.

[150] W. Mortelmans et al. "Epitaxial registry and crystallinity of MoS2 via molecular beam and metalorganic vapor phase van der Waals epitaxy". *Applied Physics Letters* 117.3 (2020), 6. DOI: 10.1063/5.0013391.

[151] C. Vergnaud et al. "New approach for the molecular beam epitaxy growth of scalable WSe2 monolayers". *Nanotechnology* 31.25 (2020), 7. DOI: 10.1088/1361-6528/ab80fe.

[152] S. Cadot. "Synthesis of group 6 transition metal dichalcogenide monolayers by surface organometallic chemistry". PhD thesis. Laboratoire de Chimie, Catalyse, Polymères et Procédés, R 5265 (C2P2), 2016.

[153] W. Jeon et al. "Wafer-Scale Synthesis of Reliable High-Mobility Molybdenum Disulfide Thin Films via Inhibitor-Utilizing Atomic Layer Deposition". *Advanced Materials* 29.47 (2017), 8. DOI: 10.1002/adma.201703031.

[154] B. Groven et al. "Two-Dimensional Crystal Grain Size Tuning in WS2 Atomic Layer Deposition: An Insight in the Nucleation Mechanism". *Chemistry of Materials* 30.21 (2018), 7648–7663. DOI: 10.1021/acs.chemmater.8b02924.

[155] M. Mattinen et al. "Atomic Layer Deposition of Crystalline MoS2 Thin Films: New Molybdenum Precursor for Low-Temperature Film Growth". *Advanced Materials Interfaces* 4.18 (2017), 1700123. DOI: https://doi.org/10.1002/admi.201700123.

[156] Y.-T. Ho et al. "Layered MoS2 grown on c-sapphire by pulsed laser deposition". *physica status solidi (RRL) – Rapid Research Letters* 9.3 (2015), 187–191. DOI: https://doi.org/10.1002/pssr.201409561.

[157] S. Seo et al. "Growth of Centimeter-Scale Monolayer and Few-Layer WSe2 Thin Films on SiO2/Si Substrate via Pulsed Laser Deposition". *Advanced Materials Interfaces* 5.20 (2018), 8. DOI: 10.1002/admi.201800524.

[158] J. D. Yao, Z. Q. Zheng, and G. W. Yang. "Production of large-area 2D materials for high-performance photodetectors by pulsed-laser deposition". *Progress in Materials Science* 106 (2019), 64. DOI: 10.1016/j.pmatsci.2019.100573.

[159] K. M. McCreary et al. "Synthesis of High-Quality Monolayer MoS2 by Direct Liquid Injection". *Acs Applied Materials & Interfaces* 12.8 (2020), 9580–9588. DOI: 10.1021/acsami.9b19561.

[160] Y.-H. Lee et al. "Synthesis of Large-Area MoS2 Atomic Layers with Chemical Vapor Deposition". *Advanced Materials* 24.17 (2012), 2320–2325. DOI: https://doi.org/10.1002/adma.201104798.

[161] J. Zhang et al. "Scalable Growth of High-Quality Polycrystalline MoS2 Monolayers on SiO2 with Tunable Grain Sizes". *ACS Nano* 8.6 (2014), 6024–6030. DOI: 10.1021/nn5020819.

[162] S. Wang et al. "Shape Evolution of Monolayer MoS2 Crystals Grown by Chemical Vapor Deposition". *Chemistry of Materials* 26.22 (2014), 6371–6379. DOI: 10.1021/cm5025662.

[163] D. Dumcenco et al. "Large-Area Epitaxial Mono layer MoS2". *ACS Nano* 9.4 (2015), 4611–4620. DOI: 10.1021/acsnano.5b01281.

[164] K. K. H. Smithe et al. "Low Variability in Synthetic Monolayer MoS2 Devices". *ACS Nano* 11.8 (2017), 8456–8463. DOI: 10.1021/acsnano.7b04100.

[165] S. Chowdhury et al. "Two-Dimensional to Three-Dimensional Growth of Transition Metal Diselenides by Chemical Vapor Deposition: Interplay between Fractal, Dendritic, and Compact Morphologies". *Acs Applied Materials & Interfaces* 12.13 (2020), 15885–15892. DOI: 10.1021/acsami.9b23286.

[166] A. G. Thompson. "MOCVD technology for semiconductors". *Materials Letters* 30.4 (1997), 255–263. DOI: 10.1016/s0167-577x(96)00215-7.

[167] B. Kalanyan et al. "Rapid Wafer-Scale Growth of Polycrystalline 2H-MoS2 by Pulsed Metal-Organic Chemical Vapor Deposition". *Chemistry of Materials* 29.15 (2017), 6279–6288. DOI: 10.1021/acs.chemmater.7b01367.

[168] M. Seol et al. "Triboelectric Series of 2D Layered Materials". *Advanced Materials* 30.39 (2018), 8. DOI: 10.1002/adma.201801210.

[169] N. B. Shinde et al. "Rapid wafer-scale fabrication with layer-by-layer thickness control of atomically thin MoS2 films using gas-phase chemical vapor deposition". *Apl Materials* 7.8 (2019), 8. DOI: 10.1063/1.5095451.

[170] M. Macha et al. "Wafer-scale MoS2 with water-vapor assisted showerhead MOCVD". *Nanoscale Advances* (2022). DOI: 10.1039/D2NA00409G.

[171] A. C. Jones and M. L. Hitchman. *Chemical Vapour Deposition: Precursors, Processes and Applications.* Royal Society of Chemistry, 2009.

[172] F. Maury. "Recent trends in the selection of metal-organic precursors for MOCVD process". *Journal De Physique Iv* 5.C5 (1995), 449–463. DOI: 10.1051/jphyscol:1995552.

[173] W. M. Haynes. *CRC Handbook of Chemistry and Physics.* CRC Press, 2016.

[174] D. Fu et al. "Molecular Beam Epitaxy of Highly Crystalline Monolayer Molybdenum Disulfide on Hexagonal Boron Nitride". *Journal of the American Chemical Society* 139.27 (2017), 9392–9400. DOI: 10.1021/jacs.7b05131.

[175] Y.-Y. Lai et al. "Substrate Lattice-Guided MoS2 Crystal Growth: Implications for van der Waals Epitaxy". *ACS Applied Nano Materials* 4.5 (2021), 4930–4938. DOI: 10.1021/acsanm.1c00469.

[176] T. Li et al. "Epitaxial growth of wafer-scale molybdenum disulfide semiconductor single crystals on sapphire". *Nature Nanotechnology* 16.11 (2021), 1201–1207. DOI: 10.1038/s41565-021-00963-8.

[177] M. Marx et al. "Metalorganic Vapor-Phase Epitaxy Growth Parameters for Two-Dimensional MoS2". *Journal of Electronic Materials* 47.2 (2018), 910–916. DOI: 10.1007/s11664-017-5937-3.

[178] H. Kim et al. "Suppressing Nucleation in Metal-Organic Chemical Vapor Deposition of MoS2 Monolayers by Alkali Metal Halides". *Nano Letters* 17.8 (2017), 5056–5063. DOI: 10.1021/acs.nanolett.7b02311.

[179] L. K. Tan et al. "Atomic layer deposition of a MoS2 film". *Nanoscale* 6.18 (2014), 10584–10588. DOI: 10.1039/C4NR02451F.

[180] J. G. Song et al. "Catalytic chemical vapor deposition of large-area uniform two-dimensional molybdenum disulfide using sodium chloride". *Nanotechnology* 28.46 (2017), 8. DOI: 10.1088/1361-6528/aa8f15.

[181] T. A. Ho et al. "Edge-On MoS2 Thin Films by Atomic Layer Deposition for Understanding the Interplay between the Active Area and Hydrogen Evolution Reaction". *Chemistry of Materials* 29.17 (2017), 7604–7614. DOI: 10.1021/acs.chemmater.7b03212.

[182] A. U. Mane et al. "Atomic layer deposition of molybdenum disulfide films using MoF6 and H2S". *Journal of Vacuum Science & Technology A* 36.1 (2018), 9. DOI: 10.1116/1.5003423.

[183] Y. Kim et al. "Synthesis of two-dimensional MoS2/graphene heterostructure by atomic layer deposition using MoF6 precursor". *Applied Surface Science* 494 (2019), 591–599. DOI: 10.1016/j.apsusc.2019.07.168.

[184] L. Tang et al. "Vertical Chemical Vapor Deposition Growth of Highly Uniform 2D Transition Metal Dichalcogenides". *ACS Nano* 14.4 (2020), 4646–4653. DOI: 10.1021/acsnano.0c00296.

[185] Dockweiler Chemicals GmbH. *BTBMMo - Bis(tert-butylimino)bis(diethylamino) molybdenum(VI) ((CH3)3CN)2Mo(N(CH3)2)2 - Standard Molybdenum precursor for MOCVD. Product Data Sheet.* Marburg, Germany. DOI: https://dockchemicals.com/wp-content/uploads/2022/02/DOCK-C{_}Product{_}Datasheet{_}BTBMMo.pdf.

[186] A. Sharma et al. "Low-temperature plasma-enhanced atomic layer deposition of 2-D MoS2: large area, thickness control and tuneable morphology". *Nanoscale* 10.18 (2018), 8615–8627. DOI: 10.1039/c8nr02339e.

[187] A. J. Mughal et al. "Effect of substrate on the growth and properties of MoS2 thin films grown by plasma-enhanced atomic layer deposition". *Journal of Vacuum Science & Technology A* 37.1 (2019), 6. DOI: 10.1116/1.5074201.

[188] V. K. Kumar et al. "A predictive approach to CVD of crystalline layers of TMDs: the case of MoS2". *Nanoscale* 7.17 (2015), 7802–7810. DOI: 10.1039/c4nr07080a.

[189] J. Mun et al. "Low-temperature growth of layered molybdenum disulphide with controlled clusters". *Scientific Reports* 6 (2016), 7. DOI: 10.1038/srep21854.

[190] T. H. Choudhury et al. "Chalcogen Precursor Effect on Cold-Wall Gas-Source Chemical Vapor Deposition Growth of WS2". *Crystal Growth & Design* 18.8 (2018), 4357–4364. DOI: 10.1021/acs.cgd.8b00306.

[191] Y. Shi et al. "Engineering Wafer-Scale Epitaxial Two-Dimensional Materials through Sapphire Template Screening for Advanced High-Performance Nanoelectronics". *ACS Nano* 15.6 (2021), 9482–9494. DOI: 10.1021/acsnano.0c07761.

[192] A. T. Hoang et al. "Epitaxial Growth of Wafer-Scale Molybdenum Disulfide/Graphene Heterostructures by Metal-Organic Vapor-Phase Epitaxy and Their Application in Photodetectors". *ACS Applied Materials & Interfaces* 12.39 (2020), 44335–44344. DOI: 10.1021/acsami.0c12894.

[193] Y. Fan et al. "Understanding metal organic chemical vapour deposition of monolayer WS2: the enhancing role of Au substrate for simple organosulfur precursors". *Nanoscale* 12.43 (2020), 22234–22244. DOI: 10.1039/d0nr06459a.

[194] H. Y. Cun et al. "Wafer-scale MOCVD growth of monolayer MoS2 on sapphire and SiO2". *Nano Research* 12.10 (2019), 2646–2652. DOI: 10.1007/s12274-019-2502-9.

[195] G. Jin et al. "Heteroepitaxial van der Waals semiconductor superlattices". *Nature Nanotechnology* (2021). DOI: 10.1038/s41565-021-00942-z.

[196] S. Boandoh et al. "A Novel and Facile Route to Synthesize Atomic-Layered MoS2 Film for Large-Area Electronics". *Small* 13.39 (2017), 9. DOI: 10.1002/smll.201701306.

[197] M. Seol et al. "High-Throughput Growth of Wafer-Scale Monolayer Transition Metal Dichalcogenide via Vertical Ostwald Ripening". *Advanced Materials* 32.42 (2020), 8. DOI: 10.1002/adma.202003542.

[198] A. Grundmann et al. "H2S-free Metal-Organic Vapor Phase Epitaxy of Coalesced 2D WS2 Layers on Sapphire". *Mrs Advances* 4.10 (2019), 593–599. DOI: 10.1557/adv.2018.669.

[199] A. Cohen et al. "Growth-Etch Metal–Organic Chemical Vapor Deposition Approach of WS2 Atomic Layers". *ACS Nano* 15.1 (2020), 526–538. DOI: 10.1021/acsnano.0c05394.

[200] A. Ohtake et al. "Surface structures of GaAs(111)A,B - (2x2)". *Physical Review B* 64.4 (2001), 45318. DOI: 10.1103/PhysRevB.64.045318.

[201] W. Braun and J. Mannhart. "Film deposition by thermal laser evaporation". *AIP Advances* 9.8 (2019), 85310. DOI: 10.1063/1.5111678.

[202] T. J. Smart, J. Mannhart, and W. Braun. "Thermal laser evaporation of elements from across the periodic table". *Journal of Laser Applications* 33.2 (2021), 22008. DOI: 10.2351/7.0000348.

[203] D. H. Lee et al. "Metal-organic chemical vapor deposition of 2D van der Waals materials-The challenges and the extensive future opportunities". *APL Materials* 8.3 (2020), 18. DOI: 10.1063/1.5142601.

[204] S. Tiefenbacher et al. "EPITAXIAL-FILMS OF WS2 BY METAL-ORGANIC VAN-DER-WAALS EPITAXY (MO-VDWE)". *Surface Science* 318.1-2 (1994), L1161–L1164. DOI: 10.1016/0039-6028(94)90331-x.

[205] S. Tiefenbacher, C. Pettenkofer, and W. Jaegermann. "van der Waals epitaxy of transition metal dichalcogenides using metal organic precursors (MOVDWE)". *Thin Films - Structure and Morphology.* Ed. by S. C. Moss et al. Vol. 441. Materials Research Society Symposium Proceedings. Materials Research Society, 1997, 591–595. DOI: 10.1557/PROC-441-591.

[206] W. Hieber and E. Romberg. "Concerning metal carbonyls XXI Thermochemical analyses on metal hexacarbonyls". *Zeitschrift Fur Anorganische Und Allgemeine Chemie* 221.4 (1935), 332–336. DOI: 10.1002/zaac.19352210403.

[207] L. H. Kaplan and F. M. Dheurle. "DEPOSITION OF MOLYBDENUM AND TUNGSTEN FILMS FROM VAPOR DECOMPOSITION OF CARBONYLS". *Journal of the Electrochemical Society* 117.5 (1970), 693–&. DOI: 10.1149/1. 2407607.

[208] A. Brenner and D. A. Hucul. "REMARKABLE DECARBONYLATION RE-ACTION OF CHROMIUM, MOLYBDENUM, AND TUNGSTEN HEXACAR-BONYLS SUPPORTED ON SILICA AND USE OF THESE MATERIALS AS HETEROGENEOUS CATALYSTS". *Abstracts of Papers of the American Chemical Society* 175.MAR (1978), 125.

[209] C. C. Cho and S. L. Bernasek. "MOLYBDENUM DEPOSITION FROM THE DECOMPOSITION OF MOLYBDENUM HEXACARBONYL". *Journal of Applied Physics* 65.8 (1989), 3035–3043. DOI: 10.1063/1.342695.

[210] T. Ohta et al. "Static vapor pressure measurement of low volatility precursors for molecular vapor deposition below ambient temperature". *Chemical Vapor Deposition* 7.1 (2001), 33–37. DOI: 10.1002/1521-3862(200101)7:1<33::aid-cvde33>3.3.co;2-p.

[211] J. W. Faller, K. M. Brummond, and B. Mitasev. "Hexacarbonylmolybdenum". *Encyclopedia of Reagents for Organic Synthesis.* 2006. DOI: https://doi.org/10. 1002/047084289X.rh004.pub2.

[212] B. Kalanyan et al. "MoS2 thin films from a ((NBu)-Bu-t)(2)(NMe2)(2)Mo and 1-propanethiol atomic layer deposition process". *Journal of Vacuum Science & Technology A* 37.1 (2019), 11. DOI: 10.1116/1.5059424.

[213] T. S. Kim et al. "Gas-Phase Alkali Metal-Assisted MOCVD Growth of 2D Transition Metal Dichalcogenides for Large-Scale Precise Nucleation Control". *Small* 18.20 (2022), 2106368. DOI: https://doi.org/10.1002/smll.202106368.

[214] C. L. Yaws. *The Yaws Handbook of Vapor Pressure: Antoine Coefficients.* Elsevier Science, 2015. DOI: 10.1016/C2014-0-03590-3.

[215] D. R. Stull. "Vapor pressure of pure substances - organic compounds". *Industrial and Engineering Chemistry* 39.4 (1947), 517–540. DOI: 10.1021/ie50448a022.

[216] D. W. Scott et al. "3,4-Dithiahexane: Heat Capacity, Heats of Fusion and Vaporization, Vapor Pressure, Entropy, and Thermodynamic Functions1". *Journal of the American Chemical Society* 74.10 (1952), 2478–2483. DOI: 10.1021/ ja01130a009.

[217] Dockweiler Chemicals GmbH. *DTBS - Ditertiarybutylsulphide C8H18S - Sulphur Precursor for CVD application. Product Data Sheet.* Marburg, Germany.

[218] D. W. Scott et al. "2,3-Dithiabutane: Low Temperature Heat Capacity, Heat of Fusion, Heat of Vaporization, Vapor Pressure, Entropy and Thermodynamic Functions1,2". *Journal of the American Chemical Society* 72.6 (1950), 2424–2430. DOI: 10.1021/ja01162a021.

[219] D. W. Osborne, R. N. Doescher, and D. M. Yost. "The Heat Capacity, Heats of Fusion and Vaporization, Vapor Pressure and Entropy of Dimethyl Sulfide". *Journal of the American Chemical Society* 64.1 (1942), 169–172. DOI: 10.1021/ja01253a045.

[220] R. O. Beauchamp et al. "A Critical Review of the Literature on Hydrogen Sulfide Toxicity". *CRC Critical Reviews in Toxicology* 13.1 (1984), 25–97. DOI: 10.3109/10408448409029321.

[221] T. L. Guidotti. "Hydrogen Sulfide: Advances in Understanding Human Toxicity". *International Journal of Toxicology* 29.6 (2010), 569–581. DOI: 10.1177/1091581810384882.

[222] J. Jiang et al. "Hydrogen Sulfide—Mechanisms of Toxicity and Development of an Antidote". *Scientific Reports* 6.1 (2016), 20831. DOI: 10.1038/srep20831.

[223] G. LJUNGGREN and B. O. NORBERG. "On the Effect and Toxicity of Dimethyl Sulfide, Dimethyl Disulfide and Methyl Mercaptan". *Acta Physiologica Scandinavica* 5.2-3 (1943), 248–255. DOI: 10.1111/j.1748-1716.1943.tb02053.x.

[224] W. BOURNE. "ON THE EFFECTS OF ACETALDEHYDE, ETHER PEROXIDE, ETHYL MERCAPTAN, ETHYL SULPHIDE, AND SEVERAL KETONES—DIMETHYL, ETHYL METHYL AND DI-ETHYL—WHEN ADDED TO ANAESTHETIC ETHER". *Journal of Pharmacology and Experimental Therapeutics* 28.3 (1926), 409 LP –432.

[225] X. T. Zhang et al. "Influence of Carbon in Metalorganic Chemical Vapor Deposition of Few-Layer WSe2 Thin Films". *Journal of Electronic Materials* 45.12 (2016), 6273–6279. DOI: 10.1007/s11664-016-5033-0.

[226] J. A. R. Coope and W. A. Bryce. "The thermal decomposition of dimethyl disulphide". *Canadian Journal of Chemistry-Revue Canadienne De Chimie* 32.8 (1954), 768–779. DOI: 10.1139/v54-097.

[227] E. H. Braye, A. H. Sehon, and B. D. B. Darwent. "THERMAL DECOMPOSITION OF SULFIDES". *Journal of the American Chemical Society* 77.20 (1955), 5282–5285. DOI: 10.1021/ja01625a019.

[228] L. G. S. Shum and S. W. Benson. "The pyrolysis of simethyl sulfide, kinetics and mechanism". *International Journal of Chemical Kinetics* 17.7 (1985), 749–761. DOI: 10.1002/kin.550170705.

[229] S. H. Mousavipour, L. Emad, and S. Fakhraee. "Theoretical study on the unimolecular dissociation of CH3SCH3 and CH3SCH2". *Journal of Physical Chemistry A* 106.11 (2002), 2489–2496. DOI: 10.1021/jp010990q.

[230] A. G. Vandeputte, M. F. Reyniers, and G. B. Marin. "Theoretical Study of the Thermal Decomposition of Dimethyl Disulfide". *Journal of Physical Chemistry A* 114.39 (2010), 10531–10549. DOI: 10.1021/jp103357z.

[231] L. M. Fillman and S. C. Tang. "Thermal decomposition of metal carbonyls: A thermogravimetry-mass spectroscopy study ". *Thermochimica Acta* 75.1-2 (1984), 71–84. DOI: 10.1016/0040-6031(84)85008-x.

[232] I. Usoltsev et al. "Decomposition studies of group 6 hexacarbonyl complexes. Part 1: Production and decomposition of Mo(CO)6 and W(CO)6". *Radiochimica Acta* 104.3 (2016), 141–151. DOI: 10.1515/ract-2015-2445.

[233] I. Usoltsev, R. Eichler, and A. Turler. "Decomposition studies of group 6 hexacarbonyl complexes. Part 2: Modelling of the decomposition process". *Radiochimica Acta* 104.8 (2016), 531–537. DOI: 10.1515/ract-2015-2447.

[234] C. M. Schaefer et al. "Carbon Incorporation in MOCVD of MoS2 Thin Films Grown from an Organosulfide Precursor". *Chemistry of Materials* (2021). DOI: 10.1021/acs.chemmater.1c00646.

[235] K. Momeni et al. "Multiscale computational understanding and growth of 2D materials: a review". *Npj Computational Materials* 6.1 (2020), 18. DOI: 10.1038/s41524-020-0280-2.

[236] K. Momeni et al. "A computational framework for guiding the MOCVD-growth of wafer-scale 2D materials". *npj Computational Materials* 8.1 (2022), 240. DOI: 10.1038/s41524-022-00936-y.

[237] J.-H. Park et al. "Synthesis of High-Performance Monolayer Molybdenum Disulfide at Low Temperature". *Small Methods* 5.6 (2021), 2000720. DOI: https://doi.org/10.1002/smtd.202000720.

[238] H. Tian et al. "C-O Bond Dissociation and Induced Chemical Ionization Using High Energy (CO2)n+ Gas Cluster Ion Beam". *Journal of the American Society for Mass Spectrometry* 30.3 (2019), 476–481. DOI: 10.1007/s13361-018-2102-z.

[239] Y. C. Lin et al. "Realizing Large-Scale, Electronic-Grade Two-Dimensional Semiconductors". *ACS Nano* 12.2 (2018), 965–975. DOI: 10.1021/acsnano.7b07059.

[240] M. Ohring and S. P. Baker. *Materials Science of Thin Films: Deposition and Structure*. Elsevier Science, 2016. DOI: 10.1016/B978-0-12-524975-1.X5000-9.

[241] A. Koma. "Van der Waals epitaxy for highly lattice-mismatched systems". *Journal of Crystal Growth* 201-202 (1999), 236–241. DOI: https://doi.org/10.1016/S0022-0248(98)01329-3.

[242] L. Zhang, J. Dong, and F. Ding. "Strategies, Status, and Challenges in Wafer Scale Single Crystalline Two-Dimensional Materials Synthesis". *Chemical Reviews* 121.11 (2021), 6321–6372. DOI: 10.1021/acs.chemrev.0c01191.

[243] A. Koma, K. Sunouchi, and T. Miyajima. "Fabrication and characterization of heterostructures with subnanometer thickness". *Microelectronic Engineering* 2.1 (1984), 129–136. DOI: https://doi.org/10.1016/0167-9317(84)90057-1.

[244] K. Ueno et al. "Epitaxial growth of transition metal dichalcogenides on cleaved faces of mica". *Journal of Vacuum Science & Technology A* 8.1 (1990), 68–72. DOI: 10.1116/1.576983.

[245] A. Koma, K. Saiki, and Y. Sato. "Heteroepitaxy of a two-dimensional material on a three-dimensional material". *Applied Surface Science* 41-42 (1990), 451–456. DOI: https://doi.org/10.1016/0169-4332(89)90102-5.

[246] A. Koma. "Van der Waals epitaxy—a new epitaxial growth method for a highly lattice-mismatched system". *Thin Solid Films* 216.1 (1992), 72–76. DOI: https://doi.org/10.1016/0040-6090(92)90872-9.

[247] K. Ueno et al. "Heteroepitaxial growth of layered transition metal dichalcogenides on sulfur-terminated GaAs{111} surfaces". *Applied Physics Letters* 56.4 (1990), 327–329. DOI: 10.1063/1.102817.

[248] L. Liu et al. "Uniform nucleation and epitaxy of bilayer molybdenum disulfide on sapphire". *Nature* 605.7908 (2022), 69–75. DOI: 10.1038/s41586-022-04523-5.

[249] Y. Xiang et al. "Monolayer MoS2 on sapphire: An azimuthal reflection high-energy electron diffraction perspective". *2D Materials* 8 (2020). DOI: 10.1088/2053-1583/abce08.

[250] X. Zhang et al. "Hidden Vacancy Benefit in Monolayer 2D Semiconductors". *Advanced Materials* 33.7 (2021), 2007051. DOI: https://doi.org/10.1002/adma.202007051.

[251] F. Zhang et al. "Full orientation control of epitaxial MoS2 on hBN assisted by substrate defects". *Physical Review B* 99.15 (2019), 155430. DOI: 10.1103/PhysRevB.99.155430.

[252] Q. Ji et al. "Unravelling Orientation Distribution and Merging Behavior of Monolayer MoS2 Domains on Sapphire". *Nano Letters* 15.1 (2015), 198–205. DOI: 10.1021/nl503373x.

[253] J. Dong et al. "The epitaxy of 2D materials growth". *Nature Communications* 11.1 (2020), 5862. DOI: 10.1038/s41467-020-19752-3.

[254] W. Mortelmans et al. "On the van der Waals Epitaxy of Homo-/Heterostructures of Transition Metal Dichalcogenides". *ACS Applied Materials & Interfaces* 12.24 (2020), 27508–27517. DOI: 10.1021/acsami.0c05872.

[255] J. Li et al. "Single-Crystal MoS2 Monolayer Wafer Grown on Au (111) Film Substrates". *Small* 17.30 (2021), 2100743. DOI: https://doi.org/10.1002/smll.202100743.

[256] Y. Wan et al. "Wafer-scale single-orientation 2D layers by atomic edge-guided epitaxial growth". *Chemical Society Reviews* 51.3 (2022), 803–811. DOI: 10.1039/D1CS00264C.

[257] K. Suenaga et al. "Surface-Mediated Aligned Growth of Monolayer MoS2 and In-Plane Heterostructures with Graphene on Sapphire". *ACS Nano* 12.10 (2018), 10032–10044. DOI: 10.1021/acsnano.8b04612.

[258] A. Aljarb et al. "Substrate Lattice-Guided Seed Formation Controls the Orientation of 2D Transition-Metal Dichalcogenides". *ACS Nano* 11.9 (2017), 9215–9222. DOI: 10.1021/acsnano.7b04323.

[259] H. Zhu et al. "Step engineering for nucleation and domain orientation control in WSe2 epitaxy on c-plane sapphire". *Nature Portfolio* PREPRINT (Version 1) available at Research Square (2022). DOI: 10.21203/rs.3.rs-2180223/v1.

[260] J. R. Gaines, M. D. Healy, and L. Rankin. "Backstreaming of pump oil vapors in vacuum systems". *Vakuum in Forschung und Praxis* 33.1 (2021), 28–32. DOI: https://doi.org/10.1002/vipr.202100755.

[261] D. Reifsnyder Hickey et al. "Illuminating Invisible Grain Boundaries in Coalesced Single-Orientation WS2 Monolayer Films". *Nano Letters* 21.15 (2021), 6487–6495. DOI: 10.1021/acs.nanolett.1c01517.

[262] B. Qin et al. "Substrates in the Synthesis of Two-Dimensional Materials via Chemical Vapor Deposition". *Chemistry of Materials* 32.24 (2020), 10321–10347. DOI: 10.1021/acs.chemmater.0c03549.

[263] Plan Optik AG. *SCG 94 - clear high transmission crown-glass (modified soda-lime glass). Material Data Sheet.* Elsoff, Germany.

[264] Paul Marienfeld GmbH & Co. KG. *Marienfeld Superior - Microscope slides made of soda lime glass of the 3rd hydrolytic class. Material Data Sheet.* Lauda-Königshofen, Germany, 2020.

[265] Schott AG / Advanced Optics. *B270i - clear high transmission crown-glass (modified soda-lime glass). Material Data sheet.* Mainz, Germany.

[266] M. Ju et al. "Universal Substrate Trapping Strategy To Grow Strictly Monolayer Transition Metal Dichalcogenides Crystals". *Chemistry of Materials* 29.14 (2017), 6095–6103. DOI: 10.1021/acs.chemmater.7b01984.

[267] J. Y. Chen et al. "Chemical Vapor Deposition of Large-Size Monolayer MoSe2 Crystals on Molten Glass". *Journal of the American Chemical Society* 139.3 (2017), 1073–1076. DOI: 10.1021/jacs.6b12156.

[268] P. F. Yang et al. "Batch production of 6-inch uniform monolayer molybdenum disulfide catalyzed by sodium in glass". *Nature Communications* 9 (2018), 10. DOI: 10.1038/s41467-018-03388-5.

[269] F. Cuccureddu et al. "Surface morphology of c-plane sapphire (alpha-alumina) produced by high temperature anneal". *Surface Science* 604.15-16 (2010), 1294–1299. DOI: 10.1016/j.susc.2010.04.017.

[270] S. Curiotto and D. Chatain. "Surface morphology and composition of c-, a- and m-sapphire surfaces in O2 and H2 environments". *Surface Science* 603.17 (2009), 2688–2697. DOI: https://doi.org/10.1016/j.susc.2009.07.004.

[271] C. A. Schneider, W. S. Rasband, and K. W. Eliceiri. "NIH Image to ImageJ: 25 years of image analysis". *Nature Methods* 9.7 (2012), 671–675. DOI: 10.1038/nmeth.2089.

[272] Z. Püspöki et al. "Transforms and Operators for Directional Bioimage Analysis: A Survey." *Advances in anatomy, embryology, and cell biology* 219 (2016), 69–93. DOI: 10.1007/978-3-319-28549-8{_}3.

[273] H. S. Lee et al. "Identifying multiexcitons in MoS2 monolayers at room temperature". *Physical Review B* 93.14 (2016), 6. DOI: 10.1103/PhysRevB.93.140409.

[274] C. Lee et al. "Anomalous Lattice Vibrations of Single- and Few-Layer MoS2". *ACS Nano* 4.5 (2010), 2695–2700. DOI: 10.1021/nn1003937.

[275] K. M. McCreary et al. "A- and B-exciton photoluminescence intensity ratio as a measure of sample quality for trancition metal dichalcogenide monolayers". *Apl Materials* 6.11 (2018), 9. DOI: 10.1063/1.5053699.

[276] T. Gross et al. "An XPS analysis of different SiO2 modifications employing a C1s as well as an Au 4f7/2 static charge reference". *Surface and Interface Analysis* 18.1 (1992), 59–64. DOI: 10.1002/sia.740180110.

[277] J. F. Moulder and J. Chastain. *Handbook of X-ray Photoelectron Spectroscopy: A Reference Book of Standard Spectra for Identification and Interpretation of XPS Data.* Physical Electronics Division, Perkin-Elmer Corporation, 1992.

[278] D. Ganta, S. Sinha, and R. T. Haasch. "2-D Material Molybdenum Disulfide Analyzed by XPS". *Surface Science Spectra* 21.1 (2014), 19–27. DOI: 10.1116/11.20140401.

[279] H. C. Diaz, R. Addou, and M. Batzill. "Interface properties of CVD grown graphene transferred onto MoS2(0001)". *Nanoscale* 6.2 (2014), 1071–1078. DOI: 10.1039/c3nr03692h.

[280] G. F. Harrington and J. Santiso. "Back-to-Basics tutorial: X-ray diffraction of thin films". *Journal of Electroceramics* 47.4 (2021), 141–163. DOI: 10.1007/s10832-021-00263-6.

[281] Y.-C. Chien et al. "Charge Carrier Mobility and Series Resistance Extraction in 2D Field-Effect Transistors: Toward the Universal Technique". *Advanced Functional Materials* (2021), 2105003. DOI: https://doi.org/10.1002/adfm.202105003.

[282] A. Sebastian et al. "Benchmarking monolayer MoS2 and WS2 field-effect transistors". *Nature Communications* 12.1 (2021), 693. DOI: 10.1038/s41467-020-20732-w.

[283] Z. Cheng et al. "How to Report and Benchmark Emerging Field-Effect Transistors". *Nature Electronics* 5 (2022), 416–423. DOI: 10.1038/s41928-022-00798-8.

[284] A. Ortiz-Conde et al. "A review of recent MOSFET threshold voltage extraction methods". *Microelectronics Reliability* 42.4 (2002), 583–596. DOI: https://doi.org/10.1016/S0026-2714(02)00027-6.

[285] M. Chhowalla, D. Jena, and H. Zhang. "Two-dimensional semiconductors for transistors". *Nature Reviews Materials* 1.11 (2016), 16052. DOI: 10.1038/natrevmats.2016.52.

[286] S. B. Mitta et al. "Electrical characterization of 2D materials-based field-effect transistors". *2D Materials* 8.1 (2020), 12002. DOI: 10.1088/2053-1583/abc187.

[287] K. Xu and S. K. Fullerton-Shirey. "Electric-double-layer-gated transistors based on two-dimensional crystals: recent approaches and advances". *Journal of Physics-Materials* 3.3 (2020), 13. DOI: 10.1088/2515-7639/ab8270.

[288] W. Zhu et al. "Electronic transport and device prospects of monolayer molybdenum disulphide grown by chemical vapour deposition". *Nature Communications* 5.1 (2014), 3087. DOI: 10.1038/ncomms4087.

[289] D. Dev et al. "High quality gate dielectric/MoS2 interfaces probed by the conductance method". *Applied Physics Letters* 112.23 (2018), 232101. DOI: 10.1063/1.5028404.

[290] S. M. Shinde et al. "Surface-Functionalization-Mediated Direct Transfer of Molybdenum Disulfide for Large-Area Flexible Devices". *Advanced Functional Materials* 28.13 (2018), 11. DOI: 10.1002/adfm.201706231.

[291] D. Chiappe et al. "Layer-controlled epitaxy of 2D semiconductors: bridging nanoscale phenomena to wafer-scale uniformity". *Nanotechnology* 29.42 (2018), 9. DOI: 10.1088/1361-6528/aad798.

[292] C.-S. Lee et al. "Programmed Band Gap Modulation within van der Waals Semiconductor Monolayers by Metalorganic Vapor-Phase Epitaxy". *Chemistry of Materials* 32.12 (2020), 5084–5090. DOI: 10.1021/acs.chemmater.0c00949.

[293] A. Kozhakhmetov et al. "Scalable Substitutional Re-Doping and its Impact on the Optical and Electronic Properties of Tungsten Diselenide". *Advanced Materials* (), 9. DOI: 10.1002/adma.202005159.

[294] Y. Kobayashi et al. "Continuous Heteroepitaxy of Two Dimensional Heterostructures Based on Layered Chalcogenides". *ACS Nano* 13.7 (2019), 7527–7535. DOI: 10.1021/acsnano.8b07991.

[295] S. E. Xie et al. "Coherent, atomically thin transition-metal dichalcogenide superlattices with engineered strain". *Science* 359.6380 (2018), 1131–1135. DOI: 10.1126/science.aao5360.

[296] M. Heuken et al. "(Invited) Recent Progress in Large Area MOCVD Growth of 2D Materials". *ECS Meeting Abstracts* MA2021-02.12 (2021), 606. DOI: 10.1149/ma2021-0212606mtgabs.

[297] S. Dhar et al. "Chemical vapor deposition of MoS2 layers from Mo-S-C-O-H system: thermodynamic modeling and validation". *Physical Chemistry Chemical Physics* 18.22 (2016), 14918–14926. DOI: 10.1039/c6cp01617k.

[298] S. Dhar et al. "Thermodynamic Modeling of W-C-O-H-S System for Controlled Growth of WS2 Atomic Layers by True CVD". *Emerging Materials for Post Cmos Devices/Sensing and Applications 8*. Ed. by D. Misra et al. Vol. 77. ECS Transactions. Electrochemical Soc Inc, 2017, 49–59. DOI: 10.1149/07702.0049ecst.

[299] K. J. Ivin, M. H. J. Wijnen, and E. W. R. Steacie. "Reactions of ethyl radicals". *Journal of Physical Chemistry* 56.8 (1952), 967–972. DOI: 10.1021/j150500a009.

[300] X. Zheng et al. "Experimental and computational study of diethyl sulfide pyrolysis and mechanism". *Proceedings of the Combustion Institute* 32 (2009), 469–476. DOI: 10.1016/j.proci.2008.06.176.

[301] G. Martin and N. Barroeta. "Gas-phase thermolysis of sulfur-compounds. 2. Dirtertiary butyl sulfide". *International Journal of Chemical Kinetics* 12.10 (1980), 699–716. DOI: 10.1002/kin.550121004.

[302] C. A. Class et al. "Automatic mechanism generation for pyrolysis of di-tert-butyl sulfide". *Physical Chemistry Chemical Physics* 18.31 (2016), 21651–21658. DOI: 10.1039/C6CP02202B.

[303] T. Liang et al. "Intrinsically Substitutional Carbon Doping in CVD-Grown Monolayer MoS2 and the Band Structure Modulation". *ACS Applied Electronic Materials* 2.4 (2020), 1055–1064. DOI: 10.1021/acsaelm.0c00076.

[304] K. A. Cochrane et al. "Intentional carbon doping reveals CH as an abundant charged impurity in nominally undoped synthetic WS2 and WSe2". *2d Materials* 7.3 (2020), 6. DOI: 10.1088/2053-1583/ab8543.

[305] J. Jeon et al. "Epitaxial Synthesis of Molybdenum Carbide and Formation of a Mo2C/MoS2 Hybrid Structure via Chemical Conversion of Molybdenum Disulfide". *ACS Nano* 12.1 (2018), 338–346. DOI: 10.1021/acsnano.7b06417.

[306] S. P. Kelty, G. Berhault, and R. R. Chianelli. "The role of carbon in catalytically stabilized transition metal sulfides". *Applied Catalysis a-General* 322 (2007), 9–15. DOI: 10.1016/j.apcata.2007.01.017.

[307] H. Zhang, H. Lin, and Y. Zheng. "Deactivation study of unsupported nano MoS2 catalyst". *Carbon Resources Conversion* 3 (2020), 60–66. DOI: https://doi.org/10.1016/j.crcon.2019.09.003.

[308] W. Vogel. *Glaschemie.* Springer Berlin Heidelberg, 1992.

[309] S. H. Choi et al. "Water-Assisted Synthesis of Molybdenum Disulfide Film with Single Organic Liquid Precursor". *Scientific Reports* 7.1 (2017), 8. DOI: 10.1038/s41598-017-02228-8.

[310] S. M. Eichfeld et al. "Highly Scalable, Atomically Thin WSe2 Grown via Metal-Organic Chemical Vapor Deposition". *ACS Nano* 9.2 (2015), 2080–2087. DOI: 10.1021/nn5073286.

[311] M. J. Ludowise. "Metalorganic chemical vapor deposition of III-V semiconductors". *Journal of Applied Physics* 58.8 (1985), R31–R55. DOI: 10.1063/1.336296.

[312] M. M. Benameur et al. "Visibility of dichalcogenide nanolayers". *Nanotechnology* 22.12 (2011), 125706. DOI: 10.1088/0957-4484/22/12/125706.

[313] H. Zhang et al. "Interference effect on optical signals of monolayer MoS2". *Applied Physics Letters* 107.10 (2015), 101904. DOI: 10.1063/1.4930257.

[314] T. Zhao et al. "Substrate engineering for wafer-scale two-dimensional material growth: strategies, mechanisms, and perspectives". *Chemical Society Reviews* (2023). DOI: 10.1039/D2CS00657J.

[315] C. Ahn et al. "Growth of Monolayer and Multilayer MoS2 Films by Selection of Growth Mode: Two Pathways via Chemisorption and Physisorption of an Inorganic Molecular Precursor". *ACS Applied Materials & Interfaces* 13.5 (2021), 6805–6812. DOI: 10.1021/acsami.0c19591.

[316] Z. Q. Jiang and W. X. Huang. "Comparative Investigation of Mo(CO)(6) Adsorption on Clean and Oxidized Si(111) Surfaces". *Chinese Journal of Chemical Physics* 24.6 (2011), 729–734. DOI: 10.1088/1674-0068/24/06/729-734.

[317] L. Zeng et al. "Modified atomic layer deposition of MoS2 thin films". *Journal of Vacuum Science & Technology A* 38.6 (2020), 60403. DOI: 10.1116/6.0000641.

[318] Y. Xuan et al. "Multi-scale modeling of gas-phase reactions in metal-organic chemical vapor deposition growth of WSe2". *Journal of Crystal Growth* 527 (2019), 11. DOI: 10.1016/j.jcrysgro.2019.125247.

[319] N. Nayir. "Theoretical Investigation of W(CO)6 and CO Selenization Process". *Journal* 26.2 (2022), 283–291.

[320] S. Tang et al. "Migration-Enhanced Metal–Organic Chemical Vapor Deposition of Wafer-Scale Fully Coalesced WS2 and WSe2 Monolayers". *Crystal Growth & Design* (2023). DOI: 10.1021/acs.cgd.2c01134.

[321] S. M. Eichfeld et al. "Controlling nucleation of monolayer WSe2 during metal-organic chemical vapor deposition growth". *2d Materials* 3.2 (2016), 6. DOI: 10.1088/2053-1583/3/2/025015.

[322] X. Zhang et al. "Diffusion-Controlled Epitaxy of Large Area Coalesced WSe2 Monolayers on Sapphire". *Nano Letters* 18.2 (2018), 1049–1056. DOI: 10.1021/acs.nanolett.7b04521.

[323] P. Morin et al. "(Invited) Addressing Key Process and Material Challenges to Enable 2D Transition Metal Dichalcogenide Channels in Advanced Logic Devices". *ECS Meeting Abstracts* MA2022-02.15 (2022), 822. DOI: 10.1149/MA2022-0215822mtgabs.

[324] D. R. Hickey et al. "Formation of metal vacancy arrays in coalesced WS2 monolayer films". *2d Materials* 8.1 (2021), 10. DOI: 10.1088/2053-1583/abc905.

[325] C. Boudias and D. Monceau. *CaRIne Crystallography v3.1*. Senlis, France, 1998.

[326] D. Lopez-Diaz et al. "Evolution of the Raman Spectrum with the Chemical Composition of Graphene Oxide". *Journal of Physical Chemistry C* 121.37 (2017), 20489–20497. DOI: 10.1021/acs.jpcc.7b06236.

[327] L. G. Cancado et al. "General equation for the determination of the crystallite size L-a of nanographite by Raman spectroscopy". *Applied Physics Letters* 88.16 (2006), 3. DOI: 10.1063/1.2196057.

[328] A. C. Ferrari and J. Robertson. "Interpretation of Raman spectra of disordered and amorphous carbon". *Physical Review B* 61.20 (2000), 14095–14107. DOI: 10.1103/PhysRevB.61.14095.

[329] S. L. Shang et al. "Lateral Versus Vertical Growth of Two-Dimensional Layered Transition-Metal Dichalcogenides: Thermodynamic Insight into MoS2". *Nano Letters* 16.9 (2016), 5742–5750. DOI: 10.1021/acs.nanolett.6b02443.

[330] J. Sitek et al. "Substrate-Induced Variances in Morphological and Structural Properties of MoS2 Grown by Chemical Vapor Deposition on Epitaxial Graphene and SiO2". *ACS Applied Materials & Interfaces* 12.40 (2020), 45101–45110. DOI: 10.1021/acsami.0c06173.

[331] P. Afanasiev and C. Lorentz. "Oxidation of Nanodispersed MoS2 in Ambient Air: The Products and the Mechanistic Steps". *The Journal of Physical Chemistry C* 123.12 (2019), 7486–7494. DOI: 10.1021/acs.jpcc.9b01682.

[332] K. F. Mak et al. "Tightly bound trions in monolayer MoS2". *Nature Materials* 12.3 (2013), 207–211. DOI: 10.1038/nmat3505.

[333] Q. Wang et al. "Layer-by-layer epitaxy of multi-layer MoS2 wafers". *National Science Review* 9.6 (2022), nwac077. DOI: 10.1093/nsr/nwac077.

[334] J. C. Wildervanck and F. Jellinek. "Preparation and crystallinity of molybdenum and tungsten sulfides". *Zeitschrift fuer Anorganische und Allgemeine Chemie (1950) (DE)* 328 (1964), 309–318.

[335] S. Cadot et al. "A novel 2-step ALD route to ultra-thin MoS2 films on SiO2 through a surface organometallic intermediate". *Nanoscale* 9.2 (2017), 538–546. DOI: 10.1039/c6nr06021h.

[336] H. Simchi et al. "Sulfidation of 2D transition metals (Mo, W, Re, Nb, Ta): thermodynamics, processing, and characterization". *Journal of Materials Science* 52.17 (2017), 10127–10139. DOI: 10.1007/s10853-017-1228-x.

[337] C. Kastl et al. "The important role of water in growth of monolayer transition metal dichalcogenides". *2d Materials* 4.2 (2017), 10. DOI: 10.1088/2053-1583/aa5f4d.

[338] M. A. Baker et al. "XPS investigation of preferential sputtering of S from MoS2 and determination of MoSx stoichiometry from Mo and S peak positions". *Applied Surface Science* 150.1-4 (1999), 255–262. DOI: 10.1016/s0169-4332(99)00253-6.

[339] I. S. Kim et al. "Influence of Stoichiometry on the Optical and Electrical Properties of Chemical Vapor Deposition Derived MoS2". *ACS Nano* 8.10 (2014), 10551–10558. DOI: 10.1021/nn503988x.

[340] T. L. Barr and S. Seal. "Nature of the use of adventitious carbon as a binding energy standard". *Journal of Vacuum Science and Technology A: Vacuum, Surfaces and Films* 13.3 (1995), 1239–1246. DOI: 10.1116/1.579868.

[341] J. Liang et al. "Impact of Post-Lithography Polymer Residue on the Electrical Characteristics of MoS2 and WSe2 Field Effect Transistors". *Advanced Materials Interfaces* 6.3 (2019), 1801321. DOI: https://doi.org/10.1002/admi.201801321.

[342] M. Führer, T. van Haasterecht, and J. H. Bitter. "Molybdenum and tungsten carbides can shine too". *Catalysis Science & Technology* 10.18 (2020), 6089–6097. DOI: 10.1039/D0CY01420F.

[343] A. Levasseur, P. Vinatier, and D. Gonbeau. "X-ray photoelectron spectroscopy: A powerful tool for a better characterization of thin film materials". *Bulletin of Materials Science* 22.3 (1999), 607–614. DOI: 10.1007/bf02749975.

[344] H. Chin. "Preparation and characterization of carbon-sulfur surface compounds". *Carbon* 19.3 (1981), 175–186. DOI: https://doi.org/10.1016/0008-6223(81)90040-3.

[345] V. K. Abdelkader-Fernandez et al. "Expanding graphene properties by a simple S-doping methodology based on cold CS2 plasma". *Carbon* 144 (2019), 269–279. DOI: 10.1016/j.carbon.2018.12.045.

[346] Y. Lei et al. "Graphene and Beyond: Recent Advances in Two-Dimensional Materials Synthesis, Properties, and Devices". *ACS Nanoscience Au* (2022). DOI: 10.1021/acsnanoscienceau.2c00017.

[347] N. M. J. Conway et al. "Defect and disorder reduction by annealing in hydrogenated tetrahedral amorphous carbon". *Diamond and Related Materials* 9.3-6 (2000), 765–770. DOI: 10.1016/s0925-9635(99)00271-x.

[348] H. Ye et al. "Flake Size Limits for Growth of Vertically Stacked Two-Dimensional Materials by Analytical Diffusion-Based Kinetic Model". *Crystal Growth & Design* 22.9 (2022), 5264–5271. DOI: 10.1021/acs.cgd.2c00389.

[349] B. M. Vogelaar et al. "Deactivation of Mo/Al2O3 and NiMo/Al2O3 catalysts during hydrodesulfurization of thiophene". *Applied Catalysis a-General* 251.1 (2003), 85–92. DOI: 10.1016/s0926-860x(03)00305-3.

[350] L. Lin et al. "Investigation of carbon deposition induced by pyrolytic decomposition of ethylene". *RSC Advances* 7.47 (2017), 29639–29644. DOI: 10.1039/C7RA04282E.

[351] F. Gao, Y. Wang, and W. T. Tysoe. "Ethylene hydrogenation on Mo(CO)6 derived model catalysts in ultrahigh vacuum: From oxycarbide to carbide to MoAl alloy". *Journal of Molecular Catalysis A: Chemical* 249.1 (2006), 111–122. DOI: https://doi.org/10.1016/j.molcata.2006.01.016.

[352] Y. Beckmann et al. "Role of Surface Adsorbates on the Photoresponse of (MO)CVD-Grown Graphene–MoS2 Heterostructure Photodetectors". *ACS Applied Materials & Interfaces* 14.30 (2022), 35184–35193. DOI: 10.1021/acsami.2c06047.

[353] S. Dubey et al. "Weakly Trapped, Charged, and Free Excitons in Single-Layer MoS2 in the Presence of Defects, Strain, and Charged Impurities". *ACS Nano* 11.11 (2017), 11206–11216. DOI: 10.1021/acsnano.7b05520.

[354] D. Andrzejewski et al. "Improved luminescence properties of MoS2 monolayers grown via MOCVD: role of pretreatment and growth parameters". *Nanotechnology* 29.29 (2018), 10. DOI: 10.1088/1361-6528/aabbb9.

[355] Z. Li et al. "Graphene Quantum Dots Doping of MoS2 Monolayers". *Advanced Materials* 27.35 (2015), 5235–5240. DOI: https://doi.org/10.1002/adma.201501888.

[356] D. Pierucci et al. "Large area molybdenum disulphide-epitaxial graphene vertical Van der Waals heterostructures". *Scientific Reports* 6 (2016), 10. DOI: 10.1038/srep26656.

[357] S. Mouri, Y. Miyauchi, and K. Matsuda. "Tunable Photoluminescence of Monolayer MoS2 via Chemical Doping". *Nano Letters* 13.12 (2013), 5944–5948. DOI: 10.1021/nl403036h.

[358] M. M. Ugeda et al. "Giant bandgap renormalization and excitonic effects in a monolayer transition metal dichalcogenide semiconductor". *Nature Materials* 13.12 (2014), 1091–1095. DOI: 10.1038/nmat4061.

[359] R. E. Wood et al. "Evidence for the Dominance of Carrier-Induced Band Gap Renormalization over Biexciton Formation in Cryogenic Ultrafast Experiments on MoS2 Monolayers". *Journal of Physical Chemistry Letters* 11.7 (2020), 2658–2666. DOI: 10.1021/acs.jpclett.0c00169.

[360] D. Pierucci et al. "Band Alignment and Minigaps in Monolayer MoS2-Graphene van der Waals Heterostructures". *Nano Letters* 16.7 (2016), 4054–4061. DOI: 10.1021/acs.nanolett.6b00609.

[361] M. Berg et al. "Layer dependence of the electronic band alignment of few-layer MoS2 on SiO2 measured using photoemission electron microscopy". *Physical Review B* 95.23 (2017), 235406. DOI: 10.1103/PhysRevB.95.235406.

[362] T. Zhao et al. "Ultrafast growth of nanocrystalline graphene films by quenching and grain-size-dependent strength and bandgap opening". *Nature Communications* 10.1 (2019), 4854. DOI: 10.1038/s41467-019-12662-z.

[363] Z. Luo et al. "Modulating the electronic structures of graphene by controllable hydrogenation". *Applied Physics Letters* 97.23 (2010), 233111. DOI: 10.1063/1.3524217.

[364] A. Behranginia et al. "Direct Growth of High Mobility and Low-Noise Lateral MoS2–Graphene Heterostructure Electronics". *Small* 13.30 (2017), 1604301. DOI: https://doi.org/10.1002/smll.201604301.

[365] K. Keyshar et al. "Experimental Determination of the Ionization Energies of MoSe2, WS2, and MoS2 on SiO2 Using Photoemission Electron Microscopy". *ACS Nano* 11.8 (2017), 8223–8230. DOI: 10.1021/acsnano.7b03242.

[366] S. Y. Lee et al. "Large Work Function Modulation of Monolayer MoS2 by Ambient Gases". *ACS Nano* 10.6 (2016), 6100–6107. DOI: 10.1021/acsnano.6b01742.

[367] I. Shlyakhov et al. "Band alignment at interfaces of synthetic few-monolayer MoS2 with SiO2 from internal photoemission". *APL Materials* 6.2 (2017), 26801. DOI: 10.1063/1.5002617.

[368] Q. Ji et al. "Revealing the Brønsted-Evans-Polanyi relation in halide-activated fast MoS2 growth toward millimeter-sized 2D crystals". *Science Advances* 7.44 (2022), eabj3274. DOI: 10.1126/sciadv.abj3274.

[369] K. H. Zhang et al. "Considerations for Utilizing Sodium Chloride in Epitaxial Molybdenum Disulfide". *ACS Applied Materials & Interfaces* 10.47 (2018), 40831–40837. DOI: 10.1021/acsami.8b16374.

[370] J. Lei et al. "Salt-Assisted MoS2 Growth: Molecular Mechanisms from the First Principles". *Journal of the American Chemical Society* 144.16 (2022), 7497–7503. DOI: 10.1021/jacs.2c02497.

[371] X. F. Li et al. "Surfactant-Mediated Growth and Patterning of Atomically Thin Transition Metal Dichalcogenides". *ACS Nano* 14.6 (2020), 6570–6581. DOI: 10.1021/acsnano.0c00132.

[372] S. Li et al. "Vapour–liquid–solid growth of monolayer MoS2 nanoribbons". *Nature Materials* 17.6 (2018), 535–542. DOI: 10.1038/s41563-018-0055-z.

[373] J. D. Zhou et al. "A library of atomically thin metal chalcogenides". *Nature* 556.7701 (2018), 355–+. DOI: 10.1038/s41586-018-0008-3.

[374] P. Wang et al. "Mechanism of Alkali Metal Compound-Promoted Growth of Monolayer MoS2: Eutectic Intermediates". *Chemistry of Materials* 31.3 (2019), 873–880. DOI: 10.1021/acs.chemmater.8b04022.

[375] L. Taotao et al. "Halide Vapor Phase Epitaxy of Monolayer Molybdenum Diselenide Single Crystals". *National Science Open* (2023). DOI: https://doi.org/10.1360/nso/20220055.

[376] T. Gnanasekaran et al. "Phase diagram studies on the Na-Mo-O system". *Journal of Nuclear Materials* 165.3 (1989), 210–216. DOI: https://doi.org/10.1016/0022-3115(89)90197-9.

[377] H. Kim et al. "Role of alkali metal promoter in enhancing lateral growth of monolayer transition metal dichalcogenides". *Nanotechnology* 28.36 (2017), 36LT01. DOI: 10.1088/1361-6528/aa7e5e.

[378] Y. Shi et al. "Na-assisted fast growth of large single-crystal MoS$_2$ on sapphire". *Nanotechnology* 30.3 (2018), 34002. DOI: 10.1088/1361-6528/aaea3f.

[379] N. A. Simonson et al. "Low-temperature metalorganic chemical vapor deposition of molybdenum disulfide on multicomponent glass substrates". *Flatchem* 11 (2018), 32–37. DOI: 10.1016/j.flatc.2018.11.004.

[380] E. H. Snow et al. "Ion Transport Phenomena in Insulating Films". *Journal of Applied Physics* 36.5 (1965), 1664–1673. DOI: 10.1063/1.1703105.

[381] S. Subramanian et al. "Caveats in obtaining high-quality 2D materials and property characterization". *Journal of Materials Research* 35.8 (2020), 855–863. DOI: 10.1557/jmr.2019.394.

[382] M.-Y. Choi et al. "Substrate-Dependent Growth Mode Control of MoS2 Monolayers: Implications for Hydrogen Evolution and Field-Effect Transistors". *ACS Applied Nano Materials* 5.3 (2022), 4336–4342. DOI: 10.1021/acsanm.2c00369.

[383] W. Hong et al. "Enhanced Electrical Properties of Metal-Organic Chemical Vapor Deposition-Grown MoS2 Thin Films through Oxygen-Assisted Defect Control". *Advanced Electronic Materials* 8.7 (2022), 2101325. DOI: https://doi.org/10.1002/aelm.202101325.

[384] Y. Park et al. "Critical Role of Surface Termination of Sapphire Substrates in Crystallographic Epitaxial Growth of MoS2 Using Inorganic Molecular Precursors". *ACS Nano* (2023). DOI: 10.1021/acsnano.2c08983.

[385] W. Mortelmans et al. "Peculiar alignment and strain of 2D WSe2 grown by van der Waals epitaxy on reconstructed sapphire surfaces". *Nanotechnology* 30.46 (2019), 10. DOI: 10.1088/1361-6528/ab3c9b.

[386] N. Nayir et al. "A ReaxFF Force Field for 2D-WS2 and Its Interaction with Sapphire". *The Journal of Physical Chemistry C* 125.32 (2021), 17950–17961. DOI: 10.1021/acs.jpcc.1c03605.

[387] S. Najmaei et al. "Vapour phase growth and grain boundary structure of molybdenum disulphide atomic layers". *Nature Materials* 12.8 (2013), 754–759. DOI: 10.1038/nmat3673.

[388] A. M. van der Zande et al. "Grains and grain boundaries in highly crystalline monolayer molybdenum disulphide". *Nature Materials* 12.6 (2013), 554–561. DOI: 10.1038/nmat3633.

[389] T. H. Ly et al. "Misorientation-angle-dependent electrical transport across molybdenum disulfide grain boundaries". *Nature Communications* 7.1 (2016), 10426. DOI: 10.1038/ncomms10426.

[390] A. Grundmann et al. "MOVPE of Large-Scale MoS2/WS2, WS2/MoS2, WS2/Graphene and MoS2/Graphene 2D-2D Heterostructures for Optoelectronic Applications". *Mrs Advances* 5.31-32 (2020), 1625–1633. DOI: 10.1557/adv.2020.104.

[391] X. L. Liu et al. "Rotationally Commensurate Growth of MoS2 on Epitaxial Graphene". *ACS Nano* 10.1 (2016), 1067–1075. DOI: 10.1021/acsnano.5b06398.

[392] X. T. Zhang et al. "Defect-Controlled Nucleation and Orientation of WSe2 on hBN: A Route to Single-Crystal Epitaxial Monolayers". *ACS Nano* 13.3 (2019), 3341–3352. DOI: 10.1021/acsnano.8b09230.

[393] K. Saiki et al. "Application of Van der Waals epitaxy to highly heterogeneous systems". *Journal of Crystal Growth* 95.1 (1989), 603–606. DOI: https://doi.org/10.1016/0022-0248(89)90475-2.

[394] J. Hu et al. "Epitaxial Growth of High-Quality Monolayer MoS2 Single Crystals on Low-Symmetry Vicinal Au(101) Facets with Different Miller Indices". *ACS Nano* 17.1 (2023), 312–321. DOI: 10.1021/acsnano.2c07978.

[395] D. Ruzmetov et al. "Vertical 2D/3D Semiconductor Heterostructures Based on Epitaxial Molybdenum Disulfide and Gallium Nitride". *ACS Nano* 10.3 (2016), 3580–3588. DOI: 10.1021/acsnano.5b08008.

[396] W. S. Lin et al. "Selection Role of Metal Oxides into Transition Metal Dichalcogenide Monolayers by a Direct Selenization Process". *ACS Applied Materials & Interfaces* 10.11 (2018), 9645–9652. DOI: 10.1021/acsami.7b17861.

[397] P. Zheng et al. "Universal epitaxy of non-centrosymmetric two-dimensional single-crystal metal dichalcogenides". *Nature Communications* 14.1 (2023), 592. DOI: 10.1038/s41467-023-36286-6.

[398] W. Zhou et al. "Intrinsic Structural Defects in Monolayer Molybdenum Disulfide". *Nano Letters* 13.6 (2013), 2615–2622. DOI: 10.1021/nl4007479.

[399] M. Batzill. "Mirror twin grain boundaries in molybdenum dichalcogenides". *Journal of Physics: Condensed Matter* 30.49 (2018), 493001. DOI: 10.1088/1361-648X/aae9cf.

[400] H. Liu et al. "Dense Network of One-Dimensional Midgap Metallic Modes in Monolayer MoSe2 and Their Spatial Undulations". *Physical Review Letters* 113.6 (2014), 66105. DOI: 10.1103/PhysRevLett.113.066105.

[401] L. Du et al. *The Effect of Twin Grain Boundary Tuned by Temperature on the Electrical Transport Properties of Monolayer MoS2*. 2016. DOI: 10.3390/cryst6090115.

[402] J. H. Kim et al. "Antiphase Boundaries as Faceted Metallic Wires in 2D Transition Metal Dichalcogenides". *Advanced Science* 7.15 (2020), 2000788. DOI: https://doi.org/10.1002/advs.202000788.

[403] X. Zou, Y. Liu, and B. I. Yakobson. "Predicting Dislocations and Grain Boundaries in Two-Dimensional Metal-Disulfides from the First Principles". *Nano Letters* 13.1 (2013), 253–258. DOI: 10.1021/nl3040042.

[404] H. Tang et al. "Nucleation and coalescence of tungsten disulfide layers grown by metalorganic chemical vapor deposition". *Journal of Crystal Growth* (2023), 127111. DOI: https://doi.org/10.1016/j.jcrysgro.2023.127111.

[405] J. Mo et al. "Importance of the substrate's surface evolution during the MOVPE growth of 2D-transition metal dichalcogenides". *Nanotechnology* 31.12 (2020), 7. DOI: 10.1088/1361-6528/ab5ffd.

[406] V. Spampinato et al. "Correlated Intrinsic Electrical and Chemical Properties of Epitaxial WS2 via Combined C-AFM and ToF-SIMS Characterization". *Advanced Materials Interfaces* n/a.n/a (2023), 2202016. DOI: https://doi.org/10.1002/admi.202202016.

[407] R. Dong et al. "The Intrinsic Thermodynamic Difficulty and a Step-Guided Mechanism for the Epitaxial Growth of Uniform Multilayer MoS2 with Controllable Thickness". *Advanced Materials* n/a.n/a (2022), 2201402. DOI: https://doi.org/10.1002/adma.202201402.

[408] L. Chen et al. "Step-Edge-Guided Nucleation and Growth of Aligned WSe2 on Sapphire via a Layer-over-Layer Growth Mode". *ACS Nano* 9.8 (2015), 8368–8375. DOI: 10.1021/acsnano.5b03043.

[409]   X. Chen et al. "Orientation domain dispersions in wafer scale epitaxial monolayer WSe2 on sapphire". *Applied Surface Science* 567 (2021), 150798. DOI: https://doi.org/10.1016/j.apsusc.2021.150798.

[410]   K. V. Bets, N. Gupta, and B. I. Yakobson. "How the Complementarity at Vicinal Steps Enables Growth of 2D Monocrystals". *Nano Letters* 19.3 (2019), 2027–2031. DOI: 10.1021/acs.nanolett.9b00136.

[411]   Y. Hwang and N. Shin. "Hydrogen-assisted step-edge nucleation of MoSe2 monolayers on sapphire substrates". *Nanoscale* 11.16 (2019), 7701–7709. DOI: 10.1039/c8nr10315a.

[412]   S. Tang et al. "Detailed study on MOCVD of wafer-scale MoS2 monolayers: From nucleation to coalescence". *MRS Advances* (2022). DOI: 10.1557/s43580-022-00312-4.

[413]   A. Roy et al. "Structural and Electrical Properties of MoTe2 and MoSe2 Grown by Molecular Beam Epitaxy". *ACS Applied Materials & Interfaces* 8.11 (2016), 7396–7402. DOI: 10.1021/acsami.6b00961.

[414]   H. G. Ji et al. "Hydrogen-Assisted Epitaxial Growth of Monolayer Tungsten Disulfide and Seamless Grain Stitching". *Chemistry of Materials* 30.2 (2018), 403–411. DOI: 10.1021/acs.chemmater.7b04149.

[415]   M. Chubarov et al. "In-plane x-ray diffraction for characterization of monolayer and few-layer transition metal dichalcogenide films". *Nanotechnology* 29.5 (2018), 8. DOI: 10.1088/1361-6528/aaa1bd.

[416]   G. Renaud et al. "Atomic Structure of the a-Al2O3(0001) sqrt(31)×sqrt(31)R9° Reconstruction". *Physical Review Letters* 73.13 (1994), 1825–1828. DOI: 10.1103/PhysRevLett.73.1825.

[417]   I. Vilfan et al. "Structure determination of the (3sqt(3)×3sqrt(3)) reconstructed α-Al2O3(0001)". *Surface Science* 505 (2002), L215–L221. DOI: https://doi.org/10.1016/S0039-6028(02)01380-8.

[418]   R. Sant et al. "Decoupling Molybdenum Disulfide from Its Substrate by Cesium Intercalation". *The Journal of Physical Chemistry C* (2020). DOI: 10.1021/acs.jpcc.0c00970.

[419]   L. Peters et al. "Directing the Morphology of Chemical Vapor Deposition-Grown MoS2 on Sapphire by Crystal Plane Selection". *physica status solidi (a)* 217.15 (2020), 2000073. DOI: https://doi.org/10.1002/pssa.202000073.

[420]   R. Verre et al. "Equilibrium faceting formation in vicinal Al2O3 (0001) surface caused by annealing". *Surface Science* 606.23 (2012), 1815–1820. DOI: https://doi.org/10.1016/j.susc.2012.07.024.

[421]   Y. Hayashi et al. "Heteroepitaxy between wurtzite and corundum materials". *Journal of Applied Physics* 113.18 (2013), 8. DOI: 10.1063/1.4804328.

[422]   L. Pham Van, O. Kurnosikov, and J. Cousty. "Evolution of steps on vicinal (0001) surfaces of α-alumina". *Surface Science* 411.3 (1998), 263–271. DOI: https://doi.org/10.1016/S0039-6028(98)00329-X.

[423]   O. Kurnosikov, L. Pham Van, and J. Cousty. "About anisotropy of atomic-scale height step on (0001) sapphire surface". *Surface Science* 459.3 (2000), 256–264. DOI: https://doi.org/10.1016/S0039-6028(00)00452-0.

[424] O. Kurnosikov, L. Pham Van, and J. Cousty. "High-temperature transformation of vicinal (0001) Al2O3-α surfaces: an AFM study". *Surface and Interface Analysis* 29.9 (2000), 608–613. DOI: https://doi.org/10.1002/1096-9918(200009)29:9<608::AID-SIA906>3.0.CO;2-B.

[425] P. R. Ribič and G. Bratina. "Behavior of the (0001) surface of sapphire upon high-temperature annealing". *Surface Science* 601.1 (2007), 44–49. DOI: https://doi.org/10.1016/j.susc.2006.09.003.

[426] J. R. Heffelfinger, M. W. Bench, and C. B. Carter. "Steps and the structure of the (0001)alpha-alumina surface". *Surface Science* 370.1 (1997), L168–L172. DOI: 10.1016/s0039-6028(96)01123-5.

[427] K. H. Zhang et al. "Deconvoluting the Photonic and Electronic Response of 2D Materials: The Case of MoS2". *Scientific Reports* 7 (2017), 8. DOI: 10.1038/s41598-017-16970-6.

[428] W. D. Kaplan et al. "Ca Segregation to Basal Surfaces in α-Alumina". *Journal of the American Ceramic Society* 78.10 (1995), 2841–2844. DOI: https://doi.org/10.1111/j.1151-2916.1995.tb08064.x.

[429] T. M. French and G. A. Somorjai. "Composition and surface structure of the (0001) face of alpha-alumina by low-energy electron diffraction". *The Journal of Physical Chemistry* 74.12 (1970), 2489–2495. DOI: 10.1021/j100706a014.

[430] E. A. A. Jarvis and E. A. Carter. "Metallic Character of the Al2O3(0001)-sqrt(31)×sqrt(31)R±9° Surface Reconstruction". *The Journal of Physical Chemistry B* 105.18 (2001), 4045–4052. DOI: 10.1021/jp003587c.

[431] J. V. Lauritsen et al. "Atomic-Scale Structure and Stability of the sqrt(31)×sqrt(31)R9° Surface of Al2O3(0001)". *Phys. Rev. Lett.* 103.7 (2009), 76103. DOI: 10.1103/PhysRevLett.103.076103.

[432] D. S. Milakhin et al. "Peculiarities of the AlN crystalline phase formation in a result of the electron-stimulated reconstruction transition sqrt(31)×sqrt(31)R±9° - (1 × 1)". *Applied Surface Science* 541 (2021), 148548. DOI: https://doi.org/10.1016/j.apsusc.2020.148548.

[433] N. Mishra et al. "Wafer-Scale Synthesis of Graphene on Sapphire: Toward Fab-Compatible Graphene". *Small* 15.50 (2019), 1904906. DOI: 10.1002/smll.201904906.

[434] A. Tosaka et al. "Influence of step morphology on the structural phase transition of the α-Al2O3(0001) surface". *Applied Physics Letters* 104.22 (2014), 221601. DOI: 10.1063/1.4881334.

[435] S. Hasegawa. *Reflection High-Energy Electron Diffraction*. 2012. DOI: https://doi.org/10.1002/0471266965.com139.

[436] K. Trepka. "Quantifying epitaxial growth using a purely topographical signal". *NanoScientific Magazine* 21 (2021), 19–24. DOI: 10.48550ARXIV.2101.08455.

[437] Y. Xiang et al. "Domain boundaries in incommensurate epitaxial layers on weakly interacting substrates". *Journal of Applied Physics* 130.6 (2021), 65301. DOI: 10.1063/5.0057417.

[438] C. M. Schaefer, A. Pedroso López, and J. Santiso. *In-plane and out-of-plane structural analysis of epitaxial 2D MoS2 thin films MOCVD-grown on distinct Al2O3(0001) surfaces [Data set]. European Synchrotron Radiation Facility.* Tech. rep. Grenoble: Eurpoean Synchrotron Radiation Facility, 2025. DOI: 10.15151/ESRF-ES-891425217.

[439] D. S. Milakhin et al. "Nitridation of an unreconstructed and reconstructed sqrt(31)×sqrt(31)R±9° (0001) sapphire surface in an ammonia flow". *Semiconductors* 49.7 (2015), 905–910. DOI: 10.1134/S1063782615070180.

[440] H. Gao et al. "Graphene at Liquid Copper Catalysts: Atomic-Scale Agreement of Experimental and First-Principles Adsorption Height". *Advanced Science* 9.36 (2022), 2204684. DOI: https://doi.org/10.1002/advs.202204684.

[441] K. Saito and T. Ogino. "Direct Growth of Graphene Films on Sapphire (0001) and (1120) Surfaces by Self-Catalytic Chemical Vapor Deposition". *The Journal of Physical Chemistry C* 118.10 (2014), 5523–5529. DOI: 10.1021/jp408126e.

[442] K.-G. Zhou et al. "Raman Modes of MoS2 Used as Fingerprint of van der Waals Interactions in 2-D Crystal-Based Heterostructures". *ACS Nano* 8.10 (2014), 9914–9924. DOI: 10.1021/nn5042703.

[443] B. Chakraborty et al. "Symmetry-dependent phonon renormalization in monolayer MoS${}_{2}$ transistor". *Physical Review B* 85.16 (2012), 161403. DOI: 10.1103/PhysRevB.85.161403.

[444] G. Kukucska and J. Koltai. "Theoretical Investigation of Strain and Doping on the Raman Spectra of Monolayer MoS2". *physica status solidi (b)* 254.11 (2017), 1700184. DOI: https://doi.org/10.1002/pssb.201700184.

[445] M. R. Laskar et al. "Large area single crystal (0001) oriented MoS2". *Applied Physics Letters* 102.25 (2013), 252108. DOI: 10.1063/1.4811410.

[446] W. Mortelmans et al. "Fundamental limitation of van der Waals homoepitaxy by stacking fault formation in WSe2". *2d Materials* 7.2 (2020), 10. DOI: 10.1088/2053-1583/ab70ec.

[447] H. Ryu et al. "Two-dimensional material templates for van der Waals epitaxy, remote epitaxy, and intercalation growth". *Applied Physics Reviews* 9.3 (2022), 31305. DOI: 10.1063/5.0090373.

[448] H. Liu et al. "Atomic layer deposited 2D MoS2 atomic crystals: from material to circuit". *Nano Research* (), 7. DOI: 10.1007/s12274-020-2787-8.

[449] X. H. Zheng et al. "Determination of twist angle of in-plane mosaic spread of GaN films by high-resolution X-ray diffraction". *Journal of Crystal Growth* 255.1 (2003), 63–67. DOI: https://doi.org/10.1016/S0022-0248(03)01211-9.

[450] K. S. Kim et al. "Atomic Layer Etching Mechanism of MoS2 for Nanodevices". *ACS Applied Materials & Interfaces* 9.13 (2017), 11967–11976. DOI: 10.1021/acsami.6b15886.

[451] F. C. Eversteyn et al. "A Stagnant Layer Model for the Epitaxial Growth of Silicon from Silane in a Horizontal Reactor". *Journal of The Electrochemical Society* 117.7 (1970), 925. DOI: 10.1149/1.2407685.

[452] K. Momeni et al. "Multiscale framework for simulation-guided growth of 2D materials (vol 2, 27, 2018)". *Npj 2d Materials and Applications* 2 (2018), 1. DOI: 10.1038/s41699-018-0081-3.

[453] F. H. Yang. "2 - Modern metal-organic chemical vapor deposition (MOCVD) reactors and growing nitride-based materials". Ed. by J. Huang, H.-C. Kuo, and S.-C. B. T. .-. N. S. L.-E. D. (Shen. Woodhead Publishing, 2014, 27–65. DOI: https://doi.org/10.1533/9780857099303.1.27.

[454] L. Hui. *Mass transport analysis of a showerhead MOCVD reactor.* 2011. DOI: 10.1088/1674-4926/32/3/033006.

[455] Z. Ma et al. "Epitaxial Growth of Rectangle Shape MoS2 with Highly Aligned Orientation on Twofold Symmetry a-Plane Sapphire". *Small* 16.16 (2020), 2000596. DOI: https://doi.org/10.1002/smll.202000596.

[456] J. Wang et al. "Dual-coupling-guided epitaxial growth of wafer-scale single-crystal WS2 monolayer on vicinal a-plane sapphire". *Nature Nanotechnology* 17.1 (2022), 33–38. DOI: 10.1038/s41565-021-01004-0.

[457] R. Zhao et al. "Incorporating Niobium in MoS2 at BEOL-Compatible Temperatures and its Impact on Copper Diffusion Barrier Performance". *Advanced Materials Interfaces* 6.1901055 (2019), 7. DOI: 10.1002/admi.201901055.

[458] A. Kozhakhmetov et al. "Scalable BEOL compatible 2D tungsten diselenide". *2d Materials* 7.1 (2020), 8. DOI: 10.1088/2053-1583/ab5ad1.

[459] J. Mun et al. "High-Mobility MoS2 Directly Grown on Polymer Substrate with Kinetics-Controlled Metal-Organic Chemical Vapor Deposition". *ACS Applied Electronic Materials* 1.4 (2019), 608–616. DOI: 10.1021/acsaelm.9b00078.

[460] A. J. Watson et al. "Transfer of large-scale two-dimensional semiconductors: challenges and developments". *2D Materials* 8.3 (2021), 32001. DOI: 10.1088/2053-1583/abf234.

[461] A. Gurarslan et al. "Surface-Energy-Assisted Perfect Transfer of Centimeter-Scale Mono layer and Few-Layer MoS2 Films onto Arbitrary Substrates". *ACS Nano* 8.11 (2014), 11522–11528. DOI: 10.1021/nn5057673.

[462] F. Zhang et al. "Etchant-free transfer of 2D nanostructures". *Nanotechnology* 29.2 (2018), 5. DOI: 10.1088/1361-6528/aa9c21.

[463] M. Thakur et al. "Wafer-Scale Fabrication of Nanopore Devices for Single-Molecule DNA Biosensing using MoS2". *Small Methods* (), 10. DOI: 10.1002/smtd.202000072.

[464] J. Kim et al. "Layer-Resolved Graphene Transfer via Engineered Strain Layers". *Science* 342.6160 (2013), 833–836. DOI: 10.1126/science.1242988.

[465] J. Kang et al. "Selective Transfer of Rotationally Commensurate MoS2 from an Epitaxially Grown van der Waals Heterostructure". *Chemistry of Materials* 30.23 (2018), 8495–8500. DOI: 10.1021/acs.chemmater.8b03128.

[466] J. D. Caldwell et al. "Technique for the Dry Transfer of Epitaxial Graphene onto Arbitrary Substrates". *ACS Nano* 4.2 (2010), 1108–1114. DOI: 10.1021/nn901585p.

[467] K. Kang et al. "Layer-by-layer assembly of two-dimensional materials into wafer-scale heterostructures". *Nature* 550.7675 (2017), 229–233. DOI: 10.1038/nature23905.

[468] J. H. Kim et al. "Centimeter-scale Green Integration of Layer-by-Layer 2D TMD vdW Heterostructures on Arbitrary Substrates by Water-Assisted Layer Transfer". *Scientific Reports* 9 (2019), 10. DOI: 10.1038/s41598-018-37219-w.

[469] J. Kang et al. "Efficient Transfer of Large-Area Graphene Films onto Rigid Substrates by Hot Pressing". *ACS Nano* 6.6 (2012), 5360–5365. DOI: 10.1021/nn301207d.

[470] T. Y. Zhang et al. "Clean Transfer of 2D Transition Metal Dichalcogenides Using Cellulose Acetate for Atomic Resolution Characterizations". *ACS Applied Nano Materials* 2.8 (2019), 5320–5328. DOI: 10.1021/acsanm.9b01257.

[471] H. Yang et al. "Enhanced Electrical Properties of Lithography-Free Fabricated MoS2 Field Effect Transistors with Chromium Contacts". *The Journal of Physical Chemistry Letters* 12.11 (2021), 2705–2711. DOI: 10.1021/acs.jpclett.1c00231.

[472] R. Mahlouji et al. "On the Contact Optimization of ALD-Based MoS2 FETs: Correlation of Processing Conditions and Interface Chemistry with Device Electrical Performance". *ACS Applied Electronic Materials* 3.7 (2021), 3185–3199. DOI: 10.1021/acsaelm.1c00379.

[473] N. Schaefer et al. "Improved metal-graphene contacts for low-noise, high-density microtransistor arrays for neural sensing". *Carbon* 161 (2020), 647–655. DOI: https://doi.org/10.1016/j.carbon.2020.01.066.

[474] P. Bolshakov et al. "Contact Engineering for Dual-Gate MoS2 Transistors Using O2 Plasma Exposure". *ACS Applied Electronic Materials* 1.2 (2019), 210–219. DOI: 10.1021/acsaelm.8b00059.

[475] K. M. Freedy et al. "MoS2 cleaning by acetone and UV-ozone: Geological and synthetic material". *Applied Surface Science* 478 (2019), 183–188. DOI: https://doi.org/10.1016/j.apsusc.2019.01.222.

[476] A. Azcatl et al. "HfO2 on UV–O3 exposed transition metal dichalcogenides: interfacial reactions study". *2D Materials* 2.1 (2015), 14004. DOI: 10.1088/2053-1583/2/1/014004.

[477] Y. C. Lin et al. "Graphene Annealing: How Clean Can It Be?" *Nano Letters* 12.1 (2012), 414–419. DOI: 10.1021/nl203733r.

[478] Y. Ahn et al. "Thermal annealing of graphene to remove polymer residues". *Materials Express* 6.1 (2016), 69–76. DOI: 10.1166/mex.2016.1272.

[479] C. D. English et al. "Improved Contacts to MoS2 Transistors by Ultra-High Vacuum Metal Deposition". *Nano Letters* 16.6 (2016), 3824–3830. DOI: 10.1021/acs.nanolett.6b01309.

[480] K. Schauble et al. "Uncovering the Effects of Metal Contacts on Monolayer MoS2". *ACS Nano* 14.11 (2020), 14798–14808. DOI: 10.1021/acsnano.0c03515.

[481] R. Li et al. "Determination of PMMA Residues on a Chemical-Vapor-Deposited Monolayer of Graphene by Neutron Reflection and Atomic Force Microscopy". *Langmuir* 34.5 (2018), 1827–1833. DOI: 10.1021/acs.langmuir.7b03117.

[482] Kayaku Advanced Materials. *PMMA and Copolymer - Technical Data Sheet.* 2020. DOI: https://kayakuam.com/wp-content/uploads/2019/09/PMMA{_}Data{_}Sheet.pdf.

[483] Kayaku Advanced Materials. *Remover PG - Technical data sheet.* 2020. DOI: https://kayakuam.com/wp-content/uploads/2020/11/KAM-Remover-PG-TDS.10.29.20-final.pdf.

[484] M. Reisch. "SOLVENT USERS LOOK TO REPLACE NMP". *Chemical & Engineering News Archive* 86.29 (2008), 32. DOI: 10.1021/cen-v086n029.p032.

[485] TECHNIC France. *TechniStrip NI555 - Technical Data sheet.* Saint Denis la Plaine (France), 2017. DOI: https://www.microchemicals.net/micro/msds/TF{_}TDS{_}SPEC/TDS/tds{_}technistrip{_}ni555.pdf.

[486] K. Murayama et al. "Height Measurement Using High-Precision Atomic Force Microscope Scanner Combined with Laser Interferometers". *Japanese Journal of Applied Physics* 45.11R (2006), 8832. DOI: 10.1143/JJAP.45.8832.

[487] C. Möller et al. "Tapping-Mode Atomic Force Microscopy Produces Faithful High-Resolution Images of Protein Surfaces". *Biophysical Journal* 77.2 (1999), 1150–1158. DOI: https://doi.org/10.1016/S0006-3495(99)76966-3.

[488] A. J. Pollard. "Metrology for Graphene and 2-D Materials". *International Congress of Metrology* (2015).

[489] MicroChem Corp. *Remover PG - Safety data sheet.* Newton, MA 02464 (USA), 2001. DOI: https://kayakuam.com/wp-contehttps://kayakuam.com/wp-content/uploads/2019/09/PMMA{_}Data{_}Sheet.pdf.

[490] H. Qiu et al. "Electrical characterization of back-gated bi-layer MoS2 field-effect transistors and the effect of ambient on their performances". *Applied Physics Letters* 100.12 (2012), 123104. DOI: 10.1063/1.3696045.

[491] A. Leonhardt et al. "Improving MOCVD MoS2 Electrical Performance: Impact of Minimized Water and Air Exposure Conditions". *Ieee Electron Device Letters* 38.11 (2017), 1606–1609. DOI: 10.1109/led.2017.2752424.

[492] A. J. Cho et al. "Multi-Layer MoS2 FET with Small Hysteresis by Using Atomic Layer Deposition Al2O3 as Gate Insulator". *Ecs Solid State Letters* 3.10 (2014), Q67–Q69. DOI: 10.1149/2.0111409ssl.

[493] C. J. McClellan et al. "High Current Density in Monolayer MoS2 Doped by AlOx". *ACS Nano* 15.1 (2021), 1587–1596. DOI: 10.1021/acsnano.0c09078.

[494] D. Jena and A. Konar. "Enhancement of Carrier Mobility in Semiconductor Nanostructures by Dielectric Engineering". *Physical Review Letters* 98.13 (2007), 136805. DOI: 10.1103/PhysRevLett.98.136805.

[495] S. McDonnell et al. "HfO2 on MoS2 by Atomic Layer Deposition: Adsorption Mechanisms and Thickness Scalability". *ACS Nano* 7.11 (2013), 10354–10361. DOI: 10.1021/nn404775u.

[496] H. Zhang et al. "Nucleation and growth mechanisms of Al2O3 atomic layer deposition on synthetic polycrystalline MoS2". *Journal of Chemical Physics* 146.5 (2017), 10. DOI: 10.1063/1.4967406.

[497] J. Wang et al. "Integration of High-k Oxide on MoS2 by Using Ozone Pre-treatment for High-Performance MoS2 Top-Gated Transistor with Thickness-Dependent Carrier Scattering Investigation". *Small* 11.44 (2015), 5932–5938. DOI: https://doi.org/10.1002/smll.201501260.

[498] S. Park et al. "Interface Properties of Atomic-Layer-Deposited Al2O3 Thin Films on Ultraviolet/Ozone-Treated Multilayer MoS2 Crystals". *ACS Applied Materials & Interfaces* 8.18 (2016), 11189–11193. DOI: 10.1021/acsami.6b01568.

[499] L. X. Cheng et al. "Atomic Layer Deposition of a High-k Dielectric on MoS2 Using Trimethylaluminum and Ozone". *ACS Applied Materials & Interfaces* 6.15 (2014), 11834–11838. DOI: 10.1021/am5032105.

[500] K. M. Price et al. "Uniform Growth of Sub-5-Nanometer High-κ Dielectrics on MoS2 Using Plasma-Enhanced Atomic Layer Deposition". *ACS Applied Materials & Interfaces* 9.27 (2017), 23072–23080. DOI: 10.1021/acsami.7b00538.

[501] H. Kim et al. "Optimized single-layer MoS2 field-effect transistors by non-covalent functionalisation". *Nanoscale* 10.37 (2018), 17557–17566. DOI: 10.1039/c8nr02134a.

[502] H. D. Zhang et al. "MoS2 Functionalization with a Sub-nm Thin SiO2 Layer for Atomic Layer Deposition of High-kappa Dielectrics". *Chemistry of Materials* 29.16 (2017), 6772–6780. DOI: 10.1021/acs.chemmater.7b01695.

[503] S. Son et al. "Improved high temperature integration of Al2O3 on MoS2 by using a metal oxide buffer layer". *Applied Physics Letters* 106.2 (2015), 4. DOI: 10.1063/1.4905634.

[504] B. Fallahazad et al. "Dielectric thickness dependence of carrier mobility in graphene with HfO2 top dielectric". *Applied Physics Letters* 97.12 (2010), 123105. DOI: 10.1063/1.3492843.

[505] C. G. C. H. M. Fabrie et al. "Conversion from Al to Al2O3 of subnanometer barriers for magnetic tunnel junctions monitored in real time". *Journal of Applied Physics* 99.8 (2006), 08T303. DOI: 10.1063/1.2159419.

[506] G. Lin et al. "Performance enhancement of monolayer MoS2 transistors by atomic layer deposition of high-k dielectric assisted by Al2O3 seed layer". *Journal of Physics D: Applied Physics* 53.10 (2019), 105103. DOI: 10.1088/1361-6463/ab605b.

[507] J. R. Lince, D. J. Carré, and P. D. Fleischauer. "Schottky-barrier formation on a covalent semiconductor without Fermi-level pinning: The metal-MoS2(0001) interface". *Physical Review B* 36.3 (1987), 1647–1656. DOI: 10.1103/PhysRevB.36.1647.

[508] H. Kroemer. "Nobel Lecture: Quasielectric fields and band offsets: teaching electrons new tricks". *Reviews of Modern Physics* 73.3 (2001), 783–793. DOI: 10.1103/RevModPhys.73.783.

[509] D. M. Fleetwood. "'Border traps' in MOS devices". *IEEE Transactions on Nuclear Science* 39.2 (1992), 269–271. DOI: 10.1109/23.277495.

[510] D. M. Fleetwood et al. "Effects of oxide traps, interface traps, and "border traps" on metal-oxide-semiconductor devices". *Journal of Applied Physics* 73.10 (1993), 5058–5074. DOI: 10.1063/1.353777.

[511] Y. Y. Illarionov et al. "Energetic mapping of oxide traps in MoS2 field-effect transistors". *2D Materials* 4.2 (2017), 25108. DOI: 10.1088/2053-1583/aa734a.

[512] A. Valsaraj et al. "Theoretical and experimental investigation of vacancy-based doping of monolayer MoS2 on oxide". *2D Materials* 2.4 (2015), 45009. DOI: 10.1088/2053-1583/2/4/045009.

[513] P. D. Kirsch et al. "Dipole model explaining high-k/metal gate field effect transistor threshold voltage tuning". *Applied Physics Letters* 92.9 (2008), 92901. DOI: 10.1063/1.2890056.

[514] P. Zhao et al. "Evaluation of border traps and interface traps in HfO2/MoS2 gate stacks by capacitance–voltage analysis". *2D Materials* 5.3 (2018), 31002. DOI: 10.1088/2053-1583/aab728.

[515] A. Gaur et al. "Analysis of admittance measurements of MOS capacitors on CVD grown bilayer MoS2". *2D Materials* 6.3 (2019), 35035. DOI: 10.1088/2053-1583/ab20fb.

[516] A. Piacentini et al. "Stable Al2O3 Encapsulation of MoS2-FETs Enabled by CVD Grown h-BN". *Advanced Electronic Materials* (2022). DOI: https://doi.org/10.1002/aelm.202200123.

[517] S. Y. Kim, H. I. Yang, and W. Choi. "Photoluminescence quenching in monolayer transition metal dichalcogenides by Al2O3 encapsulation". *Applied Physics Letters* 113.13 (2018), 133104. DOI: 10.1063/1.5048052.

[518] J. Tao et al. "The energy-band alignment at molybdenum disulphide and high-k dielectrics interfaces". *Applied Physics Letters* 104.23 (2014), 232110. DOI: 10.1063/1.4883865.

[519] A. Michail et al. "Optical detection of strain and doping inhomogeneities in single layer MoS2". *Applied Physics Letters* 108.17 (2016), 5. DOI: 10.1063/1.4948357.

[520] C. Lee et al. "Density functional theory investigation of the electronic structure and thermoelectric properties of layered Mo S2, Mo Se2 and their mixed-layer compound". *Journal of Solid State Chemistry* 211 (2014), 113–119.

[521] R. Yan et al. "Raman and Photoluminescence Study of Dielectric and Thermal Effects on Atomically Thin MoS2". *arXiv: Materials Science* (2012).

[522] G. Plechinger et al. "Low-temperature photoluminescence of oxide-covered single-layer MoS2". *physica status solidi (RRL) – Rapid Research Letters* 6.3 (2012), 126–128. DOI: https://doi.org/10.1002/pssr.201105589.

[523] A. Molina-Sánchez and L. Wirtz. "Phonons in single-layer and few-layer MoS2 and WS2". *Physical Review B* 84.15 (2011), 155413. DOI: 10.1103/PhysRevB.84.155413.

[524] T. Li et al. "Electrical performance of multilayer MoS2 transistors on high-κ Al2O3 coated Si substrates". *AIP Advances* 5.5 (2015), 57102. DOI: 10.1063/1.4919800.

[525] C. J. Powell. "Practical guide for inelastic mean free paths, effective attenuation lengths, mean escape depths, and information depths in x-ray photoelectron spectroscopy". *Journal of Vacuum Science & Technology A* 38.2 (2020), 14. DOI: 10.1116/1.5141079.

[526] S. Gurban et al. "Experimental determination of the inelastic mean free path (IMFP) of electrons in selected oxide films applying surface excitation correction". *Surface and Interface Analysis* 38.4 (2006), 624–627. DOI: https://doi.org/10.1002/sia.2302.

[527] B. R. Strohmeier. "An ESCA method for determining the oxide thickness on aluminum alloys". *Surface and Interface Analysis* 15.1 (1990), 51–56. DOI: https://doi.org/10.1002/sia.740150109.

[528] A. G. Shard. "Practical guides for x-ray photoelectron spectroscopy: Quantitative XPS". *Journal of Vacuum Science & Technology A* 38.4 (2020), 41201. DOI: 10.1116/1.5141395.

[529] I. T. McGovern et al. "Soft X-ray photoemission spectroscopy of metal-molybdenum bisulphide interfaces". *Surface Science* 152-153 (1985), 1203–1212. DOI: https://doi.org/10.1016/0039-6028(85)90540-0.

[530] W. Song and M. Yoshitake. "A work function study of ultra-thin alumina formation on NiAl(110) surface". *Applied Surface Science* 251.1 (2005), 14–18. DOI: https://doi.org/10.1016/j.apsusc.2005.03.116.

[531] O. A. Dicks et al. "The origin of negative charging in amorphous Al2O3 films: the role of native defects". *Nanotechnology* 30.20 (2019), 205201. DOI: 10.1088/1361-6528/ab0450.

[532] K. Hirose et al. "Photoelectron spectroscopy studies of SiO2/Si interfaces". *Progress in Surface Science* 82.1 (2007), 3–54. DOI: https://doi.org/10.1016/j.progsurf.2006.10.001.

[533] K. S. Liang, G. J. Hughes, and R. R. Chianelli. "UPS investigation of poorly crystallized MoS2". *Journal of Vacuum Science & Technology A* 2.2 (1984), 991–994. DOI: 10.1116/1.572499.

[534] K. Henkel, M. Kot, and D. Schmeißer. "Localized defect states and charge trapping in atomic layer deposited-Al2O3 films". *Journal of Vacuum Science & Technology A* 35.1 (2016), 01B125. DOI: 10.1116/1.4971991.

[535] M. Kefi et al. "Hybridization of Al and O states in alpha- and gamma-alumina". *Journal of Physics: Condensed Matter* 5.45 (1993), 8629–8642. DOI: 10.1088/0953-8984/5/45/016.

[536] E. O. Filatova and A. S. Konashuk. "Interpretation of the Changing the Band Gap of Al2O3 Depending on Its Crystalline Form: Connection with Different Local Symmetries". *The Journal of Physical Chemistry C* 119.35 (2015), 20755–20761. DOI: 10.1021/acs.jpcc.5b06843.

[537] R. Besse et al. "Beyond the Anderson rule: importance of interfacial dipole and hybridization in van der Waals heterostructures". *2D Materials* 8.4 (2021), 41002. DOI: 10.1088/2053-1583/ac1902.

[538] R. Degraeve et al. "Trap Spectroscopy by Charge Injection and Sensing (TSCIS): A quantitative electrical technique for studying defects in dielectric stacks". *2008 IEEE International Electron Devices Meeting*. 2008, 1–4. DOI: 10.1109/IEDM.2008.4796812.

[539] Y. Zhao et al. "Electrical spectroscopy of defect states and their hybridization in monolayer MoS2". *Nature Communications* 14.1 (2023), 44. DOI: 10.1038/s41467-022-35651-1.

[540] P. Zhao et al. "Effects of annealing on top-gated MoS2 transistors with HfO2 dielectric". *Journal of Vacuum Science & Technology B* 35.1 (2017), 01A118. DOI: 10.1116/1.4974220.

[541] Y. Zhang et al. "Ambipolar MoS2 Thin Flake Transistors". *Nano Letters* 12.3 (2012), 1136–1140. DOI: 10.1021/nl2021575.

[542] F. Wang et al. "Ionic Liquid Gating of Suspended MoS2 Field Effect Transistor Devices". *Nano Letters* 15.8 (2015), 5284–5288. DOI: 10.1021/acs.nanolett.5b01610.

[543] P. D. Patil et al. *Electric Double Layer Field-Effect Transistors Using Two-Dimensional (2D) Layers of Copper Indium Selenide (CuIn7Se11)*. 2019. DOI: 10.3390/electronics8060645.

[544] J. Pu et al. "Highly Flexible MoS2 Thin-Film Transistors with Ion Gel Dielectrics". *Nano Letters* 12.8 (2012), 4013–4017. DOI: 10.1021/nl301335q.

[545] M. M. Perera et al. "Improved Carrier Mobility in Few-Layer MoS2 Field-Effect Transistors with Ionic-Liquid Gating". *ACS Nano* 7.5 (2013), 4449–4458. DOI: 10.1021/nn401053g.

[546] A. T. Wong et al. "Impact of gate geometry on ionic liquid gated ionotronic systems". *APL Materials* 5.4 (2017), 42501. DOI: 10.1063/1.4974485.

[547] T. Sato, G. Masuda, and K. Takagi. "Electrochemical properties of novel ionic liquids for electric double layer capacitor applications". *Electrochimica Acta* 49.21 (2004), 3603–3611. DOI: https://doi.org/10.1016/j.electacta.2004.03.030.

[548] N. Miyakawa et al. *Drift Suppression of Solution-Gated Graphene Field-Effect Transistors by Cation Doping for Sensing Platforms*. 2021. DOI: 10.3390/s21227455.

[549] D. J. Late et al. "Hysteresis in Single-Layer MoS2 Field Effect Transistors". *ACS Nano* 6.6 (2012), 5635–5641. DOI: 10.1021/nn301572c.

[550] S. McDonnell et al. "MoS2–Titanium Contact Interface Reactions". *ACS Applied Materials & Interfaces* 8.12 (2016), 8289–8294. DOI: 10.1021/acsami.6b00275.

[551] A. Singh and A. K. Singh. "Origin of n-type conductivity of monolayer MoS2". *Physical Review B* 99.12 (2019), 121201. DOI: 10.1103/PhysRevB.99.121201.

[552] W. S. Leong et al. "Tuning the threshold voltage of MoS2 field-effect transistors via surface treatment". *Nanoscale* 7.24 (2015), 10823–10831. DOI: 10.1039/C5NR00253B.

[553] J. Yang et al. "Electrical Doping Effect of Vacancies on Monolayer MoS2". *The Journal of Physical Chemistry C* 123.5 (2019), 2933–2939. DOI: 10.1021/acs.jpcc.8b10496.

[554] J. Robertson. "High dielectric constant oxides". *European Physical Journal-Applied Physics* 28.3 (2004), 265–291. DOI: 10.1051/epjap:2004206.

[555] D. Edelberg et al. "Approaching the Intrinsic Limit in Transition Metal Dise-lenides via Point Defect Control". *Nano Letters* 19.7 (2019), 4371–4379. DOI: 10.1021/acs.nanolett.9b00985.

[556] M. Amani et al. "Near-unity photoluminescence quantum yield in MoS2". *Science* 350.6264 (2015), 1065–1068. DOI: 10.1126/science.aad2114.

[557] M. Amani et al. "High Luminescence Efficiency in MoS2 Grown by Chemical Vapor Deposition". *ACS Nano* 10.7 (2016), 6535–6541. DOI: 10.1021/acsnano. 6603443.

[558] A. Alharbi, P. Zahl, and D. Shahrjerdi. "Material and device properties of superacid-treated monolayer molybdenum disulfide". *Applied Physics Letters* 110.3 (2017), 33503. DOI: 10.1063/1.4974046.

[559] Z. Yu et al. "Towards intrinsic charge transport in monolayer molybdenum disulfide by defect and interface engineering". *Nature Communications* 5.1 (2014), 5290. DOI: 10.1038/ncomms6290.

[560] A. Förster et al. "Chemical and Electronic Repair Mechanism of Defects in MoS2 Monolayers". *ACS Nano* 11.10 (2017), 9989–9996. DOI: 10.1021/acsnano. 7b04162.

[561] S. M. Feng et al. "Synthesis of Ultrahigh-Quality Monolayer Molybdenum Disulfide through In Situ Defect Healing with Thiol Molecules". *Small* (2020), 9. DOI: 10.1002/smll.202003357.

[562] P. Bampoulis et al. "Defect Dominated Charge Transport and Fermi Level Pinning in MoS2/Metal Contacts". *ACS Applied Materials & Interfaces* 9.22 (2017), 19278–19286. DOI: 10.1021/acsami.7b02739.

[563] B. Schuler et al. "How Substitutional Point Defects in Two-Dimensional WS2 Induce Charge Localization, Spin–Orbit Splitting, and Strain". *ACS Nano* 13.9 (2019), 10520–10534. DOI: 10.1021/acsnano.9b04611.

[564] K. Sotthewes et al. "Universal Fermi-Level Pinning in Transition-Metal Dichalco-genides". *The Journal of Physical Chemistry C* 123.9 (2019), 5411–5420. DOI: 10.1021/acs.jpcc.8b10971.

[565] Y. Wan et al. "Low-defect-density WS2 by hydroxide vapor phase deposition". *Nature Communications* 13.1 (2022), 4149. DOI: 10.1038/s41467-022-31886-0.

[566] S. Barja et al. "Identifying substitutional oxygen as a prolific point defect in monolayer transition metal dichalcogenides". *Nature Communications* 10.1 (2019), 3382. DOI: 10.1038/s41467-019-11342-2.

[567] J. A. Robinson and B. Schuler. "Engineering and probing atomic quantum defects in 2D semiconductors: A perspective". *Applied Physics Letters* 119.14 (2021), 140501. DOI: 10.1063/5.0065185.

[568] J. Yang et al. "Improved Growth Behavior of Atomic-Layer-Deposited High-k Dielectrics on Multilayer MoS2 by Oxygen Plasma Pretreatment". *ACS Applied Materials & Interfaces* 5.11 (2013), 4739–4744. DOI: 10.1021/am303261c.

[569] W. Yang et al. "The Integration of Sub-10nm Gate Oxide on MoS2 with Ultra Low Leakage and Enhanced Mobility". *Scientific Reports* 5.1 (2015), 11921. DOI: 10.1038/srep11921.

[570] J. G. Song et al. "Effect of Al2O3 Deposition on Performance of Top-Gated Monolayer MoS2-Based Field Effect Transistor". *ACS Applied Materials & Interfaces* 8.41 (2016), 28130–28135. DOI: 10.1021/acsami.6b07271.

[571] J. Zhou et al. "Non-invasive digital etching of van der Waals semiconductors". *Nature Communications* 13.1 (2022), 1844. DOI: 10.1038/s41467-022-29447-6.

[572] P. Zhao et al. "Understanding the Impact of Annealing on Interface and Border Traps in the Cr/HfO2/Al2O3/MoS2 System". *ACS Applied Electronic Materials* 1.8 (2019), 1372–1377. DOI: 10.1021/acsaelm.8b00103.

[573] Y. Cui et al. "High-Performance Monolayer WS2 Field-Effect Transistors on High-κ Dielectrics". *Advanced Materials* 27.35 (2015), 5230–5234. DOI: https://doi.org/10.1002/adma.201502222.

[574] B. H. Wang et al. "High-k Gate Dielectrics for Emerging Flexible and Stretchable Electronics". *Chemical Reviews* 118.11 (2018), 5690–5754. DOI: 10.1021/acs.chemrev.8b00045.

[575] P. A. Caban et al. "The role of hydrogen in carbon incorporation and surface roughness of MOCVD-grown thin boron nitride". *Journal of Crystal Growth* 498 (2018), 71–76. DOI: https://doi.org/10.1016/j.jcrysgro.2018.06.001.

[576] C. Wen et al. "Dielectric Properties of Ultrathin CaF2 Ionic Crystals". *Advanced Materials* 32.34 (2020), 2002525. DOI: https://doi.org/10.1002/adma.202002525.

[577] J.-K. Huang et al. "High-κ perovskite membranes as insulators for two-dimensional transistors". *Nature* 605.7909 (2022), 262–267. DOI: 10.1038/s41586-022-04588-2.

[578] A. J. Yang et al. "Van der Waals integration of high-κ perovskite oxides and two-dimensional semiconductors". *Nature Electronics* 5.4 (2022), 233–240. DOI: 10.1038/s41928-022-00753-7.

[579] L. Wang et al. "A general one-step plug-and-probe approach to top-gated transistors for rapidly probing delicate electronic materials". *Nature Nanotechnology* 17.11 (2022), 1206–1213. DOI: 10.1038/s41565-022-01221-1.

[580] A. Guimerà-Brunet et al. "Novel transducers for high-channel-count neuroelectronic recording interfaces". *Current Opinion in Biotechnology* 72 (2021), 39–47. DOI: https://doi.org/10.1016/j.copbio.2021.10.002.

[581] N. Schaefer et al. "Multiplexed neural sensor array of graphene solution-gated field-effect transistors". *2d Materials* 7.2 (2020), 10. DOI: 10.1088/2053-1583/ab7976.

[582] R. Garcia-Cortadella et al. "Distortion-Free Sensing of Neural Activity Using Graphene Transistors". *Small* 16.16 (2020), 1906640. DOI: 10.1002/smll.201906640.

[583] N. Pérez-Prieto and M. Delgado-Restituto. "Recording Strategies for High Channel Count, Densely Spaced Microelectrode Arrays". *Frontiers in Neuroscience* 15 (2021). DOI: 10.3389/fnins.2021.681085.

[584] B. C. Raducanu et al. *Time Multiplexed Active Neural Probe with 1356 Parallel Recording Sites.* 2017. DOI: 10.3390/s17102388.

[585] J. Viventi et al. "Flexible, foldable, actively multiplexed, high-density electrode array for mapping brain activity in vivo". *Nature Neuroscience* 14.12 (2011), 1599–1605. DOI: 10.1038/nn.2973.

[586] M. A. Escabí et al. "A high-density, high-channel count, multiplexed μECoG array for auditory-cortex recordings". *Journal of Neurophysiology* 112.6 (2014), 1566–1583. DOI: 10.1152/jn.00179.2013.

[587] C.-H. Chiang et al. "Development of a neural interface for high-definition, long-term recording in rodents and nonhuman primates". *Science Translational Medicine* 12.538 (2020), eaay4682. DOI: 10.1126/scitranslmed.aay4682.

[588] K. D. Harris, A. L. Elias, and H.-J. Chung. "Flexible electronics under strain: a review of mechanical characterization and durability enhancement strategies". *Journal of Materials Science* 51.6 (2016), 2771–2805. DOI: 10.1007/s10853-015-9643-3.

[589] S.-I. Park et al. "Theoretical and Experimental Studies of Bending of Inorganic Electronic Materials on Plastic Substrates". *Advanced Functional Materials* 18.18 (2008), 2673–2684. DOI: https://doi.org/10.1002/adfm.200800306.

[590] S. Hong et al. "Multifunctional molybdenum disulfide flash memory using a PEDOT:PSS floating gate". *NPG Asia Materials* 13.1 (2021), 38. DOI: 10.1038/s41427-021-00307-x.

[591] H.-Y. Chang et al. "High-Performance, Highly Bendable MoS2 Transistors with High-K Dielectrics for Flexible Low-Power Systems". *ACS Nano* 7.6 (2013), 5446–5452. DOI: 10.1021/nn401429w.

[592] S. Hong et al. "Highly sensitive active pixel image sensor array driven by large-area bilayer MoS2 transistor circuitry". *Nature Communications* 12.1 (2021), 3559. DOI: 10.1038/s41467-021-23711-x.

[593] S. Kim et al. "Active-matrix monolithic gas sensor array based on MoS2 thin-film transistors". *Communications Materials* 1.1 (2020), 86. DOI: 10.1038/s43246-020-00086-y.

[594] Y. J. Park et al. "All MoS2-Based Large Area, Skin-Attachable Active-Matrix Tactile Sensor". *ACS Nano* 13.3 (2019), 3023–3030. DOI: 10.1021/acsnano.8b07995.

[595] C. Boehler et al. "Tutorial: guidelines for standardized performance tests for electrodes intended for neural interfaces and bioelectronics". *Nature Protocols* 15.11 (2020), 3557–3578. DOI: 10.1038/s41596-020-0389-2.

[596] C. Mackin et al. "A Current–Voltage Model for Graphene Electrolyte-Gated Field-Effect Transistors". *IEEE Transactions on Electron Devices* 61.12 (2014), 3971–3977. DOI: 10.1109/TED.2014.2360660.

[597] H.-M. Li et al. "Metal-Semiconductor Barrier Modulation for High Photoresponse in Transition Metal Dichalcogenide Field Effect Transistors". *Scientific Reports* 4.1 (2014), 4041. DOI: 10.1038/srep04041.

[598] J. Lee et al. "Multi-finger flexible graphene field effect transistors with high bendability". *Applied Physics Letters* 101.25 (2012), 252109. DOI: 10.1063/1.4772541.

[599] R. Garcia-Cortadella et al. "Switchless Multiplexing of Graphene Active Sensor Arrays for Brain Mapping". *Nano Letters* (2020). DOI: 10.1021/acs.nanolett.0c00467.

[600] M. Naqi et al. "Pulsed Gate Switching of MoS2 Field-Effect Transistor Based on Flexible Polyimide Substrate for Ultrasonic Detectors". *Advanced Functional Materials* 31.7 (2021), 2007389. DOI: https://doi.org/10.1002/adfm.202007389.

[601] A. Pirkle et al. "The effect of chemical residues on the physical and electrical properties of chemical vapor deposited graphene transferred to SiO2". *Applied Physics Letters* 99.12 (2011), 122108. DOI: 10.1063/1.3643444.

[602] V. Woods et al. "Long-term recording reliability of liquid crystal polymer µECoG arrays". *Journal of Neural Engineering* 15.6 (2018), 66024. DOI: 10.1088/1741-2552/aae39d.

[603] E. Reato et al. "Zero-Bias Power-Detector Circuits based on MoS2 Field-Effect Transistors on Wafer-Scale Flexible Substrates". *Advanced Materials* n/a.n/a (2022), 2108469. DOI: https://doi.org/10.1002/adma.202108469.

[604] M. E. P. Tweedie et al. "Transparent ultrathin all-two-dimensional lateral Gr:WS2:Gr photodetector arrays on flexible substrates and their strain induced failure mechanisms". *Materials Today Advances* 6 (2020), 100067. DOI: https://doi.org/10.1016/j.mtadv.2020.100067.

[605] J. Cisneros-Fernández et al. "A 1024-Channel 10-Bit 36-μW/ch CMOS ROIC for Multiplexed GFET-Only Sensor Arrays in Brain Mapping". *IEEE Transactions on Biomedical Circuits and Systems* 15.5 (2021), 860–876. DOI: 10.1109/TBCAS.2021.3113556.

[606] Y. Liu et al. "Promises and prospects of two-dimensional transistors". *Nature* 591.7848 (2021), 43–53. DOI: 10.1038/s41586-021-03339-z.

[607] Z. Lin et al. "Defect engineering of two-dimensional transition metal dichalcogenides". *2d Materials* 3.2 (2016), 21. DOI: 10.1088/2053-1583/3/2/022002.

[608] G. Yannick et al. "Impact of synthesis temperature and precursor ratio on the crystal quality of MOCVD WSe2 monolayers". *Nanotechnology* (2023).

[609] S. K. Pandey et al. "Controlled p-type substitutional doping in large-area monolayer WSe2 crystals grown by chemical vapor deposition". *Nanoscale* 10.45 (2018), 21374–21385. DOI: 10.1039/c8nr07070a.

[610] K. H. Zhang et al. "Tuning the Electronic and Photonic Properties of Monolayer MoS2 via In Situ Rhenium Substitutional Doping". *Advanced Functional Materials* 28.16 (2018), 7. DOI: 10.1002/adfm.201706950.

[611] K. H. Zhang and J. Robinson. "Doping of Two-Dimensional Semiconductors: A Rapid Review and Outlook". *Mrs Advances* 4.51-52 (2019), 2743–2757. DOI: 10.1557/adv.2019.391.

[612] M. A. Land, K. N. Robertson, and S. T. Barry. "Ligand-Assisted Volatilization and Thermal Stability of Bis(imido)dichloromolybdenum(VI) ([(t-BuN=)2MoCl2]2) and Its Adducts". *Organometallics* 39.7 (2020), 916–927. DOI: 10.1021/acs.organomet.9b00578.

[613] M. A. Land et al. "Thermal Stability and Decomposition Pathways in Volatile Molybdenum(VI) Bis-imides". *Inorganic Chemistry* 61.12 (2022), 4980–4994. DOI: 10.1021/acs.inorgchem.1c03817.

[614] J. Zhu. "High performance MoS transistors based on wafer-scale low-temperature MOCVD synthesis". PhD thesis. Massachussetts Institute of Technology, 2021.

[615] C. Ahn et al. "Low-Temperature Synthesis of Large-Scale Molybdenum Disulfide Thin Films Directly on a Plastic Substrate Using Plasma-Enhanced Chemical Vapor Deposition". *Advanced Materials* 27.35 (2015), 5223–5229. DOI: 10.1002/adma.201501678.

[616] P. M. Campbell et al. "Plasma-assisted synthesis of MoS2". *2d Materials* 5.1 (2018), 12. DOI: 10.1088/2053-1583/aa8c96.

[617] H. Seok et al. "Low-Temperature Synthesis of Wafer-Scale MoS2–WS2 Vertical Heterostructures by Single-Step Penetrative Plasma Sulfurization". *ACS Nano* 15.1 (2021), 707–718. DOI: 10.1021/acsnano.0c06989.

[618] A. Bala et al. "Low-Temperature Plasma-Assisted Growth of Large-Area MoS2 for Transparent Phototransistors". *Advanced Functional Materials* n/a.n/a (2022), 2205106. DOI: https://doi.org/10.1002/adfm.202205106.

[619] W. H. Chang et al. "Sb2Te3/MoS2 Van der Waals Junctions with High Thermal Stability and Low Contact Resistance". *Advanced Electronic Materials* n/a.n/a (2023), 2201091. DOI: https://doi.org/10.1002/aelm.202201091.

[620] Y. Wang et al. "P-type electrical contacts for 2D transition-metal dichalcogenides". *Nature* (2022). DOI: 10.1038/s41586-022-05134-w.

[621] Z. Dai et al. "Mechanics at the interfaces of 2D materials: Challenges and opportunities". *Current Opinion in Solid State and Materials Science* 24.4 (2020), 100837. DOI: https://doi.org/10.1016/j.cossms.2020.100837.

[622] J. Kang et al. "Tough-interface-enabled stretchable electronics using non-stretchable polymer semiconductors and conductors". *Nature Nanotechnology* (2022). DOI: 10.1038/s41565-022-01246-6.

[623] E. Parzinger et al. "Photocatalytic Stability of Single- and Few-Layer MoS2". *ACS Nano* 9.11 (2015), 11302–11309. DOI: 10.1021/acsnano.5b04979.

[624] E. Parzinger et al. "Hydrogen evolution activity of individual mono-, bi-, and few-layer MoS2 towards photocatalysis". *Applied Materials Today* 8 (2017), 132–140. DOI: 10.1016/j.apmt.2017.04.007.

[625] B. Han and Y. H. Hu. "MoS2 as a co-catalyst for photocatalytic hydrogen production from water". *Energy Science & Engineering* 4.5 (2016), 285–304. DOI: https://doi.org/10.1002/ese3.128.

[626] G. Q. Li et al. "All The Catalytic Active Sites of MoS2 for Hydrogen Evolution". *Journal of the American Chemical Society* 138.51 (2016), 16632–16638. DOI: 10.1021/jacs.6b05940.

[627] J. P. Shi et al. "Controllable Growth and Transfer of Mono layer MoS2 on Au Foils and Its Potential Application in Hydrogen Evolution Reaction". *ACS Nano* 8.10 (2014), 10196–10204. DOI: 10.1021/nn503211t.

[628] L. Q. Dong et al. "Activating MoS2 basal planes for hydrogen evolution through direct CVD morphology control". *Journal of Materials Chemistry A* 7.48 (2019), 27603–27611. DOI: 10.1039/c9ta08738a.

[629] V. T. Nguyen et al. "Large-scale chemical vapor deposition growth of highly crystalline MoS2 thin films on various substrates and their optoelectronic properties". *Current Applied Physics* 19.10 (2019), 1127–1131. DOI: 10.1016/j.cap.2019.07.007.

[630] D. M. Andoshe et al. "Directly Assembled 3D Molybdenum Disulfide on Silicon Wafer for Efficient Photoelectrochemical Water Reduction". *Advanced Sustainable Systems* 2.3 (2018), 1700142. DOI: https://doi.org/10.1002/adsu.201700142.

[631] S. Boandoh et al. "Wafer-Scale van der Waals Heterostructures with Ultraclean Interfaces via the Aid of Viscoelastic Polymer". *ACS Applied Materials & Interfaces* 11.1 (2019), 1579–1586. DOI: 10.1021/acsami.8b16261.

[632] R. K. Biroju et al. "Hydrogen Evolution Reaction Activity of Graphene–MoS2 van der Waals Heterostructures". *ACS Energy Letters* 2.6 (2017), 1355–1361. DOI: 10.1021/acsenergylett.7b00349.

[633] H.-U. Kim et al. "Low-temperature wafer-scale growth of MoS2-graphene heterostructures". *Applied Surface Science* 470 (2019), 129–134. DOI: https://doi.org/10.1016/j.apsusc.2018.11.126.

[634] K. C. Kwon et al. "Memristive Devices Based on Two-Dimensional Transition Metal Chalcogenides for Neuromorphic Computing". *Nano-Micro Letters* 14.1 (2022), 58. DOI: 10.1007/s40820-021-00784-3.

[635] J. Yuan and J. Lou. "Memristor goes two-dimensional". *Nature Nanotechnology* 10.5 (2015), 389–390. DOI: 10.1038/nnano.2015.94.

[636] V. K. Sangwan et al. "Gate-tunable memristive phenomena mediated by grain boundaries in single-layer MoS2". *Nature Nanotechnology* 10.5 (2015), 403–406. DOI: 10.1038/nnano.2015.56.

[637] R. Xu et al. "Vertical MoS2 Double-Layer Memristor with Electrochemical Metallization as an Atomic-Scale Synapse with Switching Thresholds Approaching 100 mV". *Nano Letters* 19.4 (2019), 2411–2417. DOI: 10.1021/acs.nanolett.8b05140.

[638] S. M. Hus et al. "Observation of single-defect memristor in an MoS2 atomic sheet". *Nature Nanotechnology* 16.1 (2021), 58–62. DOI: 10.1038/s41565-020-00789-w.

[639] F. Zhang et al. "Electric-field induced structural transition in vertical MoTe2- and Mo1–xWxTe2-based resistive memories". *Nature Materials* 18.1 (2019), 55–61. DOI: 10.1038/s41563-018-0234-y.

[640] X. Zhu et al. "Ionic modulation and ionic coupling effects in MoS2 devices for neuromorphic computing". *Nature Materials* 18.2 (2019), 141–148. DOI: 10.1038/s41563-018-0248-5.

[641] M. Belete et al. "Nonvolatile Resistive Switching in Nanocrystalline Molybdenum Disulfide with Ion-Based Plasticity". *Advanced Electronic Materials* 6.3 (2020), 7. DOI: 10.1002/aelm.201900892.

[642] S. Papadopoulos et al. "Ion Migration in Monolayer MoS2 Memristors". *Physical Review Applied* 18.1 (2022), 14018. DOI: 10.1103/PhysRevApplied.18.014018.

[643] F. D. Broccard et al. "Neuromorphic neural interfaces: from neurophysiological inspiration to biohybrid coupling with nervous systems". *Journal of Neural Engineering* 14.4 (2017), 41002. DOI: 10.1088/1741-2552/aa67a9.

[644] M. Naqi et al. "Multilevel artificial electronic synaptic device of direct grown robust MoS2 based memristor array for in-memory deep neural network". *npj 2D Materials and Applications* 6.1 (2022), 53. DOI: 10.1038/s41699-022-00325-5.

[645] Y. Li and K.-W. Ang. "Hardware Implementation of Neuromorphic Computing Using Large-Scale Memristor Crossbar Arrays". *Advanced Intelligent Systems* 3.1 (2021), 2000137. DOI: https://doi.org/10.1002/aisy.202000137.

[646] P. Hohenberg and W. Kohn. "Inhomogeneous Electron Gas". *Phys. Rev.* 136.3B (1964), B864–B871. DOI: 10.1103/PhysRev.136.B864.

[647] W. Kohn and L. J. Sham. "Self-Consistent Equations Including Exchange and Correlation Effects". *Phys. Rev.* 140.4A (1965), A1133–A1138. DOI: 10.1103/PhysRev.140.A1133.

[648] J. M. Soler et al. "The {SIESTA} method forab initioorder-Nmaterials simulation". *Journal of Physics: Condensed Matter* 14.11 (2002), 2745–2779. DOI: 10.1088/0953-8984/14/11/302.

[649] E. Artacho et al. "The {SIESTA} method$\mathsemicolon$ developments and applicability". *Journal of Physics: Condensed Matter* 20.6 (2008), 64208. DOI: 10.1088/0953-8984/20/6/064208.

[650] J. P. Perdew, K. Burke, and M. Ernzerhof. "Generalized Gradient Approximation Made Simple". *Phys. Rev. Lett.* 77.18 (1996), 3865–3868. DOI: 10.1103/PhysRevLett.77.3865.

[651] N. Troullier and J. L. Martins. "Efficient pseudopotentials for plane-wave calculations". *Phys. Rev. B* 43.3 (1991), 1993–2006. DOI: 10.1103/PhysRevB.43.1993.

[652] L. Kleinman and D. M. Bylander. "Efficacious Form for Model Pseudopotentials". *Physical Review Letters* 48.20 (1982), 1425–1428. DOI: 10.1103/PhysRevLett.48.1425.

[653] E. Artacho et al. "Linear-Scaling ab-initio Calculations for Large and Complex Systems". *physica status solidi (b)* 215.1 (1999), 809–817. DOI: https://doi.org/10.1002/(SICI)1521-3951(199909)215:1<809::AID-PSSB809>3.0.CO;2-0.

[654] A. Love, S. Middleman, and A. K. Hochberg. "The dynamics of bubblers as vapor delivery systems". *Journal of Crystal Growth* 129.1-2 (1993), 119–133. DOI: 10.1016/0022-0248(93)90441-x.

[655] Swagelok Company. *Valve Sizing - Technical Bulletin.* Solon, USA, 2007.

[656] Swagelok Company. *Metering valves (S, M, L, and 31 Series., Product Data Sheet.* Solon, USA, 2021. DOI: https://www.swagelok.com/downloads/webcatalogs/en/MS-01-142.pdf.

[657] Schott AG / Advanced Optics. *B270i, Technische Sicherheitsinformation. Material Safety Data Sheet.* Mainz, Germany, 2015.

[658] A. Rai et al. "Progress in Contact, Doping and Mobility Engineering of MoS2: An Atomically Thin 2D Semiconductor". *Crystals* 8.8 (2018), 84. DOI: 10.3390/cryst8080316.

[659] K. M. Freedy et al. "Titanium contacts to $\mathrm{Mo}{\mathrm{S}}_{2}$ with interfacial oxide: Interface chemistry and thermal transport". *Physical Review Materials* 3.10 (2019), 104001. DOI: 10.1103/PhysRevMaterials.3.104001.

[660] K. Verguts et al. "Epitaxial Al2O3(0001)/Cu(111) Template Development for CVD Graphene Growth". *The Journal of Physical Chemistry C* 120.1 (2016), 297–304. DOI: 10.1021/acs.jpcc.5b09461.

[661] B. Chamlagain and S. I. Khondaker. "Rapid Degradation of the Electrical Properties of 2D MoS2 Thin Films under Long-Term Ambient Exposure". *ACS Omega* 6.37 (2021), 24075–24081. DOI: 10.1021/acsomega.1c03522.

[662] Q. H. Thi et al. "Coating two-dimensional MoS2 with polymer creates a corrosive non-uniform interface". *Npj 2d Materials and Applications* 2 (2018), 7. DOI: 10.1038/s41699-018-0079-x.

[663] R. Sant. "Synchrotron x-ray exploration of growth and structure in 2D dichalcogenides". PhD thesis. Université Grenoble Alpes, 2019. DOI: https://tel.archives-ouvertes.fr/tel-02940600.

[664] B. Deng et al. "Anisotropic Strain Relaxation of Graphene by Corrugation on Copper Crystal Surfaces". *Small* 14.22 (2018), 1800725. DOI: https://doi.org/10.1002/smll.201800725.

[665] A. L. Mazzoni et al. "Process Development for Reactive-Ion Etching of Molybdenum Disulfide (MoS2) Utilizing a Poly(methyl methacrylate) (PMMA) Etch Mask". 2017.

[666] S. Xiao et al. "Atomic-layer soft plasma etching of MoS2". *Scientific Reports* 6.1 (2016), 19945. DOI: 10.1038/srep19945.

[667] F. Ghasemi, A. Abdollahi, and S. Mohajerzadeh. "Controlled Plasma Thinning of Bulk MoS2 Flakes for Photodetector Fabrication". *ACS Omega* 4.22 (2019), 19693–19704. DOI: 10.1021/acsomega.9b02367.

[668] Y. C. Kung et al. "Air and Water-Stable n-Type Doping and Encapsulation of Flexible MoS2 Devices with SU8". *Advanced Electronic Materials* 5.1 (2019), 7. DOI: 10.1002/aelm.201800492.

[669] S. Chen et al. "Tip-Based Cleaning and Smoothing Improves Performance in Monolayer MoS2 Devices". *ACS Omega* 6.5 (2021), 4013–4021. DOI: 10.1021/acsomega.0c05934.

[670] B.-K. Kim et al. "Origins of genuine Ohmic van der Waals contact between indium and MoS2". *npj 2D Materials and Applications* 5.1 (2021), 9. DOI: 10.1038/s41699-020-00191-z.

[671] A. Matković et al. "Interfacial Band Engineering of MoS2/Gold Interfaces Using Pyrimidine-Containing Self-Assembled Monolayers: Toward Contact-Resistance-Free Bottom-Contacts". *Advanced Electronic Materials* 6.5 (2020), 2000110. DOI: https://doi.org/10.1002/aelm.202000110.

[672] G. J. Lee et al. "Stress Release Effect of Micro-hole Arrays for Flexible Electrodes and Thin Film Transistors". *ACS Applied Materials & Interfaces* 12.16 (2020), 19226–19234. DOI: 10.1021/acsami.0c02362.

[673] M. D. Groner et al. "Gas diffusion barriers on polymers using Al2O3 atomic layer deposition". *Applied Physics Letters* 88.5 (2006), 51907. DOI: 10.1063/1.2168489.

[674] P. F. Carcia et al. "Ca test of Al2O3 gas diffusion barriers grown by atomic layer deposition on polymers". *Applied Physics Letters* 89.3 (2006), 31915. DOI: 10.1063/1.2221912.

[675] M. Westerhausen et al. "Characterization of Biostable Atomic Layer Deposited (ALD) Multilayer Passivation Coatings for Active Implants". *2019 41st Annual International Conference of the IEEE Engineering in Medicine and Biology Society (EMBC)*. 2019, 3927–3930. DOI: 10.1109/EMBC.2019.8856574.

[676] A. Bulusu et al. "Engineering the mechanical properties of ultrabarrier films grown by atomic layer deposition for the encapsulation of printed electronics". *Journal of Applied Physics* 118.8 (2015), 85501. DOI: 10.1063/1.4928855.

[677] D. Schaubroeck et al. "Polyimide-ald-polyimide layers as hermetic encapsulant for implants". *XXXI International Conference on Surface Modification Technologies (SMT31)*. Mons, 2017, 1–6.

[678] P. Čvančara et al. "Stability of flexible thin-film metallization stimulation electrodes: analysis of explants after first-in-human study and improvement of in vivo performance". *Journal of Neural Engineering* 17.4 (2020), 46006. DOI: 10.1088/1741-2552/ab9a9a.

[679] N. B. Babaroud et al. "Investigation of the long-term adhesion and barrier properties of a PDMS-Parylene stack with PECVD ceramic interlayers for the conformal encapsulation of neural implants". *2021 23rd European Microelectronics and Packaging Conference & Exhibition (EMPC)*. 2021, 1–7. DOI: 10.23919/EMPC53418.2021.9584961.

[680] M. Vomero et al. "Electrocorticography Arrays: Incorporation of Silicon Carbide and Diamond-Like Carbon as Adhesion Promoters Improves In Vitro and In Vivo Stability of Thin-Film Glassy Carbon Electrocorticography Arrays (Adv. Biosys. 1/2018)". *Advanced Biosystems* 2.1 (2018), 1870001. DOI: https://doi.org/10.1002/adbi.201870001.

Appendices

Appendix A

Background, Materials & Methods

A.1 Precursor bond dissociation energy

To determine dissociation energies of some selected precursors used in MOCVD of TMDs, theoretical calculations from first principles were performed. Bogdan Guster[1] is acknowledged for carrying out the simulations.

Computational details

Bond dissociation energies (BDE) were calculated from the energy difference before and after dissociation using a density functional theory (DFT) method. The geometric optimizations and electronic structure calculations were carried out using a numerical atomic orbitals density functional theory (DFT) [646, 647] approach implemented in the SIESTA code [648, 649]. The Perdew-Burke-Ernzerhof functional was used to account for the exchange-correlation energy [650]. The core electrons have been replaced by norm-conserving scalar relativistic pseudopotentials [651] factorized in the Kleinman-Bylander form [652]. A split-valence double-ζ basis set, including polarization functions [653], was used. In all calculations, a cutoff of 400 Ry for the real space integrals, and a tolerance of 10^{-4} and 10^{-3} eV were used on the density matrix and the total energy, respectively, for the convergence of the self-consistent field cycle. In the case of the geometric optimizations, the atomic coordinates were relaxed until the forces on the atoms were below $0.01\,\mathrm{eV\,\mathring{A}^{-1}}$. The molecules were placed in a box with the side of $25\,\mathring{A}$ to dismiss spurious interactions with neighbouring supercell images. Due to the DFT method used, a counterpoise correction was applied to account for the basis set superposition error.

---

[1]https://orcid.org/0000-0003-1305-1862, currently affiliated at the University of Liege (Belgium)

Table A1 Bond dissociation energies (BDE) of transition-metal and chalcogen precursors by DFT simulation from first principles. BDEs are calculated along the dissociation pathway for different Mo, W, S, Se, and Te molecular precursors and compared to literature. Reference values are typically reported as the first (1st) dissociation in a series of steps or averaged (Av.) BDEs from the multi-step dissociation pathway, as indicated. Precursors used in this work are underlined.

Precursor		Educt	Products	BDE (eV)	BDE (1st/Av.) [ref] (eV)
Mo	MHC	$Mo(CO)_6$	$Mo(CO)_5 + CO$	1.73	1.75 (1st) [232]
		$Mo(CO)_5$	$Mo(CO)_4 + CO$	2.63	
		$Mo(CO)_4$	$Mo(CO)_3 + CO$	1.68	
		$Mo(CO)_3$	$Mo(CO)_2 + CO$	1.52	1.70 (Av.) [153]
		$Mo(CO)_2$	$Mo(CO) + CO$	1.89	
		$Mo(CO)$	$Mo + CO$	0.37	
W	WHC	$W(CO)_6$	$W(CO)_5 + CO$	2.15	2.07 (1st) [232]
		$W(CO)_5$	$W(CO)_4 + CO$	4.25	
		$W(CO)_4$	$W(CO)_3 + CO$	2.08	2.52 ± 0.59 (Av.) [321]
		$W(CO)_3$	$W(CO)_2 + CO$	2.48	
		$W(CO)_2$	$W(CO) + CO$	2.33	
		$W(CO)$	$W + CO$	2.34	
S	H_2S	H-S-H	HS + H	3.66	
		HS	H + S	3.19	
	DMS	CH_3-S-CH_3	CH_3-S + CH_3	3.38	
		CH_3-S	CH_3 + S	3.09	
	DES	CH_3-CH_2-S-CH_2-CH_3	CH_3-S + CH_3	3.44	
		CH_3-CH_2-S	CH_3-CH_2 + S	3.06	3.00 [153]
	DMDS	CH_3-S-S-CH_3	CH_3-S-S + CH_3	2.96	
		CH_3-S-S-CH_3	CH_3-S + S-CH_3	2.84	
	DEDS	CH_3-CH_2-S-S-CH_2-CH_3	CH_3-CH_2-S-S + CH_2-CH_3	-	2.70 [153]
		CH_3-CH_2-S-S-CH_2-CH_3	CH_3-CH_2-S + S-CH_2-CH_3	-	2.00 [153]
	DTBS	$(CH_3)_3$-CH_2-S-CH_2-$(CH_3)_3$	$(CH_3)_3$-CH_2-S + CH_2-$(CH_3)_3$	2.58	
		$(CH_3)_3$-CH_2-S	$(CH_3)_3$-CH_2 + S	2.60	
	H_2Se	H-Se-H	HSe + H	3.55	4.78 ± 0.06 (Av.) [321]
		H-Se-H	H + Se	3.32	
Se	DMSe	CH_3-Se-CH_3	CH_3-Se + CH_3	3.12	3.78 ± 0.19 (Av.) [321]
		CH_3-Se	CH_3 + Se	3.20	
	DTBSe	$(CH_3)_3$-CH_2-Se-CH_2-$(CH_3)_3$	$(CH_3)_3$-CH_2-Se + CH_2-$(CH_3)_3$	-	3.06 ± 0.28 (Av.) [321]
		$(CH_3)_3$-CH_2-Se	$(CH_3)_3$-CH_2 + Se	-	
Te	H_2Te	H-Te-H	HTe + H	3.10	4.28 ± 0.06 (Av.) [321]
		H-Te-H	H + Te	2.92	
	DMTe	CH_3-Se-CH_3	CH_3-S + CH_3	2.45	3.38 ± 0.10 (Av.) [321]
		CH_3-Te	CH_3 + Te	2.70	
	DTBTe	$(CH_3)_3$-CH_2-Te-CH_2-$(CH_3)_3$	$(CH_3)_3$-CH_2-Te + CH_2-$(CH_3)_3$	-	2.62 ± 0.18 (Av.) [321]
		$(CH_3)_3$-CH_2-Te	$(CH_3)_3$-CH_2 + Te	-	

A.2 MOCVD reactors, procedures and precursor flow estimations

ICN2 reactor – Growth procedure

Substrates (SiO_2 or soda-lime glass) were diced into typically $1{\times}1\,cm^2$ to $2{\times}2\,cm^2$ sized chips, sonicated in acetone/isopropanol for 5 min each, and blow-dried with N_2. Then, they were mounted face-down onto the vertical quartz bar sample holder using silver paste (OK-SPI, SPI supplies, USA). A thermocouple and temperature controller were used to measure and set the temperature at the sample, referred to as "growth temperature". Optionally, for alkali-assisted growth specified in the text (section 3.4.1.1), a sample holder to which a crucible underneath the sample was fixed and filled with 20 mg of previously dehydrated NaCl (Alfa Aesar, 10862, $\gtrsim$99.999 % trace metals basis) for co-evaporation experiments.

Following the growth process outlined in the main text (Fig. 2.13), the reactor was ramped to the desired growth temperature at a rate of around $40\,°C\,min^{-1}$ under an inert purge gas flow of 100 sccm high-purity Ar (Air Liquide, Alphagaz 1, 99.999 %). Then, Ar was switched off and MoS_2 growth was initiated by vapor draw of molybdenum hexacarbonyl $Mo(CO)_6$ (Sigma-Aldrich, 577766, $\geq$99.9 % trace metals basis) and diethyl sulfide $(C_2H_5)_2S$ (DES, Sigma-Aldrich, 107247, $\geq$98 %) from dedicated canisters without any carrier gas. $Mo(CO)_6$ powder was bedded on glass beads for high surface area during sublimation [131, 178]. $Mo(CO)_6$ and DES precursors were held in stainless steel canisters at 30 °C and 12 °C, respectively. Their flow was independently regulated by needle metering valves (SS-SS4-VH, Swagelok, USA). Nominal $Mo(CO)_6$ flows between 0.02 sccm and DES flows between 0.03 sccm and 13.2 sccm were used, based on estimations described in detail in section A.2. Additionally, high-purity H_2 gas (Air Liquide, Alphagaz 1, 99.999 %) with flows between 0 and 30 sccm was injected. Typical working pressures were in the range of 1×10^{-2} and 1×10^{-1} Torr. Growth was stopped by stopping the $Mo(CO)_6$, DES, and H_2 flow; then, the reactor was cooled down to room temperature under 100 sccm Ar flow before sample removal. After each run, the reactor was annealed at 800 °C in Ar/H_2 flow to remove residual reaction products (Fig. 2.13). In between runs, the reactor was held under vacuum at around 1×10^{-3} Torr base pressure. During sample loading/unloading, 150 sccm Ar was flowed to minimize ambient exposure of the tube. Samples were stored in a vacuum desiccator after growth.

ICN2 reactor – Precursor injection by vapor draw

In this section, an estimation of precursor flow for the vapor draw MOCVD process is given. The source flow Q_S from a precursor-filled canister at pressure P_S to the reactor chamber at pressure P_{ch} can be estimated by a simple model according to Fig. A1a. It is assumed that the source pressure P_S equals the vapor pressure $P_{vap}(T_S)$ of the source material at a given source temperature T_S in full saturation, and that the source pressure stays constant over time. P_S is continously monitored by pressure gauges connected to the canister [654]. Vapor pressure data is typically reported by a simplified version of the Clausius-Clapeyron equation, which is known as the Antoine eq. (A.1) with the parameters $A[\text{Torr}, °\text{C}]$, $B[\text{Torr}, °\text{C}]$ and $C[\text{Torr}, °\text{C}]$. Compilations of these parameters for a variety of chemical compounds with reference to the original data are listed in databases, such as the *Chemistry WebBook* from the United States' National Institute of Standards and Technology (NIST).

$$log_{10}(P_{vap}(T_S)) = A - \frac{B}{T + C} \tag{A.1}$$

Fig. A1b shows the vapor pressure curves for DES and $Mo(CO)_6$ as a function of temperature based on literature as well as on own data. In case of a "high pressure drop" where $P_{ch} < 0.5P_S$, the flow Q is only dependent on the inlet pressure $P_S = P_{vap}(T_S)$, the temperature T_S (in K), specific gas gravity G_S (molecular weight of species divided by molecular weight of air; resulting in 3.11 for DES and 9.11 for $Mo(CO)_6$), and is independent on the pressure difference between source and chamber due to a „choked flow" [655]. According to equation eq. (A.2), control over Q is possible by varying T_S or by varying the flow coefficient $C_V(t)$ of the needle metering rotary valve by the number of turns t. These can be extracted as a polynomial function from the valve product specification sheet [656], according to equation eq. (A.3):

$$Q_S[\text{sccm}] = 3273450 \cdot C_V(t) \cdot P_{vap}(T_S)[\text{Torr}, \text{K}] \cdot \sqrt{\frac{1}{G_S T_S}} \tag{A.2}$$

, with

$$C_V(t) = a_0 + a_1 t + a_2 t^2 + a_3 t^3 + a_4 t^4 + a_5 t^5 + a_6 t^6 + a_7 t^7 + a_8 t^8 + a_9 t^9 \tag{A.3}$$

Fig. A1(c-d) show the estimated flow of $Mo(CO)_6$ and DES as a function of needle valve turns and for different source temperatures. In the ICN2 MOCVD reactor,
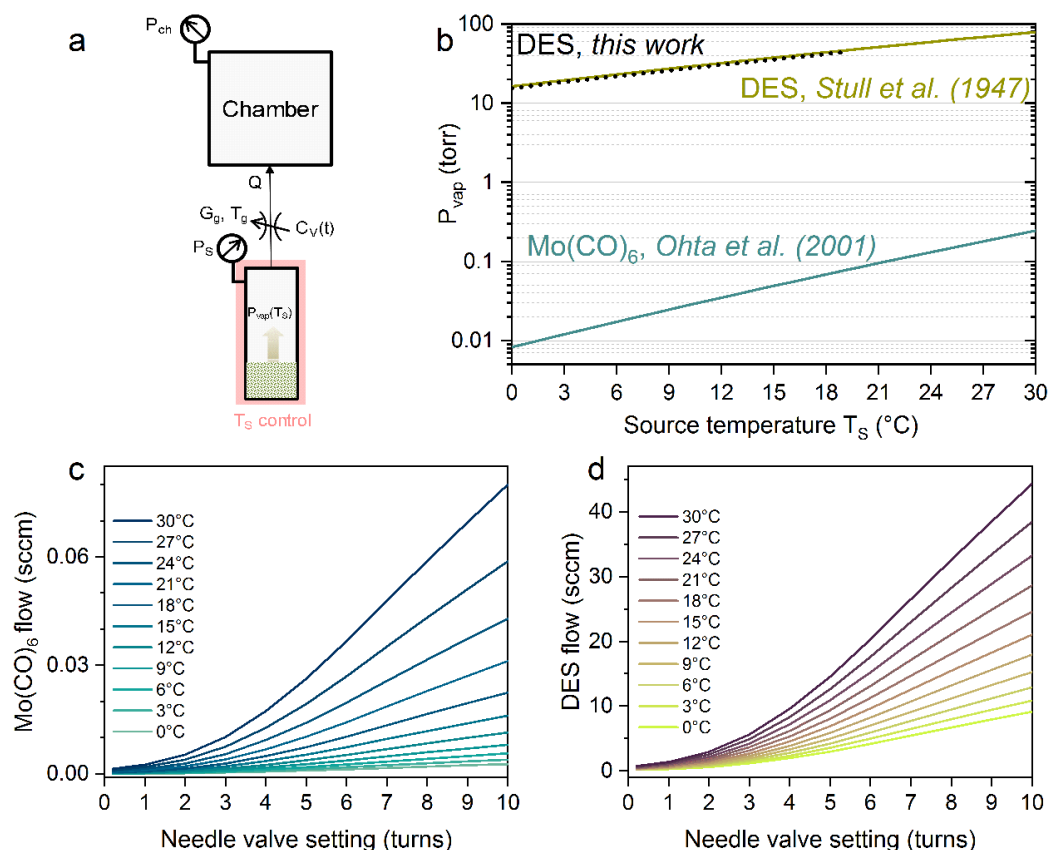
Figure A1 Precursor flow estimation for vapor draw. **(a)** Schematic model for precursor flow Q_S drawn from the canister to the low-pressure reactor chamber. The canister source pressure P_S is assumed to be equal to the vapor pressure $P_{vap}(T_S)$ of filled source material at canister temperature T_S. **(b)** Vapor pressure P_{vap} as function of T_S for DES and $Mo(CO)_6$. based on literature data [215, 210]. The flow Q_S of **(c)** $Mo(CO)_6$ and **(d)** DES can be controlled by T_S and/or by the needle metering valve as function of handle turns.

precursor flow was adjusted by varying the needle valve setting and keeping source temperatures constant.

It should be remarked that this simple estimation assumes that the precursor flow in the reaction zone of the chamber equals the flow Q_S passing through the needle valve. However, in the real situation of a hot-wall MOCVD process the actual precursor flow reaching the substrate might be lower due to pre-decomposition or pre-reactions of precursors upstream the sample position. In the case of $Mo(CO)_6$, with low decomposition temperature of around $150\,°C$ [231, 232, 233], the real flow might be overestimated and significantly smaller than Q_S. Consequently, for a constant needle valve setting the precursor concentration becomes a function of growth temperature, gas flow (residence time) and position in the reactor as well.

Yonsei reactor – Growth procedure

SiO_2 and/or Al_2O_3 substrates were sonicated in acetone/isopropanol for 5 min each, blow-dried with N_2, and placed vertically on a quartz holder perpendicular to the tube axis and gas flow direction. The sample position was set at 19 cm from the furnace entrance (Fig. 2.14(a), "wafer run"), which is a critical parameter optimized specifically for this setup due to the decomposition profile and precursor concentration gradients along the hot-wall tube (also see Fig. 2.10). Alternative to full wafer runs, chips with smaller dimensions ($2 \times 2\,cm^2$ SiO_2, and/or quarter 2" wafer Al_2O_3, "chip run") were placed for comparative growth parameter studies. Prior the growth run, substrates were "flash" annealed with the furnace open air at $700\,°C$ for 10 min to burn off adventitious carbons. This procedure resulted in enlarged grain sizes (Fig. C13). Optionally, for alkali-assisted growth, NaCl was placed upstream the sample (inset in Fig. 2.14(a)). For this, a slurry of NaCl and distilled water was evenly distributed on a 4" SiO_2/Si wafer, dried on a hotplate, and centered at the furnace entrance edge, before starting the growth run.

MoS_2 was grown from $Mo(CO)_6$ (Sigma Aldrich, 577766, $\geq 99.9\,\%$) and *anhydrous* DMS (Sigma-Aldrich, 274380, $\geq 99.9\,\%$), which are kept as a solution in the bubbler, carried with Ar from a bottle at 1765 Torr controlled by a MFC downstream the bubbler. If not otherwise indicated concentrations of 65 mg $Mo(CO)_6$ dissolved in 12 mL DMS were used. Additionally, Ar and H_2 are injected controlled by MFCs that enter the chamber together with the $Mo(CO)_6$/DMS flow pre-mixed at the reactor inlet. More detailed information on the estimation of precursor flow is given in section A.2. A scheme of a typical growth process is shown in the main text (Fig. 2.15a). First, a flow of 5 sccm H_2, 100 sccm Ar and pressure of 10 Torr were set and kept throughout the whole process. Then, all three zones of the furnace were ramped to the growth temperature (e.g. $600\,°C$) at a rate of around $20\,°C\,min^{-1}$, where growth was initiated by injecting $Mo(CO)_6$/DMS with 1 sccm Ar pick-up during 16 h to obtain submonolayer coverage thin films. For 1-2L films the growth phase was extended for another 6 h at accelerated growth rate with 1.6 sccm Ar. After the growth stage, $Mo(CO)_6$/DMS flow and heaters were switched off, the furnace was opened and quenched down to room temperature. Finally, the sample was removed and the reactor with the tube was annealed at $900\,°C$ open to air for tube cleaning before the subsequent growth run (Fig. 2.15b).

Yonsei reactor – Precursor injection by carrier gas

The precursor source flow rate Q_S from a canister into the reactor chamber by use of a carrier gas can be simply estimated by Amagat's law in eq. (A.4) [322]:

$$Q_S = \frac{n_S \cdot Q_{carrier}}{1 - n_S} \tag{A.4}$$

, where n_S is the mole fraction of the precursor source, obtained from Dalton's law in eq. (A.5):

$$n_S = \frac{P_{vap}(T_S)}{P_S} \tag{A.5}$$

, where $P_{vap}(T_S)$ is the precursor vapor pressure at canister source temperature T_S, and P_S is the canister pressure. For a canister pressure of 1765 Torr controlled by the Ar inlet pressure, and at a room temperature of 25 °C, an Ar carrier gas flow of 1 sccm, and $Mo(CO)_6$ and DMS vapor pressures of 0.15 Torr and 484 Torr , respectively, the precursor flow for $Mo(CO)_6$ and DMS can be calculated to be 0.4 sccm and 8.3×10^{-5} sccm, respectively, resulting in an approximate S/Mo precursor ratio of around 4560. For an Ar carrier gas flow of 1.6 sccm, the precursor flow for $Mo(CO)_6$ and DMS increase to 0.6 sccm and 1.3×10^{-4} sccm at unchanged ratio of 4560. The orders of magnitude lower, growth-rate-controlling $Mo(CO)_6$ flow in the Yonsei growth reactor as compared to the flows used in the ICN2 vapor draw process in previous section A.2, require significantly longer growth times to obtain monolayer coverage in the Yonsei reactor.

Substrate properties and preparation

Material properties of soda-lime glasses

Table A2 Material properties of commercial soda-lime silicate glasses after manufacturer's data: SCG 94 (Plan Optik AG, Elsoff, Germany) [263], Marienfeld Superior (Paul Marienfeld GmbH & Co. KG, Lauda-Königshofen, Germany) [264], and B270®i (Schott AG, Mainz, Germany) [265][657]

	Marienfeld Superior	Plan Optik SCG 94	Schott B270®i
Description	microscope slide float-glass	high transmission crown-glass	high transmission crown-glass
Physical and mechanical properties			
Thickness (mm)	1.0	0.7	0.5
Density ($g\,cm^{-3}$)	6.23	0.91	5.2
Young's modulus (GPa)	70.0	73.6	71.1
Composition (%)			
SiO_2 "silicate"	72.6	69.5	70-80
Na_2O "soda"	13.0	8.1	10-20
K_2O	0.3	8.3	1-10
CaO "lime"	8.8	2.1	1-10
MgO	4.3	-	-
BaO	-	4.2	1-10
ZnO	-	0.5	1-10
TiO_2	-	0.5	<1
Sb_2O_3	-	0.5	0.5
Al_2O_3	0.6	-	-
Fe_2O_3	0.1	-	-
SO_3	0.2	-	-
Thermal properties			
Linear thermal expansion coefficient[a] (10^{-6} K^{-1})	9.0	9.4	9.4
Strain point[b] (°C)	530	511	507
Annealing point[c] (°C)	557	541	535
Softening point[d] (°C)	726	724	711

[a] temperature range [20-300 °C]
[b] $log(\eta) = 14.5\,Pa \cdot s$
[c] $log(\eta) = 13.0\,Pa \cdot s$
[d] $log(\eta) = 7.6\,Pa \cdot s$
,where η is the viscosity

Sapphire surface preparation

Sapphire substrates were annealed inside appropriate-sized alumina crucibles (99.7 % purity, Nanoker Research S.L., Spain) and covered with an alumina lid, as shown in

the main text (Fig. 2.17d). It is remarked that covering the crucibles was essential to obtain regularly stepped surfaces (see Fig. C2). Two dedicated furnaces were used, as shown in Fig. 2.17a. For annealing of up to 2"-sized sapphire wafers in ambient air conditions at $1050\,°C$, a box muffle furnace 30/1100 LSF01 (SNOL, Lithuania) was used. For chip-scale annealing in controlled gas atmosphere up to $1350\,°C$, a high-temperature furnace ST.16 6060 (Hobersal S.L., Spain) with horizontal alumina tube was used, which was equipped with a mass flow controller through which either 50 sccm O_2, referred to as "O_2-annealing", or 50 sccm of $5\,\%H_2/95\,\%Ar$ mix referred to as "H_2-annealing", was injected. Depending on the studied conditions indicated in the results section, the annealing program shown in Fig. 2.17d consisted in ramping the temperature at $10\,°C/min$ to the annealing temperature of either $1050\,°C$, $1200\,°C$, or $1350\,°C$, where samples were dwelled for 2, 6 or $12\,h$, and finally cooled down $(-5\,°C/min)$ to room temperature. Annealing was carried out at atmospheric pressure; in the case of O_2/H_2-annealing the gas flow was kept throughout the whole process. One annealing experiment was performed at low pressure ($10\,Torr$) and highly reductive condition in $50\,sccm$ pure H_2 at $1050\,°C$ for $2\,h$ in a programmable MOCVD reactor (BM NOVO Lite, Aixtron Ltd., UK).

For analyzing the wetting behaviour of sapphire surfaces, the static contact angle of distilled water was measured with a Drop Shape Analyzer DSA25 (KRÜSS GmbH, Germany) and averaged from three measurements. Droplets were applied with a $5\,µL$ micro-pipette. Fully spreading/wetting droplets were designated as "WET".

A.3   Microfabrication methods

Microfabrication and wafer processing was carried out at the ICN2 Nanofabrication facility and CNM-IMB (CSIC) cleanroom. The main microfabrication techniques used in this thesis include photolithography, etching, metallization, and dielectric integration, which are briefly described in the following.

Photolithography

Optical photolithography is the most common method to pattern thin film materials coated over a wafer substrate into device structures by selectively protecting certain areas during subsequent processing steps (metallization, etching, layer deposition and transfer, oxide integration etc.). Typically, ultraviolet (UV) light is used to project and

transfer the image from an aligned, optical photomask containing the geometric device structures to a light-sensitive polymeric photoresist on the substrate. The photoresist is previously applied by spin-coating, pre-baked and, in the exposure step, irradiated by UV light, where it either breaks down (positive resist) or hardens (negative resist) in defined areas. In the development step, the patterned film structure is then obtained by removing the softer parts of the photoresist with suitable solvents, and fully removing the resist layer by solvents ("stripping") or plasma oxidation ("ashing") when not needed anymore. These standard procedures can be applied to pattern 2D materials, such as graphene and MoS_2; however, care needs to be taken during processing. For example, photoresist or polymer layers may not be completely removed during development. Even small amounts of residue underneath or on top of 2D materials may adversely affect the device performance. Therefore, residue removal may be an important processing step in 2D manufacturing, which can be done by UV-ozone [473], annealing in vacuum, inert or forming gas [478, 18], or by appropriate chemical solvents [55].

The used equipment (spin-coater, mask aligner, UV-ozone cleaner) and chemicals (photoresists, strippers) are given in table D5 and table D4, respectively. Photolithography recipes are given in the respective process protocols in section D.4.

Etching of 2D materials and via-holes

Etching is an important process in micro- and nanofabrication to chemically remove material from the wafer surface. Often, an etch-resistant or sufficiently thick photoresist mask previously patterned by photolithography protects designated parts of the wafer from etching. For etching processes it is critical to precisely control etching time and depth by a known etch rate. There are liquid-phase ("wet") and plasma-phase ("dry") etching processes available.

Inductively coupled plasma - reactive ion etching (ICP-RIE) is a dry etching technique combining chemical and physical etching for material removal. ICP-RIE is carried out under vacuum conditions in chemically reactive plasma of high-energetic, charged ions generated from gases flown into the reaction chamber. Dry etching offers excellent process control for large-scale wafer processing. An PlasmaPro Cobra 100 ICP-RIE (Oxford Instruments, UK) equipped with a laser interferometer for etch monitoring was used in the MoS_2 and graphene patterning steps. Detailed etch recipes are given in section D.4. Wet etching uses chemically reactive etching solutions of caustics or acids depending on the material to be etched, and into which the wafer

is immersed and regions of interest are dissolved. A nitric/phosphoric acid-based aluminium etchant (TechniEtch Al80, Microchemicals GmbH, Germany) was used to open via-holes through Al_2O_3 oxide dielectric and encapsulation layers for contacting gate, source and drain of embedded MoS_2 transistors.

Metallization of contacts and conductive tracks

Metallization is an important step in electronic device fabrication to create electrically conducting tracks and contacts and can be achieved by different methods, such as sputtering, electroplating, chemical or physical vapor deposition. In this thesis, physical vapor deposition (PVD) by electron-beam evaporation is used, in which an intense electron beam is generated from a filament and steered via electric and magnetic fields to strike and vaporize a source material (e.g. metal pellets) within a vacuum environment. The source material is heated by the electron impact and energy transfer its surface atoms will have sufficient energy to leave the surface, and coat a substrate positioned above the evaporating material. The trajectory of the physically evaporated atoms is directional. Compared to thermal evaporation, e-beam evaporation is able to transfer higher energies into the material to be evaporated and has the advantage of thin films of high density and purity. By using a multiple crucible system, several different materials can be sequentially deposited, such as for Ti/Au contacts and tracks, without breaking the vacuum and avoiding interlayer contamination. In posterior photomask lift-off processes, Ti/Au provides good adhesion to the device substrates (SiO_2, polyimide) and forms a reasonable good contact to MoS_2 [550]. However, alternative contact materials may be better suited to improve contact resistance and device performance in the future [49, 479, 658, 67, 69].

For deposition of Ti/Au and Ni/Au contacts and Al for self-oxidized AlO_x seed layers onto 4" wafer an AJA International Inc. ATC-8E Orion e-beam evaporator was used, working at $8\,kV$. The system operated with a turbopumped loadlock chamber and cryopumped main chamber with typical working pressure during evaporation in the high vacuum range of $1 \times 10^{-7}\,mbar$, which has implications due to possible oxidation of reactive metals like Ti during deposition in high vacuum conditions [550, 659, 474, 480]. Source material was evaporated from liner crucibles in a multiple source rotary pocket. A quartz crystal balance was used for thickness monitoring and deposition was initiated and stopped by a shutter system.

Oxide integration for dielectrics and encapsulation by ALD

Atomic layer deposition (ALD) is a thin film deposition process based on the sequential injection of gas-phase precursors. The precursors react with the surface sites of a material (functional groups, dangling bonds, defects etc.) in an alternating, self-limiting manner separated by inert gas purges in each cycle. ALD provides excellent control over atomic layer thickness and conformality and has become a standard technique for oxide and dielectric integration in semiconductor device manufacturing. In MoS_2 thin film transistors, AlO_x oxide sandwich encapsulation of the 2D transistor channel has led to improved device performance [41].

A Cambridge NanoTech Savannah S100 reactor was used for AlO_x dielectric and encapsulation layers of MoS_2 transistor devices. Trimethylaluminum (TMA, Sigma-Aldrich, 663301-25G) and H_2O served as the precursors in a thermal ALD process carried out at $200\,°C$ using a continuous $20\,sccm$ N_2 flow at a working pressure of $\sim270\,mTorr$. Precursor canisters were kept at room temperature. Precursor pulse and purge sequences for one ALD cycle were as follows: TMA ($0.15\,s$), N_2 ($5\,s$), H_2O ($0.05\,s$), N_2 ($5\,s$. Oxide thickness and a growth-per-cycle of $\sim1.27\,Å/cycle$ were verified for layers deposited on Si reference substrates by X-ray reflectometry (XRR) with a PANalytical X'PERT PRO MRD.

Appendix B

MOCVD of MoS$_2$ thin films grown from organosulfide precursors

B.1   Growth parameter studies
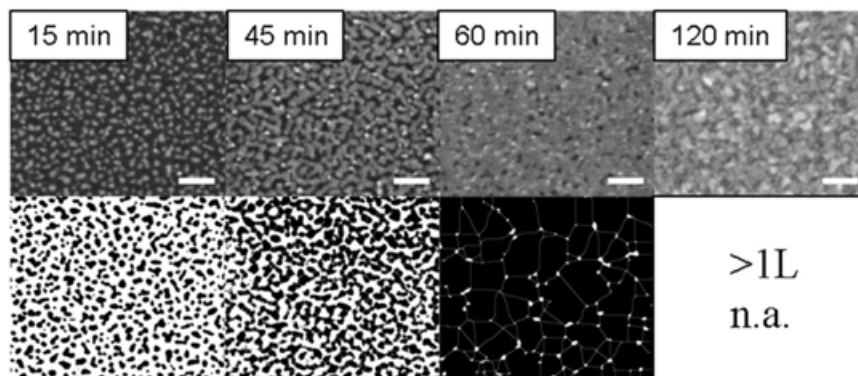
Figure B1 Growth time study. Image analysis of MoS$_2$ thin films grown at 700 °C by co-injection of 0.02 sccm Mo(CO)$_6$ and 0.3 sccm sccm DES flow for different growth times. Original images (top) and corresponding binary images after execution of the image analysis algorithm (below). The scale bars are 100 nm.
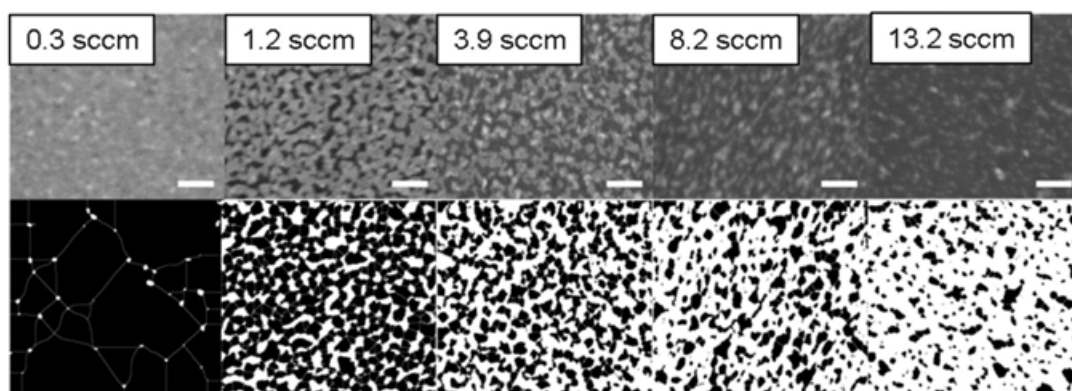
Figure B2 DES flow study. Image analysis of MoS$_2$ films grown at 700 °C (60 min) by co-injection of 0.02 sccm Mo(CO)$_6$ and different DES flows. Original images (top) and corresponding binary images after execution of the image analysis algorithm (below). The scale bars are 100 nm.
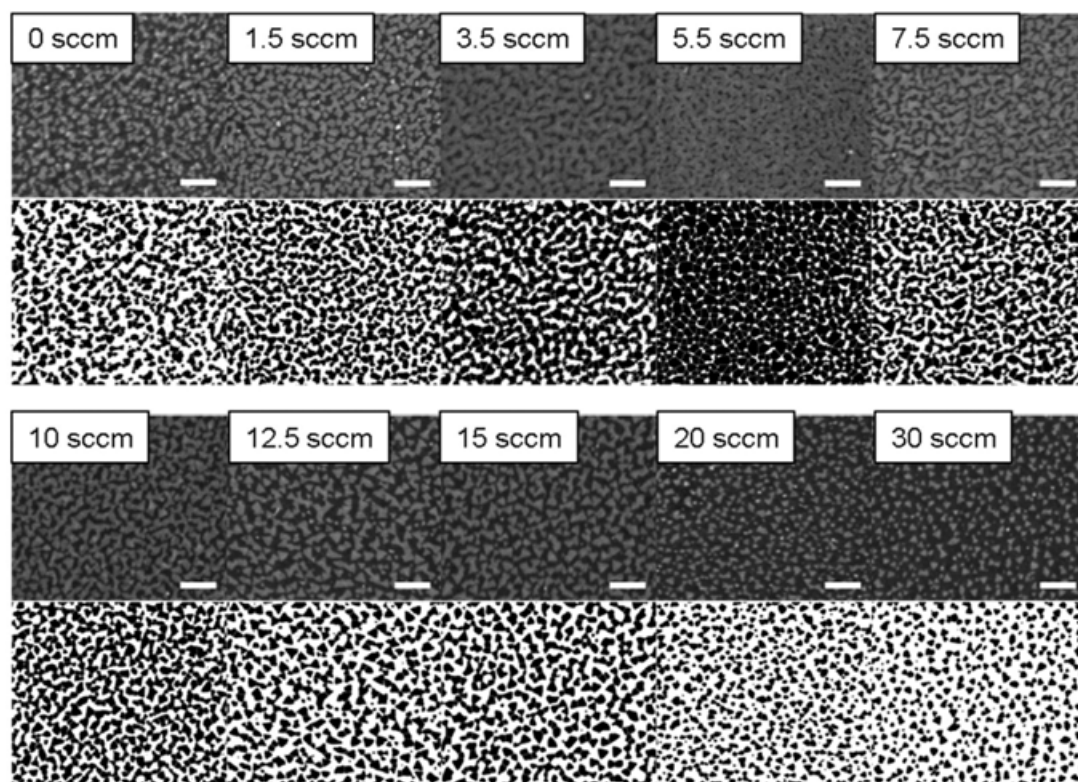
Figure B3 H_2 flow study. Image analysis of MoS_2 films grown at 700 °C (60 min) by co-injection of 0.02 sccm $Mo(CO)_6$ and different DES flows. Original images (top) and corresponding binary images after execution of the image analysis algorithm (below). The scale bars are 100 nm.
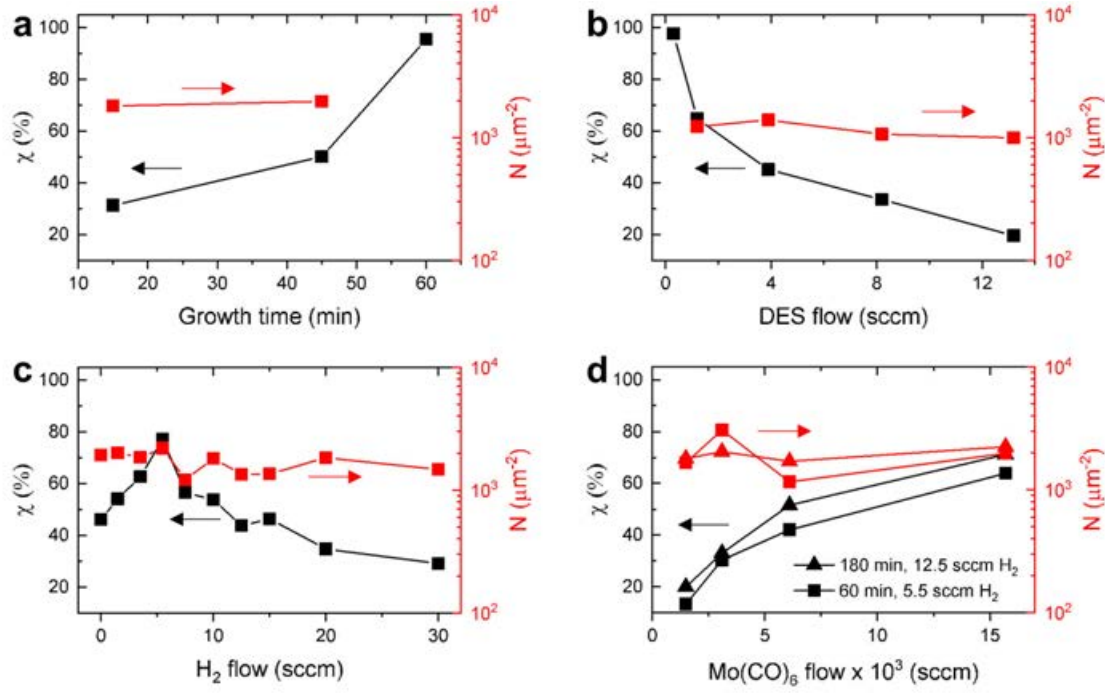
Figure B4 Coverage χ and nucleation densities N extracted from SEM images for MoS$_2$ thin films growth at $700\,°C$ at varied growth parameters: **(a)** Growth time, **(b)** DES flow, **(c)** H$_2$ flow, and **(d)** Mo(CO)$_6$ flow.
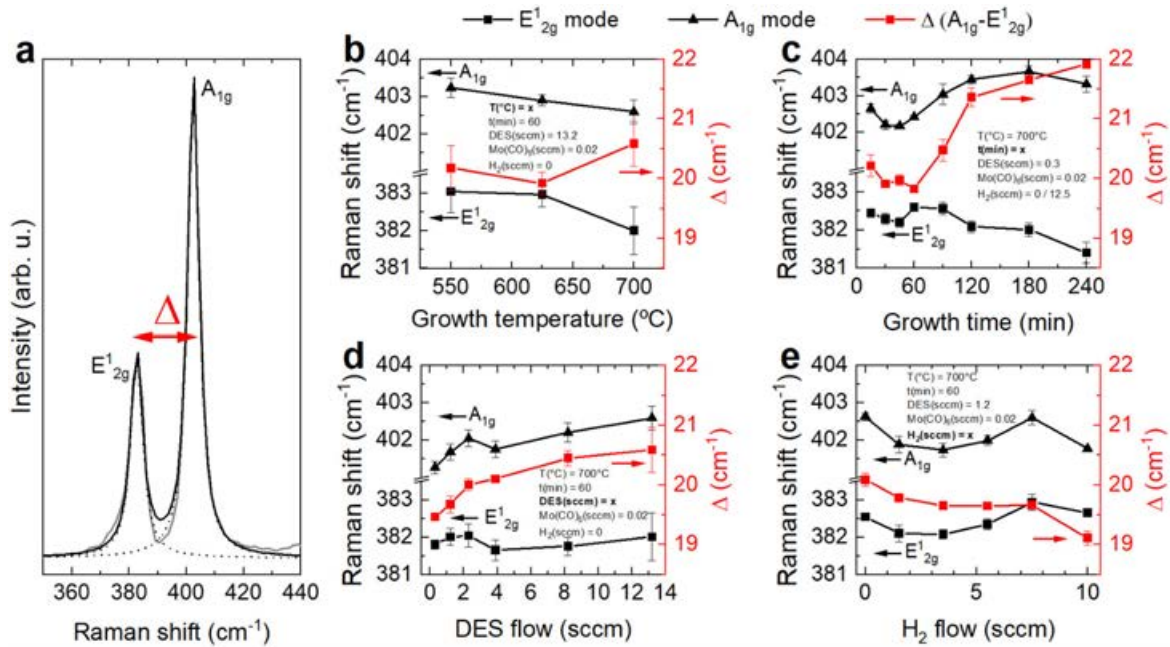
Figure B5 In-plane E_{2g} and out-of-plane A_{1g} MoS$_2$-mode positions and frequency difference $\Delta = A_{1g} - E_{2g}^1$ for MoS$_2$ thin films grown for varied growth parameters: **(a)** Growth temperature, **(b)** growth time, **(c)** DES flow, and **(d)** H$_2$ flow.

Table B1 XPS fitting parameters and constraints.

#	Element/ Transition	Assignment	Peak position constraint (eV)	FWHM constraint (eV)	Peak area constraint	Peak shape	Literature/ sample ref
A	C 1 s	C-C (sp^2)	284.2±0.2 vary	1.0±0.1 vary	vary	A(0.4,0.25,0)GL(60)	*
B	C 1 s	C-H/C-C	284.7±0.2 vary	1.4±0.1 vary	vary	GL(30)	**, [340]
C	C 1 s	C-O-C	B+1.7	1.5±0.1 vary	B*0.17	GL(30)	**, [340]
D	C 1 s	O-C=O	B+4.3	1.4±0.1 vary	B*0.10	GL(30)	**, [340]
E	Mo^{IV-y} 3 d$_{5/2}$	MoS$_{2-x}$	(228.9-229.1) ±0.1	1.1±0.1 vary	vary	GL(80)	[338], [339]
F	Mo^{IV-y} 3 d$_{3/2}$	MoS$_{2-x}$	E+3.15	E*1	E*2/3	GL(80)	[338], [339]
G	Mo^{IV} 3 d$_{5/2}$	MoS$_2$	229.3±0.1 vary	0.7±0.1 eV vary	vary	GL(80)	***
H	Mo^{IV-y} 3 d$_{3/2}$	MoS$_2$	G+3.15	G*1	G*2/3	GL(80)	***
I	Mo^{VI} 3 d$_{5/2}$	MoO$_3$	232.5±0.2 vary	1.8±0.4 vary	vary	GL(80)	***
J	Mo^{VI} 3 d$_{3/2}$	MoO$_3$	I+3.15	I*1	I*2/3	GL(80)	***
K	S 2 s	C$_x$S$_y$	228.0±0.1 vary	L*1 vary	(M/O)*L	GL(90)	****
L	S^{-II} 2 s	MoS$_2$	226.5±0.1 vary	1.8±0.1 vary	vary	GL(90)	***
M	S 2 p$_{3/2}$	C$_x$S$_y$	163.6±0.2 vary	0.8±0.1 vary	vary	GL(90)	****
N	S 2 p$_{1/2}$	C$_x$S$_y$	M+1.18	M*1	M*1/2	GL(90)	****
O	S^{-II} 2 p$_{3/2}$	MoS$_2$	162.1±0.1 vary	0.7±0.1 vary	vary	GL(90)	***
P	S^{-II} 2 p$_{1/2}$	MoS$_2$	O+1.18	O*1	M*1/2	GL(90)	***
Q	Si 2 p	SiO$_2$	103.3	1.5±0.1 vary	vary	GL(30)	[276]

*graphitic C(sp^2): MoS$_2$ grown for 60 min at 700 °C with Mo(CO)$_6$: 0.02 sccm and DES: 13.2 sccm, after removal of adv. carbon by 500 °C *in situ* annealing in XPS chamber

**adventitious C: SiO$_2$ substrate, after standard cleaning procedure and ambient exposure

***MoS$_2$/MoO$_3$: natural MoS$_2$ crystal

****C$_x$S$_y$: SiO$_2$ after single-source exposure of 13.2 sccm DES for 60 min at 700 °C
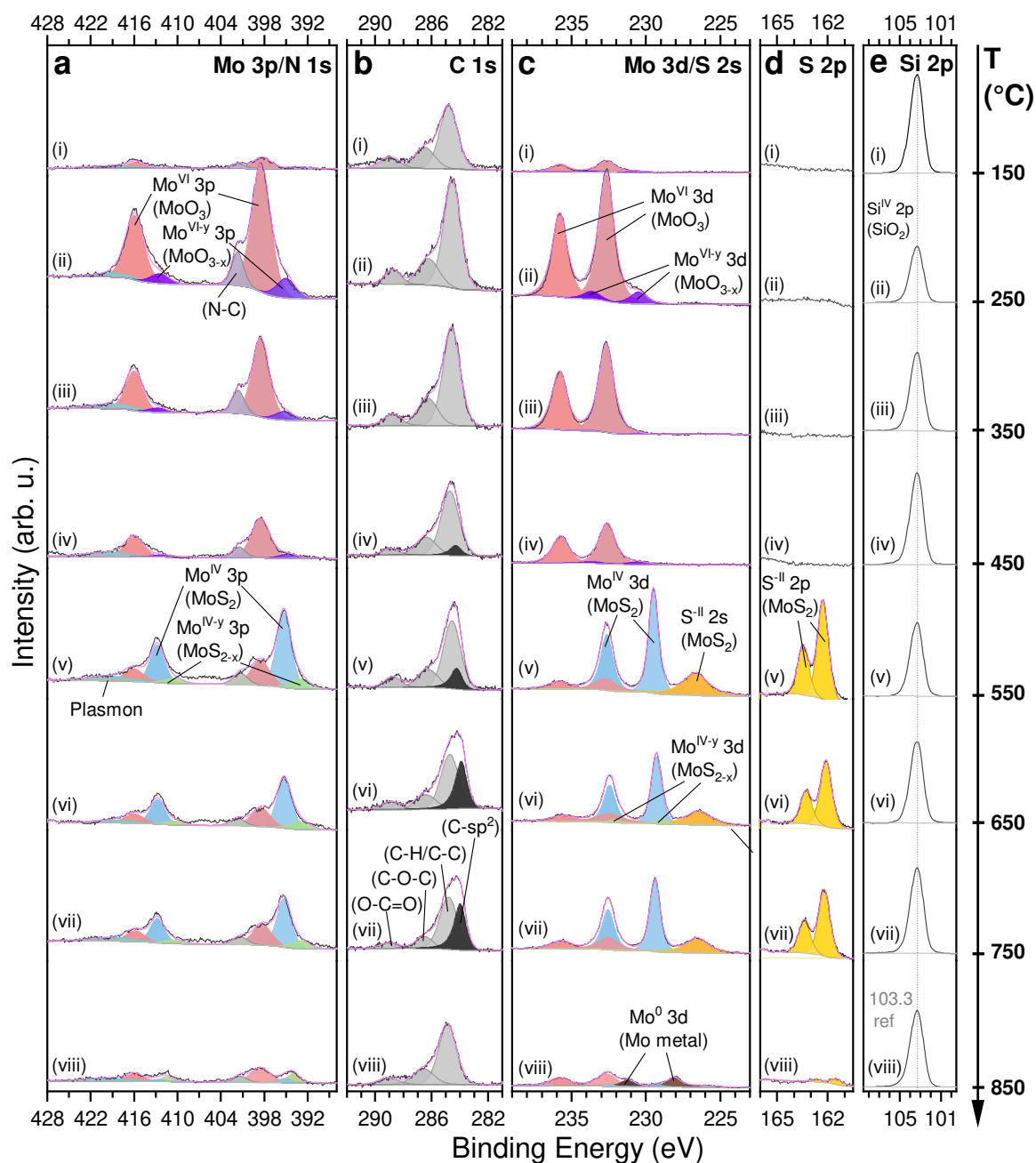
Figure B6 Growth temperature study - XPS analysis. XPS analysis showing the effect of growth temperature on chemical composition of thin films grown *without* H$_2$ (60 min) on SiO$_2$; The following core level regions are shown: **(a)** /Mo 3p, **(b)** C 1s, **(c)** Mo 3d/S 2s, **(d)** /S 2p, **(e)** Si 2p, where black lines in (i-viii) show the measured spectra for temperatures T between 150 °C and 850 °C, as indicated by the scale on the right. Colored areas under singlet/doublets represent fits assigned to the same features/chemical species. Pink lines show the synthetic fitting envelopes of summed peaks. All spectra are calibrated to the SiO$_2$ substrate peak at 103.3 eV and are plotted with the same intensity scale among the series of same core levels.
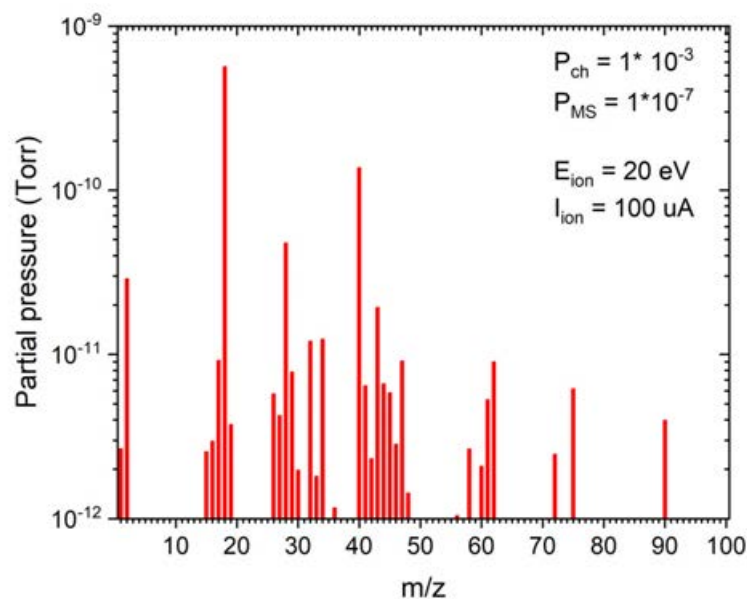
Figure B7 ICN2 reactor vacuum background. Exemplary spectrum aquired with residual gas analyzer at indicated reactor base pressure P_{ch}, electron ionization energy E_{ion}, ionization current I_{ion}, and mass spectrometer pressure P_{MS}. The prominent peak at $m/z = 18$ is assigned to residual H_2O in the background. DES-related peaks ($m/z = 90, 75, 62, 61$ etc.) are always present in the background – even if no DES is injected.
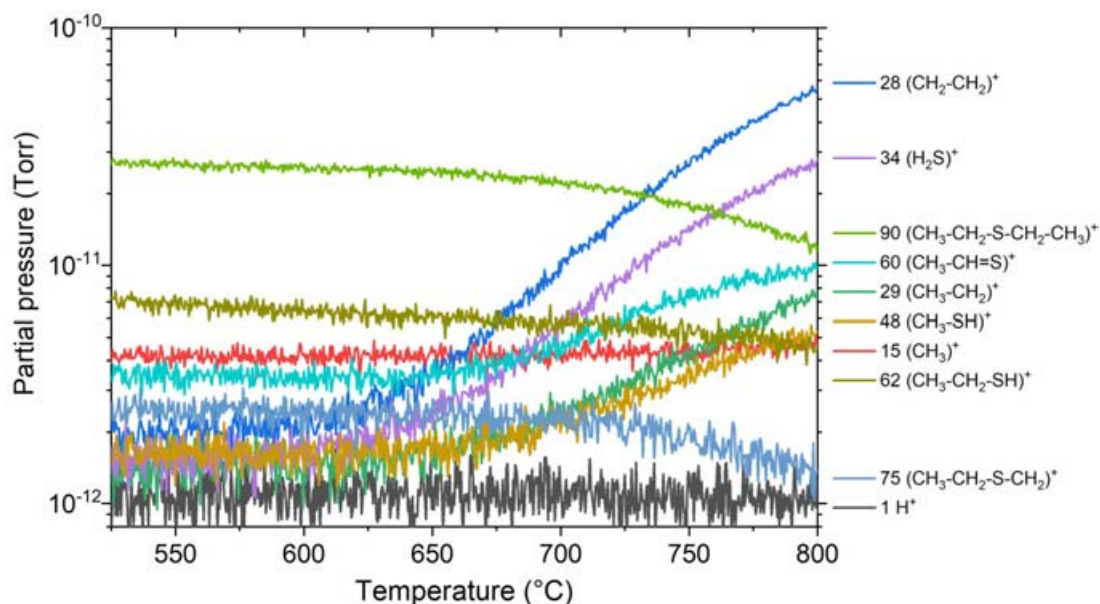
Figure B8 Temperature-dependent DES pyrolysis monitoring by low energy electron ionization at 12 eV and DES flow of 13.2 sccm. Evolution of partial pressures of the unfragmented molecular DES ion and its main fragments as a function of growth temperature. Different colors correspond to different single-ionized fragments assigned by their m/z-ratio and chemical formulas.
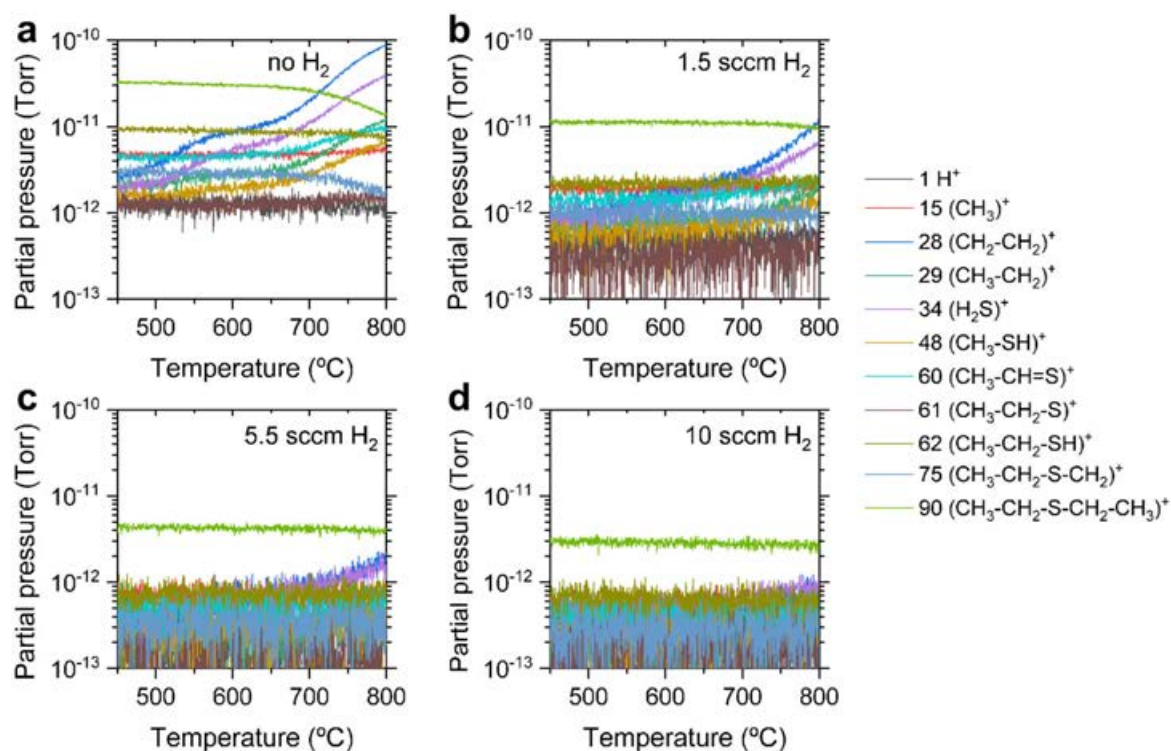
Figure B9 Temperature-dependent DES pyrolysis monitoring by low energy electron ionization at 12 eV for a gas-mixture of 0.02 sccm Mo(CO)$_6$, 1.2 sccm DES, and indicated H$_2$ flow. Evolution of partial pressures of the unfragmented molecular DES ion and its main fragments as a function of growth temperature. Different colors mark different single-ionized fragments assigned by their m/z-ratio and respective chemical formulas.
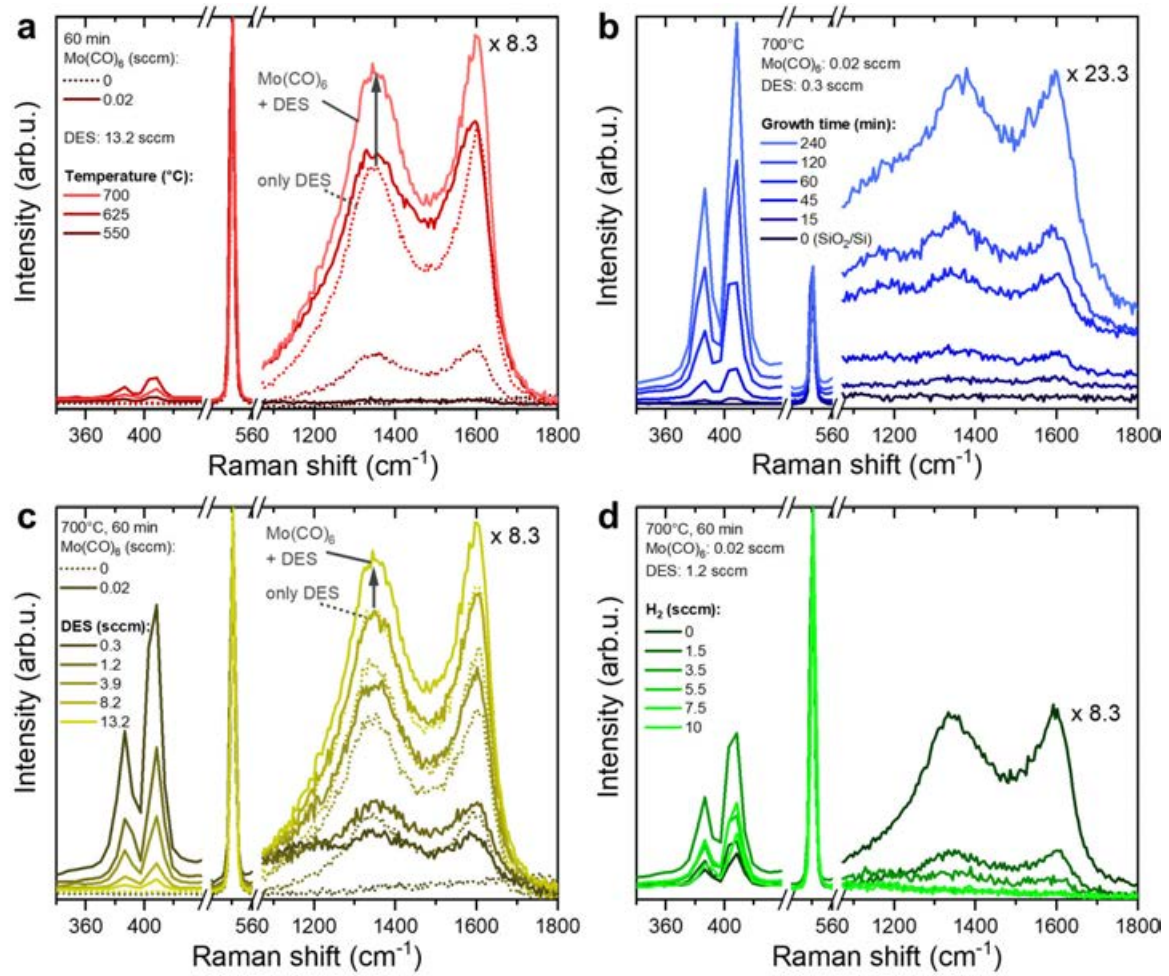
Figure B10 Raman spectra for different growth parameter studies showing the effect of **(a)** temperature for single source DES and DES+Mo(CO)$_6$ exposure, **(b)** growth time, **(c)** DES flow for single-source DES and DES+Mo(CO)$_6$ exposure, and **(d)** H$_2$ flow. Synthesis conditions are given in the graphs. Regions of MoS$_2$-related E^1_{2g} and A_{1g} phonon modes, Si peak and C-related D and G bands are shown with magnification factors, as indicated. All spectra are normalized to the Si peak at $521\,\mathrm{cm}^{-1}$.
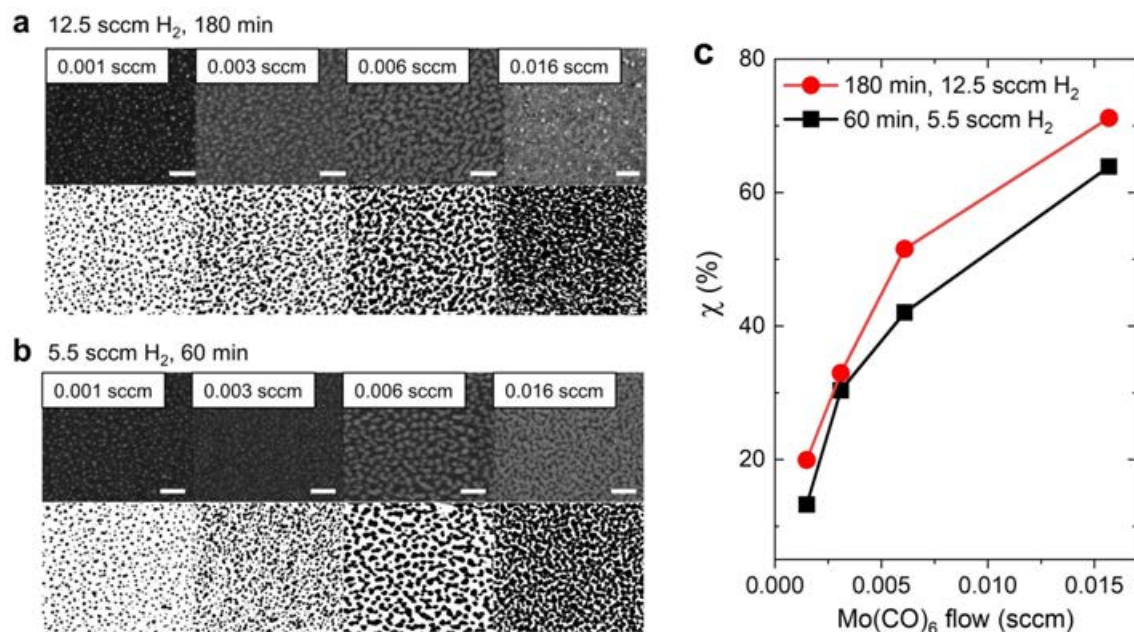
Figure B11 Mo(CO)$_6$ and H$_2$ flow study. MoS$_2$ thin films grown on SiO$_2$ for varied Mo(CO)$_6$ flow and two sets of added H$_2$ flow and growth times: **(a)** 12.5 sccm H$_2$, 180 min, and **(b)** 5.5 sccm H$_2$, 60 min. SEM images in the top row and their corresponding binary images for image analysis. **(c)** Monolayer coverage as a function of estimated Mo(CO)$_6$ flow extracted from the binary images.
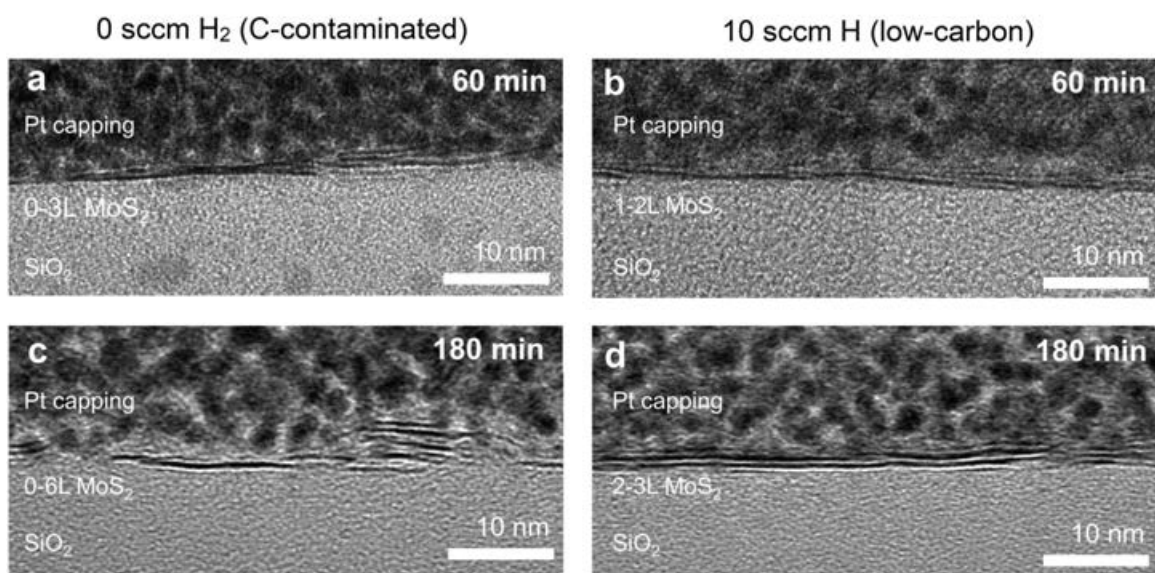
Figure B12 TEM cross-sections of MoS$_2$ thin films grown from 0.02 sccm Mo(CO)$_6$ and 1.2 sccm DES for varied growth times and H$_2$ flows: **(a)** 60 min, 0 sccm H$_2$, **(b)** 60 min, 10 sccm H$_2$, **(c)** 180 min, 0 sccm H$_2$, and **(d)** 180 min, 10 sccm H$_2$.

Table B2 PL spectra fitting parameters and constraints.

| Component | Variable | | Start value | Vary | Constraints | | Unit |
					Lower	Upper	
	y_0	Baseline	0	no			CCD cts
A^- trion	x_0	Position	1.86	yes	1.84	1.88	eV*CCD cts
	w_0	FWHM	0.06	yes	0.00	0.07	eV
	A_0	Area		yes	0.00		eV
A^0 exciton	x_1	Position	1.86	yes	1.88	1.91	eV*CCD cts
	w_1	FWHM	0.06	yes	0.00	0.07	eV
	A_1	Area		yes	0.00		eV
B exciton	x_2	Position	2.03	yes	2.00	2.06	eV*CCD cts
	w_2	FWHM	0.07	yes	0.00		eV
	A_2	Area		yes	0.00		eV
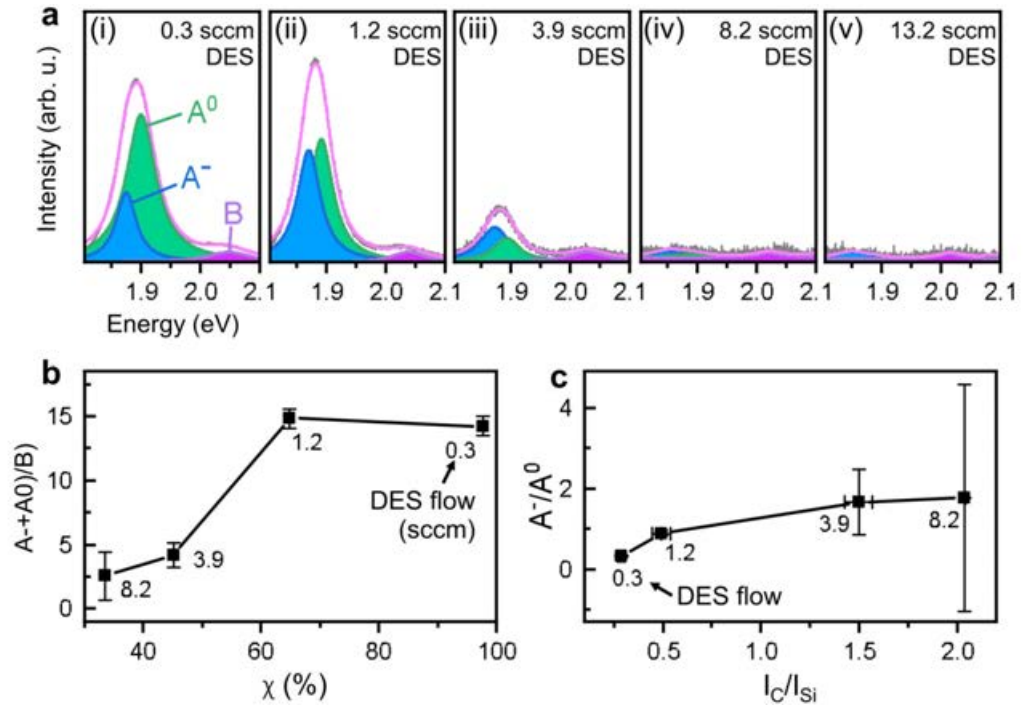
Figure B13 (a) PL spectra of MoS_2 thin films grown at $700\,°C$ ($60\,min$) from $0.02\,sccm$ $Mo(CO)_6$ and DES flow varying between 0 and $13.2\,sccm$, as indicated. Lorentzian peak deconvolution marks contributions of trions A^- (blue), neutral excitons A^0 (green) and B excitons (purple). The fitting envelopes are shown by the pink lines. Spectra were normalized to the B exciton intensity. **(b)** PL integral ratio $(A^- + A^0)/B$ as function of monolayer coverage for MoS_2 films grown with different DES flows, as indicated next to each measurement point. **(c)** Trion-to-exciton ratio A^-/A^0 as function of carbon content, represented by I_C/I_{Si} Raman integral ratio, for MoS_2 films grown with different DES flows, as indicated next to each measurement point.
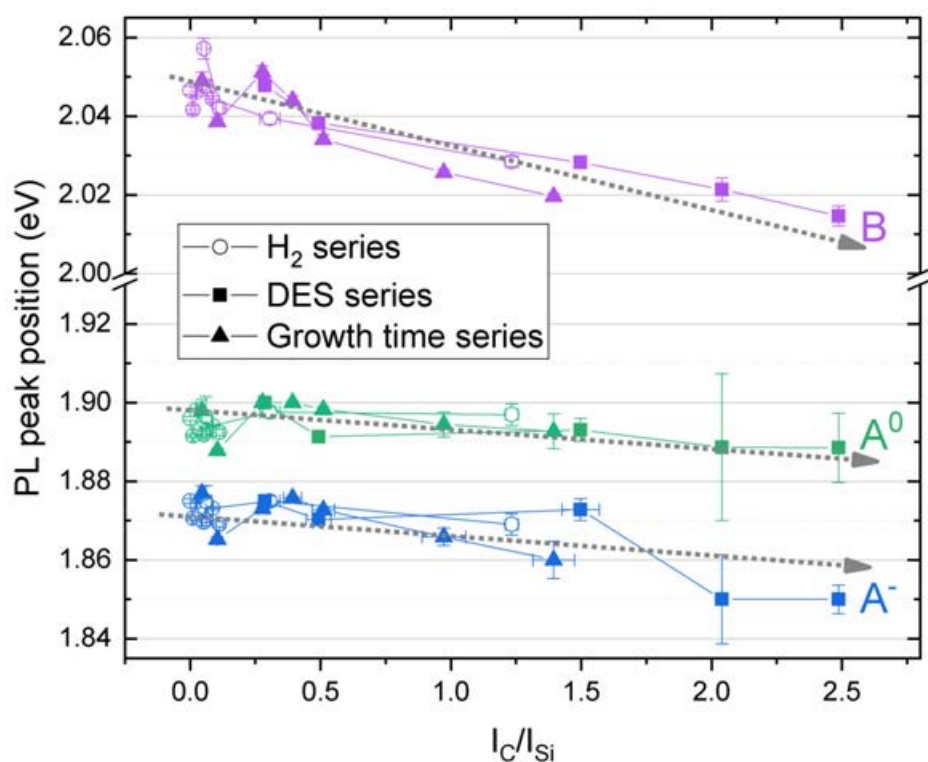
Figure B14 C-induced charge transfer doping and PL Stokes redshift in MoS$_2$ thin films. PL peak position of A^- trions (blue), neutral excitons A^0 (green) and B excitons (purple) as extracted from Lorentzian peak deconvolution of PL spectra from various parameter studies (H$_2$, DES, growth time) of this work as function of their respective C content, as represented by the I_C/I_{Si} Raman integral ratio. The general trend of red-shifting PL peak positions with increasing C content is depicted with gray arrows. This Stokes red-shift has been reported to indicate increased n-type doping of MoS$_2$ thin films [332].
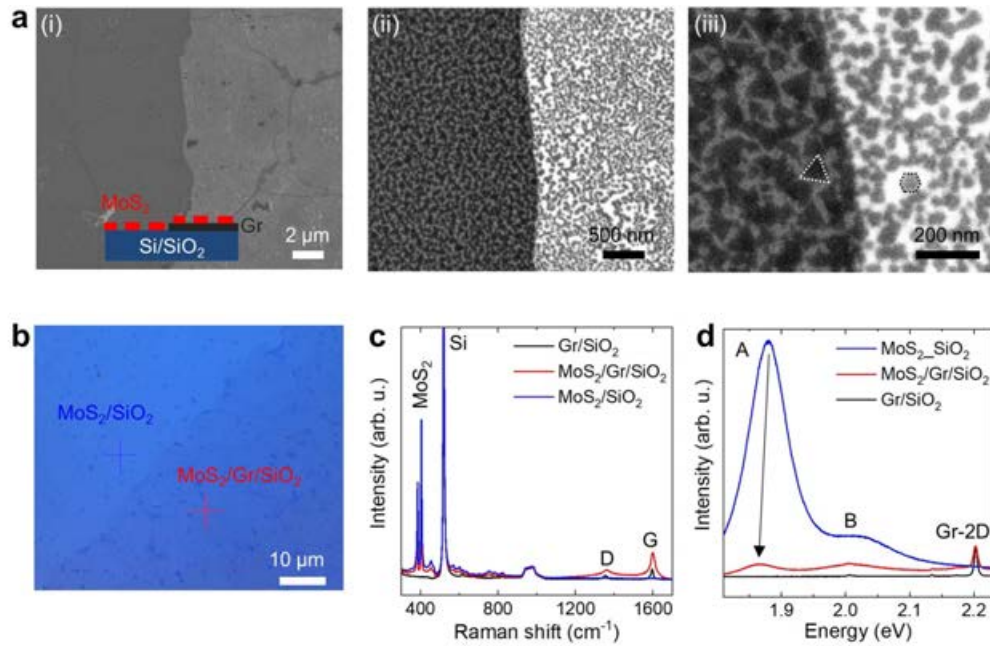
Figure B15 MoS$_2$ thin films grown at 700 °C (60 min) from 0.02 sccm Mo(CO)$_6$, 1.2 sccm DES flow, and 10 sccm H$_2$ on transferred CVD-graphene (Gr) and SiO$_2$ (see Fig. D4,Fig. D5). **(a)**(i-iii) SEM images taken at the edge of the graphene sheet, as illustrated by the schematic. **(b)** Microscope image. Points marked for spectroscopic analysis of MoS$_2$/Gr and MoS$_2$/SiO$_2$. **(c)** Raman spectra. **(d)** PL spectra.
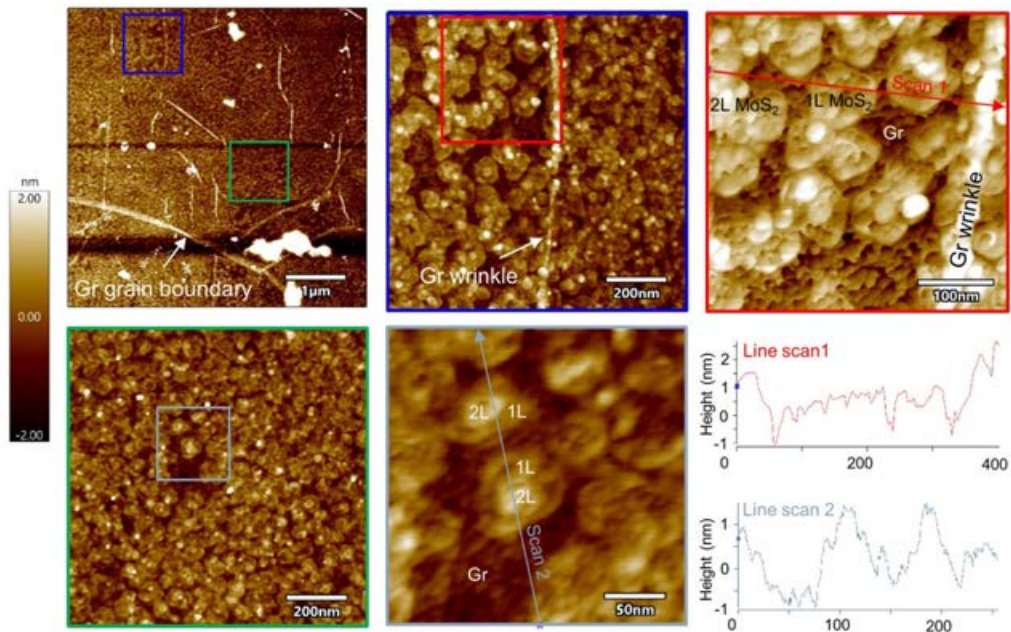
Figure B16 AFM of MoS$_2$ thin films grown at 700 °C (60 min) from 0.02 sccm Mo(CO)$_6$, 1.2 sccm DES flow, and 10 sccm H$_2$ on graphene/SiO$_2$. Scanned regions corresponding to colored frames. Line profile scans are highlighted.

B.2 Alkali-assisted growth
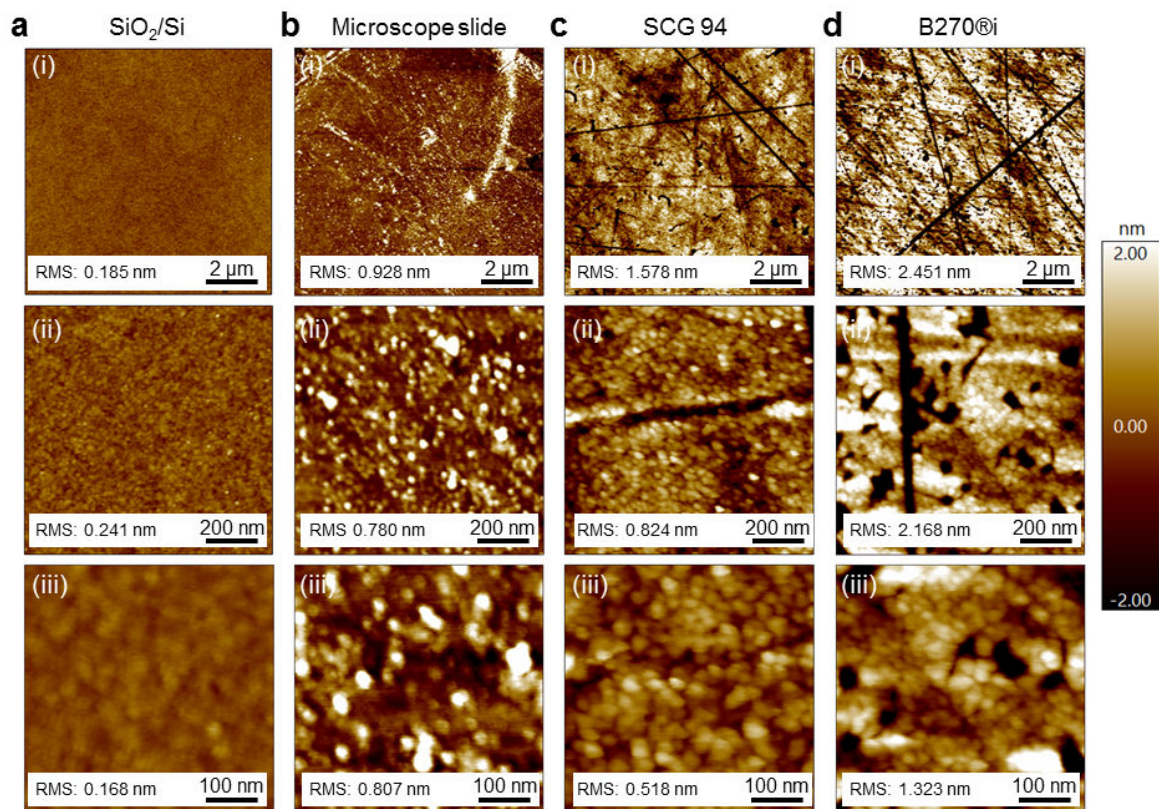
Figure B17 AFM of SiO$_2$/Si and soda-lime glass substrates: **(a)** Dry thermal oxide SiO$_2$(285nm)/Si, **(b)** microscope slide float-glass Marienfeld Superior, **(c)** Plan Optik SCG 94 crown-glass, and **(d)** Schott B270®i crown-glass. Three different scan sizes are given for each sample: (i) 10×10 µm^2, (ii) 1×1 µm^2, (iii) 1×1 µm^2. Root-mean-square (RMS) are given on the bottom left of each AFM scan.
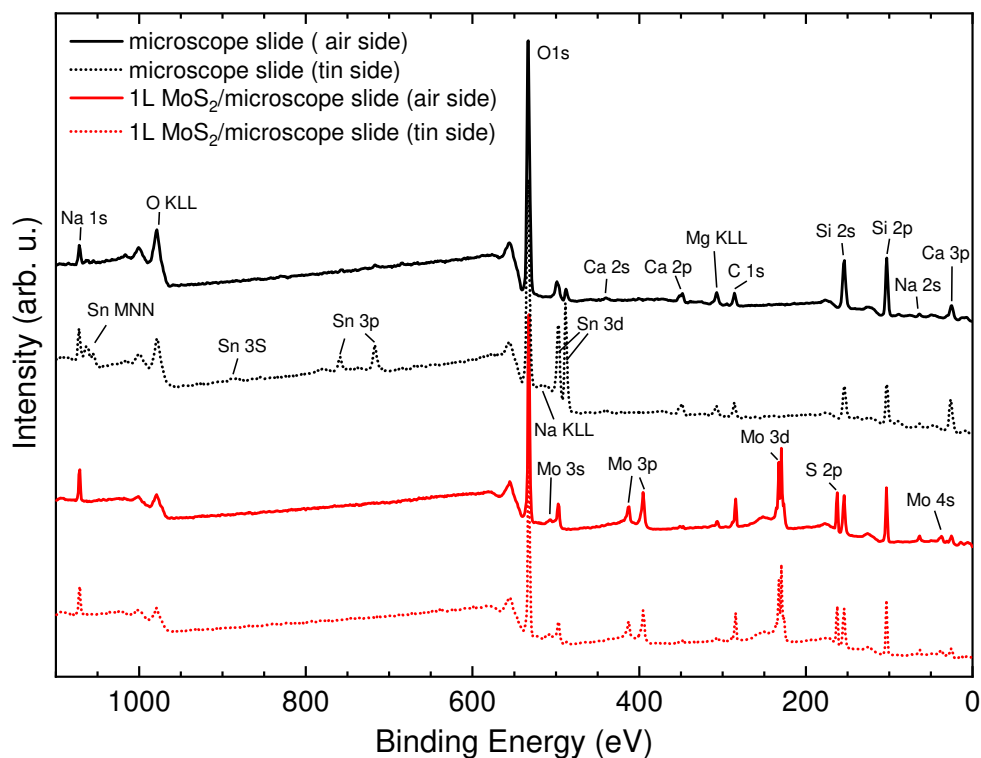
Figure B18 XPS overview spectra of as-received microscope float-glass (Marienfeld Superior), including bottom "tin side" facing the tin melt bed during glass production, top "air side", and 1L-MoS$_2$ thin films grown on both sides, respectively, from Mo(CO)$_6$ and DES at 700 °C. Core levels of different elements are designated.
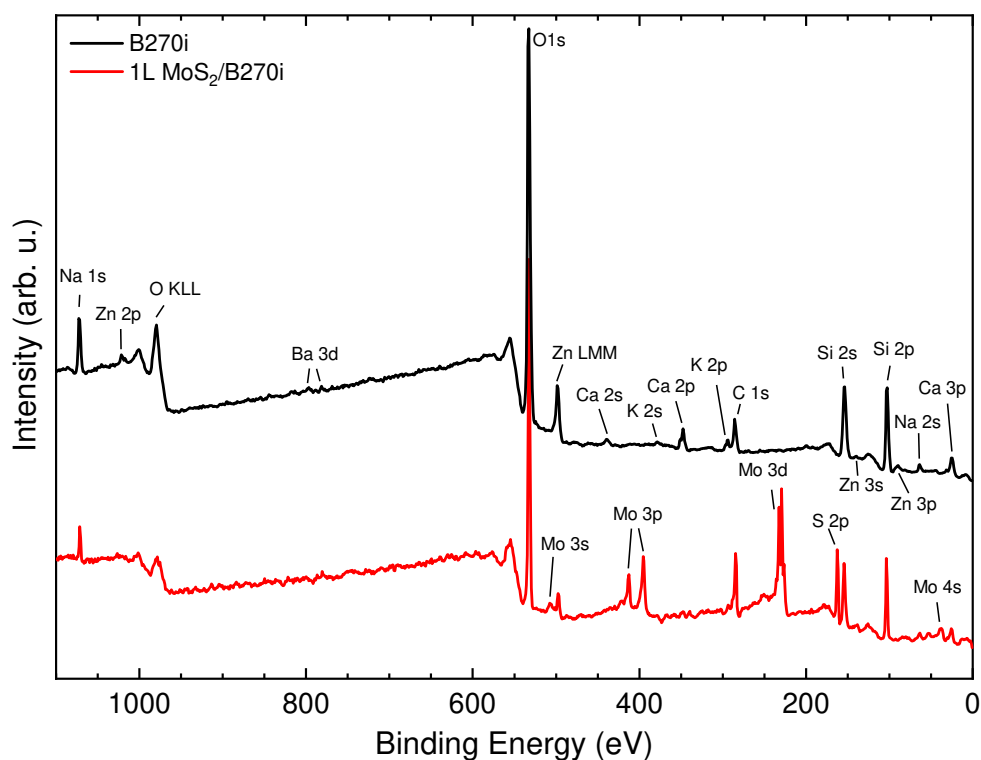
Figure B19 XPS overview spectra of B270®i crown-glass and 1L-MoS$_2$ thin films grown from Mo(CO)$_6$ and DES at 700 °C. Core levels of different elements are designated.
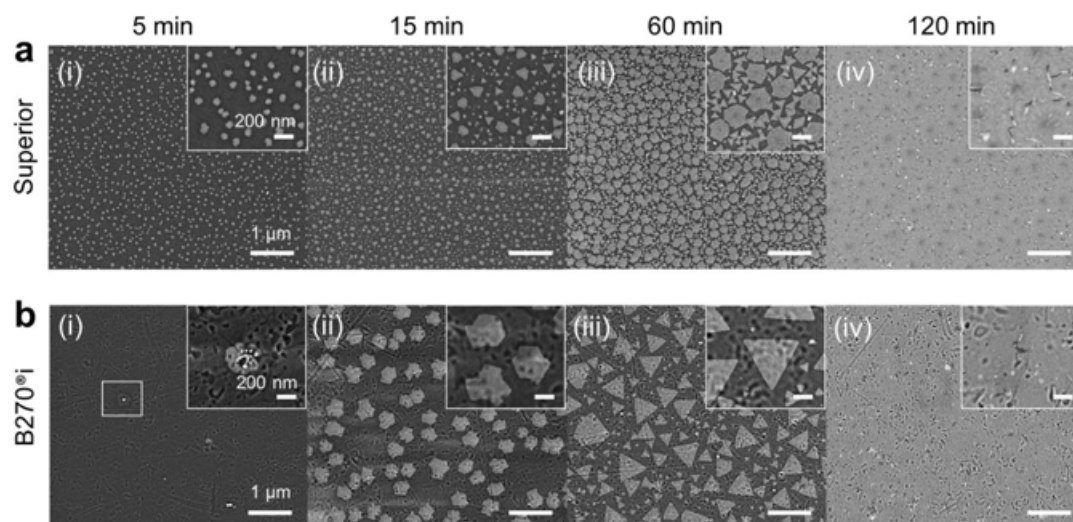
Figure B20 Growth time study for MoS$_2$ thin films grown on soda-lime glass at 700 °C. SEM images with magnified insets are shown for growth on **(a)** Marienfeld Superior, and **(b)** Schott B270®i crown-glass for (i) 5 min, (ii) 15 min, and (iii) 60 min, and (iv) 120 min.
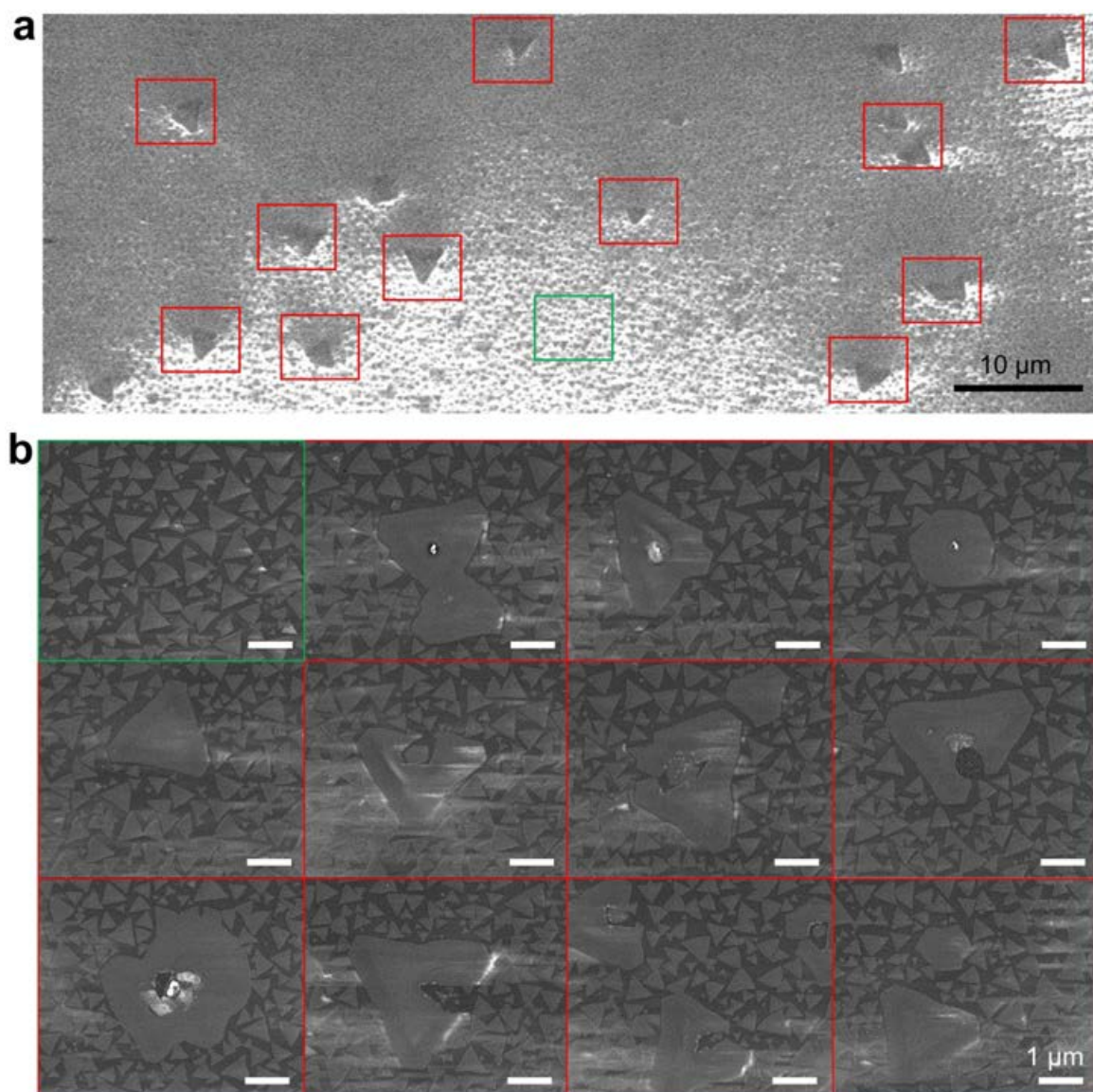
Figure B21 MoS$_2$ thin films grown on B270®i crown-glass grown from Mo(CO)$_6$ and DES at 700 °C (60 min). **(a)** Overview SEM image, and **(b)** magnified SEM images of "small" grain size area (green), and "large" grain size area with low melting point compound nucleation cluster still present, or evaporated.
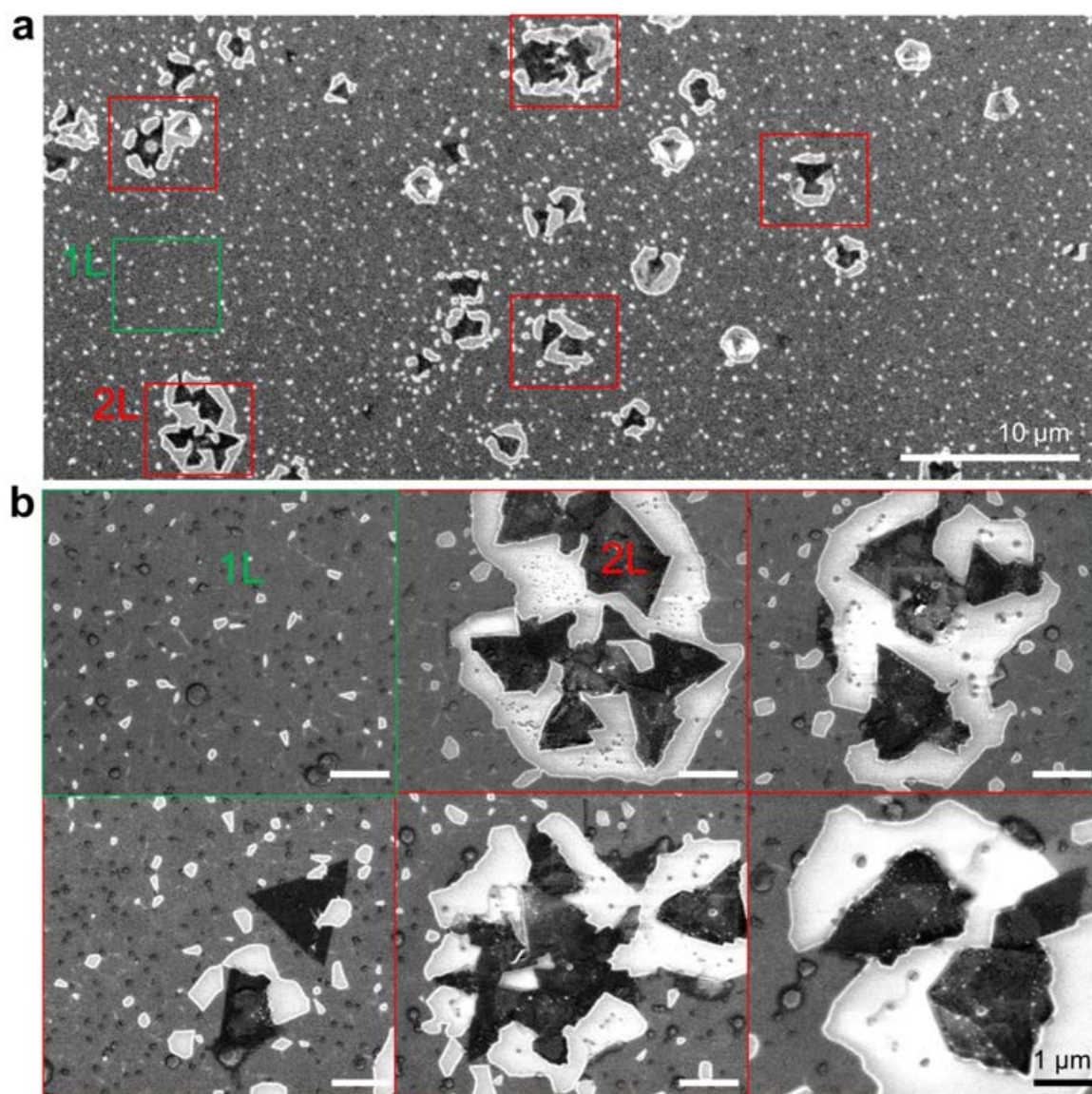
Figure B22 MoS$_2$ thin films grown on B270®i crown-glass grown from Mo(CO)$_6$ and DES at 700 °C (180 min). **(a)** Overview SEM image, and **(b)** magnified SEM images of 1L monolayer area (green), and bilayer nucleation areas with solidified, eutectic melt around 2L domain edges (red).
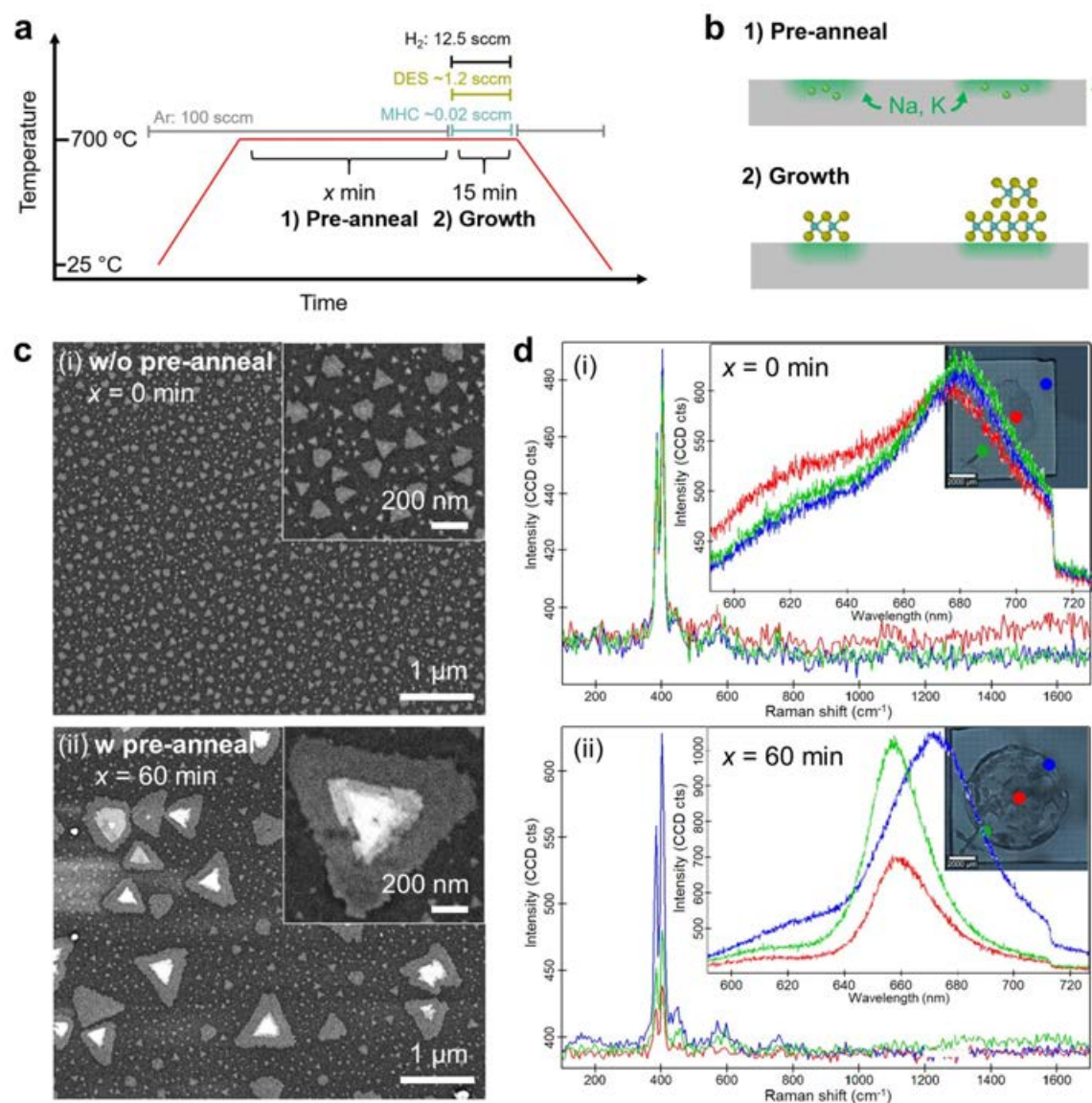
Figure B23 MoS$_2$ growth on pre-annealed soda-lime glass (microscope slide, air side). **(a)** Schematic of growth process, in which the soda-lime glass substrate is annealed at 700 °C prior growth start. **(b)** Illustration of alkali (Na,K) diffusion from bulk to surface during annealing process and domain growth of mono- and few layer MoS$_2$ thin films on alkali-enriched surface. **(c)** SEM images of sample (i) without pre-anneal, and (ii) with 60 min pre-anneal prior 15 min growth. **(d)** Corresponding Raman and PL spectra (inset) for the three measurement spots (green, red, and blue), as marked in the photograph.
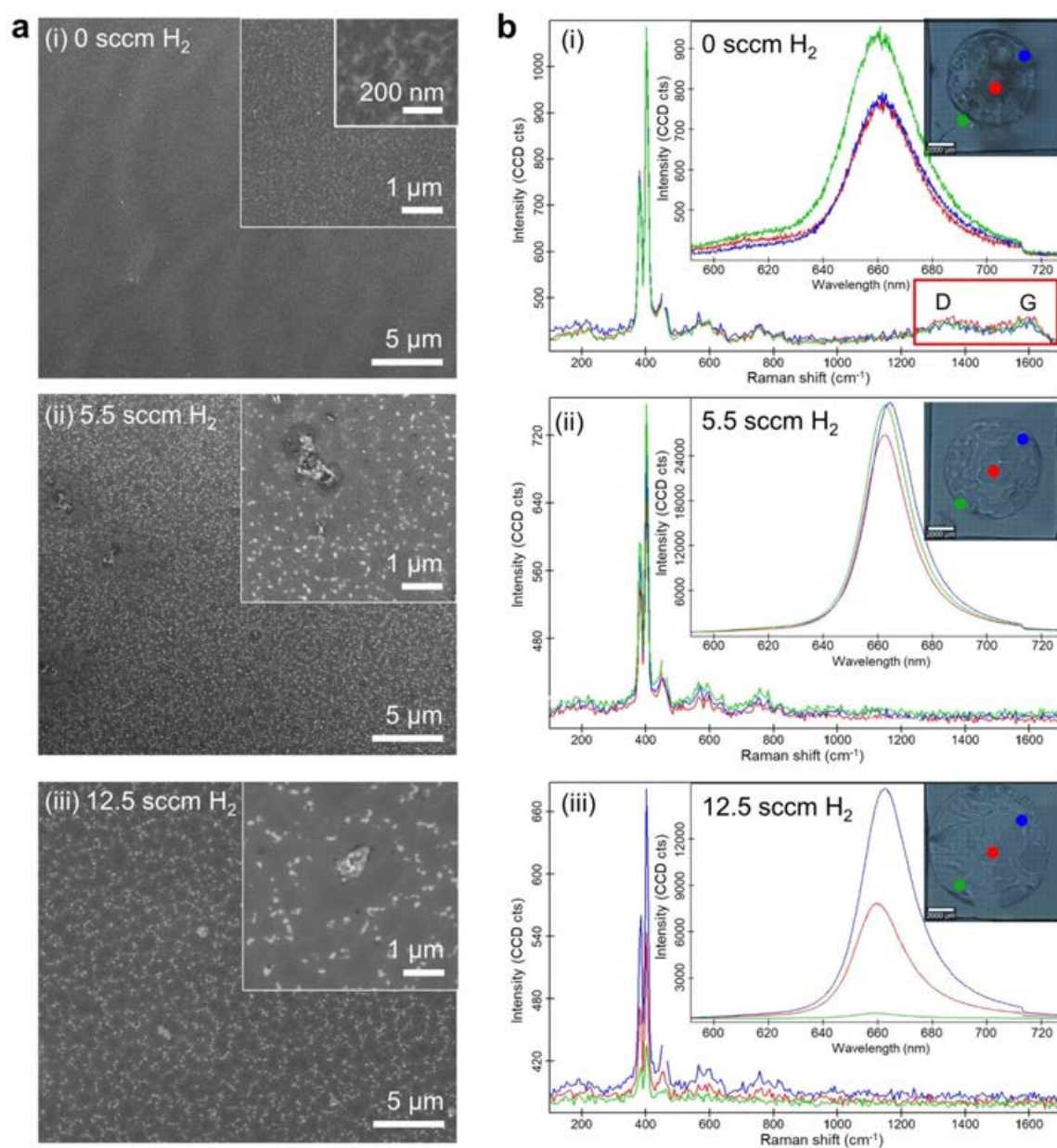
Figure B24 H$_2$ flow study for MoS$_2$ growth on Schott B270®i crown-glass. Thin films were grown at 700 °C (150 min) for different H$_2$ flows: (i) 0 sccm, (ii) 5.5 sccm, and (iii) 12.5 sccm. **(a)** SEM images with magnified insets. **(b)** Corresponding Raman and PL spectra (inset) for the three measurement spots (green, red, and blue), as marked in the photograph.
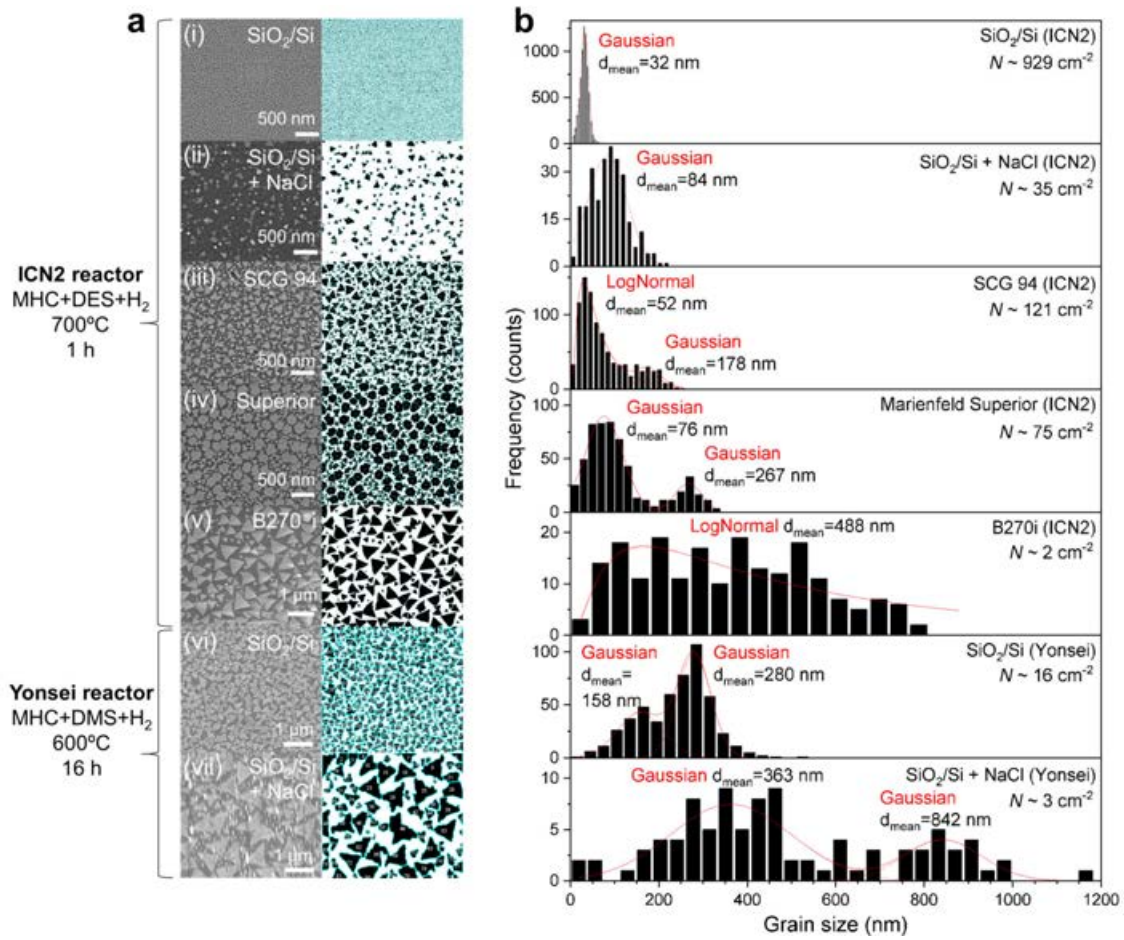
Figure B25 Comparison of grain size distributions for MoS_2 thin films grown in the ICN2 and Yonsei reactor on different substrates and with/without NaCl-assisted growth. **(a)** SEM images and corresponding binary images after execution of ImageJ analysis algorithm. **(b)** Histograms of grain size distribution (based on side length of an approximated, equilateral triangle). The data was fitted with Gaussians/LogNormal functions and the mean grain sizes d_{mean} were extracted from the peak centers. Nucleation densities N are given.

B.3   MoS$_2$ HER catalysis
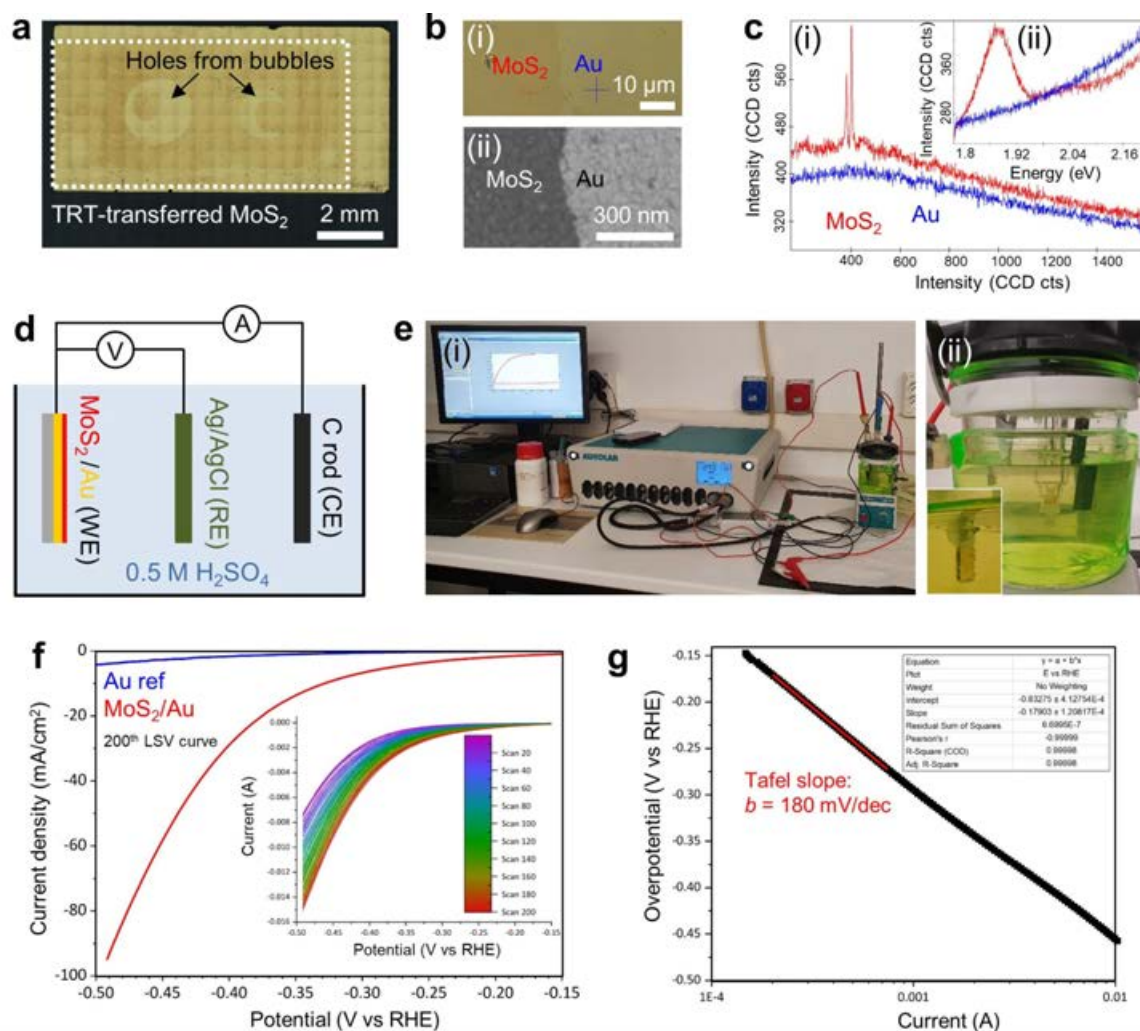
Figure B26 MoS$_2$-catalyzed hydrogen evolution reaction (HER) catalysis. **(a)** Photograph of 1L MoS$_2$ thin film transferred onto Au/SiO$_2$. The marked holes were not taken into account for area extraction and current density calculations below. **(b)** Edge of the 1L MoS$_2$ film on Au. (i) Magnified microscopic image. (ii) SEM image. **(c)** (i) Raman spectrum (ii) PL spectrum. **(d)** Schematic of HER measurement setup with MoS$_2$/Au as the working electrode (WE), Ag/AgCl (3 M KCl) as reference electrode (RE), and a graphite rod as counter electrode (CE). **(e)** (i) Photograph of HER measurement setup (ii) Electrochemical cell. The inset shows H$_2$ bubble creation on the MoS$_2$/Au surface. **(f)** Linear sweep voltammetry (LSV) after 200 cycles. Current density over potential versus reversible hydrogen electrode (RHE). Insets shows evolution of LSV from 1 to 200 cycles. **(g)** Tafel plot.

Appendix C

MOCVD of epitaxial MoS$_2$ thin films

C.1 Sapphire surface preparation
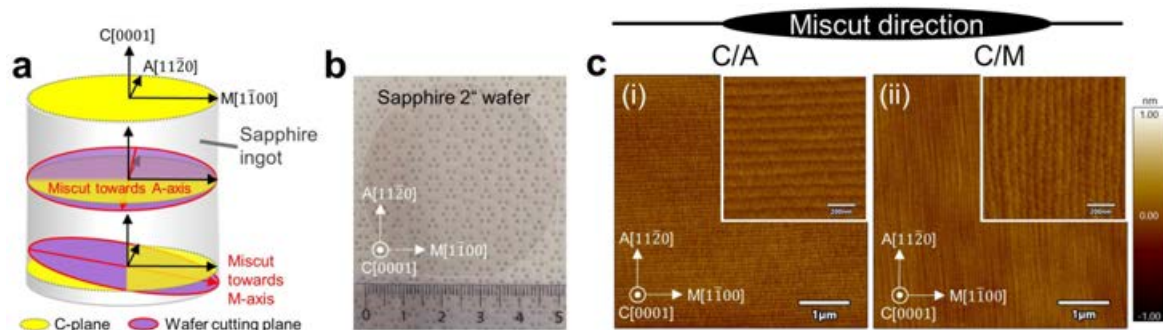
Figure C1 Sapphire miscut direction. **(a)** Schematic of a single-crystal sapphire ingot with indicated crystallographic axes. Wafer cutting planes (purple) with miscut tilted from the C-plane (yellow) towards the A- and M-axis. **(b)** Photograph of a c-sapphire wafer. **(c)** AFM images of vicinal c-sapphire surfaces annealed at 1050 °C with nominal 0.2° miscut tilted (i) along A-axis (C/A), and (ii) along M-axis (C/M). Insets show magnified scans.
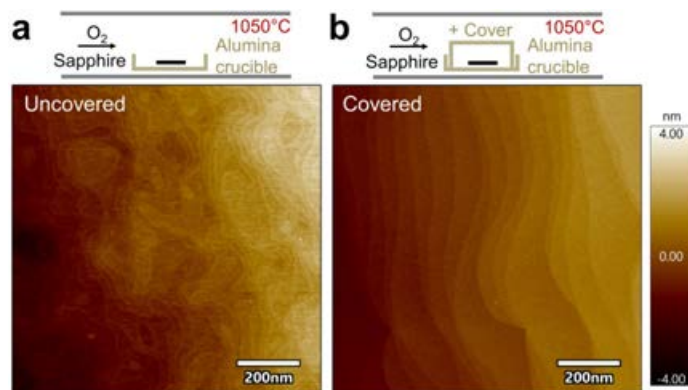
Figure C2 Importance of annealing crucible. AFM images of sapphire surfaces annealed at 1050 °C placed inside an **(a)** uncovered, and **(b)** covered alumina crucible.
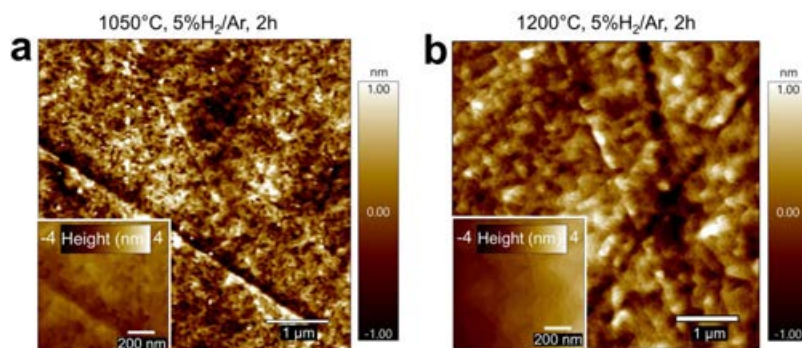
Figure C3 Topographic AFM images after direct 5 %H$_2$/Ar-annealing of c-sapphire (0.2° miscut) for 2 h at **(a)** 1050 °C and **(b)** 1200 °C.
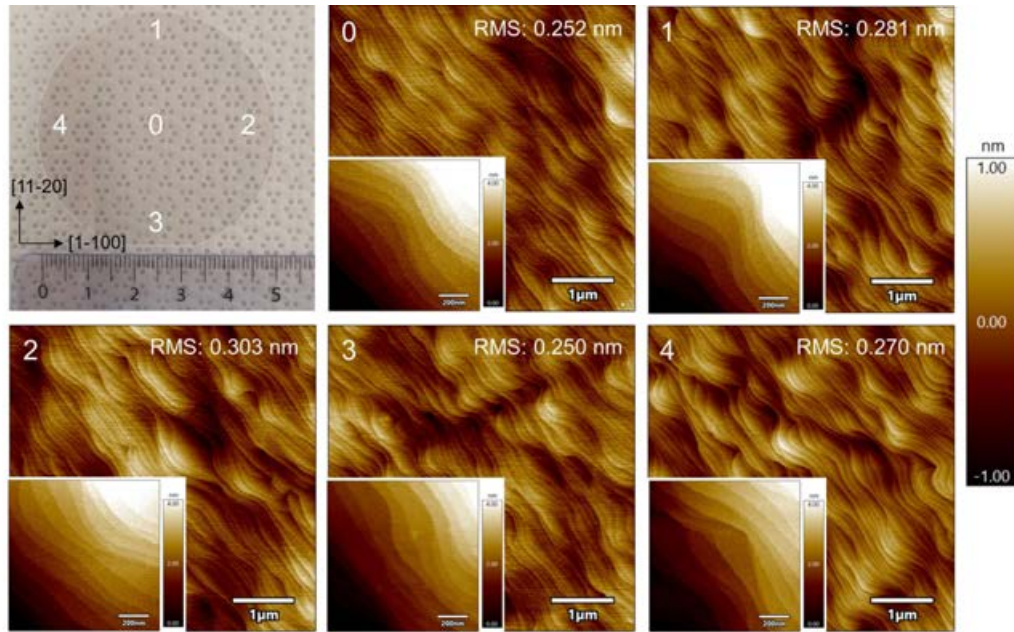
Figure C4 Wafer-scale homogeneity of 0.2° sapphire surface after annealing at 1050 °C in air for 2 h. The large, flattened AFM images correspond to the positions marked in the photo of the wafer (remark: RMS values of flattened images measured over step edges do not reflect the on-terrace roughness). Insets show magnified, plane-fitted images.
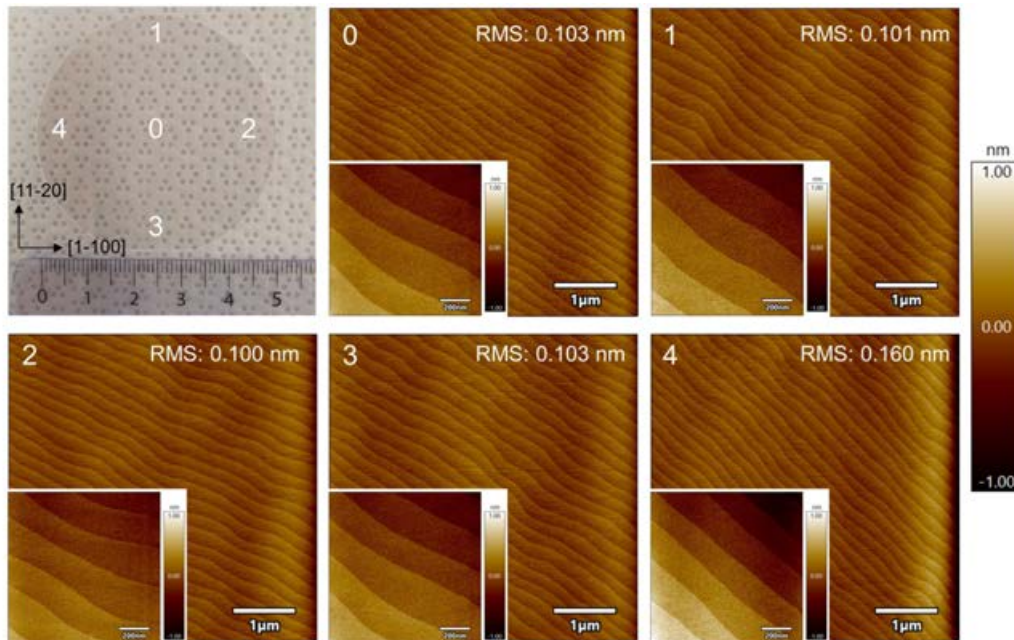
Figure C5 Wafer-scale homogeneity of 0.05° sapphire surface after annealing at 1050 °C in air for 2 h. The large, flattened AFM images correspond to the positions marked in the photo of the wafer (remark: RMS values of flattened images measured over step edges do not reflect the on-terrace roughness). Insets show magnified, plane-fitted images.
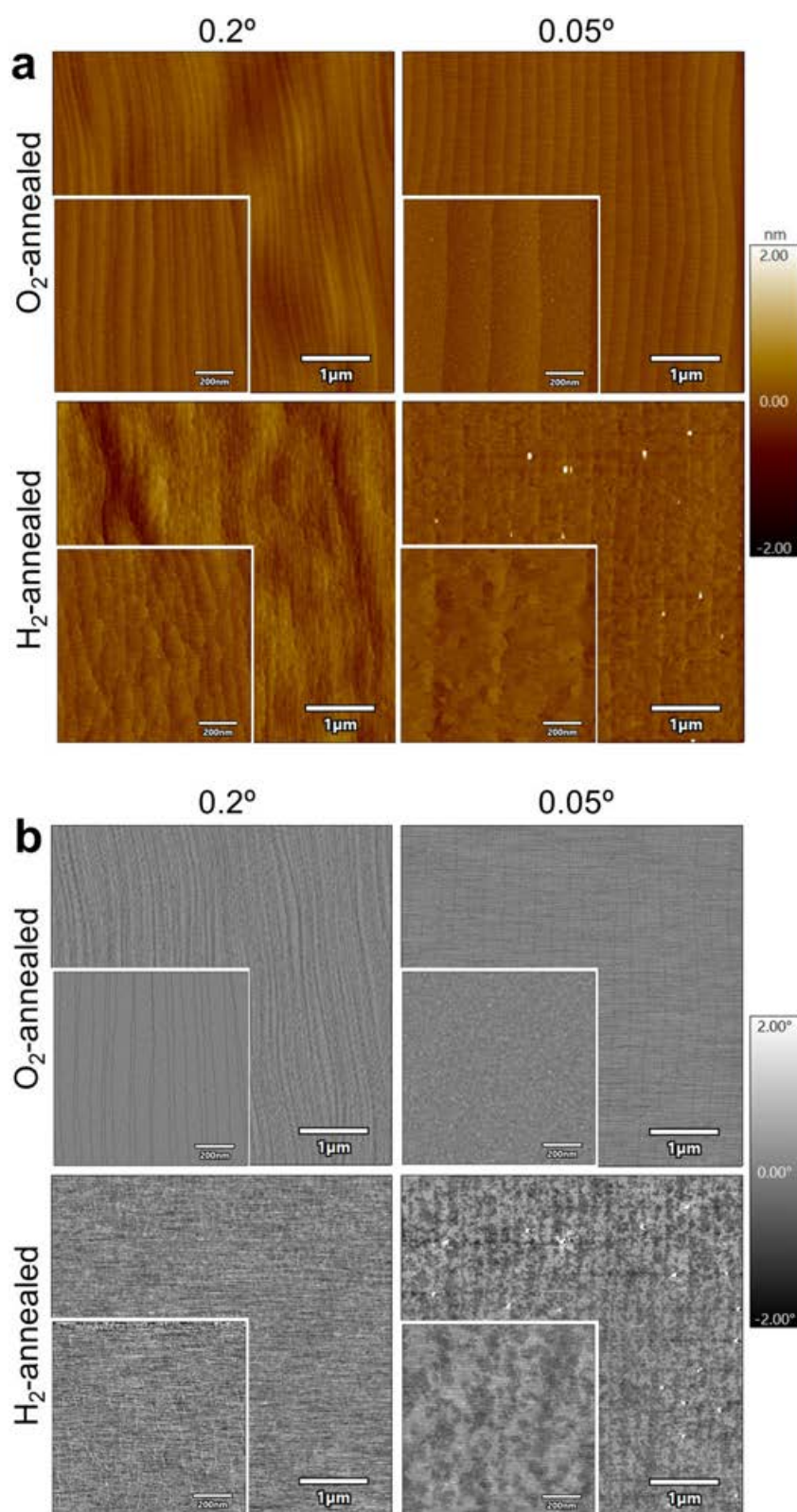
Figure C6 AFM study of 0.2° and 0.05° miscut c-sapphire surfaces after 1200 °C annealing (2 h) in O$_2$-rich and H$_2$-rich atmosphere. **(a)** Flattened, topographic images. **(b)** Flattened, phase images.
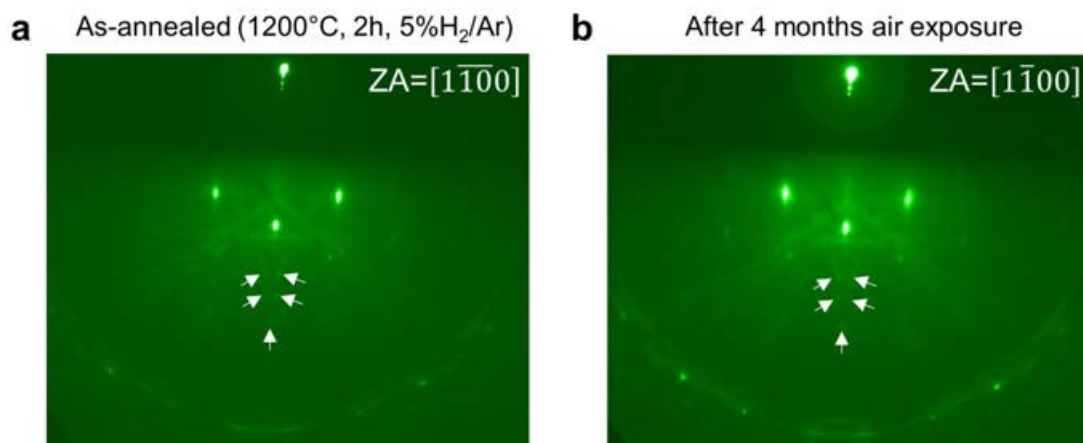
Figure C7 Stability of sapphire surface reconstruction. Characteristic RHEED patterns of the $(\sqrt{31} \times \sqrt{31})\pm$ R9°surface reconstruction **(a)** as-annealed, and **(b)** four months after annealing.
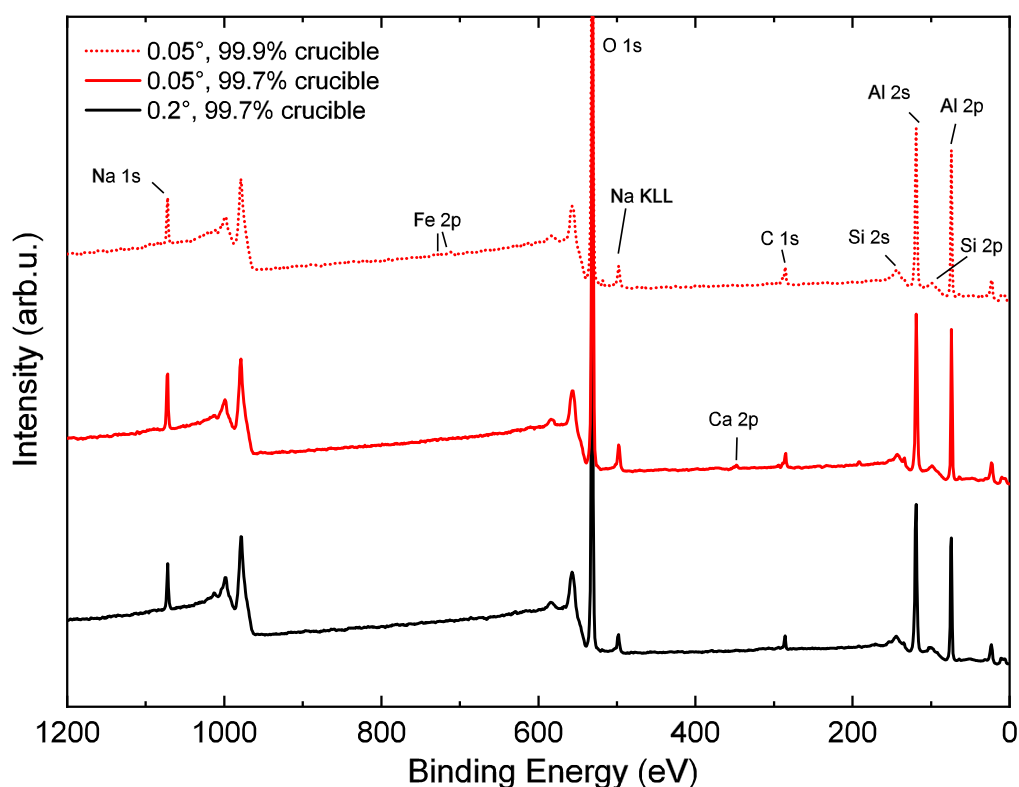
Figure C8 Sapphire surface impurities. XPS overview spectra of c-sapphire (SIEGERT Wafer GmbH, Germany) O_2-annealed at 1200 °C for 2h placed inside alumina crucibles of 99.7 % and 99.9 % purity. Na, Ca, Si, and Fe species can be attributed to impurities from the alumina annealing crucible, consistent with information provided by the manufacturer.

C.2 MOCVD and analysis of epitaxial MoS$_2$ films
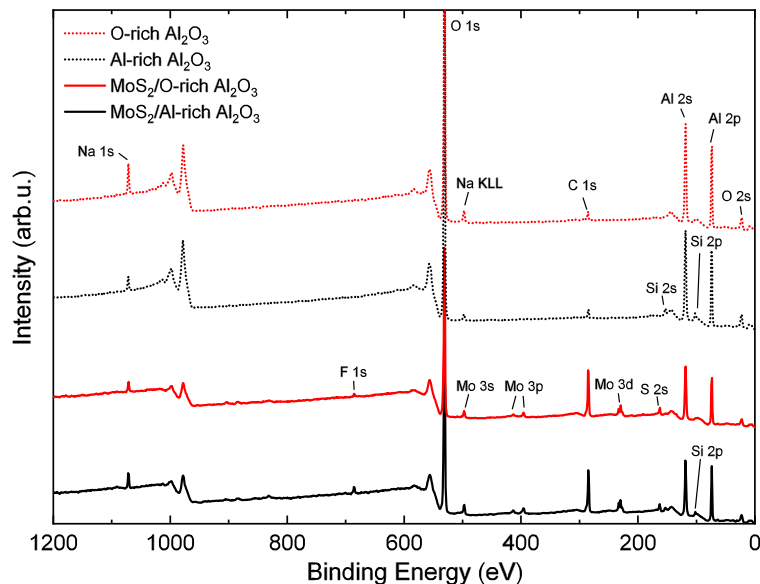
Figure C9 MoS$_2$/sapphire XPS overview spectra. From top to bottom: as-annealed O-rich Al$_2$O$_3$ (1200 °C, O$_2$, 2 h), Al-rich Al$_2$O$_3$ (1200 °C, 5 % H$_2$/Ar, 2 h), as-grown MoS$_2$/O-rich Al$_2$O$_3$. Na and Si impurities from annealing crucibles. Origin of F impurities unknown, maybe from long-term sample storage in PTFE boxes [660].
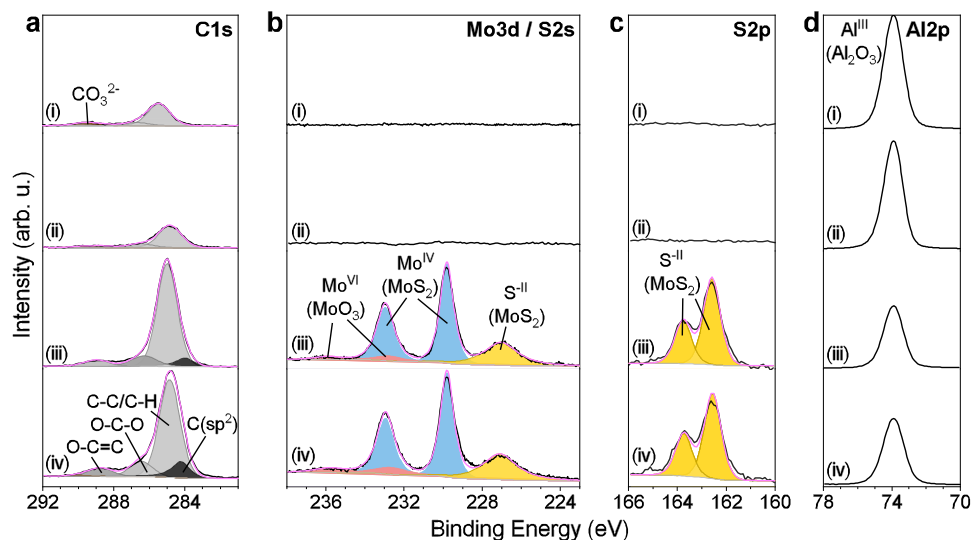
Figure C10 XPS analysis of as-annealed sapphire substrates and as-grown, epitaxial MoS$_2$ thin films, showing core level spectra for **(a)** C1s **(b)** Mo 3d, **(c)** S 2p, **(d)** Al 2p. Spectra from top to bottom correspond to (i) O-rich Al$_2$O$_3$, (ii) Al-rich Al$_2$O$_3$, (iii) MoS$_2$/O-rich Al$_2$O$_3$, and (iv) MoS$_2$/Al-rich Al$_2$O$_3$.
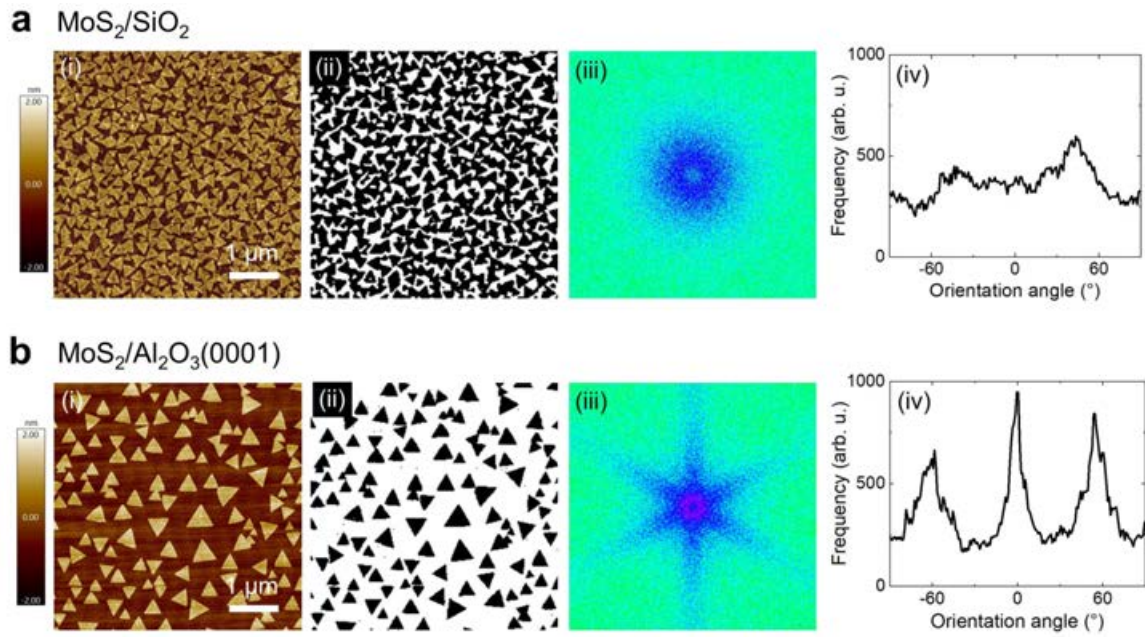
Figure C11 Comparison of MoS$_2$ thin films grown on **(a)** SiO$_2$ with random domain orientation, and **(b)** on 1200°-annealed Al$_2$O$_3$(0001) with epitaxially aligned domains: (i) AFM images, (ii) corresponding binary images, (iii) Fast-Fourier transform (FFT), and (iv) histogram of domain orientation obtained after analysis with the software IMAGEJ 1.53 [271] by using the plugin ORIENTATIONJ v2.0.5 [272].
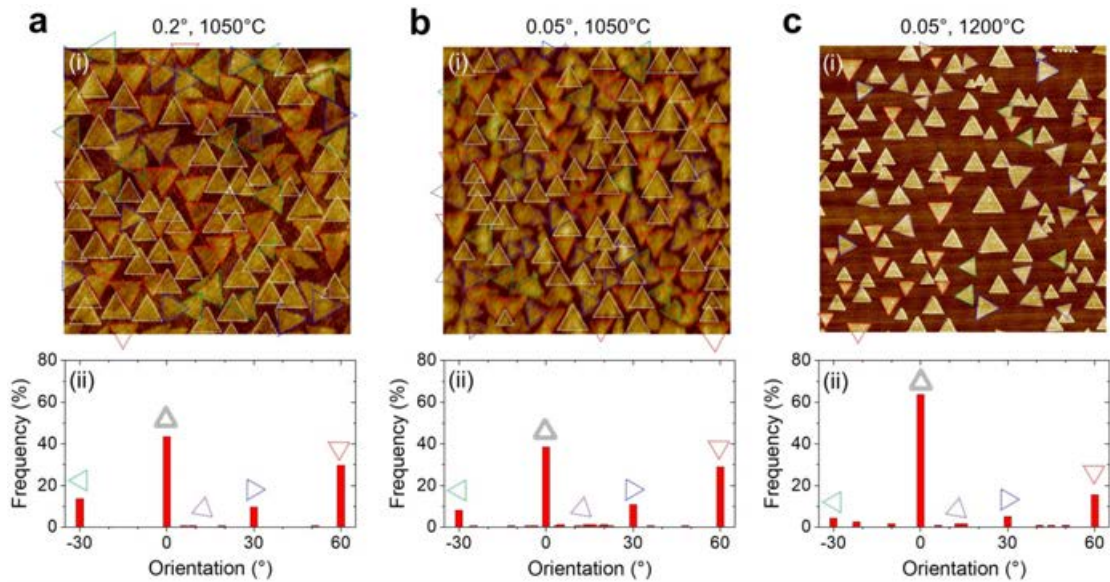

Figure C12 AFM domain orientation analysis. MoS$_2$ thin films grown at 600 °C on O-rich sapphire with **(a)** 0.2° miscut annealed at 1050 °C (2 h), **(b)** 0.05° miscut annealed at 1050 °C (2 h), **(c)** 0.05° miscut annealed at 1200 °C (2 h). (i) AFM images with color-classified domains by orientation: −30° (green), 0° (white), 30° (blue), 60° (red), random alignment (purple) and corresponding (ii) domain orientation histograms.
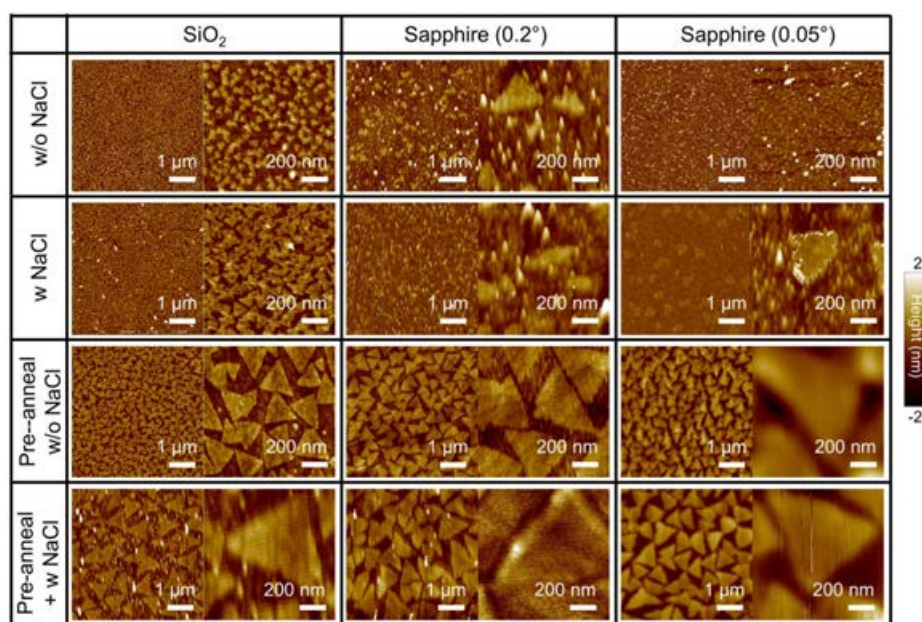
Figure C13 Overview of MOCVD of MoS$_2$ thin films grown on SiO$_2$ and sapphire substrates in Yonsei reactor at 600 °C for 16 h. The AFM images show four sample batches grown without NaCl, with NaCl, and without and with an additional 700 °C pre-anneal (10 min) inside the reactor tube open to ambient air just prior the growth process. The sapphire substrates had been annealed at 1050 °C to obtain an atomically-smooth surface a few weeks before the growth process. The intention of the pre-anneal was to burn off adventitious carbons for a clean starting surface.
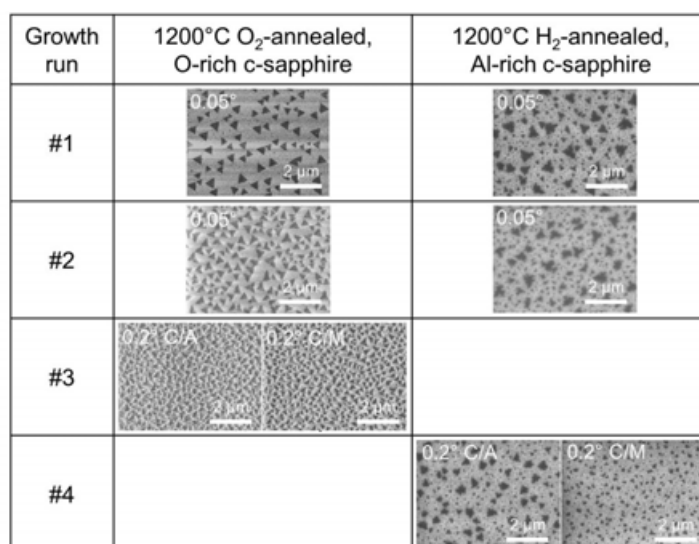
Figure C14 SEM images of MoS$_2$ thin films grown in subsequent growth runs on 1200 °C O$_2$- an H$_2$-annealed c-sapphire with different miscut angles (0.05 and 0.2°) and miscut orientations (towards A and M-directions), as indicated. Growth was carried out in the Yonsei reactor with Mo(CO)$_6$/DMS precursors at 600 °C.
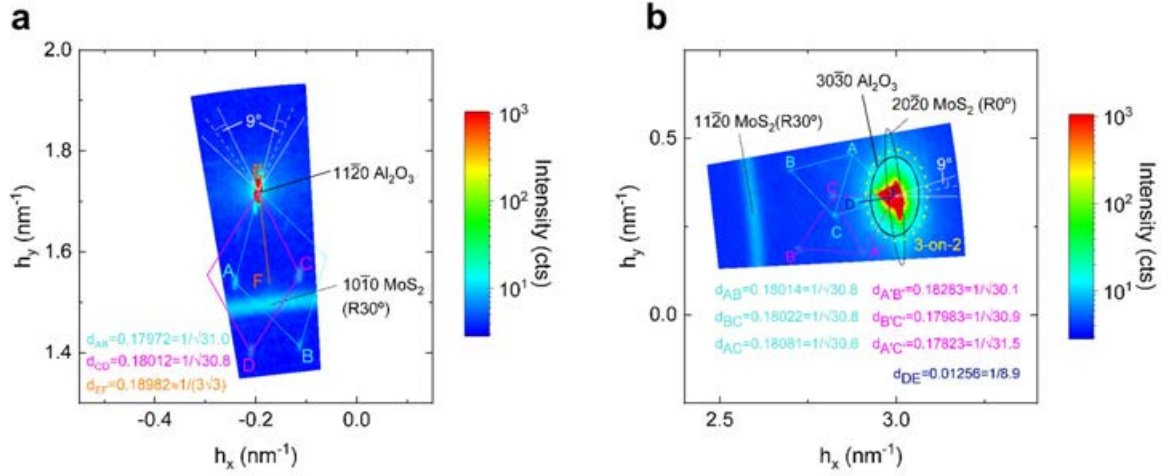
Figure C15 Magnified Al$_2$O$_3$(0001) surface reconstruction patterns. Reciprocal space mapping was performed around the **(a)** $(11\,\overline{2}\,0)$Al$_2$O$_3$ peak, and **(b)** $(3\,0\,\overline{3}\,0)$Al$_2$O$_3$ peak. The diffraction spots with symmetry of $\pm 9°$-rotated rhombs and depicted spot-to-spot distances are compatible with the $(\sqrt{31} \times \sqrt{31})\pm R9°$ surface reconstruction. This proves the stability of this reconstruction during MoS$_2$ growth by MOCVD at 600 °C. Also a diffraction spot matching the $(3\sqrt{3} \times 3\sqrt{3})\pm R30°$ reconstruction is observed from the distance d_{EF} in (a).
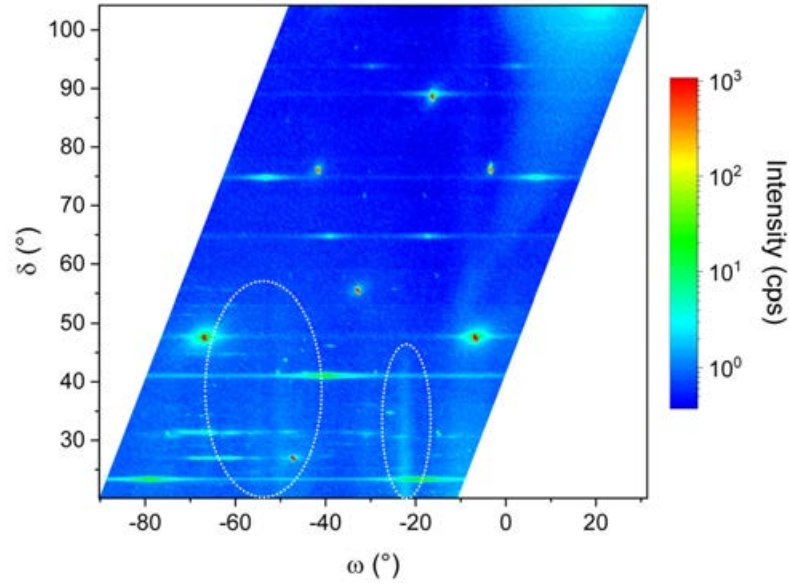

Figure C16 Reciprocal space map artifacts. A $\delta - \omega$ plot of the reciprocal space map of epitaxial MoS$_2$ grown on c-sapphire reveals that the marked, streaky background features are constant in ω. Therefore, they might be related to artifacts not coming from the sample, but another source such as the reflections from the Be window etc.
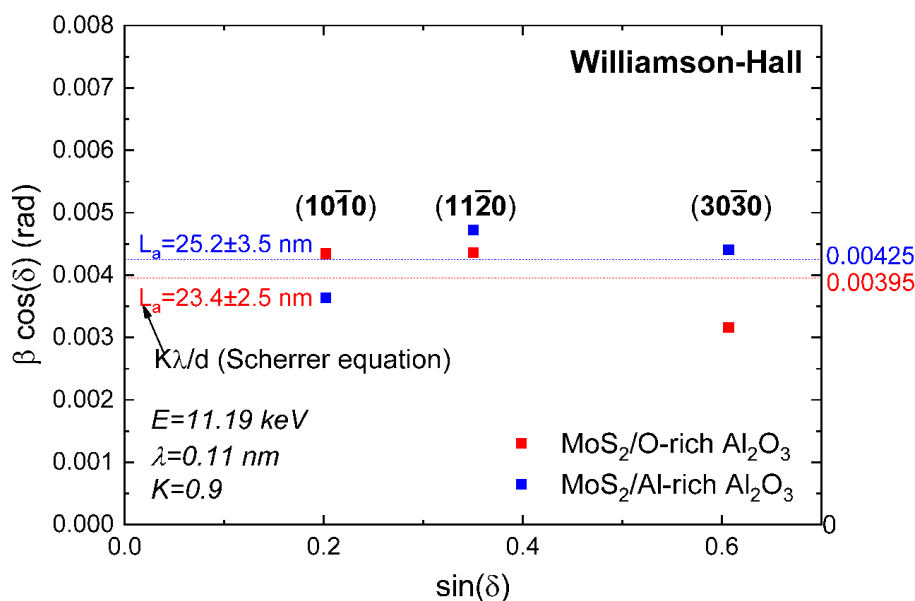
Figure C17 Williamson-Hall plot used to distinguish the origin of peak broadening of the in-plane ($h\,k\,i\,0$) Bragg reflections of radial scans in Fig. 4.13d. A constant trend indicates peak broadening related to crystallite size L_a rather than microstrain [280]. L_a can be extracted via the Scherrer equation from the intercept via $L_a = K\lambda/\beta cos(\delta)$, where K is a geometric shape factor, β is the peak broadening (FWHM) and the angle δ is defined according to the diffractometer geometry depicted in Fig. C24c.
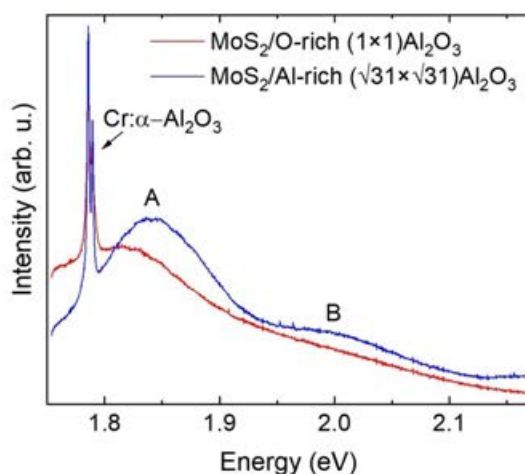

Figure C18 PL spectroscopy of MoS$_2$ thin films grown at 600 °C on O-rich (1×1) and Al-rich ($\sqrt{31} \times \sqrt{31}$)±R9° surfaces. The data represents total average spectra extracted from 225 points of a 5×5 µm map recorded with a 488 nm laser at 1.5 mW.
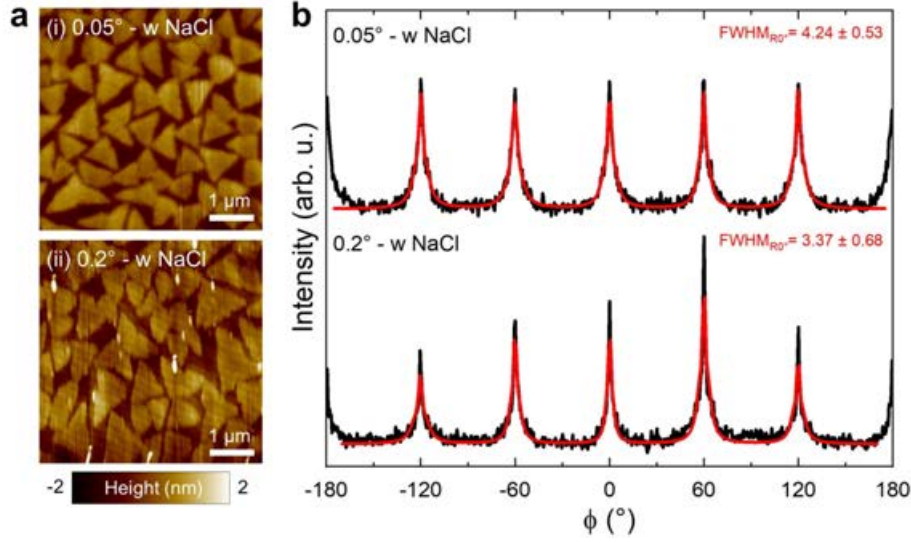
Figure C19 Impact of sapphire miscut angle on NaCl-assisted MoS$_2$ epitaxy. **(a)** AFM images of MoS$_2$ grown on 1050 °C-annealed sapphire with miscut angle (i) 0.05°, and (ii) 0.2° **(b)** GIXRD in-plane, azimuthal ϕ-scans around the MoS$_2$\{11$\bar{2}$0\} reflections, where $\phi = 0$ is defined along the Al$_2$O$_3$(11$\bar{2}$0) direction. NaCl was placed at the furnace entrance.
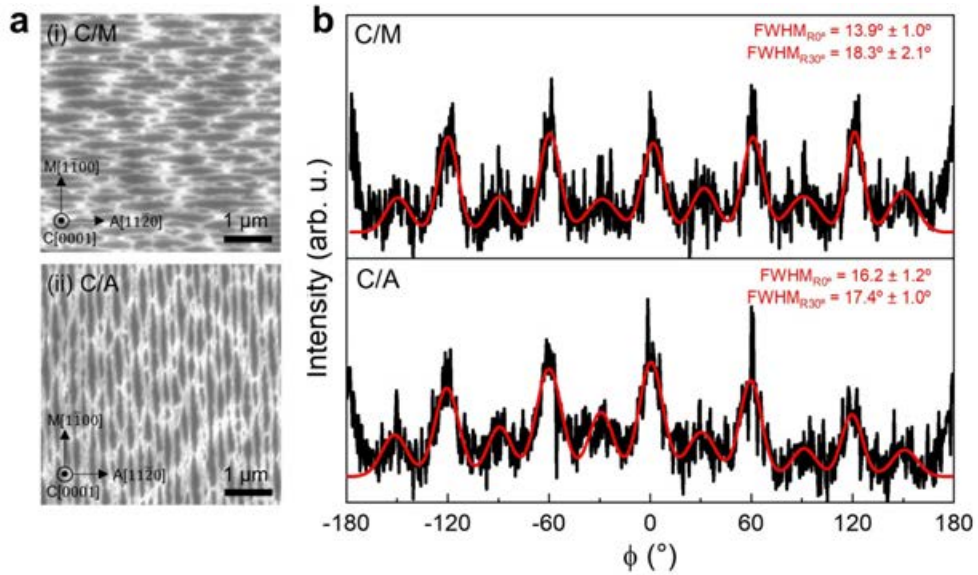

Figure C20 Impact of sapphire miscut orientation on MoS$_2$ epitaxy. **(a)** SEM images of MoS$_2$ grown on O-rich sapphire with 0.2°-miscut (i) towards M-axis, and (ii) A-axis. **(b)** GIXRD in-plane, azimuthal ϕ-scans around the MoS$_2$\{11$\bar{2}$0\} reflections, where $\phi = 0$ is defined along the Al$_2$O$_3$(11$\bar{2}$0) direction. (Samples were grown in Yonsei reactor, analyzed by SEM, coated with PMMA, shipped to ICN2, and measured with the PMMA coating by GIXRD several months after growth. The effect of PMMA-coating on MoS$_2$ quality and degradation has been controversially discussed both in favor of protecting MoS$_2$ from and accelerating MoS$_2$ aging [121, 661, 662].
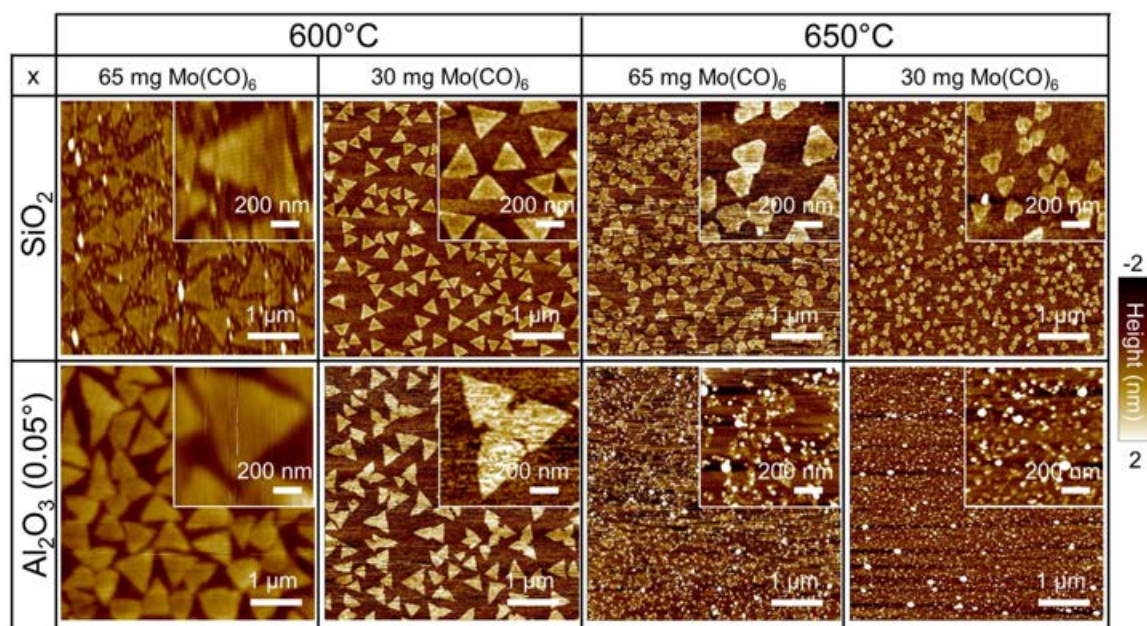
Figure C21 Impact of growth temperature and S:Mo ratio. AFM images for MoS$_2$ thin films grown on SiO$_2$ and 1050 °C-annealed O-rich sapphire with 0.05°-miscut at 600 °C and 650 °C, respectively, for Mo(CO)$_6$/DMS precursor solution concentrations of x mg/12 mL. NaCl was used in all growth runs.
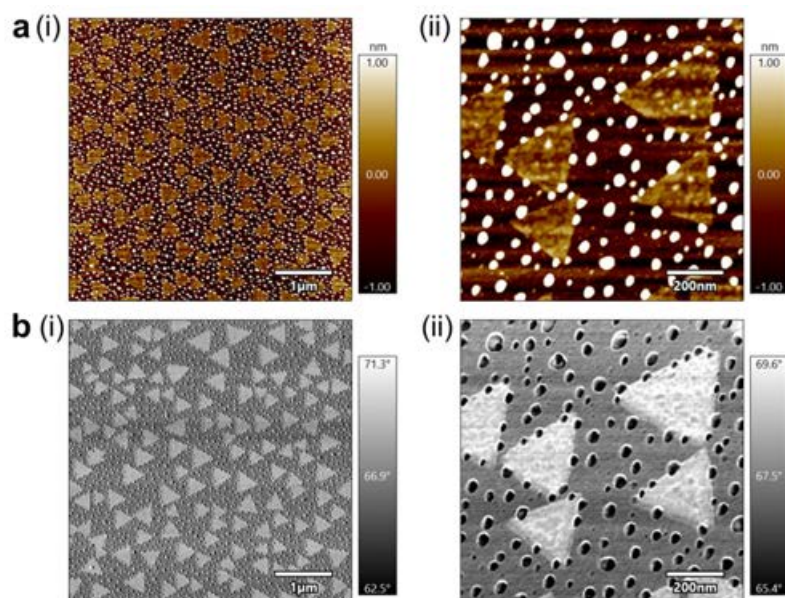

Figure C22 Particle formation in 5 day aged, air exposed, epitaxial MoS$_2$ thin films. **(a)** Topographical AFM images, and **(b)** phase images of (i) 5×5 µm^2 and (ii) 1×1 µm^2 area scans.

Table C1 Literature comparison of TMD epitaxy on sapphire, including available information about substrate preparation, growth method/condition, preferentially found epitaxial relationships and mosaic spread (FWHM) of TMD films.

| Material	Substrate condition	Growth method	Growth condition	Epi. relation	Mosaic spread (°)	[ref]
1L MoS$_2$	0.2/1° off A, 1000 °C-annealed (Ar/O$_2$), Al$_2$O$_3$(0001)	CVD (Mo+O$_2$+S)	850–1000 °C	R30°		[176]
2L MoS$_2$	1° off A, 1350 °C-annealed (air) Al$_2$O$_3$(0001)	CVD (Mo+O$_2$+S)	850–1000 °C	R30°	0.26	[248]
1L MoS$_2$	0.2°, Al$_2$O$_3$(0001)	CVD (Mo+O$_2$+S)	O-rich, 790 °C	R0°		[175]
1L MoS$_2$	0.2°, Al$_2$O$_3$(0001)	CVD (Mo+O$_2$+S)	S-rich, 790 °C	R30°		[175]
1L MoS$_2$	0.2°, 1000 °C-annealed (air) Al$_2$O$_3$(0001)	CVD (MoO$_3$+S)	700 °C	R0°		[163]
1L MoS$_2$	as-received, Al$_2$O$_3$(0001)	CVD (MoO$_3$+S)	S-poor, 930 °C	R0°		[257]
1L MoS$_2$	as-received, Al$_2$O$_3$(0001)	CVD (MoO$_3$+S)	S-rich, 930 °C	R30°		[257]
1L MoS$_2$	1200 °C-annealed, ($\sqrt{31}\times\sqrt{31}$)±R9°Al$_2$O$_3$(0001)	MBE (Mo+H$_2$S-plasma)	S-rich, 450 °C	R30°		[150]
1L MoS$_2$	1200 °C-annealed, ($\sqrt{31}\times\sqrt{31}$)±R9°Al$_2$O$_3$(0001)	MOCVD (Mo(CO)$_6$+H$_2$S)	700 °C	R30°		[150]
1L MoS$_2$	0.2° off M,1200 °C-annealed (H$_2$), Al$_2$O$_3$(0001)	MOCVD (W(CO)$_6$+DTBS)	700 °C	R30°	~3.8–3.9	[404]
1L MoS$_2$	1175 °C-annealed, ($\sqrt{31}\times\sqrt{31}$)±R9°Al$_2$O$_3$(0001)	MOCVD (Mo(CO)$_6$+H$_2$S)	700 °C	R30°	~5–16	[405]
1L MoS$_2$	1175 °C-annealed, ($\sqrt{31}\times\sqrt{31}$)±R9°Al$_2$O$_3$(0001)	MOCVD (Mo(CO)$_6$+H$_2$S)	1000 °C	R0°	~10–14	[405]
1L MoS$_2$	1000 °C-annealed, (1×1)Al$_2$O$_3$(0001)	IMCVD (MoOCl$_4$+H$_2$S)	600 °C	R0°/R30°	random	[384]
1L MoS$_2$	1000 °C-annealed, (1×1)Al$_2$O$_3$(0001)	IMCVD (MoOCl$_4$+H$_2$S)	700 °C	R0°/R30°	~5.4°	[384]
1L MoS$_2$	1000 °C-annealed, (1×1)Al$_2$O$_3$(0001)	IMCVD (MoOCl$_4$+H$_2$S)	800 °C	R0°/R30°	~4.7°	[384]
1L MoS$_2$	1000 °C-annealed, (1×1)Al$_2$O$_3$(0001)	IMCVD (MoOCl$_4$+H$_2$S)	900 °C	R0°	~4.2°	[384]
1L MoS$_2$	Al$_2$O$_3$(0001)	PLD (MoS$_2$ target)	800 °C	R30°		[156]
1L WSe$_2$	Al$_2$O$_3$(0001)	MBE (W+Se), buffer	450 °C growth/900 °C anneal	R0°	8.8	[149]
1L WSe$_2$	Al$_2$O$_3$(0001)	MBE (W+H$_2$Se-plasma)	450 °C growth/850 °C anneal	R0°	~24	[385]
1L WSe$_2$	Al$_2$O$_3$(0001), S-passivated	MOCVD (Mo(CO)$_6$+H$_2$S)	1000 °C	R0°	16–23	[249]
1L MoS$_2$	Al$_2$O$_3$(0001)	MOCVD (Mo(CO)$_6$+DES)	900 °C	R0°	0.4	[369]
1L WSe$_2$	Al$_2$O$_3$(0001)	MOCVD (W(CO)$_6$+H$_2$S)	750 °C	R0°	0.28	[322]
1L WSe$_2$	0.2° off M, Al$_2$O$_3$(0001), Se-passivated	MOCVD (W(CO)$_6$+H$_2$S)	750–1000 °C	R0°	0.16–0.47	[259]
1L WSe$_2$	as-received, Al$_2$O$_3$(0001)	MOCVD (W(CO)$_6$+H$_2$S)	850–1000 °C	R0°	0.09–1.13	[48]
1L MoS$_2$	0.05°, 1200 °C-annealed (H$_2$/Ar), ($\sqrt{31}\times\sqrt{31}$)±R9°Al$_2$O$_3$(0001)	MOCVD (Mo(CO)$_6$+DMS)	600 °C	R0°/R30°	19.3	This work
1L MoS$_2$	1050 °C-annealed (air), (1×1)Al$_2$O$_3$(0001)	MOCVD (Mo(CO)$_6$+DMS)	S-rich, 600–700 °C	R30°	7.5–8.5	This work
1L MoS$_2$	0.05/0.2°, 1050–1200 °C-annealed (air/O$_2$), (1×1)Al$_2$O$_3$(0001)	MOCVD (Mo(CO)$_6$+DMS)	600–700 °C	R0°	1.8–5.2	This work

C.3 GIXRD setups
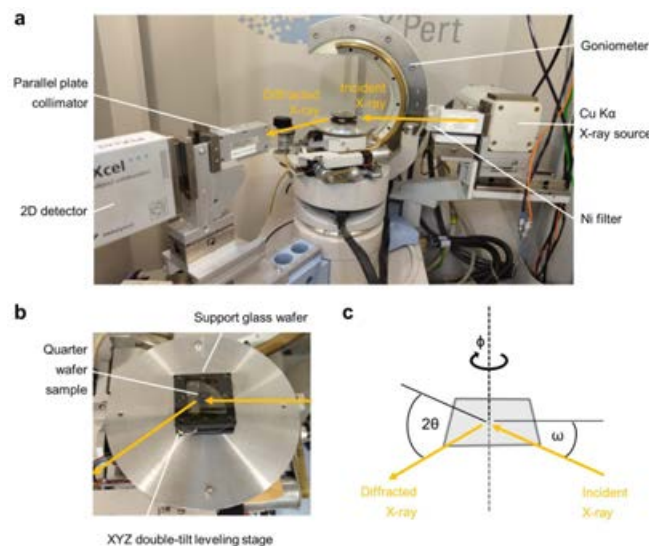
Figure C23 Laboratory diffractometer setup PANalytical X'PERT PRO MRD (ICN2). **(a)** Photo of the instrument located at the ICN2 diffraction facility. **(b)** Photo of the sample stage. **(c)** Schematic illustration of the in-plane $\omega - 2\theta$ diffraction geometry.
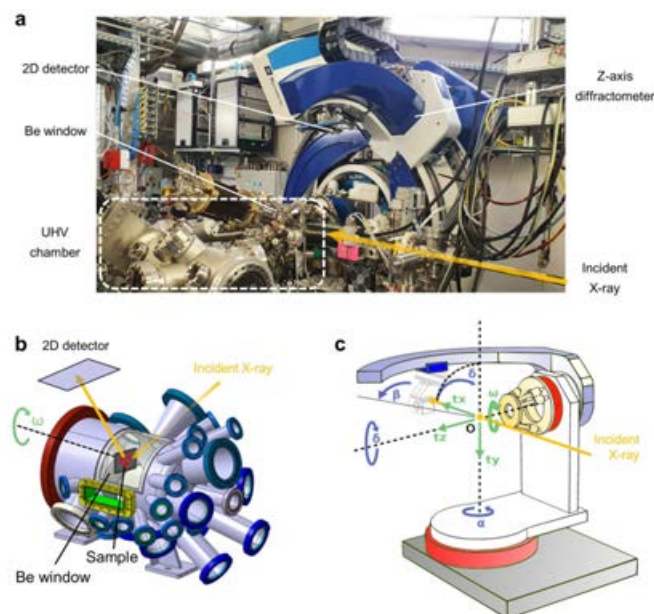
Figure C24 Synchrotron diffractometer setup at BM32 (ESRF, Grenoble). **(a)** Photo of the instrument in the INS2 hutch (Interface and Nanostructure and Surfaces). **(b)** Technical drawing of the UHV analysis chamber. **(c)** Schematic illustration of the z-axis diffractometer. Adapted from [663]. More information about the setup can be found online.

Appendix D

MoS$_2$ integration and transistor technology for flexible electronics

D.1 MoS$_2$ transfer

Wet transfer

First, the MoS$_2$ sample was blown with N$_2$ and a sacrificial polymer support layer (PMMA 950K A4, MicroChem, USA) was spin coated (3000 rpm, 60 s) and hard-baked on a hotplate (180 °C, 30 s). A blade was used to scratch away PMMA/MoS$_2$ around the edges of the substrate. The edge of the sample was dipped into 1 M NaOH(aq) solution (Sigma Aldrich, 137031) and moved in and out in a ∼45° angle to detach the PMMA/MoS$_2$ stack from the substrate. Then, the PMMA/MoS$_2$ sheet was subsequently transferred into two fresh water baths for 20 min. The PMMA/MoS$_2$ sheet was fished onto an arbitrary target substrate and put onto a hotplate for 10 min at 50 °C, and additional 10 min at 70 °C to dry, dewrinkle and promote adhesion of the transferred film. Finally, the PMMA/MoS$_2$/target substrate was immersed into a suitable solvent (e.g. acetone, Remover PG) at 50 °C for 1 h for dissolution of the PMMA support layer, transferred into isopropanol for washing off organic residuals (10 min), further rinsed with isopropanol from a spray bottle, and blow dried by N$_2$.
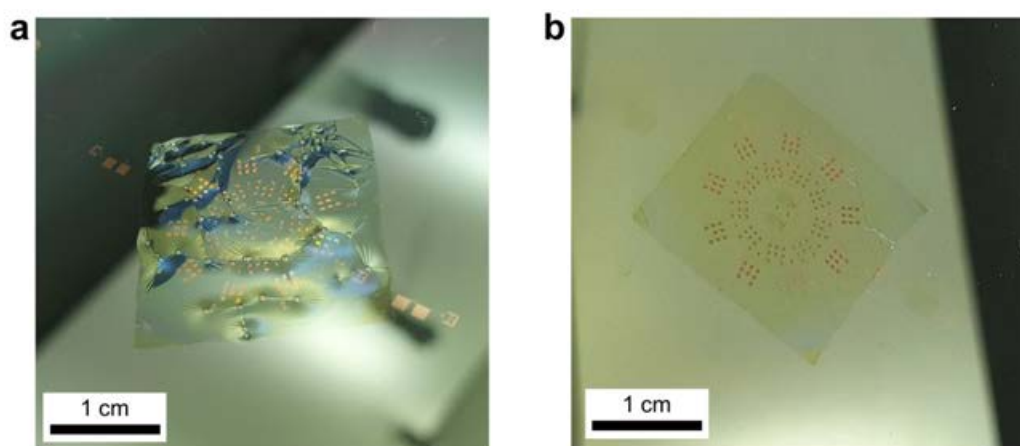

Figure D1 Non-optimized MoS$_2$ wet transfer. Photos of transferred PMMA/MoS$_2$ sheet **(a)** right after fishing with trapped water and bubbles underneath and wrinkle defects, and **(b)** after completed hotplate drying for layer adhesion. Although some wrinkles smooth out, some defects remain.

Thermal release tape transfer

The semi-dry thermal release tape (TRT) transfer process is schematically illustrated in the main text (Fig. 5.2). Further information and photos of each step can be found

in Fig. D2. Similarly to the wet transfer, the MoS$_2$ sample was blowed with N$_2$ and a sacrificial PMMA layer was spin coated (3000 rpm, 60 s) and hard-baked on a hotplate (180 °C, 30 s). Then, a blade was used to scratch away PMMA/MoS$_2$ around the border edges of the substrate to later facilitate water intercalation for MoS$_2$ detachment. Next, a TRT (REVALPHA 3195V, Nitto Denko, Japan) is precut with dimensions slightly exceeding the three side widths of the PMMA/MoS$_2$ region and the forth with an overlapping flap to facilitate later sheet removal. The sample was blowed with N$_2$ and the TRT was gently applied onto the PMMA/MoS$_2$ by evenly distributing pressure with a roller and removing potential air bubbles. A water droplet was placed on top with a pipet and covered with an overlapping polydimethlysiloxane sheet (PDMS, Gel-Pak, USA) that spreads out the droplet and acts as a compliant layer in the next step. The stack was placed into a pressing dye to apply uniaxial pressure. The pressure squeezes the water sideways to the edges of the layer stack where it intercalates at the MoS$_2$/substrate interface by capillary force [461]. The layer stack is unmounted from the dye, the PDMS sheet was removed, and the TRT/PMMA/MoS$_2$ stack was slowly detached ($\sim$1 mm s^{-1}) from the growth substrate with a tweezer pulling from the TRT flap. Residual droplets from the water-repelling MoS$_2$ side were blow-dried with N$_2$ and the TRT/PMMA/MoS$_2$ was gently transferred onto the target substrate, making this step essentially a dry process. The color contrast change seen through the semi-transparent thermal tape verified that the MoS$_2$ film was well-adhered. Gently pulling with a cotton bud may assist the adhesion process in case of trapped air bubbles. The sample was then placed onto a hotplate and ramped to 155 °C at $\sim$7 °C min^{-1} to enhance MoS$_2$/target substrate adhesion during ramping, the TRT was peeled off from the PMMA/MoS$_2$/target substrate when the TRT lost its adhesion strength at the release point at around 155 °C [291]. Then, the protective PMMA layer was dissolved at 50 °C (1 h) in a suitable solvent (e.g. acetone, Remover PG, see section 5.1.2). Finally, the sample was washed from organic residuals in isopropanol (10 min), further rinsed with isopropanol from a spray bottle, and blow dried by N$_2$.
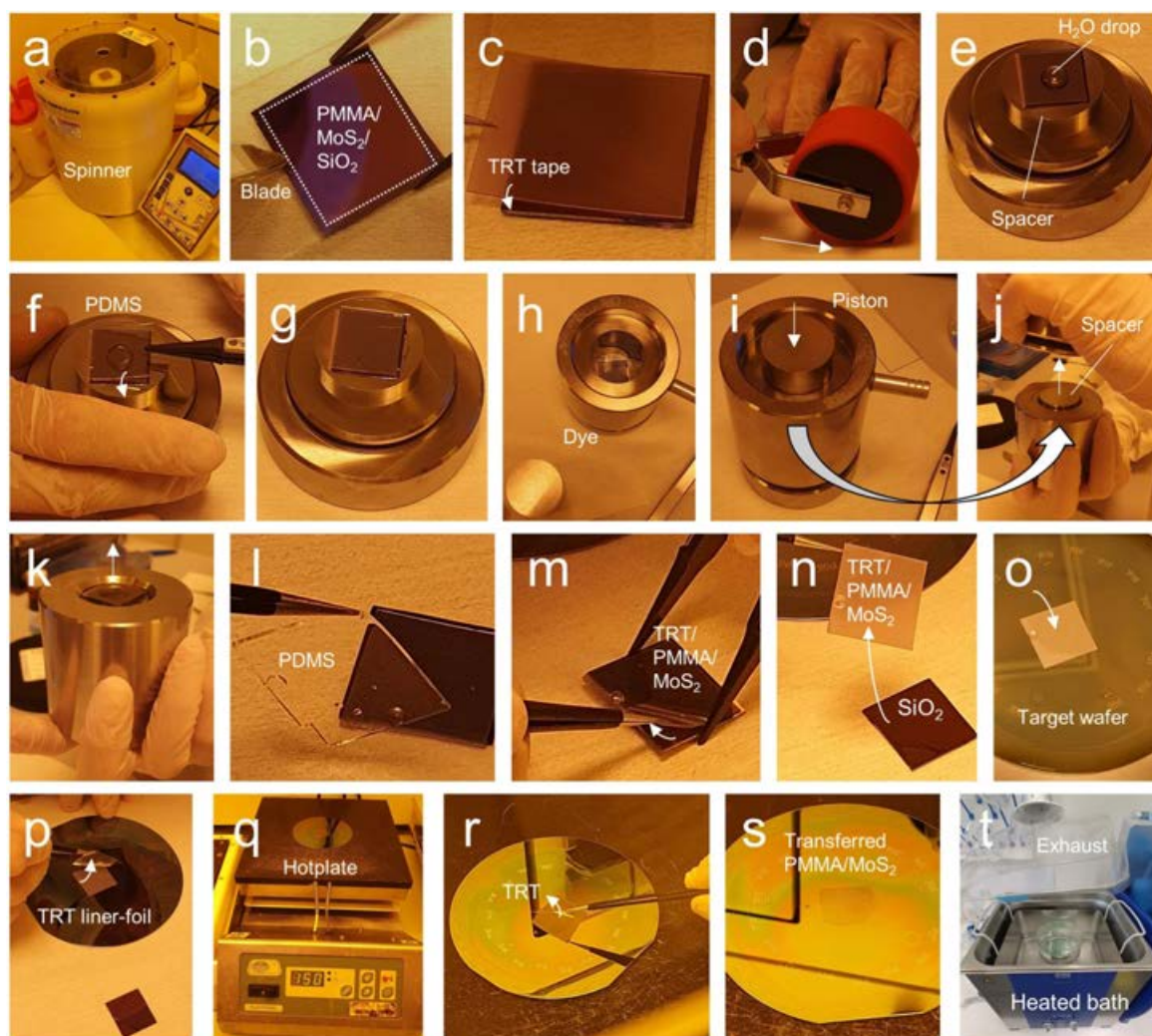
Figure D2 MoS$_2$ TRT transfer procedure. **(a)** Spin PMMA onto the as-grown MoS$_2$. **(b)** Scratch around 2 mm of PMMA/MoS$_2$ from the edges. **(c-d)** Apply thermal release tape (TRT) and ensure even adhesion with roller or by softly stroking with a cotton bud. **(e)** Put sample onto pressing chamber and place a droplet of water on top of the TRT stack. **(f-g)** Place PDMS onto the stack. **(h)** Assemble the rest of the compression chamber and **(i)** allow gravity to compress the piston. **(j-k)** Disassemble the compression chamber. **(l)** Remove PDMS from the stack. **(m-n)** Detach TRT/PMMA/MoS$_2$ stack from the growth substrate. **(o)** Apply stack to target sample and allow to slowly adhere. **(p)** Remove film from second side of TRT. **(q)** Place sample on hotplate at room temperature and ramp at $\sim$10 °C min^{-1} to 155 °C. **(r-s)** Once the TRT releases from the surface, peel it away. **(t)** Remove PMMA using Remover PG at 50 °C (covered beaker under fume exhaust).
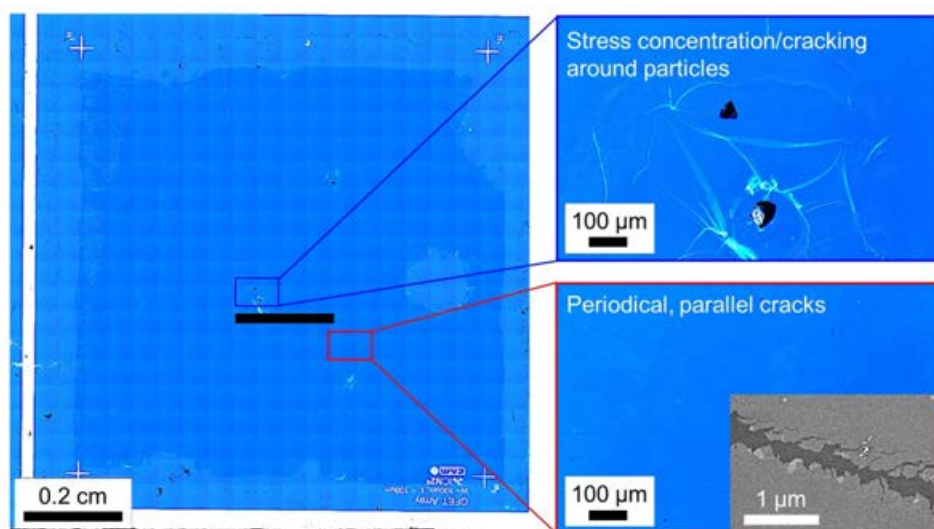
Figure D3 Non-optimized MoS$_2$ transfer by TRT method. The microscope image shows sheet cracking in regions around particles (blue frame) that were included underneath the TRT, and regions with fracture patterns of parallel cracks due to excessive tensile strain (red frame), further magnified by the SEM image inset.

D.2   Graphene growth and transfer

Chemical vapor deposition

Chemical vapor deposition (CVD) of single-layer graphene used in this work was performed in the reactor shown in Fig. D4(a-b), following an established growth procedure from methane precursor in an Ar/H$_2$ gas mixture catalyzed on Cu surface, which is illustrated in Fig. D4c.

As growth substrate a Cu foil (Graphene Platform Corp., Tokyio , Japan) with purity 98.5 %, sheet size of $8{\times}4\,\text{cm}^2$, and thickness of 0.035 mm was used. Prior to growth, the Cu foil was electropolished for 5 min at a fixed current density of $62\,\text{mA}\,\text{cm}^{-2}$ in a solution of 1 L distilled water, 0.5 L phosphoric acid H$_3$PO$_4$, 0.5 L of ethanol, 0.1 L isopropanol, and 10 g urea. The Cu foil was then placed onto a quartz frame inside the inner quartz tube (length: 330 mm, diameter: 53 mm), and subsequently loaded into the horizontal quartz tube reactor (length: 1600 mm, diameter: 60 mm) heated by a three-zone furnace (Fig. D4). The growth procedure includes a thermal annealing of the Cu foil for 80 min at 1050 °C under 400 sccm Ar flow at 100 mbar pressure, controlled by the needle valve bypass. Then, for the 15 min graphene growth step, a gas mixture of 1000 sccm of Ar, 20 sccm of H$_2$ and 0.7 sccm of methane is injected at

26 mbar pressure. Finally, the sample is quenched down to room temperature under a flow of 400 sccm of Ar by removing the tube from the heating zone with a swivel arm.

After the growth, graphene is inspected by Raman spectroscopy, showing the characteristic G and 2D modes, as shown in Fig. D4d. The absence of a D peak proves good quality. The SEM images in Fig. D4e reveal the polycrystalline structure of Cu foil with different grain orientations and grain sizes of the order of 50 to 200 µm, on which coalesced single-layer graphene with domain sizes on the order of typically 10 to 20 µm has grown. The AFM image in Fig. D4f reveals graphene grain boundaries and patterns of roughened, corrugated sheet morphology, which is caused by strain relaxation on the Cu crystal surface [664].
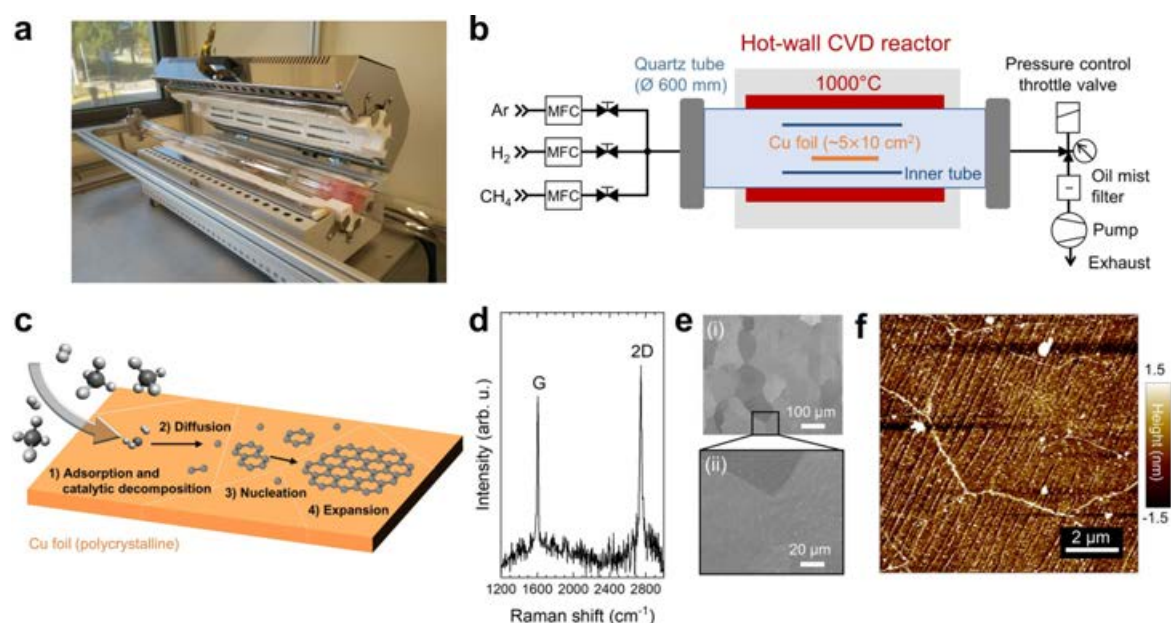

Figure D4 Chemical vapor deposition (CVD) of graphene on Cu foil. **(a)** Photo of CVD reactor with designated components. The inset shows the Cu foil with typical dimensions. **(b)** Schematic illustration of the reactor with gas-injection system using mass flow controllers (MFCs). **(c)** Schematic illustration of catalytic graphene growth on polycrystalline Cu from methane precursor with designated growth steps. **(d)** Raman spectrum of graphene with characteristic G and 2D modes. **(e)** SEM images for magnifications of (i) 500×, revealing the polycrystalline grain structure of the Cu foil, and (ii) 2500×, showing the domain structure of coalesced, polycrystalline single-layer graphene. **(f)** AFM image revealing graphene grain boundary and sheet morphology.

PMMA-assisted graphene transfer

To transfer the graphene film from Cu foil to an arbitrary target wafer a conventional polymer-assisted wet transfer was used, as illustrated in Fig. D5. First, poly(methyl methacrylate) (PMMA A4 950K, MicroChem Corp., USA) was spun onto the graphene/Cu stack at 3000 rpm for 30 s and dried at room temperature for 12 h. Then, graphene grown on the backside of the Cu foil was removed by ICP-RIE (PlasmaPro Cobra 100, Oxford Instruments, UK) in oxygen plasma (O_2: 40 sccm, Ar: 40 sccm, 40 W, 6 min at 20 °C), and the sample was cut into pieces of proper target size. Afterwards, an etching solution was prepared by dissolving 20.27 g $FeCl_3$ in 330 g H_2O and adding 120 mL HCl, in which the PMMA/graphene/Cu sample was kept floating for at least 6 h to dissolve the Cu substrate. Subsequently, the PMMA/graphene was fished with a SiO_2 wafer and transferred onto two cleaning baths of deionized water for 1 h each, before being transferred onto the target wafer. The PMMA/graphene/wafer was then dried on a hotplate at 40 °C for 2 h, and then thermally annealed in ultra-high vacuum (6 °C min^{-1} ramp-up, 180 °C dwell for 1 min, 6 °C min^{-1} cool-down). Finally, the stack was immersed in acetone (50 °C, 20 min) for PMMA removal, rinsed with fresh acetone, put into a bath of isopropanol for 5 min, rinsed with isopropanol, and blow-dried with N_2.
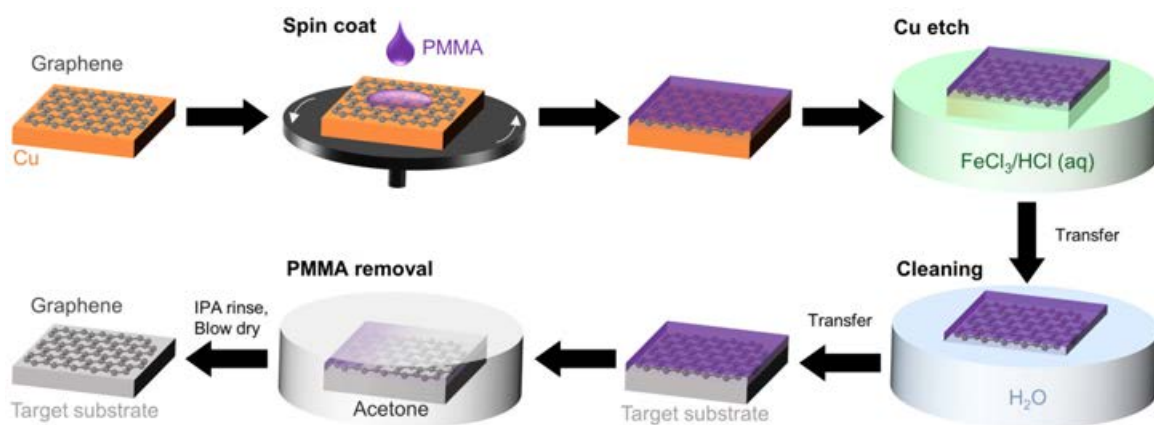

Figure D5 Graphene transfer. Schematic of the sequential steps of the polymer-assisted wet transfer from Cu foil to an arbitrary, target substrate.
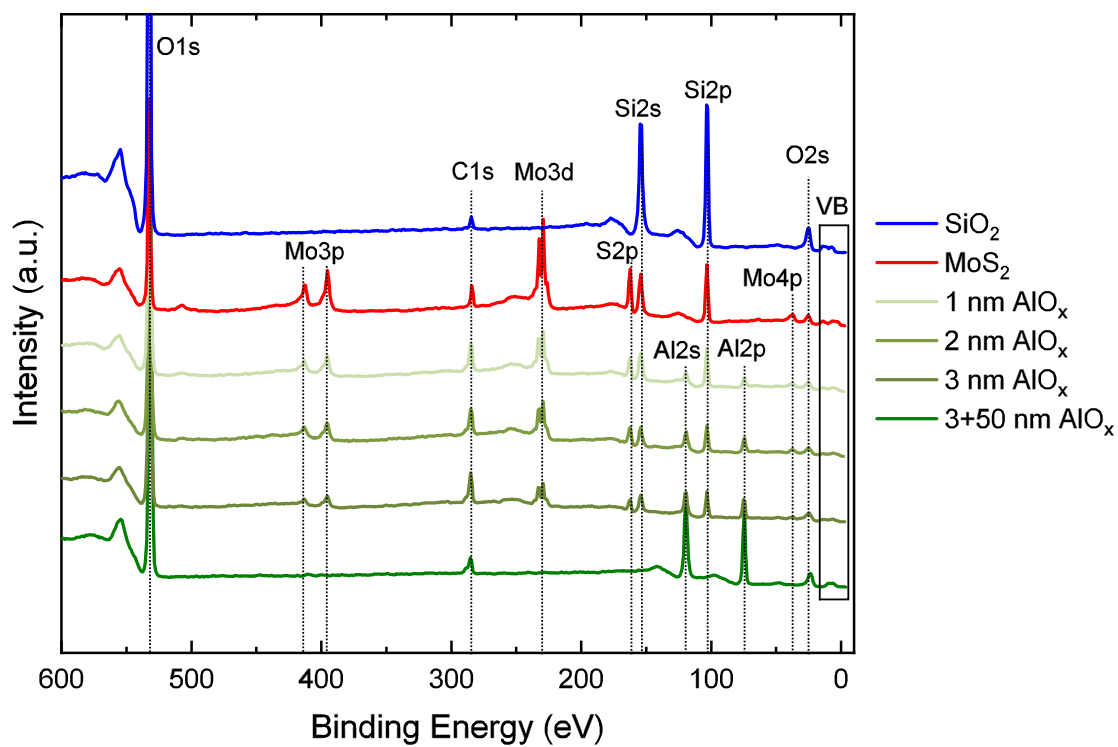
D.3 MoS$_2$ dielectric integration and encapsulation

Figure D6 XPS overview spectra of SiO$_2$ substrate and MoS$_2$/SiO$_2$, after capping with 1, 2, 3 nm AlO$_x$ seed layer and after 50 nm ALD encapsulation.
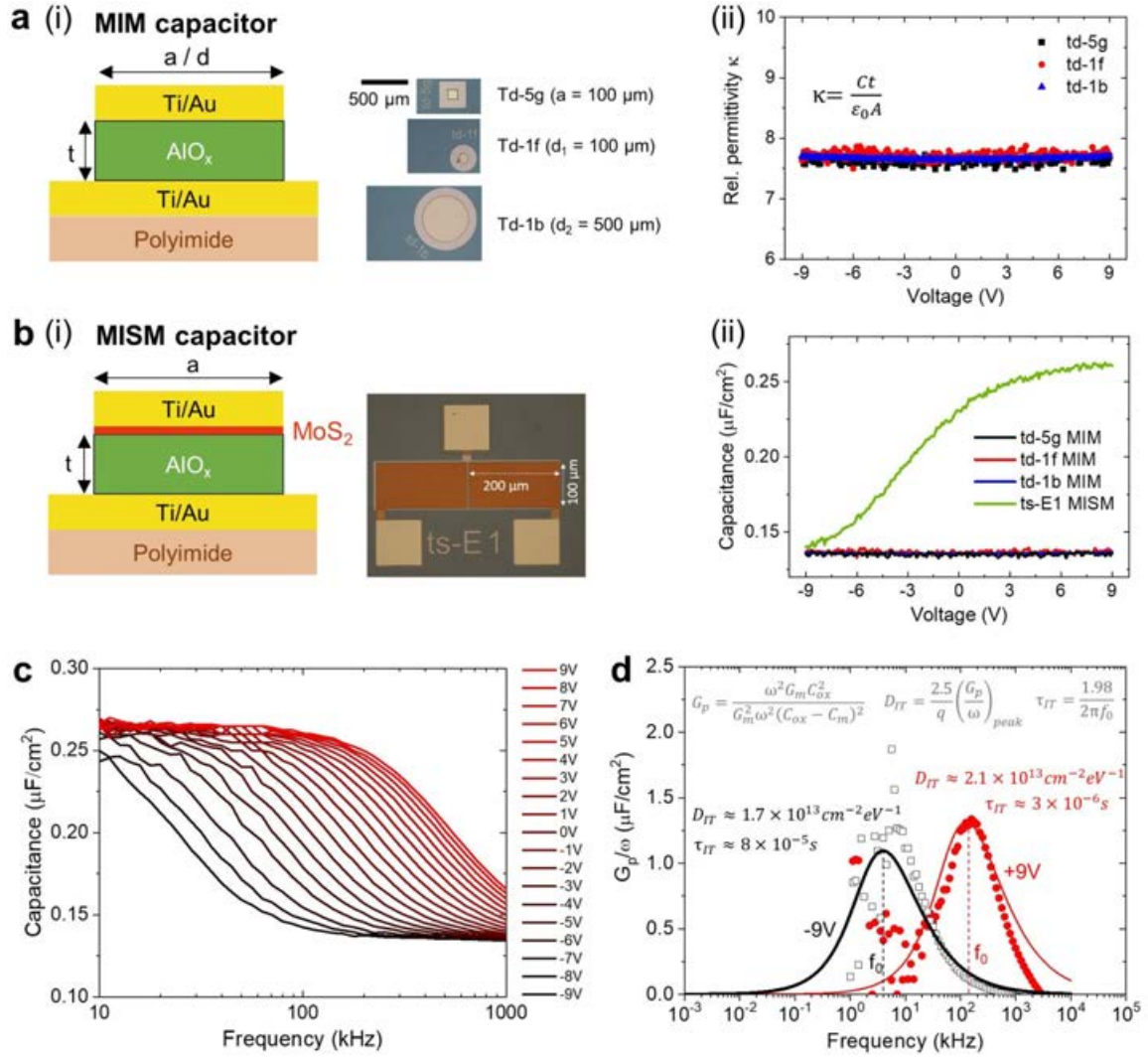
Figure D7 Metal-insulator-metal (MIM) and metal-insulator-semiconductor-metal (MISM) capacitor characterization. **(a)** MIM test structure. (i) Schematic illustration of layer stack cross-section and top-view optical microscopy images. Oxide thickness t, capacitor diameter d (round design) and capacitor side length a (square design) are indicated. (ii) C-V measurement (at $100\,\mathrm{kHz}$) translated into AlO$_x$ dielectric constant κ as function of voltage, using the indicated formula. **(b)** MISM test structure. (i) Schematic illustration of layer stack cross-section and top-view optical microscopy images. MoS$_2$ was MOCVD-grown in the Yonsei reactor. (ii) C-V measurement. **(c)** Multi-frequency C-V measurement of MISM structure for analysis of MoS$_2$/AlO$_x$ interface. **(d)** Determination of trap density D_{IT} and time constant τ_{IT} via conductance method [289, 286, 259].
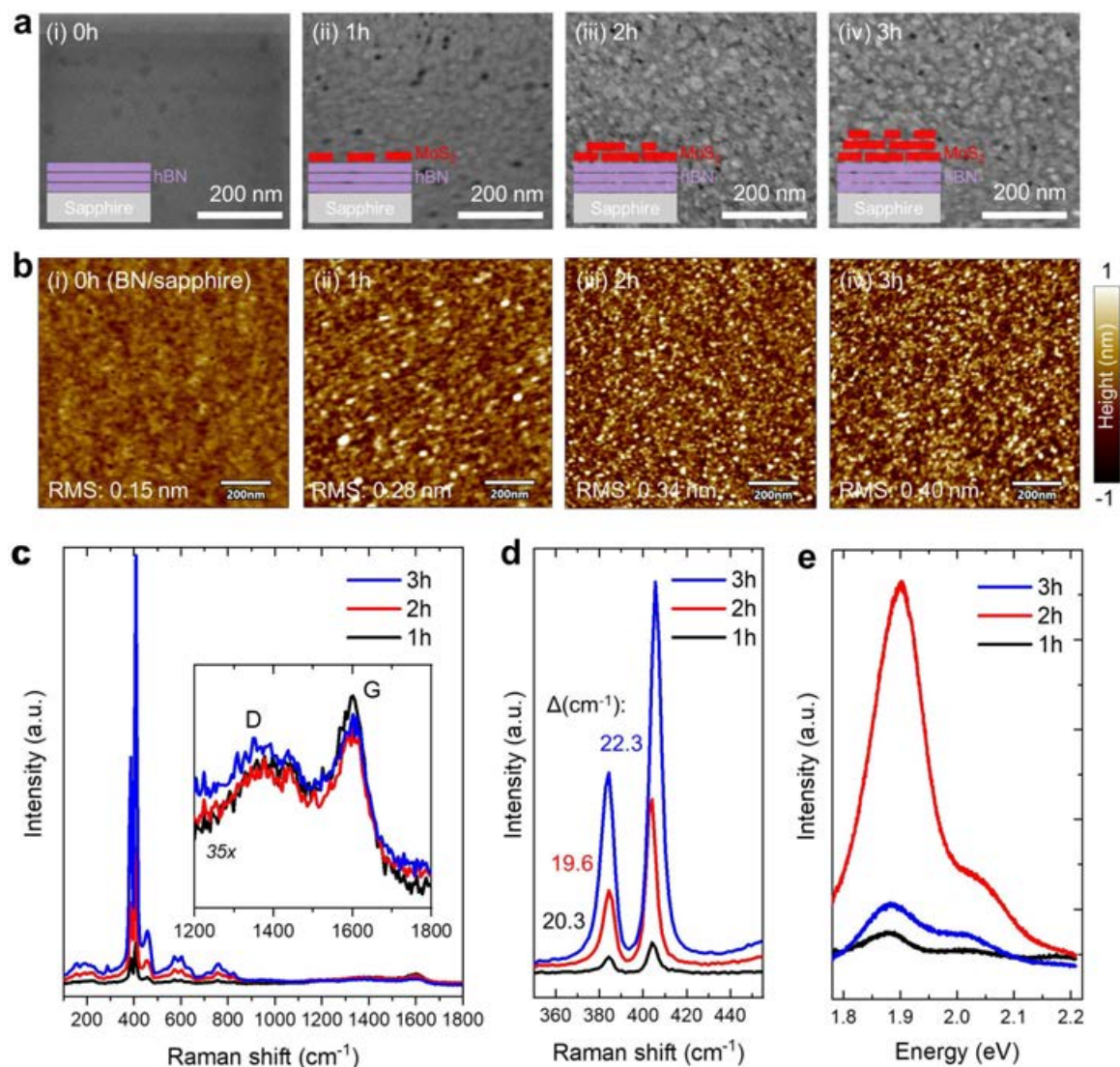
Figure D8 MoS$_2$ growth onto hBN/sapphire in ICN2 reactor at 700 °C. **(a)** SEM images, and **(b)** AFM images with extracted RMS roughness values of (i) hBN/sapphire growth substrate, and MoS$_2$ thin films for growth times of (ii) 1h, (iii), 2h, and (iii) 3h, respectively. Corresponding **(c)** Raman overview spectra with inset of carbon D and G band region, **(d)** magnified MoS$_2$ band region, and **(e)** PL spectra for the different growth times. The hBN/sapphire samples were obtained by a previously reported 2″ wafer-scale MOCVD process [575].
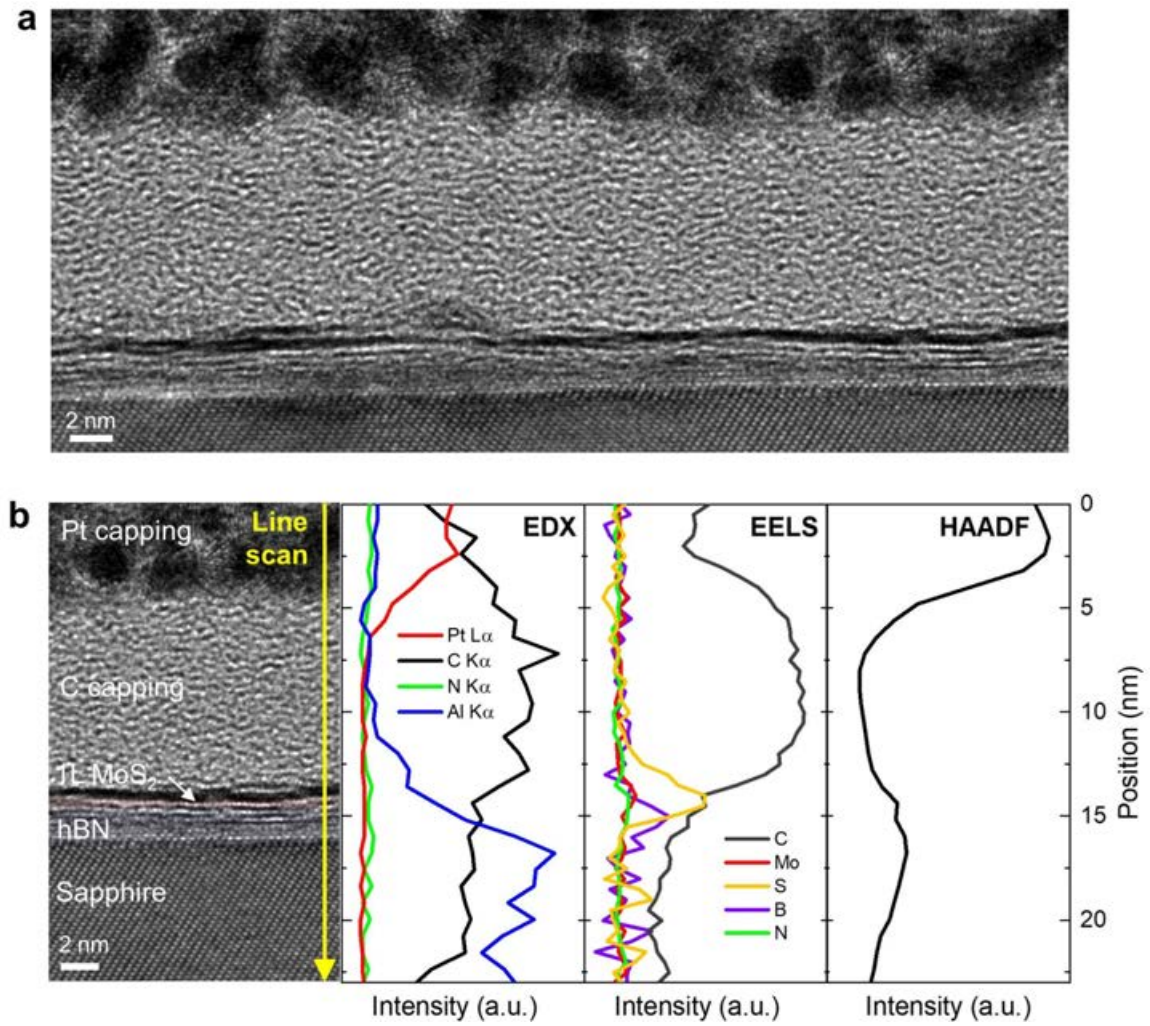
Figure D9 1L MoS$_2$ thin film grown onto 3L hBN/sapphire substrate at 700 °C (1h). **(a)** Cross-sectional TEM image of the van der Waals heterostructure capped by a C/Pt-protection layer. **(b)** Chemical analysis of heterostructure by EDX, EELS, and HAADF line scans. The hBN/sapphire samples were obtained by a 2" wafer-scale previously reported MOCVD process [575].

D.4 MoS$_2$-FET technology

MoS$_2$-FET fabrication protocols

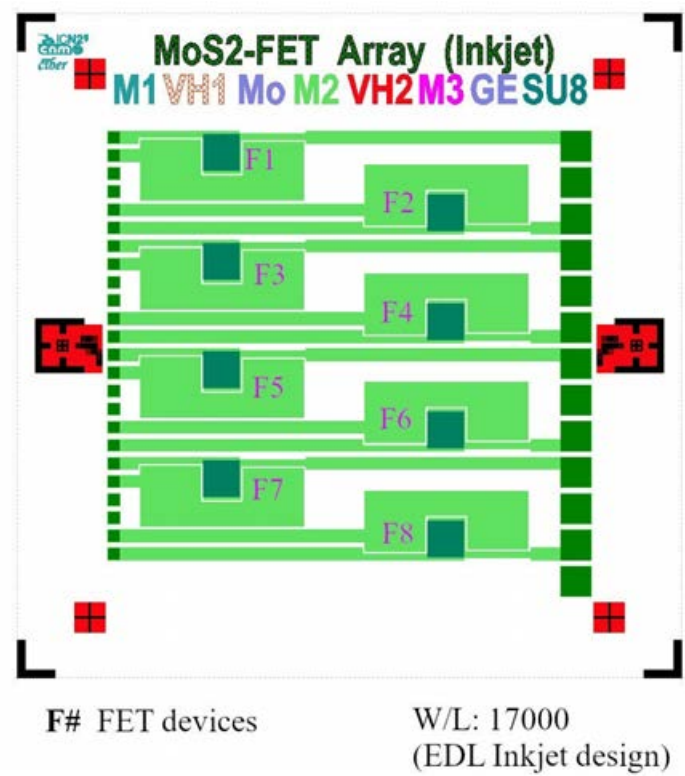### Liquid-gated MoS$_2$-FETs

Figure D10 Liquid-gated MoS$_2$-FET mask design.

Table D1 Fabrication protocol for liquid-gated MoS$_2$-FETs on rigid SiO$_2$ chips produced in CNM and ICN2 cleanrooms.

#	Fabrication step	Protocol
1	**MoS$_2$ transfer (unless as-grown films used)**	<u>Transfer</u> see section 5.1 <u>Vacuum annealing for layer adhesion</u> 180°C, 1', $<1 \times 10^{-7}$ mbar <u>PMMA removal</u> Remover PG, 50°C, 15'

2	**MoS$_2$ definition**	<u>PMMA protection for clean removal after etch</u> Spin PMMA A4 950K ($\sim$0.22 µm), 3000 rpm Bake on hotplate, 180ºC, 30" <u>Photolithography</u> Spin-coat HiPR 6512 (1.2 µm) Developing in OPD-4262, 50" <u>MoS$_2$ channel etch</u> ICP-RIE, O$_2$ plasma Note: Etch progress monitored by interferometer, oscillation flatlines when SiO$_2$ is reached <u>PMMA/HiPR 6512 resist removal</u> Remover PG, 50ºC, 10' <u>Vacuum annealing for residue removal</u> 350°C, 2h, $<1 \times 10^{-7}$ mbar
3	**Metallization of source-drain, side gate, metal tracks/pads**	<u>Photolithography</u> Spin coat invertible resist AZ 5214E (-1.7 µm) Developing in AZ 726 MIF <u>Metallization</u> E-beam evaporation: Ti/Au (5/35 nm), $<5 \times 10^{-7}$ mbar Lift-off in acetone <u>Vacuum annealing</u> 250°C, 2h, $<1 \times 10^{-7}$ mbar
4	**Ionic liquid/gel drop-casting**	Drop-cast ionic liquid

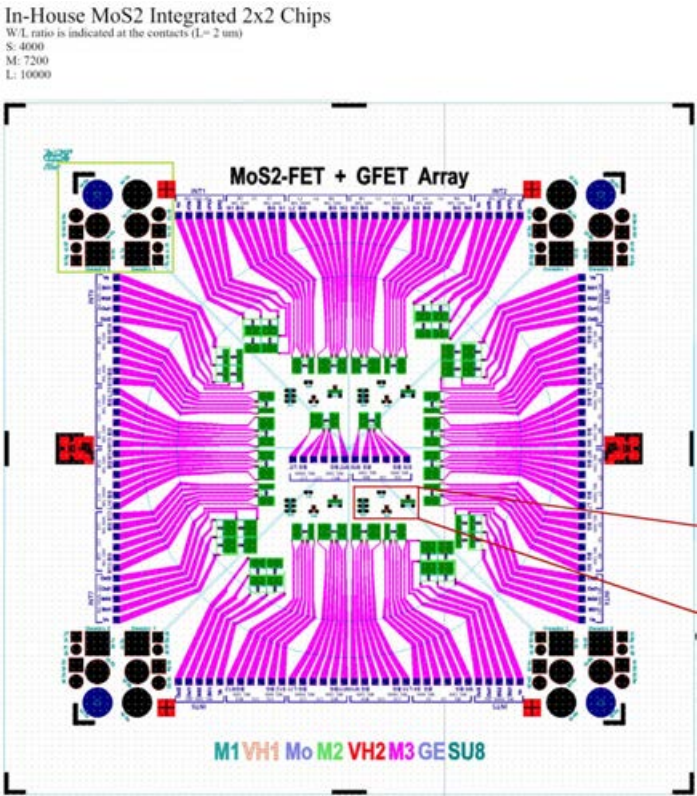**Rigid AlO$_x$-encapsulated MoS$_2$-FETs**

Figure D11 Rigid AlO$_x$-encapsulated MoS$_2$-FET mask design

Table D2 Fabrication protocol for rigid AlO$_x$-encapsulated MoS$_2$-FETs produced in CNM and ICN2 cleanrooms.

#	Fabrication step	Protocol
1	Gate Metal	Photolithography
		Spin coat invertible resist AZ 5214E ($-1.7\,\mu m$)
		Developing in AZ 726 MIF
		Metallization
		E-beam evaporation: Ti/Au (3/30nm), $< 5 \times 10^{-7}$ mbar
		Lift-off in acetone
2	Gate dielectric +Via-hole 1 etch	Al$_2$O$_3$ seed layer deposition + self-oxidation
		Al deposition: 3 x 1 nm, $< 5 \times 10^{-7}$ mbar
		Unload, let sample oxidize in ambient, 60'

Al$_2$O$_3$ oxide dielectric deposition
ALD of Al$_2$O$_3$ (50 nm)

Photolithography
Spin-coat HiPR 6512 (1.2 µm)
Developing in OPD-4262, 50"

Via-hole 1 etch
DRIE, most of Al$_2$O$_3$ layer (40 nm), 1000W, C$_4$F$_8$/CH$_4$/He
Finish by wet etch with TecniEtch Al80, 45°C
Verify etch completion by ellipsometry

3	**MoS$_2$ transfer**	Surface preparation of target wafer

Surface preparation of target wafer
UVO treatment, 3'

Transfer
Thermal release tape transfer, see section D.1

Vacuum annealing for layer adhesion
180°C, 1', $<1 \times 10^{-7}$ mbar

PMMA removal
Remover PG, 50°C, 15'

4	**MoS$_2$ definition**	PMMA protection for clean removal after etch

PMMA protection for clean removal after etch
Spin PMMA A4 950K ($\sim$0.22 µm), 3000 rpm
Bake on hotplate, 180ºC, 30"

Photolithography
Spin-coat HiPR 6512 (1.2 µm)
Developing in OPD-4262, 50"

MoS$_2$ channel etch
ICP-RIE, O$_2$ plasma, 220W
Note: Etch progress monitored by interferometer with laser
spot placed onto Al$_2$O$_3$ island (flatlined curve when etch complete)

PMMA/HiPR 6512 resist removal
Remover PG. 50ºC, 10'

Vacuum annealing for residue removal
250°C, 2h, $<1 \times 10^{-7}$ mbar

5	**MoS$_2$ contacts**	Photolithography Spin coat invertible resist AZ 5214E ($-1.7\,\mu$m) Developing in AZ 726 MIF, 40" Metallization E-beam evaporation: Ti/Au (5/35 nm), $<5 \times 10^{-7}$ mbar Lift-off in acetone Vacuum annealing 250°C, 2h, $<1 \times 10^{-7}$ mbar
6	**MoS$_2$ encapsulation + Via-hole 2**	Al$_2$O$_3$ seed layer deposition + self oxidation Al deposition: 3 x 1 nm @$<$ 5*10–7 mbar Unload, let sample oxidize in ambient. 60' Al$_2$O$_3$ oxide encapsulation ALD of Al$_2$O$_3$ (50 nm) Photolithography Spin-coat HiPR 6512 (1.2 μm) Developing in OPD-4262 Via-hole 2 etch DRIE, most of Al$_2$O$_3$ layer (40 nm) 1000W, C$_4$F$_8$/CH$_4$/He, 15/10/10 sccm Finish by wet etch with TecniEtch Al80, 45°C
7	**Metal tracks**	Photolithography Spin coat invertible resist AZ 5214E ($-1.7\,\mu$m) Developing in AZ 726 MIF Metallization E-beam evaporation: Ti/Au (10/100nm), $<5 \times 10^{-7}$ mbar Lift-off in acetone

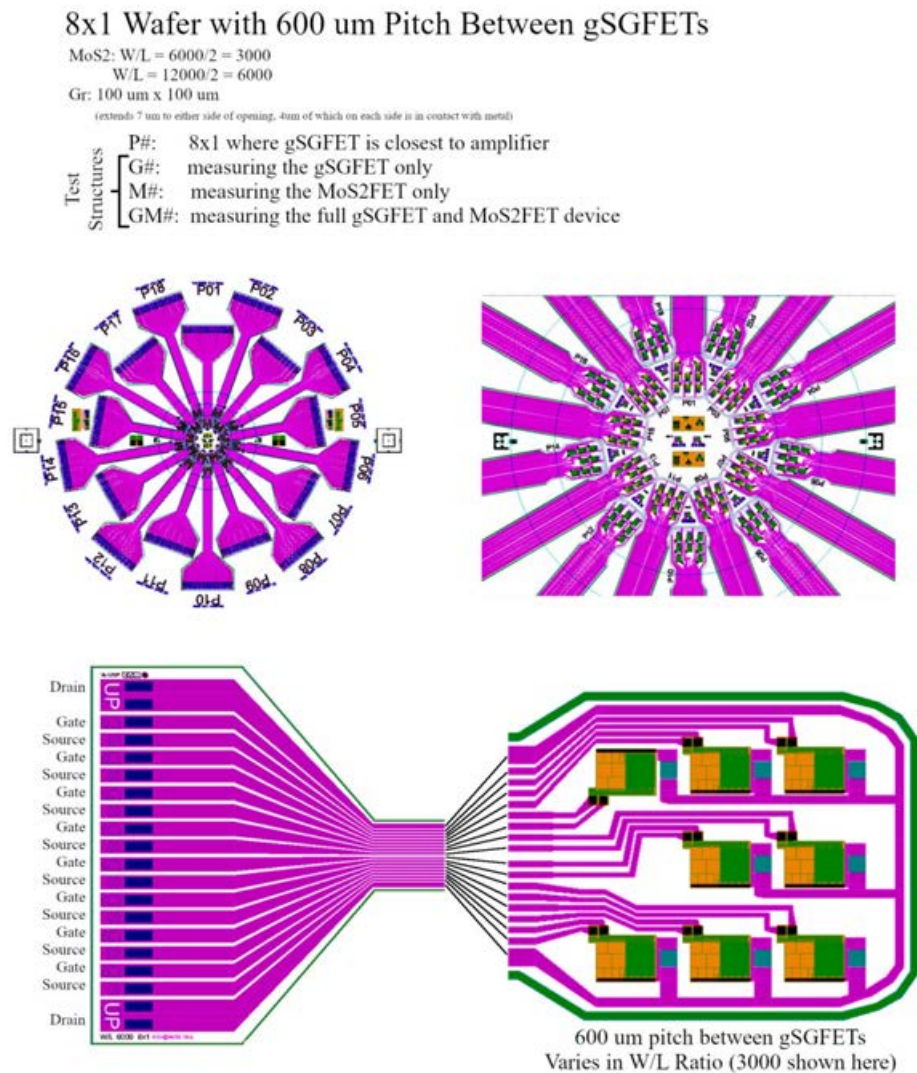## MoS$_2$-FET/Gr-SGFET flex hybrid probes

Figure D12 MoS$_2$-FET/Gr-SGFET flex probe mask design

Table D3 Fabrication protocol for MoS$_2$/Gr hybrid ECoG probes produced in CNM and ICN2 cleanrooms.

#	Fabrication step	Protocol
1	**Flexible polyimide substrate**	<u>Wafer clean</u>
		Dehydrate 4 inch SiO2/Si support wafer, 200°C
		Surface cleaning, O$_2$ plasma
		<u>Polyimide coating</u>

Spin-coat PI-2611 (7.5 μm)

Soft-bake
Dwell 120°C, 2'

Hard-bake
Cure at 350°C, 60'

2	**Gate Metal**	<u>Photolithography</u> Spin coat resist AZ 5214E (−1.7 μm) Developing with AZ 726 MIF <u>Metallization</u> E-beam evaporation: Ti/Au (3/30nm), $< 5 \times 10^{-7}$ mbar Lift-off in acetone
3	**Gate dielectric +Via-hole 1 etch**	<u>Al$_2$O$_3$ seed layer deposition + self-oxidation</u> Al deposition: 3 x 1 nm, $< 5 \times 10^{-7}$ mbar Unload, let sample oxidize in ambient, 60' <u>Al$_2$O$_3$ oxide dielectric deposition</u> ALD of Al$_2$O$_3$ (50 nm) <u>Photolithography</u> Spin-coat HiPR 6512 resist (1.2 μm) Developing in OPD-4262 <u>Via-hole 1 etch</u> DRIE, most of Al$_2$O$_3$ layer (40 nm) Verify etch completion by ellipsometry Finish by wet etch with TecniEtch Al80
4	**MoS$_2$ transfer**	<u>Surface preparation of target wafer</u> UVO treatment, 3' <u>Transfer</u> Thermal release tape transfer, see section D.1 <u>Vacuum annealing for layer adhesion</u> 180°C, $<1 \times 10^{-7}$ mbar <u>PMMA removal</u> Remover PG, 50°C, 15'

5	**MoS$_2$ definition**	PMMA protection for clean removal after etch
		Spin PMMA A4 950K ($\sim$0.22 μm)
		Bake on hotplate, 180ºC, 30"
		Photolithography
		Spin-coat HiPR 6512 (1.2 μm)
		Developing in OPD-4262, 50"
		MoS$_2$ channel etch
		ICP-RIE O$_2$ plasma
		PMMA/HiPR 6512 resist removal
		Remover PG, 50ºC, 10'
		Vacuum annealing for residue removal
		250°C, 2h, $<1 \times 10^{-7}$ mbar
6	**MoS$_2$ contacts**	Photolithography
		Spin coat invertible resist AZ 5214E (-1.7 μm)
		Developing in AZ 726 MIF
		Metallization
		E-beam evaporation: Ti/Au (5/35 nm), $<5 \times 10^{-7}$ mbar
		Lift-off in acetone
		Vacuum annealing
		250°C, 2h, $<1 \times 10^{-7}$ mbar
7	**MoS$_2$ encapsulation + Via-hole 2**	Al$_2$O$_3$ seed layer deposition + self oxidation
		Al deposition: 3 x 1 nm @$<$ 5*10–7 mbar
		Unload, let sample oxidize in ambient, 60'
		Al$_2$O$_3$ oxide encapsulation
		ALD of Al$_2$O$_3$ (50 nm)
		Photolithography
		Spin-coat HiPR 6512 (1.2 μm)
		Developing in OPD-4262, 50"
		Via-hole 2 etch
		DRIE, most of Al$_2$O$_3$ layer (40 nm)

Finish by wet etch with TecniEtch Al80, 45°C, 3'

8	**Metal tracks/ Graphene bottom-contacts**	Photolithography
		Spin coat invertible resist AZ 5214E ($-1.7\,\mu$m)
		Developing in AZ 726 MIF
		Metallization
		E-beam evaporation: Ti/Au (10/100nm), $<5 \times 10^{-7}$ mbar
		Lift-off in acetone

9	**Graphene transfer**	Surface preparation of target wafer
		UVO-cleaning, 3'
		PMMA-assisted transfer
		see Fig. D5
		Vacuum annealing for adhesion
		180°C, 1', $<1 \times 10^{-7}$ mbar
		PMMA removal
		Acetone, 50°C, 20'

#	**Graphene definition**	Photolithography
		Spin-coat HiPR 6512 (1.2 μm)
		Developing in OPD-4262, 50"
		Graphene etch
		ICP-RIE, O$_2$ plasma
		HiPR 6512 resist removal
		Acetone, 50°C, 20'

#	**Graphene top-contacts**	Photolithography
		Spin coat invertible resist AZ 5214E ($-1.7\,\mu$m)
		Developing in AZ 726 MIF, 40"
		Metallization
		E-beam evaporation: Ni/Au (20/200nm), $<5 \times 10^{-7}$ mbar
		Lift-off in acetone

#	**Probe passivation**	Photolithography
		Spin-coat SU-8 (5 μm)

<u>Pre-exposure bake on hotplate</u>
65°C, 3'
Ramp to 95ºC, 5°C/min
Bake, 95°C, 8'

<u>Post-exposure bake on hotplate</u>
65ºC, 2'
Ramp to 95ºC, 5°C/min
Bake, 95°C, 3'
Develop in mr-Dev 600, 50"

<u>Hard-bake on hotplate</u>
120°C, 30', N$_2$ atmosphere

#	**Probe definition**	<u>Photolithography</u> Spin-coat AZ 10XT (16 µm) Develop in AZ 400K:H20 (1:3 ratio), 3' <u>Probe structure etch</u> Deep reactive ion etching, 1200W Remove photoresist, IPA, 5'
#	**Probe removal**	Peel-off probes from rigid carrier wafer

Microfabrication chemicals and equipment lists

Table D4 Microfabrication chemicals list.

Description	Name	Supplier
Polyimide (flexible substrate)	PI-2611	HD MicroSystems
SU-8 epoxy (passivation)	SU-8 2005	MicroChem Corp.
Positive Photoresist	HiPR 6512	Fujifilm
Invertible Photoresist (for high res)	AZ 5214E	MicroChemicals GmbH
Thick photoresist (for high res)	AZ10XT	MicroChemicals GmbH
Developer	AZ 726 MIF	MicroChemicals GmbH
SU-8 Developer	Mr-DEV 600	Micro resist technology GmbH
Developer	AZ 400K	MicroChemicals GmbH
Polymer support layer (transfers)	PMMA A4 950 K	MicroChem Corp.
Positive Photoresist Developer	OPD 4262	Fujifilm
Photoresist stripper	MicroStrip 2001	Fujifilm
Aluminum ALD-precursor	Trimethylaluminum (663301-25G)	Sigma-Aldrich
NMP-based solvent stripper	Remover PG	Kayaku Advanced Materials
Al etchant (for Al$_2$O$_3$ etch)	TecniEtch Al80	MicroChemicals GmbH

Table D5 Microfabrication equipment list.

Description	Name/Model	Manufacturer	Location
Oven for dehydration	UT6060	Heraeus	CNM
Oven for PI hard-bake	N 67	Ovenvan	CNM
Spin coater	WS-650Mz-23NPPB	Laurell Technologies	ICN2
Spin coater	Delta 20 (AZ/HiPR)	Karl Süss	CNM
Spin coater	Delta 80 (for SU-8)	Karl Süss	CNM
Ultra-sonic bath	Elmasonic P 180 H	Elma Schmidbauer GmbH	ICN2
Atomic layer deposition (ALD)	Savannah S100	Cambridge nanoTech Inc.	ICN2
Photolithography Mask aligner	MA6 & MA/BA6	Karl Süss	CNM
Metallization (e-beam evaporator)	ATC-8E Orion	AJA International Inc.	ICN2
Metallization (e-beam evaporator)	UNIVEX 450B	Oerlikon / Leybold	CNM
Oxygen plasma asher	Gigabatch 360M	PVA TePla AG	CNM
UVO-cleaner	Model-30-220	Jelight	ICN2
Inductively-coupled reactive-ion etching	PlasmaPro Cobra 100	Oxford Instruments	ICN2
Deep reactive ion etching (AlOx etch)	SI 500 I	Sentech	CNM
Deep reactive ion etching (probe/Gr etch)	AMS 110 DE	Alcatel	CNM
Annealing oven (vacuum anneal)	Home-made vacuum oven equipped with Turbo HiPace 300 and 5 inch hotplate	Pfeiffer Vacuum	ICN2

MoS$_2$-FET device analysis
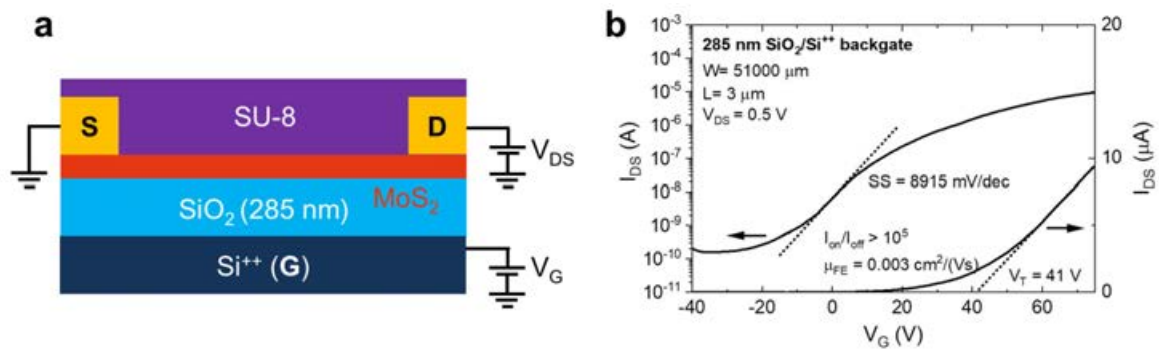
Figure D13 SiO$_2$-backgated MoS$_2$-FET. **(a)** Schematic of FET architecture using the 285 nm dry thermal SiO$_2$ with highly p-doped Si++ as back-gate. **(b)** Transfer curve.
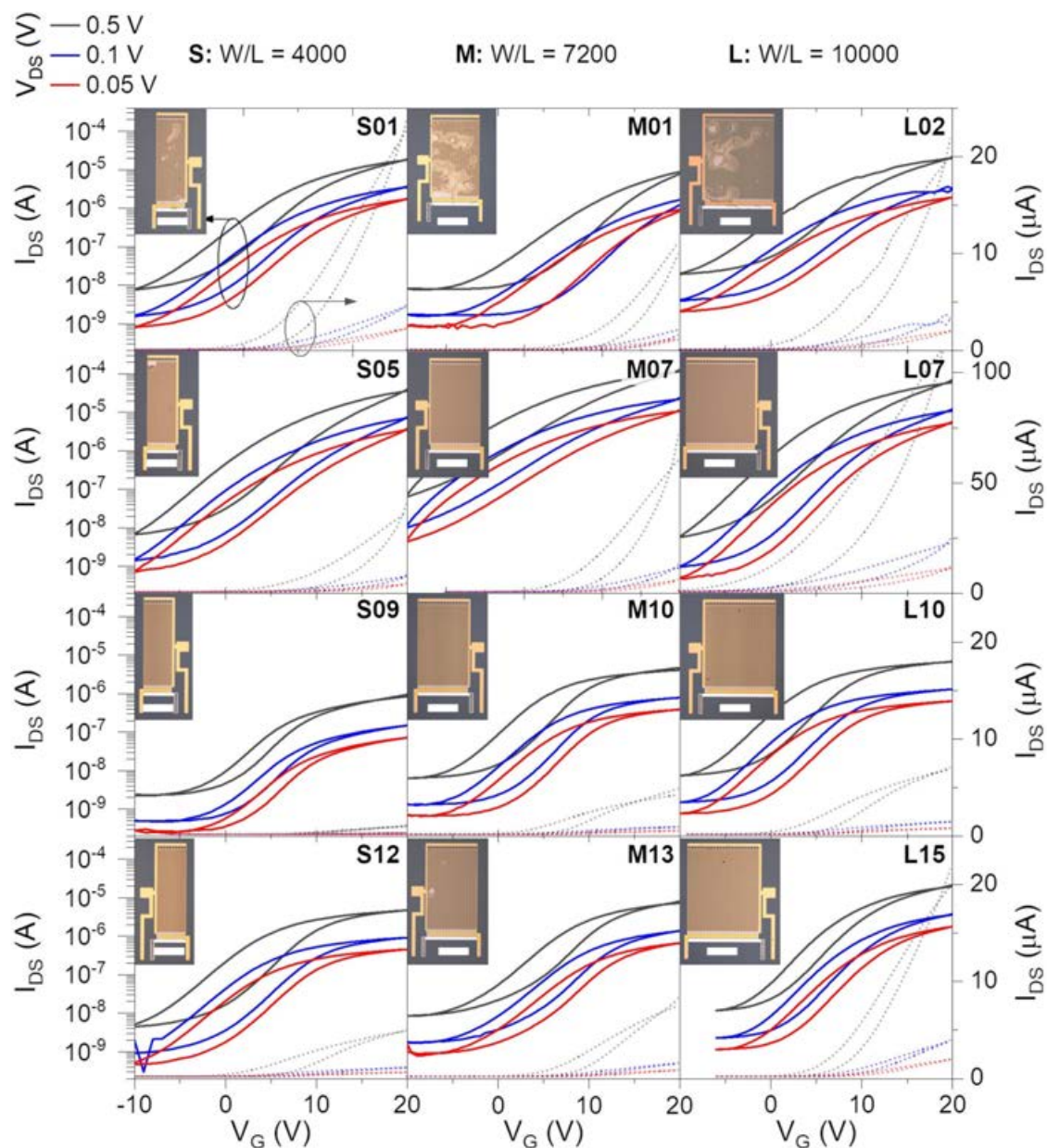
Figure D14 Testing of rigid AlO$_x$-encapsulated MoS$_2$-FETs devices. Transfer characteristics of 12 FET devices fabricated on the same chip with interdigitated source-drain contacts of different W/L-ratios: 4000 (S), 7200 (M), 10 000 (L). Transfer curves are shown for varied source-drain voltages V_{DS}, as indicated, and represented in both logarithmic scale (left, full lines) and linear scale (right, dashed lines). Microscopy images of each device are given as insets with 100 nm scale bar.
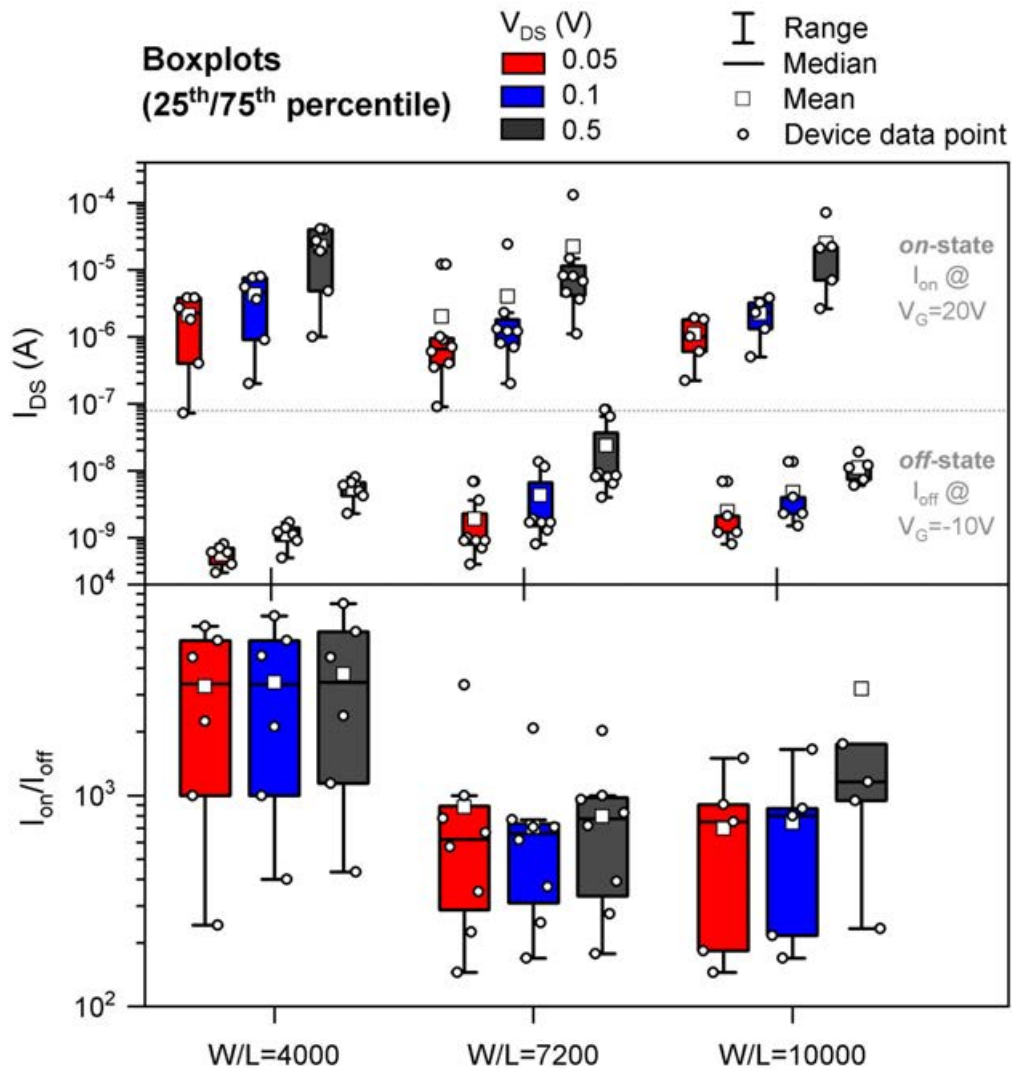
Figure D15 Rigid AlO$_x$-encapsulated MoS$_2$-FET on/off current statistics of devices shown in Fig. D14. 25th/75th percentile boxplots for 6 small size ($W/L = 4000$) , 8 medium size ($W/L = 7200$), and 5 large size ($W/L = 10000$) interdigitated FETs fabricated on the same chip. The top graph shows I_{on} and I_{off} currents extracted from the transfer curves at $V_G = 20$ V (*on*-state) and $V_G = -10$ V (*off*-state), respectively, and the bottom shows corresponding I_{on}/I_{on} ratio. No clear trend of increasing I_{on}-current with W/L can be observed. Possibly, the larger device areas for increased W/L result in higher probability of fabrication-related channel defects, which degrades the intended current output enhancement. Devices with $W/L = 4000$ and smallest area footprint show the highest I_{on}/I_{on}-ratios beyond 10^3.
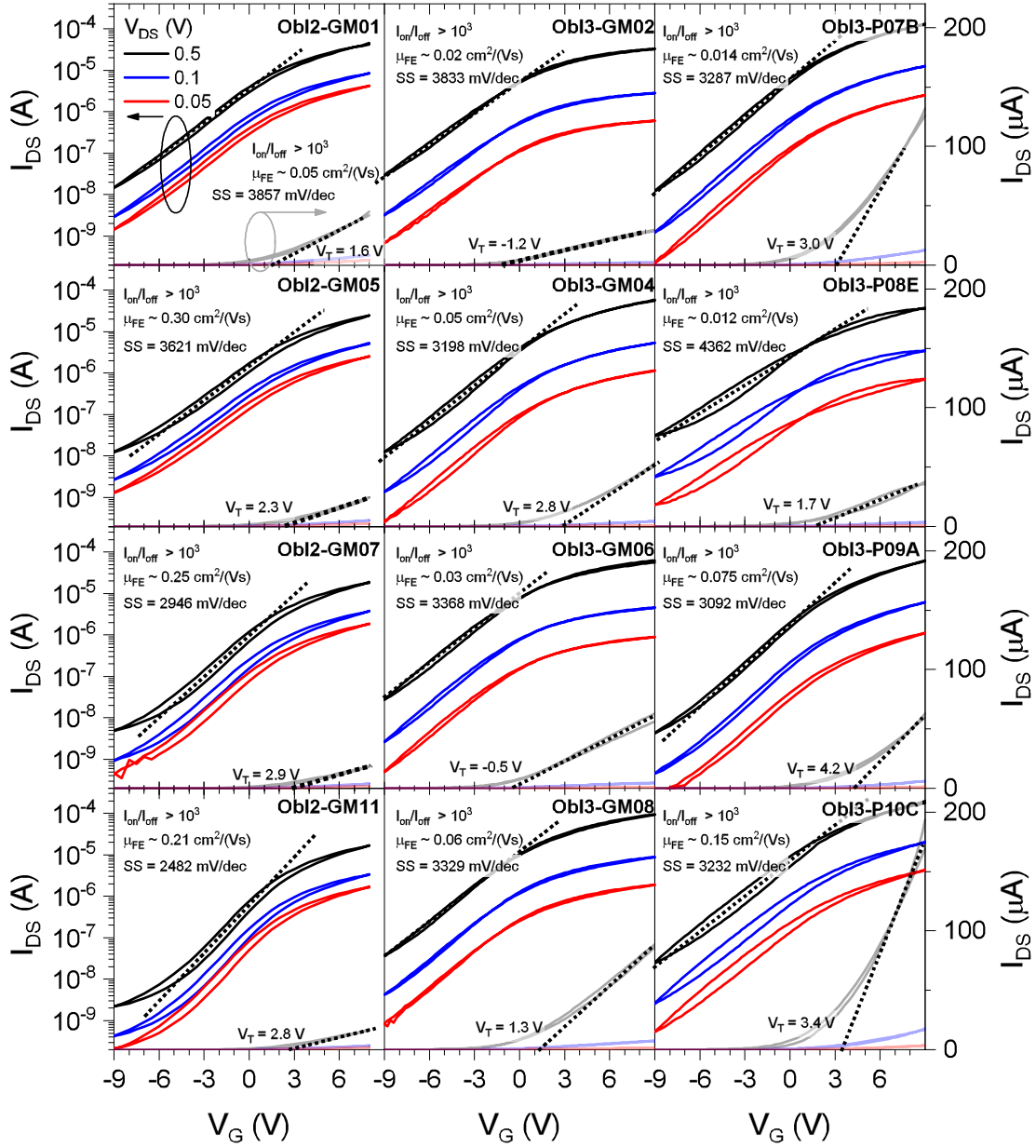
Figure D16 Flexible AlO$_x$-encapsulated MoS$_2$-FETs device testing. Transfer characteristics of 12 FET devices fabricated on two different wafers (Obl-2, Obl-3) on polyimide with interdigitated source-drain contacts ($W/L = 3000$). Transfer curves are shown for varied source-drain voltages V_{DS}, as indicated, and represented in both logarithmic scale (left, full lines) and linear scale (right, extenuated lines).
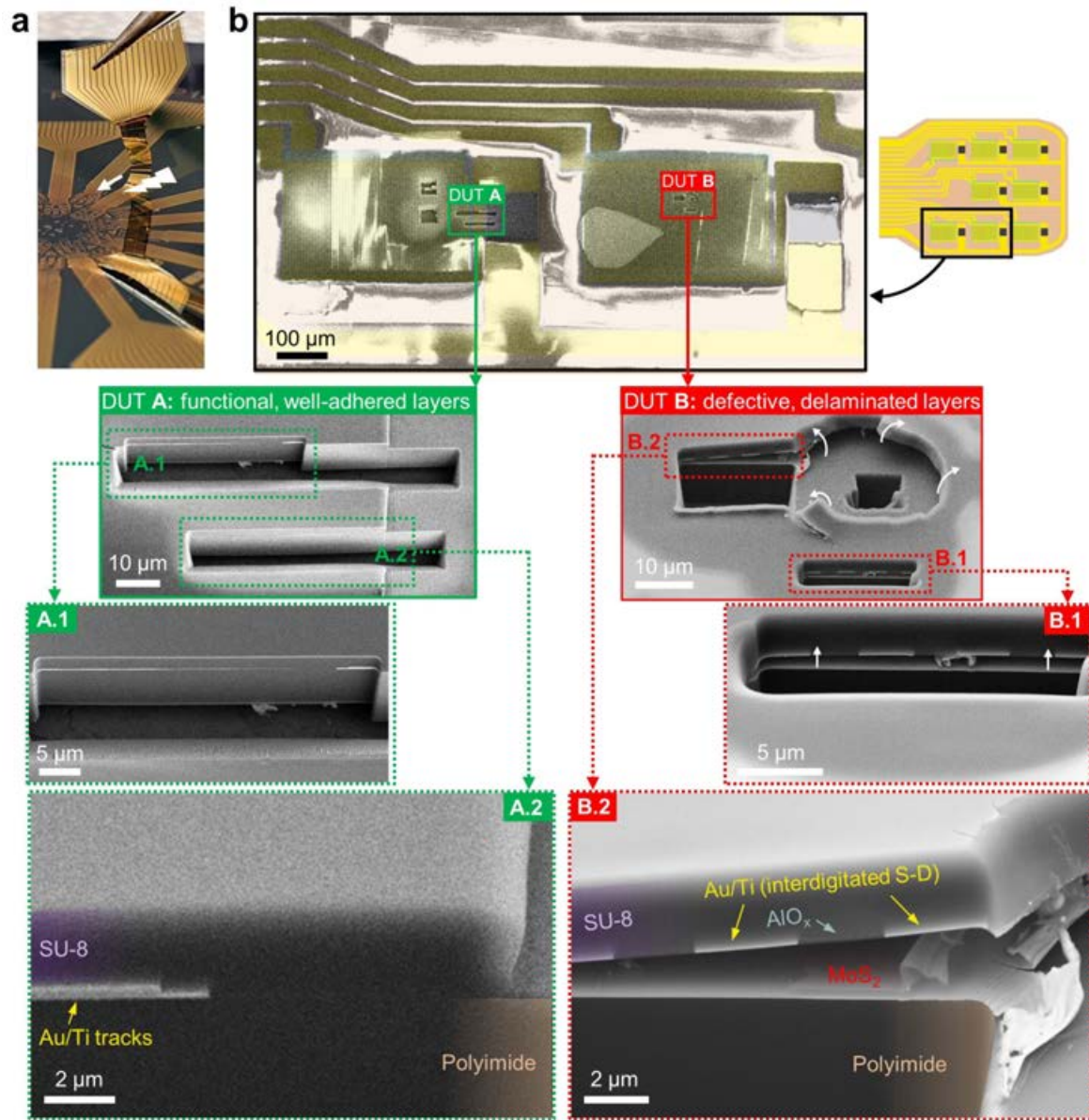
Figure D17 FIB cross-section failure analysis of flexible ECoG probes. **(a)** Photograph of flexible probe during peeling from carrier wafer. The process induces bending stress/strain and might be a reason for device degradation/failure. **(b)** FIB cross-sections cut into the devices under test (DUTs) were analyzed by SEM imaging. These devices were tested after peel-off and after electrical "dry"-testing of the MoS₂-FETs in air. In the electrical testing DUT A and DUT B had been previously identified as functional and defective, respectively. The layer delamination observed in DUT B explains the electrical non-functionality.

Table D6 Challenges, assessment and mitigation strategies for technology improvements of flexible MoS$_2$-FET/Gr-SGFET devices.

Challenges	Assessment methods	Mitigation strategies
Fabrication issues / device yield (currently $\sim 70\%$ with $\sim 55\%$ "useful" devices) limited by critical steps:	Microscopic/electrical inspection, device statistics	Optimization of critical fabrication steps:
MoS$_2$ transfer: sheet cracking, adhesion issues during TRT removal, variation due to manual process in ambient, stress concentration due to particles		Tune temperature/time during TRT removal [191, 291], avoid shear/instabilities for damage-free transfer [54], automatized transfer in vacuum [467], avoid transfer by direct MOCVD MoS$_2$ growth at polymer-compatible temperatures [459, 237], focus on alternative methods, reconsider wet transfer for research scale fabrication
MoS$_2$ S-D top-contacts photolithography developing step (developer intercalates underneath MoS$_2$		Careful, minimal wafer movements during developing, water-free photolithography process [471]
Metal lift-off of finely interdigitated S-D structures difficult without sonication		Highly interdigitated structure not required anymore once MoS$_2$ performace is sufficient, alternative device structure by MoS$_2$ transfer onto bottom-contacts avoiding photolithography and metal-lift-off on top of MoS$_2$
Shorting of metal tracks due to metal particle redeposition during lift-off		Optimize lift-off step
PI delamination/bubble formation during wafer processing		Optimize PI-wafer adhesion by surface treatment or PI adhesion promotor, e.g. HD Microsystems VM651/VM652, innovate device architecture/fabrication order, "polyimide-last" [56, 579]
Incomplete MoS$_2$ etch by O$_2$-RIE, MoO$_3$ residues	XPS, etching study	Development of fluorine-based/assisted etch process (SF$_6$, CF$_4$, CHF$_3$) [665, 666, 667]
MoS$_2$-FET performance		
on/off-ratios	Electrical characterization [286, 283]	
Subthreshold slope SS	IV-transfer curve	Reduce interface trap density D_{IT}
		Improve MoS$_2$ channel quality (reduce 1D, 2D, 3D defects/impurities), e.g. epitaxial MoS$_2$ [282, 248]
Mobility μ_{FE}	IV-transfer curve	Improve AlO$_x$/MoS$_2$ interface quality, especially top-encapsulation
	Spectroscopy (Raman, PL, XPS), see section 5.2.2	Optimize (oxide) encapsulation, see section 5.3:
		Increase gate capacitance by sub-10 nm, pin-hole-free oxide encapsulation [569, 500], pre/post-encapsulation annealing steps [493], MoS$_2$ encapsulation by polymer instead of oxide [668], dangling-bond free buffer layers, e.g. hBN [516], decrease fabrication-induced residues [341, 601, 669], controlled process environment [57]
Contact resistance R_C	Transfer length method (TLM)	Schottky barrier reduction, contact engineering, avoid reactive metals like Ti, use better suited contact materials: (Au [493, 480], In [67, 670], Bi [69]), non-damaging contact deposition [68], tunnel- or edge contacting schemes [658]
	Y-function method	
	4 point probe (4PP)	

|		
		Transfer onto (functionalized) bottom-contacts to avoid metal deposition damage and photolithography on top of MoS2 [671]
Device failure		
Common failure modes in packaged, flex devices [38, 588], including:	Failure mode assessment [604]	Minimize stress/strain by maintaining active device zone (MoS2/Gr-FETs) in neutral axis of flexible device [38], adapt layer thicknesses accordingly
1) Delamination at various interfaces: Delamination of few layer MoS$_2$ (low adhesion vdW interfaces) [46], AlO$_x$/MoS$_2$ (elastic mismatch), AlO$_x$/PI, AlO$_x$/SU-8, PI/SU-8, PI/PI (low adhesion)	Cross-sectional microscopies (FIB, SEM, TEM), see Fig. D17	Reduce fabrication-induced stress (steps involving thermal annealing etc.) [604], adapt elastic moduli of surrounding materials, e.g. 2D dielectrics or organic dielectric materials, plasma treatments/annealing steps to improve interlayer adhesion, standardize probe peel-off from carrier wafer avoiding excessive strain/too small bending radii [603]
2) Layer slipping, buckling [38]		Use monolayer MoS$_2$ instead of multilayer, layer number trade-off [38]
3) Layer cracking, e.g. materials with lowest fracture strain, such as AlO$_x$ oxide dielectric/encapsulation [591]	Localize breakage by probe dissection	Use materials with higher strain limits (hBN), improve strain limits by reducing grain boundary defects in MoS$_2$ [91], increase interfacial toughness by polymer engineering [622]
Fatigue under repeated bending	Cyclic bending tests with controlled bending radii [588, 38, 41, 590, 591, 603]	Ensure durability by probe layout engineering, geometrical design, guided crack propagation [672, 589, 92]
Hermeticity / ECoG device stability in liquid environment		Engineering of probe design/hermetic packaging:
polymer water uptake/interface soaking, passivation pin-holes	Permeability test by water vapor transmission rate [673, 674], accelerated aging tests *in vitro* [675]	Alternatives for polymer support/encapsulation, e.g. fused liquid crystal polymer (LCP) instead of PI/SU-8 [602, 587]
Current leakage from powered metal tracks in contact with penetrating liquid	Aging tests with/without track bias	Hermetic, biostable ALD AlO$_x$ barrier layers avoiding water/gas uptake/transmission [676, 673, 677, 675]: SiN, SiC or SiO$_2$ barrier and adhesion layers [598, 678, 679, 680] (AlO$_x$-)encapsulation of powered tracks Low-power MoS$_2$ switch, reduce gate track bias (below 1.2 V water window)
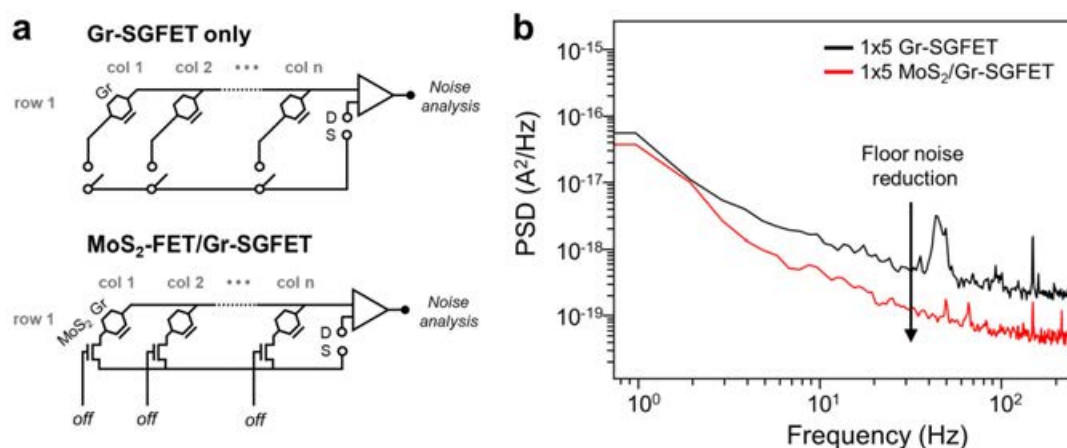
Figure D18 Floor noise benchmarking for time-division multiplexing with external and integrated switches. **(a)** Schematic circuits of a row of n columns of externally switched Gr-SGFET sensors (top) and on-site switched MoS$_2$-FET/Gr-SGFETs sensors (bottom). **(b)** Frequency-dependent power spectral density (PSD) of de-multiplexed channels of an externally switched 1×5 Gr-SGFET-only array and on-site switched 1×5 MoS$_2$/Gr-SGFET array. The on-site switched array shows reduced floor noise thanks to noise cancellation by the high-impedance, integrated MoS$_2$ elements [605].